*Crystallography Reports, Vol. 45, No. 2, 2000, pp. 169–171. Translated from Kristallografiya, Vol. 45, No. 2, 2000, pp. 199–201.*


## DIFFRACTION AND SCATTERING OF X-RAY AND SYNCHROTRON RADIATION

# Specific Features of Diffraction Patterns from Weakly Absorbing Objects Recorded by the "Refection" Method

**A. V. Kurdyumov**

*Frantsevich Institute of Problems of Materials Science, National Academy of Sciences of Ukraine, ul. Krzhizhanovskogo 3, Kiev, 252680 Ukraine*

Received December 15, 1997; in final form, June 16, 1998

**Abstract**—Some practical recommendations for phase analysis and precision determination of the lattice parameters of weakly absorbing objects studied by X-ray "reflection" method have been given. A method is suggested for taking into account the displacements of the diffraction intensity maxima caused by penetration of X-rays into the sample depth. *© 2000 MAIK "Nauka/Interperiodica".*

"Reflection method" is one of the most widely used procedures for recording X-ray diffraction patterns from flat weakly absorbing objects. Among such objects, there are a broad class of materials consisting of light chemical elements and their compounds and also samples of other materials whose thickness is less than the effective penetration depth of X-rays.

The diffraction lines from weakly absorbing objects are asymmetric and can be considerably displaced from their true positions, whereas their intensities are essentially dependent on glancing angle and sample thickness. However, the above-indicated effects are often ignored in the analysis of diffraction patterns, which results in considerable errors in the determination of the phase composition and the structure of weakly absorbing materials.

The aim of the present study is to draw attention of all those engaged in studying structures of weakly absorbing objects to the necessity of taking into account the above indicated specific features in the analysis of the X-ray scattering intensities, the quantitative phase analysis, and the determination of the lattice parameters. We also give some practical recommendations and suggest a method for taking into account line displacements, which can be used in the measurements of the intensity maxima and determination of the centers of gravity of the lines.

## INTENSITIES OF DIFFRACTION LINES

As is well known, the intensity of the *hkl* line on a powder diffraction pattern from a one-phase sample is determined by the expression

$$I_{hkl} = KQ_{hkl}AV, \quad (1)$$

where $K$ is the factor including the intensity of the primary beam and the constants associated with the specific features of X-ray scattering, $Q_{hkl}$ is the reflectivity of the ($hkl$) planes, $A$ is the absorption factor for X-rays in the sample, and $V$ is the irradiated volume of the sample with the subtraction of the pores. The product $AV = \alpha$ is the sample volume really participating in the formation of the diffraction pattern. In the "reflection" method, a primary beam is incident onto a flat sample at an angle $\theta$ [1, 2] entering the expression:

$$\alpha = \frac{[1 - \exp(-2\mu h/\sin\theta)]S}{2\mu}, \quad (2)$$

where $S$ is the area of the primary-beam cross section, $\mu$ is the linear absorption coefficient, and $h$ is the sample thickness. If the product $2\mu h$ has a sufficiently high value [$\exp(-2\mu h/\sin\theta) \approx 0$], equation (2) is reduced to the well known expression $\alpha = \frac{1}{2}\mu$ (with due regard for the fact that $S$ = const).

At the same time, the exponent in (2) for a weakly absorbing substance can differ from zero. Then, one has necessarily to take into account the dependence of the absorption factor on sample thickness and reflection angle on order to avoid considerable errors in the line intensities. These errors can be essentially pronounced for powder samples whose densities $\rho'$ are considerably lower than their theoretical values $\rho$. Thus, in accordance with (2), the intensities of high-angle reflections ($\theta > 60°$) on powder diffraction patterns from samples with density $\rho' = 0.2\rho$ and thickness 0.5 mm obtained using the Cu$K_\alpha$ radiation are considerably distorted: the intensities lines at $\theta > 60°$ on diffraction pattern from beryllium, graphite, and diamond are lower by factors of 20, 3.5, and 3 in comparison with those lines on the diffraction patterns from pore-free samples of the same materials. It should also be noted that the dependence of $\alpha$ on $h$ and $\theta$ is even more pronounced for the transmission diffraction patterns (this problem is considered in detail elsewhere [3]). Thus, the line intensities given for weakly absorbing materials without the indication of the sample characteristics ($\rho'$, $h$), the radiation wave-

1063-7745/00/4502-0169$20.00 © 2000 MAIK "Nauka/Interperiodica"

length, and the geometry of the diffraction experiment cannot be used for any quantitative estimates.

## PHASE ANALYSIS

The intensity of the *hkl* line of the *i*th phase in the *n*-phase sample is proportional to its volume content, $V_i$. Substituting the volume fractions by the weight ones, $m_i$ ($V_i = \rho m_i/\rho_i$), and using the relationships $V = \rho' V'/\rho$ and $\mu = \rho \sum_{i=1}^{n} m_i \mu_i^*$, where $\mu^*$ is the coefficient of mass absorption, we obtain from (1) and (2)

$$I_{i(hkl)} = kQ_{i(hkl)} \frac{1 - \exp\left(-2\rho' n \sum_{i=1}^{n} m_i \mu_i^* / \sin\theta\right)}{\rho_i \sum_{i=1}^{n} m_i \mu_i^*} m_i, \quad (3)$$

where $k = SK/2$. It should be emphasized that the exponent includes the real density ($\rho'$) of the *n*-phase sample, whereas the denominator includes the theoretical density of the *i*th phase ($\rho_i$). For polymorphous modifications of the substance, we have $\sum_{i=1}^{n} m_i \mu_i^* = \mu^*$. Then

$$I_{i(hkl)} = kQ^*_{i(hkl)} \sigma m_i, \quad (4)$$

where $Q^*_{i(hkl)} = Q_{i(hkl)}/\mu_i$ is the quantity characterizing only the *i*th phase, and $\sigma = 1 - \exp(-2\mu^*\rho' h/\sin\theta)$ is the correction that should necessarily be taken into account in the analysis of a diffraction pattern from the weakly absorbing *n*-phase sample.

If the values of $Q^*_{i(hkl)}$ are calculated in the same units, they can be used for the quantitative phase analysis using the intensity ratios for various phases on one X-ray diffraction pattern (the so-called standard-free method). Let us estimate the error caused by the neglect of the weak-absorption factor $\sigma$ in the phase analysis of the mixture of three polymorphous modifications of boron nitride—a graphite-like ($BN_{gr}$), wurtzite-like ($BN_w$), and sphalerite-like ($BN_{sp}$) phases. We use the $Q_{i(hkl)}$ values for these phases calculated in [4]. For simplicity, we assume that the amounts of all three modifications in the mixture are the same. We also assume that the sample thickness is small ($h = 0.02$ cm), $\rho' = 0.2\rho$, and that the reflection diffraction pattern is obtained using the Cu$K_\alpha$ radiation. It should be remembered that the lines due to the $BN_{sp}$ phase and the lines due to the $BN_{gr}$ or $BN_w$ phase are superimposed ($111_{sp}$–$0.002_w$, $200_{sp}$–$102_w$, $220_{sp}$–$110_w$, etc.) [4]. Analyzing the "mixed" (superimposed) $220_{sp}$–$110_w$ line and the pure $002_{gr}$ and $101_w$ lines, we can calculate their expected intensities for such a sample by formula (4). Then, assuming that $\sigma = 1$ and using the intensities determined, we obtain $m_{gr} = 0.30$, $m_w = 0.45$, and $m_{sp} = 0.25$ instead of $m_{gr} = m_w = m_{sp} = 1/3$.

Another method of the quantitative phase analysis is based on the comparison of the intensity of the *hkl* reflection due to the *i*th phase on the diffraction pattern from the *n*-phase sample with the intensity of the one-phase standard. It follows from (4) that

$$X = \frac{[I_{i(hkl)}]_{sample}}{[I_{i(hkl)}]_{st}} = \frac{[\sigma_{i(hkl)}]_{sample}}{[\sigma_{i(hkl)}]_{st}} m_i \quad (5)$$

under the condition that $k$ = const. In the analysis of a weakly absorbing object, it is important either to take into account $\sigma$ or to fulfill the condition $\sigma$ = const at which $X = m_i$.

A modification of the method of standard is the procedure in which a sample is added a certain amount of the *i*th phase [5]. For a weakly absorbing object, it is necessary that the addition of the amount $t$ of the *i*th phase would not change the total mass of the sample (the preliminary removal from the sample of the mass $\Delta M = t$). Then it can readily be shown that

$$m_i = \frac{xt}{M - xM - xt}, \quad (6)$$

where $x$ is the intensity ratio of the *hkl* lines of the *i*th phase prior to and upon the addition of the *i*th phase.

## DETERMINATION OF THE LATTICE PARAMETER

Since X-rays penetrate the sample depth, the diffraction lines on the reflection diffraction pattern are displaced toward small angles, whereas their profile is asymmetric. In order to determine the displacement of the center of gravity of the line, we obtained the analytical dependences $\Delta 2\theta(\theta, h)$ and the functions providing the angular extrapolations to $\theta = 90°$ [1]. To measure the intensity maxima ($2\theta_m$), it is expedient to use the extrapolation methods and to choose the corresponding function empirically, because the analytical expressions are too complicated for the practical use. Thus, the lattice parameters of polymorphous BN modifications were determined by extrapolating $a_{obs}(1/\theta)$; the dependences obtained were linear in the whole angular range of $\theta$ angles (20°–70°) [6].

With a decrease of the sample thickness, the weak absorption-induced displacement of the line tends to zero. Therefore, one can determine the lattice parameters of the weakly absorbing objects by extrapolating $a_{obs}(h)$ to $h = 0$. We studied this dependence on the sphalerite modification of boron nitride ($BN_{sp}$) and the natural graphite of the trade mark C-1. The point-to-point photographing (at a step of 0.02°) was performed on a HZG-diffractometer ($\lambda_{\alpha 1} = 1.540593$ Å [7]). The $\alpha_1$ component was determined by the Renninger method. The sample thicknesses varied from 0.1 to

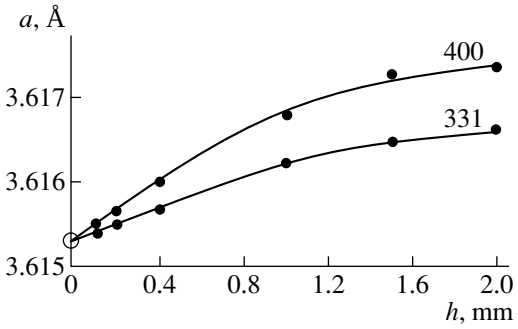


Lattice parameter of $BN_{sp}$ determined from the intensity maxima of the 400 and 331 lines as a function of sample thickness $h$.

2 mm, $\rho' = 0.2\rho$. The statistical measurement error $2\theta_m$ did not exceed ±0.02°.

The dependences of $a_{obs}(h)$ for $BN_{sp}$ determined from the 400 and 331 lines are shown in figure. Both curves converge at one point at $h = 0$ corresponding to the value $a = 3.6153 \pm 0.0001$ Å, which agrees quite well with the data of the angular extrapolation [6]. At small $h$, both dependences are satisfactorily approximated by straight lines. A similar behavior was also observed for graphite. The $a$ parameter equals $2.4613 \pm 0.0001$ Å.

It should also be noted that the angular extrapolation can be made only if the large-angle lines are rather strong and sharp. If it is not so, one has either to construct the dependences $a_{obs}(h)$ or to obtain the diffraction pattern with a standard. If one uses an external standard, the latter can be chosen in such a way that the products $\mu h$ for the sample and the standard should be equal.

## ACKNOWLEDGMENTS

The author is grateful to V.B. Zelyavskiĭ for his participation in X-ray diffraction measurements.

## REFERENCES

1. D. M. Kheiker and A. S. Zevin, *X-ray Diffractometry* (Gos. Izd. Fiz.-Mat. Lit., Moscow, 1963).
2. A. A. Rusakov, *X-ray Diffraction Study of Metals* (Atomizdat, Moscow, 1977).
3. A. Taylor, *Crystallographic Data on Metal and Alloy Structures* (Dover, New York, 1963; Metallurgiya, Moscow, 1965).
4. A. V. Kurdyumov, V. G. Malogolovets, N. V. Novikov, *et al.*, *Handbook of Polymorphous Modifications of Carbon and Boron Nitride* (Metallurgiya, Moscow, 1994).
5. G. W. Brindley, *The X-ray Identification and Crystal Structures of Clay Minerals* (Mineralogical Society, Clay Minerals Group, London, 1961; Mir, Moscow, 1965).
6. A. V. Kurdyumov, V. L. Solozhenko, and W. B. Zelyavskiĭ, J. Appl. Crystallogr. **28**, 540 (1995).
7. J. Hartwig, S. Grosswig, P. Becker, and D. Windisch, Phys. Status Solidi A **125**, 79 (1991).

*Translated by L. Man*

*Crystallography Reports, Vol. 45, No. 2, 2000, pp. 172–181. Translated from Kristallografiya, Vol. 45, No. 2, 2000, pp. 202–212.*


**THEORY OF CRYSTAL STRUCTURES**

# Search for Possible Structures of Cubic Approximants of Icosahedral Quasicrystals

**A. A. Gorokhovskiĭ**

*Shubnikov Institute of Crystallography, Russian Academy of Sciences, Leninskiĭ pr. 59, Moscow, 117333 Russia*

Received March 20, 1997; in final form, March 12, 1998

**Abstract**—Admissible structures of the approximants are obtained within the model of the dodecahedral local order (DLO) with due regard for the constraints imposed by the space symmetry. It is shown that the number of cubic approximants of icosahedral quasicrystals having a certain order and dodecahedral local order is finite and that the number of positions that can be occupied by the atoms from the unit cells of an approximant of each order is also finite. The corresponding estimates from above are made. In particular, it is shown that there exists only one structure for the 1/–1 approximant. It is also shown that it is possible to determine all the structures for any approximant of any order. The corresponding algorithm of the exhaustive search for these structures is suggested. The implementation of this algorithm provided the determination of all the structures of the 0/1 approximants and also some possible structures of the 0/1 and 1/1 approximants. The tables of possible approximant structures can be useful in the studies of new phases having approximant structures. © *2000 MAIK "Nauka/Interperiodica".*

## INTRODUCTION

An important characteristic of quasicrystals distinguishing them from conventional crystals is the simultaneous existence of the long-range order, nonperiodicity, and noncrystallographic symmetry. Thus, there exist some experimentally detected and theoretically described structures with the five- [1, 2], eight- [3], 10- [4], and twelvefold [5] axes inconsistent with the crystallographic symmetry, according to which all the crystals are characterized by three-dimensional translational invariance and, as a result, can have only two-, three-, four-, and sixfold axes. The parameters of new phases distinguish them from crystals, twinned crystals, and commensurate phases, and, thus, are related to a separate class of quasicrystals, which can have elements of both classical symmetry and quasisymmetry. The quasisymmetry has it that to any infinitely large fragment of an infinite transformed structure, there should correspond another congruent part of the same structure [6].

It is also assumed that a three-dimensional structure is the projection of a structure from a space of higher dimension (this statement is merely an assumption and, thus, is not the unique one). Thus, one-dimensional quasicrystals can be described using the two-dimensional space, two-dimensional quasicrystals can be described using the four- and five-dimensional spaces, and icosahedral crystals can be described using the six-dimensional space. In the latter cases, the axial quasisymmetry of the *n*th order can be related to the conventional *n*-fold symmetry axis in the space of a higher dimension.

Quasicrystals do not form an independent class of structures—there also exist strictly periodic structures called approximants. Each approximant possessing the cubic symmetry (a cubic approximant) can be assigned a natural number or order. A sequence of structures with the order parameter increasing from unity to an infinite number are characterized by infinitely increasing lattice parameters and, in the limit, should form a quasicrystalline structure. It is clear, that beginning with a certain number of the approximant sequence, all the following approximants become experimentally indistinguishable from quasicrystals. Therefore, the approximant-based approach is of no less importance than the approach of the *n*-dimensional crystallography. Moreover, the further study of approximants is also stimulated by the opinion (although not widespread one) that no real quasicrystals can exist at all. The structures considered to be quasicrystals are, in fact, the approximants of very high orders. Even if it were possible to prove that atoms in a certain sample of a hypothetical quasicrystal are ordered in an absolutely nonperiodic way, the finite dimensions of the sample would not have allowed to prove that such structure is a fragment of an approximant with the unit cell dimensions exceeding the dimensions of the experimental sample.

In analogy with three-dimensional quasicrystals, one can model the approximant structures in a six-dimensional space. In this approach, one assumes that there is a periodic lattice in an abstract six-dimensional space that can be projected into the physical three-dimensional space (the so-called projection method). Only those lattice points are projected which lie in the

1063-7745/00/4502-0172$20.00 

"tube" of the six-dimensional space, a region infinite along three linearly independent directions (the so-called parallel space) and finite along three other dimensions (the perpendicular space). If the tangents of the angle of tube inclination with respect to the directions of the six-dimensional lattice are rational numbers, then we arrive at a periodic structure in the physical space; if they are irrational, we arrive at the quasiperiodic structure in the physical space. Since any irrational number can be represented as a limit of an infinite sequence of the ratios of rational numbers, then, in a certain sense, the quasicrystal structures can be considered as the limit of the periodic sequences, i.e., the approximants. A modification of the projection method is the cut method, in which all the sites of the six-dimensional lattice are assumed to be decorated with non-point objects (e.g., atomic surfaces), which intersect the physical space and yield the points forming the real structure. However, such a description of quasicrystals and approximants has an essential shortcoming—insufficiently justified assumption about the physical nature of the six-dimensional space, and, moreover, of the multidimensional atomic surfaces representing the points in our three-dimensional world.

Some attempts were made to use purely three-dimensional models of quasicrystals and approximants, in which the space is filled with unit cells (building blocks of a certain type such as, e.g., Ammann rhombohedra) which fill the space periodically or quasiperiodically without leaving any empty spaces. The major disadvantage of such models is the necessity of decorating these cells with atoms, i.e., the necessity of constructing a real atomic structure from the abstract cellular one. Another possibility to describe quasicrystals in three-dimensional space is the use of geometrically ordered atomic clusters, i.e., the Mackay icosahedra. However, in this case, one has to introduce the so-called "glue atoms" to fill the space between the clusters, which results in an unjustified "singling out" of some atoms from all the other ones.

With due regard for the above stated, the description of the quasicrystal structures with the aid of the dodecahedral local order has some obvious advantages. Thus, crystal is considered only in the three-dimensional space, all the atoms of such structure are equivalent, etc.

The present study is devoted to the theoretical consideration of the structures of cubic approximants of icosahedral quasicrystals, i.e., the structures periodic along three directions and described by one of the cubic space groups. In the limit of infinitely large periods, these approximants are transformed into quasicrystals with the icosahedral (quasi)symmetry. Below, we consider the possibility of the exhaustive theoretical search for all the admissible approximant structures for each term of the Fibonacci series in the model of the dodecahedral local order.

## 1. DODECAHEDRAL LOCAL ORDER AND FIBONACCI SERIES

Below, we describe the approximants using the model of dodecahedral local order (DLO) quite justified for structure motifs observed in the simplest approximants having the FeSi- and CsCl-type structures [7]. This model proved to be very useful not only in the description of the structures of higher-order approximants but also in the prediction of new structures. A number of phases were discovered, which, being approximants of icosahedral quasicrystals, possess the dodecahedral local order [8]. This DLO-model was successfully applied to simulate growth of quasicrystals. The "computer-grown" quasicrystals have a clearly pronounced dodecahedral faceting [9, 10].

The essence of the dodecahedral local order (DLO) model reduces to the following. A special condition is imposed onto the arrangement of atoms: the nearest neighbors of each atom (i.e., the atoms from the first coordination sphere) should be located at the vertices of a dodecahedron circumscribed around this atom, although not all the dodecahedron vertices should necessarily be occupied [11]. The orientations and dimensions of dodecahedra circumscribed around different atoms should coincide. The orientations of the reference unit vectors in Fig. 1. are chosen in such a way that the directions of four threefold axes (of the total number of ten) should coincide with four threefold axes of the cubic lattice (we consider the cubic space groups). The distance from the center of a dodecahedron to its vertex is determined by the minimum possible interatomic distance. Since the length of the dodecahedron edge is less than the distance from its center to a vertex, only some of the dodecahedron vertices can be simultaneously occupied by the atoms. One can readily show that the maximum possible number of the nearest neighbors in a regular DLO packing equals eight. The ratio of the lattice period to the minimum possible interatomic distance in the approximants of the Fibonacci series increases as $\tau^n$ ($n$ is the approximant order):

$$a_n = 2r_{\min}\tau^{(n-1)}/\sqrt{3} = a_1\tau^{n-1} = a_1(F_{n-1}\tau + F_{n-2}),$$

where $\tau = 1.61803\ldots = (1 + \sqrt{5})/2$ is the golden mean; $r_{\min}$ is the minimum possible interatomic distance; $F_n$ is the Fibonacci series of numbers ($F_1 = F_2 = 1$, $F_{n+2} = F_{n+1} + F_n$, and $n$ is an integer) possessing a remarkable property—the ratio of two neighboring terms converges to the golden mean $\tau$; $a_1 = 2r_{\min}/\sqrt{3}$ is the lattice parameter of the simplest approximant, CsCl, described below ($2/\sqrt{3}$ is the ratio of the cube side to the half of its principal diagonal).

The approximant with the ratio of the lattice parameter to the minimum interatomic distance equal to $a_n$ is the $n$th term of the Fibonacci series and is denoted as $F_{n-2}/F_{n-3}$ [12].

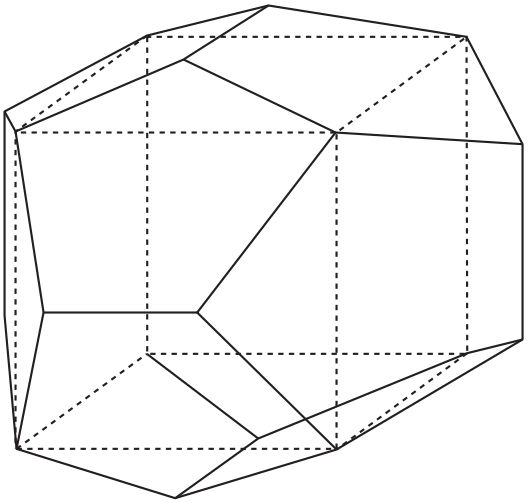

**Fig. 1.** A cube inscribed into a dodecahedron. It is seen that the mutual orientation of the cube and the dodecahedron provides the coincidence of some of their two- and threefold axes.

The simplest example of a DLO-approximant is the 1/–1 approximant ($n = 1$, $F_{-1} = -1$, $F_{-2} = 1$) with two atoms in the unit cell. Its structure is described by a unit cell of the CsCl-type: one atom in the cubic unit cell is located at the cube vertex, whereas the second one is located in its center. The approximant structure can also be illustrated by one of the following simplest approximants—a cubic FeSi crystal with the lattice parameter 4.6 Å, sp. gr. $P2_13$, with eight atoms per unit cell (the 0/1 approximant, $n = 2$). The Fe and Si atoms in this crystal occupy the special ($x$, $x$, $x$) positions with $x_{Si} = (\tau - 1)/4 \approx 0.155$ and for $x_{Fe} = (5 - \tau)/4 \approx 0.845$. Each atom in this structure is surrounded with seven other atoms occupying the dodecahedron vertices. Such a simple structure provides the formation of a system of Bragg reflections similar to that observed for icosahedral crystals. Such a "latent" icosahedral symmetry of a FeSi crystal affects its physical properties—all the elastic shear moduli of the crystal are almost equal.

## 2. ORIENTATION OF INTERATOMIC VECTORS WITH RESPECT TO THE SYMMETRY AXES

As is readily seen from Fig. 1, a dodecahedron can be circumscribed around a cube by two ways that differ by the rotation by an angle of $\pi/4$ about one of the coordinate axes. The dodecahedron orientation with respect to the symmetry elements (axes, planes, etc.) of the symmetry group (related to a cube as to a lattice cell) is of great importance, because it can indicate the existence of various structures for different dodecahedron orientations. Therefore, it is important to show that this ambiguity of the dodecahedron orientation can be avoided if one chooses appropriately the coordinate system by rotating the dodecahedron by an angle of $\pi/4$ around one of the coordinate axes.

In order to prove this statement without a possible "loss" of an entire class of possible approximant structures, we make use of the following fact: the geometry of the symmetry elements of the group $P2_13$ is such that, being rotated by $\pi/4$ around one of the coordinate axes with the simultaneous translation by a quarter of period along the [111] direction in the lattice, these elements are transformed into themselves. Let us assume that we have two classes of structures—those of type *A* and type *B*. By definition, the structures of these types differ by the orientation of the symmetry elements with respect to the reference dodecahedron, in full accordance with the above-stated. There are only two such orientations. Consider an arbitrary structure of type *A* and modify its coordinate system by rotating the initial coordinate system by $\pi/4$ around one of the coordinate axes and then displace the origin of the coordinate system by a quarter-period along the [111] direction. In this case, the orientation and the location of the symmetry elements in the new coordinate system are the same as in the initial one, whereas the orientation of the reference dodecahedron would change to the opposite one. In other words, we obtained the structure of type *B* from the structure of type *A*. Thus, the assignment of a structure to the *A* or the *B* type depends on the choice of the coordinate system; e.g., one can take that all the DLO structures are of type *A* or, in other words, in this case we can give the symmetrically equivalent description of these two structures.

Similar considerations can also be made for other cubic groups. In particular, in the group $P23$, no translation is needed to bring into coincidence the symmetry axes rotated by $\pi/4$ about one of the coordinate axes. Otherwise, the above consideration and the conclusion are the same.

## 3. MATHEMATICAL DESCRIPTION OF DODECAHEDRAL LOCAL ORDER

In order to describe the DLO in terms of mathematics, one has, first, to choose one atom and to write the coordinates of all the remaining atoms as the linear combination (with the integral coefficients) of twenty vectors directed from the center of the reference dodecahedron to its vertices. Since, of the total twenty vectors, only six are linearly independent on the ring of integers, the coordinates of each atoms (with respect to the first one) are conditionally called the relative coordinates and can be reduced to a linear combination with integral coefficients of six vectors. For example, these vectors can be chosen as is illustrated by Fig. 2:

$$\mathbf{e}_1 = \lambda_n(\tau^2, 0, 1),\ \mathbf{e}_4 = \lambda_n(-\tau^2, 0, 1),$$

$$\mathbf{e}_2 = \lambda_n(1, \tau^2, 0),\ \mathbf{e}_5 = \lambda_n(1, -\tau^2, 0),$$

$$\mathbf{e}_3 = \lambda_n(0, 1, \tau^2),\ \mathbf{e}_6 = \lambda_n(0, 1, -\tau^2),$$

where $\lambda_n$ is the scale factor. For the crystallographic normalization, where the lattice period is taken to be unity, $\lambda_n = \tau^{-n}/2$. We believe that the convenient normalization is that with $\lambda_n = 1$. In this case, the lattice period equals $2\tau^n$ (where $n$ is the ordinal number of the approximant). Then, in order to pass to the conventional normalization, one has to divide all the coordinates into the lattice constant, i.e., $2\tau^n$. Below, we use only the normalization with $\lambda_n = 1$.

Since each coordinate of the basic vectors has the form $m_1\tau + m_2$ (where $m_1$ and $m_2$ are integers), the relative coordinates of each atom (i.e., the coordinates with respect to any other atoms of the structure) have the same form. With due regard for this fact, one can show that the constraints imposed by the cubic space groups result in the fact that the atomic coordinates in the standard crystallographic Cartesian coordinate system (on a noncrystallographic scale, where the lattice parameter equals $2\tau^n$ and not unity) are the combinations of natural unity and the golden mean with half-integral coefficients. In other words, these coordinates can be represented in the form

$$(m_{1x}\tau + m_{2x})/2. \quad (3.1)$$

To prove this statement, consider the difference between any two (including equivalent) positions ("relative coordinates") in the form

$$\mathbf{x} - \mathbf{y} = n_1\mathbf{e}_1 + \ldots + n_6\mathbf{e}_6, \quad (3.2)$$

where $n_1, \ldots, n_6$ are integers. It should be noted that the right-hand side in (3.2) has the form

$$(m_{1x}\tau + m_{2x}, m_{1y}\tau + m_{2y}, m_{1z}\tau + m_{2z}), \quad (3.3)$$

where $m_{1x}$, $m_{2x}$, $m_{1y}$, $m_{2y}$, $m_{1z}$, and $m_{2z}$ are the integers.

The difference between two positions, $(x, y, z)$ and $(-x, y, z)$, transformed into one another by the rotation by an angle of $\pi$ around the $OX$-axis, equals $(2x, 0, 0)$. Equating this difference to (3.3), we obtain $x$ in the form $(m_1\tau + m_2)/2$. For two remaining coordinates, a similar consideration yields the identical result.

Thus, it is seen that the atoms in a DLO structure can occupy not arbitrary positions but only those ones which are set by expression (3.3), i.e., the positions forming a discrete set.

Expression (3.1) is the most general form of the atomic coordinates for all the space groups, although in highly symmetric groups some additional constraints can be imposed on $m_1$ and $m_2$, for example, it can be necessary that the numbers $m_1$ and $m_2$ be only even. Some additional constraints imposed on $m_1$ and $m_2$ in various cubic space groups (specific "selection rules") are listed in Table 1. These rules can be obtained in the following way: the difference between two arbitrary positions (including equivalent ones), i.e., the relative coordinates, should be written in the form

$$\mathbf{x} - A\mathbf{x} = n_1\mathbf{e}_1 + \ldots + n_6\mathbf{e}_6, \quad (3.4)$$

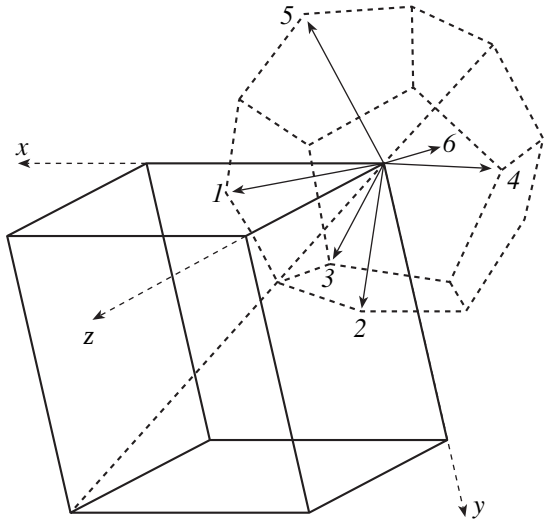


**Fig. 2.** Orientation of the basis vectors for the dodecahedral local order (*1*) $\mathbf{e}_1$, (*2*) $\mathbf{e}_2$, and (*6*) $\mathbf{e}_6$.

where $n_i$ are integers and $A$ is the symmetry operation transforming one position into another. Setting a certain position $(x, y, z)$ and a space group, and performing an exhaustive search for all the symmetry operations of this group, one arrives at the system of linear equations containing the atomic coordinates $x$, $y$, $z$ and a certain set of integers.

Upon some simplifications and substitutions, the thus written set of equations for each operation $A$ of the given space group can be reduced to the simplest one; it is also possible to determine the relationships between $n_j$: the $x$, $y$, and $z$ coordinates can be expressed in terms of $n_j$. Thus, one arrives at the expressions for $z$ equivalent to the selection rules listed in Table 1.

Since a translation is also a symmetry element, and some symmetry elements of cubic groups (i.e., screw axes and glide planes) include the lattice constant as a parameter, the solution of system (3.4) also yields the selection rules for lattice constant also indicated in Table 1.

Thus, for the simplest approximant, CsCl, whose sp. gr. $Pm3m$ is the supragroup of $Pm3$, the selection rules are determined to be the same as for $Pm3$.

## 4. SIMPLIFICATION OF SYSTEM OF EQUATIONS

Although system of equations (3.4) is infinite and the numbers of symmetry elements in the space group (with due regard for translations) and the set of variables are infinite as well, the system can readily be simplified, because the number of independent equations does not exceed the number of the group generators. Therefore, in order to simplify this system, it is sufficient to consider only the equations derived from (3.4)

**Table 1.** General form of DLO-positions for cubic groups

| Sp. gr. | General form of position $(x, y, z)$ | Constraints | Admissible lattice constant |
|---|---|---|---|
| $P23$ ($T^1$) | $(p_1 + p_2\tau, p_3 + p_4\tau, p_5 + p_6\tau)$ | | $2m_1 + 2m_2\tau$ |
| $F23$ ($T^2$) | $(p_1 + p_2\tau, p_3 + p_4\tau, p_5 + p_6\tau)$ | | $4m_1 + 4m_2\tau$ |
| $I23$ ($T^3$) | $(p_1 + p_2\tau, p_3 + p_4\tau, p_5 + p_6\tau)$ | | $4m_1 + 2m_2\tau$ |
| $P2_13$ ($T^4$) | $(p_1 + p_2\tau, p_3 + p_4\tau, p_5 + p_6\tau)/2$ | $p_4 - p_6 = 2l_1\ p_4 - p_2 = 2l_2$ | $2m_1 + 2m_2\tau$ |
| | | $p_1 - p_5 = 2l_1 + 4l_5$ | parity of $m_1$ as for $p_2$: |
| | | $p_3 - p_5 = 2l_2 + 4l_4$ | parity of $m_2$ as for $p_1 - p_2$ |
| $I2_13$ ($T^5$) | $(p_1 + p_2\tau, p_3 + p_4\tau, p_5 + p_6\tau)/2$ | $p_4 - p_6 = 2l_1\ p_4 - p_2 = 2l_2$ | $4m_1 + 2m_2\tau$, $p_2$ is even; |
| | | $p_1 - p_5 = 2l_1 + 4l_5$ | parity of $m_2$ as for $p_1 - p_2$ |
| | | $p_3 - p_5 = 2l_2 + 4l_4$ | |
| $Pm3$ ($T_h^1$) | $(p_1 + p_2\tau, p_3 + p_4\tau, p_5 + p_6\tau)$ | | $2m_1 + 2m_2\tau$ |
| $Pn3$ ($T_h^2$) | $(p_1 + p_2\tau, p_3 + p_4\tau, p_5 + p_6\tau)$ | | $4m_1 + 2m_2\tau$ |
| $Fm3$ ($T_h^3$) | $(p_1 + p_2\tau, p_3 + p_4\tau, p_5 + p_6\tau)$ | | $4m_1 + 4m_2\tau$ |
| $Fd3$ ($T_h^4$) | $(p_1 + p_2\tau, p_3 + p_4\tau, p_5 + p_6\tau)$ | | $8m_1 + 4m_2\tau$ |
| $Im3$ ($T_h^5$) | $(p_1 + p_2\tau, p_3 + p_4\tau, p_5 + p_6\tau)$ | | $4m_1 + 2m_2\tau$ |
| $Pa3$ ($T_h^6$) | $(p_1 + p_2\tau, p_3 + p_4\tau, p_5 + p_6\tau)/2$ | $p_4 - p_6 = 2l_1\ p_4 - p_2 = 2l_2$ | $2m_1 + 2m_2\tau$ |
| | | $p_1 - p_5 = 2l_1 + 4l_5$ | parity of $m_1$ as for $p_2$: |
| | | $p_3 - p_5 = 2l_2 + 4l_4\ p_1 = 2k$ | parity of $m_2$ as for $p_1 - p_2$ |
| $Ia3$ ($T_h^7$) | $(p_1 + p_2\tau, p_3 + p_4\tau, p_5 + p_6\tau)$ | | $4m_1 + 4m_2\tau$ |

Note: Table 1 shows the general form and the additional constraints on the form of the admissible positions in the DLO structures. The data are given only for twelve cubic groups; in order to determine the necessary constraints for cubic groups not listed in Table 1, one can use the constraints indicated in this table for the corresponding subgoups. Notation: $l_1$, $l_2$, $l_4$, $l_5$, $m_1$, $m_2$, $k$ are certain (arbitrary) integers. The last column shows the translations admitted by the space group (within the normalization used, the lattice constant is not equal to unity; for details, see the text).

by substituting there the group generators. With this aim, we have to prove that the equations

$$\mathbf{x} - A\mathbf{x} = m_1\mathbf{e}_1 + \ldots + m_6\mathbf{e}_6$$

and

$$\mathbf{x} - B\mathbf{x} = n_1\mathbf{e}_1 + \ldots + n_6\mathbf{e}_6$$

necessarily yield that

$$\mathbf{x} - AB\mathbf{x} = l_1\mathbf{e}_1 + \ldots + l_6\mathbf{e}_6. \quad (4.1)$$

Now, prove this statement.

Let $A = (A|\mathbf{a})$ and $B = (B|\mathbf{b})$, then $AB = (AB|\mathbf{a} + A\mathbf{b})$ and we have

$$\mathbf{x} - (A|\mathbf{0})\mathbf{x} - \mathbf{a} = m_j\mathbf{e}_j, \quad (4.2)$$

$$\mathbf{x} - (B|\mathbf{0})\mathbf{x} - \mathbf{b} = n_j\mathbf{e}_j \quad (4.3)$$

(the summation is performed over the repeating indices). Applying the transformation $A = (A|\mathbf{a})$ to (4.3), we obtain

$$(A|\mathbf{a})(\mathbf{x} - (B|\mathbf{0})\mathbf{x} - \mathbf{b}) = (A|\mathbf{a})n_i\mathbf{e}_i,$$

$$(A|\mathbf{0})\mathbf{x} - (AB|\mathbf{0})\mathbf{x} + \mathbf{a} - (A|\mathbf{0})\mathbf{b} = n_i(A|0)\mathbf{e}_i + \mathbf{a}, \quad (4.4)$$

$$(A|\mathbf{0})\mathbf{x} - (AB|\mathbf{0})\mathbf{x} - (A|\mathbf{0})\mathbf{b} = (A|\mathbf{0})n_i\mathbf{e}_i.$$

Summing up (4.4) and (4.2), we have

$$\mathbf{x} - AB\mathbf{x} = (A|\mathbf{0})n_i\mathbf{e}_i + m_i\mathbf{e}_i. \quad (4.5)$$

Comparing (4.5) with (4.1), we can see that, in fact, they coincide, if any linear combination of the basis vectors subjected to the operations of the point symmetry group can be transformed into a linear combination of the same basis vectors with integral coefficients, i.e.,

$$(A|\mathbf{0})(n_j\mathbf{e}_j) = k_j\mathbf{e}_j, \quad (4.6)$$

where $k_i$ are integers and $k_i = l_i - m_i$. In turn, in order to prove the validity of (4.6) one has to prove that each of the basis vectors transformed by the symmetry operation of the point symmetry group becomes a combination of the basis vectors with integral coefficients.

Such a multiplication of any basis vector by all possible operations of the point group of the cubic space groups yields 40 vectors, whose ends form the vertices

of two dodecahedra which differ, as has already been indicated only by the rotation by $\pi/4$ about one of the coordinate axis. Since the choice of six "dodecahedral vectors" from the total twenty vectors forming the vertices of one dodecahedron is dictated by the requirement of their linear independence on the ring of integers, formula (4.6) is valid for the operations that do not transform one dodecahedron into another (related to the first one). Thus, we only have to prove that formula (4.6) is also valid for any operation relating these dodecahedra, in particular, the rotation by $\pi/4$ around the *OX*-axis.

Eight vertices of total twenty vertices of one dodecahedron coincide with those of the related dodecahedron (these are the vertices along the [111] directions), whereas the remaining twelve vertices (along the $[\tau^2 01]$ directions differ from one another by the rotation by $\pi/4$ about the *OX*-axis. As has already been shown, formula (4.6) is valid for eight dodecahedron vertices coinciding with eight vertices of the reference dodecahedron. The $(\tau^2 10)$ directions differ from $(\tau^2 01)$ directions by the rotation by $\pi/4$ about the *OX*-axis. Then, since by definition of the dodecahedral local order, the orientations of the reference dodecahedra around each atom of the structure are the same, such interatomic vectors cannot exist in the DLO-structures. Thus, it is not necessary to prove the validity of (4.6) for these directions.

Thus, the initial statement has been proven.

It should be emphasized that, in accordance with the definition of the DLO, the impossibility of a simultaneous presence in the structure of the related local directions imposes no constraints on the symmetry, including the symmetry operations relating the dodecahedra (e.g., the rotation by $\pi/4$ about the *OX*-axis). Nevertheless, the set of the local vectors in such groups is somewhat reduced in comparison with the conventional set for DLO-structures or, as was shown above, the DLO structures with such symmetry groups can have only eight interatomic vectors equivalent to the [111] direction. Thus, in the simplest approximant, CsCl, with the sp. gr. *Pm*3*m*, there are only the [111] type vectors.

## 5. NUMBER OF ATOMS IN THE APPROXIMANT UNIT CELL

As was shown above, the positions of the atoms in the unit cells of cubic approximants are discrete. It is possible to impose some additional constraints onto the atomic positions; i.e., to show that the numbers $m_1$ and $m_2$ can take only a limited set of values not exceeding $3N_n$, where $N_n$ is the maximum possible number of atoms in the unit cell of the approximant of order *n*.

To prove this statement, estimate $N_n$ from above. In the $F_{n-2}/F_{n-3}$ approximants, the unit cell of the dimension $2r_{\min}\tau^{n-1}/\sqrt{3}$ and the minimum possible interatomic distance $r_{\min}$ allows the arrangement of not more than $16\tau^{3n-3}/(\pi\sqrt{3})$ atoms (an atom is represented by a rigid sphere with the radius equal to a half of the allowed minimum interatomic distance).

Thus, we have $N_n < \dfrac{16\tau^{3n-3}}{\pi\sqrt{3}}$, $N_n < 2, 12, 52, 223, \ldots$ $(n = 1, 2, 3\ldots)$.

Obviously, since the packing of imaginary rigid spheres has some voids, the above numbers are somewhat overestimated in comparison with the data determined for some DLO-structures. In a cubic face-centered packing of equivalent rigid spheres (having the highest possible density among all the other known packings), the fraction of the total volume occupied by the atoms is $\pi\sqrt{2}/6 \approx 74\%$. With due regard for this fact, it is possible to introduce a certain correction (a coefficient 0.74) into the above estimated number of atoms in the unit cell of the approximant, which would reduce the estimated number of atoms. A more realistic estimate can be obtained if one takes into account that of all the known structures of cubic approximants, the closest packing is possessed by the body-centered cubic unit cell of CsCl (the 1/–1 approximant). Then the correction coefficient can be reduced to 0.68, but the reliability of the above estimate of $N_n$ becomes lower.

Taking into account the number of special and general positions in cubic space groups, we can see from the estimate made above that the structure of the CsCl-type is the only possible structure for the 1/–1 approximant.

## 6. NUMBER OF APPROXIMANTS

Despite the fact that the general number of the approximant structures is infinite (because the series of approximants is infinite), the numbers $M_n$ of the structures of each order are limited. Let us prove this statement and estimate the number $M_n$ from above.

The consideration is made in terms of vectors, but, in fact, we imply here atomic positions. The basic equation (for the relative atomic coordinates **y** with respect to the coordinates of atom **x**) is

$$\mathbf{y} - \mathbf{x} = n_1\mathbf{e}_1 + n_2\mathbf{e}_2 + \ldots + n_6\mathbf{e}_6.$$

We proceed from the estimate of the maximum number $N_n$ (or, for the sake of simplification, *N*) of atoms in the unit cell of the approximant made above. If the atom described by **y** is one of the nearest neighbors of the atom described by **x**, then some of the $n_j$ numbers are equal to unity, whereas some other are equal to zero. Moving from the atom described by **y** to any of its nearest neighbors, with the vector **x** being fixed, we see that some of the $n_j$ coefficients change by unity at each step, whereas some other numbers remain constant. Moving from the fixed point described by the

**x** value, one can reach any of the $N$ atoms in the unit cell using less than $N$ steps. Therefore, the integral $n_j$ values can range from $-N$ to $N$.

Let us choose the vector **y** be determined by two positions equivalent to the vector **x**, namely, $C_{2x}\mathbf{x}$ and $C_{2y}\mathbf{x}$ (second-order rotations around the $X$- and $Y$-axes, respectively):

$$\mathbf{x} - C_{2x}\mathbf{x} = l_1\mathbf{e}_1 + l_2\mathbf{e}_2 + \ldots + l_6\mathbf{e}_6,$$

$$\mathbf{x} - C_{2x}\mathbf{x} = k_1\mathbf{e}_1 + k_2\mathbf{e}_2 + \ldots + k_6\mathbf{e}_6.$$

The above equations have the following solution

$$\mathbf{x} = (k_1 + k_2 - l_1 + (k_1 - l_1)\tau,$$

$$l_2 + l_3 - k_3 + l_2\tau, l_1 + k_3 + k_3\tau),$$

$$l_j = (l_1, l_2, l_3, l_1, -l_2, l_3 - 2k_3),$$

$$k_j = (k_1, k_2, k_3, 2l_1 - k_1, k_2, -k_3).$$

Thus, each atomic position is determined by the following six integral parameters: $l_1$, $l_2$, $l_3$, $k_1$, $k_2$, and $k_3$ taking the values in the range from $-N$ to $N$. This signifies that each unit cell has less than $(2N + 1)^6$ positions that can be filled with the DLO-atoms. There are $(2N + 1)^6 = C^1_{(2N+1)^6}$ ways to construct a DLO structure with only one atom in the unit cell, $C^2_{(2N+1)^6}$ ways to construct the structure with two atoms per unit cell, and $C^N_{(2N+1)^6}$ ways to construct the structure with $N$ atoms per unit cell. Thus, the total number of the DLO-approximants $F_{n-2}/F_{n-3}$ with the fixed $n$ is less than

$$M_n < C^1_{(2N+1)^6} + C^2_{(2N+1)^6} + C^3_{(2N+1)^6} + \ldots + C^N_{(2N+1)^6} < 2^{(2N+1)^6}.$$

The first of the above estimates can be additionally reduced using the fact that the interatomic distance can be covered within about $\sqrt[3]{N_n}$ steps. Therefore, the number of the approximants is estimated as $M_n \leqslant 4^{N_n^2}$.

It should be emphasized that all the above figures are overestimated; i.e., they increase with an increase of the approximant number so fast that soon they loose any physical sense: even at low $n$ values, the estimated number of atoms exceeds the number of atoms in the whole Universe. Thus, the studies in this field should be continued.

## 7. ALGORITHM OF THE SEARCH FOR APPROXIMANT STRUCTURES

Thus, the number of the approximants of each order is limited and therefore one can formulate the problem of the exhaustive theoretical search for all the structures of approximants of each order. The above estimates yield enormous numbers of approximants rapidly increasing with an increase of the approximant order. Therefore, the exhaustive search for the approximant structures was made on a personal computer. Below, we describe the suggested algorithm of the exhaustive search.

Since all the cubic groups are supragroups of one of two space groups, $P23$ or $P2_13$, we considered only the constraints imposed onto the atomic positions of these two groups. The structures possessing a higher symmetry were obtained as the particular cases of the atomic arrangement described by these two groups.

The search algorithm is based on the combinatorial approach and can be described as follows.

1. The position (point) of the first atom is selected from a set of possible atomic positions (as was shown above, this set is finite).

2. The thus given point is multiplied by all the symmetry elements of the space group ($P23$ or $P2_13$).

3. The thus obtained structure is checked against two physical criteria—the criterion of the absence of interatomic distances shorter than the minimum admissible interatomic distance and the DLO-criterion. If a structure is low probable in terms of physics and is not a DLO-structure, it is discarded, and the search is started anew from step 1.

4. "Crystal growth" of the structure obtained at step 3 is performed by adding another (a neighboring) atom located at the minimum possible interatomic distance along the direction from the first atom to one of the twenty dodecahedron vertices.

5. A new atomic position is also multiplied by all the symmetry elements of the space group.

6. The physical sense of the thus obtained new structure is considered and also checked against the DLO criterion. If the structure does not satisfy these two criteria, it is discarded.

7. Steps 4, 5, 6 are repeated until "crystal growth" (an increase of the atomic density) loses any physical sense or results in violation of the DLO criterion. The thus obtained final crystal has the maximum density and is included into the list of DLO-structures.

At each step providing an increase of the atomic density (beginning from the selection of the initial atomic position) and selection of one of twenty possible directions to the dodecahedron vertices, we have to solve the same problem—selection of one element from a finite number of elements. This process can be illustrated by invoking a tree. The number of branching levels for a tree is limited by the maximum number $N_n$ of atoms in the unit cell of the approximant. The number of branches at each "junction" is also limited. Therefore, the exhaustive search for all such branch junctions would correspond to the exhaustive search for all the structures of the approximant of the $n$th order.

This algorithm was implemented in a computer program. As a result, we performed an exhaustive search for all the 0/1 approximants. In other words, we man-

**Table 2.** Admissible approximant structures

| 1/0 | $P2_13$ | 1/0 | $P2_13$ | 1/0 | $P2_13$ |
|---|---|---|---|---|---|
| 0.036 0.036 0.036 | 4/28 | 0.036 0.155 0.345 | 12/32 | 0.036 0.845 0.155 | 12/32 |
| 0.082 0.345 0.155 | 12/28 | 0.155 0.464 0.345 | 12/32 | 0.155 0.155 0.155 | 4/32 |
| 0.273 0.536 0.345 | 12/28 | 0.655 0.655 0.655 | 4/32 | 0.155 0.155 0.536 | 12/32 |
| | | 0.845 0.845 0.845 | 4/32 | 0.345 0.345 0.345 | 4/32 |

| 1/0 | $P23$ |
|---|---|
| 0.000 0.000 0.000 | 1/27 |
| 0.000 0.500 0.309 | 6/27 |
| 0.191 0.191 0.191 | 4/27 |
| 0.191 0.309 0.500 | 12/27 |
| 0.809 0.809 0.809 | 4/27 |

| 1/1 | $P23$ | 1/1 | $P23$ | 1/1 | $P23$ | 1/1 | $P23$ |
|---|---|---|---|---|---|---|---|
| 0.000 0.191 0.264 | 12/121 | 0.000 0.191 0.264 | 12/112 | 0.000 0.191 0.264 | 12/106 | 0.000 0.191 0.264 | 12/106 |
| 0.000 0.191 0.500 | 6/112 | 0.000 0.191 0.500 | 6/112 | 0.000 0.809 0.500 | 6/106 | 0.000 0.809 0.500 | 6/106 |
| 0.000 0.500 0.309 | 6/112 | 0.000 0.500 0.309 | 6/112 | 0.073 0.073 0.073 | 4/106 | 0.073 0.382 0.264 | 12/106 |
| 0.073 0.073 0.073 | 4/112 | 0.073 0.382 0.118 | 12/112 | 0.073 0.382 0.264 | 12/106 | 0.118 0.691 0.382 | 12/106 |
| 0.073 0.382 0.118 | 12/112 | 0.118 0.691 0.382 | 12/112 | 0.118 0.691 0.382 | 12/106 | 0.191 0.191 0.191 | 4/106 |
| 0.118 0.691 0.382 | 12/112 | 0.191 0.191 0.191 | 4/112 | 0.191 0.191 0.191 | 4/106 | 0.191 0.264 0.382 | 12/106 |
| 0.191 0.191 0.191 | 4/112 | 0.191 0.264 0.382 | 12/112 | 0.191 0.264 0.382 | 12/106 | 0.191 0.500 0.382 | 12/106 |
| 0.191 0.264 0.382 | 12/112 | 0.191 0.500 0.382 | 12/112 | 0.191 0.500 0.382 | 12/106 | 0.191 0.882 0.382 | 12/106 |
| 0.191 0.500 0.382 | 12/112 | 0.191 0.882 0.382 | 12/112 | 0.191 0.882 0.382 | 12/106 | 0.309 0.382 0.500 | 12/106 |
| 0.191 0.882 0.382 | 12/112 | 0.309 0.382 0.500 | 12/112 | 0.309 0.382 0.500 | 12/106 | 0.691 0.691 0.691 | 4/106 |
| 0.309 0.382 0.500 | 12/112 | 0.691 0.691 0.691 | 4/112 | 0.691 0.691 0.691 | 4/106 | 0.809 0.809 0.809 | 4/106 |
| 0.691 0.691 0.691 | 4/112 | 0.809 0.809 0.809 | 4/112 | 0.809 0.809 0.809 | 4/106 | 0.927 0.927 0.927 | 4/106 |
| 0.809 0.809 0.809 | 4/112 | 0.927 0.927 0.927 | 4/112 | | | | |

| 1/1 | $P2_13$ | 1/1 | $P2_13$ | 1/1 | $P2_13$ | 1/1 | $P2_13$ | 1/1 | $P2_13$ |
|---|---|---|---|---|---|---|---|---|---|
| 0.036 0.155 0.345 | 12/132 | 0.036 0.155 0.345 | 12/132 | 0.036 0.155 0.345 | 12/128 | 0.036 0.155 0.345 | 12/128 | 0.036 0.155 0.345 | 12/128 |
| 0.036 0.155 0.727 | 12/132 | 0.036 0.155 0.727 | 12/132 | 0.036 0.155 0.727 | 12/128 | 0.036 0.155 0.727 | 12/128 | 0.036 0.155 0.727 | 12/128 |
| 0.036 0.155 0.964 | 12/132 | 0.036 0.155 0.964 | 12/132 | 0.036 0.155 0.964 | 12/128 | 0.036 0.227 0.155 | 12/128 | 0.036 0.227 0.155 | 12/128 |
| 0.036 0.227 0.155 | 12/132 | 0.036 0.227 0.155 | 12/132 | 0.036 0.227 0.536 | 12/128 | 0.036 0.227 0.536 | 12/128 | 0.036 0.227 0.536 | 12/128 |
| 0.036 0.227 0.536 | 12/132 | 0.036 0.227 0.536 | 12/132 | 0.036 0.773 0.345 | 12/128 | 0.036 0.464 0.155 | 12/128 | 0.036 0.464 0.155 | 12/128 |
| 0.036 0.845 0.155 | 12/132 | 0.155 0.345 0.418 | 12/132 | 0.036 0.845 0.155 | 12/128 | 0.036 0.536 0.345 | 12/128 | 0.036 0.536 0.345 | 12/128 |
| 0.155 0.345 0.418 | 12/132 | 0.155 0.418 0.227 | 12/132 | 0.155 0.345 0.418 | 12/128 | 0.036 0.845 0.155 | 12/128 | 0.155 0.345 0.418 | 12/128 |
| 0.155 0.418 0.227 | 12/132 | 0.155 0.655 0.227 | 12/132 | 0.155 0.418 0.227 | 12/128 | 0.155 0.345 0.418 | 12/128 | 0.155 0.655 0.227 | 12/128 |
| 0.155 0.655 0.227 | 12/132 | 0.155 0.727 0.418 | 12/132 | 0.155 0.655 0.227 | 12/128 | 0.155 0.655 0.227 | 12/128 | 0.155 0.727 0.418 | 12/128 |
| 0.227 0.227 0.227 | 4/132 | 0.227 0.227 0.227 | 4/132 | 0.227 0.227 0.227 | 4/128 | 0.227 0.227 0.227 | 4/128 | 0.227 0.227 0.227 | 4/128 |
| 0.345 0.345 0.345 | 4/132 | 0.345 0.345 0.345 | 4/132 | 0.345 0.345 0.345 | 4/128 | 0.345 0.345 0.345 | 4/128 | 0.345 0.345 0.345 | 4/128 |
| 0.464 0.464 0.464 | 4/132 | 0.464 0.464 0.464 | 4/132 | 0.464 0.464 0.464 | 4/128 | 0.464 0.464 0.464 | 4/128 | 0.464 0.464 0.464 | 4/128 |
| 0.582 0.582 0.582 | 4/132 | 0.582 0.582 0.582 | 4/132 | 0.845 0.845 0.845 | 4/128 | 0.845 0.845 0.845 | 4/128 | 0.845 0.845 0.845 | 4/128 |
| 0.845 0.845 0.845 | 4/132 | 0.845 0.845 0.845 | 4/132 | 0.964 0.964 0.964 | 4/128 | 0.964 0.964 0.964 | 4/128 | 0.964 0.964 0.964 | 4/128 |
| 0.964 0.964 0.964 | 4/132 | 0.964 0.964 0.964 | 4/132 | | | | | | |

Note: Table 2 lists several promising DLO structures from those determined as a result of the exhaustive search for possible approximant structures. All the structures are divided into several groups according to their symmetry groups and approximant order. There are two columns for each approximant: the column indicating atomic coordinates (in the conventional crystallographic normalization) and the column indicating the numbers of equivalent atoms in the unit cell corresponding to the given position (only nonequivalent positions are indicated).

aged to show that there are no other new structures for 0/1 approximants in addition to the already known ones.

We also studied the 1/0 and 1/1 approximants. Since the set of structures for the exhaustive search dramatically increases with an increase of the approximant order, the exhaustive search for the 1/0 and 1/1 approximants within the suggested algorithm on modern computers should take from several years to several decades.

An additional, but not the main, selection rule used in the exhaustive search for the approximant structures can be conditionally called "the rule of the second coordination sphere". The point is that the radius of the second coordination spheres in the CsCl structure exceeds that of the first coordination sphere by a factor of $2/\sqrt{3}$. Therefore, it is logical to assume that the radii of the second and the first coordination spheres of the approximants would differ in the same way. Within the above algorithm, the 1/0 and 1/1 approximants form the structures with the radius ratio less than the indicated value. Such structures are usually characterized by a lower atomic density than the structures with the radius ratio exactly equal to $\sqrt{3}/2$. Thus, using the radius ratio for the first and the second coordination spheres, one can increase the speed of the exhaustive search by the above algorithm. In fact, this requirement was used at the initial stages of the search, when the use of the second coordination-sphere rule considerably reduced the list of newly generated structures. At the final steps of the search, the structure density was rather high, and the requirement imposed onto the radius of the second coordination sphere was lifted, because an additional atom could be introduced into the dense structure only by violating the basic principles.

## 8. RESULTS OF EXHAUSTIVE SEARCH

Some of the possible structures determined for the 1/0 and 1/1 approximants are listed in Table 2, which shows only the best of all the generated structures, differing from one another only by the choice of the coordinate system or the operation of mirror reflection (only one of the structures forming the pair is indicated). In all the structures obtained, we also analyzed the radii of the second coordination sphere.

For the 1/0 approximants, Table 2 lists all the structures with more than 27 atoms per unit cell. The maximum possible number of atoms in the unit cell determined from the estimate made above ranges within 52–74%, i.e, is about 38 atoms. Table 2 does not indicate several structures having the same density (above 27 atoms per unit cell) but "bad radius" of the second coordination sphere (in the above indicated sense) for at least one of the atomic positions.

For the 1/1 approximants, all the structures with the density above 100 and 128 atoms per unit cell (for the $P23$ and $P2_13$ groups, respectively) are indicated. For comparison, the estimate made above yields the maximum number of atoms in the unit cell of the 1/1 approximant ranging within 223 × 68%, i.e., about 152 atoms. At present, the densest structure of the cubic 1/1 approximants is an atomic analogue of the structure with 136 atoms in the unit cell suggested in [13]. We obtained a close result—132 atoms in the unit cell.

Comparing the structures obtained, one can see that different structures have many equivalent positions, because they were "grown" and selected simultaneously. Therefore, they can be divided into pairs related by the so-called phason hoppings. Two structures of each pair differ only by the fact that in the transition from one structure to another, one of the structure atoms (or, strictly speaking, atoms in all the atomic positions equivalent to it) performs a "hopping" into another position located at a distance less than the minimum admissible interatomic distance to occupy a DLO position. In the sp. gr. $P23$, the phason pairs are represented by structures 1 and 2 and also structures 2 and 3. In the sp. gr. $P2_13$, they form structures 1 and 2 and also 4 and 5. In all these cases, the cells indicating the coordinates of hopping atoms in Table 2 are of grey color. At first glance, the third of the $P2_13$ structures has its own place, but, in fact, it is related to the first $P2_13$ structure, which, upon elimination of one atomic position (in order to obtain the structure with the same number of atoms per unit cell), forms with it a phason pair.

It should be emphasized that in terms of the second coordination-sphere rule, all the listed $P2_13$-ст structures are "good" ones, whereas the $P23$ structures in Table 2 are not, because the second coordination sphere of one of the atoms has a too small radius. It should be noted that the role of such atoms in all the structures obtained is played by the atoms with phason degrees of freedom (the corresponding cell in Table 2 is grey).

In addition to the new structures listed in Table 2, we also considered the structures determined earlier, in particular, those for which the corresponding real structures are known. For the structure of the 1/1 cubic approximant determined in [11], we also found its "phason partner"—a structure obtained upon the phason hopping of an atom from the position (0.227, 0.536, 0.655) to the position (0.036, 0.227, 0.536).

## CONCLUSIONS

Thus, it is shown that the number of the approximants of each order is finite and their number is estimated from above. The number of atoms in the unit cell is also estimated from above. The number of positions occupied by the atoms in the unit cell of the approximant of each order is finite. There is only one structure for the 1/–1 approximant.

It is established that it is possible to perform the exhaustive search for all the structures of the approximants of each order. The algorithm of such search is

suggested. The algorithm of the exhaustive search suggested in this study provided the determination of all the structures of the 0/1 approximants and also of several possible structures of the 1/0 and 1/1 approximants.

The tables of possible structures of the approximants can be of interest for the experimenters working with new phases having approximants with unknown structures.

The investigation should be continued for the 1/0, 1/1, and higher-order approximants. It is most probable, that the number of possible DLO-structures would be much less than the number estimated obtained in this study. It seems that the algorithm of the exhaustive search for possible structures would be much faster if one imposes some additional constraints onto the structures by checking them against various physical criteria. One of such criterion is the rule of the second coordination sphere. Of special interest is the question of whether the violation of this rule and the simultaneous existence of a phason degrees of freedom is merely a coincidence or two interrelated facts.

In terms of physics, the effect of such constraints on the structure quality is still unclear (although, one can also invoke some energy considerations) and should be studied further.

Still another object of such studies can be the approximants with noncubic symmetries and those of the so-called Lucas series.

## ACKNOWLEDGMENTS

The author is grateful to V. A. Koptsik and V. E. Dmitrienko for useful remarks. The study was supported by the Russian Foundations for Basic Research, project no. 95-02-05746-a.

## REFERENCES

1. D. Shechtman, I. Blech, D. Gratias, *et al.*, Phys. Rev. Lett. **53**, 1951 (1984).
2. D. Shechtman, I. Blech, *et al.*, Metall. Trans. A **16**, 1005 (1985).
3. N. Wang *et al.*, Phys. Rev. Lett. **59**, 1010 (1987).
4. L. A. Bendersky, Phys. Rev. Lett. **55**, 1461 (1985).
5. T. Ishimasa *et al.*, Phys. Rev. Lett. **55**, 511 (1985).
6. B. K. Vaĭnshteĭn, *Modern Crystallography* (Nauka, Moscow, 1979; Springer, Berlin, 1994).
7. V. E. Dmitrienko, J. Phys. (Paris) **51**, 2717 (1990).
8. V. E. Dmitrienko, Acta Crystallogr., Sect. A: Found. Crystallogr. **50**, 515 (1994).
9. V. E. Dmitrienko and S. B. Astaf'ev, Pis'ma Zh. Éksp. Teor. Fiz. **61**, 316 (1995) [JETP Lett. **61**, 331 (1995)].
10. V. E. Dmitrienko and S. B. Astaf'ev, Phys. Rev. Lett. **75**, 1538 (1995).
11. V. E. Dmitrienko, Mater. Forum **150**, 199 (1994).
12. V. Elser and C. L. Henley, Phys. Rev. Lett. **55**, 2883 (1985).
13. M. E. J. Newman, C. L. Henley, and M. Oxborrow, Philos. Mag. B **71**, 991 (1995).

*Translated by L. Man*

*Crystallography Reports, Vol. 45, No. 2, 2000, pp. 182–186. Translated from Kristallografiya, Vol. 45, No. 2, 2000, pp. 213–217.*


## THEORY OF CRYSTAL STRUCTURES

# Hydrodynamics of Layered and Cubic Quasicrystals

**O. A. Belyaev and V. A. Koptsik**

*Moscow State University, Vorob'evy gory, Moscow, 119899 Russia*

Received May 13, 1998

**Abstract**—The dissipative processes associated with sound absorption in layered and cubic quasicrystals have been studied within the framework of the hydrodynamic approach. The decagonal, octagonal, and dodecagonal quasicrystals are considered as layered quasicrystals. Proceeding from the general theory, the complex law of dispersion is calculated for various directions of the propagation and polarization of sonic waves in layered and cubic quasicrystals. The effect of the phason modes on the process of sound absorption and the role of symmetry constraints are analyzed. The validity of the macroscopic consideration is discussed in terms of the theory of the generalized color symmetry. *© 2000 MAIK "Nauka/Interperiodica".*

Symmetry and structural features of the quasicrystalline state manifest themselves in the elastic properties of quasicrystals. The main method of their experimental study is acoustic measurements. Both linear and nonlinear acoustic properties of icosahedral quasicrystals, the most widespread class of quasicrystals, were studied experimentally [1] and theoretically [2].

Another important class of quasicrystals are layered quasicrystals—decagonal quasicrystals with the point group 10/*m* or 10/*mmm*, octagonal quasicrystals with the point group 8/*m* or 8/*mmm*, and dodecagonal quasicrystals with the point group 12/*m* or 12/*mmm*.

Nonlinear acoustic effects for such structures associated with the third-order elasticity moduli were considered in [3].

All the above-cited studies had one common shortcoming—they ignored the dissipative processes and the existence of phason modes in these quasicrystals. However, phasons, which are not propagating excitations and do not affect the sound propagation (in particular, its velocity), can influence absorption of sound in quasicrystals.

Sound absorption in quasicrystals and the related dissipative processes can be described within the hydrodynamic approach [4–6] reducing to the following [7]. If a system with numerous degrees of freedom (a crystal, a liquid crystal, or a quasicrystal) is taken away from the state of the thermodynamic equilibrium and then is not subjected to the action of any factor, the majority of the degrees of freedom relax to the equilibrium states for short periods determined by microscopic interactions such as interatomic collisions. However, there exist collective excitations which would decay for longer periods of time proportional to a certain power of their wave length. Such long-living states are described by hydrodynamics. The existence of these modes can be associated either with the laws of conservation or (in ordered systems) with the break of continuous symmetries.

In the present study, we aimed to estimate theoretically the sound absorption in layered and cubic quasicrystals using the hydrodynamic approach.

Being compared to icosahedral quasicrystals, layered quasicrystals seem to be of more interesting, at least, because of two reasons. First, layered quasicrystals are characterized by both periodic order along the high-order symmetry axis and quasiperiodic order along two perpendicular directions. Second, the experimental study of the physical properties of layered quasicrystals show their considerable anisotropy. Thus, it was established [8] that electric conductivity along the periodic direction in a decagonal quasicrystal can be twenty times higher than the conductivity along the perpendicular direction. The resistivity of a decagonal $Al_{70}Ni_{15}Co_{15}$ quasicrystal along the tenfold axis is $50\ \mu\Omega$ cm, whereas in the plane perpendicular to this direction, it ranges within 1100–1400 $\mu\Omega$ cm, which corresponds to the resistivity of stable icosahedral quasicrystals.

Cubic quasicrystals are structures in which the cubic point symmetry is combined with the quasiperiodic order in the atomic arrangement [9–12].

Consider a quasicrystal of rank *r*. We say that a quasicrystal has the rank *r*, if the dimension of its Fourier module equals *r*, or, in other words, if the reciprocal lattice of a quasicrystal has not more than *r* vectors with rational coefficients on the ring of rational numbers (hereafter called for brevity the rationally independent vectors). In this case, a three-dimensional quasicrystal has $(r - 3)$ additional (in comparison with a conventional crystal) hydrodynamic variables related to the phason degrees of freedom. The total number of the hydrodynamic variables for a quasicrystal is $(r + 5)$: the phonon and the phason variables are complemented with three density components of the momentum density **g**, the densities of mass, $\rho$, and energy, $\epsilon$.

1063-7745/00/4502-0182$20.00 © 2000 MAIK "Nauka/Interperiodica"

The general hydrodynamic equations for quasicrystals have the form [5, 6]:

$$\partial_t \rho + \nabla \mathbf{g} = 0 \quad (1)$$

$$\partial_t g_i + \nabla(\mathbf{v} g_i) - \nabla_j(\eta_{ijkl}\nabla_k g_l) = -(\delta_{ij} - \nabla_i u_j)\frac{\delta H}{\delta u_j} + (\nabla_i w_j)\frac{\delta H}{\delta w_j} - \rho\nabla_i\frac{\delta H}{\delta \rho}, \quad (2)$$

$$(\partial_t + \nabla\mathbf{v})u_i + \Gamma_u\frac{\delta H}{\delta u_i} - v_i = 0, \quad (3)$$

$$(\partial_t + \nabla\mathbf{v})w_i + \Gamma_w\frac{\delta H}{\delta w_i} = 0. \quad (4)$$

An elastic Hamiltonian of a quasicrystal in (1)–(4) has the form

$$H = \int d^3x\left[\frac{1}{2}\rho v^2 + \frac{1}{2}A(\delta\rho/\rho_0)^2 + \frac{1}{2}B(\delta\rho/\rho_0)\nabla\mathbf{u} + F(u, w)\right],$$

where $\rho$ is the nonequilibrium density of a quasicrystal, $\rho_0$ is its equilibrium density, $\delta\rho = \rho - \rho_0$ is the deviation of the quasicrystal density from its equilibrium value, $\mathbf{g}$ is the momentum density, i.e., the momentum of a unit volume of a quasicrystal, $\mathbf{v} = \mathbf{g}/\rho$ is the velocity, and $\eta_{ijkl}$ are the components of the viscosity-tensor coefficients possessing the following properties of the thermodynamic (permutational) symmetry

$$\eta_{ijkl} = \eta_{jikl} = \eta_{klij} = \eta_{ijlk}.$$

The number of independent components of the tensor $\eta$ is determined by the macroscopic symmetry group of a quasicrystal. As usual, $u_i$ and $w_i$ are the components of the phonon and phason displacements, respectively.

Equation (1) is a conventional continuity equation describing the conservation of mass. Equation (2) is a generalized Navier–Stokes law and is, in fact, nothing but the local formulation of the second Newton law equating the velocity of the momentum variation to the sum of elastic forces associated with the pressure and the deformation of a quasilattice and the forces of viscous friction. Equations (3) and (4) describe the diffusion relaxation of phase variables in the absence of a macroscopic velocity field. Since this relaxation for phonons and phasons is of the same physical nature, it is reasonable to assume that $\Gamma_w$ value is of the same order of magnitude as $\Gamma_u$, a coefficient of diffusion mobility of vacancies, which for typical metals, has the value of the order of $10^{-14}$ m$^2$/s.

The elastic energy of a quasicrystal is a function of the tensors of the phonon ($u_{ij}$) and phason ($\partial_j w_i$) deformations. The density of the elastic energy F can be expanded into a Taylor series in the vicinity of $u_{ij} = 0$ and $\partial_j w_i = 0$ within the accuracy of the second-order terms,

$$F(u, w) = \frac{1}{2}C_{ijkl}u_{ij}u_{kl} + \frac{1}{2}K_{ijkl}\partial_j w_i\partial_l w_k + \frac{1}{2}R_{ijkl}u_{ij}\partial_l w_k + \frac{1}{2}R'_{ijkl}\partial_j w_i u_{kl},$$

where

$$C_{ijkl} = \left(\frac{\partial^2 F}{\partial u_{ij}\partial u_{kl}}\right)_0$$

are the stiffness constants in the classical theory of elasticity obeying the relationships

$$C_{ijkl} = C_{klij} = C_{jikl} = C_{ijlk},$$

and

$$K_{ijkl} = \left(\frac{\partial^2 F}{\partial(\partial_j w_i)\partial(\partial_l w_k)}\right)_0$$

are the constants of phason elasticity symmetric with respect to the permutation of the pairs of indices

$$K_{ijkl} = K_{klij},$$

and

$$R_{ijkl} = \left(\frac{\partial^2 F}{\partial u_{ij}\partial(\partial_l w_k)}\right)_0,$$

$$R'_{ijkl} = \left(\frac{\partial^2 F}{\partial(\partial_j w_i)\partial u_{kl}}\right)_0$$

are the elastic constants associated with the phonon–phason interaction. It is clear that

$$R_{ijkl} = R_{jikl}, \quad R'_{ijkl} = R'_{ijlk}, \quad R'_{klij} = R_{ijkl},$$

but, at the same time, that

$$R_{ijkl} \neq R_{klij}, \quad R'_{ijkl} \neq R'_{jikl}.$$

Upon the linearization and the Fourier transformation in space and time, equations (1)–(4) take the form

$$-i\omega\delta\rho + \mathbf{qg} = 0, \quad (5)$$

$$-i\omega\mathbf{g} = -\eta(\mathbf{q})\mathbf{g} - C(\mathbf{q})\mathbf{u} - R(\mathbf{q})\mathbf{w} + B\mathbf{q}(\mathbf{qu}) - i(A - B)\mathbf{q}(\delta\rho/\rho_0), \quad (6)$$

$$-i\omega\mathbf{u} = \mathbf{g}/\rho_0 - \Gamma_u\left[-i\mathbf{q}B\frac{\delta\rho}{\rho_0} + C(\mathbf{q})\mathbf{u} + R(\mathbf{q})w\right], \quad (7)$$

$$-i\omega\mathbf{w} = -\Gamma_w[K(\mathbf{q})\mathbf{w} + R^T(\mathbf{q})\mathbf{u}], \quad (8)$$

where the matrix components, $\eta(\mathbf{q})$, $C(\mathbf{q})$, $K(\mathbf{q})$, and $R(\mathbf{q})$, are the following convolutions:

$$\eta_{ik} = \eta_{ijkl}q_j q_l, \quad C_{ik} = C_{ijkl}q_j q_l,$$

$$K_{ik} = K_{ijkl}q_j q_l, \quad R_{ik} = \frac{1}{2}(R_{ijkl} + R'_{kjil})q_j q_l.$$

The requirement of tensor invariance with respect to the symmetry transformation of the point group of a quasicrystal results in the fact that only the components of the tensors of phason elastic constants listed below have the nonzero values [13–15]:

For quasicrystals with the point symmetry groups 10/*mmm* and 10/*m*, these are

$$K_{1111} = K_{2222} = K_{2121} = K_{1212},$$
$$K_{1313} = K_{2323}, \quad K_{1122} = K_{2211};$$
$$R_{1221} = -R_{1212} = 2R_{1111} = -2R_{2211} = 2R_{1122} = -2R_{2222};$$

for quasicrystals with the point group 10/*m*, these are

$$2R_{1121} = -2R_{2221} = -2R_{1112} = 2R_{2212} = -R_{1211} = -R_{1222};$$

for the quasicrystals with the point groups 8/*mmm* and 12/*mmm*, these are

$$K_{1111} = K_{2222}, \quad K_{1313} = K_{2323}, \quad K_{1122} = K_{2211},$$
$$K_{2121} = K_{1212} = K_{1111} + K_{1221} + K_{1122}, K_{2112} = K_{1221};$$

and, finally, for quasicrystals with the point groups 8/*m* and 12/*m*, these are

$$K_{1121} = -K_{2221} = K_{1112} = -K_{2212}.$$

Quasicrystals with the point groups 8/*m* and 8/*mmm* have the same nonzero components $R_{ijkl}$ of the phonon–phason elasticity constants as quasicrystals with the point groups 10/*m* and 10/*mmm*, namely,

$$R_{1221} = -R_{1212} = 2R_{1111} = -2R_{2211} = 2R_{1122} = -2R_{2222};$$

for quasicrystals with the point group 8/*m*, the nonzero components are also

$$2R_{1121} = -2R_{2221} = -2R_{1112} = 2R_{2212} = -R_{1211} = -R_{1222}.$$

For quasicrystals with the point groups 12/*m* and 12/*mmm*, all the $R_{ijkl}$ moduli are identical zeroes.

A cubic quasicrystal has the following nonzero phason-elasticity moduli [16]:

$$K_{1111} = K_{2222} = K_{3333}, \quad K_{1122} = K_{1133} = K_{2233},$$
$$K_{2323} = K_{1313} = K_{1212} = K_{3232} = K_{1313} = K_{2121},$$
$$K_{2332} = K_{3113} = K_{1221};$$
$$R_{1111} = R_{2222} = R_{3333}, \quad R_{1212} = R_{2323} = R_{3131};$$
$$R_{1122} = R_{1133} = R_{2211} = R_{2233} = R_{3311} = R_{3322}.$$

Omitting here the derivation of the complex dispersion law from the system of the linearized hydrodynamic equations in the general form (see Appendix), consider only some particular cases for various directions of sound propagation and polarizations, which allow to obtain a clear picture of the effect of a quasicrystal structure. If a sound wave is polarized in the quasicrystal plane of a layered quasicrystal and propagates in this plane (i.e., the directions of wave propagation and wave polarization are perpendicular to the high-order symmetry axis), the expressions for the dispersion law are the direct two-dimensional analogues of the corresponding expressions for three-dimensional icosahedral quasicrystal [5, 6]. For the longitudinal mode, we have

$$\omega = c_L q - \frac{i}{2}\left[\eta_{1111}q^2 + \frac{\Gamma_w}{\rho_0 c_L^2}\frac{Tr(QRR^T)}{q^2}\right],$$

where the elements of the matrix $Q$ are given by the relationships

$$Q_{ij} = \frac{q_i q_j}{q^2},$$

and the longitudinal sound velocity $c_L$ is determined from the condition

$$\rho_0 c_L^2 = A + C_{1111} - 2B.$$

For the transversal mode, we have

$$\omega = c_T q - \frac{1}{2}iq^2\left[(\eta_{1212} + \Gamma_u C_{1212}) + \frac{\Gamma_w}{c_{1212}q^4}\lambda\right],$$

where the transverse sound velocity is determined from the condition

$$\rho_0 c_T^2 = C_{1212},$$

and $\lambda$ is the only nonzero eigenvalue of the matrix $PRR^TP$ for the particular case under study, where $P$ is the matrix of the projection operator with the matrix elements

$$P_{ij} = \delta_{ij} - Q_{ij}.$$

If a sonic wave propagates along the high-order symmetry axis and is polarized in the quasicrystal plane, the dispersion law in the approximation under consideration has the form

$$\omega = \sqrt{\frac{C_{11}}{\rho_0}} - \frac{i}{2}(\eta_{11} + \Gamma_u C_{11}).$$

For a wave polarized in the periodic direction, we have

$$\omega = \sqrt{\frac{C_{33}}{\rho_0}} - \frac{i}{2}(\eta_{33} + \Gamma_u C_{33}),$$

if the sonic wave propagates in the quasicrystal plane, and

$$\omega = \sqrt{\frac{C_{33} + A - 2B}{\rho_0}} - \frac{i}{2}(\eta_{33} + \Gamma_u C_{33})$$

if the wave propagates along the periodic direction.

Thus, if the vector of the direction of the wave propagation or the polarization vector of a sonic wave is parallel to the periodic direction in a layered quasicrystal, the phonon–phason elasticity moduli do not enter the expression for a complex dispersion law, i.e., do not affect the sound absorption in the approximation used. When deriving the above formula, we made use of the fact (see Appendix) that, for small $q$ values (to which

the thermodynamic approach is applicable), the term $K(\mathbf{q})\mathbf{w}$ in the right-hand side of (8) can be neglected in comparison with the term $R^T(\mathbf{q})\mathbf{u}$. If one takes into account the rejected term, the phason elasticity provides a contribution to the sound absorption in a layered quasicrystal irrespectively of the directions of polarization and propagation, but, because of smallness of $q$, this contribution is negligibly small. In the general case, we arrive at the conclusion that, in the approximation used, phasons makes the contribution to the sound absorption in octagonal and decagonal quasicrystals via the phonon–phason elasticity moduli only if the vector of sound propagation and the polarization vector have nonzero components in the quasiperiodic plane. Since all the phonon–phason elasticity constants in a dodecagonal quasicrystal are equivalent zeroes, the phason elasticity does not make any contribution to the sound absorption for any propagation and polarization directions.

For a cubic quasicrystal and a sonic wave propagating and polarized in the [100] direction, the complex dispersion law for the longitudinal mode can be written, in the first approximation, as

$$\omega = c_L q - \frac{i}{2}\left[\eta_{1111}q^2 + \frac{\Gamma_w}{\rho_0 c_L^2}\frac{R_{11}^2}{q^2}\right], \quad (9)$$

whereas the longitudinal sonic velocity $c_L$ is determined from the condition

$$\rho_0 c_L^2 = A + C_{1111} - 2B.$$

For a wave propagating in the same direction, but polarized along the [010] direction, we have

$$\omega = \sqrt{\frac{C_{1212}}{\rho_0}}q - \frac{i}{2}q^2\left(\eta_{1212} + \Gamma_u C_{1212} + \frac{\Gamma_w R_{22}^2}{C_{1212}q^4}\right), \quad (10)$$

and for polarization in the [001] directions, we have

$$\omega = \sqrt{\frac{C_{1313}}{\rho_0}}q - \frac{i}{2}q^2\left[\eta_{1313} + \Gamma_u C_{1313} + \frac{\Gamma_w R_{33}^2}{C_{1313}q^4}\right]. \quad (11)$$

The expressions for the complex dispersion law for waves propagating along the [010] direction and polarized along the [010], [001], and [100] directions and also for waves propagating along [001] direction and polarized along the [001], [100], and [010] directions are obtained automatically from formulas (9)–(11) with the use of appropriate cyclic permutation of subscripts 1, 2, and 3. This follows from the fact that in a conventionally oriented cubic quasicrystal (with the three unit vectors of the Cartesian coordinate system being directed along three mutually perpendicular symmetry axes) these axes are physically "equivalent".

In a cubic quasicrystal, phasons make contributions into sound absorption via the phonon–phason elasticity moduli irrespectively of the propagation and polarization directions.

It is well known that the specific features of an icosahedral quasicrystal distinguishing it from conventional crystals are seen from the acoustic properties of a single crystal specimen even in the linear range. Similar to isotropic media, icosahedral crystals have a lower number (2) of linear elastic constants than conventional crystals. The transition to the first nonlinear approximation, i.e., to the third-order elastic moduli, allows one to study the symmetric aspects of the acoustic behavior of layered quasicrystals [3] and to follow the symmetric differences in the acoustic properties of icosahedral quasicrystals and isotropic media [1, 2].

In terms of symmetry, the sound propagation in cubic quasicrystals does not differ from the sound propagation in a cubic crystal because their point symmetries are exactly the same. However, the situation is quite different for sound absorption: in quasicrystals, the effect of phasons manifests itself via the phonon–phason elastic constants. In layered quasicrystals, this effect is seen only for a sound propagating and polarized in the quasiperiodic plane, which is a bright physical demonstration of the two-dimensional nature of quasicrystallinity of such systems. A cubic quasicrystal differs from a cubic crystal by the contribution made by the phason modes to the sound absorption via the constants of the phonon–phason elasticity irrespectively of the direction of sound propagation and polarization seen already in the first approximation.

Concluding the article, we should like to emphasize that the present study of the particular form of the hydrodynamic equations for layered and cubic quasicrystals is made within the approximation of an anisotropic continuous medium. In terms of the generalized color symmetry, the anisotropy in elasticity can be taken into account by using, in this approximation, the classical point symmetry groups $G(3)$ (the factor-groups of the corresponding three-dimensional space groups $\Phi(3) = T(3)\lambda G(3)$). It can be made because the positional color groups $\Phi(3)^{W_p(d)}$ adequately describing the microsymmetry of quasicrystals [17, 18] and possessing the corresponding homomorphism or the symmetry groups isomorphic to them in the imaginary $n = 3 + d$-dimensional space (introduced for the restoration of the broken translation periodicity of quasicrystals [19]) are characterized by the same sets of the vector $V(G(3)) \longleftrightarrow V(G^{W_p}(3)) \longleftrightarrow V(G(3 + d))$ and the tensor $V^s(G(3)) \longleftrightarrow V^s(G^{W_p}(3)) \longleftrightarrow V^s(G(3 + d))$ ($V^s = \underbrace{V \times \ldots \times V}_{s \text{ times}}$) representations. The differences between the true $\Phi(3)^{W_p(d)}$ and the fictitious $\Phi(3 + d)$ microsymmetries of quasicrystals should affect the local microscopic properties of quasicrystals, in particular, their vibrational and electronic spectra [20, 21]. However, this subject is beyond the scope of the present article.

## *APPENDIX*

In the general case, the complex dispersion law for acoustic waves in a quasicrystal is obtained from the condition of the existence of nontrivial solutions of a system of equations linear with respect to the components of the vector **u**

$$L\mathbf{u} = 0, \tag{12}$$

obtained by combining equations (5)–(8) with due regard for the fact that in the range of applicability of hydrodynamics, i.e., at small $q$ values, we have $\omega \sim q$, so that, in the first approximation, the first term in (8) can be ignored when substituting this equation into (6) and (7).

The matrix $L$ has the form

$$L = i\omega I + \frac{1}{\rho_0}(1 + \Gamma_u BQ/w)N^{-1}M$$

$$-\Gamma_u C(\mathbf{q}) - \Gamma_u\Gamma_w \frac{R(\mathbf{q})R^T(\mathbf{q})}{i\omega},$$

where $I$ is the unit matrix, and the matrix $M$ is

$$M = i\omega\frac{A-B}{B}I - \frac{A}{B}\Gamma_u C(\mathbf{q}) - \frac{A}{B}\Gamma_u\Gamma_w\frac{R(\mathbf{q})R^T(\mathbf{q})}{i\omega},$$

and the matrix $N$ is

$$N = \eta\mathbf{q} - i\omega I - \frac{A-B}{B\rho_0}I,$$

where the elements of the matrix $Q$ are set by the relationships

$$Q_{ij} = \frac{q_i q_j}{q^2}.$$

The requirement that the system of equations (12) should have a nonzero solution has the form $\det L = 0$ and is described by the relationship implicitly implying the dependence $\omega(\mathbf{q})$, which allows one to find the complex dispersion law for each mode. The nonzero solutions of this system of equations sets the polarization of the propagating sonic waves.

## REFERENCES


1. Y. Amazit, M. Fisher, B. Perrin, *et al.*, Europhys. Lett. **25**, 441 (1994).
2. S. Y. Goshen and J. L. Birman, J. Phys. (Paris) **4**, 1077 (1994).
3. O. A. Belyaev and V. A. Koptsik, Kristallografiya **42**, 225 (1997) [Crystallogr. Rep. **42**, 888 (1997)].
4. D. Levine, T. C. Lubensky, S. Ostlund, *et al.*, Phys. Rev. Lett. **54**, 1520 (1985).
5. T. C. Lubensky, in *Aperiodicity and Order*, Vol. 1. Introduction to Quasicrystals (Academic, Boston, 1988), p. 199.
6. T. C. Lubensky, S. Ramaswamy, and J. Toner, Phys. Rev. B: Condens. Matter **32**, 7444 (1985).
7. P. S. Martin, O. Parodi, and P. S. Pershan, Phys. Rev. A **6**, 2401 (1972).
8. T. Shibya, T. Hashimoto, and S. Takeuchi, J. Phys. Soc. Jpn. **59**, 1917 (1990).
9. Y. C. Feng, G. Lu, and R. L. Withers, J. Phys.: Condens. Matter **1**, 3695 (1989).
10. Y. C. Feng, G. Lu, H. Q. Ye, *et al.*, J. Phys.: Condens. Matter **2**, 3695 (1990).
11. R. Wang, C. Qin, G. Lu, *et al.*, Acta Crystallogr., Sect. A: Found. Crystallogr. **50**, 366 (1994).
12. P. Donnadieu, M. Harmelin, H.-L.Su, *et al.*, Z. Metallkd. **88**, 33 (1997).
13. D. Ding, W. Yang, C. Hu, and R. Wang, Phys. Rev. B: Condens. Matter **48**, 7003 (1993).
14. J. E. S. Socolar, Phys. Rev. B: Condens. Matter **39**, 10519 (1989).
15. W. Yang, R. Wang, D. Ding, *et al.*, J. Phys.: Condens. Matter **7**, 7099 (1995).
16. W. Yang, R. Wang, D. Ding, *et al.*, Phys. Rev. B: Condens. Matter **48**, 6999 (1993).
17. V. A. Koptsik, Comput. Math. Applic. **16**, 407 (1988).
18. V. A. Koptsik, in *Proceedings of the XVIII International Colloquium, Moscow, USSR 1990*, Ed. by V. V. Dodonov and V. I. Man'ko (Springer, Berlin, 1991), p. 588.
19. T. Janssen, Rep. Prog. Phys. **168**, 55 (1988).
20. I. I. Nebola, N. R. Kharkhalis, and V. A. Koptsik, Fiz. Tverd. Tela (Leningrad) **29**, 3223 (1987).
21. I. I. Nebola, N. R. Kharkhalis, and V. A. Koptsik, Fiz. Tverd. Tela (Leningrad) **32**, 972 (1990).


*Translated by L. Man*

*Crystallography Reports, Vol. 45, No. 2, 2000, pp. 187–194. Translated from Kristallografiya, Vol. 45, No. 2, 2000, pp. 218–226.*


**THEORY OF CRYSTAL STRUCTURES**

# Hyperphasons and the Effect of Incommensurate Modulation on Elastic Properties of Quasicrystals

**O. A. Belyaev**

*Moscow State University, Vorob'evy gory, Moscow, 119899 Russia*

Received October 1, 1998; in final form, April 20, 1999

**Abstract**—Possible descriptions of phasons in incommensurate crystal phases and quasicrystals have been reviewed in terms of the theory of elasticity and superspace symmetry. The superspace symmetry of incommensurately modulated quasicrystals and its relation to the concept of the generalized symmetry are discussed. A new concept of hyperphasons, excited states of a solid characteristic of incommensurately modulated quasicrystals, is introduced using the formalism of the Landau density waves. Hyperphasons are characterized in terms of the generalized unit cells. The expression for the contribution of a hyperphason to the elastic free energy is derived, and the experimental examples of quasicrystals are considered. © *2000 MAIK "Nauka/Interperiodica".*

## INTRODUCTION

Quasicrystals are characterized by an aperiodic long-range order [1]. The absence of the translation invariance can result in the appearance of the five- [2], eight- [3], ten- [4], and twelvefold [5] symmetry axes. There also exist quasicrystal structures with cubic point groups [6, 7].

The aperiodic long-range order of a quasicrystal manifests itself in the appearance of phasons in the excitation spectra. The concept of phasons was first introduced in the studies of the phason contribution to the Debye–Waller factor in neutron diffraction scattering [8] for one class of incommensurate phases—the structures with the charge-density waves [9]. Under certain assumptions, both incommensurate phases and quasicrystals can be described in terms of the atomic (mass) density waves [10]. In distinction from conventional crystals, this formalism in the hydrodynamic limit $\omega\tau \ll 1$ [11, 12] gives rise to $(r - 3)$ new hydrodynamic variables and $(r - 3)$ Goldstone phason modes corresponding to spontaneously broken symmetry of phase shifts [11, 12]. Here $r$ is the maximum number of "rationally independent" reciprocal-lattice vectors of the aperiodic structure or, in the algebraic language, the dimension of the Fourier module.

For incommensurate phases, these excitations make contributions to the elastic properties of systems under study [13, 14]. However, in distinction from, e.g., acoustic phonons with the dispersion law $\omega \sim cq$ (where $\omega$ is the frequency, $c$ is the sonic velocity, and $q$ is the wave-vector length), the phason modes are usually not the propagating but rather the diffusing modes with $\omega \sim iDq^2$ (where $D$ is the diffusion coefficient) [15]. Crystal imperfection and the effects of the lattice discretness can lead to pinning of the modulation wave and formation of a gap in the energy spectrum [16]. This limits the applicability range of the continuum theory [17] dealing only with sliding gapless modes. In terms of crystallography, phasons in an incommensurate phase are characterized by a displacement of the modulation structure providing the formation of satellite reflections on the diffraction pattern, whereas the basic structure provides the formation of the main reflections in the reciprocal space.

Both incommensurate modulated structure [18] and quasicrystal [19] can be obtained in $n$-dimensions by projecting a part of $r$-dimensional periodic lattice onto the $n$-dimensional hyperplane $V^{\parallel}$ along the $(r–n)$-dimensional hyperplane $V^{\perp}$. The $r$-dimensional Euclidean space $V(r)$ is represented as a direct sum of the orthogonal subspaces $V^{\parallel}$ and $V^{\perp}$, i.e., $V(r) = V^{\parallel} \oplus V^{\perp}$. The space $V^{\parallel}$ is called the parallel, physical, or external space, and the space $V^{\perp}$, the perpendicular or internal space. The elastic deformation of a quasicrystal is described by the $r$-dimensional displacement vector $\tilde{u} = u \oplus w$, where $u$ is the $n$-dimensional phonon displacement and $w$ is the $(r - n)$-dimensional phason displacement. Spatially uniform variations of $u$ and $w$ provide no contributions to the free elastic energy, which depends on deformations $\partial_i u_j$ and $\partial_i w_k$, where $j = 1, \ldots, n$; $k = 1, \ldots, r - n$; $\partial_i = \partial/\partial x_i$, $x \equiv \{x_1, \ldots, x_n\}$, $r \in V^{\parallel}$ [20, 21]. Assuming that the elastic energy is an analytical function, the elastic energy is expanded into a series in powers of the deformation-tensor components beginning with the squared terms. The expansion coefficients play the part of elastic moduli. In the case of noncrystallographic point groups, the phonon and the phason variables are transformed by different irreducible representations of the point group of a quasicrystal, whereas in the case of the crystallographic symmetry, they are transformed by the same irreducible representations. This elasticity theory was developed for pen-

1063-7745/00/4502-0187$20.00 

tagonal [22], cubic [23], icosahedral [24] and layered (decagonal, octagonal, and dodecagonal) quasicrystals [24, 25]. For icosahedral and layered quasicrystals, the values of nonlinear third-order elastic constants were determined in [26]. The elastic properties of quasicrystals with two-dimensional quasiperiodicity and noncrystallographic symmetry axes of the order different from the fifth, eighth, tenth, and twelfth order were also studied. Thus, the structures with the seven-, fourteen-, and eighteenfold symmetry axes were obtained by projection from the six-dimensional space. They have two phason branches per one phonon branch [27]. However, it was shown theoretically [28] that, in fact, to obtain such crystals is rather difficult because it is necessary to satisfy the local matching rules.

As is well known, phonons in quasicrystals correspond to the translational displacements and local distortions of the unit cells, whereas phasons correspond to specific rearrangement of unit cells accompanied by discrete atomic hoppings. The topological considerations [29], show that phasons cannot propagate in quasicrystals, whence it becomes clear why they were ignored in the consideration of the acoustic properties of quasicrystals in the absence of absorption [30, 31].

The simplest model of diffraction from an ideal quasicrystal predicts infinitely narrow δ-function-like Bragg maxima [32] corresponding to the correlation length $r_c = \infty$, whereas the real Al–Mn specimens provided the formation of reflections of width $\Delta q = 0.01$ Å$^{-1}$ corresponding to the correlation lengths 100–300 Å [33]. Such small correlation lengths could not be explained by the instrumental factors and the conventional mechanisms of reflection broadening and thus indicated the considerable degree of disorder in the structure. One of the possible explanation of this inconsistency and the interpretation of displacements of maxima from their positions for the ideal structure (which are inversely proportional to their intensities) is the existence of phason deformations, "frozen" into the structure during the preparation of quasicrystalline material [34–36]. Relaxation of such deformations due to diffusion motion of atoms at conventional temperatures occurs very slowly and cannot be completed within the short quenching time of the melt. The distortions observed on electron diffraction patterns were interpreted in terms of frozen phason deformations [37, 38]. The X-ray diffraction method allowed one to evaluate the phason deformations [39, 40]. It was also suggested to consider some phase transformations of the type icosahedral quasicrystal–crystal as certain "lock-in transitions" occurring with lowering of the point symmetry from the icosahedron group to one of its subgroups associated with the phason degree of freedom [41]. In this model, the phason deformation played the role of an order parameter.

The complete experimental studies of specific physical properties of quasicrystals and, in particular, of the phason dynamics can be made only on large pure single quasicrystals. However, the first discovered quasicrystals (Al–Mn and some other quasicrystals, see review [42]) were metastable and could be obtained only by fast cooling. The rate of the temperature lowering attained $10^6$ for spinning [1] and $10^{13}$ K/s for ion-beam mixing [43]. It is clear that under such conditions, no large single-domain specimens could be obtained.

The situation has completely changed with the discovery of the fact that a stable $Al_6Li_3Cu$ quasicrystal can be obtained by slow cooling of the corresponding melt [44]. Then, a thermodynamically stable quasicrystal of the approximate composition $Al_{65}Cu_{20}Fe_{15}$ with a small number of defects of the phason-deformation type was obtained [45].

However, the thermodynamic stability is not the only theoretically and practically important property of the Al–Cu–Fe quasicrystal. It is well known that three-dimensional icosahedral quasicrystals can have a primitive, a body- or a face-centered six-dimensional hypercubic lattice [46] (and, primitive, face and body-centered reciprocal lattice, respectively). Whereas the majority of icosahedral quasicrystals, such as Al–Mn and Al–Ni–Cu, are described with the aid of a primitive hyperlattice and the six-dimensional sp. gr. $P\bar{5}\bar{3}m$, the Al–Cu–Fe quasicrystal has a face-centered (body-centered in the reciprocal space) lattice corresponding to six-dimensional sp. gr. $F\bar{5}\bar{3}m$ [47]. The formation of face-centered structure is attributed to chemical ordering of atoms in the alloy [48] with the formation of the most symmetric superstructure in the primitive lattice [49].

It was also established that an "intermediate product" of the quasicrystal transformation into the crystal in the $Al_{63.5}Cu_{24}Fe_{12.5}$ alloy is an icosahedrally modulated icosahedral phase [50–52]. The present study is devoted to the theory of the elastic properties of such phases with due regard for phasons and new modes (hyperphasons) characteristic of incommensurately modulated quasicrystals. The crystallographic aspects proper are considered only where necessary. We also make some generalizations, providing, in particular, the consideration of the recently discovered two-dimensionally periodic modulation in the Al–Li–Cu quasicrystals [53]. However, it should be emphasized that the development of the general method does not exclude the necessity of analyzing the elastic properties of each of the modulated phases separately. In this article, we deliberately avoid the consideration of dislocations and their effect on the elastic properties. This will be the subject of another article.

## MODULATION AND HYPERPHASONS

We shall call modulated quasicrystals those quasicrystals in which, in addition to the conventional quasiperiodic order in the atomic arrangement, there also exists some periodic or quasiperiodic order with

respect to a certain structural or physical characteristic. Experimentally, the modulation manifests itself in the formation of some additional or satellite reflections that cannot be formed on the diffraction pattern because of the main quasilattice. The set of such satellite reflections factorized using the set of points of the main quasilattice is called either the modulation lattice (if it is characterized by a periodic order) or the quasilattice (if it is characterized by a quasiperiodic order).

Similar to the case of crystals, one can separate the following possible physical mechanisms of modulations. In deformed modulated structures (sometimes also called the structures with the displacive-type modulation), an additional order is formed because of displacements of atoms from their positions in the basic structure. In modulated structures, an additional order can be provided by several factors. (i) The probability function of filling the atomic positions of the basic structures; (ii) in spin modulated structures, an additional order is formed due to spins of one or several atoms; (iii) in the structures with the charge-density waves, the modulation is caused by the ordered distribution of an electric charge and the corresponding atomic displacements, and finally, (iv) in the structures with surface modulations, their source can be flat surfaces that can be either translational surfaces (antiphase and interphase boundaries, stacking faults, and the planes of crystallographic shear, twinning, and their combinations).

A modulated quasicrystal can be considered as an ideal crystal in the following generalized sense. An "ideal crystal" is understood as the distribution of the matter with the Fourier wave vectors expressed as the linear combinations with the integral coefficients (hereafter called for brevity the integral linear combinations) of a finite number of the vectors $s$ with the discrete set of the Bragg maxima which can be indexed by a set $s$ of integers $h_1, h_2, \ldots, h_s$. The number $s$ is called the rank of the generalized ideal crystal. The above definition ignores the diffraction intensities less than a certain threshold value, which allows us to identify and to index the Bragg maxima even in the case where $s$ is higher than the crystal dimension $n$ usually equal to three. In this case, which encompasses incommensurately modulated conventional crystals, quasicrystals, and also modulated quasicrystals, the Bragg maxima densely fill the whole reciprocal space. In other words, any neighborhood of any Bragg maximum contains an infinitely large number of other maxima, but most of them have negligibly low intensities.

The quasicrystal modulation is called incommensurate if the rank $s$ of the modulated quasicrystal exceeds the rank $r$ of an unmodulated quasicrystal; i.e., at least one of the modulation vectors cannot be an integral linear combination of vectors forming the basis of the Fourier module of an unmodulated quasicrystal.

Thus, the discrete set of diffraction vectors of a modulated quasicrystal structure can be uniquely indexed as [54]

$$\mathbf{G} = \sum_{i=1}^{r} h_i \mathbf{k}_i + \sum_{j=1}^{q} m_j \mathbf{q}_j = \mathbf{G}_r + \mathbf{G}_q,$$

where $\{\mathbf{k}_i\}$ is the basis set of independent wave vectors on the ring of the rational numbers, hereafter called for brevity the rationally independent wave vectors, associated with the quasilattice of basic reflections, whereas $\{\mathbf{q}_i\}$ is a set of rationally independent modulation vectors. For the basic reflections, all the $m_j$ have the zero values, $m_j = 0$, whereas for the satellite reflections, at least some $m_j$ have nonzero values, $m_j \neq 0$. The vectors $\mathbf{q}_i$ can be chosen in such a way that for any point-symmetry operation $R$ (in the conventional three-dimensional space) and any diffraction vector $\mathbf{G} = \mathbf{G}_r + \mathbf{G}_q$, the transformed vector $\mathbf{G}' = R\mathbf{G} = \mathbf{G}'_r + \mathbf{G}'_q$ would satisfy the following relationships

$$\mathbf{G}'_r = R\mathbf{G}_r, \quad \mathbf{G}'_q = R\mathbf{G}_q. \tag{1}$$

In accordance with the general principles of multidimensional crystallography, to each modulated quasicrystal of rank $s$ there corresponds an ideally periodic crystal in the $s$-dimensional space.

The point-symmetry operation $R_s(R)$ of such a crystal in the superspace is given by the $s \times s$ matrix which sets the point-symmetry transformation of the diffraction vector $\mathbf{G}$ in terms of its integral $s$ components $(h_i, m_j)$ in the chosen indexing basis.

It follows from (1) that the matrices $R_s$ are reducible and, in the chosen basis $\{\mathbf{k}_i, \mathbf{q}_j\}$, have the block-diagonal form

$$R_s(R) = \begin{pmatrix} R^r & 0 \\ 0 & R^q \end{pmatrix}.$$

Considering a modulated quasicrystal as an ideal crystal in the $s$-dimensional Euclidean space $V(s)$ and the corresponding unmodulated quasicrystal as an ideal crystal in the $r$-dimensional Euclidean space $V(r)$, we can write the elements of the $s$-dimensional space group as $\{R|\mathbf{t}, \mathbf{v}\}$, where $\mathbf{t}$ and $\mathbf{v}$ are the constraints of the translation symmetry transformations of the space $V(s)$ imposed onto the space $V(r)$ and its orthogonal complement $V(q)$ such that $V(s) = V(r) \oplus V(q)$.

The multiplication law for this group has the form

$$\{R_2|\mathbf{t}_2, \mathbf{v}_2\}\{R_1|\mathbf{t}_1, \mathbf{v}_1\}$$
$$= \{R_2R_1|R^r(R_2)\mathbf{t}_1 + \mathbf{t}_2,\ R^q(R_2)\mathbf{v}_1 + \mathbf{v}_2\}.$$

In other words, a modulated quasicrystal can be characterized by a pair of groups $\{R^r|\mathbf{t}\}$ and $\{R^q|\mathbf{v}\}$ (of super-

space symmetry whose operations are defined in the spaces $V(r)$ and $V(q)$, respectively).

An alternative approach based on the superspace symmetry consists in the description of quasicrystals in terms of the generalized (color) symmetry. Earlier, this approach was used for ideal unmodulated quasicrystals [55, 56]. Within this approach, a modulated quasicrystal can be characterized by a pair of color groups $\Phi(n)^{W_p(r-n)}$ and $\Phi(m)^{W_p(q-m)}$ for an incommensurately modulated quasicrystal with the quasiperiodic modulation and by a pair consisting of the generalized group $\Phi(n)^{W_p(r-n)}$ and the conventional space group $\Phi(m)$ for a periodically modulated quasicrystal. Here, $n$ is the conventional physical dimension of a quasicrystal, and $m$ is the dimension of the modulation, i.e., the number of space dimensions along which modulations are observed. The analysis performed in [55, 56] shows that these groups are isomorphic to the groups introduced above, which are, generally speaking, superspace groups. Thus, for a quasiperiodically modulated quasicrystal, we have the following isomorphic correspondences

$$\Phi(n)^{W_p(r-n)} \longleftrightarrow \{\{R^r|\mathbf{t}\}\},$$
$$\Phi(m)^{W_p(q-m)} \longleftrightarrow \{\{R^q|\mathbf{v}\}\}.$$

In crystallography, one traditionally uses two methods for the analysis of the hydrodynamic modes (long-wavelength excitations introducing a certain contribution to the elastic energy) [20]—the phenomenological Landau method of the mass-density waves and a more detailed crystallographic method of generalized unit cells.

In the density-wave formalism, the mass density $\rho(\mathbf{r})$ of an ordered solid is expanded into a Fourier series

$$\rho(\mathbf{r}) = \sum_{\mathbf{G} \in L_R} \rho_{\mathbf{G}} \exp(i\mathbf{G}\mathbf{r}),$$

where $\mathbf{G}$ is the reciprocal-lattice vector and $L_R$ is the reciprocal lattice. Each factor $\rho_{\mathbf{G}}$ is a complex number with the amplitude $|\rho_{\mathbf{G}}|$ and the phase $\phi_{\mathbf{G}}$. Since $\rho(\mathbf{r})$ is real and $\rho_{\mathbf{G}} = \rho_{-\mathbf{G}}$, then also $\phi_{\mathbf{G}} = \phi_{-\mathbf{G}}$. The free energy of the ordered phase can be expanded into a Landau series with the $k$th term in the form [20]

$$F^{(k)} = A_k \sum_{n1, n2, \ldots, nk} \int d\mathbf{r} \rho_{\mathbf{G}_{n1}} \rho \mathbf{G}_{n2} \ldots \rho \mathbf{G}_{nk} \exp\left(\sum_{i=1}^{k} \mathbf{G}_{ni}\mathbf{r}\right) \quad (2)$$
$$= VA_k \sum_{n1, n2, \ldots, nk} \Delta\left(\sum_{i=1}^{k} \mathbf{G}_{ni}\right) \cos\left(\sum_{i=1}^{k} \phi G_{ni}\right) \prod_{i=1}^{k} |\rho \mathbf{G}_{ni}|,$$

where $V$ is the specimen volume. The factor $\Delta(x) \equiv \delta_{x,0}$ shows that only the terms with $\sum_{n=1}^{k} \mathbf{G}_n = 0$ can give the contribution into the sum in equation (2). The free-energy expansion is phenomenological in the sense that the coefficients $A_k$ depend on the characteristics of the physical system (kind of the constituent atoms, atomic interactions, temperature, pressure, etc.). The equilibrium ordered state is characterized by $\rho_{\mathbf{G}}$ values which minimize $F$. The description in terms of the density waves requires the determination of certain common general properties of the ordered states dependent on the symmerties and the conservation laws but independent of the choice of $A_k$. Thus, it is sufficient to consider a small finite subset $\{\rho_{\mathbf{G}_n}\}$ of the Fourier components of $\rho_{\mathbf{G}}$. The set $\{\rho_{\mathbf{G}_n}\}$ should include the minimum set of $\rho_{\mathbf{G}}$ corresponding to such $N_R$ vectors of the reciprocal space $\mathbf{G}_n$ that any reciprocal-lattice vector $\mathbf{G} \in L_R$ can be written as a integral linear combination $\mathbf{G}_n$. The set $\{\rho_{\mathbf{G}_n}\}$ should include the inversion images $\{\rho_{-\mathbf{G}_n}\}$ (in order to provide the real values of the mass density upon summing over all the waves), plus all the vectors that can be derived from this minimum set using the transformations of the point-symmetry group of a solid.

The minimization of $F$ with respect to $|\rho_{\mathbf{G}}|$ and $\phi_{\mathbf{G}}$ fixes all the variables except of $N_R$ phases. It follows from (2) that for any set $\mathbf{G}_n$ satisfying the conditions $\sum \mathbf{G}_n = 0$, the $F$ value depends on the value of $\sum \phi_{\mathbf{G}_n}$.

Since homogeneous shifts over $N_R$ phases do not affect $F$, they correspond to the theoretical hydrodynamic variables. The homogeneous phase shifts $\phi_{\mathbf{G}_n}$, which change the sums of the phases, also change the energy.

In a modulated quasicrystal, $N_R = s$. Within the ideal model considered here, to a spontaneous break of any of $N_R$ continuous phase symmetries there corresponds a Goldstone gapless mode. Taking into account that the number of analogous modes for an ideal unmodulated quasicrystal equals $r$, we arrive at the conclusion that incommensurately modulated quasicrystals should additionally possess $q = s - r$ excited states in comparison with their unmodulated analogues. Hereafter, these new hydrodynamic modes are called hyperphasons.

Consider some experimental examples. In an $Al_{63.5}Cu_{24}Fe_{12.5}$ quasicrystal, the structure with the temperature-dependent displacive-type modulation is formed as an intermediate phase upon the phase transition from the icosahedral quasicrystal into a rhombohedral crystal [50–52]. Each basic Bragg maximum had twelve satellite reflections located along the fivefold axes. Within the above scheme based on the detailed experimental diffraction data, this structure can be

brought into correspondence with the twelve-dimensional group

$$(H_r, H_q) = (F\bar{5}\bar{3}m, P\bar{5}\bar{3}m).$$

In terms of mass-density waves, we can draw a conclusion that the number of the degrees of freedom of the degeneracy parameter $\phi$ and, therefore, the number $q$ of new hydrodynamic modes (hyperphasons) should be six. In an Al–Li–Cu quasicrystal, a periodic two-dimensional surface deformation modulation was observed [53], which can be fully defined by two reciprocal-lattice vectors. Thus, in this case, $q = 2$.

For a quasiperiodic incommensurate modulation, the $q$-dimensional representation $\Gamma_{(q)}$ of the rotation subgroup $R^q$ of the $q$-dimensional space group $\{R^q|\mathbf{v}\}$ can be represented as a direct sum of irreducible representations

$$\Gamma_{(q)} = \Gamma_{(m)} \oplus \Gamma_{(q-m)}. \quad (3)$$

In view of the results obtained in [28], the right-hand side of (3) can hardly include three or more direct terms.

Then $q$ new phase hydrodynamic degrees of freedom can be parametrized by an $m$-dimensional vector $v^\mu$ and the $(q - m)$-dimensional vector $v^w$, which are transformed according to irreducible representations $\Gamma_{(m)}$ and $\Gamma_{(q-m)}$, respectively. The excited states of a modulated quasicrystal described with the aid of the components of the vector $v^\mu$ are, hereafter, called phonon-type hyperphasons, whereas the excitations described by the components of the vector $v^w$, the phason-type hyperphasons.

Although the method of density waves allows the reliable identification of the hydrodynamic degrees of freedom, a more detailed crystallographic description is achieved by the method of generalized unit cells.

Consider an integral linear shell $\mathbf{G}_q = \sum_{j=1}^{q} m_j \mathbf{q}_j$ of the basis vectors of the modulation $\mathbf{q}_1, \ldots, \mathbf{q}_q$, which, in terms of algebra, is one of the elements of the factor-module of the Fourier module of the modulated quasicrystal by the Fourier module of an unmodulated quasicrystal (in particular, corresponding to the zero vector). If among $\{\mathbf{q}_i\}$ vectors, $m$ are linearly independent above the field of real numbers, one can choose the finite number of $m$-dimensional polyhedra with the vertices located at the points corresponding to the satellite reflections of the same main reflection, in such a way that these polyhedra would tile the whole $m$-dimensional space without empty spaces and overlaps. These polyhedra are selected in such a way that they cannot be divided into smaller ones that would fully tile the above indicated space. These polyhedra are called the generalized unit cells of the modulation quasilattice. The rule according to which the generalized unit cells tile the space are called the modulation matching rules.

Proceeding from the general principles of describing the quasicrystal structures in terms of the generalized unit cells [20], we can state that the setting of the point symmetry and the unit-cell shape is insufficient for the unique space tiling. There exist an infinite number of sets of generalized unit cells whose diffraction patterns are determined by the same sets of the reciprocal-lattice vectors, but have different intensities of the Bragg maxima. These tiling patterns can be distributed over the classes of local isomorphism (LI) in such a way that two tiling patterns belong to the same class of local isomorphism if and only if each limited unit-cell configuration of one tiling pattern can also be found in another tiling pattern. Two tiling patterns belong to the same class if these patterns provide the same results irrespectively of the number of measurements on finite samples. Thus, tiling patterns belonging to the same LI class are physically in distinguishable and have the identical diffraction properties, including the reflection intensities. The configurations belonging to the same LI class are characterized by the same density of the free energy $F$, whereas the tiling patterns belonging to different LI classes would have different densities of free energies $F$ in all the cases except of the cases of random degeneracy.

Consider a quasicrystal with the quasiperiodic incommensurate modulation. To the uniform increments in phonon-type hyperphason variable there correspond pure translations of the modulation quasilattice. The space variations of the parameter $v^\mu$ lead to the deformation of the generalized unit cells of the modulation but do not change the configuration of the set of unit cells forming the tiling pattern. In a similar way, repeating the reasoning used earlier in the consideration of quasilattices of ideal unmodulated quasicrystals also for the (factorized) modulation quasilattice, we arrive at the conclusion that the uniform increments to the variable $v^w$ should not lead to any translation displacements and deformations of the generalized unit cells of the modulation quasilattice. Such increments only lead to specific rearrangements of the tiles (polyhedra) of the tiling pattern and thus transform it into another tiling within the given LI class. The spatial variations of $v^w$ are associated with the transition from one LI class to another and are accompanied by the violation of the matching rules in different regions of the tiling.

It should be noted that for a periodic incommensurate modulation, the set of satellite reflections of a basic reflection is characterized by the translation invariance. As was to be expected, in the transition to the quasiperiodic (in the rigorous sense of the word) modulated quasicrystals, this invariance is lost. However, it can be restored in a certain generalized sense [56] if the translations are complemented with some compensating local transformations in such a way that the compositions of the translations and these generalized transformations bring the modulated structure into coincidence

with itself. These transformations are the transformations of the generalized (color) symmetry of the modulation, which physically correspond to the rearrangement in the structure possible within the given class of the local modulation or, which is the same, to the degeneracy of elastic free energy over the phason-type hyperphason variables.

Above, we considered new hyperphason modes introduced on within the approach of multidimensional crystallography and superspatial symmetry. However, this approach is not the only possible method of describing aperiodic crystal structures. One of the alternatives is the description and the classification of the quasicrystal symmetry groups in the three-dimensional space in terms of the symmetries of the quasicrystal reciprocal space bringing the Fourier-expansion of the density function into coincidence with itself. Although the latter approach has a number of common features with the one used above for the phenomenological identification of hyperphason modes, it should rather be used to classify of the space groups of unexcited states.

The already mentioned color-symmetry approach was used to describe optical phonons in the consideration of the spectrum of elementary excitations of the multiatomic sodium chloride-type crystals [57]. The generalization of this approach would allow one to describe the phason modes in incommensurately modulated crystals and quasicrystals. Nebola *et al.* [57] considered not only the translational space symmetry transformations that bring a sodium chloride crystal into itself, but also the transformations of the generalized symmetry. This allowed them to take into account all the symmetry details of a multiatomic lattice. Nebola *et al.* introduced a new variable, which took the values of the atom mass at the given point and thus having two different values for the diatomic crystal. Then, it became possible to introduce an operation of the generalized symmetry, which is the composition of the spatial translation and the change in the mass value. New symmetry transformations are related, in the most natural way, to the optical phonon model. Thus, the translation symmetry of a quasicrystal lost in the transition to quasiperiodicity can be restored in the generalized sense as the composition of a translation for a certain vector and the compensating local transformation of an inflation–deflation type. These transformations can be related to phason modes. This approach seems to be most efficient for the symmetry analysis of the microscopic mechanisms of the physical properties associated with the details of the phason spectrum. However, at the macroscopic level, one can limit the consideration to the traditional point group, because if one ignores the details of the quasicrystal structure, the color symmetry group can be transformed into this point group.

## HYPERPHASON CONTRIBUTION TO ELASTICITY

Similar to phasons, the hyperphason-type long-wavelength excitations can sometimes be described in the continuum approximation with the aid of the continuously changing (in the space) variables whose gradients influence the elastic free energy.

In the linear approximation with due regard for the hyperphason modes, the elastic free energy of a modulated quasicrystal has the form

$$F(u_{ij}, \partial_j w_i, \partial_j v_i^u, \partial_j v_i^w) = F_0 + F_m,$$

where the elastic energy of an unmodulated quasicrystal equals

$$F_0(u, w) = (1/2)C_{ijkl}^{uu}u_{ij}u_{kl} + (1/2)C_{ijkl}^{ww}\partial_j w_i \partial_l w_k + (1/2)C_{ijkl}^{uw}u_{ij}\partial_l w_k + (1/2)C_{ijkl}^{wu}\partial_j w_i u_{kl},$$

where $C_{ijkl}^{uu} = (\partial^2 F/\partial u_{ij}\partial u_{kl})_0$ are stiffness constants of the classical elasticity theory obeying the relationships

$$C_{ijkl}^{uu} = C_{klij}^{uu} = C_{jikl}^{uu} = C_{ijlk}^{uu}, \text{ and}$$
$$C_{ijkl}^{ww} = (\partial^2 F/\partial(\partial_j w_i)\partial(\partial_l w_k))_0$$

are the phason-elasticity constants symmetric with respect to the permutation of the pairs of indices

$$C_{ijkl}^{ww} = C_{klij}^{ww}, \text{ and } C_{ijkl}^{uw} = (\partial^2 F/\partial u_{ij}\partial(\partial_l w_k))_0$$
$$\text{and } C_{ijkl}^{wu} = (\partial^2 F/\partial(\partial_j w_i)\partial u_{kl})_0$$

are the elastic constants associated with the phonon–phason interactions.

It is clear that

$$C_{ijkl}^{uw} = C_{jikl}^{uw}, \quad C_{ijkl}^{wu} = C_{ijlk}^{wu}, \quad C_{klij}^{wu} = C_{ijkl}^{uw},$$

but at the same time

$$C_{ijkl}^{uw} \neq C_{klij}^{uw}, \quad C_{ijkl}^{wu} \neq C_{jikl}^{wu}.$$

The modulation contribution to the free energy is given by the expression

$$F_m = F_{m1} + F_{m2},$$

where the contribution linear with respect to the hyperphason distortions is

$$F_{m1} = \frac{1}{2}C_{ijkl}^{uv^u}u_{ij}\partial_l v_k^u + \frac{1}{2}C_{ijkl}^{v^u u}\partial_j v_i^u u_{kl} + \frac{1}{2}C_{ijkl}^{uv^w}u_{ij}\partial_l v_k^w + \frac{1}{2}C_{ijkl}^{v^w u}\partial_j v_i^w u_{kl} + \frac{1}{2}C_{ijkl}^{wv^u}\partial_j w_i \partial_l v_k^u + \frac{1}{2}C_{ijkl}^{v^u w}\partial_j v_i^u \partial_l w_k + \frac{1}{2}C_{ijkl}^{wv^w}\partial_j w_i \partial_l v_k^w + \frac{1}{2}C_{ijkl}^{v^w w}\partial_j v_i^w \partial_l w_k,$$

and the term quadratic with respect to the hyperphason

distortions is given by the expression

$$F_{m2} = \frac{1}{2}C_{ijkl}^{v^u v^u}\partial_j v_i^u \partial_l v_k^w + \frac{1}{2}C_{ijkl}^{v^u v^w}\partial_j v_i^u \partial_l v_k^w + \frac{1}{2}C_{ijkl}^{v^w v^u}\partial_j v_i^w \partial_l v_k^u + \frac{1}{2}C_{ijkl}^{v^w v^w}\partial_j v_i^w \partial_l v_k^w.$$

The above expressions include the constants of hyperphason elasticity

$$C_{ijkl}^{uv^u} = (\partial^2 F/\partial u_{ij}\partial(\partial_l v_k^u))_0 \text{ and}$$

$$C_{ijkl}^{v^u u} = (\partial^2 F/\partial(\partial_j v_i^u)\partial u_{kl})_0,$$

which are the elastic moduli associated with the phonon-type phonon–hyperphason interactions typical of a modulated quasicrystal. Hereafter, these moduli are referred to as phonon-type phonon–hyperphason elastic constants.

In a similar way, we can also introduce the constants of the phason–phonon-type hyperphason–hyperphason elasticity

$$C_{ijkl}^{uv^w} = (\partial^2 F/\partial u_{ij}\partial(\partial_l v_k^w))_0 \text{ and}$$

$$C_{ijkl}^{v^w u} = (\partial^2 F/\partial(\partial_j v_i^w)\partial u_{kl})_0,$$

the phonon-type phason–hyperphason elasticity

$$C_{ijkl}^{wv^u} = (\partial^2 F/\partial(\partial_j w_i)\partial(\partial_l v_k^u))_0$$

$$\text{and } C_{ijkl}^{v^u w} = (\partial^2 F/\partial(\partial_j v_i^u)\partial(\partial_l w_k))_0,$$

the phason-type phason–hyperphason elasticity

$$C_{ijkl}^{wv^w} = (\partial^2 F/\partial(\partial_j w_i)\partial(\partial_l v_k^w))_0 \text{ and}$$

$$C_{ijkl}^{v^w w} = (\partial^2 F/\partial(\partial_j v_i^w)\partial(\partial_l w_k))_0,$$

the phonon–phonon-type hyperphason–hyperphason elasticity

$$C_{ijkl}^{v^u v^u} = (\partial^2 F/\partial(\partial_j v_i^u)\partial(\partial_l v_k^u))_0,$$

the phonon–phason-type hyperphason–hyperphason elasticity

$$C_{ijkl}^{v^w v^u} = (\partial^2 F/\partial(\partial_j v_i^w)\partial(\partial_l v_k^u))_0,$$

the phason–phonon-type hyperphason–hyperphason elasticity

$$C_{ijkl}^{v^w v^w} = (\partial^2 F/\partial(\partial_j v_i^w)\partial(\partial_l v_k^w))_0.$$

Of course, one has to take into account the symmetry of each concrete modeled quasicrystal. Thus, for the already mentioned modulated Al–Cu–Fe phase, the components of the vector $v^u$ (similar to the components of the vector $u$) are transformed according to the three-dimensional irreducible representation $\Gamma_3$ of the symmetry group of an icosahedron, whereas the components of the vector $v^w$ (similar to the components of the vector $w$), are transformed according to another three-dimensional irreducible representation $\Gamma_{3'}$ of the same group. Taking into account that the components of the gradient vector are transformed according to the representation $\Gamma_3$, one can establish the laws of transformation for the components of the hyperphason elasticity tensors. Thus, $C_{ijkl}^{uv^w}$ is transformed according to $\Gamma_3 \otimes \Gamma_3 \otimes \Gamma_3 \otimes \Gamma_{3'}$. Knowing the laws of the transformations of the components of the hyperphason elasticity tensors, one can determine the nonzero components by taking into account the point symmetry. Omitting the long list of the nonzero components of hyperphason elastic constants for this case, we only indicate here the number of independent components. This number equals unity for $uv^w$, $wv^u$, and $v^u v^w$, and two for $uv^u$, $wv^w$, $v^u v^u$, and $v^w v^w$. It should be indicated that for the most often encountered weak modulation (observed experimentally in $Al_{63.5}Cu_{24}Fe_{12.5}$), the contribution to the elastic energy, which is quadratic with respect to the hyperphason variables, can be ignored.

In another experimental example, Al–Li–Cu, the experimentally observed modulation breaks the point symmetry of the initial structure. However, the allowance for the fact that the modulated structure is formed as a result of the phase transition and exists only in a narrow temperature range in the vicinity of the transformation point, one can use the ideology of the Landau theory and assume that in this case, the spontaneous break of the symmetry manifests itself in the fact that the newly formed physical states (hyperphason modes) break the symmetry of a quasicrystal, however the elastic energy (Hamiltonian) of the quasicrystal is transformed according the irreducible representations of the highly symmetric icosahedral group. The Frenkel–Kontorova model used earlier to describe incommensurate phases in crystals was extended to the Fibonacci chains [58]. It was shown that the above continuum description of hyperphasons is also applicable at low values of the potential of interaction between the basic structure and a modulation wave. At higher values of this potential, hyperphasons are pinned at the potential barrier, the energy changes in jumpwise manner, and the continuum approximation becomes invalid.

In conclusion, we should like to indicate that, proceeding from the general considerations and, in particular, from the analysis of modulated phases in crystals, one can predict that the hyperphasons contribution to elasticity of a modulated quasicrystal would be small and the existence of hyperphasons in the spectrum would determine certain specific features of the physical behavior of the system. In some situations, these specific features can be analyzed, e.g., by considering hyperphason excitations as the soft modes corresponding to the phase transformation of an ideal quasicrystalline phase into a modulated one.

## ACKNOWLEDGMENTS

I am grateful to V.A. Koptsik for his constant interest in this study and valuable remarks.

## REFERENCES


1. D. Levine and P. J. Steinhardt, Phys. Rev. Lett. **53**, 2477 (1984).
2. D. Shechtman, I. Blech, D. Gratias, *et al.*, Phys. Rev. Lett. **53**, 1951 (1984).
3. N. Wang. H. Chen, and K.H. Kuo, Phys. Rev. Lett. **59**, 1010 (1987).
4. L. A. Bendersky, Phys. Rev. Lett. **55**, 1461 (1985).
5. T. Ihimasa, H. U. Nissen, and Y. Fukano, Phys. Rev. Lett. **55**, 511 (1984).
6. R. Wang, C. Qin, G. Lu, *et al.*, Acta Crystallogr., Sect. A: Found. Crystallogr. **50**, 366 (1994).
7. P. Donnadieu, M. Harmelin, H.-L. Su, *et al.*, Z. Metallkd. **88**, 33 (1997).
8. A. W. Overhauser, Phys. Rev. B: Solid State **3**, 3173 (1971).
9. T. Janssen and A. Janner, Adv. Chem. Phys. **36**, 519 (1987).
10. P. Bak, Phys. Rev. B: Condens. Matter **32**, 5764 (1985).
11. P. S. Martin, O. Parodi, and P. S. Pershan, Phys. Rev. A **6**, 2401 (1972).
12. D. Forster, *Hydrodynamic Fluctuations, Broken Symmetry, and Correlation Functions*, Ed. by W. A. Benjamin (Reading, Mass. 1975; Atomizdat, Moscow, 1980).
13. J. D. Axe and P. Bak, Phys. Rev. B: Condens. Matter **26**, 4963 (1982).
14. H. Brand and P. Bak, Phys. Rev. A **27**, 1062 (1983).
15. R. Zeyler and W. Finger, Phys. Rev. Lett. **49**, 1833 (1982).
16. G. Papavassiliou, A. Anagnostopoulos, F. Milia, *et al.*, Phys. Rev. B: Condens. Matter **44**, 7283 (1991).
17. R. A. Cowley and A. D. Bruce, J. Phys. C: Solid State Phys. **11**, 3577 (1978).
18. A. Janner and T. Janssen, Phys. Rev. B: Solid State **15**, 643 (1977).
19. A. Katz and M. Duneau, J. Phys. (Paris) **47**, 181 (1986).
20. J. E. S. Socolar, T. C. Lubensky, and P. J. Steinhardt, Phys. Rev. B: Condens. Matter **34**, 3345 (1986).
21. T. C. Lubensky, in *Aperiodicity and Order* (Academic, Boston, 1988), Vol. 1, p. 199.
22. P. De and R. A. Pelcovitz, Phys. Rev. B: Condens. Matter **35**, 8609 (1987).
23. W. Yang, R. Wang, D. Ding, *et al.*, Phys. Rev. B: Condens. Matter **48**, 6999 (1993).
24. D. Ding, W. Yang, C. Hu, *et al.*, Phys. Rev. B: Condens. Matter **48**, 7003 (1993).
25. J. E. S. Socolar, Phys. Rev. B: Condens. Matter **39**, 10519 (1989).
26. W. Yang, D. Ding, C. Hu, *et al.*, Phys. Rev. B: Condens. Matter **49**, 12656 (1994).
27. W. Yang, R. Wang, D. Ding, *et al.*, J. Phys.: Condens. Matter **7**, 7099 (1995).
28. L. S. Levitov, Zh. Éksp. Teor. Fiz. **93**, 1832 (1987).
29. D. M. Frenkel, C. L. Henley, and E. D. Siggia, Phys. Rev. B: Condens. Matter **34**, 3649 (1986).
30. S. Y. Goshen and J. L. Birman, J. Phys. (Paris) **4**, 1077 (1994).
31. O. A. Belyaev and V. A. Koptsik, Kristallografiya **42**, 225 (1997) [Crystallogr. Rep. **42**, 188 (1997)].
32. V. Elser, Phys. Rev. B: Condens. Matter **32**, 4892 (1985).
33. P. A. Bancel, P. A. Heiney, P. W. Stephens, *et al.*, Phys. Rev. Lett. **54**, 2422 (1985).
34. T. C. Lubensky, J. E. S. Socolar, P. J. Steinhardt, *et al.*, Phys. Rev. Lett. **57**, 1440 (1986).
35. P. M. Horn, W. Malzfeldt, and D. P. DiVincenzo, Phys. Rev. Lett. **57**, 1444 (1986).
36. J. E. S. Socolar and D. C.Wright, Phys. Rev. Lett. **59**, 221 (1987).
37. K. Hiraga and M. J. Hirabayashi, J. Electron Microsc. **36**, 353 (1987).
38. K. Hiraga, *Quasicrystals. The State of the Art*, Ed. by D. P. DiVincenzo and P. J. Steinhardt (World Scientific, Singapore, 1991).
39. J. D. Budai, J. Z. Tischler, A. Habenschuss, *et al.*, Phys. Rev. Lett. **58**, 2304 (1987).
40. D. C. Follstaedt and J. A. Knapp, J. Mater. Res. **4**, 1398 (1989).
41. Y. Ishii, Phys. Rev. B **39**, 11862 (1989).
42. R. J. Shaefer, and L. A. Bendersky, in *Aperiodicity and Order* (Academic, Boston, 1988), Vol. 1, p. 143.
43. J. Tartas and E. J. Knystautas, J. Mater. Sci. **29**, 6011 (1994).
44. B. Dubost, J. M. Lang, M. Tanaka, *et al.*, Nature (London) **324**, 48 (1986).
45. A. P. Tsai, A. Inoue, and T. Matsumoto, Jpn. J. Appl. Phys. **26**, 1505 (1987).
46. N. D. Mermin and D. C. Wright, Phys. Rev. B: Condens. Matter **35**, 5487 (1987).
47. M. Cornier-Quiquandon, A. Quivy, E. Elkaim, *et al.*, Phys. Rev. B: Condens. Matter **44**, 2071 (1991).
48. S. Ebalard and F. Spaepen, J. Mater. Res. **5**, 62 (1990).
49. J. Devaud-Rzepski, A. Quivy, Y. Calvayrac, *et al.*, Philos. Mag. B **60**, 855 (1989).
50. C. Janot, M. Audier, and M. De Boissieu, Europhys. Lett. **14**, 355 (1991).
51. M. Audier, Y. Bréchet, M. De Boissieu, *et al.*, Philos. Mag. B **63**, 1375 (1991).
52. N. Menguy, M. De Boissieu, P. Guyot, *et al.*, J. Phys. (Paris) **3**, 1953 (1993).
53. D. P. Yu and Z. Zhang, Philos. Mag. A **73**, 499 (1996).
54. J. M. Pérez-Mato and L. Elcoro, J. Phys. (Paris) **4**, 1341 (1994).
55. V. A. Koptsik, Comput. Math. Applic. **16**, 407 (1988).
56. V. A. Koptsik, in *Proceedings of the XVIII International Colloquium, Moscow, USSR 1990*, Ed. by V. V. Dodonov and V. I. Man'ko (Springer, Berlin, 1991), p. 588.
57. I. I. Nebola, N. R. Kharkhalis, and V. A. Koptsik, Fiz. Tverd. Tela (Leningrad) **29**, 3223 (1987).
58. O. A. Belyaev, Kristallografiya **43**, 398 (1998) [Crystallogr. Rep. **43**, 360 (1998).


*Translated by L. Man*

*Crystallography Reports, Vol. 45, No. 2, 2000, pp. 195–198. Translated from Kristallografiya, Vol. 45, No. 2, 2000, pp. 227–230.*




# Reliability of Maximum Likelihood-Based Figures of Merit

**T. P. Skovoroda and V. Yu. Lunin**

*Institute of Mathematical Problems of Biology, Russian Academy of Sciences, Pushchino, Moscow oblast, 142292 Russia*

Received February 19, 1997; in final form, February 3, 1998

**Abstract**—Various schemes for determining the maximum likelihood-based figures of merit for phases of structure factors have been considered. It is shown that the use of the likelihood function of all the available structure factors provides the adequate estimates of the accuracy of phases calculated for the atomic models with independent errors in the coordinates, but, at the same time, systematically overestimates the figures of merit for models preliminarily refined in the reciprocal space. It is shown that the use of the marginal likelihood function calculated from the control set of reflections allows the elimination of the systematic bias estimates. A method for reducing the statistical dispersion of the estimates based on a small number of control reflections is suggested. © *2000 MAIK "Nauka/Interperiodica".*

## INTRODUCTION

In crystallography of macromolecules, the Fourier maps of electron density are often calculated with the use of the coefficients

$$m_{\mathbf{s}} F_{\mathbf{s}}^{obs} \exp(i\varphi_{\mathbf{s}}^{mod}), \qquad (1)$$

where **s** is the reciprocal-lattice point, $F_{\mathbf{s}}^{obs}$ is the experimentally determined structure-factor modulus, and $\varphi_{\mathbf{s}}^{mod}$ is the structure-factor phase calculated for a certain preliminarily chosen atomic model of the structure. The weighting factor $m_{\mathbf{s}}$ (the so-called figure of merit of the phase determination) is introduced to compensate possible errors in the Fourier coefficient caused by the discrepancy between the experimentally determined phase $\varphi_{\mathbf{s}}^{mod}$ and the true phase $\varphi_{\mathbf{s}}^{true}$. The probabilistic assumptions about the accidental nature of the errors in the preliminary atomic model of the structure allow one to determine the weights $m_{\mathbf{s}}$ as the mathematical expectations of the quantities $\cos(\varphi_{\mathbf{s}}^{true} - \varphi_{\mathbf{s}}^{mod})$ [1] and lead to the widely used formula

$$m_{\mathbf{s}} = \Lambda(t_{\mathbf{s}} F_{\mathbf{s}}^{obs} F_{\mathbf{s}}^{mod}/\varepsilon_{\mathbf{s}}), \qquad (2)$$

where the function $\Lambda(x)$ is either the hyperbolic tangent (for centrosymmetric reflections) or the ratio of the modified Bessel functions $I_1(2x)/I_0(2x)$ (for the noncentrosymmetric ones), $F_{\mathbf{s}}^{mod}$ is the structure-factor modulus calculated for the preliminarily model, and $\varepsilon_{\mathbf{s}}$ is the coefficient compensating the differences between the average intensities of reflections of various types. The parameter $t_{\mathbf{s}}$ in (2) reflects the errors made in the construction of the preliminary model. The correct estimate of this error (i.e., the estimate of the adequacy of the preliminary model) is the key factor in the determination of the weights $m_{\mathbf{s}}$.

On the average, the "appropriately calculated" weights $m_{\mathbf{s}}$ should correspond (be close) to the real values of $\cos(\varphi_{\mathbf{s}}^{true} - \varphi_{\mathbf{s}}^{mod})$. The degree of this correspondence can be checked in some test situations; i.e., in the situations where, in addition to the preliminary model, one also uses sufficiently reliable "sought" atomic structure such that the phases determined for this structure can be assumed to be the true ones. Such a test performed by Read [2] showed that many of the procedures suggested earlier for calculating the parameters $t_{\mathbf{s}}$ yielded unrealistic figures of merits, and that the best results are obtained within the maximum likelihood approach [2–5]. However, as was indicated in [2–5], the use of this approach gives rise to some difficulties in the work with the preliminary models subjected earlier to crystallographic refinement. Below, we analyze some modifications of this method that allow one to obtain the realistic figure of merits for the phases calculated for the preliminarily refined atomic models.

The tests were performed on the experimental data for Protein *G* (sp. gr. $P2_12_12_1$, the unit cell dimensions $34.9 \times 40.3 \times 42.2$ Å) with the known atomic structure determined at a high resolution.

The refinement of the test preliminary models was performed with the use of the FROG complex of programs [6], the maximum likelihood-based estimates (the ML estimates) and the estimates based on the maximization of the marginal likelihood function (the MML estimates) and the LBEST program [7] specially

1063-7745/00/4502-0195$20.00 © 2000 MAIK "Nauka/Interperiodica"

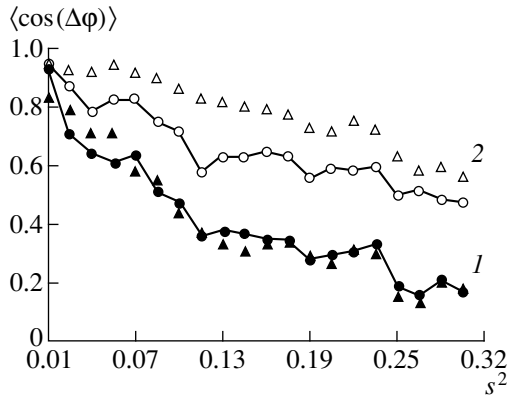


**Fig. 1.** Cosines of phase errors predicted from ML estimates (triangles) and the real values (circles) for (*1*) the model with independent errors in the atomic coordinates and (*2*) for the same model upon 12 cycles of its refinement in the reciprocal space.

designed in this study in accordance with the method considered elsewhere [3, 5].

## ML-ESTIMATES OF THE PARAMETERS OF PROBABILITY DISTRIBUTIONS

The essence of the probabilistic approach to the estimation of the errors in the phases [8–10] is the allowance for the additional information about the object under study in the form of a statistical hypothesis on the character of error distribution in the preliminary model. The simplest and the most rigorous variant of this hypothesis reduces to the assumption that all the errors are reduced to the errors in the atomic coordinates and that they are independent and distributed according to the normal law with the nonzero mean and the same dispersions (more complicated examples were considered in [5, 7, 11]). Similar hypotheses allow one to consider the values of the structure factors as random quantities and obtain the expressions for their probability distributions. The resulting distributions for a large class of initial hypotheses are described by the same formula,

$$P(F_s, \varphi_s) \propto F_s \exp\{-|F_s \exp(i\varphi_s) - \alpha_s F_s^{mod} \exp(i\varphi_s^{mod})|^2/\varepsilon_s\beta_s\} \quad (3)$$

and differ only by the form of the functional dependences of $\alpha_s$ and $\beta_s$ on the parameters describing the error distribution in the atomic model. Therefore, there is no need to fix any concrete hypothesis about the atomic model. We proceed from the assumption that the probability distribution for a structure factor is described by formula (3) with certain parameters $\alpha_s$ and $\beta_s$. The mathematical expectation of the cosine of the phase error in this case is given by formula (2) with $t_s = \alpha_s/\beta_s$. Thus, we arrive at one of the standard problems of the mathematical statistics—the problem of selection of the distribution from class (3) or the problem of estimating the parameters $\alpha_s$ and $\beta_s$.

The maximum likelihood-based methods of estimating the $\alpha_s$ and $\beta_s$ parameters were described elsewhere [2–5]. The method reduces to the following. The estimates of the $\alpha_s$ and $\beta_s$ quantities for a thin spherical layer of the reciprocal space are taken to be the constants maximizing the probability of coincidence of the structure-factor moduli distributed according law (3) and the $\{F_s^{obs}\}$ values obtained in the real experiment.

## ESTIMATES OF FIGURES OF MERITS

Within the framework of the approach used, the figures of merits calculated by formula (2) are also random quantities possessing all the characteristics typical of random quantities. One of the most important statistical characteristics of such estimates is the bias—the deviation of the expected value of the estimate from its true value. Another important characteristic is the expected root-mean-square deviation of the estimate from its true value (the estimate dispersion).

The first run of the tests was devoted to the study of the bias of the figure of merit calculated from ML estimates for the $\alpha_s$ and $\beta_s$ parameters. In order to exclude the effect of the experimental errors and inaccuracy of the initial model, we used the data calculated for the structure of *Protein G* without water molecules as the exact values of the phases and the experimental values of the structure factor moduli. The same model but with deliberately introduced independent random errors in the atomic coordinates (the mean absolute value 0.8 Å) was used as the starting model for the further refinement. Figure 1 shows the results of the use of the ML estimates for the starting model and for the mode upon twelve cycles of its refinement in the reciprocal space. It is clearly seen that the figures of merits based on ML estimates show no bias in independent errors in the atomic coordinates of the model, but are systematically overestimated for the preliminarily refined models.

## ELIMINATION OF BIAS. MML ESTIMATES

Earlier, we suggested the modified method for determining the $\alpha_s$ and $\beta_s$ parameters [5] based on the Brünger *R*-free likelihood-based method [12] also used in [13–15]. The likelihood function in this method is calculated using only the reflections, which were preliminarily excluded from the refinement process. Hereafter the parameter values obtained by maximization of this marginal likelihood function are called the MML estimates. Our further experiments were directed to the determination of the bias of the figures of merit based on the MML estimates for the $\alpha_s$ and $\beta_s$ parameters. In each test, the refinement procedure was preceded by the selection of a control set of reflections that should be excluded from the refinement and should be used for

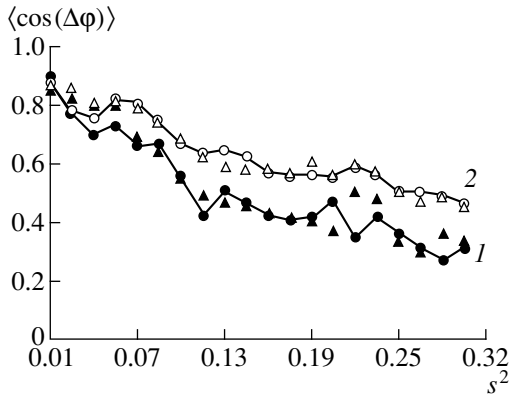


**Fig. 2.** Cosines of phase errors predicted from MML estimates (triangles) and the real values (circles) for the refinement (*1*) without and (*2*) with the stereochemical restraints. Model data.

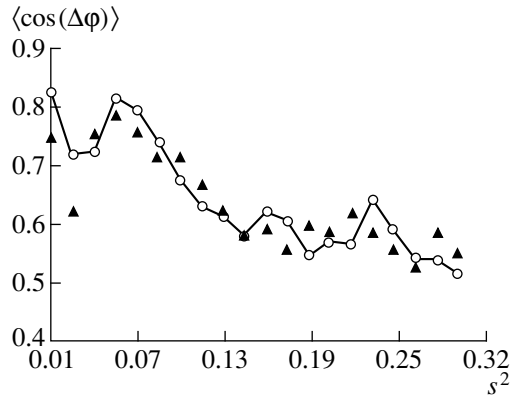


**Fig. 3.** Cosines of phase errors predicted from MML estimates (triangles) and the real values (circles) for the model refined over 50% of the experimental data.

the subsequent estimation of the $\alpha_s$ and $\beta_s$ parameters. Then the figure of merits were calculated for all the reflections using formula (2) with $t_s = \alpha_s/\beta_s$.

Figure 2 shows the results of such calculation for two different refinement strategies. Using the first strategy, we performed 24 cycles of refinement not imposing any the stereochemical restraints; the second strategy included 12 cycles of refinement under the stereochemical restraints. In order to reduce the dispersion in the estimates arising in the determination of the distribution parameters from a small number of experimental data, we first used quite a large number of control reflections (up to 50% of all the reflections from the zone of a 1.8 Å resolution). It is seen from Fig. 2, that both strategies resulted in no bias; the predicted mean values of cos(Δφ) are rather close to the true ones and reflect different quality of the models obtained upon the refinement.

All the subsequent tests were performed using the same starting model, but the refinement, the estimation of the $\alpha_s$ and $\beta_s$ parameters, and the calculation of the figures of merit were made with the use of the real experimental data. In these cases, the exact phase values were taken to be the phases calculated using all the atoms from the model of *Protein G* (including water molecules). It should be emphasized, that in this case, the sources of the errors in the phases calculated according to the model were both positional errors for the atoms of the model and some missing atoms (those of water molecules). The results obtained in this case with the use of MML estimates are shown by triangles in Figs. 3 and 4. The control set of reflections in these tests attained about 50 (Fig. 3) or 10% (Fig. 4) of the total number of reflections. It is seen that there the estimates have no bias with respect to their true values.

## REDUCTION OF STATISTICAL DISPERSION OF MML ESTIMATES

As showed our calculations, a reduction of the percentage of control reflection from 50% to a more realistic 10% of the total number of reflections without introducing any bias into the estimates results in an almost double increase of the dispersion in the predicted figures of merit. The statistical dispersion in such estimates can be reduced by different methods. The first method consists in the use of some additional hypotheses on the character of the errors in the atomic model and, thus, in a decrease of the number of the parameters to be determined and, at the same time, an increase of the ratio of the number of measurements to the number of the parameters to be determined. For example, one can assume that the model includes all the structure atoms and that the errors in their coordinates are independent and distributed over the radial-symmetric normal law with the same (although unknown)

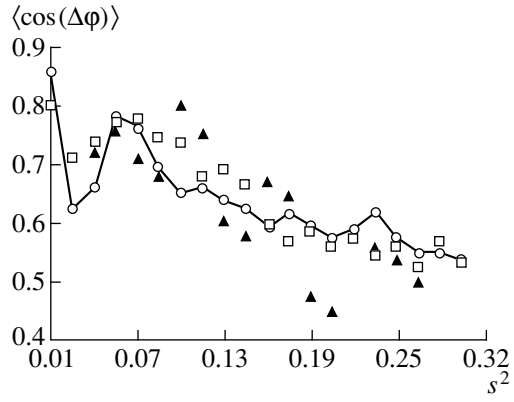


**Fig. 4.** Cosines of phase errors predicted from MML (triangles) and smoothed MML (squares) estimates and their true values (circles) for the model refined over 90% of the experimental data.

standard deviation $\nu$. Assuming that the structure factors are normalized, we can show that the following relationships are valid

$$\alpha_s = \exp(-2\pi^2\nu^2 s^2), \quad \beta_s = 1 - \alpha_s^2. \qquad (4)$$

Thus, we reduced the problem to the determination of one parameter $\nu$ instead of two ($\alpha$ and $\beta$) for each zone of the reciprocal space. A somewhat more general variant of this approach was considered in [15], where instead of the additional assumption on the character of the coordinate errors, it was assumed that the $\alpha_s$ and $\beta_s$ parameters obey a relationship of type (4). The advantage of the latter approach consists in the considerable improvement of the ratio of the number of measurements to the number of the parameters to be determined, which, in turn, reduces the statistical dispersion of the estimates. On the other hand, this approach requires the use of some new, not always obvious, assumptions. The problem of search for the optimum parameters becomes much more complicated and hinders the search for the global minimum. Thus, in such a situation, Brigogne and Irwin [15] had to use only the local likelihood maximization.

Another approach to the reduction of the statistical dispersion of the estimates consists in the change of the requirement of a fixed functional dependence of the $\alpha$ and $\beta$ parameters on **s** to the requirement that these dependences should be smooth. Such a requirement can be taken into account, e.g., by introducing a simple correction in the functional to be maximized, in which a penalty is applied where the value lies far from the line connecting two neighbors [13]. However, in this case as well, one has to use only the local optimization.

However, the additional requirement of smoothness can be implemented in a simpler way. As earlier, the initial values of the $\alpha$ and $\beta$ parameters for each zone are determined from the condition of the global maximum. Then, the thus obtained values are smoothed out using one of the standard schemes. The simplest smoothing procedure is illustrated by Fig. 4. The ratio $t = \alpha/\beta$, initially determined for each zone of the reciprocal space, was then substituted by the values averaged over the previous, the current, and the following zones. The thus obtained smoothed $t$ values were used to calculate figures of merit by formula (2). It is also seen from Fig. 4 that this procedure considerably reduces the errors in the calculated estimates and allows one to use a relatively small number of control reflections without any negative effect on the refinement process.

## ACKNOWLEDGMENTS

This study was supported by the Russian Foundation for Basic Research, project nos.94-04-12844 and 97-04-48319.

## REFERENCES

1. D. M. Blow and F. H. C. Crick, Acta Crystallogr. **12**, 794 (1959).
2. R. J. Read, Acta Crystallogr., Sect. A: Found. Crystallogr. **42**, 140 (1986).
3. V. Yu. Lunin, Preprint No. 22, NTsBI AN SSSR (Center of Biological Studies, Soviet Academy of Sciences, Pushchino, Moscow Area, 1982).
4. V. Yu. Lunin and A. G. Urzhumtsev, Acta Crystallogr., Sect. A: Found. Crystallogr. **40**, 269 (1984).
5. V. Yu. Lunin and T. P. Skovoroda, Acta Crystallogr., Sect. A: Found. Crystallogr. **51**, 880 (1995).
6. A. G. Urzhumtsev, V. Yu. Lunin, and E. A. Vernoslova, J. Appl. Crystallogr. **22**, 500 (1989).
7. A. G. Urzhumtsev, T. P. Skovoroda, and V. Yu. Lunin, J. Appl. Crystallogr. **29**, 741 (1996).
8. V. Luzzati, Acta Crystallogr. **5**, 802 (1952).
9. G. A. Sim, Acta Crystallogr. **12**, 813 (1959).
10. R. Srinivasan and S. Parthasarathy, *Some Statistical Applications in X-ray Crystallography* (Pergamon, Oxford, 1976; Mir, Moscow, 1979).
11. R. J. Read, Acta Crystallogr., Sect. A: Found. Crystallogr. **46**, 900 (1990).
12. A. T. Brünger, Nature **355**, 472 (1992).
13. N. S. Pannu and R. J. Read, Acta Crystallogr., Sect. A: Found. Crystallogr. **52**, 659 (1996).
14. G. N. Murshudov, E. J. Dodson, and A. A. Vagin, in *Macromolecular Refinement. Proceedings of the CCP4 Study Weekend*, January, 1996, p. 93.
15. G. Bricogne and J. Irwin, in *Macromolecular Refinement. Proceedings of the CCP4 Study Weekend*, January, 1996, p. 85.

*Translated by L. Man*

*Crystallography Reports, Vol. 45, No. 2, 2000, pp. 199–202. Translated from Kristallografiya, Vol. 45, No. 2, 2000, pp. 231–234.*




# Simple Criterion of Division of Two-Dimensional Space of a Periodic Lattice into Arbitrarily Shaped Polyominoes

**V. G. Rau**

*Vladimir State Pedagogical University, Vladimir, Russia*

Received March 24, 1998

**Abstract**—The method of discrete modeling of molecular packings in crystals is further developed. A criterion of the translational division of the two-dimensional space into arbitrarily shaped polyominoes based on the comparison of the vector systems of the polyomino points with the points of the packing multispace is suggested. The analysis of the properties of this multispace has been performed for the first time in the present study. *© 2000 MAIK "Nauka/Interperiodica".*

Earlier [1], considering the major concepts of the method of discrete modeling of packings [2], we suggested the algorithmic criterion of possible translational division of the $n$-dimensional pseudo-Euclidean space into $n$-dimensional polyominoes with the packing coefficient $k = r/N$, where $r$ is the number of polyomino cells sharing the $(n-1)$-dimensional face and $N$ is the order of the packing space (the sublattice index). According to [2], a packing space (PS) is a set of unit cells or points of one of the supracells of the crystal lattice, each of which is attributed a certain index ("weight" with respect to mod $N$) in such a way that the translationally nonidentical points have different weights, whereas the translationally identical points have the same weights. In this case, the packing criterion is formulated in the following way [1]. In order that the given $n$-dimensional polyominoes $\{\beta_i | i = 1, 2, \ldots, r\}$ can translationally pack the $n$-dimensional space with the packing coefficient $k = r/N$, the following necessary and sufficient condition should be fulfilled: at least one packing space of the order $N$ should exist such that its $r$ points with coordinates $\{\beta_i + x_0 | i = 1, 2, \ldots, r\}$ (where $x_0$ is any arbitrary integral vector) have different weights. Using this criterion, Maleev developed an algorithm and the program of exhaustive search for all possible translation packings of two- and three-dimensional polyominoes of the given shape in the two- and three-dimensional spaces with the packing coefficient $k = r/N$.

Below, we suggest the criterion for division ($k = 1$) of the two-dimensional space into arbitrarily shaped $N$-minoes, which does not require a direct exhaustive search for all the packing spaces. We believe that this criterion can considerably simplify some calculations especially for packing spaces of large orders with a large number of divisors $d|N$, because the number of spaces of the $N$th order is determined by the sum of divisors including unity and $N$ [2].

In accordance with the algorithm of exhaustive search for packing spaces of the $N$th order [1], we can write the matrices of the packing space whose diagonal elements are the expansions of the order $N$ in terms of pairs of cofactors in the form

$$\begin{pmatrix} N & 0 \\ C_0 & 1 \end{pmatrix}, \begin{pmatrix} d_1 & 0 \\ C_1 & N/d_1 \end{pmatrix}, \begin{pmatrix} d_2 & 0 \\ C_2 & N/d_2 \end{pmatrix}, \ldots,$$

$$\begin{pmatrix} d_i & 0 \\ C_i & N/d_i \end{pmatrix}, \ldots, \begin{pmatrix} 1 & 0 \\ 0 & N \end{pmatrix}, \quad (1)$$

$$C_0 = 0, 1, \ldots, N, \; C_1 = 0, 1, \ldots, d_1,$$

$$C_2 = 0, 1, \ldots, d_2, \ldots, C_i = 0, 1, \ldots, d_i.$$

Obviously, the number of matrices $\sigma(d) = \sum_{d|N} d$ corresponds to the number of packing spaces of order $N$.

The geometric sense of the matrices is quite clear—they are the basic vectors of the unit cells of the packing spaces. Figure 1 shows that to each matrix of the packings space of order $N = 6$, there corresponds a certain unit cell of the packing space.

The integral coordinates of the unit-cell sites of the packing space are determined by the rows of matrix (1), where the numbers in the left-hand column belong to the $0x$-axis, whereas the numbers in the right-hand column, to the $0y$-axis. The sites with the coordinates multiple to the coordinates of the sites of the packing-space unit cell form a sublattice in the lattice of the integral coordinates.

Now, let us define the packing multispace of the sublattice (PMS of the $N$th order) as a multilattice formed by all the sublattices generated by the packing-space matrix of form (1). In this case, irrespectively of the symmetry of each packing space, their combination into the packing multispace does not "remove" the

1063-7745/00/4502-0199$20.00 

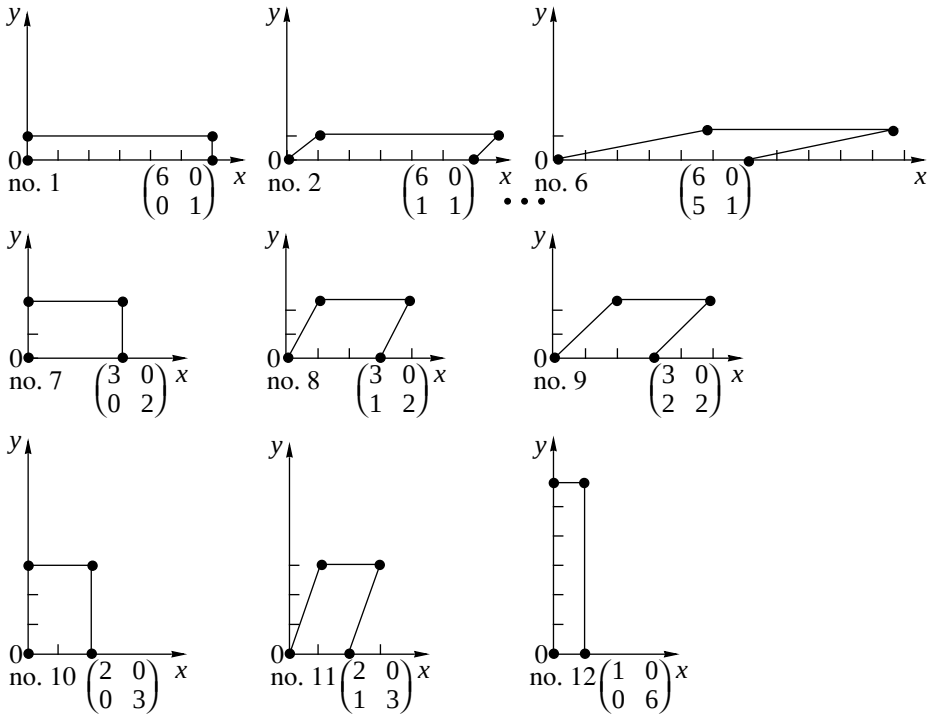


**Fig. 1.** Unit cells (nos. 1–12) of packing spaces of the 6th order with the corresponding matrices.

symmetry element common for all the packing spaces—the center of inversion (the consequence of the Neumann–Curie principle). Figure 2 shows an example of the packing multispace of the 6th order. Each site of the packing multispace is attributed the number of the sublattice of the packing space to which it belongs. All the sites with the same numbers obviously belong to the nodal line of the direct packing multispace drawn from the origin (0, 0) to the point with the coordinates $(C_i, N/d_i)$, i.e., to the straight line set by the unit-cell periods of the selected packing space. A straight line in a packing multispace is considered as a set of sites belonging to one of the sublattices generated by packing-space matrices (1). In terms of classical crystallography, the site coordinates $(C_i, N/d_i)$ are, in fact, the $h$ and $k$ indices of the nodal line.

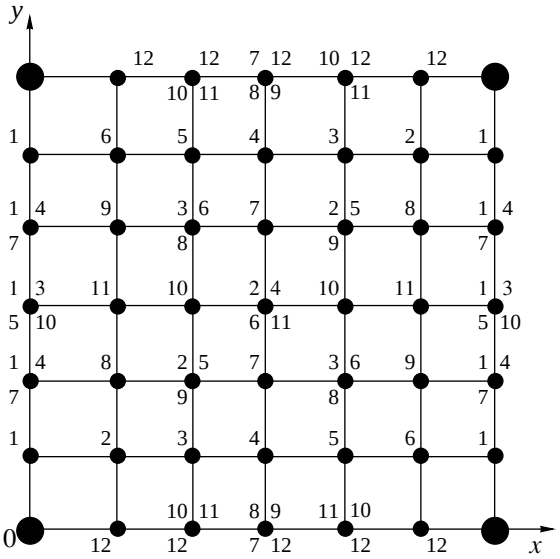

**Fig. 2.** Packing multispace of the 6th order. The site numbers correspond to the sublattices of the packing space of the 6th order in Fig. 1.

Using the first basic theorem of the lattice crystallography (see, e.g., [3]), the "subsequent nodal planes of the *hkl* family intersect the *a*, *b*, and *c* edges of the primitive unit cell into *h*, *k*, and *l* segments, respectively, the body diagonal, into the $h + k + l$ segments, and the face diagonals, into $k + l$, $l + h$, and $h + k$ segments". For packing multispace in the two-dimensional case, this leads to the fact that any nodal line of the packing space has the same number of the sites equal to $N$. Finally, the following statement is also valid: at least one nodal line passes through each point of the packing multispace, because there always exists a nodal line passing through the given point, and, if there is no corresponding sublattice of the packing space, this nodal line should be considered as a unit-cell vector not taken into account in the list of matrices (1). In other words, the number of packing spaces exceeds the number given by the theorem proven in [1].

If several lines pass through a certain point of the packing multispace, it becomes necessary to introduce one more characteristics of the multispace—the degree

$m$ of the nodal point equal to the number of the lines passing through this point (if to assume that this point is a vertex of a graph, then the degree of the graph vertex is $2m$, because the straight lines (graph edges) not only "enter" this vertex but also "leave" it. Now, consider the distribution of the degrees of the sites of the packing multispace along a certain direction drawn from the origin of coordinate system. If an arbitrary sublattice of the packing multispace is determined by the matrix of the form

$$\begin{pmatrix} d_i & 0 \\ C_i & N/d_i \end{pmatrix}, \tag{1'}$$

then the coordinates of its sites can be written as

$$\begin{pmatrix} p_i d_i & 0 \\ q_i C_i & q_i N/d_i \end{pmatrix}, \tag{2}$$

where $p_i$ and $q_i$ are the integers (with respect to mod$N$), and the intersection of the straight lines belonging to various lattices of the packing spaces can be written as

$$\begin{pmatrix} p_i d_i & 0 \\ q_i C_i & q_i N/d_i \end{pmatrix} = \begin{pmatrix} p_j d_j & 0 \\ q_j C_j & q_j N/d_j \end{pmatrix} \tag{3}$$

whence follows the system of equations to be compared:

$$\begin{aligned} p_i d_i &\equiv p_j d_j \pmod{N}, \\ q_i C_i &\equiv q_j C_j \pmod{N}, \\ q_i N/d_i &\equiv q_j N/d_j \pmod{N}. \end{aligned} \tag{4}$$

Without detracting from the general character of the theory, we can consider an example of the packing space with the matrix $\begin{pmatrix} 1 & 0 \\ 0 & N \end{pmatrix}$ and calculate the degrees of the sites along the straight line $\begin{pmatrix} p_i 1 & 0 \\ 0 & N \end{pmatrix}$ passing from the origin of the coordinate system along the $0x$ axis. The quantity $p_i$ determines the number of the site on the straight line under consideration. Equation (3) is valid if the first equations to be compared from (4) are valid,

$$p_i \times 1 \equiv p_j d_j (\mathrm{mod} N), \tag{5}$$

which signifies that there exists a sublattice, one of the sites of which coincides with the site $p_i$

$$\begin{pmatrix} p_i \times 1 & 0 \\ 0 & N \end{pmatrix} = \begin{pmatrix} p_j d_j & 0 \\ C_j & N/d_j \end{pmatrix}. \tag{6}$$

The number of equations similar to (6) equals the number of the values of $C_j$, i.e., $d_j$. Thus, if $N = 16$ and $p_i = 8$, the eighth point of the line along the $0x$-axis has the degree $m = 8 + 4 + 2 + 1$ in virtue of the condition

$$\begin{aligned} \begin{pmatrix} 8 \times 1 & 0 \\ 0 & N \end{pmatrix} &= \begin{pmatrix} 1 \times 8 & 0 \\ C_j & N/8 \end{pmatrix} = \begin{pmatrix} 2 \times 4 & 0 \\ C_j & N/4 \end{pmatrix} \\ C_j &= 0, 1, \ldots, 7 \qquad C_j = 0, 1, 2, 3 \\ &= \begin{pmatrix} 4 \times 2 & 0 \\ C_j & N/2 \end{pmatrix}, \\ C_j &= 0, 1. \end{aligned} \tag{3'}$$

Thus, generalizing the above result, we can draw a conclusion that at each $p_i$th point $(p_i|N)$ of the selected direction, the number of the intersecting lines is equal to the sum of the divisors of the number $p_i$. One can readily see that, of them, only those lines are nonrepeating which correspond to the maximum value in the sum of the divisors $N$, i.e., to the number $p_i$. All the other properties of the packing multispace can be studied within the same scheme.

Thus, the analysis performed allows us to formulate the following properties of the packing multispace:

1. The unit cell $N \times N$ of the packing multispace contains the information about all the packing spaces of the $N$th order, whose number is equal to $\sigma(d) = \sum_{d|N} d$.

2. The $N \times N$ cell of the packing multispace is centrosymmetric.

3. The number of points on the nodal line belonging to any packing space coincides with the space order $(N)$.

4. At least one line belonging to the sublattice of the packing space should pass through each point of the packing multispace.

5. At each point with the number $p_i$ (a divisor of $N$) lying on the nodal line of the packing multispace and drawn from the origin of the coordinate system, the $m = \sum_{d|N} d$ lines belonging to different packing spaces are intersected.

6. Through a point on the nodal line with the number $p_i$, which is not a divisor and has no common divisors with any of the $N$ divisors, only one line can pass.

7. The point with the number $p_i$, which is not a divisor of $N$ and has no common divisors with $d|N$, has the same order as the points with the numbers corresponding to these divisors.

8. The points with the coordinates $x = d_j$ and $y = N/d_j$ belong to the same line, which passes from the origin of the coordinate system in the direction of the sites $x = d_j$, $y = 0$ and $x = 0$, $y = N/d_j$. The coordinates of all the other

nodal points satisfying relationship (3) at all the possible values of $p_i$, $p_j$, $q_i$, and $q_j$ are located at the intersections of the corresponding nodal lines.

The last four properties of the packing multispace allow one to pass to the integral criterion of the space division into arbitrarily shaped polyominoes.

Let us set a polyomino by the corresponding graph of the neighboring cells, i.e. substitute each cell by a point. Obviously, the polyominoes characterize a set of points, which are the vertices of a graph with integral coordinates in the system of lattice points having the integral coordinates. If this set of $N$ points (the main system of points) has at least one interpoint distance coinciding with the distance between the sites of the sublattice of any packing space of the $N$th order, then this space cannot have a packing with $k = 1$. The set of all the interpoint distances in the initial polyomino forms a vector point system [4], which has a center of symmetry. Therefore, it is sufficient to compare only the independent part of the vector point system of points of polyominoes with the packing multispace upon the bringing into coincidence the origins of their coordinate systems. Then the division criterion can be formulated in the following way. Superimposing the vector point system onto the packing multispace, we see that all the points of the vector space coincide with the sites of the packing multispace at which, in general, all the lines corresponding to the complete set of the packing spaces are intersected, then such polyominoes cannot translationally tile the space. And *vice versa*, if a certain number of the packing space is missing in the "list" of the lines at the points of the multispace occupied by the points of the vector system of polyominoes, then such polyominoes can tile the packing space.

The knowledge of the degrees of the sites of the successive series of points on each line of the packing multispace is sufficient to answer the question of possible division of the space into the polyominoes of the given shape according to the vector system constructed at the polyomino points. The algorithm of the corresponding checking is implemented in several stages in the following sequence:

(i) Using the integral coordinates of $N$ points of polyominoes, one constructs the function of interpoint distances (the vector system of polyominoes points).

(ii) A bundle of straight lines is drawn from the origin of the vector system through each point of the independent part of the vector system.

(iii) The numbers corresponding to the $N$ divisors are indicated along each line in the order of their increase, which thus determine the number of independent directions $\delta$ coinciding with the vector system.

(iv) Exclude from the general list of directions $\delta$ all the repeating lines (in accordance with property 8) and denote their number as $\pi$.

(v) Calculate $\sigma$, the total sum of all the divisors $N$.

(vi) Calculate the difference $\Delta = (\delta - \pi) - \sigma$.

If $\Delta \geq 0$, then the initial polyominoes cannot translationally divide or tile the space.

If $\Delta < 0$, then this quantity determines the number of packing spaces that can be divided into the given polyominoes.

Concluding the article, we should like to note that the implementation of this algorithm on a computer with due regard for the above suggested criterion should be preceded by checking the coincidence of the points of the vector systems of polyominoes with the points of the multispace numbered in accordance with the packing-space matrices. The analysis of the results obtained in such calculations gives the answer not only to the question of space division but indicates those packing spaces in which such a division is possible.

## ACKNOWLEDGMENTS

The authors is grateful to V.G. Zhuravlev from the Vladimir State Pedagogical Institute for useful discussion of the general problems of space division into polyominoes.

## REFERENCES

1. A. V. Maleev, Kristallografiya **40**, 394 (1995) [Crystallogr. Rep. **40**, 354 (1995)].
2. A. V. Maleev, V. G. Rau, K. A. Potekhin, *et al.*, Dokl. Akad. Nauk SSSR **315**, 1382 (1990).
3. N. V. Belov, *Essays on Structural Crystallography and Space Groups* [in Russian] (Nauka, Moscow, 1986).
4. M. J. Buerger, *Vector Space and Its Application in Crystal Structure Investigation* (Wiley, New York, 1959; Inostrannaya Literatura, Moscow, 1961).

*Translated by L. Man*

*Crystallography Reports, Vol. 45, No. 2, 2000, pp. 203–205. Translated from Kristallografiya, Vol. 45, No. 2, 2000, pp. 235–237.*


**THEORY OF CRYSTAL STRUCTURES**

# Mathematical Dynamics and Migration of Silver Ions in Superionic Conductor AgI

**V. I. Polyakov**

*Chemistry Faculty, Saratov State University, Astrakhanskaya ul. 83, Saratov, 410071 Russia*

Received December 29, 1998

**Abstract**—It is established that the mathematical dynamics and the dynamics of silver ion migration represented by equipotential surfaces of interionic potential for the superionic conductor AgI are rather similar. The parameters of the interionic potential are determined in terms of the effective pair potential of the EXAFS method. © *2000 MAIK "Nauka/Interperiodica".*

According to Andersson *et al.*, the mathematical dynamics is the rearrangement and the merge of the surface of the function level on an exponential scale $f[x, y, z] = C$ with the change in the parameter $C$. They determined simple mathematical functions describing such important structures as the primitive, body- and face-centered cubic packings, and also diamond-, cristobalite-, sphalerite-, CsCl, $CaF_2$, $ReO_3$, and sodalite-types structures [1]. Thus, the upper row in figure show the surfaces described by the equations

$$\exp\{\cos[2\pi(x-y)]\} + \exp\{\cos[2\pi(x+y)]\}$$
$$+ \exp\{\cos[2\pi(y-z)]\} + \exp\{\cos[2\pi(z-x)]\}$$
$$+ \exp\{\cos[2\pi(x+z)]\} + \exp\{\cos[2\pi(y+z)]\} = C.$$

At lower values of the constant $C$, the surface is represented by isolated "bubbles" at the vertices of a truncated octahedron (I in figure). An increase in $C$ results in broadening of the isolated regions, their approach, merge of their boundaries, and the formation of a periodic structure bound over the whole volume (II and III). At large $C$-values, the surface is transformed into the nodal IWP-type surface (IV) [2]. It was discovered that this mathematical dynamics is closely related to the real dynamics of silver ion migration in a superionic conductor AgI.

The lower row in figure shows the equipotential surfaces of the interionic potential in AgI in whose field a silver ion migrates. The interionic potential is constructed as the superposition of the lattice sum of the Lennard–Jones pair potentials $V_{Ag–I}(r)$ describing the interaction between the iodine and silver ions and the potential $V_{Ag–Ag}(R)$ acting from the side of the uniform charge distribution of silver ions onto the $Ag^+$ ion migrating inside the unit cell. The pair potential is set in the form $V_{Ag–I}(r) = A\,r^{-1} - B\,r^{-n}$, where the quantity $n = 7$ determines the soft-core repulsive potential term [3]. Summation is performed over the bcc lattice of iodine atoms inside a sphere with the center $O$ located at the lattice point and having a radius of $3^{1/2}a$, where $a$ is the lattice parameter of the highly conducting AgI phase (thus, five coordination spheres of iodine ions with respect to the sphere center, were taken into account, i.e., altogether 59 atoms).

The $V_{Ag–Ag}(R)$ potential is the potential inside a uniformly charged sphere; $V_{Ag–Ag}(R) = \frac{3}{2}N/(3^{1/2}a) - R^2/2\,N/(3^{1/2}a)^3$, where $R$, the distance between the sphere center and a mobile ion, is limited by the unit-cell dimensions ($N$ is the number of silver ions inside the sphere, which is determined from the condition of the electric neutrality). The larger the sphere dimensions, the less the $V_{Ag–Ag}(R)$-value differs from the first $R$-independent term. Therefore, in what follows we assumed that $V_{Ag–Ag}(R) \approx \text{const} = D$.

The construction of the parametric three-dimensional interionic potential $V_{3D}$ is completed with the optimization of its parameters $A$, $B$, and $D$ by the least-squares method in a way to approach the effective pair-interaction potential between iodine and silver ions, $V_{eff}$, in the EXAFS method [4]. The $V_{eff}$ potential is one-dimensional, and therefore it is necessary to choose a ray originating at the center $O$ along which $V_{3D}$ should vary in a way to fit $V_{eff}$. The optimum direction is that from $O$ to the truncated cuboctahedron vertex. Fitting along this direction gives the best results. This direction is the most important for the distribution density of $Ag^+$-ions, because the most stable positions of mobile silver ions are located in the vicinity of the truncated cuboctahedron vertices [5].

At energies lower than the activation energy $E_a$ = 0.1 eV [5], the regions of $Ag^+$ migration are isotropic and localized. At energies close to $E_a$, the migration regions first are broadened (I in the lower part of figure) and then, with a further increase in the energy, start merging together (II), thus forming a network of conductivity channels (which explains the structural features of the superionic state of AgI). The narrow places

1063-7745/00/4502-0203$20.00 

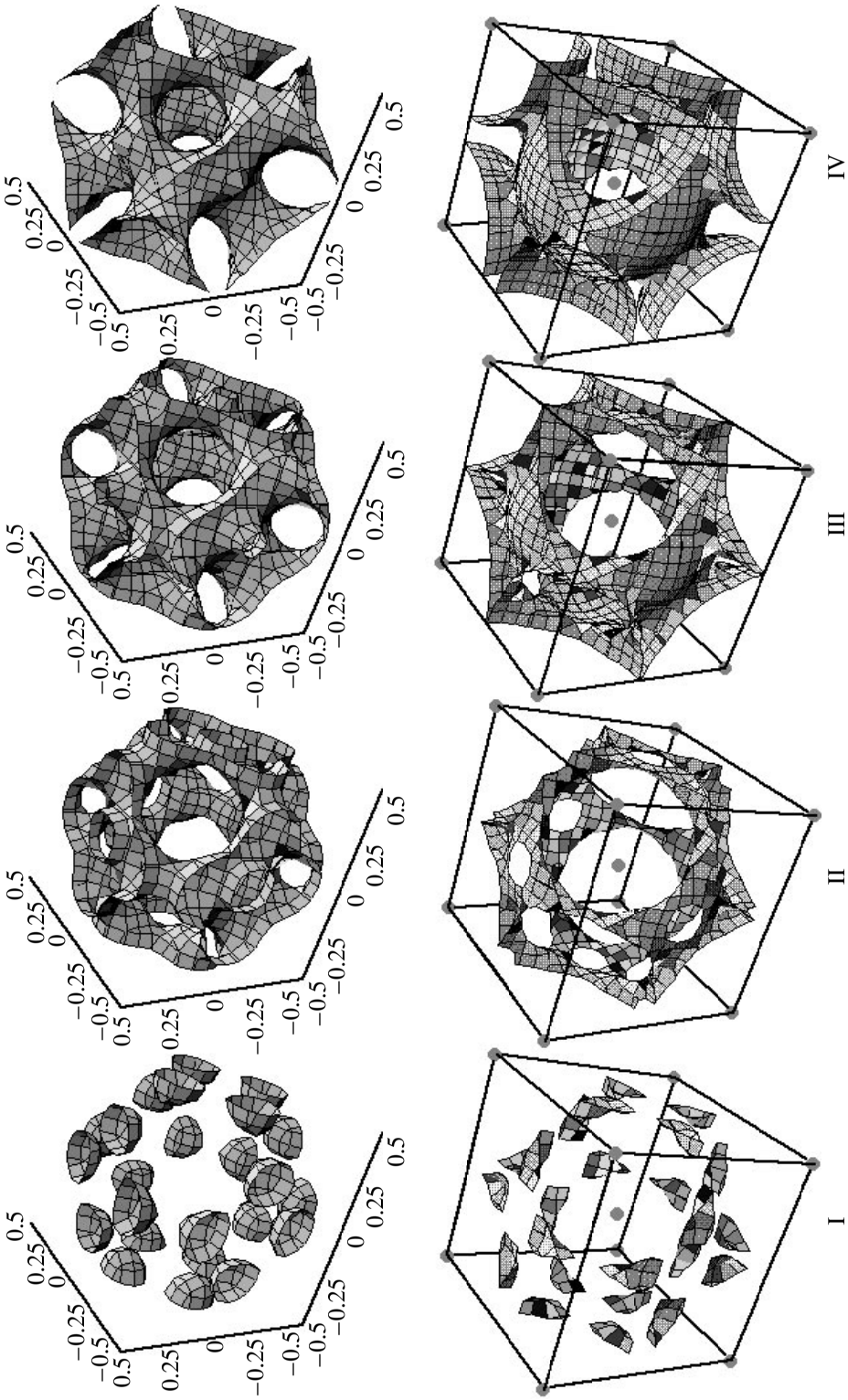


Mathematical dynamics (above) and the equipotential surfaces of the interionic Ag I potential Δ (below). In the upper part: the unit cell is given by varying *x*, *y*, and *z* from –0.5 to 0.5. For I–IV, the values of the parameter *C* are equal to 5.5, 6.0, 6.5, and 7.0, respectively. In the lower part: the energy values for I–IV are equal to 0.14, 0.20, 0.40, and 1.15 eV, respectively.

on the "necks" of surface II coincide with the so-called trigonal positions (saddle point of the silver-ion density distribution). The centers of square faces (octahedrally coordinated sites) first are "avoided" by ions (remain empty), but with an increase of the energy (III) become more available for them. At high energies, there are no specific positions for migration—surface IV consists of the external parts of the bcc system of intersecting spheres.

It is quite surprising how close the results are of the mathematical dynamics and the evolution of the equipotential surfaces, two approaches of quite different origins—purely mathematical and purely physical. The interpretation of these similar results and some other examples of superionic conductors will be considered in our following studies.

## REFERENCES

1. S. Andersson, S. Lidin, and M. Jacob, Z. Kristallogr. **210**, 826 (1995).
2. H. G. Schnering and R. Nesper, Z. Phys. B: Condens. Matter **83**, 407 (1991).
3. Y. Kaneko, A. Ueda, and Y. Hiwatari, J. Phys. Soc. Jpn. **55**, 1244 (1986).
4. G. Dalba, P. Fornasini, R. Gotter, *et al.*, Philos. Mag. B **71**, 751 (1995).
5. *Physics of Superionic Conductors*, Ed. by M. B. Salamon (Zinatne, Riga, 1982).

*Translated by L. Man*

*Crystallography Reports, Vol. 45, No. 2, 2000, pp. 206–209. Translated from Kristallografiya, Vol. 45, No. 2, 2000, pp. 238–241.*


**STRUCTURES OF INORGANIC COMPOUNDS**

# Synthesis, IR Spectra, and Structures of Double Metaphosphates $M$Ni$(PO_3)_3$ ($M$ = Na or K)

**A. A. Kapshuk, P. G. Nagornyĭ, and O. V. Petrenko**

*Kiev State University, ul. Glushkova 6, Kiev, 252127 Ukraine*

Received January 12, 1998

**Abstract**—Double metaphosphates of the composition $M$Ni$(PO_3)_3$ ($M$ = Na or K) were prepared by spontaneous crystallization from melts in the $M_2O$–$P_2O_5$–NiO system. Their thermal properties were studied, and the IR spectra were analyzed. The complete X-ray structure analysis of the compounds synthesized was performed. The NaNi$(PO_3)_3$ crystals are orthorhombic with the unit-cell parameters $a$ = 13.781(2) Å, $b$ = 10.584(2) Å, $c$ = 9.873(1) Å, sp. gr. *Pcca*. The KNi$(PO_3)_3$ crystals belong to the sp. gr. $R3$ with the unit-cell parameters $a$ = 10.076(2) Å and $c$ = 9.623(5) Å. The structures of the studied phosphates are compared with the structures of the related compounds. © *2000 MAIK "Nauka/Interperiodica".*

When studying the behavior of transition metal oxides (Fe, Co, or Ni) in melted phosphate systems of alkali metals over a wide range of $M_2O$ : $P_2O_5$ ratios ($M$ = Li, Na, or K), we obtained a number of complex phosphates of alkali and divalent metals in slowly cooled oxide-saturated systems. These compounds possess some specific properties and, similar to phosphate systems themselves, find wide use as catalysts, special phosphate cements, high-temperature lubricants, etc. [1–3]. Hence, the studies of the structural characteristics of these phosphate compounds are of both theoretical and practical interest.

We synthesized complex $M$Ni$(PO_3)_3$ phosphates, where $M$ = Li, Na, or K, and studied the structures of the corresponding sodium and potassium salts. Phosphates of the compositions KNi$(PO_3)_3$ and KCo$(PO_3)_3$ were synthesized earlier and were characterized by X-ray diffraction studies [4]. Analogous lithium- and sodium-containing compounds with divalent metals (Zn, Cu, or Mg) were also studied, but the complete X-ray structure analysis was performed only for NaMg$(PO_3)_3$ [5–7]. All the compounds were synthesized by sintering the corresponding charges. The corresponding single crystals were usually obtained by recrystallization from sodium metaphosphate melt.

## EXPERIMENTAL

Double sodium (potassium) and nickel phosphates were prepared by slow cooling of the melts in the nickel-oxide saturated $M_2O$–$P_2O_5$–NiO systems (the $M_2O$ : $P_2O_5$ ratio was varied in the range from 1 : 1.5 to 1 : 1.7) at temperatures from 950 to 720–700°C. The cooling rate was 1–3°/h. Upon cooling, the liquid melt was poured off, and the crystals formed were washed in dilute HCl at moderate heating. The compositions of the phases obtained were determined by the chemical analysis. The nickel and phosphorus presence was determined according to procedures described in [8] and [9], respectively. The alkali metal content was determined on an S-302 atomic absorption spectrophotometer.

For NaNi$(PO_3)_3$, anal. calcd. (%): $Na_2O$, 9.72; NiO, 23.51; $P_2O_5$, 66.77; found (%): $Na_2O$, 10.03; NiO, 23.73; $P_2O_5$, 66.89.

For KNi$(PO_3)_3$, anal. calcd. (%): $K_2O$, 14.03; NiO, 22.39; $P_2O_5$, 63.58; found (%): $K_2O$, 14.25; NiO, 22.48; $P_2O_5$, 63.76.

The IR spectra of the compounds under study were recorded on a UR-20 instrument in the spectral range 400–1400 $cm^{-1}$. The samples were prepared as KBr-containing pellets. The thermograms were obtained on a Q-1500 derivatograph. The heating rate of the samples was 7.5°/min.

The X-ray diffraction data were collected on an Enraf-Nonius CAD-4 diffractometer (Mo$K_\alpha$ radiation, graphite monochromator, $\omega/2\theta$ scanning techniques). The principal crystallographic parameters of the compounds under study and the details of X-ray data collection are given in Table 1.

The structures were solved by the direct method and were refined anisotropically by the full-matrix least-squares method. The experimental data were corrected for the Lorentz and the polarization factors, with absorption being ignored. All the computations were performed using the SHELX program package adapted for an IBM PC. The positional and the thermal parameters of the atoms in the structures of the sodium and potassium salts are listed in Tables 2 and 3, respectively.

1063-7745/00/4502-0206$20.00 

**Table 1.** Crystallographic data

| Formula | $NaNi(PO_3)_3$ | $KNi(PO_3)_3$ |
|---|---|---|
| Sp. gr. | *Pcca* | *R*3 |
| *a*, Å | 13.781(2) | 10.076(2) |
| *b*, Å | 10.584(2) | – |
| *c*, Å | 9.863(1) | 6.9623(5) |
| *V*, Å$^3$ | 1438.6(4) | 612.2(2) |
| *Z* | 8 | 3 |
| *d*, g/cm$^3$ | 2.94 | 2.72 |
| μ, mm$^{-1}$ | 3.45 | 3.50 |
| *F*(000) | 1248 | 492 |
| $\theta_{max}$, deg | 25 | 30 |
| Number of measured reflections | 1488 | 412 |
| Number of independent reflections | 1267 | 409 |
| Number of reflections used in the least-squares refinement | 1258 | 405 |
| Maximum peak on the difference electron density map, e/Å$^3$ | 0.565 | 1.188 |
| *R* | 0.030 | 0.026 |

**Table 2.** Coordinates ($\times 10^4$) and equivalent thermal parameters (Å$^2 \times 10^3$) of the basic atoms in the $NaNI(PO_3)_3$ structure

| Atom | *x* | *y* | *z* | $U_{eq}$ |
|---|---|---|---|---|
| Ni(1) | 5000 | 0 | 0 | 6(1) |
| Ni(2) | 7500 | 5000 | 287(1) | 6(1) |
| P(1) | 6478(1) | 446(1) | –2371(1) | 5(1) |
| P(2) | 6253(1) | 2525(1) | –459(1) | 6(1) |
| P(3) | 6016(1) | 4745(1) | –2146(1) | 5(1) |
| O(1) | 7500 | 0 | –2949(3) | 8(1) |
| O(2) | 6084(2) | –479(2) | –1384(2) | 11(1) |
| O(3) | 5893(2) | 831(2) | –3559(2) | 10(1) |
| O(4) | 6799(2) | 1699(2) | –1573(2) | 9(1) |
| O(5) | 5527(2) | 1764(2) | 288(2) | 9(1) |
| O(6) | 7027(2) | 3174(2) | 317(2) | 10(1) |
| O(7) | 5649(2) | 3522(2) | –1329(2) | 9(1) |
| O(8) | 6493(2) | 4317(2) | –3398(2) | 12(1) |
| O(9) | 6529(2) | 5613(2) | –1207(2) | 10(1) |
| O(10) | 5000 | 5385(3) | –2500 | 8(1) |
| Na | 6245(1) | –2482(1) | –128(2) | 23(1) |

## RESULTS AND DISCUSSION

The $NaNi(PO_3)_3$ structure is based on infinite zigzag polyphosphate chains, running along the *x*-axis of the crystal and forming a three-dimensional framework linked by Ni ions. The structure projection onto the *xy* plane is shown in Fig. 1. The unit cell contains two crystallographically nonequivalent Ni atoms, of which one is located in the inversion center, and the second one lies on the twofold axis. The coordination polyhedra of both Ni atoms are octahedra. All the terminal O atoms of the complex anions interact with the cations. Within the independent fragment of the polyphosphate chain, the coordination is such that two of total four terminal oxygen atoms of the adjacent units are involved in the formation of six-membered metallocycles with the nickel atoms, whereas the third and fourth oxygen atoms complement the coordination spheres of the Ni(1) and Ni(2) atoms, respectively, and vice versa.

Sodium atoms also play an important role in the framework formation. One can separate infinite …Ni(1)–Na–Ni(2)–Na… columns of polyhedra sharing the edges and oriented parallel to the [210] direction. Such an arrangement provide the formation of eight-membered rings consisting of a sodium atom and three links of the polyphosphate chain. Similar columns of alternating sodium and magnesium polyhedra were also observed in the $NaMg(PO_3)_3$ structure [7]. In these structures, the modes of coordination of an anion by cations are also identical, but the conformation of the chain in magnesium phosphate is essentially different.

The Ni–O distances in both coordination polyhedra are not equivalent. Thus, the bonds between the Ni(1) and the O(2) and O(3) atoms located at the edge of the $PO_4$ tetrahedron and linking two equivalent Ni atoms (2.087(2) and 2.076(2) Å, respectively) are noticeably elongated in comparison with the Ni(1)–O(5) bond (2.024(2) Å). The neighboring Ni(2) atoms are "bonded" by the O(8)–O(9) edge of the tetrahedron, with the Ni(2)–O(9) distance being the maximal in the coordination environment of this atom (2.093(2) Å). On the whole, the Ni–O bond lengths have values typical of the sixfold-coordinated nickel atom.

The coordination polyhedron of the Na atom can be described as a distorted octahedron elongated in the direction of the threefold axis. The Na–O distances range within 2.313(2)–2.608(2) Å. The longer bonds the Ni–O bonds, the shorter the bonds between the Na atom and the same O atoms. The distribution of the

**Table 3.** Coordinates ($\times 10^4$) and equivalent thermal parameters (Å$^2 \times 10^3$) of the basic atoms in the $KNi(PO_3)_3$ structure

| Atom | *x* | *y* | *z* | $U_{eq}$ |
|---|---|---|---|---|
| Ni | 0 | 0 | 0 | 6(1) |
| K | 0 | 0 | 4933(1) | 18(1) |
| P | 3435(1) | 2386(1) | 1360(2) | 7(1) |
| O(1) | 1875(5) | 1092(5) | 1778(3) | 11(11) |
| O(2) | 3530(4) | 3004(4) | –779(5) | 10(1) |
| O(3) | 4785(4) | 2191(4) | 1616(6) | 9(1) |

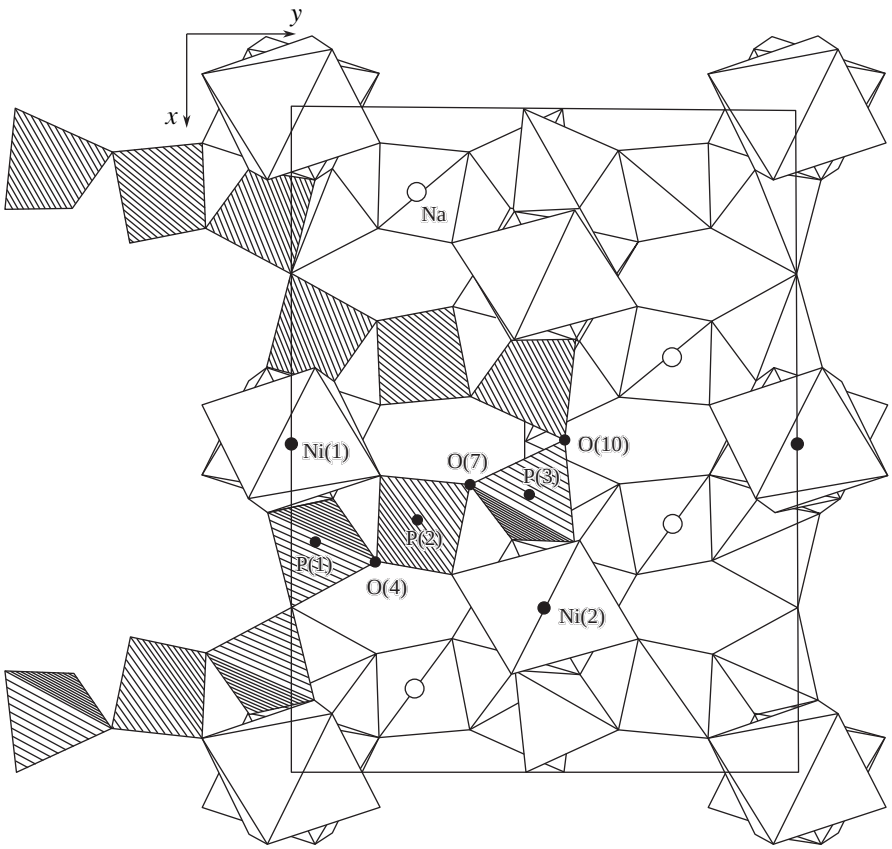


**Fig. 1.** $NaNi(PO_3)_3$ structure projected onto the *xy* plane.

bond lengths and bond angles in the phosphate tetrahedra corresponds to their conventional distribution.

The unit cell of $KNi(PO_3)_3$ projected onto the *xy* plane is shown in Fig. 2. The compound has a framework structure formed by infinite polyphosphate chains along the *z*-axis. Three chains are linked by potassium and nickel atoms located on the threefold axis. Despite the fact that, at first glance, the structure of potassium–nickel phosphate is different, it has some features typical of the sodium salt. Thus, the alternating K and Ni polyhedra share the edges to form columns along the *z*-axis of the crystal. The mode of coordination of the polyphosphate chain is retained—two neighboring links include the edge of the nickel octahedron, whereas three following links include the edge of the potassium polyhedron. An interesting feature of the

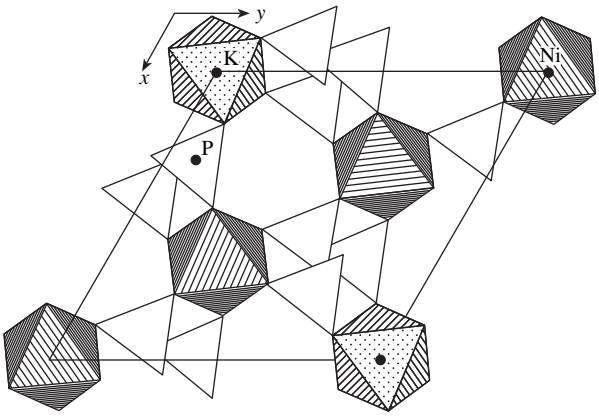


**Fig. 2.** $KNi(PO_3)_3$ structure projected onto the *xy* plane.

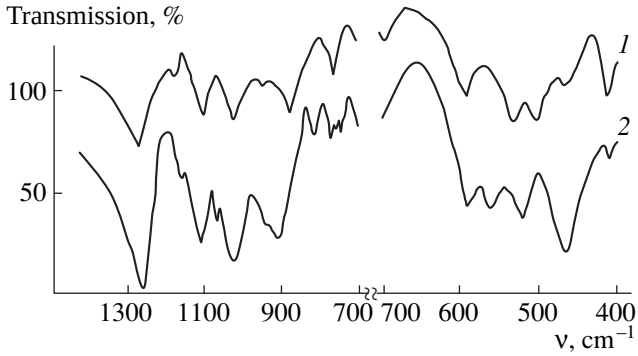


**Fig. 3.** IR spectra of (*1*) $KNi(PO_3)_3$ and (*2*) $NaNi(PO_3)_3$.

structure is the formation of channels (with about 3.5 Å diameter) penetrating the crystal along the *z*-axis. This reduced the density of potassium phosphate in comparison with the density of the Na salt (Table 1).

A Ni atom is located in the center of an almost regular octahedron with the average Ni–O distance of 2.049 Å. The coordination polyhedron of a K atom can be described as a distorted tricapped trigonal prism.

A large number of double polyphosphates of alkali and divalent metals were studied in [12]. Double polyphosphates have several structural types, namely, those of benitoites [for K*M*$(PO_3)_3$, where *M* = Co, Mn, Mg, or Zn], high-temperature benitoite $(NH_4)Ni(PO_3)_3$, and of compounds with the orthorhombic structures of the type $(NH_4)Co(PO_3)_3$, etc. [11].

The specific feature of the benitoite-type structures is the presence of three-membered $(PO_3)_3$ rings located normally to the sixfold axis. The compounds with the high-temperature benitoite structure are characterized by the presence of threefold screw axes with infinite chains of $PO_4$ tetrahedra around them, which remind similar fragments in the structure of $KNi(PO_3)_3$ under study. However, the coordination number in the latter structure ($KNi(PO_3)_3$) equals 9, whereas the coordination number in the high-temperature benitoite equals 12. Double polyphosphates with the orthorhombic and the monoclinic structural types are characterized by infinite polyphosphate chains with the repetition period equal to six $PO_4$ tetrahedra, oriented along the *b*-axis [12, 13]. In $NaNi(PO_3)_3$, the repetition period of the polyphosphate chain equals 12 and the chains are parallel to the *a*-axis. The structure under consideration differs from the structure described earlier in [7] because it contains polyphosphate chains of a rather peculiar configuration. The angles between the tetrahedron triads in this chain substantially differ from the right angle. Moreover, the structure under consideration is characterized by the coordination number on Na atoms different from the coordination number of the above-mentioned monoclinic and orthorhombic structures.

The IR spectra of the compounds synthesized are given in Table 3. The spectra have the absorption bands typical of polyphosphates, namely, P–O–P stretching vibration bands $\nu_{as}$ (at 700, 740, 765, and 810 $cm^{-1}$) and P–O–P bands $\nu_s$ (at 910–940 $cm^{-1}$) and also $PO_2$ vibration bands $\nu_s$ and $\nu_{as}$ in the range 1030–1260 $cm^{-1}$ for $NaNi(PO_3)_3$. The absorption bands in the range of 410–595 $cm^{-1}$ may be attributed P–O–P bands $\nu_{as}$ and $\nu_s$. The $\nu$ vibrations of *M*–O are also observed in the same range.

The $KNi(PO_3)_3$ double phosphate is also characterized by absorption bands in the same range (Fig. 3), but the P–O–P bands stretching $\nu_{as}$ and $\nu_s$ are observed only at 695, 765, and 875 $cm^{-1}$. This fact can be explained by the presence of a more symmetric polyphosphate chain than that in $NaNi(PO_3)_3$, where several angles of the chain considerably differ from one another.

The thermal studies of the compounds synthesized showed that they undergo phase transitions at 640 and 895°C. The melting points of the $NaNi(PO_3)_3$ and $KNi(PO_3)_3$, compounds were determined as 970 and 980°C, respectively.

## REFERENCES


1. N. V. Litvin and V. A. Masloboev, *Rare Earth Phosphates* (Nauka, Leningrad, 1989).
2. B. Thonnerieux, J.-C. Grenier, and A. Durif, C. R. Acad. Sci., Ser. IIb: Mec., Phys., Chim., Astron. **267**, 718 (1968).
3. R. Masse, J.-C. Grenier, and M. T. Averbuch-Pouchot, Bull. Soc. Fr. Mineral. Cryst. **90**, 158 (1967).
4. E. L. Krivovyazov and P. M. Fedorov, Izv. Akad. Nauk SSSR, Neorg. Mater. **11**, 307 (1976).
5. E. L. Krivovyazov, K. K. Palkina, and I. K. Voskresenskaya, Dokl. Akad. Nauk SSSR **174**, 610 (1967).
6. A. Durif and C. Martin, Acta Crystallogr., Sect. B: Struct. Crystallogr. Cryst. Chem. **28**, 2348 (1972).
7. Yu. F. Shepelev, Yu. I. Smolin, A. M. Domanskiĭ, and A. V. Lavrov, Dokl. Akad. Nauk SSSR **272**, 610 (1983) [Sov. Phys.-Doklady **28**, 710 (1983)].
8. V. G. Zharovskiĭ, A. T. Pilipenko, and I. V. Pyatnitskiĭ, *Analytical Chemistry* (Vyscha Shkola, Kiev, 1969).
9. W .F. Hillebrandt and G. E. F. Lundell, *Applied Inorganic Analysis with Special Reference to the Analysis of Metals, Minerals and Rocks*, 2nd ed. Revised by G. E. F. Lundell, H. A. Bright, and J. I. Hoffman (Wiley, New York, 1953; Khimiya, Moscow, 1957).
10. R. Masse, J.-C. Grenier, and M. T. Averbuch-Pouchot, Bull. Soc. Fr. Mineral. Cryst. **93**, 394 (1970).
11. M. Laugt, M. Scory, and A. Durif, Mater. Res. Bull. **3**, 963 (1968).
12. A. Durif, Rev. Chem. Mineral. **6**, 109 (1969).
13. O. Tranqui, J.-C. Grenier, and A. Durif, Bull. Soc. Fr. Mineral. Cryst. **90**, 252 (1967).


*Translated by T. Safonova*

*Crystallography Reports, Vol. 45, No. 2, 2000, pp. 210–214. Translated from Kristallografiya, Vol. 45, No. 2, 2000, pp. 242–246.*


## STRUCTURES OF INORGANIC COMPOUNDS

# Crystal Structure of Loparite

**N. V. Zubkova*, A. V. Arakcheeva**, D. Yu. Pushcharovskiĭ*, E. I. Semenov***, and D. Atencio******

** Moscow State University, Vorob'evy gory, Moscow, 119899 Russia*

*** Baĭkov Institute of Metallurgy and Materials Technology, Russian Academy of Sciences, Leninskiĭ pr. 49, Moscow, 117334 Russia*

**** Mineralogical Museum, Russian Academy of Sciences, Leninskiĭ pr. 18, Moscow, 117071 Russia*

***** Institute of Geoscience, University of São Paulo, Caixa Postal 11348–05422-970, São Paulo, Brazil*

Received September 1, 1998

**Abstract**—The crystal structure of the cubic modification of the natural mineral loparite has been studied for the first time by the methods of the X-ray diffraction analysis ($\lambda$Mo$K_\alpha$ radiation, 105 independent reflections with $I > 3\sigma(I)$, $R = 0.041$ in the anisotropic approximation). The structure belongs to the perovskite type ($ABO_3$) with the double period of the cubic unit cell, $a = 7.767(1)$ Å (sp. gr. $Pn3m$; $Z = 2$ for the composition $(Ca,Na,Ce)(Na,Ce)_3(Ti,Nb)_2Ti_2O_{12}$. Period doubling is explained by ordering of cations both in the *A* and the *B* positions. © *2000 MAIK "Nauka/Interperiodica".*

## INTRODUCTION

The Khibiny and the Lovozero alkaline complexes are the world's largest massifs of nepheline syenites. Until recently, only two minerals of the perovskite group were found in these massifs, namely, perovskite $CaTiO_3$ proper from ultrabasic xenoliths and loparite $(Ce,Ca,Na,M)(Ti,Nb)O_3$ (*M* = Sr, *TR*, Th, etc.) discovered in nepheline syenites associated with pegmatites and metasomatites [1]. In 1997, this mineralogical group was extended due to the discovery of isolueshite $(Na,La,Ce)(Nb,Ti)O_3$ related to hydrothermally modified pegmatite lodes of the Khibiny alkaline complex [2].

Despite the first indications of the existence of loparite having appeared more than a hundred years ago [3], the data on its structure are ambiguous because no reliable single-crystal studies have been performed. Most publications consider loparite as a perovskite-like mineral, whose cubic structure with the parameter $a = 3.886(1)$ Å and sp. gr. $Pm3m$ is identical to the structures of the cubic modification of perovskite $CaTiO_3$ and its strontium analog tausonite, $SrTiO_3$. Unlike these two minerals, loparite is characterized by a much larger "isomorphous capacity" of both positions occupied by large cations (*A* position), in which, in addition to Ca cations, a large number of Ce, Na, Sr, Th, and rare-earth cations can also be located, and by small cations (*B* position), in which Ti is partly replaced by Nb. Loparite [1] and Sr-loparite (South Africa) [4] are distinguished by the prevalence of a certain kind of cations in the *A* position. The Sr-loparite was considered as a solid solution of perovskite and tausonite [4].

Apparently, the variety of chemical compositions of loparites provide various distortions of the perovskite structure, which may result from the complete or partial ordering of cations in both positions. Thus, a trigonal modification of loparite with the unit-cell parameters $a = 5.50$ and $c = 6.71$ Å and $Z = 3$ was found in the Lovozero alkaline complex [5]. It was assumed that in this modification, the ordered distribution of the *A* cations (Ce, Ca, and Na) takes place. It should be indicated that in most studies, the propensity of loparites to twinning was indicated.

Finally, it is noteworthy to mention "nioboloparite" discovered in 1957 and later also found in different regions of the Khibiny and the Lovozero massifs. However, the detailed study of this mineral undertaken in 1996 [6] demonstrated that it was loparite, in fact, with the average $Nb_2O_5$ content not exceeding 11%. Therefore, "nioboloparite" as a mineral type has been discarded.

All the above-mentioned structural data on loparite, to a large extent hypothetical, gave an impetus to its further experimental study. Therefore, the present article is devoted to the study of the loparite structure.

## EXPERIMENTAL

The loparite crystals chosen for the X-ray structure study were found by E.I. Semenov in the Alluaiv mountain of the Lovozero alkaline massif. This mineral is related to the trigonal loparite modification discovered in the Punkaruaiv mountain of the same massif [5] because both modifications were found in the enclosing rocks having similar compositions, namely, in agpaitic

1063-7745/00/4502-0210$20.00 © 2000 MAIK "Nauka/Interperiodica"

nepheline syenites. Usually, these rocks contain eudialyte and are formed on the contacts with pegmatites, whose core forms a characteristic ultrasodium mineral—ussingite ($Na_2AlSi_3O_8(OH)$).

The chemical composition of the crystals was determined on a Camebax SX50 X-ray microanalyzer. Processing of the data obtained yielded the following formula:

$$(Na_{0.48}Ca_{0.12}Ce_{0.19}La_{0.08}Nd_{0.04}Th_{0.01}Sr_{0.05}Pr_{0.01}Eu_{0.01}Sm_{0.01})(Ti_{0.87}Nb_{0.13})O_3.$$

This formula was taken as the basis for the subsequent refinement of the crystal structure.

The refraction indices measured using the method of immersion liquids performed by I.V. Pekov confirmed the isotropic nature of the optical properties of loparite.

A $0.1 \times 0.1 \times 0.2$ mm-large loparite single crystal was chosen for the X-ray structure analysis.

All the X-ray diffraction studies were performed on a single-crystal Syntex $P\bar{1}$ diffractometer (Mo$K_\alpha$ radiation, graphite monochromator). The unit-cell parameters, determined with the use of 15 reference reflections with $2\theta < 15°$ showed that the period of the cubic unit-cell is doubled in comparison with that indicated by the published data for the perovskite-type structures. The values determined were refined using two groups of strong high-angle ($2\theta = 36°$–$40°$) ($\pm 4 \pm 4 \pm 4$) and ($\pm 6 \pm 4 \pm 2$) reflections indicated that cubic symmetry ($a$ = 7.767(1) Å, $\alpha = 90.03(1)°$) is highly probable and confirmed the doubling of the unit cell parameter of loparite.

To reveal possible twinning in the crystals, we obtained profiles of different types of reflections using the $\omega$ and $2\theta/\theta$ scanning techniques. The presence of narrow symmetric peaks (their $2\theta$ and $\omega$ widths did not exceed 1° and 0.6°, respectively) excluded the presence of twins with the disordered lattice vectors. This allowed us to conclude that the only possible twinning, if at all, can be merohedral twinning.

The complete set of X-ray diffraction data was collected using the $2\theta/\theta$ scanning technique within a reciprocal-space hemisphere ($\sin\theta/\lambda < 1.1$) and amounted to 2398 independent reflections. The intensities of 1434 reflections exceeding $3\sigma(I)$ were used in the subsequent calculations.

The experimental intensities were recalculated into structure amplitudes with due regard for the Lorentz and the polarization factors. All the computations were performed by the AREN program package [7].

Upon averaging of the crystallographically equivalent reflections within the diffraction class $m3m$ ($R_{int}$ = 0.047), 105 independent reflections were used for further computations. The double unit cell parameter of the loparite crystal was chosen because 39 reflections had odd $h, k, l$ indices.

The analysis of the systematic extinctions for the $hk0$-types reflections with $h + k = 2n + 1$ indicated the sp. gr. $Pn3m$. Because of possible merohedral twinning not excluded at this stage of the study, the structure was also refined within the acentric sp. gr. $P4_232$.

In both symmetry groups, the $A$ and $B$ cations in the perovskite structure occupy two independent positions—namely, twofold and sixfold positions ($A$ cations) and two fourfold positions ($B$ cations). Taking into account the interatomic distances in the coordination polyhedra, the refined occupancies of the cationic positions, and the isotropic thermal parameters we used, the Ti and ($Ti_{0.73}$ + $Nb_{0.27}$) scattering curves for two $B$ positions and the mixed scattering curves (0.47Ca + 0.13Na + 0.4$M$) and (0.59Na + 0.41$M$) for the $A$ positions, where $M$ = $Ce_{0.19}La_{0.08}Nd_{0.04}Th_{0.01}Sr_{0.05}Pr_{0.01}Eu_{0.01}Sm_{0.01}$.

The computations performed within the sp. gr. $Pn3m$ gave the lower reliability factor, $R$ = 0.041. Examination of different modes of merohedral twinning showed that there are no twinning components. No additional significant peaks were observed on the difference electron-density map constructed with the use of the final atomic coordinates.

The positional and the thermal parameters of the atoms and the position occupancies are given in Table 1.

**Table 1.** Characteristics of the atomic positions in the structure of loparite

| Position | Occupancy | $x/a$ | $y/b$ | $z/c$ | $B_{eq}$ |
|---|---|---|---|---|---|
| $B'$: 4$b$ | Ti | 0.0 | 0.0 | 0.0 | 0.98(4) |
| $B''$: 4$c$ | $Ti_{0.73}$ + $Nb_{0.27}$ | 0.5 | 0.5 | 0.5 | 0.85(3) |
| $A'$: 2$a$ | $Ca_{0.47}$ + $Na_{0.13}$ + $M$* | 0.25 | 0.25 | 0.25 | 0.44(5) |
| $A''$: 6$d$ | $Na_{0.59}$ + $M$ | 0.25 | 0.75 | 0.75 | 0.90(3) |
| O : 24$k$ | O | 0.4778(1) | 0.4778(1) | 0.2483(1) | 4.31(4) |

* Here and in Table 2, $M$ = $Ce_{0.19}La_{0.08}Nd_{0.04}Th_{0.01}Sr_{0.05}Pr_{0.01}Eu_{0.01}Sm_{0.01}$.

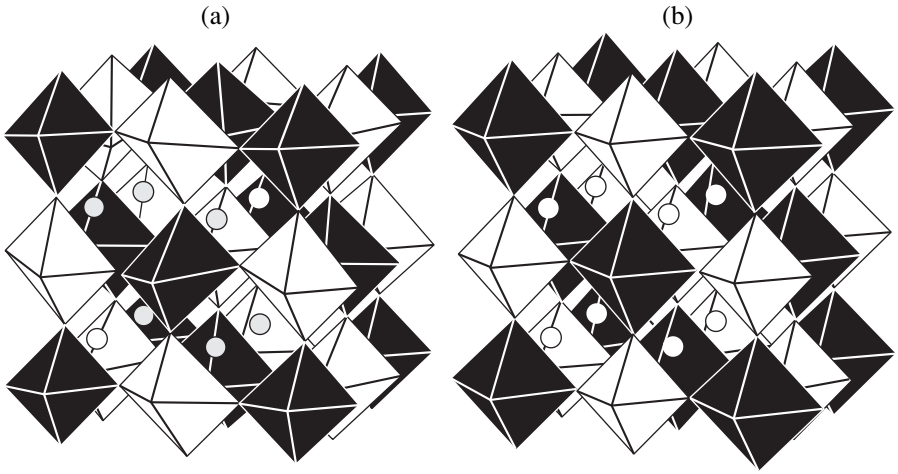


**Fig. 1.** Perovskite-type cubic structures with double unit-cell parameters of (a) loparite and (b) $Ca_2TiSiO_6$. (Ti-octahedra are black; (Ti,Nb) octahedra in the loparite structure and Si-octahedra in the $Ca_2TiSiO_6$ structure are white); (a) two positions of large cations are indicated by circles—empty for Ca and hatched for Na.

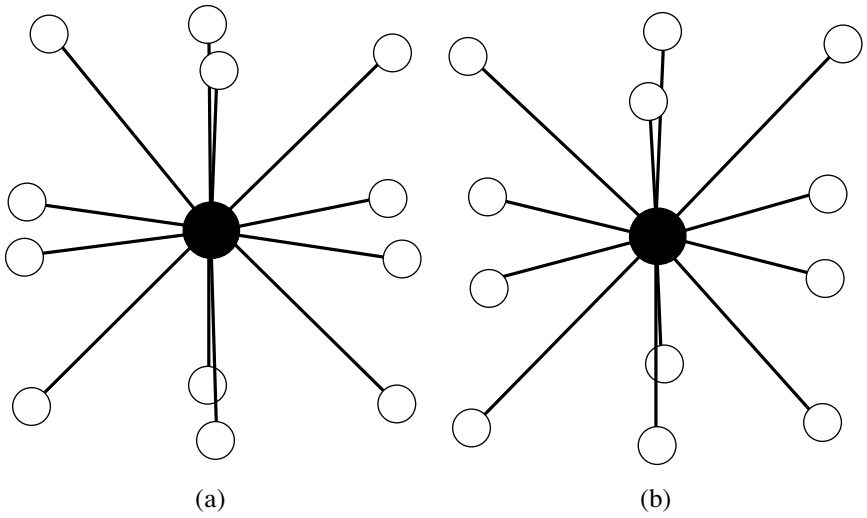


**Fig. 2.** The first coordination spheres of atoms in the *A* positions: (a) Ca position and (b) Na position.

The corresponding interatomic distances in the coordination polyhedra are as follows: *B*'–O, 1.94(1) Å, *B*''–O, 1.96(1) Å, *A*'–O, 2.50(1) Å, and *A*''–O, 2.75(1) Å × 8 and 2.98(1) Å × 4. The cation distribution over the crystallographically nonequivalent positions was confirmed by the calculations of the balance of valence strengths at the anions (the "quality" criterion $D = 0.009$).

The X-ray powder diffraction pattern of the loparite crystal was obtained on a DRON-M3 diffractometer (Cu$K_\alpha$ radiation, pyrographite monochromator) and indexed using the Lazy Pulverix program [8] (Table 2). The presence of a reflection with the odd indices confirmed the doubling of the loparite unit-cell parameter in this case as well.

## RESULTS AND DISCUSSION

Similar to all the structures of the perovskite type, the loparite framework is formed by small-cation octahedra sharing their vertices. The Ti atoms in the 4*b* (*B*') position are located in the octahedra with all the Ti–O distances being equal to 1.94 Å and the O–Ti–O angles ranging within 79.6(4)°–100.3(4)°. A slightly larger (Ti,Nb) polyhedron (position 4*c* (*B*'')) is also an almost regular octahedron. The O–(Ti,Nb)–O angles range within 79.4(4)°–100.5(4)°. These two types of chemically different octahedra are arranged in the structure in the chess-board manner (Fig. 1a). Large *A* cations occupy the cuboctahedral cavities of the framework; they are partly ordered. As a result, all the Ca atoms occupy one twofold position (2*a*), whereas almost all

the Na atoms occupy the sixfold position (6*d*) (Table 1). The Ca polyhedron (*A*') is slightly smaller and is virtually undistorted (all the twelve cation–oxygen distances equal 2.50 Å). The first coordination sphere of the *A*' cation is shown in Fig. 2a. The Na polyhedron (*A*") is larger and more distorted: the *A*–O distances range within 2.75–2.99 Å, with the average value being 2.83 Å. The cuboctahedron is slightly elongated in the direction of the fourfold axis. The first coordination sphere of the *A*" cation is shown in Fig. 2b.

The distribution of the cations over various polyhedra is characterized by different degrees of deformation observed in the loparite structure demonstrates that, on the one hand, the cations in the Ca–Na and Nb–Ti pairs are crystallochemically different. On the other hand, this distribution shows that we deal with a new structural type of perovskite, in which such cation separation becomes possible. It is this ordered distribution of the *A* and *B* cations that accounts for doubling of the unit-cell parameters of loparite.

This type of cation ordering in the perovskite type structure was observed for the first time. It can be described as follows: $A'A''_3\,B'_2\,B''_2\,O_{12}$; sp. gr. $Pn3m$; *A*': 2*a*, $\bar{4}\,3m$, (0.25, 0.25, 0.25); *A*": 6*d*, $\bar{4}\,2m$, (0.25, 0.75, 0.75); *B*': 4*b*, $\bar{3}\,m$, (0, 0, 0); *B*": 4*c*, $\bar{3}\,m$, (0.5, 0.5, 0.5); O: 24*k*, *m*, (*x*, *x*, *z*). For the crystal under study, $x = 0.4778(1)$ and $z = 0.2483(1)$.

The cations in this structural type are ordered over different positions because O atoms can be displaced from their positions to form two chemically different *B* octahedra of different sizes which are rotated with respect to one another and two twelve-vertex polyhedra *A* of different sizes. One of them (*A*') is an almost regular cuboctahedron, whereas the second one (*A*") is a considerably distorted cuboctahedron.

Now compare the revealed ordering in the perovskite structure with the characteristic double unit-cell parameter *a*, with the well known type of ordering in perovskite-like compounds described by the general formula $A_2B'B''O_6$ [9]. The latter compounds are also crystallized in the cubic cell with a double period, but are described by the sp. gr. $Fm3m$. Using the analogy with the above-mentioned type of ordering, the ordering in these compounds can be represented as follows: $A_2B'B''O_6$; sp. gr. $Fm3m$; *A*: 8*c*, $\bar{4}\,3m$, (0.25, 0.25, 0.25); *B*': 4*a*, $m3m$, (0, 0, 0); *B*": 4*b*, $m3m$, (0.5, 0.5, 0.5); O: 24*e*, 4*mm*, (*x*, 0, 0).

For the $Ca_2TiSiO_6$ compound, $x = 0.2372(4)$ [9]. The comparison of the structural types, shows that they have common features, namely, cationic positions have no degrees of freedom, there is only one oxygen position possessing the positional degrees of freedom, and the *B* positions are divided into two positions. The differences between these two types of ordering reduce to the following: the first case, the A cations can be ordered in (two *A* positions), while in the second case such ordering is impossible (one *A* position). Moreover, the polyhedra in the first structural type can be distorted more pronouncedly, because the oxygen atoms have one additional degree of freedom.

**Table 2.** Comparison of the experimental and calculated X-ray powder diffraction patterns of loparite

| *h k l* | $I_{calcd}$ | $I_{exp}$ | $d_{calcd}$, Å | $d_{exp}$, Å |
|---|---|---|---|---|
| 1 1 0 | 3 | 8 | 5.492 | 5.496 |
| 2 2 0 | 100 | 100 | 2.746 | 2.748 |
| 2 2 2 | 11 | 11 | 2.242 | 2.242 |
| 4 0 0 | 39 | 53 | 1.942 | 1.943 |
| 4 2 2 | 36 | 41 | 1.585 | 1.589 |
| 4 4 0 | 13 | 12 | 1.373 | 1.373 |
| 6 2 0 | 13 | 9 | 1.228 | 1.227 |
| 4 4 4 | 5 | 4 | 1.121 | 1.123 |
| 6 4 2 | 16 | 6 | 1.038 | 1.040 |

The structure of loparite under study and that of $Ca_2TiSiO_6$ characterized by the double unit-cell parameter are shown in Fig. 1. It is seen that the octahedra occupied by the chemically different *B* cations in both structures are arranged in a chess-board manner. In the structure of $Ca_2TiSiO_6$, chemically different *B* octahedra have noticeably different dimensions (Ti–O is 1.947(3) and Si–O is 1.758(3) Å [9]), whereas in the loparite structure the difference between these polyhedra is only feebly marked (Ti–O is 1.95(1) and (Ti,Nb)–O is 1.97(1) Å), but, at the some time, the *B*' and *B*" octahedra are rotated with respect to one another.

In conclusion, it should be noted that the loparite structure under consideration with the double unit-cell parameter substantially differs from the loparite structures described earlier. Thus, one cannot exclude the probability that loparites having another chemical composition would also have some other structural changes.

## ACKNOWLEDGMENTS

We are grateful to I.V. Pekov for performing optical measurements, N.N. Kononkova for carrying out the chemical analysis, and G.U. Lubman for his help in performing X-ray diffraction studies.

The study was supported by the Russian Foundation for Basic Research, project nos. 99-05-39019 and 00-05-65399, by the Foundation of the Ministry of General and Vocational Education of the Russian Federation, and by the Program *Russian Universities*.

## REFERENCES

1. In *Geochemistry, Mineralogy and Genetic Types of Deposits of Rare Elements*, Ed. by K. A. Vlasova (Nauka, Moscow, 1964).
2. A. Chakhmouradian, V. Yakovemchuk, R. Mitchell, *et al.*, Eur. J. Mineral. **9**, 483 (1997).
3. W. Ramsay and V. Hackman, Fennia **11**, 1 (1894).
4. S. E. Haggerty and A. N. Mariano, Contrib. Mineral. Petrol. **84**, 365 (1983).
5. E. I. Semenov, *Mineralogy of Rare Earth Elements* (Nauka, Moscow, 1963).
6. R. Mitchell, A. Chakhmouradian, and V. Yakovemchuk, Can. Mineral. **34**, 991.
7. V. I. Andrianov, Kristallografiya **34**, 592 (1989) [Sov. Phys.-Crystallogr. **34**, 352 (1989)].
8. K. Yvon, W. Jeitschko, and E. Parthé, J. Appl. Crystalogr. **10**, 73 (1977).
9. K. Leinenweber and J. Parise, Am. Mineral. **82**, 475 (1997).

*Translated by T. Safonova*

*Crystallography Reports, Vol. 45, No. 2, 2000, pp. 215–218. Translated from Kristallografiya, Vol. 45, No. 2, 2000, pp. 247–250.*


**STRUCTURES OF INORGANIC COMPOUNDS**

# Low-Temperature X-ray Studies of Crystal-Lattice Parameters and Thermal Expansion of $KTiOPO_4$ Crystals

**A. U. Sheleg, E. M. Zub, L. A. Stremoukhova, and S. A. Guretskiĭ**

*Institute of Solid-State and Semiconductor Physics, National Academy of Sciences of Belarus, ul. Brovki 17, Minsk, 220072 Belarus*

Received June 8, 1998; in final form, December 15, 1998

**Abstract**—The unit-cell parameters *a*, *b*, and *c* of $KTiOPO_4$ crystals have been measured by the X-ray diffraction method in the temperature range 80–320 K. The parameters obtained were used to determine the thermal expansion coefficients $\alpha_{[100]}$, $\alpha_{[010]}$, and $\alpha_{[001]}$ along the principal crystallographic axes. It was established that thermal expansion in the crystals is essentially anisotropic and that $\alpha_{[010]} > \alpha_{[100]}$, whereas $\alpha_{[001]}$ is close to zero.


## INTRODUCTION

Potassium-titanyl phosphate crystals are considered to be a very promising nonlinear-optical material for laser technology and micro- and optoelectronics. These crystals are also the object of intense studies because of a set of unique physical properties. In addition to high value of the nonlinearity coefficient of optical properties, they are also characterized by high optical stability and ionic conductivity and possess ferroelectric and pyroelectric properties [1–5].

The crystal structure of $KTiOPO_4$ crystals is described by the noncentrosymmetric orthorhombic point group *mm*2, sp. gr. $Pna2_1$, with the unit-cell parameters at room temperature equal to $a$ = 12.814, $b$ = 6.404, and $c$ = 10.616 Å according to [2, 6] and $a$ = 12.8164, $b$ = 6.4033, and $c$ = 10.5987 Å according to [7]. The unit cell contains eight formula units. Since $KTiOPO_4$ crystals are best known as a material for nonlinear optics, most of the published data on these crystals describe their optical properties. The crystallographic and dynamic characteristics of the crystals are studied to a considerably lesser degree, despite the fact that they are of great scientific and practical interest. Below, we present the results of the X-ray diffraction study of the variation in the unit-cell parameters *a*, *b*, *c*, the volume *V*, and thermal-expansion coefficients along the principal crystallographic directions, [100], [010], and [001], in the temperature range from 80 to 320 K.

## EXPERIMENTAL

Single crystals of the composition $KTiOPO_4$ were grown from flux in the $TiO_2$–$K_2HPO_4$–$KH_2PO_4$ system. The synthesis was performed in a device with heating carbide–silicon elements and automated control of the temperature maintained within ~0.1 K. The crystals were grown on (100)-oriented seeds (within an accuracy not less than 5′). A seed submerged into the flux was rotated at all the growth stages at rates ranging from 80 to 120 rpm depending on the dimensions of a growing crystal and the temperature gradients in the crystallization zone. The synthesis began at the temperature 1320–1360 K. The thus grown crystals had the dimensions ~50 × 40 × 12 mm.

X-ray diffraction studies of the $KTiOPO_4$ crystals grown were performed on a TUR-M62 diffractometer in a $CuK_\alpha$-monochromatized radiation by the method described elsewhere [8]. The specimens were ~5 × 2 mm plates cut out from the boules of the grown single crystals. Using the X-ray diffraction method, the plate surfaces were oriented parallel to the crystallographic (100), (010) and (001) planes within an accuracy of 3′–7′. The profiles of the X-ray diffraction spectra were recorded onto the diagram band by a counter rotating with the angular velocity of 1/4 deg/min (θ–2θ scan). The reflection angles were determined from the position of the center of gravity of the profiles within an accuracy of 0.2′–0.4′.

The unit-cell parameters determined from the reflection angles of the 14.00, 060, and 00.12 reflections at room temperature are: $a$ = 12.8187 ± 0.0002, $b$ = 6.4023 ± 0.0001, and $c$ = 10.5857 ± 0.0001 Å and agree quite well with the known data [6, 7]. Then, the same parameters were measured at different temperatures at a step of ~10 K.

The temperature dependences of the experimental geometric characteristics of the crystal lattice obtained in the temperature range 80–320 K are shown in Fig. 1. The dependences $a = f(T)$, $b = f(T)$, $c = f(T)$, and $V = f(T)$ were approximated by a polynomial of the type $L = L_0(1 + AT + BT^2 + CT^3)$. The values of the *A*, *B*, and *C*

1063-7745/00/4502-0215$20.00 © 2000 MAIK "Nauka/Interperiodica"

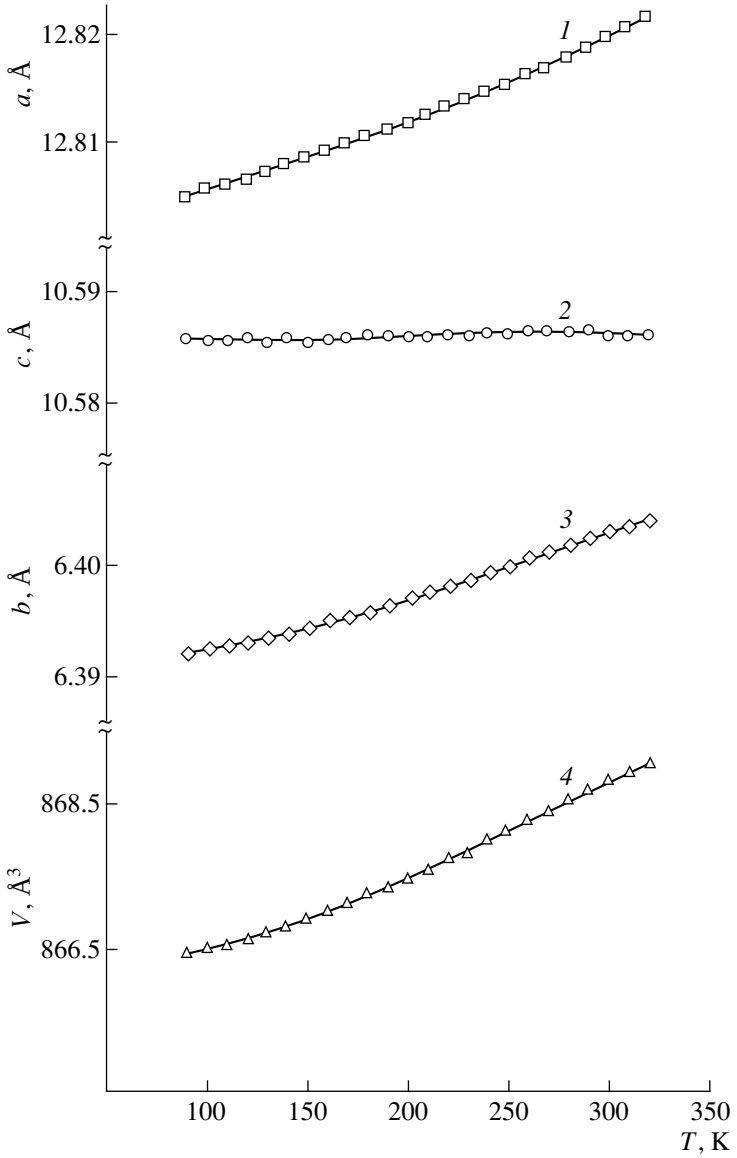


**Fig. 1.** Temperature dependences of the (*1*) *a*-, (*2*) *c*-, and (*3*) *b*-parameters, and (*4*) the unit-cell volume *V* for $KTiOPO_4$ crystals.

coefficients for the curves $a = f(T)$, $b = f(T)$, $c = f(T)$, and $V = f(T)$ are indicated in table.

As is seen from Fig. 1, the temperature dependences of the experimental lattice parameters (points) are reliably described by such a polynomial (solid lines). The *a*- and *b*-parameters and the unit-cell volume *V* smoothly (but no linearly) increase with the temperature, whereas the *c*-parameter varies only slightly in the same temperature range. Similar data were also obtained for the $TlTiOPO_4$ crystals [9]. The thermal expansion coefficients $\alpha_{[100]}$, $\alpha_{[010]}$, and $\alpha_{[001]}$ along the principal crystallographic axes and the volume coefficient of thermal expansion $\alpha_V$ were calculated from the expression $\alpha = dL/(dTL)$. The temperature dependences of the linear and volume thermal expansion coefficients with due regard for the determined coefficients *A*, *B*, and *C* can be represented in the form

$$\alpha_{[100]} = 4.292 \times 10^{-6} - 4.678 \times 10^{-9} T + 4.791 \times 10^{-11} T^2,$$

Coefficients of the polynomial $L = L_0(1 + AT + BT^2 + CT^3)$ approximating the temperature dependence of the geometrical parameters of the $KTiOPO_4$ crystals

| Parameters | $A$, $10^{-6}$ | $B$, $10^{-8}$ | $C$, $10^{-11}$ |
|---|---|---|---|
| *a* | 4.292 | −0.234 | 1.597 |
| *b* | −5.367 | 5.686 | −7.188 |
| *c* | −4.727 | 2.607 | −4.392 |
| *V* | −7.988 | 9.115 | −11.586 |

$$\alpha_{[010]} = -5.367 \times 10^{-6} + 1.137 \times 10^{-7} T - 2.156 \times 10^{-10} T^2,$$

$$\alpha_{[001]} = -4.727 \times 10^{-6} + 5.214 \times 10^{-8} T - 1.318 \times 10^{-10} T^2,$$

and

$$\alpha_V = -7.988 \times 10^{-6} + 1.823 \times 10^{-7} T - 3.477 \times 10^{-10} T^2.$$

In the graphical form, these dependences are shown in Fig. 2. It is seen that the $KTiOPO_4$ crystals are characterized by a pronounced anisotropy of thermal expansion. The thermal expansion coefficients along the [100]- and [010]-directions increase with the temperature, so that $\alpha_{[100]} = \alpha_{[010]}$ at $T \approx 105$ K, $\alpha_{[100]} > \alpha_{[010]}$ at $T < 105$ K, and $\alpha_{[010]} > \alpha_{[100]}$ at $T > 105$ K. The coefficients of thermal expansion along the [001]-direction are close to zero in the whole temperature range studied. It should be emphasized that the temperature dependence of the volume thermal expansion coefficient $\alpha_V$ and the temperature dependences of the coefficients of thermal expansion along the [010]-direction showed broad maxima at temperatures close to ~260 K. It should also be indicated that the $\varepsilon(T)$ and the $\tan\delta(T)$ curves obtained in the studies of dielectric properties of $KTiOPO_4$ crystals had kinks at $T \approx 280$ K [2], which were interpreted by the authors as the indications to the structural rearrangements in these crystals at $T \sim 280$ K. Possibly, a certain transformation occurs in the temperature range ~260–280 K, despite the fact that the anomalies observed on the $\alpha(T)$ curves during structural transformations have somewhat different form.

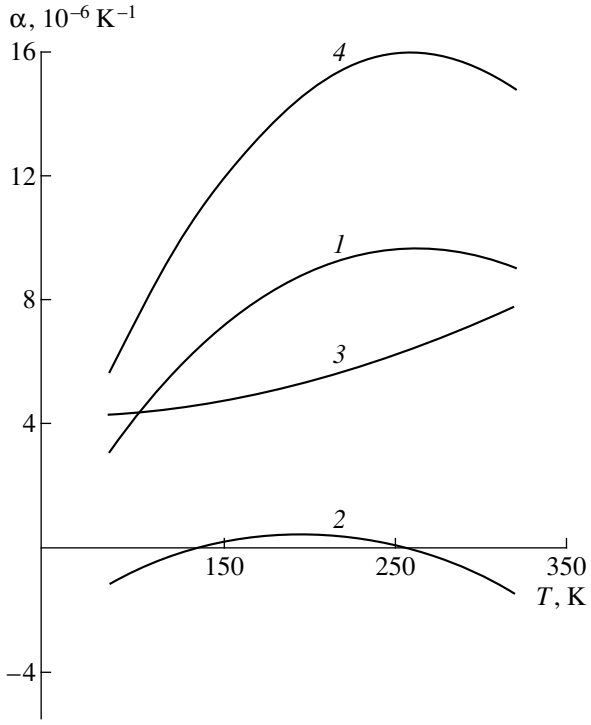


**Fig. 2.** Temperature dependences of the thermal expansion coefficients (*1*) $\alpha_{[010]}$, (*2*) $\alpha_{[001]}$, and (*3*) $\alpha_{[100]}$ and (*4*) the volume expansion coefficient $\alpha_V$ for $KTiOPO_4$ crystals.

## DISCUSSION

The experimental results obtained indicate that thermal expansion in the $KTiOPO_4$ crystals is strongly anisotropic. The thermal expansion coefficient along the [010]-direction exceeds the coefficient of thermal expansion along the [100]-direction in the largest part of the temperature range studied. It should be indicated that the thermal expansion coefficient along the [001]-direction is close to zero in the whole temperature range. The anisotropy of thermal expansion in the crystals is provided, first and foremost, by the specific features of the $KTiOPO_4$ crystal structure and, thus, by the anisotropy in atomic interactions. The structure of the $KTiOPO_4$ crystals consists of three-dimensional chains of alternating strongly distorted $TiO_6$-octahedra and slightly distorted $PO_4$-tetrahedra sharing their vertices and, thus, forming a three-dimensional anionic framework [6, 7]. The voids of the structure are occupied by $K^+$-cations located in two nonequivalent positions with respect to the *c*-axis and are displaced by 0.143 Å with respect to one another along this axis. The $K^+$ cations fill only some of the voids. The existence of empty voids located along the *c*-axis and mobile $K^+$-ions provides a high ionic conductivity and anisotropic electric conductivity in the $KTiOPO_4$ crystals [2, 10]. Both $TiO_6$-octahedra and $PO_4$-tetrahedra are the rigid formations with strong chemical bonding. Potassium ions located between these tetrahedra and octahedra can readily migrate over the voids along the polar *c*-axis. Thus, the existence of the conductivity channels along the *c*-axis results in weak chemical bonding between the octahedra and the tetrahedra in the (001) plane, whereas along the [001]-direction, the atomic interactions are very strong, which is provided by the rigid bonding inside the octahedra and the tetrahedra. It is such a character of the interaction forces between the atoms that gives rise to thermal-expansion anisotropy in the $KTiOPO_4$ crystals.

## REFERENCES

1. V. K. Yanovskiĭ, V. I. Voronkova, A. P. Leonov, *et al.*, Fiz. Tverd. Tela (Leningrad) **27**, 2516 (1985).
2. V. A. Kalesinskas, N. I. Pavlova, I. S. Rez, *et al.*, Litov. Fiz. Sb. **22**, 87 (1982).

3. F. C. Zumsteg, J. D. Bierlein, and T. E. Gier, J. Appl. Phys. **47**, 4980 (1976).
4. A. A. Bogomolov, R. M. Grechishkin, O. N. Sergeeva, *et al.*, Kristallografiya **42**, 478 (1997) [Crystallogr. Rep. **42**, 432 (1997)].
5. A. P. Leonov, V. I. Voronkova, S. Yu. Stefanovich, *et al.*, Pis'ma Zh. Éksp. Teor. Fiz. **11**, 85 (1985).
6. J. Tordjman, R. Masse, and J. R. Guitel, Z. Kristallogr. **139**, 103 (1974).
7. I. V. Voloshina, R. G. Gerr, M. Yu. Antipin, *et al.*, Kristallografiya **30**, 668 (1985).
8. A. U. Sheleg, E. M. Zub, L. A. Stremoukhova, *et al.*, Fiz. Tverd. Tela (Leningrad) **39**, 1038 (1997).
9. M. K. Blomberg, M. J. Merisalo, N. I. Sorokina, *et al.*, Kristallografiya **43**, 801 (1998) [Crystallogr. Rep. **43**, 748 (1998)].
10. V. K. Yanovskiĭ and V. I. Voronkova, Fiz. Tverd. Tela (Leningrad) **27**, 2183 (1985).

*Translated by L. Man*

*Crystallography Reports, Vol. 45, No. 2, 2000, pp. 219–221. Translated from Kristallografiya, Vol. 45, No. 2, 2000, pp. 251–253.*


## STRUCTURES OF INORGANIC COMPOUNDS

# Crystal Structure of a Hyperzirconium Analogue of Eudialyte

**R. K. Rastsvetaeva* and A. P. Khomyakov****

** Shubnikov Institute of Crystallography, Russian Academy of Sciences, Leninskiĭ pr. 59, Moscow, 117333 Russia*

*** Institute of Mineralogy, Geochemistry, and Crystal Chemistry of Rare Elements, Russian Academy of Sciences, Moscow, Russia*

Received June 11, 1999

**Abstract**—X-ray diffraction study of a new representative of the eudialyte family ($R$ = 4.5%, 2347 independent reflections) provided the establishment of a number of characteristic features of its structure associated with a high zirconium content and some other characteristics of the composition. The deficiency of Ca is compensated with Mn, Fe, rare-earth elements, Sr, and Na. The excessive Zr atoms are located in octahedra participating in the formation of a new type of a $TiZr_3$ cluster. © *2000 MAIK "Nauka/Interperiodica".*

Recently, a large number of new representatives having new chemical compositions have been found in the family of eudialyte, a mineral of a variable composition. Among these samples, there are kentbrooksite with high fluorine and manganese content [1], a high-titanium analog [2], and a low-iron analog of eudialyte [3], whose structures have already been studied. The present article describes the structural study of a new representative of the eudialyte family with an anomalously high zirconium content. The major characteristics of the mineral and the details of its single-crystal X-ray diffraction study are illustrated by Table 1. The atomic coordinates are listed in Table 2. The crystallochemical formula of eudialyte with anomalously high zirconium content can be written as follows ($Z$ = 3): $Zr_3(Ca_{2.7}MnFeNa_{0.85}Ce_{0.33}Sr_{0.12})[Si_3O_9]_2[Si_9O_{27}]_2 \times [Si_{0.5}Al_{0.5}][Si_{0.5}(Ti_{0.3}Nb_{0.2})][Zr_{1.2}Fe_{0.3}]Na_{0.87}(OH)_{1.5}] \times (Na_{15.87}K_{0.3}Sr_{0.33})Cl_{0.5}(O,OH)_{1.5}(OH)_{2.5} \cdot H_2O$. The main zirconium position in the eudialyte structure is located in the center of a regular octahedron with the distances to the nearest anions ranging within 2.018–2.097 Å. The excessive zirconium atoms in this structure form, together with iron atoms, the octahedra of

**Table 1.** Structural data and details of X-ray data collection

| Characteristic | Value |
|---|---|
| Unit-cell parameters, Å | $a$ = 14.222(3), $c$ = 30.165(5) |
| Unit-cell volume, Å$^3$ | $V$ = 5283.9 |
| Sp. gr., $Z$ | $R3m$; 3 |
| Radiation, λ, Å | Mo$K_\alpha$; 0.71073 |
| Crystal dimensions, mm | 0.14 × 0.25 × 0.33 |
| Diffractometer | Syntex $P2_1$ |
| Scanning mode | ω/2θ |
| sinθ/λ, Å$^{-1}$ | <0.809 |
| Range of data collection | $-20 < h < 20$, $0 < k < 20$, $-48 < l < 0$ |
| $R_{int}$ for equivalent reflections | 0.045 |
| Total number of reflections | 6107 $I > 2\sigma(I)$ |
| Number of independent reflections | 2347 $\|F\| > 4\sigma(F)$ |
| Program used in calculations | AREN [4] |
| Absorption correction | DIFABS [5] |
| Number of independent positions | 51 |
| $R$-factor for anisotropic refinement | 0.045 |

1063-7745/00/4502-0219$20.00 © 2000 MAIK "Nauka/Interperiodica"

**Table 2.** Coordinates, occupancies, and equivalent thermal parameters of the atoms

| Atom | *x*/*a* | *y*/*b* | *z*/*c* | *q* | $B_{eq}$, Å$^2$ |
|---|---|---|---|---|---|
| Zr(1) | 0.3333(1) | 0.1666(1) | 0.1668(1) | 1 | 1.43(1) |
| Zr(2) | 0.0126(3) | 0.5063(2) | 0.0017(1) | 0.50(1) | 3.1(1) |
| Si(1) | −0.0074(1) | 0.6044(1) | 0.0968(1) | 1 | 1.02(4) |
| Si(2) | 0.0561(1) | 0.3250(1) | 0.2369(1) | 1 | 1.06(4) |
| Si(3) | 0.0840(1) | 0.5420(1) | 0.2589(1) | 1 | 1.30(6) |
| Si(4) | 0.1395(1) | 0.0698(1) | 0.0817(1) | 1 | 1.33(6) |
| Si(5) | 0.2074(1) | 0.4148(1) | 0.0771(1) | 1 | 1.34(6) |
| Si(6) | 0.5260(2) | 0.2630(1) | 0.2525(1) | 1 | 1.71(7) |
| *T*(2) | 0.3333 | 0.6667 | 0.0885(5) | 0.50(1) | 1.8(2) |
| *T*(3) | 0.3333 | 0.6667 | 0.2455(5) | 0.46(4) | 2.2(5) |
| *T*(4) | 0.3333 | 0.6667 | 0.2833(3) | 0.52(3) | 2.2(3) |
| *M*(1) | −0.0004(1) | 0.2633(1) | 0.0006(1) | 1 | 1.42(1) |
| *M*(2) | 0.3333 | 0.6667 | 0.0407(1) | 0.50(1) | 2.1(1) |
| *M*(3) | 0.1130(2) | 0.2260(3) | 0.1530(1) | 0.80(1) | 2.7(1) |
| *M*(4) | 0.583(1) | 0.416(1) | 0.1661(9) | 0.29(1) | 5.0(2) |
| Na(1) | 0.4537(4) | 0.2270(3) | 0.0499(1) | 0.80(2) | 2.1(1) |
| Na(2) | 0.5579(3) | 0.4421(3) | 0.1791(2) | 0.71(2) | 3.0(2) |
| Na(3) | 0.2586(3) | 0.5166(5) | 0.1819(4) | 0.55(2) | 4.1(4) |
| Na(4) | 0.1957(4) | 0.0979(2) | 0.2904(1) | 0.84(2) | 2.1(1) |
| Na(5) | 0.5209(6) | 0.4791(6) | −0.0032(5) | 0.29(1) | 2.1(2) |
| Na(6) | 0.081(2) | 0.163(2) | 0.1684(9) | 0.19(1) | 2.9(4) |
| Na(7) | 0.495(1) | 0.247(1) | 0.0430(7) | 0.20(1) | 2.4(3) |
| Na(8) | 0.2401(1) | 0.1205(7) | 0.2776(6) | 0.20(1) | 1.9(3) |
| O(1) | 0.1813(3) | 0.3626(4) | 0.0292(2) | 1 | 2.7(3) |
| O(2) | 0.1788(2) | 0.3576(3) | 0.2225(2) | 1 | 1.5(2) |
| O(3) | 0.4054(4) | 0.0356(4) | 0.0453(1) | 1 | 2.2(2) |
| O(4) | 0.2587(4) | 0.0290(3) | 0.2069(1) | 1 | 2.1(1) |
| O(5) | 0.4690(6) | 0.2345(4) | 0.2043(2) | 1 | 3.8(3) |
| O(6) | 0.2243(7) | 0.1122(5) | 0.0414(3) | 1 | 4.3(5) |
| O(7) | 0.1896(6) | 0.0952(4) | 0.1294(2) | 1 | 2.6(2) |
| O(8) | 0.0991(3) | 0.3778(4) | 0.1068(1) | 1 | 1.9(1) |
| O(9) | 0.4414(6) | 0.2207(4) | 0.2921(2) | 1 | 3.2(3) |
| O(10) | 0.6043(2) | 0.3957(2) | 0.2567(2) | 1 | 2.4(2) |
| O(11) | 0.0609(2) | 0.1218(3) | 0.0789(2) | 1 | 2.0(2) |
| O(12) | 0.0474(4) | 0.6128(4) | 0.2262(1) | 1 | 2.2(2) |
| O(13) | 0.0231(6) | 0.5115(4) | 0.3050(2) | 1 | 2.5(2) |
| O(14) | 0.4103(4) | 0.3050(4) | 0.1287(1) | 1 | 2.5(2) |
| O(15) | 0.0407(3) | 0.2959(3) | 0.2883(1) | 1 | 1.7(1) |
| O(16) | 0.2740(3) | 0.5479(4) | 0.0678(3) | 1 | 3.8(4) |
| O(17) | 0.4903(3) | 0.5097(3) | 0.1147(2) | 1 | 2.0(2) |
| O(18) | 0.2092(6) | 0.6046(4) | 0.2552(1) | 1 | 3.7(3) |
| Cl | 0.0004(1) | 0.0002(1) | 0.2318(8) | 0.53(4) | 4.3(2) |
| O, OH(1) | 0.3948(9) | 0.6052(9) | 0.0050(7) | 0.50(1) | 3.9(5) |
| OH(2) | 0.3333 | 0.6667 | 0.137(1) | 0.50(1) | 0.9(1) |
| OH(3) | 0.3333 | 0.6667 | 0.1918(6) | 0.46(7) | 1.2(6) |
| OH(4) | 0.3333 | 0.6667 | 0.339(1) | 0.52(9) | 4(2) |
| OH(5) | 0.560(1) | 0.439(1) | −0.0019(9) | 0.50(2) | 5.2(5) |
| $H_2O$(1) | 0.6667 | 0.3333 | 0.048(4) | 0.50(9) | 3.3(5) |
| $H_2O$(2) | 0.6667 | 0.3333 | 0.081(4) | 0.17(5) | 4(2)* |
| $H_2O$(3) | 0 | 0 | 0.299(4) | 0.15(5) | 3(1)* |
| $H_2O$(4) | 0 | 0 | 0.262(4) | 0.16(5) | 2(1)* |

Note: The chemical compositions of the positions ($Z$ = 1): Zr(2) = 3.6Zr + 0.9Fe; *M*(1) = 8.1Ca + 3Mn + 3Fe + 2.54Na + Ce + 0.36Sr; *M*(2) = 0.9Ti + 0.6Nb; *M*(3) = 8.1Na + 0.9K; *M*(4) = 8Na + Sr; *T*(2) = 1.5Si: *T*(3) = 1.5Si; and *T*(4) = 1.5Al.

* Isotropic thermal parameters.

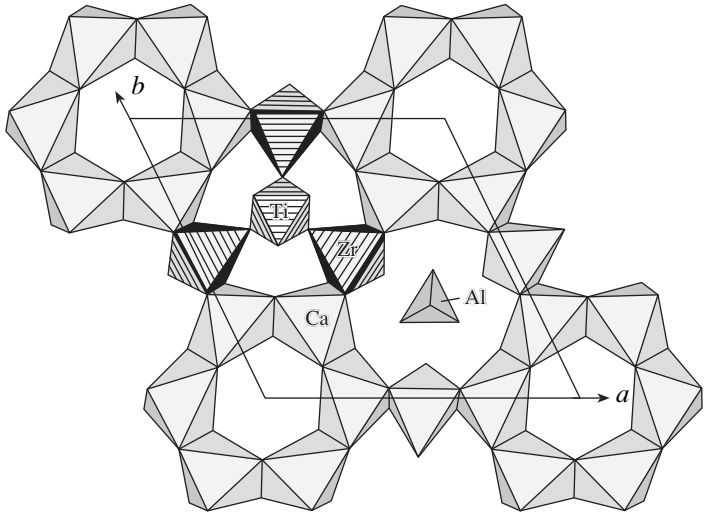


Fragment of the hyperzirconium eudialyte structure projected onto the (001) plane. A cluster of Ti- and Zr-octahedra linking three six-membered rings of the Ca-octahedra is hatched with solid lines.

the second type based on the square of the oxygen atoms. Most of Fe atoms are displaced from their usual positions toward Ca octahedra forming six-membered rings, in which Fe together with Mn, Na, Ce, and Sr isomorphically replace Ca. This statistical filling of the Ca position is one of the major features of the mineral under study. Another characteristic feature of this mineral is the formation of a new type of a $TiZr_3$ cluster (figure) consisting of a Ti-octahedron located on the threefold axis and Zr(2)-octahedra located in the vicinity of this axis.

## ACKNOWLEDGMENTS

This study was supported by the Russian Foundation for Basic Research, project no. 99-05-65035.

## REFERENCES

1. O. Johnsen, J. D. Grice, and R. A. Gault, Eur. J. Mineral. **10**, 207 (1998).
2. R. K. Rastsvetaeva and A. P. Khomyakov, Z. Kristallogr. **214**, 271 (1999).
3. R. K. Rastsvetaeva, Dokl. Akad. Nauk **362**, 784 (1998).
4. V. I. Andrianov, Kristallografiya **32**, 228 (1987) [Sov. Phys. Crystallogr. **32**, 130 (1987)].
5. N. Walker and D. Stuart, Acta Crystallogr., Sect. A: Found. Crystallogr. **39**, 158 (1983).

*Translated by T. Safonova*

*Crystallography Reports, Vol. 45, No. 2, 2000, pp. 222–226. Translated from Kristallografiya, Vol. 45, No. 2, 2000, pp. 254–258.*


**STRUCTURES OF COORDINATION COMPOUNDS**

# Crystal Structure of Cobalt(III) Compound with Ethylenediamine-*N*,*N*'-Di-3-Propionic Acid, $[Co(H_2Eddp)(HEddp)]Br_2 \cdot 4H_2O$

**I. N. Polyakova*, A. L. Poznyak**, and V. S. Sergienko***

** Kurnakov Institute of General and Inorganic Chemistry, Russian Academy of Sciences, Leninskiĭ pr. 31, Moscow, 117907 Russia*

*** Institute of Molecular and Atomic Physics, Belarussian Academy of Sciences, pr. F. Skoriny 70, Minsk, 220072 Belarus*

Received March 18, 1998

**Abstract**—The crystal structure of $[Co(H_2Eddp)(HEddp)]Br_2 \cdot 4H_2O$ is determined [$R1 = 0.0551$ and $wR2 = 0.1298$ for 2580 reflections with $I > 2\sigma(I)$]. The structure consists of the $[Co(H_2Eddp)(HEddp)]^{2+}$ cationic complexes, $Br^-$ anions, and molecules of crystallization water. Two tridentate ligands, which differ in the degree of protonation, coordinate the Co atom by two N atoms and one O atom, each forming a meridional isomer. In the complex, the configurations of the N(2) and N(4) atoms, which are included in two chelate rings each, differ from those of the N(1) and N(3) atoms, which are included only in the five-membered rings and bear uncoordinated propionate groups. The Co–N(1) and Co–N(3) bonds are longer than the Co–N(2) and Co–N(4) bonds (mean 1.987 and 1.957 Å, respectively). The Co–O(5) bond with the neutral ligand is longer than the Co–O(1) bond with the negatively charged carboxyl group (1.927 and 1.901 Å, respectively). The C(13)–O(5) carbonyl bond in the coordinated COOH group is elongated to 1.266 Å. The system of hydrogen bonds interlinks the cationic complexes, $Br^-$ anions, and water molecules into a three-dimensional framework. © *2000 MAIK "Nauka/Interperiodica".*

In the course of systematic studies of mixed-ligand metal complexes that include an anion of polyaminopolycarboxylic acid as one of the ligands, we obtained a compound, which, according to the scheme of synthesis and the data of elemental analysis, was expected to contain the cationic complexes $[Co(H_2Edtp)En]^+$, where *En* is ethylenediamine, and $H_4Edtp$ is ethylenediaminetetrapropionic acid. The X-ray diffraction study revealed that the complex actually contains two ethylenediamine fragments and four propionate groups; however, they are incorporated into the molecule and anion of ethylenediamine-*N*,*N*'-di-3-propionic acid, $H_2Eddp$ and $HEddp^-$, respectively. The composition of the crystals is described by the formula $[Co(H_2Eddp)(HEddp)]Br_2 \cdot 4H_2O$ (**I**).

## EXPERIMENTAL

We omit the description of the synthesis procedure, because it was worked out for another target product. The conventional scheme can be proposed to synthesize **I** [1, 2]: the reaction of a $Co^{2+}$ salt with $H_2Eddp$ taken in the 1 : 2 ratio followed by oxidation of $Co^{2+}$ to $Co^{3+}$.

Dark claret crystals **I** ($C_{16}H_{39}Br_2CoN_4O_{12}$) are monoclinic, $a = 18.580(4)$ Å, $b = 8.986(2)$ Å, $c = 17.614(4)$ Å, $\beta = 117.16(3)°$, $V = 2617(1)$ Å$^3$, $d_{calcd} = 1.773$ g/cm$^3$, $\mu_{Mo} = 3.774$ mm$^{-1}$, $M = 698.26$, $F(000) = 1424.0$, $Z = 4$, and space group $P2_1/c$.

The intensities of 4363 reflections were measured on a CAD-4 automated diffractometer ($\lambda MoK_\alpha$, graphite monochromator, $\omega$-$2\theta/6$ scan mode, $\theta_{max} = 26°$).

The structure was solved by the direct method (SHELXS86 [3]). All the hydrogen atoms were located from difference Fourier syntheses, but their independent refinement failed. The non-hydrogen atoms were refined by the least-squares procedure in the anisotropic approximation, and the H atoms were refined within the riding-atom model. Their thermal parameters were fixed by the values 0.01 Å$^2$ larger than $U_{eq}$ of the atoms to which they are attached. The refinement was performed with the SHELXL93 program [4]. Secondary extinction was considered [$c = 0.0006(4)$], and the weighting scheme $w = 1/[\sigma^2(F_o^2) + (0.0901P)^2]$, where $P = [\max(F_o^2, 0) + 2F_c^2]/3$, was used. The refinement led to the discrepancy factors $R1 = 0.0551$ and $wR2 = 0.1298$ for 2580 observed reflections [$I > 2\sigma(I)$]; $R1 = 0.1010$ and $wR2 = 1450$ for 3927 unique reflections; $S = 1.004$. The residual electron density on the zero Fourier synthesis lies in the range $-0.691 < \Delta\rho < 1.242$ e/Å$^3$, and the highest peaks are observed in the vicinity of the Br and Co atoms.

Atomic coordinates ($\times 10^4$) and parameters of thermal vibrations $U_{eq}$ ($\times 10^3$; for H atoms, $U_{iso}$)

| Atom | *x* | *y* | *z* | $U_{eq}/U_{iso}$, Å$^2$ |
|---|---|---|---|---|
| Co(1) | 7171(1) | 5036(1) | –94(1) | 22(1) |
| O(1) | 6068(3) | 5418(5) | –395(3) | 26(1) |
| O(2) | 4970(3) | 6700(5) | –691(3) | 38(1) |
| O(3) | 10012(4) | 1668(7) | –27(4) | 61(1) |
| O(4) | 8888(4) | 2939(7) | –721(4) | 65(2) |
| O(5) | 7339(3) | 4313(5) | 1004(3) | 31(1) |
| O(6) | 7250(4) | 2919(6) | 1976(3) | 52(2) |
| O(7) | 5536(3) | 9540(6) | –2414(3) | 49(2) |
| O(8) | 5863(3) | 9396(6) | –3475(3) | 44(1) |
| N(1) | 8330(3) | 4659(6) | 226(3) | 28(1) |
| N(2) | 7540(3) | 6949(6) | 475(3) | 25(1) |
| N(3) | 7007(3) | 5747(6) | –1229(3) | 27(1) |
| N(4) | 6797(4) | 3082(6) | –628(4) | 32(1) |
| C(1) | 8782(4) | 6086(8) | 594(5) | 35(2) |
| C(2) | 8392(4) | 6813(8) | 1073(5) | 35(2) |
| C(3) | 7048(5) | 7515(8) | 888(4) | 33(2) |
| C(4) | 6198(4) | 7860(7) | 249(4) | 30(2) |
| C(5) | 5715(4) | 6582(7) | –300(4) | 27(2) |
| C(6) | 8719(5) | 3379(9) | 800(5) | 39(2) |
| C(7) | 9514(5) | 2870(9) | 814(5) | 42(2) |
| C(8) | 9428(5) | 2535(9) | –58(6) | 40(2) |
| C(9) | 6909(5) | 4394(7) | –1759(5) | 35(2) |
| C(10) | 6401(5) | 3282(8) | –1560(4) | 39(2) |
| C(11) | 6290(5) | 2268(8) | –325(5) | 39(2) |
| C(12) | 6723(5) | 1874(8) | 592(5) | 46(2) |
| C(13) | 7100(5) | 3114(8) | 1192(5) | 37(2) |
| C(14) | 6360(4) | 6868(7) | –1667(4) | 31(2) |
| C(15) | 6409(5) | 7576(8) | –2414(4) | 36(2) |
| C(16) | 5893(4) | 8918(8) | –2751(4) | 29(2) |
| Br(1) | 2218(1) | 141(1) | 492(1) | 44(1) |
| Br(2) | 9138(1) | 475(1) | 2382(1) | 51(1) |
| O(1*w*) | 1604(4) | 3572(8) | 1498(4) | 77(2) |
| O(2*w*) | 306(3) | 6234(7) | 6705(4) | 59(2) |
| O(3*w*) | 8193(4) | 4924(7) | 2947(3) | 64(2) |
| O(4*w*) | 4704(4) | 5313(7) | 3659(4) | 74(2) |
| H(30) | 10512 | 1598 | 450 | 70 |
| H(60) | 7639 | 3549 | 2366 | 62 |
| H(80) | 5533 | 10333 | –3660 | 54 |
| H(1) | 8368 | 4389 | –217 | 38 |
| H(2) | 7563 | 7629 | 185 | 35 |
| H(3) | 7402 | 6172 | –1181 | 37 |
| H(4) | 7134 | 2602 | –522 | 42 |
| H(1*A*) | 9351 | 5838 | 941 | 45 |
| H(1*B*) | 8675 | 6531 | 94 | 45 |
| H(2*A*) | 8425 | 6289 | 1578 | 44 |

**Table** (Contd.)

| Atom | *x* | *y* | *z* | $U_{eq}/U_{iso}$, Å$^2$ |
|---|---|---|---|---|
| H(2*B*) | 8658 | 7565 | 1284 | 44 |
| H(3*A*) | 7394 | 8511 | 1285 | 42 |
| H(3*B*) | 7056 | 7001 | 1250 | 42 |
| H(4*A*) | 6144 | 8656 | –148 | 39 |
| H(4*B*) | 5810 | 8194 | 538 | 39 |
| H(6*A*) | 8194 | 2509 | 517 | 48 |
| H(6*B*) | 8829 | 3624 | 1369 | 48 |
| H(7*A*) | 9744 | 2118 | 1292 | 52 |
| H(7*B*) | 9874 | 3726 | 1006 | 52 |
| H(9*A*) | 6544 | 4452 | –2429 | 45 |
| H(9*B*) | 7383 | 4155 | –1627 | 45 |
| H(10*A*) | 5908 | 3620 | –1813 | 48 |
| H(10*B*) | 6380 | 2345 | –1870 | 48 |
| H(11*A*) | 5752 | 2751 | –547 | 48 |
| H(11*B*) | 6062 | 1390 | –623 | 48 |
| H(12*A*) | 7298 | 1228 | 792 | 56 |
| H(12*B*) | 6439 | 1603 | 737 | 56 |
| H(14*A*) | 5867 | 6422 | –1931 | 41 |
| H(14*B*) | 6568 | 7588 | –1249 | 41 |
| H(15*A*) | 6957 | 7888 | –2316 | 46 |
| H(15*B*) | 6210 | 7091 | –2883 | 46 |
| H(11) | 1493 | 4151 | 1848 | 88 |
| H(12) | 1339 | 3081 | 1423 | 88 |
| H(21) | 296 | 7353 | 6919 | 71 |
| H(22) | 49 | 6346 | 6077 | 71 |
| H(31) | 8616 | 4499 | 3032 | 79 |
| H(32) | 8185 | 5080 | 3476 | 79 |
| H(41) | 4954 | 6187 | 4041 | 82 |
| H(42) | 4798 | 5188 | 3176 | 82 |

The atomic coordinates and parameters of thermal vibrations are listed in the table.

## RESULTS AND DISCUSSION

Structure **I** consists of the $[Co(H_2Eddp)(HEddp)]^{2+}$ cationic complexes, $Br^-$ anions, and molecules of crystallization water. The structure of the cationic complex is shown in the figure. The octahedral coordination of the Co atom is formed by four N atoms and two O atoms of two tridentate ligands that differ in the degree of protonation—$H_2Eddp$ and $HEddp^-$. Each ligand closes the five-membered ethylenediamine ring (*E*) and the six-membered alaninate ring (*A*). Taking into account that nitrogen atoms in both ligands differ from one another (one of them is included in two chelate rings, whereas the other atom, only in the *E* ring), the complex can form seven geometric isomers, six of which are facial isomers. Complex **I** crystallizes in the form of the only meridional isomer.

Structure **I** provides a rare example of the aminopolycarbonate, in which the metal atom is coordinated by the neutral molecule of the ligand. Among structurally studied compounds of this type, palladium and platinum ethylenediaminetetraacetates $M(H_4Edta)Cl_2 \cdot 5H_2O$, which contain the neutral $H_4Edta$ ligand, are known [5]. In **I** and $M(H_4Edta)Cl_2 \cdot 5H_2O$, the acid protons are attached to the carboxyl groups, and the N atoms coordinate the metal atom. In $M(H_4Edta)Cl_2 \cdot 5H_2O$, all COOH groups are located outside the coordination sphere of the *M* atom. In structure **I**, the protonated C(13)O(5)O(6)H(6) group coordinates the Co(1) atom. As noted above, the independent refinement of the H atoms in the structure failed. Nonetheless, geo-

metric comparison of the coordinated carboxyl groups C(5)O(1)O(2) and C(13)O(5)O(6) provides support for the conclusion that the acid proton is located at the O(6) atom. In the former group, the ratio of the C–O bond lengths is common for the $COO^-$ groups: the bond with the coordinated O(1) atom is significantly longer than the bond with the uncoordinated O(2) atom [1.286(8) and 1.236(8) Å, respectively]. In the latter group, we observe the reverse ratio of the C–O bond lengths: the C(13)–O(6) bond is longer than the C(13)–O(5) bond [1.291(8) and 1.266(8) Å, respectively]. Moreover, the Co(1)–O(5) bond with the neutral carboxyl group [1.927(4) Å] is longer than the Co(1)–O(1) bond with the negatively charged group [1.901(4) Å]. The C(13)=O(5) carbonyl bond in **I** is stretched to a larger degree than that in the majority of other transition metal aminopolycarboxylates with coordinated COOH groups. Thus, in the compounds $[Co(HEdta)(H_2O)] \cdot 2H_2O$ [6, 7], $[Cu(H_2Nta)_2] \cdot 2H_2O$ [8], $[Cu(H_2Pddadp)] \cdot 1.5H_2O$ [9], $[Cu(H_2Cdta)] \cdot H_2O$ [10], $Ag[Cu(HEdta)(H_2O)] \cdot H_2O$ [11], and $[Fe(H_2Edta)(H_2O)] \cdot 2H_2O$ [12], the coordination of the carbonyl O atom does not cause noticeable elongation of the C=O bond (1.201–1.219 Å)[1]. In the compounds $[Zn(H_2Phdta)(H_2O)] \cdot H_2O$ [13], $[Fe(H_2O)_4][Fe(HEdta)(H_2O)]_2 \cdot 4H_2O$[12], $[Ni(H_2Cdta)(H_2O)] \cdot 4H_2O$ [10], $[Ti(HEdta)(H_2O)] \cdot H_2O$ [14], and $[V(HEdta)(H_2O)] \cdot H_2O$ [14], the corresponding bonds are elongated to 1.225–1.241 Å. The maximum elongation of the C=O bond (to 1.30 Å) is observed in the $[Ru(H_3Edta)Cl_2] \cdot 4H_2O$ structure [15].

The bonds of the Co(1) atom with the N(1) and N(3) atoms, which are involved only in one chelate ring, are noticeably longer that the bonds with the N(2) and N(4) atoms, which are included in two chelate rings each (av. 1.987 and 1.957 Å, respectively). The lengths of the latter bonds are close to the lengths of the Co–N bonds with the deprotonated $Eddp^{2-}$ ligand in different isomers of the mixed-ligand complex $[Co(Eddp)En]^+$ (1.938–1.956 Å) [16] and in the dimer complex $[Co(Eddp)(OH)]_2 \cdot 8H_2O$ (1.943 and 1.956 Å) [17]. Elongation of the metal–nitrogen bonds has been observed earlier in the compounds containing uncoordinated carboxylate arms (for example, [18]).

The angular distortions of the octahedron due to the formation of the chelate rings are small. The N(1)Co(1)N(2) and N(3)Co(1)N(4) angles in the five-membered *E* rings decrease to 85.6(2)° and 87.0(2)°, whereas the O(1)Co(1)N(2) and O(5)Co(1)N(4) angles in the six-membered *A* rings increase to 97.3° and 92.2°; all the *trans* angles are close to 180°.

The conformations of the chelate rings formed by two ligands are approximately the same. In the five-membered *E* rings, the C atoms deviate from the $CoN_2$ plane in opposite directions. In the Co(1)N(3)N(4)C(9)C(10) ring, these deviations are close in magnitude (0.346 and –0.367 Å), and in the Co(1)N(1)N(2)C(1)C(2) ring, they differ significantly (–0.189 and 0.527 Å); that is, the two rings adopt symmetric and asymmetric *gauche* conformations, respectively. The six-membered *A* rings have a sofa conformation. They contain five-atomic flattened fragments, Co(1)N(2)C(4)C(5)O(1) and Co(1)N(4)C(12)C(13)O(5), in which the mean atomic deviations from the plane are 0.034 and 0.059 Å, respectively. The C(3) and C(11) atoms deviate from these planes by 0.697 and –0.616 Å, respectively.

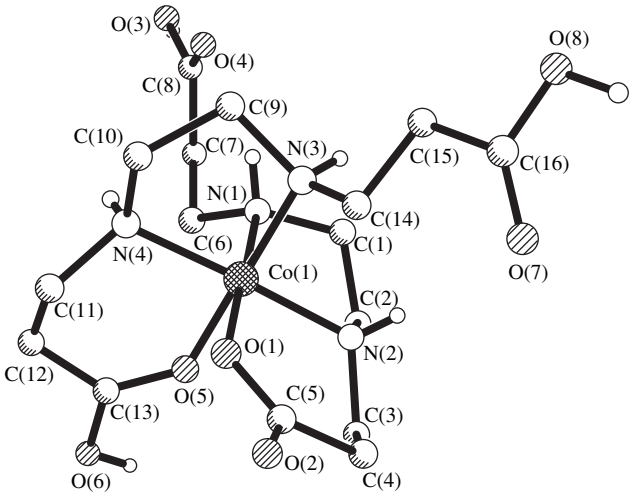


Structure of the $[Co(H_2Eddp)(HEddp)]^{2+}$ cationic complex. The H(C) atoms are omitted.

In the cationic complex, the absolute configurations of two pairs of nitrogen atoms—N(2), N(4) and N(1), N(3)—are different. In the complex shown in the figure, the configuration of the N(2) and N(4) atoms is *S*, and the configuration of the N(1) and N(3) atoms is *R*.

All the carboxyl groups perform different structural functions. The O(1) atom of the deprotonated carboxyl group C(5)O(1)O(2) coordinates the Co(1) atom, and the O(2) atom accepts two protons in hydrogen bonds. In the protonated C(13)O(5)O(6)H group, the "carbonyl" O(5) atom coordinates the Co(1) atom, and the hydroxyl O(6) atom donates its proton to a strong O–H··O hydrogen bond. Both free carboxyl groups are involved in two hydrogen bonds: C(16)O(7)O(8)H acts as an acceptor and a donor, and C(8)O(4)O(3)H acts as an acceptor of two protons.

A large number of active protons lead to the formation of a three-dimensional system of hydrogen bonds in the structure. The intramolecular N(1)–H(1)··O(4) hydrogen bond [N(1)··O(4) 2.797(9) Å] closes the six-membered ring. Two protonated carboxyl groups form strong hydrogen bonds O(6)–H(6O)··O(3*w*) [O(6)··O(3*w*) 2.551(8) Å] and O(8)–H(8O)··O(2) (1 – *x*, 0.5 + *y*, –0.5 – *z*) [O(8)··O(2) 2.600(7) Å]. The

[1] $H_4Edta$, $H_3Nta$, $H_4Pddadp$, $H_4Cdta$, $H_4Phdta$ are ethylenediaminetetraacetic, nitrilotriacetic, propanediaminediacetic-dipropionic, cyclohexanediaminetetraacetic, and phenylenediaminetetraacetic acids, respectively.

H(3O) atom of the third protonated group is not involved in hydrogen bonding. The O(8)–H(8O)··O(2') bonds link the cationic complexes into chains running along the screw axes. The chains are crosslinked through $Br^-$ anions and water molecules.

## ACKNOWLEDGMENTS

This work was supported in part by the Belarussian Republican Foundation for Basic Research, project no. F96-92.

## REFERENCES

1. A. L. Poznyak and V. E. Stel'mashok, Koord. Khim. **14**, 482 (1988).
2. H. Kawaguchi, N. Maruyama, N. Ama, *et al.*, Bull. Chem. Soc. Jpn. **65**, 175 (1992).
3. G. M. Sheldrick, Acta Crystallogr., Sect. A: Found. Crystallogr. **46**, 467 (1990).
4. G. M. Sheldrick, *SHELXL93*: *Program for the Refinement of Crystal Structures* (Univ. of Göttingen, Göttingen, 1993).
5. D. J. Robinson and C. H. L. Kennard, J. Chem. Soc., Dalton Trans., No. 7, 1008 (1970).
6. Ya. M. Nesterova, M. A. Porai-Koshits, and V. A. Logvinenko, Zh. Neorg. Khim. **26**, 1141 (1981).
7. J. D. Zubkovskĭ, D. L. Perry, E. J. Valente, *et al.*, Inorg. Chem. **34**, 6409 (1995).
8. N.-H. Dung, B. Viossat, A. Busnot, *et al.*, Inorg. Chem. **27**, 1227 (1988).
9. B. V. Prelesnik, D. D. Radanovic, Z. D. Tomic, *et al.*, Polyhedron **15**, 3761 (1996).
10. J. D. Martín-Ramos, J. M. Tercero-Moreno, A. Matilla-Hernández, *et al.*, Polyhedron **15**, 439 (1996).
11. Ch. Brouca-Cabarrecq, B. Marrot, and A. Mosset, Acta Crystallogr., Sect. A: Found. Crystallogr. **52**, 1903 (1996).
12. T. Mizuta, J. Wang, and K. Miyoshi, Inorg. Chim. Acta **230**, 119 (1995).
13. Sh. Azuma, N. Nakasuka, and M. Tanaka, Acta Crystallogr., Sect. C: Cryst. Struct. Commun. **42**, 673 (1986).
14. K. Miyoshi, J. Wang, and T. Mizuta, Inorg. Chim. Acta **228**, 165 (1995).
15. R. Vilaplana-Serrano, M. G. Basallote, C. Ruíz-Valero, *et al.*, J. Chem. Soc., Chem. Commun., No. 2, 100 (1991).
16. N. Sakagami, T. Yasui, H. Kawaguchi, *et al.*, Bull. Chem. Soc. Jpn. **67**, 680 (1994).
17. A. V. Gasparyan, L. M. Shkol'nikova, M. A. Porai-Koshits, *et al.*, Koord. Khim. **12** (10), 1408 (1986).
18. L. M. Shkol'nikova, A. L. Poznyak, and S. S. Sotman, Koord. Khim. **20**, 456 (1994).

*Translated by I. Polyakova*

*Crystallography Reports, Vol. 45, No. 2, 2000, pp. 227–229. Translated from Kristallografiya, Vol. 45, No. 2, 2000, pp. 259–261.*


**STRUCTURES OF COORDINATION COMPOUNDS**

# Crystal Structure of Aqua[*S*-Prolinato-*N*-Monoacetato)copper(II) Dihydrate [Cu(*Proma*)$H_2O$] · $2H_2O$

**I. F. Burshteĭn*, A. L. Poznyak**, and L. V. Stopolyanskaya****

** Analytical Instrumentation Department, Siemens Energy and Automation Inc., 6300 Enterprise Lane, Madison, WI, USA*

*** Institute of Molecular and Atomic Physics, Belarussian Academy of Sciences, pr. F. Skoriny 70, Minsk, 220072 Belarus*

Received April 13, 1998

**Abstract**—The crystal structure of [Cu($C_7H_9NO_4$)$H_2O$] · $2H_2O$ is determined by X-ray diffraction (λMo, $R$ = 0.0316 for 857 reflections). The crystals are tetragonal, $a$ = 8.219(1) Å, $c$ = 17.449(3) Å, $Z$ = 4, $\rho_{calcd}$ = 1.627 g cm$^{-3}$, and space group $P4_3$. The coordination polyhedron of the Cu atom is a tetragonal pyramid with the O atom of the acetate arm of the prolinatomonoacetate ion (*Proma*) in the apical position [Cu–O 2.312(6) Å]. The O atom of the water molecule and the N and O atoms of the prolinate group of the *Proma* ligand lie in the basal plane. The Cu–N bond length is 2.044(6) Å, and the Cu–O bond lengths are 1.932(7) and 1.927(6) Å. The O atom of the acetate arm of the neighboring *Proma* ion completes the basal plane [Cu–O 1.951(6) Å], thus linking the copper complexes into infinite chains. © *2000 MAIK "Nauka/Interperiodica".*

The crystal structure of the copper(II) complex with *S*-proline-*N*-monoacetic acid was determined by X-ray diffraction.

Dianions $\overline{CH(CO_2^-)CH_2CH_2CH_2}NCH_2CO_2^-$ (in abbreviated form, *Proma*) were obtained in a solution according to the procedure described in [1]. Free acid $H_2$*Proma* was not isolated, and copper(II) chloride was added to the reaction mixture. The required complexes were separated from impurities by gel filtration on a Sephadex G-10 column. Needle-like crystals of [Cu(*Proma*)$H_2O$] · $2H_2O$ (**I**) were obtained upon evaporation of the blue filtrate.

Crystals **I** are tetragonal, $a$ = 8.219(1) Å, $c$ = 17.449(3) Å, $V$ = 1178.7(3) Å$^3$, $Z$ = 4 (the formula unit is $C_7H_{15}CuNO_7$), space group $P4_3$, $d_{calcd}$ = 1.627 g cm$^{-3}$. (Space group $P4_1$ is inconsistent with the known absolute configuration of the *Proma* ligand). The intensities of reflections were measured on a Siemens *P*4 automated diffractometer (λMo$K_\alpha$, graphite monochromator, $2\theta_{max} = 45°$). The structure was solved by the direct method and refined by the full-matrix least-squares procedure in the anisotropic approximation to $R_1$ = 0.0316 and $wR_2$ = 0.0724 for 857 reflections with $I > 2\sigma(I)$. At the final stage, the hydrogen atoms are taken into account in the isotropic approximation. The hydrogen atoms of water molecules were located from the Fourier synthesis. All the were performed with the XP [2] and SHELXTL [3, 4] program packages. The atomic coordinates and equivalent thermal parameters are listed in Table 1.

## RESULTS AND DISCUSSION

The coordination polyhedron of the copper atom can be described as a distorted tetragonal pyramid. The O(1) atom of the acetate group is located on the axis of the pyramid, and the N and O(3) atoms of the proline group of the same *Proma* ligand lie in the base of the pyramid. Thus, *Proma* acts a tridentate ligand (figure).

**Table 1.** Atomic coordinates (×10$^4$) and equivalent isotropic thermal parameters (Å$^2$ × 10$^3$)

| Atom | $x/a$ | $y/b$ | $z/c$ | $U_{eq}$ |
|---|---|---|---|---|
| Cu | –2310(1) | –658(1) | 3318(1) | 33(1) |
| O(1) | –1892(7) | 570(7) | 4493(3) | 39(1) |
| O(2) | –451(6) | 24(7) | 5534(3) | 39(1) |
| O(3) | –4587(7) | –1055(8) | 3504(3) | 50(2) |
| O(4) | –6273(8) | –2058(9) | 4355(5) | 80(2) |
| O(1*w*) | –2983(9) | 1058(10) | 2630(4) | 61(2) |
| O(2*w*) | 4282(10) | 2660(10) | 2892(5) | 55(2) |
| O(3*w*) | 2275(8) | 978(8) | 4022(4) | 50(2) |
| N | –1913(8) | –2599(7) | 4025(4) | 33(2) |
| C(1) | –762(11) | –2079(9) | 4627(5) | 34(2) |
| C(2) | –1088(10) | –348(10) | 4894(5) | 33(2) |
| C(3) | –3539(10) | –3038(10) | 4364(5) | 42(2) |
| C(4) | –4915(12) | –1965(11) | 4057(5) | 46(2) |
| C(5) | –3786(13) | –4840(11) | 4184(8) | 72(3) |
| C(6) | –2284(29) | –5466(20) | 3998(22) | 56(9) |
| C(6') | –2575(40) | –5134(48) | 3491(33) | 73(15) |
| C(7) | –1341(13) | –4088(10) | 3628(6) | 57(3) |

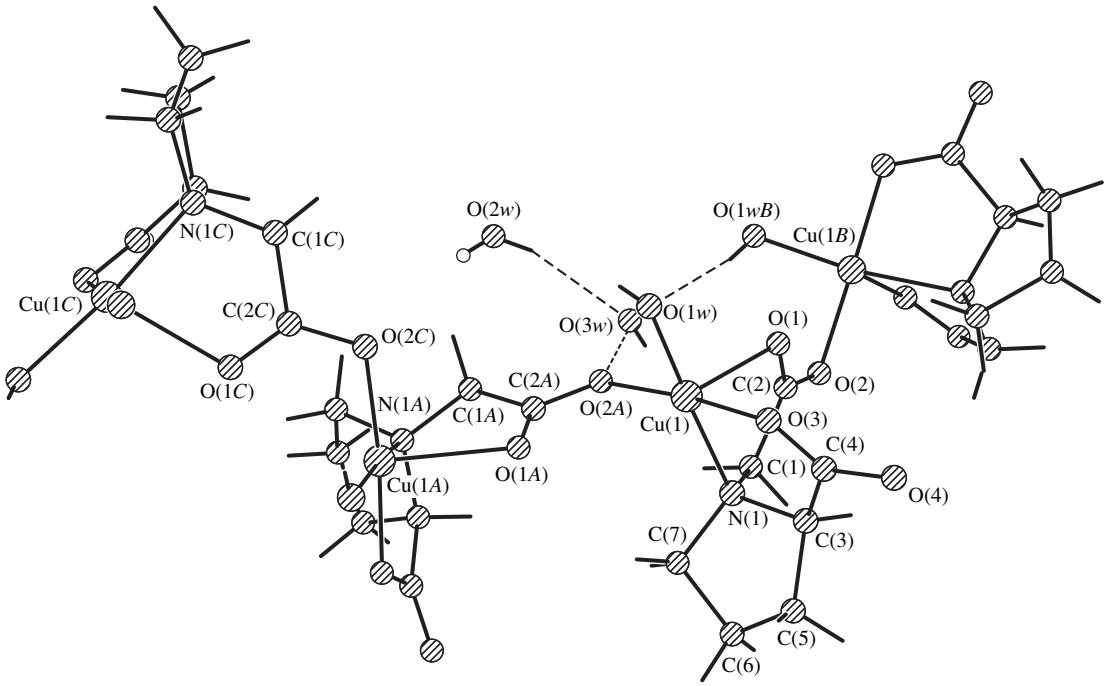


A fragment of the $\{[Cu(Proma)H_2O] \cdot 2H_2O\}_n$ chain in structure **I**. The bond lengths and angles: Cu–O(1), 2.312(6) Å; Cu–O(2*A*), 1.951(6) Å; Cu–O(3), 1.927(6) Å; Cu–O(1*w*), 1.932(7) Å; Cu–N, 2.044(6) Å; O(1)–Cu–N, 77.3(2)°; and O(3)–Cu–N, 85.5(3)°.

The two remaining sites in the basal plane of the pyramid are occupied by the O(1*w*) atom of the water molecule and the O(2*A*) atom of the acetate group of the neighboring *Proma* ion (related by the symmetry operation $-y, x, z - 1/4$). The four basal atoms deviate from their mean plane by ±0.03 Å, and the copper atom deviates from this plane by 0.085 Å in the direction of the O(1) atom. The question arises as to whether any donor atom in the second axial position completes the pyramid to an elongated octahedron. The O(1*A*) atom of the acetate group of the same neighboring *Proma* ion can be considered a candidate. The Cu-O(1*A*) distance is 2.902(6) Å, and the Cu–O(1*A*) segment is inclined relative to the mean basal plane by 52.2(1)°. Since this angle differs essentially from 90°, the Cu–O(1*A*) coordination is hardly probable.

**Table 2.** Intermolecular contacts (*d*) shorter than 3.0 Å in the structure of $[Cu(Proma)H_2O] \cdot 2H_2O$

| *A*···*B* | *d*, Å | Symmetry operation for *B* atom |
|---|---|---|
| O(1*w*)···O(2*w*) | 2.65(1) | $x - 1, y, z$ |
| O(3*w*)···O(4) | 2.83(1) | $x + 1, y, z$ |
| O(2*w*)···O(3*w*) | 2.92(1) | $x, y, z$ |
| O(1*w*)···O(3*w*) | 2.73(1) | $-y, x, z - \frac{1}{4}$ |
| O(3*w*)···O(2) | 2.81(1) | $x, y, z$ |
| O(2*w*)···O(4) | 2.72(1) | $-y, x + 1, z - \frac{1}{4}$ |

The bond lengths and angles in the coordination polyhedron are normal for the related copper(II) complexes. The pyrrolidine ring of the *Proma* ligand has the shape of an envelope with the "corner" at the C(6) atom. This carbon atom is disordered over two approximately equally occupied sites, which corresponds to opposite deviations of the "corner."

Since each *Proma* ion is bound to two Cu atoms, infinite helical chains run in the crystal along fourfold screw axes. The lengths of the intermolecular O···O contacts (Table 2) indicate that each of the three water molecules is involved in hydrogen bonds. These bonds link the chains into a three-dimensional framework.

Structure **I** resembles the structure of the Cu(II) complex with the *S*-prolinato-*N*-mono(3-propionate) ion characterized in [5]. In this complex, in distinction to **I**, the water molecule is situated *cis* relative to the N atom of the aminodicarboxylate ligand, and the polymeric chains run along the twofold screw axes. Structures of a number of 1 : 1 complexes between copper(II) and iminodiacetate ions or their analogues have also been reported. Two derivatives of *N*-phenyliminodiacetic acid form monomeric complexes [6, 7]. Crystals of other related compounds, similar to **I**, consist of polymeric chains [8–11].

## ACKNOWLEDGMENTS

This work was supported in part by the Belarussian Republican Foundation for Basic Research, project no. F96-92.

## REFERENCES

1. K. Okamoto, J. Hidaka, and Y. Shimura, Bull. Chem. Soc. Jpn. **44**, 1601 (1971).
2. *XP: Interactive Molecular Graphics Program, Version 5.03* (Siemens Analytical X-ray Instrumentation Inc., Madison, Wis., 1994).
3. G. M. Sheldrick, *SHELXTL 93: Program for the Refinement of Crystal Structures* (Univ. of Göttingen, Göttingen, 1993).
4. G. M. Sheldrick, *SHELXTL: Version 5.0, Reference Manual* (Siemens Analytical X-ray Instrumentation Inc., Madison, Wis., 1994).
5. A. B. Ilyukhin, L. M. Shkol'nikova, A. L. Poznyak, *et al.*, Kristallografiya **36**, 1155 (1991) [Sov. Phys. Crystallogr. **36**, 653 (1991)].
6. Wang Jinling, Tian Guihua, Miao Fangming, *et al.*, Jiegou Huaxue **11**, 384 (1992). Chemical Abstracts **120**, 42311d (1994).
7. M. A. Hidalgo, A. Romerosa, J. Suárez-Varela, *et al.*, Acta Crystallogr., Sect. C: Cryst. Struct. Commun. **51**, 1505 (1995).
8. S. K. Porter, R. J. Angelici, and J. Clardy, Inorg. Nucl. Chem. Lett. **10**, 21 (1974).
9. A. Podder, J. K. Dattagupta, N. N. Saha, *et al.*, Acta Crystallogr., Sect. B: Struct. Crystallogr. Cryst. Chem. **35**, 53 (1979).
10. Nguyen-Huy-Dung, B. Viossat, A. Busnot, *et al.*, Inorg. Chim. Acta **175**, 155 (1990).
11. Wang Jinling, Tian Guihua, Miao Fangming, *et al.*, Acta Crystallogr., Sect. C: Cryst. Struct. Commun. **47**, 2205 (1991).

*Translated by I. Polyakova*

*Crystallography Reports, Vol. 45, No. 2, 2000, pp. 230–233. Translated from Kristallografiya, Vol. 45, No. 2, 2000, pp. 262–265.*


## STRUCTURES OF COORDINATION COMPOUNDS

# Crystal Structure of Triethanolammonium Bis(1-Hydroxyethane-1,1-Diphosphonato)diaquazincate Pentahydrate, $[(OHCH_2CH_2)_3NH][Zn(H_2O)_2(H_{2.5}L)_2] \cdot 5H_2O$

**V. S. Sergienko*, G. G. Aleksandrov*, and E. G. Afonin****

** Kurnakov Institute of General and Inorganic Chemistry, Russian Academy of Sciences, Leninskiĭ pr. 31, Moscow, 117907 Russia*

*** State Enterprise "Chemical Engineering Laboratory," Kaluga, Russia*

Received October 22, 1997; in final form, March 25, 1999

**Abstract**—The crystal structure of $[(HOCH_2CH_2)_3NH][Zn(H_2O)_2(H_{2.5}L)_2] \cdot 5H_2O$, where $H_4L$ is 1-hydroxyethane-1,1-diphosphonic acid, was determined by X-ray diffraction. The anionic complex has a *cis*-octahedral structure. The zinc atom is coordinated by four O atoms of two bidentate chelate $H_{2.5}L^{1.5-}$ ligands and two O atoms of water molecules. The Zn–O(*L*) bond lengths range between 2.050 and 2.175 Å, and the Zn–O($H_2O$) bond lengths are 2.105 and 2.133 Å. The anionic complexes, triethanolammonium cations, and molecules of crystallization water are interlinked by an extensive network of hydrogen bonds. The crystallographic data for isostructural complexes of cobalt and nickel are given. © *2000 MAIK "Nauka/Interperiodica".*

In the course of our systematic studies of the properties and structures of the complexes between bivalent metals and 1-hydroxyethane-1,1-diphosphonic acid $CH_3C(OH)(PO_3H_2)_2$ ($H_4L$), we determined the structures of a series of compounds containing the anionic complexes of general formula $[M(H_2O)_2(H_{4-n}L)_2]^{-2n+2}$, where $n$ = 1 or 2 [1–4].

In this work, we report the results of the X-ray studies of three compounds of general formula

$$[(HOCH_2CH_2)_3NH]\,[M(H_2O)_2(H_{2.5}L)_2] \cdot 5H_2O,$$

where $M$ = Zn (**I**), Co (**II**), or Ni (**III**). Structure **I** was determined by X-ray crystallography.

**Table 1.** Crystallographic data for compounds **I**–**III**

| | Compound | | |
|---|---|---|---|
| | **I** | **II** | **III** |
| Empirical formula | $C_{10}H_{43}NO_{24}P_4Zn$ | $C_{10}H_{43}NO_{24}P_4Co$ | $C_{10}H_{43}NO_{24}P_4Ni$ |
| $a$, Å | 10.878(2) | 10.911(9) | 10.845(4) |
| $b$, Å | 12.532(2) | 12.574(9) | 12.493(3) |
| $c$, Å | 12.718(2) | 12.733(9) | 12.665(5) |
| $a$, deg | 105.89(4) | 105.90(9) | 106.18(3) |
| β, deg | 101.21(4) | 101.10(9) | 101.86(3) |
| γ, deg | 113.80(4) | 113.90(9) | 113.22(3) |
| $V$, Å$^3$ | 1431.2(4) | 1442(2) | 1414.5(8) |
| $\rho_{calcd}$, g/cm$^3$ | 1.754 | 1.726 | 1.759 |
| $\mu_{Mo}$, cm$^{-1}$ | 11.82 | 9.16 | 10.13 |
| $Z$ | 2 | 2 | 2 |
| Space group | $P\bar{1}$ | $P\bar{1}$ | $P\bar{1}$ |
| Molecular weight | 750.68 | 744.24 | 744.02 |
| $F$(000) | 786 | 780 | 782 |

1063-7745/00/4502-0230$20.00 

**Table 2.** Fractional coordinates of non-hydrogen atoms and thermal parameters $U_{eq}$ for compound **I**

| Atom | *x* | *y* | *z* | $U_{eq}$, Å$^2$ | Atom | *x* | *y* | *z* | $U_{eq}$, Å$^2$ |
|---|---|---|---|---|---|---|---|---|---|
| Zn | 0.24909(4) | −0.00437(4) | 0.24638(4) | 0.0241(1) | C(3) | −0.1213(4) | −0.2427(4) | 0.0844(3) | 0.0261(7) |
| P(1) | 0.5192(1) | −0.0633(1) | 0.2618(1) | 0.0249(2) | C(4) | −0.2796(4) | −0.3324(5) | 0.0111(4) | 0.040(1) |
| P(2) | 0.2836(1) | −0.2175(1) | 0.3345(1) | 0.0227(2) | O(15) | 0.1805(4) | 0.1655(3) | 0.5589(3) | 0.0429(8) |
| P(3) | −0.0934(1) | −0.0880(1) | 0.1774(1) | 0.0245(2) | O(16) | 0.2580(4) | 0.5336(3) | 0.4235(3) | 0.0500(9) |
| P(4) | −0.0101(1) | −0.2227(1) | −0.0076(1) | 0.0244(2) | O(17) | −0.1097(5) | 0.4371(4) | 0.3711(4) | 0.059(1) |
| O(1) | 0.4429(3) | 0.0087(3) | 0.2413(3) | 0.0285(6) | N(1) | 0.0638(4) | 0.3255(3) | 0.4522(3) | 0.0310(7) |
| O(2) | 0.6001(3) | −0.0788(3) | 0.1773(3) | 0.0343(6) | C(5) | 0.0443(5) | 0.2795(5) | 0.5487(4) | 0.038(1) |
| O(3) | 0.6322(3) | −0.0029(3) | 0.3855(3) | 0.0341(6) | C(6) | 0.0410(5) | 0.1530(4) | 0.5271(4) | 0.0371(9) |
| O(4) | 0.1999(3) | −0.1530(3) | 0.3030(2) | 0.0267(6) | C(7) | 0.1903(5) | 0.3251(4) | 0.4219(4) | 0.0359(9) |
| O(5) | 0.3848(3) | −0.1579(3) | 0.4580(2) | 0.0328(6) | C(8) | 0.2406(6) | 0.4127(5) | 0.3599(4) | 0.043(1) |
| O(6) | 0.1702(3) | −0.3581(3) | 0.3033(3) | 0.0374(7) | C(9) | −0.0709(5) | 0.2560(5) | 0.3470(5) | 0.043(1) |
| O(7) | 0.2901(3) | −0.2796(3) | 0.1178(2) | 0.0328(6) | C(10) | −0.1707(5) | 0.3107(5) | 0.3642(5) | 0.050(1) |
| O(8) | 0.0611(3) | −0.0074(3) | 0.2533(2) | 0.0283(6) | O(1*w*) | 0.3516(3) | 0.1342(3) | 0.4209(2) | 0.0330(6) |
| O(9) | −0.1966(3) | −0.1128(3) | 0.2445(3) | 0.0345(7) | O(2*w*) | 0.2899(3) | 0.1399(3) | 0.1822(3) | 0.0342(6) |
| O(10) | −0.1421(3) | −0.0297(3) | 0.0951(3) | 0.0331(6) | O(3*w*) | 0.4970(6) | 0.2002(6) | 0.0760(5) | 0.093(2) |
| O(11) | 0.1450(3) | −0.1522(3) | 0.0716(2) | 0.0275(6) | O(4*w*) | 0.5368(6) | 0.3693(6) | 0.3757(6) | 0.118(2) |
| O(12) | −0.0501(3) | −0.1612(3) | −0.0842(3) | 0.0333(6) | O(5*w*) | 0.6916(5) | 0.1214(5) | 0.0855(4) | 0.076(1) |
| O(13) | −0.0533(4) | −0.3611(3) | −0.0872(3) | 0.0438(8) | O(6*w*)* | 0.8579(9) | 0.4460(6) | 0.1209(8) | 0.055(7) |
| O(14) | −0.0802(3) | −0.2993(3) | 0.1599(3) | 0.0315(6) | O(7*w*)* | 0.953(2) | 0.492(2) | 0.023(2) | 0.175(7) |
| C(1) | 0.3857(4) | −0.2244(4) | 0.2371(3) | 0.0237(7) | O(8*w*)* | 0.604(2) | 0.465(2) | 0.220(2) | 0.150(6) |
| C(2) | 0.4546(5) | −0.3072(4) | 0.2492(4) | 0.0357(9) | O(9*w*)* | 0.712(2) | 0.438(2) | 0.182(2) | 0.184(8) |

* The site occupation factors of atoms O(6*w*–9*w*) are 0.5.

## EXPERIMENTAL

The methods used to prepare the complexes, the results of elemental analysis, and some physicochemical properties were reported in [5].

The crystallographic data for compounds **I**–**III** are summarized in Table 1.

The experimental data for **I** were obtained on an Enraf-Nonius CAD-4 automated four-circle diffractometer, and the unit cell parameters of **II** and **III** were determined on a Syntex $P2_1$ diffractometer ($\lambda$Mo$K_\alpha$, graphite monochromator).

Intensities of 6400 reflections were measured for **I** ($\omega$ scan, $2\theta_{max} = 58°$); 4741 reflections with $I \geq 2\sigma(I)$ were used for structure determination.

Structure **I** was solved by direct methods and refined in the anisotropic approximation by a least-squares procedure on $F^2$. Four oxygen atoms of crystallization water molecules O(6*w*–9*w*) are disordered; their site occupation factors were set equal to 0.5. The hydrogen atoms of the ligands (except the H atoms of methyl groups) and three alcohol groups of triethanolammonium cations, as well as ten hydrogens of five ordered water molecules O(1*w*–5*w*), were located from a difference Fourier synthesis.[1] The positions of the methyl hydrogens of the ligands, as well as of the $CH_2$ and NH hydrogens of the outer-sphere cation, were calculated from geometric considerations (C–H, 0.96 Å). All hydrogen atoms were included in the refinement at fixed positions ($U_H$ = 0.08 Å$^2$). The final discrepancy factors were $R$ = 0.0427, $R_w$ = 0.123, and *GOOF* = 1.046. The extinction coefficient was 0.004(1). The highest maximum and the deepest minima on the zero

[1] The site occupation factors of the H(O2) and H(O9) atoms are 0.5; that is, the O(2) and O(9) atoms are "half-protonated." Thus, both ligands are chemically equivalent and equally charged, $H_{2.5}L^{1.5-}$.

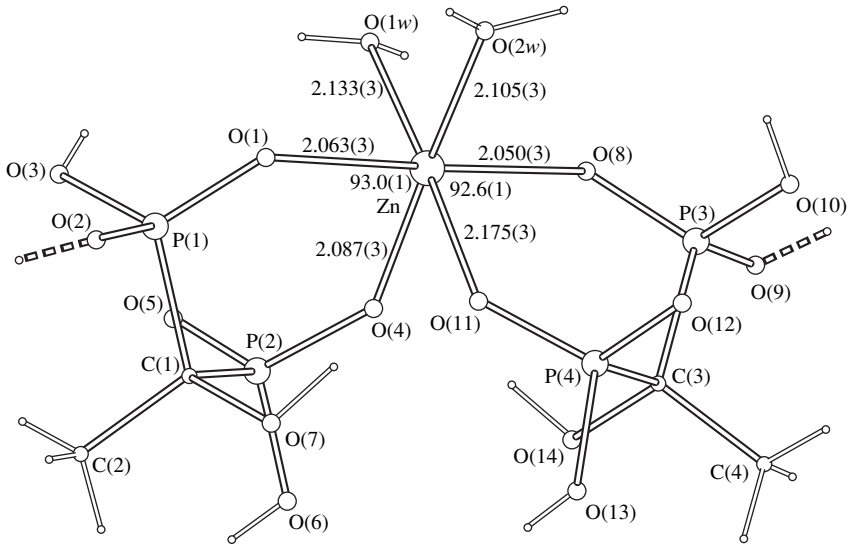


Structure of anionic complex $[Zn(H_2O)_2(H_{2.5}L)_2]^-$ in structure **I** (dashed lines indicate the O(2)–H(O2) and O(9)–H(O9) bonds involving half-protonated oxygen atoms).

Fourier synthesis were 1.158 and –0.899 eÅ$^{-3}$, respectively.

All calculations were performed with the SHELXL93 program package [6].

The atomic coordinates and thermal parameters $U_{eq}$ are listed in Table 2.

## RESULTS AND DISCUSSION

The data of the elemental and X-ray powder diffraction analyses indicate that a polycrystalline specimen of complex **I** isolated from an aqueous solution has a single-phase composition.

The structural units of crystal **I** are the $[Zn(H_2O)_2(H_{2.5}L)_2]^-$ anions, the $[(HOCH_2CH_2)_3NH]^+$ cations, and water molecules of crystallization.

In the anionic complex (figure), the octahedral coordination of the Zn atom is formed by four O(*L*) atoms of two bidentate chelate $H_{2.5}L^{1.5-}$ ligands and two O(*w*) atoms of water molecules, which are *cis* to each other. Judging by the unit cell parameters (Table 1), the similar cobalt and nickel complexes (**II** and **III**, respectively) are isostructural to zinc complex **I**. The Ni atom in the structure of $(NH_4)_2[Ni(H_2O)_2(H_2L)_2] \cdot 7H_2O$ [4] has a similar coordination. On the other hand, in the isostructural series $[(C_2H_5)_2NH_2]_2[M(H_2O)_2(H_2L)_2]$ (*M* = Cu, Co [1], Mg, Zn, Ni*, or Mn* [2]), the anionic complex has a *trans*-octahedral structure.[2] The same structure is observed for the neutral complex $[Cu(H_2O)_2(H_3L)_2]$ in β-$[Cu(H_2O)_2(H_3L)_2] \cdot 3H_2O$ [3].

[2] For two asterisked compounds, only the unit cell parameters were determined.

In each of the four phosphonate groups of two ligands, only one terminal oxygen atom is protonated. In addition, the O(2) and O(9) atoms of two ligands are "half-protonated." The short intramolecular contact O(2)···O(9) of 2.455 Å corresponds to two orientations of the proton, namely, O(2)–H(O2)···O(9) and O(9)–H(O9)···O(2) (the site occupation factors of the H(O2) and H(O9) atoms are 0.5). Hence, two $H_{2.5}L^{1.5-}$ ligands in the structure are equivalent, but in each of them, two phosphonate groups have different charges: $PO_3H_{1.5}^{0.5-}$ for P(1) and P(3), and $PO_3H^-$ for P(2) and P(4).

This charge distribution in the ligands is confirmed by the analysis of the P–O distances in structure **I**. The terminal P–O bonds and the P–O bonds with the O atoms coordinating the Zn atom are actually equal (the mean values are 1.502 ± 0.002 and 1.502 ± 0.011 Å, respectively). The P–OH bonds with the terminal protonated oxygen atoms are the longest (1.560 ± 0.010 Å). The $P–OH_{0.5}$ distances to the half-protonated oxygen atoms have intermediate values (1.530 ± 0.006 Å).

Two six-membered chelate rings $ZnO_2P_2C$ in structure **I** have sofa conformations: the C(1) and C(3) atoms deviate from the planes through the remaining five atoms of rings *A* and *B* (coplanar within ±0.03 and ±0.04 Å, respectively) by 0.87 and 0.90 Å, respectively. The *A*/*B* angle is 86.5°.

The anionic complexes, triethanolammonium cations, and crystallization water molecules are interlinked by an extensive hydrogen-bond system. In addition to the interionic and intermolecular hydrogen bonds, structure **I** is stabilized by two intramolecular contacts—O(7)–H(O7)···O(11) and O(14)–H(O14)···O(4)—involving the alcohol groups of the ligands. Due to these contacts, two seven-membered

pseudo-heterocycles Zn–O–P–C–O–H···O are closed. As noted above, four of the seven independent molecules of crystallization water occupy their positions partially (the site occupation factors are 0.5). Their complete occupation would result in unreasonably short contacts O(6*w*)···O(7*w*) (1.83 Å), O(6*w*)···O(9*w*) (1.88 Å), O(7*w*)···O(7*w*)' (1.26 Å), and O(8*w*)···O(9*w*) (1.47 Å).

## REFERENCES

1. V. S. Sergienko, G. G. Aleksandrov, and E. G. Afonin, Zh. Neorg. Khim. **42**, 1291 (1997) [Rus. J. Inorg. Chem. **42**, 1168 (1997)].
2. V. S. Sergienko, E. G. Afonin, and G. G. Aleksandrov, Zh. Neorg. Khim. **43**, 1002 (1998) [Rus. J. Inorg. Chem. **43**, 916 (1998)].
3. E. G. Afonin, G. G. Aleksandrov, and V. S. Sergienko, Koord. Khim. **23**, 846 (1997) [J. Coord. Chem. **23**, 794 (1997)].
4. V. S. Sergienko, E. G. Afonin, and G. G. Aleksandrov, Koord. Khim. **24**, 293 (1998) [J. Coord. Chem. **24**, 276 (1998)].
5. V. S. Sergienko, E. G. Afonin, and G. G. Aleksandrov, Koord. Khim. **25**, 133 (1999) [J. Coord. Chem. **25**, 123 (1999)].
6. G. M. Sheldrick, *SHELXL93: Program for the Refinement of Crystal Structures* (Univ. of Göttingen, Göttingen, 1993).

*Translated by I. Polyakova*

*Crystallography Reports, Vol. 45, No. 2, 2000, pp. 234–243. Translated from Kristallografiya, Vol. 45, No. 2, 2000, pp. 266–274.*


**STRUCTURES OF COORDINATION COMPOUNDS**

# A Study on the Phase Transition in Decamethylosmocene Crystal over a Wide Temperature Range

**I. I. Vorontsov*, K. A. Potekhin**, M. Yu. Antipin*, and I. E. Zanin***

** Nesmeyanov Institute of Organoelement Compounds, Russian Academy of Sciences, ul. Vavilova 28, Moscow, GSP-1, 117813 Russia*

*** Vladimir State Pedagogical University, pr. Stroiteleĭ 11, Vladimir, Russia*

Received April 19, 1999

**Abstract**—The reversible structural phase transition accompanied by the doubling of the unit cell parameter *c* and a change in the space group is found in the decamethylosmocene crystal $Cp_2^*Os$ at a temperature of 243 ± 5 K. In the high-temperature (HT) phase (space group $P2_1/m$, $Z = 2$), the molecule adopts an eclipsed conformation and lies in the mirror symmetry plane. In the low-temperature (LT) phase (space group $P2_1/c$, $Z = 4$), the molecule occupies the general position with a small rotation of the ligands. The structural transformations from the high-temperature phase into the low-temperature phase at 120 K are described by the deviation of the molecular axis of fivefold symmetry by 3.2(2)° and the displacement of the center of mass of the molecule by 0.173(2) Å with respect to their positions in the high-temperature phase, and also by the rotation of the *Cp** ligands in the same direction by 3.0(2)° and 5.4(2)°, respectively. © *2000 MAIK "Nauka/Interperiodica".*

## INTRODUCTION

Decamethylosmocene $(\eta^5\text{-}C_5(CH_3)_5)_2Os$ belongs to the well-known series of sandwich π-complexes $Cp_2^*M$ (*Cp** is the pentamethylcyclopentadienyl ligand), where *M* is the 3*d*, 4*d*, or 5*d* transition metal. The compounds of this series and the related metallocenes $Cp_2M$ (where $Cp = C_5H_5$) are characterized by a high rotational mobility of the *Cp* and *Cp** ligands and a wide variety of crystalline phases with different nature of ligand disordering [1]. Specifically, structural phase transitions were found in nickelocene and ferrocene [2–4], whereas the dynamic (temperature-dependent) disordering of the *Cp* rings was revealed in the formally isostructural cobaltocene [5] and vanadocene [1]. However, as a whole, the data available in the literature on the investigation into the nature of phase transitions in molecular crystals are few in number. Among the phase transitions in molecular crystals, which were studied earlier in detail by diffraction techniques, mention should be made of the "displacement"-type transitions (in chloranil [6] and *N*,*N*-dimethylnitramine [7]), the "order–disorder" transitions (in 1,4-dichloro-2,3,5,6-tetramethylbenzene [8]), and a number of works concerned with the phase transitions in polyphenyls [9–15]. These transitions occur with the retention of single crystallinity of a sample at the phase transition point; i.e., they are "continuous" transitions (or close to them). According to the classical theory, these transitions are classified as the second-order transitions or "weak" first-order transitions. Traditionally, the structural phase transitions are subdivided into the displacement transitions and the order–disorder transitions; however, closer examination showed that these transitions can be mixed in character [6]. In the present work, we studied the nature of phase transitions in the $Cp_2^*Os$ crystal by the X-ray diffraction analysis.

## EXPERIMENTAL

Decamethylosmocene crystals in the shape of prisms or thin plates were grown by slow evaporation from saturated solutions of $Cp_2^*Os$ in pentane and acetone at 20°C. The experiments were carried out with two samples stable with a decrease in the temperature, which ensured their cooling from room temperature down to a temperature of 120 K below the phase transition point without visible indications of their destruction. A total of five experiments (at 120, 153, 157, 168, and 183 K) were performed for the low-temperature (LT) phase, and four experiments (at 243, 258, and, for two samples, at 293 K) were carried out for the high-temperature (HT) phase.

The experimental data were collected on a Siemens *P*3/*PC* four-circle automated diffractometer ($MoK_\alpha$ radiation, $\lambda = 0.7107$ Å, graphite monochromator, $\theta/2\theta$ scan mode) equipped with an LT-2 low-temperature attachment (the temperature was maintained constant to within ±2 K). The unit cell parameters were refined using 24 reflections in the range $2\theta = 22°–24°$. For all the temperatures, the measurements were conducted in an independent area of the reciprocal space at $\theta \le 26°$. The scan range was 1.8°.

1063-7745/00/4502-0234$20.00 © 2000 MAIK "Nauka/Interperiodica"

**Table 1.** Main crystal data and data collection parameters

| Parameter | 120 K | 153 K* | 157 K | 168 K | 183 K* | 243 K* | 258 K* | 293 K* | 293 K |
|---|---|---|---|---|---|---|---|---|---|
| *a*, Å | 7.637(3) | 7.669(2) | 7.655(2) | 7.667(2) | 7.684(2) | 7.720(2) | 7.725(2) | 7.745(2) | 7.742(3) |
| *b*, Å | 14.486(4) | 14.546(3) | 14.509(4) | 14.527(4) | 14.567(3) | 14.597(3) | 14.610(3) | 14.639(3) | 14.629(3) |
| *c*, Å | 17.091(5) | 17.148(3) | 17.121(5) | 17.126(5) | 17.164(4) | 8.603(2) | 8.612(2) | 8.624(2) | 8.623(2) |
| β, deg | 107.12(3) | 107.04(3) | 106.97(2) | 106.98(2) | 106.94(3) | 106.78(3) | 106.70(3) | 106.46(3) | 106.45(2) |
| Space group | $P2_1/c$ | $P2_1/c$ | $P2_1/c$ | $P2_1/c$ | $P2_1/c$ | $P2_1/m$ | $P2_1/m$ | $P2_1/m$ | $P2_1/m$ |
| *Z* | 4 | 4 | 4 | 4 | 4 | 2 | 2 | 2 | 2 |
| *V*, Å$^3$ | 1807(2) | 1830(2) | 1816(2) | 1825(2) | 1838(2) | 928.2(4) | 931.0(4) | 937.7(4) | 937(1) |
| *Goof* | 0.965 | 1.030 | 0.930 | 1.030 | 1.031 | 1.200 | 1.140 | 1.150 | 1.034 |
| $R_1$ | 0.033 | 0.028 | 0.036 | 0.036 | 0.032 | 0.024 | 0.024 | 0.034 | 0.043 |
| $wR_2$ | 0.093 | 0.084 | 0.096 | 0.110 | 0.085 | 0.031 | 0.028 | 0.062 | 0.098 |
| $N(I > 2\sigma(I))$ | 2641 | 2414 | 3875 | 3370 | 3512 | 1524 | 2358 | 2700 | 2432 |

* Data for the second sample.

The structures were solved by the direct method and refined by the full-matrix least-squares procedure in the anisotropic approximation for the non-hydrogen atoms according to the SHELXTL PLUS 4.2 (refinement on $F_o$) and SHELXTL PLUS 5.0 (refinement on $F_o^2$) software packages [16, 17]. The positions of the hydrogen atoms were calculated and refined using the "rider" model with the fixed parameters $U_{iso} = 0.08$ Å$^2$ or $U_{iso} = 1.5U_{eq}$, where $U_{eq}$ are the equivalent isotropic displacement parameters for the corresponding C atoms. Absorption correction at room temperature was empirically applied by the standard procedure of Ψ-scans; then, the results obtained were used for the same samples studied at low temperatures.

The main crystal data, details of data collection, refinement parameters for all the temperatures, and the coordinates and thermal parameters $U_{eq}$ for the non-hydrogen atoms at 157 K for the low-temperature phase and at 258 K for the high-temperature phase are summarized in Tables 1 and 2. The atomic coordinates and anisotropic thermal parameters for the other temperatures are available from the authors.

In the decamethylosmocene crystal, the phase transition to the low-temperature phase is attended by the change in the space group from $P2_1/m$ to $P2_1/c$ and the doubling of the unit cell parameter *c*, which gives rise to "additional" diffraction reflections for the low-temperature phase as compared to the high-temperature phase. In [18–20], these reflections were referred to as "superstructure" reflections in order to distinguish them from the "main" reflections observed in the diffraction patterns of both phases. At 120 K, 1227 superstructure reflections were recorded, which amounts to 42% of the total number of the measured reflections with $I > 3\sigma(I)$. The mean integrated intensity comprised 9σ for the superstructure reflections and more than 50σ for the main reflections.

In order to investigate the temperature dependence of the integrated intensity for the superstructure reflections, we chose 38 reflections with $I > 40\sigma(I)$ at 120 K. The intensity of these reflections considerably decreases with an increase in the temperature from 120 to 168 K. Note that the intensity of the main reflections in the same temperature range decreases, on the average, by no more than 2σ. Consequently, the temperature dependences of the intensity of the superstructure and main reflections substantially differ from each other in the temperature range from 120 to 168 K.

To evaluate the phase transition temperature $T_{cr}$, we studied the change in intensities of two superstructure reflections (0, 2, 5/2) and (1, 3, 3/2) and one main reflection (2, 0, –3) (the indices correspond to the high-temperature phase) with a step of 5 K in the temperature range from 200 to 250 K (Fig. 1). As the temperature increases, the intensities of both superstructure reflections gradually decrease and, at $T_{cr} = 243 \pm 5$ K, become comparable with the background. In this case, the intensity of the reference main reflection remains virtually constant. A monotonic decrease in the intensity of superstructure reflections down to zero can indicate a continuous character of the structural transition.

## RESULTS AND DISCUSSION

**Thermal expansion of the decamethylosmocene crystal.** Within the limits of experimental error, the temperature dependences of the unit cell parameters of decamethylosmocene are the smooth monotonic functions in the range 120–293 K (Fig. 2). The doubled values are given for the volume and the *c* parameter above

**Table 2.** Coordinates and equivalent isotropic thermal parameters ($Å^2 \times 10^3$) for non-hydrogen atoms in decamethylosmocene crystal at 258 K (high-temperature phase) and 157 K (low-temperature phase)

| Atom | *x*/*a* | *y*/*b* | *z*/*c* | $U_{eq}$ |
|---|---|---|---|---|
| High-temperature phase | | | | |
| Os | 0.0800(1) | 1/4 | 0.2957(1) | 30(1) |
| C(1) | 0.3239(8) | 1/4 | 0.2171(9) | 52(3) |
| C(2) | 0.3234(6) | 0.1707(3) | 0.3120(6) | 43(1) |
| C(3) | 0.3262(5) | 0.2005(3) | 0.4701(5) | 35(1) |
| C(4) | –0.1661(8) | 1/4 | 0.0963(9) | 72(4) |
| C(5) | –0.1647(6) | 0.1695(4) | 0.1933(6) | 50(2) |
| C(6) | –0.1623(5) | 0.2006(3) | 0.3521(5) | 39(1) |
| C(11) | 0.3331(17) | 1/4 | 0.0440(15) | 86(6) |
| C(12) | 0.3325(10) | 0.0729(5) | 0.2618(12) | 78(3) |
| C(13) | 0.3375(9) | 0.1419(4) | 0.6154(8) | 58(2) |
| C(14) | –0.1817(16) | 1/4 | –0.0823(11) | 103(8) |
| C(15) | –0.1776(12) | 0.0721(7) | 0.1400(14) | 97(4) |
| C(16) | –0.1699(9) | 0.1421(5) | 0.4910(9) | 59(2) |
| Low-temperature phase | | | | |
| Os | 0.0803(1) | 0.2393(1) | 0.1480(1) | 15(1) |
| C(1) | 0.3251(7) | 0.2405(4) | 0.1066(3) | 24(1) |
| C(2) | 0.3312(7) | 0.1633(3) | 0.1594(3) | 22(1) |
| C(3) | 0.3333(7) | 0.1983(3) | 0.2382(3) | 19(1) |
| C(4) | 0.3267(7) | 0.2972(3) | 0.2333(3) | 19(1) |
| C(5) | 0.3195(7) | 0.3235(3) | 0.1513(3) | 22(1) |
| C(6) | –0.1682(8) | 0.2254(5) | 0.0475(3) | 30(1) |
| C(7) | –0.1578(7) | 0.1516(4) | 0.1032(3) | 25(1) |
| C(8) | –0.1571(7) | 0.1904(4) | 0.1805(3) | 21(1) |
| C(9) | –0.1685(7) | 0.2887(4) | 0.1731(3) | 24(1) |
| C(10) | –0.1740(8) | 0.3114(4) | 0.0899(3) | 28(1) |
| C(11) | 0.3306(10) | 0.2359(6) | 0.0200(4) | 43(2) |
| C(12) | 0.3509(10) | 0.0647(4) | 0.1390(4) | 39(1) |
| C(13) | 0.3515(9) | 0.1423(4) | 0.3134(3) | 31(1) |
| C(14) | 0.3293(9) | 0.3619(4) | 0.3025(3) | 32(1) |
| C(15) | 0.3165(11) | 0.4194(5) | 0.1194(5) | 47(2) |
| C(16) | –0.1805(10) | 0.2171(6) | –0.0418(3) | 44(2) |
| C(17) | –0.1606(10) | 0.0511(5) | 0.0829(4) | 40(2) |
| C(18) | –0.1580(9) | 0.1373(4) | 0.2561(3) | 32(1) |
| C(19) | –0.1797(10) | 0.3543(4) | 0.2385(4) | 35(1) |
| C(20) | –0.1962(10) | 0.4054(5) | 0.0528(5) | 45(2) |

$T_{cr}$. None of the parameters shows a jump in the phase transition range.

The principle values and the orientation of principle axes of the thermal expansion tensor were calculated in the temperature range from 120 to 293 K [21]. Since the $Cp^*_2Os$ crystal in both phases belongs to the monoclinic crystal system, one axis of the thermal expansion tensor ($a_{22}$) is always aligned parallel to the crystallographic axis *b*, and the other two axes ($a_{11}$ and $a_{33}$) lie in the *ac* plane. The orientation of the ellipsoid axes in the *ac* plane is defined by the parameter $\psi_0$—the angle between the axis of the ellipsoid, whose length is equal to $a_{11}$, and the crystal axis *a* (Fig. 3).

Note that the slopes of the tangents to the curves of the parameters $a_{11}$ and $a_{33}$ [the dependence $a_{11}(T)$ exhibits a minimum] considerably change in the range 220–250 K, i.e., in the vicinity of the $T_{cr}$ temperature. At the same time, the analysis of the thermal expansion tensor demonstrates that, in the (001) plane of the crystal, the behavior of the thermal expansion remains virtually unchanged with a change in the temperature, including the phase transition range. In this plane, the thermal expansion coefficient along the direction [010] is equal to the principal value $a_{22}$ of the thermal expansion coefficient. The linear expansion coefficient along the [100] direction is designated as $\Delta_{[100]}$ and is also depicted in Fig. 3. The weak temperature dependences of $a_{22}$ and $\Delta_{[100]}$ can indicate a system of strong intermolecular contacts in the (001) plane.

**Molecular structure of decamethylosmocene in the high-temperature and low-temperature phases.** Let us compare the obtained data on the molecular geometry of $Cp^*_2Os$ at 293 K with those reported earlier in [22]. In the high-temperature phase (space group $P2_1/m$), the molecule occupies the special position in the *m* plane passing through the Os, C(1), C(4), C(11), and C(14) atoms (Fig. 4a), and, hence, the *Cp** rings adopt an ideal eclipsed conformation. The molecule, as a whole, has approximately the $D_{5h}$ symmetry, and the angle between the normals to the root-mean-square planes of the *Cp** rings is less than 1.2(5)°. The carbon atoms of the methyl groups deviate from the planes of the cyclopentadienyl rings, on the average, by 0.08(1) Å toward the side opposite to the Os atom.

In the low-temperature phase (space group $P2_1/c$), the molecule occupies the general position (Fig. 4b), and its own symmetry lowers to $D_5$: the *Cp** ligands are rotated by the angle $\alpha$ with respect to each other. As the temperature decreases below $T_{cr}$, the $\alpha$ angle gradually increases from 0° to 2.4(5)° at 120 K. This angle is the most important parameter describing the distortion of the molecular geometry and the proper symmetry of the molecule in the crystal. The bond lengths in both modifications are virtually identical (Table 3).

A change in the position of the molecule in the crystal upon transition from the high-temperature phase to

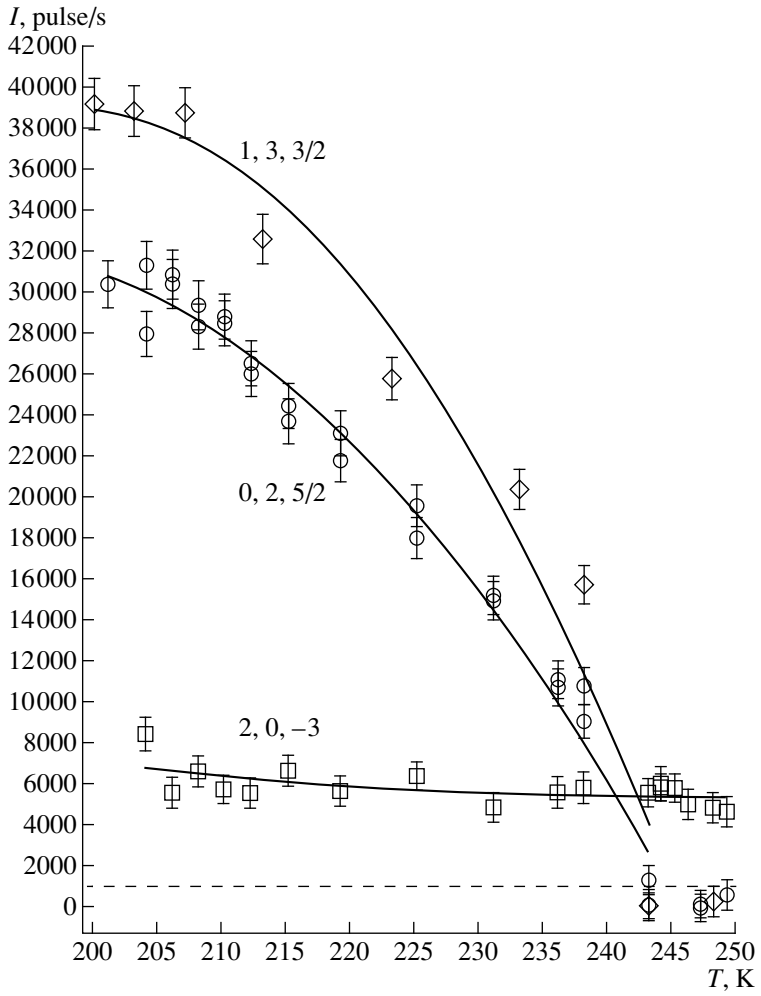


**Fig. 1.** Temperature dependences of the integrated intensity for the superstructure reflections (0, 2, 5/2) and (1, 3, 3/2) and for the main reflection (2, 0, –3). The dashed line indicates the mean background level for superstructure reflections. Errors correspond to 1 σ.

the low-temperature phase can be empirically described by four geometric parameters. The parameter $t_G$ characterizes the displacement of the center of mass from the *c* plane (in the high-temperature phase, the center of mass of the molecule lies in the mirror plane). The angular parameter ω determines the rotation of the molecule around the axis, which passes through the center of mass of the molecule and lies parallel to the *c* direction of the unit cell. Furthermore, the *Cp** ligands additionally rotate around the fivefold symmetry axis in the same direction, but through different angles $\alpha(Cp_1^*)$ and $\alpha(Cp_2^*)$; i.e., the molecule, as a whole, is rotated through the angle $(\alpha(Cp_1^*) + \alpha(Cp_2^*))/2$, and the angle of the intramolecular deformation α is equal to the difference between $\alpha(Cp_1^*)$ and $\alpha(Cp_2^*)$ (Fig. 5).

The behavior of the $t_G$, 2ω, and $2\alpha(Cp^*)$ parameters in the range 120–183 K is well approximated by the linear dependences (Fig. 6). As the $T_{cr}$ temperature is approached, the temperature dependences of these parameters apparently become nonlinear. This behavior is characteristic of the displacement-type structural transitions.

*Molecular packing and mechanism of the phase transition.* In order to describe the relative arrangement of the $Cp_2^*$ Os molecules in the crystal, we analyzed a Dirichlet packing polyhedron [23, 24]. The shape of a packing polyhedron is determined by the structure of a molecule and its nearest environment, and, hence, the features of molecular packing can be judged from the packing polyhedron shape and its variation.

It is expedient to carry out comparison between the packing polyhedra according to the boundary surfaces [25], which correspond to a set of common faces shared by a packing polyhedron of the reference molecule chosen as the origin and packing polyhedra of adjacent molecules. Table 4 lists the areas of the boundary surfaces whose contribution to the total surface area of the packing polyhedron of decamethylosmocene is more than 2%. In both phases, the number of these boundary

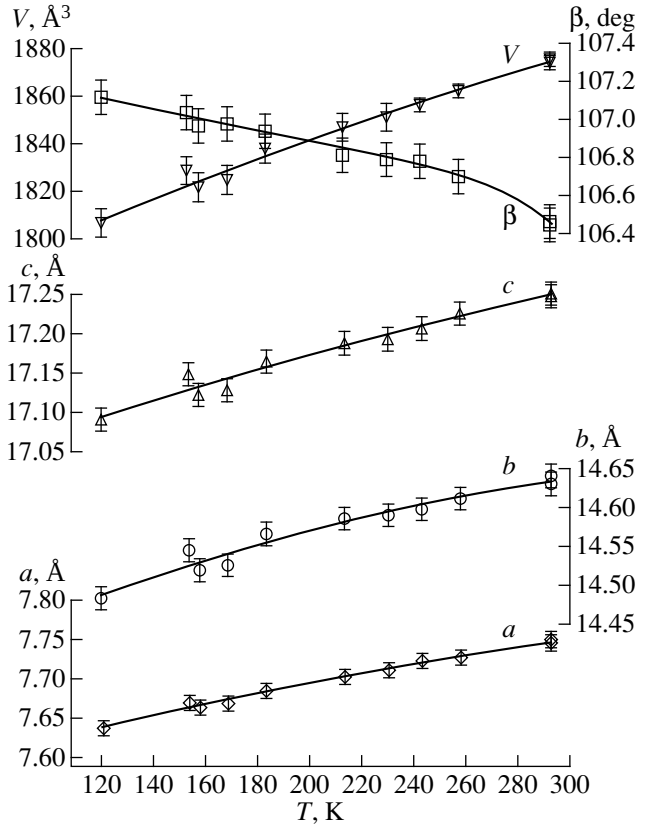


**Fig. 2.** Temperature dependences of the unit cell parameters for decamethylosmocene. Parameters $c$ and $V$ correspond to $c_{LT}$ and $V_{LT}$ at $T < T_{cr}$ and $2c_{HT}$ and $2V_{HT}$ at $T \geq T_{cr}$. Errors are equal to 3σ.

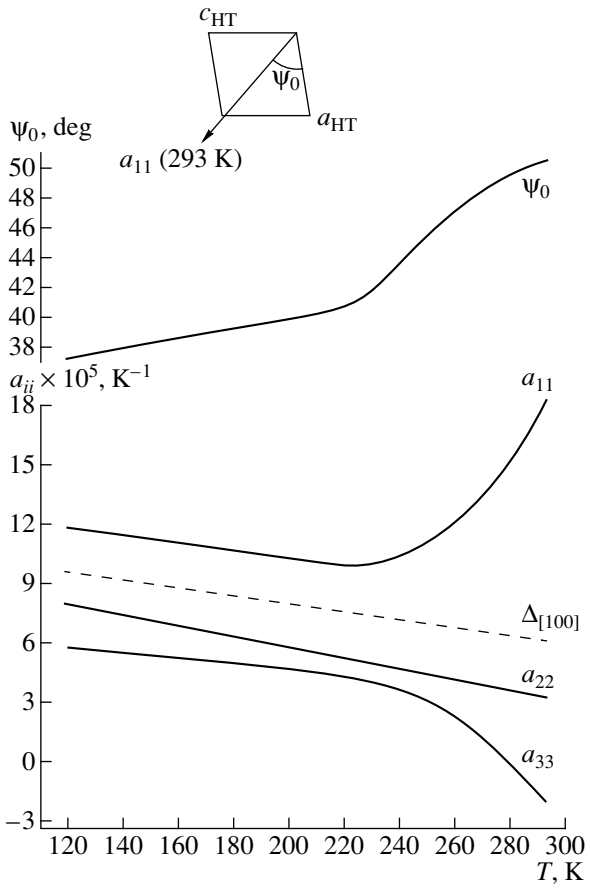


**Fig. 3.** Temperature dependences of the principal values for the thermal expansion tensor and the angle between the principal tensor axis $a_{11}$ and the crystal axis $a$. $\Delta_{[100]}$ is the linear expansion coefficient in the [100] direction. Direction of the maximum expansion at 293 K is shown in the inset.

surfaces is equal to 12, and it is possible to establish the one-to-one correspondence between them.

A common feature of the packing polyhedra in both phases (Table 4) resides in the fact that the areas of boundary surfaces with molecules 1–4 appreciably exceed all the other areas. This enables us to describe the molecular packing in the form of puckered layers running parallel to the crystallographic plane (001). In the high-temperature phase, these layers are translationally identical, whereas in the low-temperature phase, the adjacent layers are related by the glide plane *c*.

At the same time, there are considerable differences in the molecular packings of two phases. As an integrated characteristic of the degree of distinction in

**Table 3.** Bond lengths in decamethylosmocene at 120 and 293 K

| *T*, K | 120 | 293 |
|---|---|---|
| Os–C(*Cp**), Å | 2.160(7)–2.191(6) | 2.179(5)–2.193(6) |
| Mean, Å | 2.181(7) | 2.187(7) |
| *X*··*X*, Å | 3.615(6) | 3.633(6) |
| C(*Cp**)–C(*Cp**), Å | 1.416(11)–1.452(9) | 1.422(10)–1.448(9) |
| Mean, Å | 1.434(10) | 1.436(10) |
| C(*Cp**)–C(*Me*), Å | 1.488(9)–1.511(11) | 1.490(12)–1.506(10) |
| Mean, Å | 1.499(10) | 1.501(12) |

Note: *X* is the center of the pentadienyl ring.

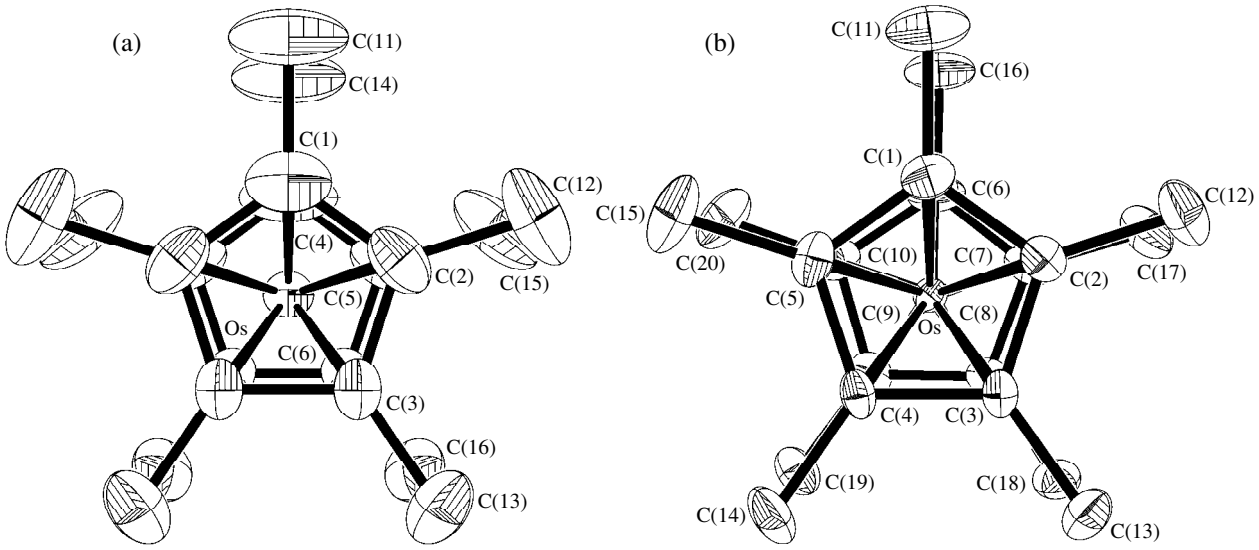


**Fig. 4.** A general view of the decamethylosmocene molecule along the fivefold symmetry axis and the atomic numbering at (a) 258 and (b) 157 K.

two packings, we used the coefficient $Ds = (\Sigma|S_{1i} - S_{2i}|)/(S_1 + S_2)$, where $S_{1i}$ and $S_{2i}$ are the areas of the $i$th boundary surfaces of the packing polyhedra, and $S_1$ and $S_2$ are the surface areas of packing polyhedra for the structures at two temperatures [25]. In the case when the packings are completely coincident, $Ds = 0$. Figure 7 displays the temperature dependence of $Ds$ (comparison was made with the structure at 120 K). A sharp increase in the $Ds$ coefficient in the temperature range 183–243 K is an important feature of its behavior. A similar temperature dependence of $Ds$ was revealed for the phase transition in chloranil [26]. Note that,

**Table 4.** Comparison between the Dirichlet packing polyhedra of decamethylosmocene at 120 (low-temperature phase) and 293 K (high-temperature phase)

| Boundary surface (low-temperature phase/high-temperature phase) | Symmetry transformations (LT phase) | $S_{1i}$, Å$^2$ (LT phase) | Symmetry transformations (HT phase) | $S_{2i}$, Å$^2$ (HT phase) | $\Delta S$, Å$^2$ |
|---|---|---|---|---|---|
| 1/1 | $-1 + X, Y, Z$ | 53.7(3) | $-1 + X, Y, Z$ | 53.8(3) | 0.1(3) |
| 2/2 | $1 + X, Y, Z$ | 53.7(3) | $1 + X, Y, Z$ | 53.8(3) | 0.1(3) |
| 3/3 | $-X, -0.5 + Y, 0.5 - Z$ | 36.7(2) | $-X, -Y, 1 - Z$ | 37.5(2) | 0.8(2) |
| 4/4 | $-X, 0.5 + Y, 0.5 - Z$ | 36.7(2) | $-X, 1 - Y, 1 - Z$ | 37.5(2) | 0.8(2) |
| 5/5 | $X, 0.5 - Y, -0.5 + Z$ | 28.7(2) | $X, Y, -1 + Z$ | 29.3(2) | 0.6(2) |
| 6/6 | $X, 0.5 - Y, 0.5 + Z$ | 28.7(2) | $X, Y, 1 + Z$ | 29.3(2) | 0.6(2) |
| 7/7 | $-X, -Y, -Z$ | 34.5(2) | $-X, -Y, -Z$ | 29.9(2) | −4.6(2) |
| 8/8 | $-X, 1 - Y, -Z$ | 26.2(2) | $-X, 1 - Y, -Z$ | 29.9(2) | 3.7(2) |
| 9/9 | $1 - X, -0.5 + Y, 0.5 - Z$ | 16.02(8) | $1 - X, -Y, 1 - Z$ | 16.78(8) | 0.76(8) |
| 10/10 | $1 - X, 0.5 + Y, 0.5 - Z$ | 16.02(8) | $1 - X, 1 - Y, 1 - Z$ | 16.78(8) | 0.76(8) |
| 11/11 | $-1 + X, 0.5 - Y, -0.5 + Z$ | 17.66(9) | $-1 + X, Y, -1 + Z$ | 17.50(9) | −0.16(9) |
| 12/12 | $1 + X, 0.5 - Y, 0.5 + Z$ | 17.66(9) | $1 + X, Y, 1 + Z$ | 17.50(9) | −0.16(9) |
| Total | | 373(2) | | 377(2) | 4(2) |

Note: The numbers of molecules whose packing polyhedra share common faces with packing polyhedra of the reference molecule are given in the first column. $S_{1i}(S_{2i})$ are the areas of the $i$th boundary surfaces of packing polyhedron. $\Delta S = S_{2i} - S_{1i}$. Symmetry transformations relating molecules in the nearest environment to the reference molecule are presented in the second and fourth columns.

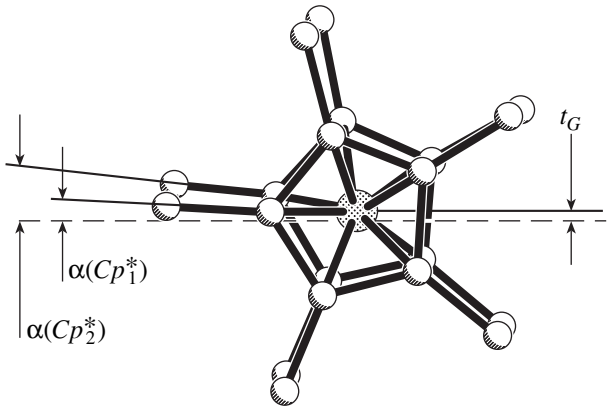


**Fig. 5.** Projection of the decamethylosmocene molecule onto the (100) plane at 120 K. Parameter $t_G$ characterizes the displacement of the center of mass of the molecule from the plane *c*, and the parameters $\alpha(Cp_1^*)$ and $\alpha(Cp_2^*)$ account for the rotation of the *Cp** ligands around the fivefold symmetry axis. The dashed line shows the glide-reflection plane *c*.

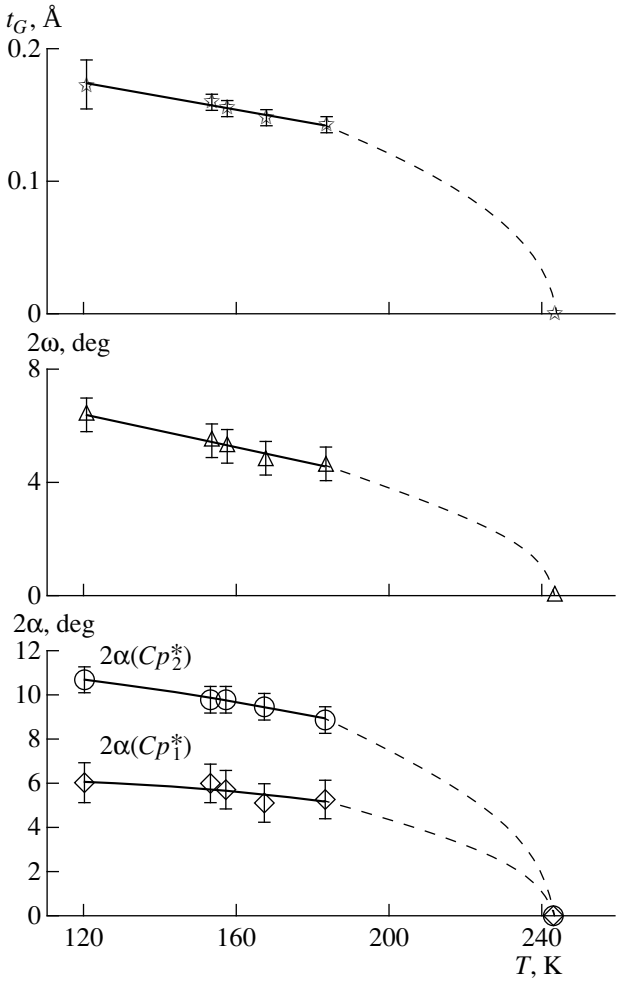


**Fig. 6.** Temperature dependences of the geometric parameters characterizing the position of the molecule in the low-temperature phase.

upon thermal expansion without phase transition, for example, in 1,4-dichlorobenzene in the temperature range 100–300 K, the *Ds* coefficient does not exceed 0.02 [27].

A considerable change in the molecular packing is associated with the parallel displacement of molecular layers parallel to the crystallographic plane (001) along the *b* axis. This shift is equal to twice the $t_G$ parameter. In the high-temperature phase, the adjacent molecular layers are arranged in such a way that "hills" of one layer are located precisely in front of "cavities" of the adjacent layer. At the same time, in the low-temperature phase, hills of the adjacent layers approach each other, which leads to the doubling of the *c* translation and the formation of the *c* plane in the crystal (Fig. 8). This displacement can arise from the change in the interaction between molecules of the adjacent layers, which is indirectly evidenced by the change in the areas of boundary surfaces 7 and 8 in the Dirichlet packing polyhedron (Table 4). The proposed mechanism of phase transition is consistent with its reversible character, because the parallel shift of molecular layers does not bring about change in the volume of the crystal and its failure.

**Analysis of thermal motion.** As expected, the anisotropic displacement ellipsoids for the carbon atoms of the *Cp** ligands, specifically in the high-temperature phase, are extended tangentially with respect to the molecular axis of fivefold symmetry $L_5$ (Fig. 4). The high values of anisotropic thermal parameters can be brought about either by the static disordering of the *Cp** ligands or by thermal librations with a large amplitude.

In order to elucidate the nature of thermal motion in the decamethylosmocene crystal, we analyzed the anisotropic displacement parameters of the non-hydrogen atoms separately for each *Cp** ring within the Schomaker–Trueblood rigid-body model [28]. The calculations were carried out using the THMA11 program package [29] according to the procedure described in [30].

The temperature dependences of the root-mean-square amplitudes of librations $\langle\phi^2\rangle$ around the fivefold symmetry axis for the $Cp_1^*$ and $Cp_2^*$ ligands are demonstrated in Fig. 9. A monotonic decrease in the $\langle\phi^2\rangle$ amplitudes with a decrease in the temperature most likely indicates the absence of static disordering of the *Cp** ligands [31], and the large anisotropic displacement parameters for the carbon atoms in decamethylosmocene are most probably caused by thermal vibrations with a large amplitude around an equilibrium position.

To evaluate the possibility of occurring the rotations of the *Cp** rings around the $L_5$ molecular axis, which also can lead to an increase in the anisotropic displacement parameters, it is necessary to compare the energy of thermal vibrations with the height of the potential barrier of rotation. In the harmonic approximation, the

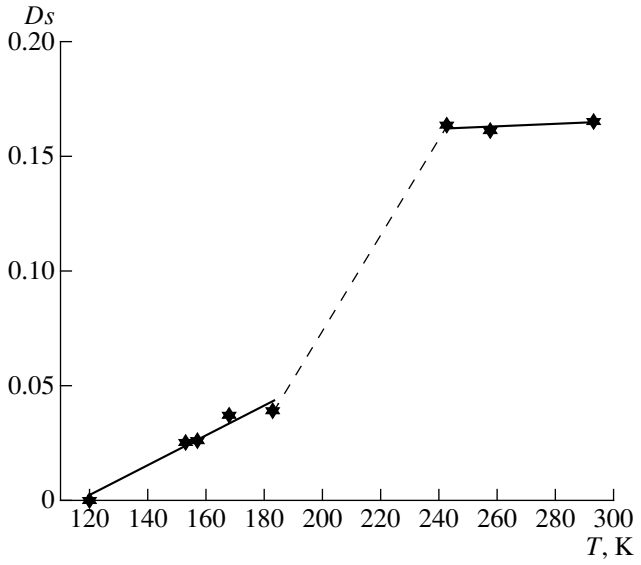


**Fig. 7.** Temperature dependence of the packing misfit coefficient *D*s.

barrier height for rotation around the fivefold symmetry axis can be estimated from the formula $B_n = 2RT/(n^2\langle\phi^2\rangle)$, where $\langle\phi^2\rangle$ is expressed in terms of rad$^2$, $n = 5$, and $R = 8.3$ J/(mol K) [30]. In the low-temperature phase, the calculated mean barrier for two rings is equal to 21(2) kJ/mol. In the high-temperature phase at 243 K, the barrier decreases to 18(2) and 14(2) kJ/mol for the $Cp_1^*$ and $Cp_2^*$ ligands, respectively. The mean barriers in the high-temperature phase are equal to 17(2) and 13(2) kJ/mol. A comparison of $B_5$ with the $RT$ value (under the assumption of the Boltzmann distribution) demonstrates that, even at 293 K, the probability of the overcoming of the potential barrier is very low, and, hence, this factor cannot substantially affect the thermal ellipsoids.

## CONCLUSION

The structural phase transition in decamethylosmocene is investigated using the traditional methods (the revelation of temperature dependences of the crystal lattice and crystal structure parameters) and also the

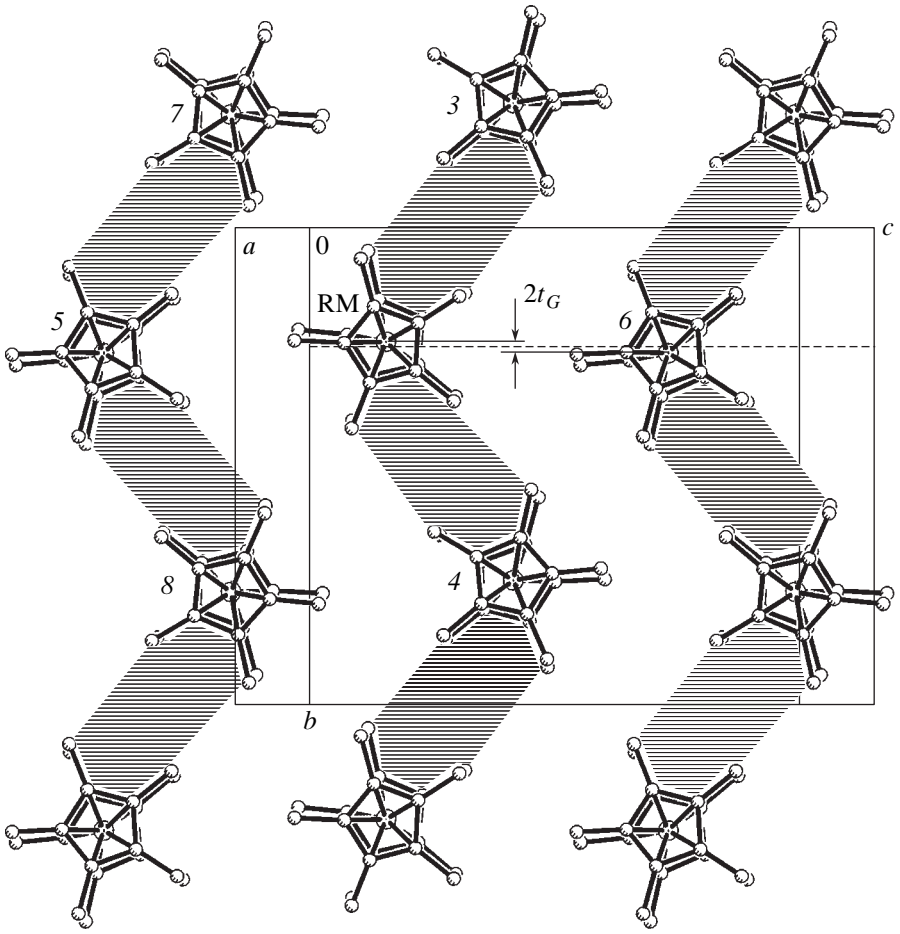


**Fig. 8.** Projection of the crystal structure of the low-temperature decamethylosmocene phase onto the (100) plane. Layers parallel to the (001) plane are hatched. Molecular numbering corresponds to that in Table 4. RM is the reference molecule.

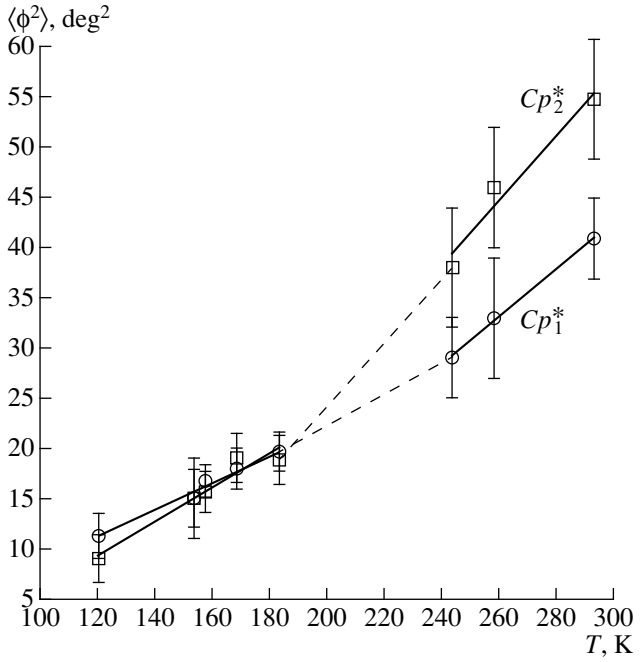


**Fig. 9.** Temperature dependences of the root-mean-square libration amplitudes for the *Cp** ligands. Errors correspond to 2σ.

analysis of the molecular packing with the Dirichlet packing polyhedra. The unit cell parameters are characterized by the smooth temperature dependences, whereas the molecular packing misfit coefficient *Ds* indicates considerable changes in the mutual arrangement of molecules upon phase transition. Analysis of the Dirichlet polyhedron made it possible to represent the packing of decamethylosmocene in the form of molecular layers and demonstrated that the structural transformations are associated with the parallel displacement of the layers with respect to each other. Moreover, the statistical analysis of the array of diffraction reflections revealed the presence of two groups of reflections differing in both the mean intensity and the temperature behavior. A close examination of the temperature dependence of the integrated intensity of reflections that correspond to the doubling of the *c* parameter in the low-temperature phase made it possible to determine the $T_{cr}$ temperature.

It is of interest to compare the crystal structures of decamethylosmocene and decamethylruthenocene $Cp_2^*$Ru [32], which crystallizes in two modifications (**I** and **II**) isostructural to the high-temperature and low-temperature phases of $Cp_2^*$Os, respectively. The static disordering of one of the *Cp** ligands over two positions in the range 153–300 K is the main difference between modification **I** of $Cp_2^*$Ru and the high-temperature phase of $Cp_2^*$Os. This distinction can be due to the difference in distances between the centers of the *Cp** rings [2.620(6) and 2.633(5) Å at 293 K for $Cp_2^*$Ru and $Cp_2^*$Os, respectively]. As a result, the adjacent *Cp** ligands in the $Cp_2^*$Os crystal can "come" nearer to the Os atoms, thus hindering the rotational motion of the rings of the initial molecule [1].

## ACKNOWLEDGMENTS

We are grateful to V. N. Panov for supplying the DIRGMU1 program used in calculations of the Dirichlet packing polyhedra and analysis of the molecular packing on the basis of the results obtained.

This work was supported by the Russian Foundation for Basic Research, project nos. 97-03-33783 and 96-15-97367.

## REFERENCES

1. M. Yu. Antipin and R. Boese, Acta Crystallogr., Sect. B: Struct. Sci. **52**, 314 (1996).
2. P. Seiler and J. D. Dunitz, Acta Crystallogr., Sect. B: Struct. Crystallogr. Cryst. Chem. **36**, 2255 (1980).
3. P. Seiler and J. D. Dunitz, Acta Crystallogr., Sect. B: Struct. Crystallogr. Cryst. Chem. **35**, 1068 (1979).
4. P. Seiler and J. D. Dunitz, Acta Crystallogr., Sect. B: Struct. Crystallogr. Cryst. Chem. **38**, 1741 (1982).
5. M. Yu. Antipin, R. Boese, N. Augart, *et al.*, Struct. Chem. **4**, 91 (1993).
6. J. L. Baudour, Y. Delugeard, H. Cailleau, *et al.*, Acta Crystallogr., Sect. B: Struct. Crystallogr. Cryst. Chem. **37**, 1553 (1981).
7. A. Filhol, G. Bravic, M. Rey-Lafon, *et al.*, Acta Crystallogr., Sect. B: Struct. Crystallogr. Cryst. Chem. **36**, 575 (1980).
8. J. C. Messager, H. Cailleau, and W. B. Yelon, Acta Crystallogr., Sect. A: Cryst. Phys., Diffr., Theor. Gen. Crystallogr. **34**, 384 (1978).
9. J. L. Baudour, Y. Delugeard, and H. Cailleau, Acta Crystallogr., Sect. B: Struct. Crystallogr. Cryst. Chem. **32**, 150 (1976).
10. Y. Delugeard, J. Desuche, and J. L. Baudour, Acta Crystallogr., Sect. B: Struct. Crystallogr. Cryst. Chem. **32**, 702 (1976).
11. G.-P. Charbonneu and Y. Delugeard, Acta Crystallogr., Sect. B: Struct. Crystallogr. Cryst. Chem. **32**, 1420 (1976).
12. G.-P. Charbonneu and Y. Delugeard, Acta Crystallogr., Sect. B: Struct. Crystallogr. Cryst. Chem. **33**, 1586 (1977).
13. J. L. Baudour, H. Cailleau, and W. B. Yelon, Acta Crystallogr., Sect. B: Struct. Crystallogr. Cryst. Chem. **33**, 1773 (1977).
14. J. L. Baudour, Y. Delugeard, and P. Rivet, Acta Crystallogr., Sect. B: Struct. Crystallogr. Cryst. Chem. **34**, 625 (1978).
15. H. Cailleau, J. L. Baudour, and C. M. E. Zeyen, Acta Crystallogr., Sect. B: Struct. Crystallogr. Cryst. Chem. **35**, 426 (1979).
16. G. M. Sheldrick, *SHELXTL PLUS: Release 4.2* (Siemens Analytical Instruments Inc., Madison, Wis., 1991).
17. G. M. Sheldrick, *SHELXTL PLUS: Release 5.0* (Siemens Analytical Instruments Inc., Madison, Wis., 1994).

18. J. L. Baudour and J. Meinnel, Acta Crystallogr., Sect. B: Struct. Crystallogr. Cryst. Chem. **38**, 472 (1982).
19. W. D. Ellenson and J. K. Kjems, J. Chem. Phys. **67**, 3619 (1977).
20. H. Terauchi, T. Sakai, and H. Chihara, J. Chem. Phys. **62**, 3832 (1975).
21. A. I. Kitaĭgorodsky, *Molecular Crystals* (Nauka, Moscow, 1971).
22. M. O. Allers, D. C. Liles, D. J. Robinson, *et al.*, Organometallics **5**, 2321 (1986).
23. W. Fischer and E. Koch, Z. Kristallogr. **150**, 245 (1979).
24. R. V. Galiulin, *Crystallographic Geometry* (Nauka, Moscow, 1984).
25. V. N. Panov, K. A. Potekhin, and A. V. Goncharov, Kristallografiya **43**, 389 (1998).
26. V. N. Panov, A. V. Goncharov, and K. A. Potekhin, in *Proceedings of National Crystallographic Conference, Chernogolovka, Russia, 1998*, Part 1, p. 95.
27. Yu. É. Ovchinnikov, K. A. Potekhin, *et al.*, Dokl. Akad. Nauk **340**, 62 (1995).
28. V. Schomaker and K. N. Trueblood, Acta Crystallogr., Sect. B: Struct. Crystallogr. Cryst. Chem. **24**, 63 (1968).
29. T. Maverick and K. N. Trueblood, *THMA-11: Thermal Motion Analysis Program* (Zurich, 1987).
30. T. Maverick and J. D. Dunitz, Mol. Phys. **62**, 451 (1987).
31. I. E. Zanin, M. Yu. Antipin, and Yu. T. Struchkov, in *Problems of Crystal Chemistry* (Nauka, Moscow, 1991), p. 65.
32. I. E. Zanin, *Analysis of Thermal Motion in Molecular Crystals from the X-ray Diffraction Experimental Data*, Candidate's Dissertation in Mathematical Physics (INÉOS, Moscow, 1991).

*Translated by O. Borovik-Romanova*

*Crystallography Reports, Vol. 45, No. 2, 2000, pp. 244–247. Translated from Kristallografiya, Vol. 45, No. 2, 2000, pp. 275–278.*


**STRUCTURES OF ORGANIC COMPOUNDS**

# Crystal and Molecular Structures of 11-Hydroxy-7-Oxodrim-8(9)-ene

**Yu. M. Chumakov*, Yu. A. Simonov*, M. D. Mazus*, D. P. Popa**†, and P. F. Vlad****

** Institute of Applied Physics, Academy of Sciences of Moldova, Academiei 5, Chisinau, 20-28 Moldova*

*** Institute of Chemistry, Academy of Sciences of Moldova, Academiei 3, Chisinau, 20-28 Moldova*

Received November 25, 1997

**Abstract**—The crystal structure of 11-hydroxy-7-oxodrim-8(9)-ene is determined. The crystals are monoclinic. The unit cell parameters are $a$ = 16.716(4) Å, $b$ = 11.052(3) Å, $c$ = 7.542(3) Å, $\gamma$ = 76.11°, $Z$ = 4, $\mu$ = 1.476 cm$^{-1}$, $\rho_{calcd}$ = 1.147 g/cm$^3$, and space group $P2_1$. The structure is solved by the direct method and refined by the least-squares procedure to $R$ = 0.045. There are two molecules of 11-hydroxy-7-oxodrim-8(9)-ene in the asymmetric unit. Both molecules have the same conformation of the skeleton and can be described as rotomers differing in orientation of the OH groups with respect to the skeleton. In both molecules, the cyclohexane rings have a usual chair conformation. In the crystal, two independent molecules are linked by a hydrogen bond. The molecular pairs related by the twofold screw axes are linked by hydrogen bonds into helices running along the $z$-axis of the crystal. The helices are bound through van der Waals interactions. © *2000 MAIK "Nauka/Interperiodica".*

In the course of studies of chemical transformations of 7-oxodrim-8(9)-ene (*1*), a natural compound belonging to an important group of drimanic sesquiterpenoids [1, 2], 11-hydroxy-7-oxodrim-8(9)-ene (*2*) was obtained among other products. Acetate of this compound (*3*) was synthesized earlier according to the multistage procedure in [3]. Owing to its structure, hydroxyketone (*2*) can serve as a starting compound in the synthesis of an important natural drimanic sesquiterpenoid warburganal (*4*), which exhibits strong antifeedant activity. In this paper, we report the results of the X-ray diffraction study of 11-hydroxy-7-oxodrim-8(9)-ene (*2*), which unambiguously confirm its structure and stereochemistry. The structural formulas of drimanic sesquiterpenoids are shown below.

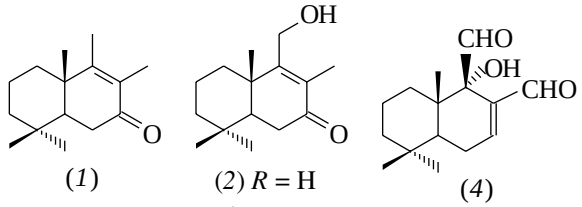


(*1*)




(*2*) $R$ = H
(*3*) $R$ = *Ac*




(*4*)

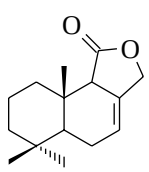


(*5*)

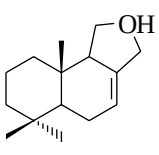


(*6*)

† Deceased.

Monoclinic colorless crystals $C_{15}H_{24}O_2$ are 0.2 × 0.2 × 0.4 mm in size. They are well faceted and have a rectangular habit. The unit cell parameters were refined by the least-squares procedure using 15 reflections in the θ range 12°–20°: $a$ = 16.716(4) Å, $b$ = 11.052(3) Å, $c$ = 7.542(3) Å, $\gamma$ = 76.11°, $Z$ = 4, $\mu$ = 1.476 cm$^{-1}$, $\rho_{calcd}$ = 1.147 g/cm$^3$, and space group $P2_1$. The intensities of 1052 nonzero reflections with $I > 3\sigma$ were measured on a DAR-UMB diffractometer in the range 1.2°–25.7° (Mo$K_\alpha$ radiation, graphite monochromator). The structure was solved by the direct method with the programs described in [4]. The non-hydrogen atoms were refined in the anisotropic approximation by the least-squares procedure with the program package [5] to $R$ = 0.045 [$R_w$ = 0.105 on $F^2$, goodness-of-fit $GOF(F^2)$ = 1.020, and the parameter of absolute configuration $g$ = 0.02(4)]. The highest peak and the lowest cavity are 0.159 and –0.147 e/Å$^3$, respectively. The hydrogen atoms of the hydroxyl groups were located from the difference Fourier syntheses, and the positions of the remaining hydrogen atoms were calculated geometrically and refined within rigid groups. The atomic coordinates are listed in Table 1.

There are two molecules of 11-hydroxy-7-oxodrim-8(9)-ene (*2*) (*a* and *b*) in the asymmetric unit of the crystal (Fig. 1). Both molecules have the same conformation of the skeleton and can be described as rotomers differing in orientation of the OH groups with respect to the C(9) carbon atom (Fig. 1). The cyclohexane rings of both molecules have a usual chair conformation. The C(2) and C(5) atoms in these rings deviate from the

1063-7745/00/4502-0244$20.00 © 2000 MAIK "Nauka/Interperiodica"

plane of the remaining four coplanar atoms C(1)C(3)C(4)C(10) (plane *I*), whose maximum deviations from their mean planes fall in the range 0.002–0.008 Å, by 0.658 and –0.581 Å in molecule *a* and 0.664 and –0.622 Å in molecule *b*. In the molecule of isodrimenin (*5*) [6], whose skeleton is close in structure to those of the compounds discussed, other atoms deviate from the corresponding mean planes: C(1) and C(4) deviate by 0.277 and –0.515 Å, respectively. The C(2)C(3)C(4)C(5) and C(2)C(1)C(10)C(5) torsion angles in the molecules studied are close to the value normal for the chair conformation (56°): they are equal to 52(1)° and –51(1)° in molecule *a* and 52(1)° and –54(1)° in molecule *b*, respectively.

In both molecules, the C(5)C(6)C(7)C(8)C(9)C(10) fragments have distorted chair conformations. The fragments C(6*a*)C(7*a*)C(8*a*)C(9*a*) (**IIa**) and C(6*b*)C(7*b*)C(8*b*)C(9*b*) (**IIb**) are almost planar; the maximum deviations of the atoms from their mean planes calculated by the least-squares method do not exceed 0.016 Å. The C(5) and C(10) atoms deviate from plane **IIa** by –0.640 and 0.062 Å and from plane **IIb** by –0.723 and 0.023 Å, respectively. The deviations of the O(2) oxygen atom and the C(11) and C(12) carbon atoms from the above planes are 0.082, 0.0, and 0.029 Å in *a* and 0.055, –0.073, and –0.034 Å in *b*, respectively. The dihedral angle between planes **IIa** and **IIIa** [C(5*a*)C(9*a*)C(10*a*)] is 29.7° in molecule *a*, and the corresponding angle is equal to 27.8° in molecule *b*. The angles between planes **I**/**II** and **I**/**III** are 35.1° and 54.1° in molecule *a* and 40.4° and 56.6° in molecule *b*, respectively. Note that, in the isodrimenin molecule, unlike the compound described here, the planar fragment includes atoms C(7), C(8), C(9), and C(10), and the C(5) and C(6) atoms deviate from it by 0.515 and 0.277 Å, respectively. Possibly, the difference in configurations of the C(1)C(6)C(7)C(8)C(9)C(10) fragments in this compound and in isodrimenin is responsible for the difference in configurations of the other cyclohexane ring in these molecules.

In the molecules studied, there is a 1,3-diaxial interaction between the C(13) and C(15) carbon atoms of the methyl groups. In molecules *a* and *b*, the C(13)··C(15) distances [3.30(1) and 3.33(1) Å, respectively] are shorter than the van der Waals contact. The corresponding distances in isodrimenin (*5*) and drimenol (*6*) are 3.250(7) and 3.359(6) Å, respectively [6]. It was noted in [7] that, for the distorted chair conformation of the cyclohexane ring, the above C··C contact should be less than 3.359(6) Å.

As noted above, molecules *a* and *b* have the same absolute configuration. They are rotamers differing in orientation of the hydroxyl groups with respect to the molecular skeleton. The O(1)–C(11) bond has a *gauche* configuration relative to the C(8)–C(9) and C(9)–C(10) bonds; the C(8)C(9)C(11)O(1) and C(10)C(9)C(11)O(1) torsion angles are equal to 95(1)° and –84(1)° in molecule *a* and –91(1)° and 92(1)° in molecule *b*, respectively. In molecule *a*, the O(1)–C(11) and C(10)–C(15) bonds are situated on the β side of the molecular skeleton, whereas in molecule *b*, these bonds lie on opposite sides of the skeleton. Bond

Atomic coordinates ($\times 10^4$) and equivalent isotropic parameters ($\times 10^3$)

| Atom | *x* | *y* | *z* | $U_{eq}$, Å$^2$ |
|---|---|---|---|---|
| O(1*a*) | 688(4) | 6606(7) | 3469(10) | 76(2) |
| O(2*a*) | 1034(4) | 8754(6) | 9852(9) | 75(2) |
| C(1*a*) | 2869(5) | 6179(8) | 4492(11) | 54(2) |
| C(2*a*) | 3690(6) | 5388(10) | 4957(14) | 77(3) |
| C(3*a*) | 4109(5) | 5955(9) | 6414(15) | 68(3) |
| C(4*a*) | 3598(5) | 6186(8) | 8122(12) | 53(3) |
| C(5*a*) | 2746(4) | 6922(7) | 7603(11) | 34(2) |
| C(6*a*) | 2170(5) | 7257(7) | 9190(10) | 41(2) |
| C(7*a*) | 1405(5) | 8126(7) | 8706(11) | 36(2) |
| C(8*a*) | 1117(5) | 8176(7) | 6841(12) | 40(2) |
| C(9*a*) | 1519(5) | 7406(7) | 5643(10) | 37(2) |
| C(10*a*) | 2288(4) | 6434(7) | 6063(10) | 35(2) |
| C(11*a*) | 1196(6) | 7472(9) | 3762(11) | 59(3) |
| C(12*a*) | 337(5) | 9072(7) | 6520(13) | 65(3) |
| C(13*a*) | 3593(5) | 4960(8) | 9096(13) | 65(3) |
| C(14*a*) | 4021(5) | 6992(8) | 9342(14) | 73(3) |
| C(15*a*) | 1974(5) | 5236(7) | 6517(12) | 51(2) |
| O(1*b*) | –1542(5) | 5318(8) | –3811(11) | 71(2) |
| O(2*b*) | –820(4) | 7814(6) | 2022(9) | 76(2) |
| C(1*b*) | –2993(5) | 7568(8) | –3415(14) | 63(3) |
| C(2*b*) | –3855(5) | 8344(9) | –3271(18) | 78(3) |
| C(3*b*) | –4124(5) | 8514(9) | –1399(16) | 65(3) |
| C(4*b*) | –3565(6) | 9107(8) | –270(13) | 58(3) |
| C(5*b*) | –2677(4) | 8376(7) | –485(11) | 43(2) |
| C(6*b*) | –2038(6) | 8840(9) | 657(12) | 67(3) |
| C(7*b*) | –1255(6) | 7904(9) | 684(14) | 58(3) |
| C(8*b*) | –1029(5) | 7157(8) | –884(13) | 46(2) |
| C(9*b*) | –1534(5) | 7250(7) | –2269(12) | 41(2) |
| C(10*b*) | –2359(5) | 8154(7) | –2393(11) | 39(2) |
| C(11*b*) | –1271(5) | 6480(8) | –3903(11) | 56(3) |
| C(12*b*) | –226(4) | 6270(7) | –783(11) | 68(3) |
| C(13*b*) | –3801(5) | 9024(10) | 1689(12) | 107(4) |
| C(14*b*) | –3687(6) | 10483(8) | –649(17) | 84(4) |

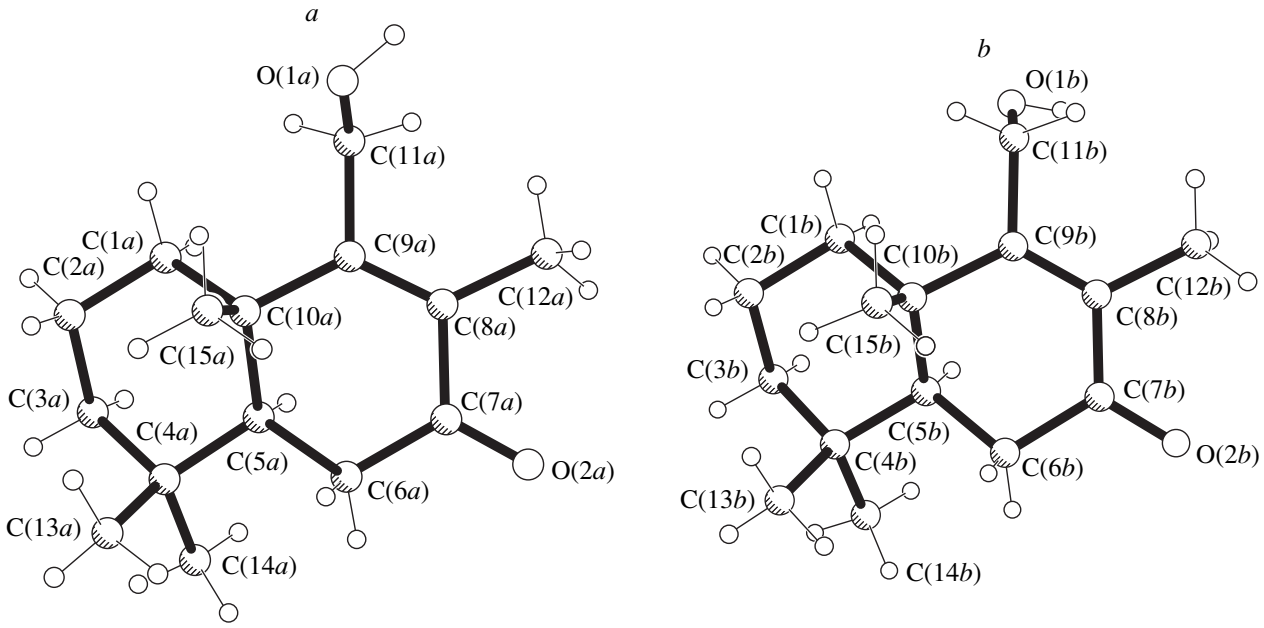


**Fig. 1.** Structures of 11-hydroxy-7-oxodrim-8(9)-ene molecules (*a* and *b*).

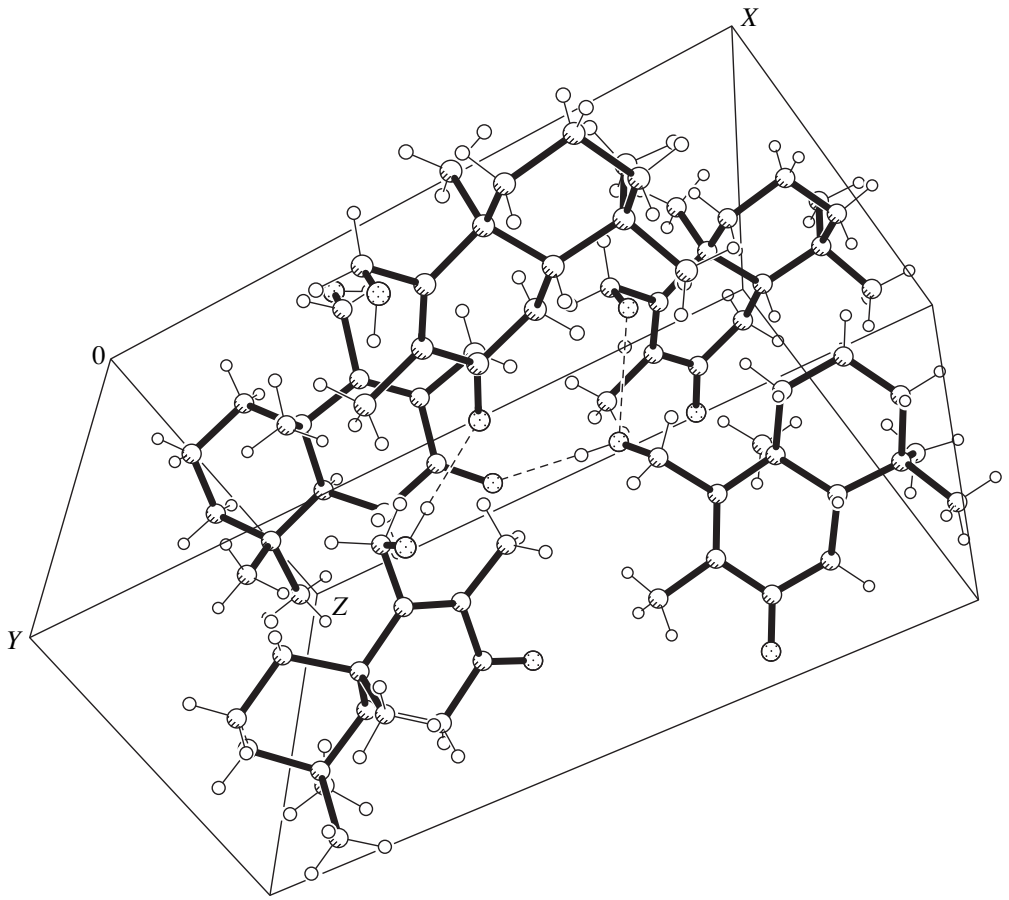


**Fig. 2.** A fragment of the molecular packing in the crystal.

lengths and angles in both molecules are close to the values observed in the related compounds [6, 7].

In the crystal, molecules *a* and *b* are linked by the hydrogen bond O(1*a*)–H(1*a*··O(2*b*) [O(1*a*)··O(2*b*), 2.8(1) Å; H(1*a*)··O(2*b*), 2.0(1) Å; O(1*a*)–H(1*a*), 0.9(1) Å; and angle O(1*a*)–H(1*a*)··O(2*b*), 179(1)°] (Fig. 2). The molecular pairs related by the twofold screw axis (–*x*, –*y* + 1, *z* – 0.5) are linked by the hydrogen bonds O(1*b*)–H(1*b*)··O(1*a*)' [O(1*b*)–H(1*b*), 0.8(1) Å; O(1*b*)··O(1*a*)', 2.9(1) Å; H(1*b*)··O(1*a*)', 2.1(1) Å; and angle O(1*b*)–H(1*b*)··O(1*a*)', 165(4)°] into helices directed along the *z*-axis of the crystal. The helices are linked by van der Waals interactions.

## REFERENCES

1. M. N. Koltsa, G. N. Mironov, S. T. Malinovskiĭ, *et al.*, Izv. Akad. Nauk, Ser. Khim., No. 1, 216 (1996).
2. M. B. J. Jansen and A. de Groot, Nat. Prod. Rep. **8**, 319 (1991).
3. A. J. Aasen, C. H. G. Vogt, and C. R. Enzell, Acta Chem. Scand. B **29**, 51 (1975).
4. G. M. Sheldrick, *SHELXS86: Crystallographic Computing 3: Data Collection, Structure Determination, Proteins, and Databases*, Ed. by G. M. Sheldrick, C. Krüger, and R. Goddard (Oxford Univ. Press, Oxford, 1985), Vol. 3, p. 175.
5. G. M. Sheldrick, *SHELXL93: Program for the Refinement of Crystal Structures* (Univ. of Göttingen, Göttingen, 1993).
6. C. Escobar and O. Wittke, Acta Crystallogr., Sect. C: Cryst. Struct. Commun. **44**, 154 (1988).
7. C. Escobar and O. Wittke, Acta Crystallogr., Sect. C: Cryst. Struct. Commun. **40**, 1461 (1984).

*Translated by I. Polyakova*

*Crystallography Reports, Vol. 45, No. 2, 2000, pp. 248–250. Translated from Kristallografiya, Vol. 45, No. 2, 2000, pp. 279–281.*


## STRUCTURES OF ORGANIC COMPOUNDS

# Crystal Structure of (*Z*)-1-(*sec*-Butyl)-3-(4-Dimethylaminophenyl)-2-(1*H*-1,2,4-Triazol-1-yl)propen-2-one

**S. T. Malinovskiĭ*, M. Z. Krimer*, E. P. Styngach*, and Yu. M. Chumakov****

**Institute of Chemistry, Academy of Sciences of Moldova, Academiei 3, Chisinau, 20-28 Moldova*

***Institute of Applied Physics, Academy of Sciences of Moldova, Academiei 5, Chisinau, 20-28 Moldova*

Received April 8, 1998

**Abstract**—The crystal structure of the title compound is determined by X-ray diffraction studies. The structure is solved by the direct method. The experimental data are obtained on a DAR-UMB diffractometer by the θ–θ/2θ scan technique using Mo$K_\alpha$ radiation. The crystal is monoclinic, $a$ = 17.913(3) Å, $b$ = 17.239(3) Å, $c$ = 5.501(5) Å, γ = 74.4(3)°, space group $P2_1/a$, $Z$ = 4 for $C_{17}H_{22}N_4O$, and $\rho_{calcd}$ = 1.211 g/cm$^3$. The molecule consists of the phenyl and triazole rings and the dimethylamino, carbonyl, and isopropyl groups attached to the rings. The dihedral angle between the rings is 67.4°. The carbonyl oxygen atom and the triazole ring are in the *trans* position relative to each other. The N–C–C–O torsion angle is 172.8°. The molecule is in the *Z* isomeric form. © *2000 MAIK "Nauka/Interperiodica".*

The discovery of a unique property of 1,2,4-triazole derivatives to inhibit the biosynthesis of ergosterins stimulated the intensive search for new active compounds [1]. This resulted in revealing high fungicide activity of a number of 1,3-diaryl-2-(1*H*-1,2,4-triazol-1-yl)propen-2-ones [2]. These compounds are known under the collective name of *N*-vinyltriazoles. They can be obtained by the condensation of aryl(1*H*-1,2,4-triazol-1-ylmethyl) ketones with aromatic aldehydes. Earlier [3], we found that diaryl-*N*-vinyltriazoles are the *Z* isomers.

Continuing our studies of *N*-vinyltriazoles in search for new active compounds, we synthesized a series of alkylaryl-*N*-vinyltriazoles. To determine specific structural features of these compounds, we performed the complete X-ray structural study of one of their representatives, namely, 1-(*sec*-butyl)-3-(4-dimethylaminophenyl)-2-(1*H*-1,2,4-triazol-1-yl)propen-2-one (**I**)

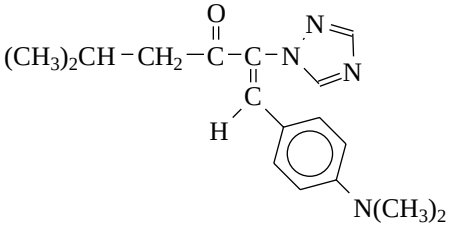


A colorless single crystal with prismatic habit 0.7 × 0.2 × 0.2 mm in size was chosen for the X-ray diffraction study. The crystal is monoclinic. The unit-cell parameters are $a$ = 17.913(3) Å, $b$ = 17.239(3) Å, $c$ = 5.501(5) Å, γ = 74.4(3)°, space group $P2_1/a$, $Z$ = 4 for $C_{17}H_{22}N_4O$, and $\rho_{calcd}$ = 1.211 g/cm$^3$. The experimental data were obtained on a DAR-UMB diffractometer by

Atomic coordinates (×10$^4$) and equivalent thermal parameters (Å$^2$ × 10$^3$)

| Atom | $x$ | $y$ | $z$ | $U_{eq}$ |
|---|---|---|---|---|
| O | 10857(2) | 1974(2) | –285(7) | 74(1) |
| N(1) | 8998(2) | 3143(2) | 1784(6) | 40(1) |
| N(2) | 8847(2) | 3630(2) | 3746(6) | 51(1) |
| N(3) | 7937(2) | 4057(2) | 881(8) | 63(1) |
| N(4) | 7889(2) | 828(2) | 10043(7) | 52(1) |
| C(1) | 9672(2) | 2471(2) | 1676(8) | 45(1) |
| C(2) | 10306(2) | 2555(3) | 57(8) | 55(1) |
| C(3) | 9755(2) | 1830(2) | 3083(8) | 48(1) |
| C(4) | 8205(2) | 4164(3) | 3107(9) | 56(1) |
| C(5) | 8458(2) | 3412(3) | 130(9) | 56(1) |
| C(6) | 9244(2) | 1605(2) | 4818(8) | 44(1) |
| C(7) | 9556(2) | 963(2) | 6391(8) | 51(1) |
| C(8) | 9124(2) | 705(2) | 8083(8) | 51(1) |
| C(9) | 8329(2) | 1079(2) | 8344(7) | 42(1) |
| C(10) | 8006(2) | 1710(2) | 6733(7) | 45(1) |
| C(11) | 8448(2) | 1956(2) | 5049(8) | 46(1) |
| C(12) | 7113(3) | 1323(3) | 10597(8) | 63(1) |
| C(13) | 8232(3) | 179(3) | 11675(9) | 64(1) |
| C(14) | 10237(2) | 3352(3) | –1158(9) | 64(1) |
| C(15) | 10963(3) | 3480(3) | –2210(10) | 70(1) |
| C(16) | 10766(4) | 4199(4) | –3930(14) | 118(2) |
| C(17) | 11522(3) | 3574(4) | –323(13) | 98(2) |

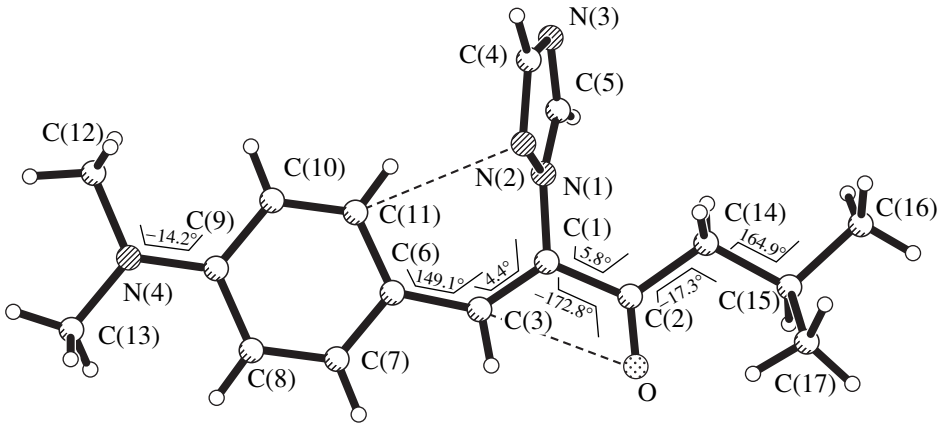


**Fig. 1.** Molecular structure of **I**.

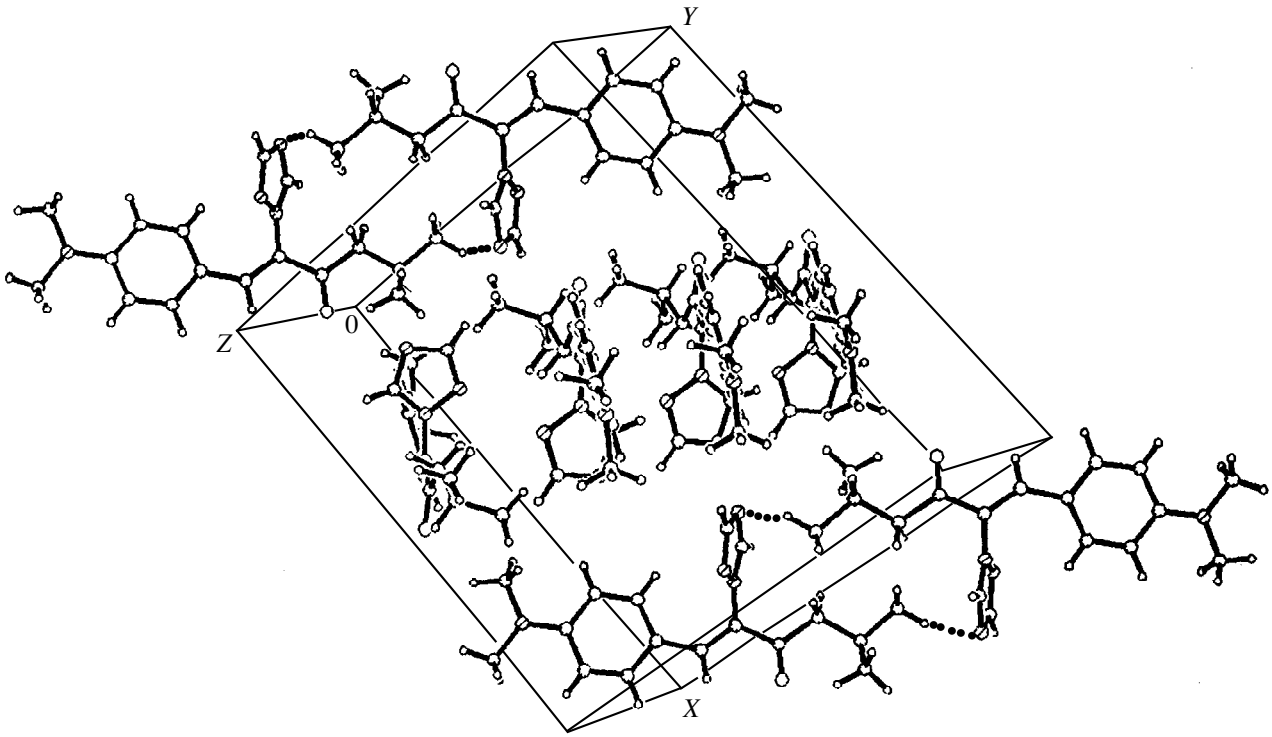


**Fig. 2.** Crystal structure of compound **I**.

the θ–θ/2θ scan technique with Mo$K_\alpha$ radiation. A total of 1474 reflections with $I \geq 3\sigma(I)$ were used for structure determination and refinement.

The structure was solved by the direct method with the SHELXS86 program package [4]. The hydrogen atoms were located from difference Fourier syntheses. The structure was refined by the least-squares procedure to $R = 0.053$. The atomic coordinates and equivalent thermal parameters with their esd's are listed in the table. The molecular structure of **I** is shown in Fig. 1. The molecule consists of the phenyl (*1*) and triazole (*2*) rings and the dimethylamine, carbonyl, and isopropyl groups attached to the rings. The phenyl ring is planar. The deviations of the carbon atoms from the rms plane are within 0.013 Å. The nitrogen atom of the dimethylamine group deviates from this plane by 0.014 Å. The C(3) atom also lies in this plane, and its deviation is 0.012 Å. The triazole ring is planar, and the atomic deviations are within 0.004 Å. Fragments *1* and *2* are in the *cis* position relative to each other and are fixed by the intramolecular contact *N*(2)···C(11) (3.13 Å). The dihedral angle between planes *1* and *2* is 67.4°. Torsion angles C(1)–C(3)–C(6)–C(11) and N(1)–C(1)–C(3)–C(6) are 14.9° and 4.4°, respectively. The carbonyl

oxygen atom is in the *trans* position relative to the triazole ring. The N(1)–C(1)–C(2)–O torsion angle is 172.8°, and 1,4-interaction between the O and C(3) atoms is 2.77 Å. The molecule can be considered as the *Z* isomer. The selected torsion angles that characterize the molecular conformation are represented in Fig. 1.

The interatomic distances and bond angles in the structure correspond to the state of hybridization of atoms and agree well with the data available in the literature on triazole-containing organic molecules [5, 6].

The crystal structure consists of alternating, mutually perpendicular chains, in which pairs of molecules are linked through the center of symmetry (Fig. 2).

The results obtained indicate that the *Z* configuration of the molecules is retained in going from diaryl-*N*-vinyltriazoles to alkylaryl-*N*-vinyltriazoles.

## REFERENCES

1. N. N. Mel'nikov and I. M. Mil'shteĭn, Agrokhimiya, No. 6, 115 (1986).
2. I. M. Mil'shteĭn, Zh. Vses. Khim. O–va im. D.I. Mendeleeva **33**, 687 (1988).
3. S. T. Malinovskiĭ, M. A. Rekhter, E. P. Styngach, *et al.*, Kristallografiya **38**, 134 (1993).
4. G. M. Sheldrick, *SHELXS86* in *Crystallographic Computing 3*, Ed. by G. M. Sheldrick, C. Krüger and R. Goddard (Oxford Univ. Press, Oxford, 1985), pp. 175–189.
5. C. Byrne, J. P. James, and C. Long, J. Chem. Soc., Chem. Commun. 945 (1996).
6. M. Fettonhi, A. Bonklari, and B. El. Otmani, Acta Crystallogr., Sect. C: Crystal Struct. Commun. **52**, 1032 (1996).

*Translated by I. Polyakova*

*Crystallography Reports, Vol. 45, No. 2, 2000, pp. 251–254. Translated from Kristallografiya, Vol. 45, No. 2, 2000, pp. 282–285.*


## STRUCTURES OF ORGANIC COMPOUNDS

# Molecular and Crystal Structures of 2-Amino-5-Benzoyl-4-(2-Nitrophenyl)-3-Cyano-4,5-Dihydrothiophene

**V. N. Nesterov*, L. N. Kuleshova*, A. A. Samet**, and A. M. Shestopalov****

** Nesmeyanov Institute of Organoelement Compounds, Russian Academy of Sciences, ul. Vavilova 28, Moscow, GSP-1, 117813 Russia*

*** Zelinskiĭ Institute of Organic Chemistry, Russian Academy of Sciences, Leninskiĭ pr. 47, Moscow, 117334 Russia*

Received March 16, 1998

**Abstract**—The crystal structure of 2-amino-5-benzoyl-4-(2-nitrophenyl)-3-cyano-4,5-dihydrothiophene is determined by X-ray diffraction analysis. The unit cell parameters are as follows: $a$ = 10.878(2) Å, $b$ = 12.890(3) Å, $c$ = 13.539(4) Å, $\alpha$ = 108.15(2)°, $\beta$ = 99.26(2)°, $\gamma$ = 107.13(2)°, $V$ = 1656(2) Å$^3$, $d_{calcd}$ = 1.410 g/cm$^3$, $Z$ = 4, and space group $P\bar{1}$. The molecules occupy two systems of independent positions in the crystal. Similar to the compounds studied earlier in this series, the *o*-nitrophenyl substituent has a synperiplanar orientation relative to the hydrogen atom at the C(4) atom of the heterocycle. *© 2000 MAIK "Nauka/Interperiodica".*

## INTRODUCTION

Considerable interest in detailed study of the geometric peculiarities in the structure of hydrogenated heterocyclic compounds is explained by the wide variety of their biological activity [1, 2]. These investigations are essential to the revelation of the dependence between the structure of these compounds and their properties [2].

Specifically, in the series of compounds under consideration [3–5], the isomerism can be caused by the presence of the substituent at the carbon atom C(4) with the $sp^3$-hybridization. A bulk radical in the *ortho* position of the substituent prevents its free rotation around the C–C single bond [6].

As a continuation of the systematic investigations on the isomerism in the series of hydrogenated heterocycles [3–5], we studied the crystal structure of 2-amino-5-benzoyl-4-(2-nitrophenyl)-3-cyano-4,5-dihydrothiophene (**I**) by the X-ray diffraction analysis.

## RESULTS AND DISCUSSION

The unit cell of compound **I** contains two symmetrically independent molecules. A general view of one of these molecules (**Ia**) is displayed in Fig. 1. The dihydrothiophene heterocycle in both independent molecules adopts an envelope conformation. The C(5) [C(5')] atom deviates from the mean plane passing through the other four atoms of the cycle [planarity to within ±0.004 Å in **Ia** (±0.007 Å in **Ib**)] by 0.479 Å in **Ia** (–0.486 Å in **Ib**). Hereafter, the values for molecule **Ib** are given in brackets. The substituents at the C(4) and C(5) atoms are in *trans* positions relative to the heterocycle plane. The torsion angles C(6)–C(4)–C(5)–C(12) and H(4)–C(4)–C(5)–H(5) are equal to –144.4° (147.2°) and 93.5° (–99.5°), respectively. The *o*-nitrophenyl substituent has a synperiplanar orientation relative to the H(4) atom. The torsion angles H(4)–C(4)–C(6)–C(7), C(4)–C(6)–C(7)–N(3), and O(1)–N(3)–C(7)–C(6) are equal to –26.2° (27.9°), 0.9° (2.7°), and

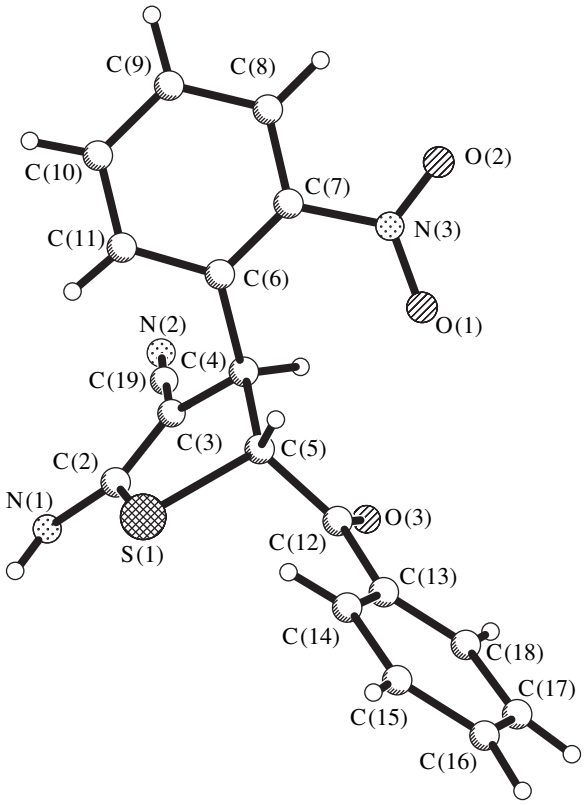


**Fig. 1.** A general view of molecule **Ia**.

1063-7745/00/4502-0251$20.00 © 2000 MAIK "Nauka/Interperiodica"

Atomic coordinates ($\times 10^4$; for H atoms, $\times 10^3$) and isotropic equivalent (isotropic for H atoms) thermal parameters $U$ for compound **I**

| Atom | *x* | *y* | *z* | *U* | Atom | *x* | *y* | *z* | *U* |
|---|---|---|---|---|---|---|---|---|---|
| Molecule **Ia** | | | | | Molecule **Ib** | | | | |
| S(1) | –1311(1) | 12892(1) | 11063(1) | 23(1) | S(1') | 1240(1) | 6978(1) | 3785(1) | 22(1) |
| O(1) | –4073(2) | 11003(2) | 7390(2) | 40(1) | O(1') | 4205(2) | 8866(2) | 7384(2) | 42(1) |
| O(2) | –3780(3) | 10021(2) | 5894(2) | 80(1) | O(2') | 4113(3) | 9949(2) | 8915(2) | 79(1) |
| O(3) | –2980(2) | 13765(2) | 9178(2) | 27(1) | O(3') | 3063(2) | 6111(2) | 5645(2) | 29(1) |
| N(1) | 1114(2) | 14464(2) | 11407(2) | 25(1) | N(1') | –1205(2) | 5488(2) | 3561(2) | 26(1) |
| N(2) | 1327(2) | 14096(2) | 8528(2) | 28(1) | N(2') | –1129(2) | 5982(2) | 6538(2) | 27(1) |
| N(3) | –3503(3) | 10420(2) | 6882(2) | 40(1) | N(3') | 3702(3) | 9488(2) | 7932(2) | 40(1) |
| C(2) | 28(2) | 13644(2) | 10646(2) | 20(1) | C(2') | –47(2) | 6282(2) | 4273(2) | 20(1) |
| C(3) | –244(2) | 13264(2) | 9548(2) | 20(1) | C(3') | 313(2) | 6662(2) | 5370(2) | 21(1) |
| C(4) | –1581(2) | 12286(2) | 8906(2) | 21(1) | C(4') | 1682(2) | 7607(2) | 5959(2) | 21(1) |
| C(5) | –2458(2) | 12308(2) | 9697(2) | 20(1) | C(5') | 2473(2) | 7536(2) | 5110(2) | 21(1) |
| C(6) | –1524(3) | 11065(2) | 8433(2) | 24(1) | C(6') | 1640(2) | 8832(2) | 6448(2) | 23(1) |
| C(7) | –2442(3) | 10188(2) | 7481(2) | 28(1) | C(7') | 2584(3) | 9707(2) | 7393(2) | 28(1) |
| C(8) | –2416(3) | 9070(2) | 7052(3) | 37(1) | C(8') | 2525(3) | 10807(2) | 7855(2) | 34(1) |
| C(9) | –1461(3) | 8793(3) | 7601(3) | 39(1) | C(9') | 1540(3) | 11084(2) | 7350(3) | 36(1) |
| C(10) | –515(3) | 9642(3) | 8535(3) | 37(1) | C(10') | 599(3) | 10252(2) | 6415(3) | 33(1) |
| C(11) | –542(3) | 10766(2) | 8940(2) | 28(1) | C(11') | 635(3) | 9136(2) | 5982(2) | 28(1) |
| C(12) | –3258(2) | 13103(2) | 9649(2) | 22(1) | C(12') | 3210(2) | 6686(2) | 5085(2) | 23(1) |
| C(13) | –4382(2) | 13025(2) | 10153(2) | 22(1) | C(13') | 4094(2) | 6576(2) | 4353(2) | 25(1) |
| C(14) | –4664(3) | 12366(2) | 10789(2) | 30(1) | C(14') | 4627(3) | 7447(3) | 3973(3) | 35(1) |
| C(15) | –5747(3) | 12311(3) | 11209(3) | 36(1) | C(15') | 5484(4) | 7315(3) | 3331(3) | 50(2) |
| C(16) | –6563(3) | 12911(3) | 10997(3) | 35(1) | C(16') | 5815(3) | 6333(3) | 3061(3) | 47(2) |
| C(17) | –6298(3) | 13557(2) | 10360(2) | 33(1) | C(17') | 5277(3) | 5459(3) | 3425(3) | 40(1) |
| C(18) | –5216(3) | 13612(2) | 9939(2) | 26(1) | C(18') | 4419(3) | 5571(2) | 4065(2) | 32(1) |
| C(19) | 637(2) | 13737(2) | 9002(2) | 20(1) | C(19') | –513(2) | 6259(2) | 5981(2) | 20(1) |
| H(1.1) | 117(3) | 1459(2) | 1207(3) | 3(1) | H(1'1) | –180(3) | 508(3) | 379(3) | 4(1) |
| H(1.2) | 169(3) | 1491(2) | 1123(2) | 2(1) | H(1'2) | –133(3) | 537(3) | 287(3) | 4(1) |
| H(4) | –200(2) | 1244(2) | 835(2) | 2(1) | H(4') | 211(3) | 743(2) | 354(2) | 3(1) |
| H(5) | –306(3) | 1156(2) | 954(2) | 2(1) | H(5') | 302(3) | 824(3) | 519(2) | 3(1) |
| H(8) | –309(3) | 849(3) | 636(3) | 3(1) | H(8') | 317(3) | 1132(3) | 847(3) | 4(1) |
| H(9) | –142(3) | 803(3) | 730(2) | 3(1) | H(9') | 149(3) | 1185(3) | 764(3) | 5(1) |
| H(10) | 17(3) | 949(3) | 890(3) | 4(1) | H(10') | –11(3) | 1043(2) | 611(2) | 3(1) |
| H(11) | 13(3) | 1133(2) | 957(2) | 2(1) | H(11') | –2(3) | 860(2) | 538(2) | 3(1) |
| H(14) | –413(3) | 1196(2) | 1097(2) | 2(1) | H(14') | 444(3) | 814(3) | 414(2) | 3(1) |
| H(15) | –595(3) | 1183(3) | 1164(3) | 4(1) | H(15') | 587(3) | 791(3) | 309(3) | 5(1) |
| H(16) | –729(3) | 1293(3) | 1131(3) | 5(1) | H(16') | 643(3) | 624(3) | 266(3) | 4(1) |
| H(17) | –684(3) | 1399(2) | 1026(2) | 3(1) | H(17') | 554(4) | 477(3) | 327(3) | 6(1) |
| H(18) | –506(2) | 1404(2) | 948(2) | 2(1) | H(18') | 407(3) | 495(3) | 435(3) | 4(1) |

–40.1° (34.6°), respectively. This leads to the formation of the short nonbonded contact O(1)··C(4) with a length of 2.783(4) Å [2.759(4) Å]. According to [7, 8], this contact can be considered an intramolecular hydrogen bond of the C–H··O type {C(4)–H(4) 0.92(3) Å [0.98(3) Å], H(4)··O(1) 2.30(3) Å [2.30(3) Å], and angle C(4)–H(4)··O 112(2)° [107(2)°]}. It is worth noting that a similar orientation of the *o*-nitrophenyl substituent relative to the 1,4-dihydropyridine heterocycle with the same contact of atoms was observed in

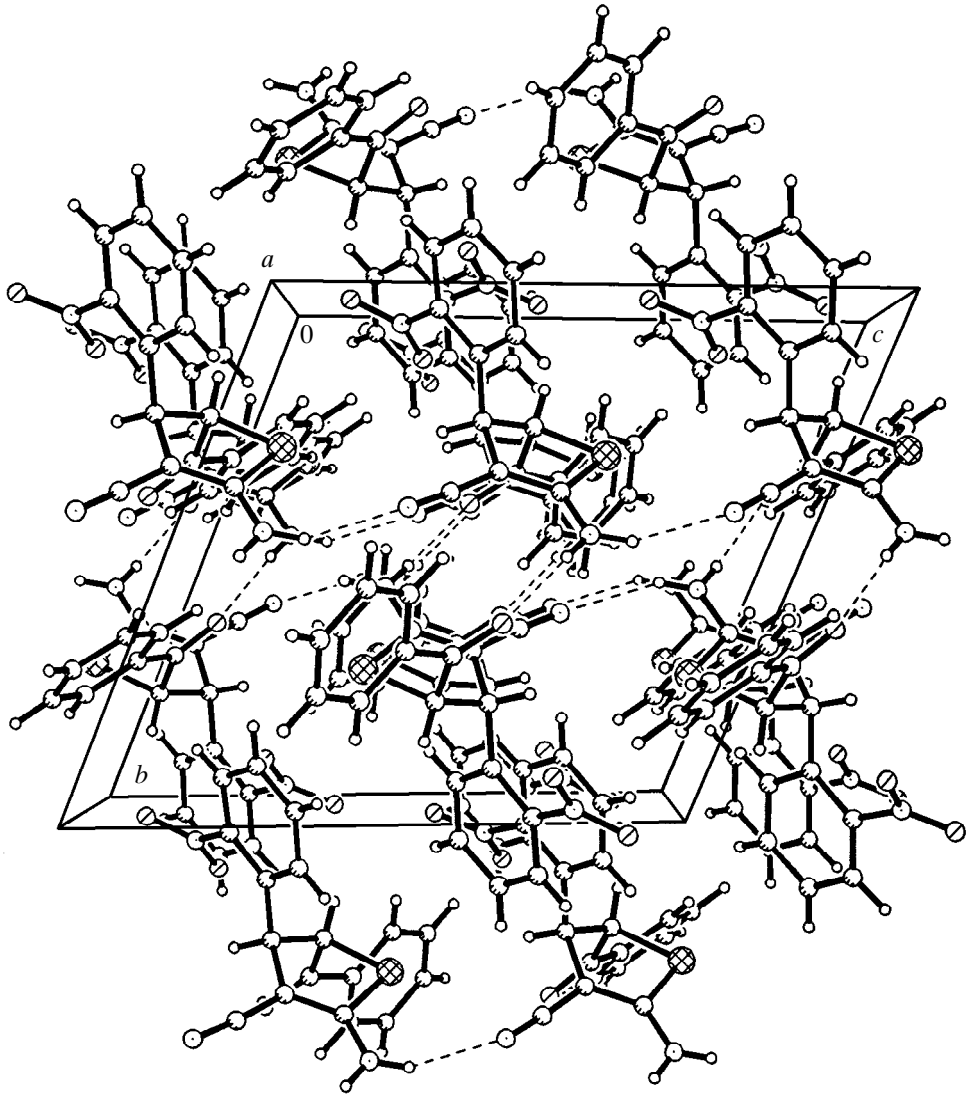


**Fig. 2.** Projection of crystal structure **I** onto the (0*yz*) plane.

the compounds studied in our earlier works [3–5]. It is significant that a similar synperiplanar orientation of the fragment under consideration remains unchanged even in the course of chemical transformations [4]. Therefore, we can believe that the conformations of both independent molecules, as a whole, are identical.

The quantitative evaluation of the geometric differences between the independent molecules **Ia** and **Ib** was performed with the method proposed in [9] for comparison of the geometric characteristics of molecules. The centers of gravity of the molecules were brought into coincidence with each other so that the distances $R_i$ between the corresponding atoms took the minimum values. Then, according to [9], the molecules are considered identical at $S = \left(\sum_{i=1}^{N} w_i R_i^2 / \sum_{i=1}^{N} w_i\right)^{1/2} < 0.1$ Å, similar at $0.1 < S < 0.2$ Å, and different at $S > 0.2$ Å. For the crystal of compound **I**, $S = 0.28$ Å; i.e., molecules **Ia** and **Ib** should be regarded as different. However, as follows from the above discussion, despite the substantial value of the *S* parameter, the independent molecules have a qualitatively identical conformation. The maximum values of $R_i$, which are found for the pairs of atoms C(14)–C(14') (0.42 Å), C(16)–C(16') (0.35 Å), C(17)–C(17') (0.79 Å), and C(18)–C(18') (0.63 Å), are likely due to different rotations of the phenyl ring of the benzoyl substituent toward the mean plane of the heterocycle.

The planar fragment of the heterocycle involves the C(2)=C(3) double bond and the functional groups $NH_2$ and CN. It seems likely that, in this fragment, there is the conjugation giving rise to the appreciable redistribution of the bond lengths as compared to the normal values [10]. Within the limits of experimental error, the remaining bond lengths and angles have the predicted values.

The independent molecules in the crystal are joined into dimers via the intermolecular hydrogen bonds N(1)–H(1.1)···N(2') (–*x*, 2 – *y*, 2 – *z*) [N(1)···N(2') 3.009(4) Å, N(1)–H(1.1) 0.85(2) Å, H(1.1)···N(2') 2.23(2) Å, angle N(1)–H(1.1)···N(2') 152.(2)°], and N(1')–H(1'2)···N(2) (–*x*, 2 – *y*, 1 – *z*) [N(1')···N(2) 3.029(4) Å, N(1')–H(1'2) 0.88(2) Å, H(1'2)···N(2) 2.21(2) Å, angle N(1')–H(1'2)···N(2) 155(2)°]. In turn, these dimers are linked together by the hydrogen bonds N(1)–H(1.2)···O(3) (–*x*, 3 – *y*, 2 – *z*) [N(1)···O(3) 2.979(4) Å, N(1)–H(1.2) 0.83(2) Å, H(1.2)···O(3) 2.16(2) Å, angle N(1)–H(1.2)···O(3) 171(2)°] and N(1')–H(1'1)···O(3') (–*x*, 1 – *y*, 1 – *z*) [N(1')···O(3') 3.020(4) Å, N(1')–H(1'1) 0.88(2) Å, H(1'1)···O(3') 2.15(2) Å, angle N(1')–H(1'1)···O(3') 170(2)°] and form the chains aligned parallel to the *c*-axis (Fig. 2).

## EXPERIMENTAL

Crystals of compound **I** are relatively stable in air; however, over the course of a month, the crystals change their color from gray to green with the subsequent destruction. This is likely due to the conversion observed in [11], during which the substituted 1,4-dihydropyridines containing the *o*-nitrophenyl fragment in the 4-position of the heterocycle transform in the presence of light into the green *o*-nitrososubstituted pyridines with the aromatization of the fragment. It is quite probable that a similar conversion proceeds in the case under investigation.

Crystals **I** ($C_{18}H_{13}N_3O_3S$) are triclinic. The unit cell parameters at –125°C are as follows: $a$ = 10.878(2) Å, $b$ = 12.890(3) Å, $c$ = 13.539(4) Å, $\alpha$ = 108.15(2)°, $\beta$ = 99.26(2)°, $\gamma$ = 107.13(2)°, $V$ = 1656(2) Å$^3$, $d_{calcd}$ = 1.410 g/cm$^3$, $Z$ = 4, and space group $P\bar{1}$. The unit cell parameters and the intensities of 6520 independent reflections were measured on a Siemens P3/PC four-circle automated diffractometer ($\lambda$Mo$K_\alpha$, graphite monochromator, $\theta/2\theta$ scan mode, $\theta_{max}$ = 28°). The structure was solved by the direct method for all the non-hydrogen atoms and refined with the full-matrix least-squares procedure in the anisotropic approximation for the non-hydrogen atoms by using 4236 reflections with $I > 4\sigma(I)$. The hydrogen atoms were independently located from a difference Fourier synthesis and then were refined in the isotropic approximation. The final discrepancy factors are as follows: $R$ = 0.038 and $R_w$ = 0.038. All the calculations were performed using the SHELXTL PLUS program package (PC version) [12]. The atomic coordinates and isotropic equivalent (isotropic for H atoms) thermal parameters are presented in the table.

## ACKNOWLEDGMENTS

This work was supported by the Russian Foundation for Basic Research, project nos. 96-15-97367 and 97-03-33783.

## REFERENCES

1. D. Lednicer and L. A. Mitscher, *The Organic Chemistry of Drug Synthesis* (Wiley, New York, 1980), Vol. 2, p. 283.
2. S. Goldmann and J. Stoltefuss, Angew. Chem., Int. Ed. Engl. **30**, 1559 (1991).
3. V. N. Nesterov, V. E. Shklover, Yu. T. Struchkov, *et al.*, Acta Crystallogr., Sect. C: Cryst. Struct. Commun. **47**, 191 (1991).
4. V. N. Nesterov, L. A. Rodinovskaya, A. M. Shestopalov, *et al.*, Khim. Geterotsikl. Soedin., No. 5, 643 (1997).
5. A. V. Samet, A. M. Shestopalov, V. N. Nesterov, *et al.*, Synthesis, No. 6, 623 (1997).
6. V. M. Potapov, *Stereochemistry* (Khimiya, Moscow, 1988).
7. L. Berkovitch-Yellin and L. Leiserowitz, Acta Crystallogr., Sect. B: Struct. Sci. **40**, 159 (1984).
8. G. R. Desiraju, Acc. Chem. Res. **24**, 290 (1991).
9. T. N. Kukina and P. M. Zorkiĭ, Vestn. Mosk. Univ., Ser. 2: Khim. **22**, 248 (1981).
10. F. H. Allen, O. Kennard, D. G. Watson, *et al.*, J. Chem. Soc., Perkin Trans. 2, S1 (1987).
11. R. Alajarin, J. J. Vaquero, J. Álvarez-Builla, *et al.*, J. Med. Chem. **38**, 2830 (1995).
12. W. Robinson and G. M. Sheldrick, *Crystallographic Computing—Techniques and New Technologies* (Oxford Univ. Press, Oxford, 1988), p. 366.

*Translated by N. Korovin*

*Crystallography Reports, Vol. 45, No. 2, 2000, pp. 255–257. Translated from Kristallografiya, Vol. 45, No. 2, 2000, pp. 286–288.*




# Molecular and Crystal Structures of 8,9-Dimethoxy-5',5'-Dimethyl-1,2,3,5,6,10*b*-Hexahydropyrrolo[2,1-*a*]isoquinoline-1-Spiro-2'-Cyclohexane-3,1',3'-Trione

**A. S. Lyakhov*, D. O. Ivashkevich*, A. A. Govorova**, and A. L. Mikhal'chuk****

** Research Institute of Physicochemical Problems, Belarussian State University, ul. Leningradskaya 14, Minsk, 220080 Belarus*

*** Institute of Bioorganic Chemistry, Belarussian Academy of Sciences, ul. Zhodinskaya 5/2, Minsk, 220141 Belarus*

Received March 18, 1998; in final form, June 16, 1998

**Abstract**—The crystal and molecular structures of 8,9-dimethoxy-5',5'-dimethyl-1,2,3,5,6,10*b*-hexahydropyrrolo[2,1-*a*]isoquinoline-1-spiro-2'-cyclohexane-3,1',3'-trione are studied by X-ray diffraction. The unit cell parameters are $a = 9.478(2)$ Å, $b = 9.844(3)$ Å, $c = 11.663(3)$ Å, $\alpha = 111.17(2)°$, $\beta = 99.56(2)°$, $\gamma = 105.82(2)°$, $Z = 2$, and space group $P1$. The structure is solved by the direct method and refined to $R = 0.0411$ [$I > 4\sigma(I)$]. Conformational and geometric characteristics of the compound studied and the molecular packing in the crystal are discussed. © *2000 MAIK "Nauka/Interperiodica".*

## INTRODUCTION

The tricyclic pyrrolo[2,1-*a*]isoquinoline skeleton is a key structural fragment in a large number of condensed azines, among them erythrine alkaloids exhibiting antidepressing activity [1, 2]. The 1-spiro-2-cyclohexane derivatives of pyrrolo[2,1-*a*]isoquinolines, which have been described recently [3], are of theoretical interest as biologically active compounds and models in studies of mutual intramolecular effects and structure–function correlations. In this connection, direct data on the molecular and crystal structure of the compounds of this series are of importance. In this work, we studied one of its representatives, namely, 8,9-dimethoxy-5',5'-dimethyl-1,2,3,5,6,10*b*-hexahydropyrrolo[2,1-*a*]isoquinoline-1-spiro-2'-cyclohexane-3,1',3'-trione (DSCT)

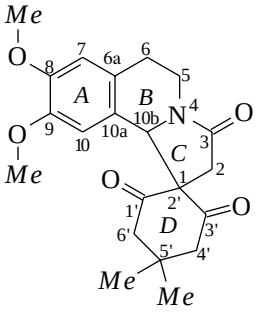


## EXPERIMENTAL

The DSCT compound was obtained according to an improved procedure of the intramolecular cyclization of *N*-acyltetrahydroisoquinolinyl[1:2']cyclohexane-1',3'-dione [4]. Detailed description of the synthesis will be published elsewhere. Single crystals for the X-ray diffraction study were obtained by crystallization of a chromatographically homogeneous sample from an acetone–ether mixture.

A three-dimensional set of X-ray diffraction data was collected on a Nicolet *R*3*m* automated four-circle diffractometer (Mo$K_\alpha$ radiation, graphite monochromator, $\theta/2\theta$ scan mode, $2\theta_{max} = 60°$). The structure was solved by the direct method. The non-hydrogen atoms were refined in the anisotropic approximation by the full-matrix least-squares procedure. The hydrogen atoms were located from a difference Fourier synthesis and refined in the isotropic approximation. All the calculations were performed with the SHELX97 program package [5–7]. The crystallographic data and parameters of structure refinement are summarized in Table 1. The atomic coordinates and equivalent thermal parameters are listed in Table 2.

## RESULTS AND DISCUSSION

A molecule of DSCT is shown in the figure. Our calculations revealed the following specific features of ring conformations in this polycyclic molecule. Benzene ring *A* is planar, and the mean atomic deviation from its plane is 0.0188 Å. The C(8) and C(9) atoms of the ring have substituents—the methoxy groups. One of them, namely, $H_3C(11)O(8)$, is situated in the plane of ring *A* [the C(11) atom deviates from this plane by only 0.033(2) Å]. The carbon atom of the other methoxy group $H_3C(12)O(9)$ deviates from the plane of the ring by 0.274(3) Å. Ring *B* has the shape of a distorted half-boat; that is, the N(4) atom and the C(5) atom deviate unidirectionally from the planar fragment of the

**Table 1.** Crystallographic data and refinement parameters for the DSCT structure

| | |
|---|---|
| Empirical formula | $C_{21}H_{25}NO_5$ |
| Molecular weight | 371.42 |
| Temperature | 293(2) K |
| Crystal system | Triclinic |
| Space group | $P\bar{1}$ |
| Unit cell parameters: | $a$ = 9.478(2) Å , α = 111.17(2)° |
| | $b$ = 9.844(3) Å , β = 99.56(2)° |
| | $c$ = 11.663(3) Å , γ = 105.82(2)° |
| $V$ | 932.9(4) Å$^3$ |
| $Z$, $d$ | 2, 1.322 g/cm$^3$ |
| μ | 0.94 cm$^{-1}$ |
| $F$(000) | 396 |
| Crystal size | 0.55 × 0.5 × 0.15 mm |
| Number of reflections: | |
| collected/unique | 5719/5456 [$R_{(int)}$ = 0.0199] |
| Refinement technique | Full-matrix least-squares procedure on $F^2$ |
| *GooF* | 1.043 |
| $R$ [$I > 4\sigma(I)$] | $R1$ = 0.0411, $wR2$ = 0.1093 |
| $R$ (all data) | $R1$ = 0.0583, $wR2$ = 0.1228 |

**Table 2.** Atomic coordinates (×10$^4$) and equivalent isotropic thermal parameters (Å$^2$ × 10$^3$) in the DSCT structure

| Atom | $x/a$ | $y/b$ | $z/c$ | $U_{eq}$ |
|---|---|---|---|---|
| C(1) | 2227(1) | 3860(1) | 1222(1) | 31(1) |
| C(2) | 2943(2) | 3006(2) | 243(1) | 42(1) |
| C(3) | 4647(1) | 3868(2) | 859(1) | 39(1) |
| N(4) | 4859(1) | 5322(1) | 1716(1) | 35(1) |
| C(5) | 6291(1) | 6353(2) | 2728(1) | 41(1) |
| C(6) | 6038(2) | 6462(2) | 4005(1) | 42(1) |
| C(6*a*) | 4744(1) | 7062(1) | 4186(1) | 32(1) |
| C(7) | 4784(1) | 8070(1) | 5411(1) | 35(1) |
| C(8) | 3727(1) | 8795(1) | 5578(1) | 33(1) |
| C(9) | 2614(1) | 8557(1) | 4490(1) | 32(1) |
| C(10) | 2549(1) | 7541(1) | 3280(1) | 30(1) |
| C(10*a*) | 3584(1) | 6750(1) | 3123(1) | 29(1) |
| C(10*b*) | 3433(1) | 5609(1) | 1788(1) | 29(1) |
| C(11) | 4850(2) | 10091(2) | 7855(1) | 49(1) |
| C(12) | 660(2) | 9299(2) | 3617(2) | 60(1) |
| C(1') | 596(1) | 3700(1) | 596(1) | 33(1) |
| C(3') | 2248(1) | 3303(1) | 2296(1) | 38(1) |
| C(4') | 1206(2) | 3627(2) | 3113(1) | 41(1) |
| C(5') | −454(1) | 3149(1) | 2309(1) | 38(1) |
| C(6') | −438(1) | 3989(2) | 1427(1) | 37(1) |
| C(7') | −1152(2) | 1378(2) | 1501(2) | 55(1) |
| C(8') | −1400(2) | 3657(2) | 3213(2) | 53(1) |
| O(3) | 5664(1) | 3364(1) | 630(1) | 57(1) |
| O(8) | 3697(1) | 9795(1) | 6739(1) | 44(1) |
| O(9) | 1665(1) | 9390(1) | 4716(1) | 46(1) |
| O(1') | 171(1) | 3319(1) | −551(1) | 51(1) |
| O(3') | 3082(1) | 2609(2) | 2447(1) | 68(1) |

ring, which passes through the C(6), C(6*a*), C(10*a*), and C(10*b*) atoms (the mean deviation of the latter atoms from their rms plane is 0.0338 Å). The deviation of the N(4) atom from the planar fragment of the ring is significantly smaller than the deviation of the C(5) atom [0.260(2) and 0.864(3) Å, respectively]. Ring *C* has the C(1)-envelope conformation; the mean deviation of the C(2), C(3), N(4), and C(10*b*) atoms, which form the planar fragment of the ring, from their rms plane is 0.0005 Å, and the C(1)-corner is bent from the planar fragment by 35.48(9)°. Ring *D* has a conformation of the C(1),C(5')-chair whose planar part is formed by the C(1'), C(3'), C(4'), and C(6') atoms (the mean deviation of these atoms from their rms plane is 0.0066 Å). The C(1)- and C(5')-corners are bent aside from the planar fragment of the ring by 30.93(9)° and 49.47(9)°, respectively; that is, the chair is far from the ideal shape, which is explained by the effect of substituents in the ring. The dihedral angles (φ) between the planar fragments of the rings have the following values: $\varphi_{AB}$ = 6.8(1)°, $\varphi_{BC}$ = 39.58(7)°, and $\varphi_{CD}$ = 71.30(5)°.

The bond lengths and angles in the part of the molecule, which involves the system of condensed rings (*A*, *B*, and *C*), agree well with the corresponding values in the molecules containing a similar fragment [8]. Note that the sum of bond angles about the N(4) atom is 357.82°; that is, this atom exhibits a planar, not pyramidal, bond configuration, which is attributable to the effect of the C(3)=O(3) carbonyl group. This effect is also indicated by the shortening of the N(4)–C(3) bond [1.353(2) Å] with respect to the N(4)–C(5) and N(4)–C(10*b*) bonds [1.455(2) and 1.464(1) Å]. The bond lengths and angles in the spiro ring *D* are normal [8].

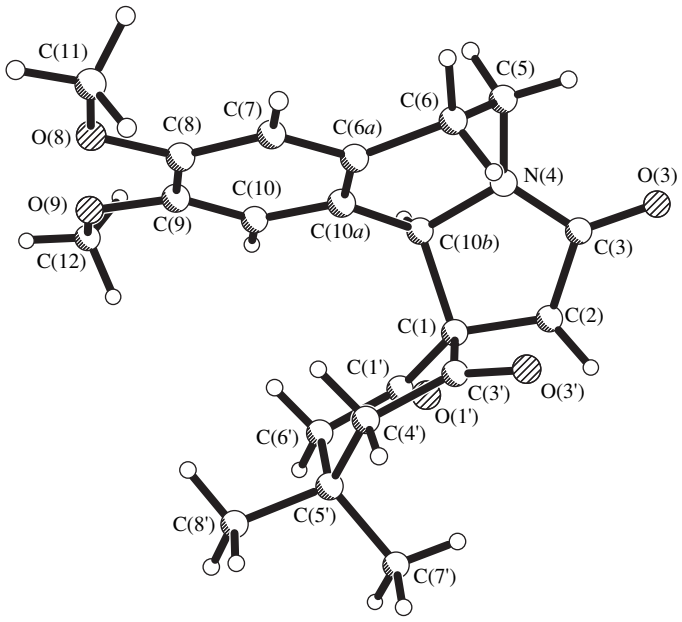


Molecular structure of DSCT in the crystal.

No short intermolecular contacts are observed in the structure, and the molecular packing is determined only by van der Waals interactions.

## ACKNOWLEDGMENTS

We acknowledge the support of the Russian Foundation for Basic Research (project no. 96-07-89187) in the payment of the licence for using the Cambridge Structural Database, which was employed in the analysis of the results obtained in this work.

## REFERENCES

1. A. G. Mikhaĭlovskiĭ and V. S. Shklyaev, Khim. Geterotsikl. Soedin., No. 3, 291 (1997).
2. B. E. Maryanoff, D. F. McComsey, J. F. Gardocki, *et al.*, J. Med. Chem. **30**, 1433 (1987).
3. A. A. Akhrem and Yu. G. Chernov, Dokl. Akad. Nauk SSSR, **301**, 354 (1988).
4. A. A. Akhrem, E. V. Borisov, and Yu. G. Chernov, Zh. Org. Khim. **26**, 1114 (1990).
5. G. M. Sheldrick, *Program for the Solution and Refinement of Crystal Structures* (Univ. of Göttingen, Göttingen, 1997).
6. G. M. Sheldrick, Acta Crystallogr., Sect. A: Found. Crystallogr. **46**, 467 (1990).
7. G. M. Sheldrick, Z. Dauter, K. S. Wilson, *et al.*, Acta Crystallogr., Sect. D: Biol. Crystallogr. **49**, 18 (1993).
8. F. H. Allen and O. Kennard, Chem. Des. Autom. News **8**, 31 (1993).

*Translated by I. Polyakova*

*Crystallography Reports, Vol. 45, No. 2, 2000, pp. 258–260. Translated from Kristallografiya, Vol. 45, No. 2, 2000, pp. 289–291.*


**STRUCTURES OF ORGANIC COMPOUNDS**

# Crystal and Molecular Structure of 11,12-Dihydroxydrim-8(9)-en-7-one

**V. Kh. Kravtsov*, E. K. Gorinchnoĭ**, G. N. Mironov**, M. N. Koltsa**, Yu. A. Simonov*, and P. F. Vlad****

**Institute of Applied Physics, Academy of Sciences of Moldova, Academiei 5, Chisinau, 20-28 Moldova*

***Institute of Chemistry, Academy of Sciences of Moldova, Academiei 3, Chisinau, 20-28 Moldova*

Received May 27, 1998; in final form, August 24, 1998

**Abstract**—The crystal structure of 11,12-dihydroxydrim-8(9)-en-7-one was determined by X-ray diffraction. The unit cell parameters are $a = 7.534(3)$, $b = 12.192(5)$, $c = 8.067(4)$ Å, $\beta = 98.01(3)$ Å, space group $P2_1$, and $Z = 2$ for $C_{15}H_{24}O_3$. The structure was solved by direct methods and refined in the anisotropic approximation to $R = 0.051$ and $R_w = 0.113$. The intramolecular O–H···O hydrogen bond [2.892(6) Å] between the hydroxy groups closes an additional seven-membered H-ring in the molecule. In the crystal, the intermolecular O–H···O hydrogen bond [2.857(4) Å] between the hydroxyl group and the carbonyl oxygen atom links the molecules related by the translation along the *c*-axis to form infinite chains. © *2000 MAIK "Nauka/Interperiodica".*

## INTRODUCTION

In the course of studies of chemical transformations of natural sesquiterpenoid drim-8(9)-en-7-one (**I**), its dibromo derivative (**II**) was obtained [1]. This compound is of specific interest, since substitution of acetoxy groups for the allyl bromine atoms should result in 11,12-diacetoxydrim-8(9)-en-7-one (**III**) [2], which is known to be an intermediate in the synthesis of the highly efficient natural antifeedant warburganal (**IV**) [2, 3].

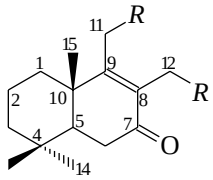


*R* = H (**I**), Br (**II**), O*Ac* (**III**), or OH (**V**)

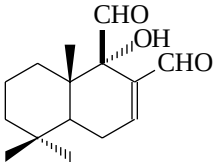


**IV**

The optically active compound **III** was described as a crystalline substance with $T_m$ = 87–88°C [3]. We obtained diacetoxy ketone **III** by nucleophilic substitution in dibromo ketone **II**. It appeared to be a liquid substance, whose spectral characteristics coincide with the literature data. All our attempts to crystallize it failed. However, the product of alkaline saponification of **III**—11,12-dihydroxydrim-8(9)-en-7-one (**V**)—is a crystalline substance. Taking into account the above contradiction and knowing that the process of nucleophilic substitution can be accompanied by molecular rearrangements, we decided to verify the structure of **V**. For this purpose, it was studied by X-ray diffraction.

## EXPERIMENTAL

Single crystals of **V** were obtained by recrystallization of the substance under study at room temperature from a solution in carbon tetrachloride. Colorless prismatic crystals are monoclinic, space group $P2_1$. A specimen, 0.20 × 0.25 × 0.35 mm in size [$\mu(MoK_\alpha)$ = 0.78 $cm^{-1}$], was chosen for the X-ray study. The experiment was performed on an oblique-type diffractometer DAR-UMB at room temperature ($MoK_\alpha$ radiation, graphite monochromator). The unit cell parameters were refined using 15 reflections measured in the 9.6°–18.2° θ-angle range to $a = 7.534(3)$, $b = 12.192(5)$, $c = 8.067(4)$ Å, and $\beta = 98.01(3)°$; $V = 733.8(6)$ $Å^3$, $d_{calcd}$ = 1.142 $g/cm^3$, and $Z = 2$ for $C_{15}H_{24}O_3$. The experimental data were obtained by the ω–θ/2θ scan technique in the range of θ angles from 2.55° to 25.1°. A total of 1066 reflections with $I \geq 2\sigma(I)$ was collected; 1000 of them are unique, $R_{int} = 0.016$.

The structure was solved by direct methods with the SHELXS86 program [4]. An *E* synthesis revealed all non-hydrogen atoms. Their positional and anisotropic thermal parameters were refined by a full-matrix least-squares procedure with the SHELXL93 program [5]. All hydrogen atoms were located in a difference synthesis calculated at this stage. Before further least-squares refinement of the structure, the geometry of the $CH_3$ and OH groups was idealized based on the orientations of the H atoms found from a difference Fourier synthesis. The remaining hydrogen atoms were assigned calculated ideal positions; in the refinement, they were rigidly bound to the corresponding carbon

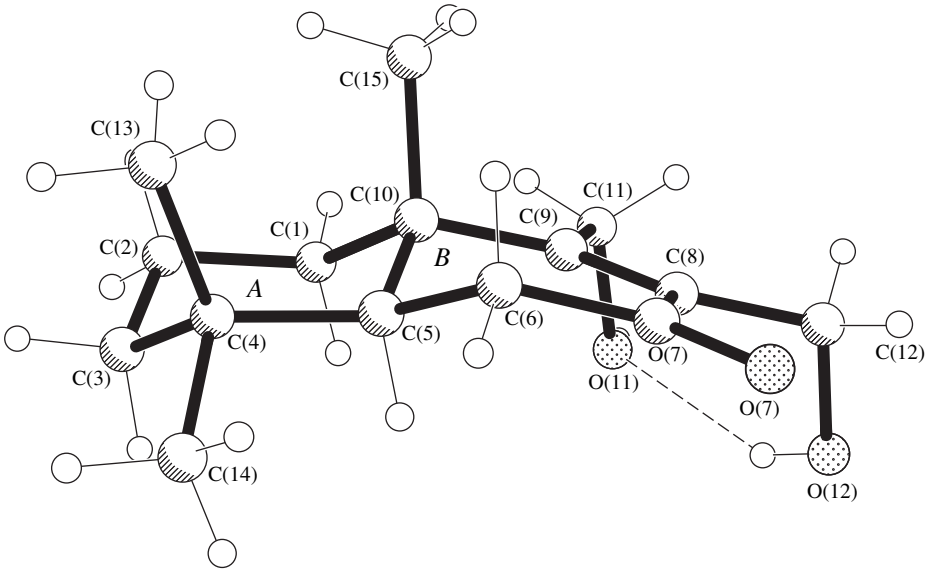


Molecular structure of 11,12-dihydroxydrim-8(9)-en-7-one.

atoms. The isotropic thermal parameters of the hydrogen atoms in the $CH_3$ and OH groups were assigned the values 1.5 times larger than the equivalent isotropic thermal parameters $U_{eq}$ of the non-hydrogen atoms to which they were attached. For the remaining hydrogen atoms, $U_{iso}$ was taken equal to $1.2U_{eq}$ of the corresponding atom. The final discrepancy factors and $R = 0.051$ and $R_w = 0.113$ and $S = 1.14$. The minimum and maximum residual peaks of the zero synthesis were –0.190 and 0.136 e Å$^{-3}$, respectively. The atomic coordinates and equivalent isotropic thermal parameters are listed in the table.

## RESULTS AND DISCUSSION

The molecular structure of **V** and the atomic numbering are shown in the figure. The X-ray analysis proved unambiguously that the structure of the crystalline product studied agrees with that in scheme **V**. As in other similar structures [1, 2], the cyclohexane fragment *A* in **V** has a chair conformation (figure). The C(1), C(2), C(4), and C(5) atoms of this fragment are coplanar within ±0.018 Å, and the C(3) and C(10) atoms are, respectively, 0.618 and –0.649 Å out of this plane. The methyl groups C(13), C(14), and C(15) deviate from this plane by –1.343, 0.954, and –2.181 Å, respectively. A short contact between two axial methyl groups is observed: the C(13)···C(15) distance is 3.354 Å. In the cyclohexane fragment, the mean C–C and C–*Me* bond lengths are 1.557 and 1.549 Å, the mean endocyclic angle is 112.3°, and the exocyclic angles at the C(4) and C(10) atoms are 104.8°–114.5°. Some spread in bond angles is due to the above-mentioned steric factors in the skeleton of the molecule. The values of the torsion angles in the cyclohexane fragment *A* also indicate a slight twisting of the cycle: starting from the C(1)–C(2) bond, –55.0(7)°, 56.1(7)°, –49.8(6)°, 49.4(5)°, –52.1(5)°, and 51.2(6)°.

Ring *B* has a half-chair conformation: the C(6), C(7), C(8), C(9), and C(10) atoms are coplanar within the limits from –0.019 to 0.016 Å, and the C(5) atom deviates from the plane through these atoms by –0.618 Å. The C(11), C(12), and O(7) atoms, which are bound to ring *B*, actually lie in the above plane; their

Atomic coordinates ($\times 10^4$) and equivalent thermal parameters ($\times 10^3$)

| Atom | *x* | *y* | *z* | $U_{eq}$, Å$^2$ |
|---|---|---|---|---|
| C(1) | 4341(7) | 195(5) | 1394(6) | 68(2) |
| C(2) | 5958(8) | –506(6) | 2114(8) | 86(2) |
| C(3) | 6855(7) | –104(5) | 3842(8) | 74(2) |
| C(4) | 5605(6) | –20(4) | 5222(7) | 47(1) |
| C(5) | 3925(5) | 632(4) | 4436(5) | 35(1) |
| C(6) | 2580(6) | 815(4) | 5676(5) | 42(1) |
| C(7) | 1218(5) | 1657(4) | 5019(5) | 35(1) |
| O(7) | 518(5) | 2238(3) | 6014(3) | 58(1) |
| C(8) | 695(5) | 1747(4) | 3140(5) | 35(1) |
| C(9) | 1497(5) | 1100(3) | 2042(5) | 34(1) |
| C(10) | 2940(6) | 268(3) | 2646(5) | 38(1) |
| C(11) | 852(7) | 1206(4) | 125(6) | 55(1) |
| O(11) | 1517(6) | 2218(3) | –438(4) | 75(1) |
| C(12) | –722(6) | 2587(4) | 2538(6) | 50(1) |
| O(12) | –21(5) | 3566(3) | 1946(5) | 71(1) |
| C(13) | 5199(7) | –1158(4) | 5892(7) | 63(2) |
| C(14) | 6606(7) | 623(5) | 6759(7) | 73(2) |
| C(15) | 1940(7) | –837(4) | 2645(7) | 62(2) |

deviations do not exceed 0.092 Å. The hydroxy groups appear on the same side of ring *B*, and their position is fixed by the intramolecular hydrogen bond O(12)–H···O(11) [O···O, 2.892(6) Å; H···O, 2.16 Å; and angle O–H···O, 148°], which closes an additional seven-membered H-ring. Note that in the molecule of 11,12-dibromodrim-8(9)-en-7-one [1], whose structure is the closest to that of **V**, the corresponding bromine atoms are situated on either side of the mean plane of ring *B*.

The bond lengths in ring *B* are, on the whole, consistent with corresponding distances in related compounds [1, 6] and other compounds with similar molecular skeletons [7–9] (structural parameters for some of the compounds cited were obtained from the Cambridge Structural Database [10]). The C(7)–O(7), C(11)–O(11), and C(12)–O(12) distances are 1.242(5), 1.429(6), and 1.414(6) Å, respectively. The double bond C(8)=C(9) observed in the ring [1.385(6) Å] is the longest among the corresponding bonds in the structurally similar compounds cited, in which the lengths range between 1.309 and 1.353 Å. This bond lengthening apparently indicates the larger degree of its conjugation and may be related to the formation of the additional fused hydrogen-containing pseudo-ring.

In the crystal, the O(11)–H···O(7) intermolecular hydrogen bond links the molecules related by the translation along the *c*-axis into infinite chains [O···O, 2.857(4) Å; H···O, 2.04 Å; and angle O–H···O, 174°]. These chains are connected only by van der Waals interactions.

ACKNOWLEDGMENTS

We are grateful to Dr. M.D. Mazus for his experimental help.

This work was supported in part by INTAS, project no. 96-1109.

REFERENCES

1. M. N. Koltsa, G. N. Mironov, S. T. Malinovskiĭ, *et al.*, Izv. Ros. Akad. Nauk, Ser. Khim., No. 1, 216 (1996).
2. T. Nakata, H. Akita, T. Naito, *et al.*, J. Am. Chem. Soc. **101**, 4400 (1979).
3. J. A. Hueso-Rodríguez and B. Rodríguez, Tetrahedron **45**, 1567 (1989).
4. G. M. Sheldrick, *SHELXS86: Program for the Solution of Crystal Structures* (Univ. of Göttingen, Göttingen, 1986).
5. G. M. Sheldrick, *SHELXL93: Program for the Refinement of Crystal Structures* (Univ. of Göttingen, Göttingen, 1993).
6. T. G. Dekker, T. G. Fourie, E. Matthee, *et al.*, S. Afr. J. Chem. **41**, 33 (1988).
7. S. D. Jolad, J. J. Hoffmann, K. H. Schram, *et al.*, J. Org. Chem. **47**, 1356 (1982).
8. D. Ávila, J. D. Medina, and A. J. Deeming, J. Nat. Prod. **55**, 845 (1992).
9. A.-A. Sánchez, B. Esquivel, A. Pera, *et al.*, Phytochemistry **26**, 479 (1987).
10. F. H. Allen and O. Kennard, Chem. Des. Autom. News **8**, 131 (1993).

*Translated by I. Polyakova*

*Crystallography Reports, Vol. 45, No. 2, 2000, pp. 261–263. Translated from Kristallografiya, Vol. 45, No. 2, 2000, pp. 292–294.*




# X-ray Mapping in Heterocyclic Design: III. Diffractometric Study of the Crystal Structure of 1-Methyl-2-Oxo-2,3-Dihydroimidazo[1,2-*a*]pyridinium Bromide

**V. B. Rybakov, S. G. Zhukov, E. V. Babaev, O. S. Mazina, and L. A. Aslanov**

*Chemistry Department, Moscow State University, Vorob'evy gory, GSP-3, Moscow, 119899 Russia*

Received May 13, 1999

**Abstract**—The crystal structure of 1-methyl-2-oxo-2,3-dihydroimidazo[1,2-*a*]pyridinium bromide $C_8H_9BrN_2O$ is determined by X-ray diffraction. The structure is solved by the direct method and refined by the least-squares procedure to $R = 0.0599$. The geometry of the pyridinium fragment observed in the molecule corresponds to the limited number of centers at which the positive charge can be delocalized. Apparently, this delocalization predominantly occurs in the NCN fragment of the imidazole ring and only slightly affects the pyridine moiety of the molecule. © *2000 MAIK "Nauka/Interperiodica".*

Earlier [1, 2], we performed structural studies characterizing the transformation of pyridine **I** into imidazopyridine **II**. This work continues our investigations into the structure of the compounds obtained by consecutive transformations of compounds **I** and **II**. Formally, compound **II** is the hydrochloride of instable free base **III**. Compound **III**, which readily enters into the reactions with electrophilic chemical agents, can be prepared by a reaction between sodium methylate and salt **II** [3]. The object of the present work was compound **IV** (a homolog of salt **II**), which was obtained by the reaction between salt **II** and the base followed by the methylation (without isolation of intermediate compound **III**):

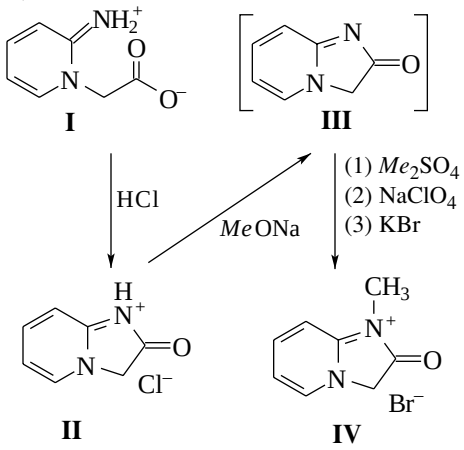


We determined the crystal structure of salt **IV** by X-ray diffraction analysis. Up to now, according to the data of the Cambridge Structural Database [4], the X-ray structure analysis of this compound has not been performed.

## EXPERIMENTAL

Salt **IV** was initially isolated as the perchlorate according to the procedure described in [3]; however, we failed to prepare the satisfactory crystals of the isolated perchlorate and transformed the compound into the bromide salt. For this purpose, an aqueous solution of the perchlorate was treated by a saturated KBr solution. The precipitate of potassium perchlorate was filtered off, and the aqueous solution of bromide **IV** was evaporated to dryness. The dry residue was recrystallized from a 1 : 1 isopropanol–water solution and used for the X-ray diffraction analysis. Transparent colorless crystals of bromide **IV** have a platelike habit.

Crystals of bromide **IV**, $C_8H_9BrN_2O$, are monoclinic. The unit cell parameters were determined and refined on a CAD4 automated diffractometer using 25 reflections in the θ range 11°–13° [5] (λMo$K_\alpha$, graphite monochromator). The crystal data are $a$ = 7.806(1) Å, $b$ = 6.404(1) Å, $c$ = 8.812(1) Å, β = 97.44(2)°, $V$ = 436.8(1) Å$^3$, $d_{calcd}$ = 1.742 g/cm$^3$, μ(λMo) = 4.656 mm$^{-1}$, $Z$ = 2, and space group $P2_1/m$. A set of 934 unique reflections with $I \geq 2\sigma(I)$ was collected in the range $\theta \leq 26°$ on the same diffractometer by the ω-scan technique. The processing of the diffraction data measured was performed with the WinGX96 program package [6]. The structure was solved by the direct method and refined in the anisotropic approximation by the least-squares procedure using the SHELX97 program package [7]. All the hydrogen atoms were located from the difference synthesis of electron density and included in the refinement in the isotropic approximation. The final discrepancy factors are $R1$ = 0.0599 and $wR2$ = 0.1374. The atomic coordinates and thermal parameters are listed in the table. The residual electron density lies between $\Delta\rho_{max}$ = 1.304 and $\Delta\rho_{min}$

Atomic coordinates ($\times 10^4$) and equivalent (isotropic) thermal parameters $U_{eq}/U_{iso}$ ($Å^2 \times 10^3$)

| Atom | *x* | *y* | *z* | $U_{eq}/U_{iso}$ |
|---|---|---|---|---|
| Br | 4404(1) | 7500 | 7737(1) | 42(1) |
| C(1) | 2386(4) | 2500 | 8644(4) | 35(1) |
| C(2) | 741(4) | 2500 | 9354(3) | 36(1) |
| O(2) | 578(3) | 2500 | 10698(3) | 53(1) |
| N(3) | −612(3) | 2500 | 8179(3) | 31(1) |
| C(3) | –2432(4) | 2500 | 8381(4) | 45(1) |
| C(4) | –12(4) | 2500 | 6777(3) | 23(1) |
| C(5) | −913(4) | 2500 | 5322(4) | 31(1) |
| C(6) | 52(5) | 2500 | 4116(4) | 33(1) |
| C(7) | 1835(5) | 2500 | 4360(4) | 35(1) |
| C(8) | 2690(4) | 2500 | 5811(4) | 31(1) |
| N(9) | 1725(3) | 2500 | 7007(3) | 26(1) |
| H(11) | 3050(24) | 1310(36) | 8835(22) | 20(5) |
| H(31) | –2694(46) | 2500 | 9425(46) | 53(12) |
| H(32) | –2983(35) | 1197(49) | 7881(34) | 69(9) |
| H(5) | –2147(41) | 2500 | 5161(38) | 33(9) |
| H(6) | −667(47) | 2500 | 3032(49) | 69(15) |
| H(7) | 2640(51) | 2500 | 3670(50) | 65(13) |
| H(8) | 3737(36) | 2500 | 6017(34) | 17(8) |

= –1.265 e/Å$^3$. Cation **IV** shown in the figure was drawn with the PLUTON96 program [8].

## RESULTS AND DISCUSSION

The bromide anion serves as a counterion in salt **IV**. The heterocyclic cation occupies a special position in the mirror plane. In the crystals of compound **IV** (in distinction to **II**), hydrogen bonds are absent.

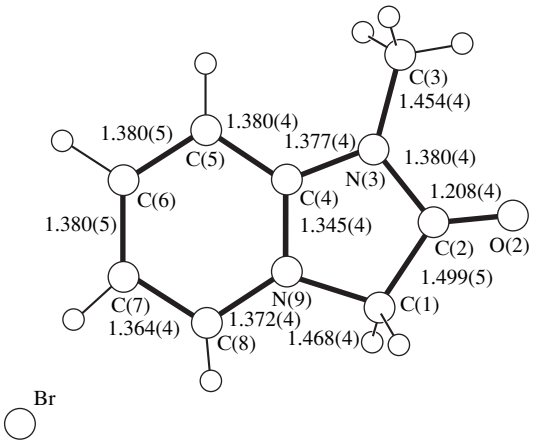


Structure of the heterocyclic cation **IV**.

A comparison of the geometries of the NH derivative **II** and the homologous $NCH_3$ derivative **IV** reveals that introduction of the methyl group results only in a slight lengthening of the C(4)–N(3) bond in compound **IV** as compared to **II**. The lengths of all the other skeleton bonds in **II** and **IV** are virtually identical. This result supports our conclusion [2] that compound **II** actually exists in the NH tautomeric form, since its structure and geometry coincide with those of the $NCH_3$ derivative **IV**.

Cations **II** and **IV** can be represented by three resonance structures—*A*, *B*, and *C* (*R* = H or $CH_3$)

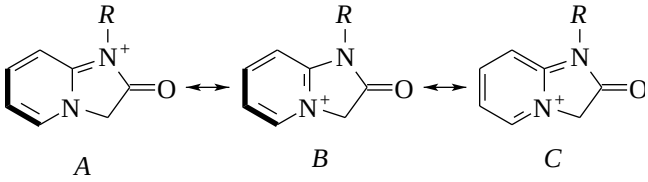


Consider the C(6)C(7)C(8) fragment (distinguished by heavy lines in structures *A* and *B*). In **II** and **IV**, the mean C(6)–C(7) bond length is 1.381(4) Å, whereas the length of the adjacent C(7)–C(8) bond is 1.362(4) Å. These bond lengths in the C(6)C(7)C(8) fragment are consistent with resonance structures *A* and *B*, but contradict structure *C*, which implies the reverse ratio of the bond lengths: the C(6)–C(7) bond should be shorter than the C(7)–C(8) bond. Of the two structures *A* and *B*, the latter structure is preferential for **IV**, since, bearing the positive charge, the nitrogen atom of the pyridine fragment should attract the bromide anion; that is, the N(9)··Br distance should be shorter than the N(3)··Br distance, which is the case in crystal structure **IV** [3.833(1) and 5.112(2) Å, respectively]. In structure **II** [2], the chloride anion approaches the N(3) atom rather than the N(9) atom [the shortest distances, other than hydrogen bonds, are N(3)··Cl = 3.045(2) Å and N(9)··Cl = 5.025(2) Å], indicating that structure *A* is preferential for **II**. A partial fixation of the geometry of the pyridine fragment results in a limited number of centers at which the positive charge can be delocalized. Apparently, this delocalization predominantly occurs in the N(9)C(4)N(3) fragment of the imidazole ring and only slightly affects the pyridine ring.

## ACKNOWLEDGMENTS

This work was supported by the Russian Foundation for Basic Research, project no. 99-03-33076a. We also acknowledge the support of this Foundation in the payment of the licence for using the Cambridge Structural Database, project no. 99-07-90133.

## REFERENCES


1. V. B. Rybakov, S. G. Zhukov, E. V. Babaev, *et al.*, Kristallografiya **44**, 1067 (1999) [Crystallogr. Rep. **44**, 997 (1999)].
2. V. B. Rybakov, S. G. Zhukov, E. V. Babaev, *et al.*, Kristallografiya **45**, 108 (2000) [Crystallogr. Rep. **45**, 103 (2000)].
3. E. D. Sych and L. T. Gorb, Ukr. Khim. Zh., No. 9, 961 (1996).
4. F. H. Allen and O. Kennard, Chem. Des. Autom. News **8**, 31 (1993).
5. *Enraf–Nonius. CAD4 Software: Version 5.0* (Enraf–Nonius, Delft, 1989).
6. L. J. Farrugia, *WinGX96: An Integrated System of Publicly Available Windows Programs for the Solution, Refinement, and Analysis of Single Crystal X-ray Diffraction Data* (Univ. of Glasgow, Glasgow, 1996).
7. G. M. Sheldrick, *SHELX97: Programs for the Solution and Refinement of Crystal Structures* (Univ. of Göttingen, Göttingen, 1997).
8. A. L. Spek, *PLUTON96: Molecular Graphics Program* (Univ. of Utrecht, Utrecht, 1996).


*Translated by I. Polyakova*

*Crystallography Reports, Vol. 45, No. 2, 2000, pp. 264–269. Translated from Kristallografiya, Vol. 45, No. 2, 2000, pp. 295–300.*


**LATTICE DYNAMICS**

# Dislocations (Solitons) in Anharmonic Crystals

**A. K. Emaletdinov**

*Ufa Institute of Service Technologies,*
*ul. Chernyshevskogo 145, Ufa, Bashkortostan, 450014 Russia*

Received November 16, 1998

**Abstract**—Static dislocations (solitons) in an anharmonic lattice are studied within the framework of the Frenkel–Kontorova model. The dislocation-induced fields corresponding to the displacement vector and the stress tensor are calculated, and their properties are analyzed. The process of soliton nucleation is discussed in terms of the kinetics of the excited phonon subsystem of a loaded crystal. The expressions describing the nucleation time and the force and the energy conditions of a dislocation (soliton) nucleation are derived. © *2000 MAIK "Nauka/Interperiodica".*

The collective excitations of the type of $2\pi$ solitons play an important role in various physical phenomena occurring such as conductivity of quasi-one-dimensional crystals, domain-wall dynamics in magnetic materials, the Josephson effect, the Frenkel–Kontorova dislocations, etc. [1, 2]. Static dislocations (solitons) induce strain and stress fields in a crystal lattice, which, in turn, determine the mechanical, electric, magnetic, and optical properties of real crystals [3]. Because of these deformations, dislocations possess an elastic energy and create internal stresses in the crystals. The expressions for the vector **u** of elastic displacements induced by static solitons [a screw and an edge dislocation with the vector $\mathbf{u}(u, 0, 0)$] in a harmonic lattice obtained by solving the sin-Gordon equation [4–8] have the characteristic form of the stationary $2\pi$ solitons $u = b\arctan(\exp(-x/2\pi b))/2\pi$, where $b$ is the Burgers vector. The elastic stress tensor $\sigma_{ij}$ for dislocations (solitons) in a harmonic lattice has the form characteristic of the long-range interaction [4–8] and is given by the expression $\sigma_{ij} = \mu b/2\pi|\mathbf{r}|$, where $|\mathbf{r}| = \sqrt{x^2 + y^2}$, **r** is the radius-vector of the dislocation axis, and $\mu$ is the shear modulus. Such stresses give rise to "nonphysical" singularities in the intrinsic elastic energy of the dislocations $E_D = \mu b^2 R\ln(R/b)/4\pi$, where $R$ is the crystal size. In the crystal with the average dislocation density $\rho_D$ there are internal stresses $\sigma_i$ with the dispersion $D\sigma_i^2 = \rho_D\mu^2 b^2\ln(R/l)/4\pi$ [9] and the average stress level $\bar{\sigma}_i = \sqrt{D\sigma_i^2} \approx 0.5\rho_D^{1/2}\mu b$. These stresses impose certain limitations on the maximum dislocation density $\rho_m$ namely, in the crystal prior to its destruction: $\rho_m \le (2\sigma_C/\mu b)^2 \approx 10^{12}$ cm$^{-2}$, where $\sigma_C$ is the destruction stress. Recently, new crystalline materials were synthesized, whose lattices possess the pronounced anharmonicity. Among such materials are strongly anharmonic crystals [10], submicron crystalline particles [11], and polycrystals formed by nanoparticles [12, 13]. It is clear that the elastic properties of dislocations in such crystals should vary, which should be seen from their micro- and macroplastic deformation determined by the kinetics of dislocation interactions and nucleation. The dynamics of homogeneous dislocation (soliton) nucleation in anharmonic crystals is one of the mechanisms of the microplastic deformation. It was studied by the methods based on the measurements of the absolute reaction rates [3, 7, 8]. It is important to consider this process in terms of the kinetics of an excited phonon system of a loaded crystal.

We had the aim to study the elastic fields of static dislocations (solitons) in an anharmonic crystal and to analyze the nucleation of dislocations as a result of the relaxation of the excited phonon subsystem of a deformed crystal.

Consider the Frenkel–Kontorova model [3, 7] of an anharmonic crystal consisting of two interacting sublattices with the same lattice period $b$ but with different number of atomic planes (an edge dislocation). The nonlinear equation for elastic displacements $u$ of atoms from their equilibrium positions, which takes into account the quadratic and the cubic terms in the potential of atomic interactions in an anharmonic lattice, $V(u)$, has the form of a modified sin-Gordon–Boussinesq equation have for variables $x = 2\pi x/b$ and $u = 2\pi u/b$ [1, 2].

$$u_{tt} - c_1^2 u_{xx} = \varepsilon c_1^2 u_x u_{xx} + \varepsilon c_1^2 \delta^2 u_{xxxx} + V_0\sin(u), \quad (1)$$

where $c_1$ is the elastic wave velocity, $\varepsilon = 2\alpha_0 b$, $\delta^2 = b^2/12$; $\varepsilon$ and $\alpha$ are the anharmonicity parameters, and the subscripts indicate the corresponding derivatives with respect to spatial variables and time. The static solutions corresponding to the $2\pi$ solitons (disloca-

tions) satisfy the specific boundary conditions: $0 \bmod(b)$ ($x \longrightarrow \pm\infty$).

The soliton solutions are obtained by the direct method based on the Hirota operators and the asymptotic expansions, which, in some instances, yield the exact solutions [1, 2]. We seek for the solution in the form $u = 4\arctan(f(x)/g(x))$, where the unknown functions $f$ and $g$ are represented as the expansions in the small parameter $\varepsilon \ll 1$,

$$f = \varepsilon f^{(1)} + \varepsilon^3 f^{(2)} + \ldots, \quad g = 1 + \varepsilon^2 g^{(1)} + \varepsilon^4 g^{(2)} + \ldots.$$

Substituting these expansions into (1) and using the Hirota operators

$$D_x^m D_t^n (ab) = \left\{\left(\frac{\partial}{\partial x} - \frac{\partial}{\partial x'}\right)^m \left(\frac{\partial}{\partial t} - \frac{\partial}{\partial t'}\right)^n [a(x,t)b(x',t')]\right\}_{\substack{x'=x \\ t'=t}}, \quad (2)$$

we arrive at the equations for functions $f$ and $g$. Equating the coefficients before the terms including $\varepsilon$ raised to the same powers, we obtain a chain of equations for functions $f^{(1)}$, $f^{(2)}$, …; $g^{(1)}$, $g^{(2)}$, … . The straightforward, although cumbersome, calculations lead to the following solution

$$u = \frac{2b}{\pi}\left\{-\frac{\pi}{4} + \arctan\left[\exp\left(\left(-\frac{2\pi x}{b}\right)\right.\right.\right. \times \left.\left.\left.(1 + \varepsilon 2x\exp(-2\pi x/b)/b(1 + 1/\sqrt{2}))\right]\right\}. \quad (3)$$

It is seen that at $\varepsilon = 0$, (3) reduces to the classical solution to the sin-Gordon equation [1–3]. Expression (3) shows that at $x < \varepsilon^{-1}b$, the solution corresponding to the linear theory of elasticity describes quite well the elastic fields induced by the dislocations ($2\pi$ solitons). In the asymptotic range $x > \varepsilon^{-1}b$, the displacements decay exponentially decrease.

To find intrinsic stresses of the stationary soliton (dislocation) in an anharmonic lattice, one has to write the stress function in the form [3]

$$\psi = \frac{\mu}{2\pi(1-\nu)}\int_{-\infty}^{\infty} dx'\left(-\frac{du}{dx}\right)_{x=x'} \times y\ln[(x-x')^2 + y^2]^{1/2}. \quad (4)$$

Substituting (3) into (4) and using the relation between the stress tensor and the stress function [7], we can determine the stress components corresponding, e.g., to an edge dislocation

$$\sigma_{xx} = -\frac{\mu b}{\pi^2(1-\nu)}\frac{\partial^2}{\partial y^2} \times \int_{-\infty}^{\infty}\left(-2\frac{d}{dx}\left\{-\frac{\pi}{4} \arctan\left[\exp\left(\left(-\frac{2\pi x}{b}\right)\right.\right.\right.\right. \times \left.\left.\left.\left.(1 + \varepsilon 2x\exp(-2\pi x/b)/b(1 + 1/\sqrt{2}))\right]\right\}\right)\Bigg|_{x=x'} \times y\ln[(x-x')^2 + y^2]^{1/2}dx',$$

$$\sigma_{xy} = \frac{\mu b}{\pi^2(1-\nu)}\frac{\partial^2}{\partial x \partial y} \times \int_{-\infty}^{\infty}\left(-2\frac{d}{dx}\left\{-\frac{\pi}{4} \arctan\left[\exp\left(\left(-\frac{2\pi x}{b}\right)\right.\right.\right.\right. \times \left.\left.\left.\left.(1 + \varepsilon 2x\exp(-2\pi x/b)/b(1 + 1/\sqrt{2}))\right]\right\}\right)\Bigg|_{x=x'} \times y\ln[(x-x')^2 + y^2]^{1/2}dx', \quad (5)$$

$$\sigma_{xz} = \frac{\mu b}{\pi^2(1-\nu)}\frac{\partial^2}{\partial x^2} \times \int_{-\infty}^{\infty}\left(-2\frac{d}{dx}\left\{-\frac{\pi}{4} \arctan\left[\exp\left(\left(-\frac{2\pi x}{b}\right)\right.\right.\right.\right. \times \left.\left.\left.\left.(1 + \varepsilon 2x\exp(-2\pi x/b)/b(1 + 1/\sqrt{2}))\right]\right\}\right)\Bigg|_{x=x'} \times y\ln[(x-x')^2 + y^2]^{1/2}dx'.$$

The general expressions for stress tensor $\sigma_{ij}$ are rather complicated. In the limiting cases, $x \ll \varepsilon^{-1}b$, they are described by conventional solutions [7]. In the asymptotic limit, $x \gg \varepsilon^{-1}b$, we have

$$\sigma_{xy}(x, 0) \cong \mu\exp(-2\pi x/b)/2\pi(1-\nu) \quad (x \gg \varepsilon^{-1}b) \quad (6)$$

and the stresses exponentially decrease. The numerical solution to equation (1) is illustrated in figure. The size of the asymptotic region is estimated as $R \approx \varepsilon^{-1}b \approx (10^3$–$10^4)b \approx 10^{-5}$–$10^{-6}$ m. Thus, at large distances, the fields of intrinsic stresses due to dislocations in an anharmonic crystal are screened. This eliminates the nonphysical singularities in the estimates of the energy and the averaged stresses. The solutions obtained are confirmed by both the numerical modeling and the consis-

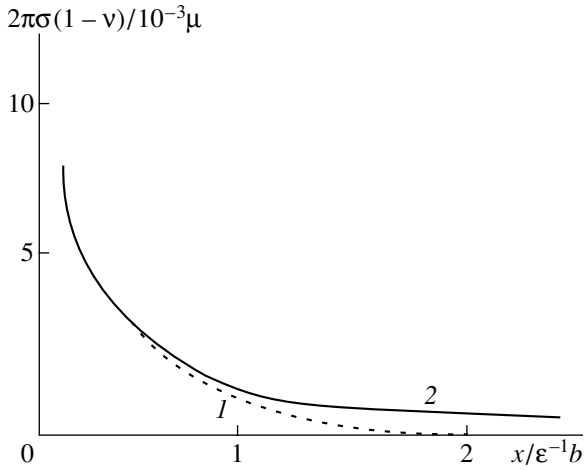


Dislocation-induced dimensionless stresses versus dimensionless distance: (*1*) in anharmonic crystal; (*2*) in a harmonic lattice

tency with the solutions obtained within the framework of the gauge theory of dislocations [14].

Now, consider the dispersion of internal stresses in a strongly anharmonic crystal. Solving equation (6) for the stresses in the asymptotic range $x > \varepsilon^{-1}b$, we determine dispersion the first approximation, as

$$D\sigma_{ia}^2 \approx \rho_D(\mu^2 b^2/4\pi)\exp(-4\pi\varepsilon). \quad (7)$$

For the mean stress level, we have

$$\bar{\sigma}_i = \sqrt{D\sigma_i^2} \approx 0.5\rho_D^{1/2}\mu b\exp(-2\pi\varepsilon). \quad (8)$$

In other words, the mean stress level in a strongly anharmonic crystal is less by a factor of $\exp(-2\pi\varepsilon)$ than that in a harmonic lattice. The maximum dislocation density in a strongly anharmonic crystal prior to its destruction is estimated as

$$\rho_m \le (2\sigma_C/\mu b)^2\exp(4\pi\varepsilon). \quad (9)$$

It is seen that the density has increased by a factor of $\exp(4\pi\varepsilon)$. In particular, the maximum dislocation density in nanocrystals can attain the values as high as $10^{-13}$ cm$^{-2}$, which is consistent with the data reported in [13]. Moreover, the stress fields and the energy characteristics of the dislocation pileups and the conditions of their formation are also modified with the formation of microcracks and other defects [3, 7].

In the framework of the synergetic approach [15, 16], the homogeneous formation of dislocations (solitons) in an anharmonic lattice is one of the factors promoting the formation of the dissipative structure of a nonequilibrium phonon system in the crystal. Consider a primitive lattice in order to reduce the number if indices. We shall study the nucleation process in the adiabatic approximation [15]. The unstable modes are confined to the narrow range of wavevectors $b_{ni}$, that is, only one or several $\Omega$ modes become unstable. A loaded crystal can be represented as a set of oscillators $\omega_{\mathbf{k}j}$ interacting with the critical mode. Now, consider a crystal with the primitive cubic lattice subjected to a uniform elastic deformation $\varepsilon_{ij}$. The atomic displacements in the strained crystal can be written in the form [10, 17]

$$u_i(l,\chi) = \sum \varepsilon_{ij}x_j(l,\chi) + d_i(l,\chi) + \xi_i(l,\chi), \quad (10)$$

where $x_j(l,\chi)$ is the coordinate of the equilibrium position of an atom, $\chi$, in the $l$th cell, $d_i(l,\chi)$ is the nonuniform strain caused by the nucleated defect, $\xi_i(l,\chi)$ are the thermal displacements of atoms in the vicinity of new equilibrium positions. The tensor $\varepsilon_{ij}$ is symmetric. The equilibrium atomic positions in the strained crystal are determined by the condition of the minimum potential energy [10, 17]

$$\left.\frac{\partial U}{\partial \xi_i}\right|_{\xi=0} = \sum Q_{ij}^{ll'}[\varepsilon_{jm}x_m(l,\chi) + d_j(l,\chi)] = 0, \quad (11)$$

whence

$$d_j(l,\chi) = \sum \varepsilon_{sm}G_{ji}^{ll'(0)}Q_{is}^{ll'}x_m(l,\chi), \quad (12)$$

where $G_{ji}^{ll'(0)}$ is the static Green function of the lattice in the harmonic approximation, which coincides up to a factor of –1 with the inverse matrix of the harmonic force constants [10]. We limit our consideration to the linear approximation with respect to strains. In what follows, the Greek subscripts $\alpha$, $\delta$, $\gamma$, and $\rho$ denote various phonon states determined by the wavevector $\mathbf{k}$ and polarization $j$, namely: $\alpha = (\mathbf{k}_1, j_1)$, $\delta = (\mathbf{k}_2, j_2)$, $\bar{\alpha} = (-\mathbf{k}_1, j_1)$.

Now express the Hamiltonian in terms of the normal coordinates:

$$H = H_0 + H_C + H_V + H_D, \quad (13)$$

where $H_0$ is the harmonic Hamiltonian of lattice phonons and $H_C$ is the Hamiltonian of the critical mode. It is convenient to express the latter Hamiltonian in terms of occupancies, choosing as the basis a set of eigenfunctions of a three-dimensional harmonic oscillator. $H_V$ is the Hamiltonian describing the interaction of the critical mode with the phonon system, $H_D$ is the Hamiltonian for the uniform strain in the crystal, which gives rise to the quasiequilibrium displacement of the distribution function. Now, write the Hamiltonians in terms of occupancies [17]:

$$H_0 = \sum_\alpha h\omega_\alpha a_\alpha^+ a_\alpha, \quad H_C = \sum_{ni} hE_{ni}b_{ni}^+ b_{ni}, \quad (14)$$

$$H_V = \frac{1}{N^{1/2}}\sum_{\alpha mn} h\omega_\alpha \beta_\alpha(mj, ni) b_m^+ b_n (a_\alpha^+ + a_\alpha) + \frac{1}{N}\sum_{\alpha\gamma} h\omega_\alpha \zeta_{\alpha\lambda}(mj, ni) b_{ni}^+ b_{mj} a_\alpha a_\gamma, \quad (15)$$

where

$$\beta_\alpha(mj, ni) = \frac{1}{h\omega_\alpha}\sum_{lk,\,\gamma\rho\delta} Q_{\gamma\rho\delta}(l\chi) \times \left(\left(\frac{h}{2M\omega_\alpha}\right)^{1/2} B_\gamma^\alpha(l\chi)\langle ni|u_\gamma u_\rho|mj\rangle\right),$$

$$\zeta_{\alpha\gamma}(mj, ni) = \frac{1}{h\omega_\alpha}\sum_{\substack{lk,\,l'k' \\ \delta\nu\rho}} Q_{\delta\nu\rho}(lk, l'k') \times \frac{h}{2\sqrt{M_k M_{k'}\omega_\alpha\omega_\gamma}} B_\delta^\alpha(lk) B_\nu^\gamma(l'k')\langle ni|u_i|mj\rangle. \quad (16)$$

Here, $B_\gamma^\alpha(l\chi)$ is the normal coordinate, $a_\alpha^+$, $a_\alpha$, $b_{ni}^+$, and $b_{ni}$ are the creation and annihilation operators for phonons and the critical mode, respectively, $Q_{\gamma\rho\delta}(l\chi)$ are the third-order force constants, $E_{ni} = h\Omega + \Delta E_{ni} \approx h\Omega$ ($\Delta E_{ni}$ is the contribution from the diagonal [with respect to $|ni\rangle$] part of the fourth-order anharmonic interaction). In the continuum approximation, the Hamiltonian of the interaction with the uniform strain can be written as [18]

$$H_D = \int \frac{d^3k}{(2\pi)^3}\sum_{\alpha\gamma} V_{\alpha\gamma}^k (a_\alpha + a_\alpha^+)(a_\gamma^+ + a_\gamma)\exp(i\Omega t), \quad (17)$$

where $V_{\alpha\gamma}^k = A_{ij}^{\alpha\gamma}\varepsilon_{ij}^k$, $A_{ij}^{\alpha\gamma} \approx 1/4\Lambda(\omega_\alpha\omega_\gamma)^{1/2}/\mu$, and $\Lambda$ is a certain average value of the third order moduli.

Eliminating the oscillatory time dependence of $a_\alpha$ and $b_\alpha$ by introducing the new variables $\tilde{a}_\alpha = a_\alpha\exp(i\omega_\alpha t)$ and $\tilde{b}_n = b_{ni}\exp(i\Omega t)$ and introducing the phenomenological terms taking into account the dissipative processes, we arrive at the Heisenberg equations of motion for operators $\tilde{a}_\alpha$ and $\tilde{b}_n$:

$$\dot{\tilde{b}}_n = -\tilde{b}_n/\tau_C + i\sum_{\alpha,\,m}\beta_\alpha(m, n)\tilde{a}_k, \quad (18)$$

$$\dot{\tilde{a}}_\alpha = -\tilde{a}_\alpha/\tau_F + i\sum_{\gamma m}\zeta_{\alpha\gamma}(m, n)\tilde{b}_n\Delta N_\alpha, \quad (19)$$

where $\tau_C$ is the decay time for the critical mode in the system and $\tau_F$ is the decay time for normal phonons of this system. The kinetic equation for an increment of the distribution function is written as

$$\Delta\dot{N} = (\Delta N_* - \Delta N)/\tau_r + 2i\sum_{\alpha\gamma}\frac{\pi}{h^2}\left|V_{\alpha\gamma}^k\right|^2(\tilde{b}_n^+\tilde{a}_\alpha - \tilde{b}_n\tilde{a}_\alpha^+), \quad (20)$$

where $\tau_r$ is the relaxation time for a nonequilibriun phonon system,

$$\Delta N_* = \frac{2\pi}{h}\left|\frac{\Lambda}{4\mu}\varepsilon_{\alpha\gamma}\right|^2(\omega_\alpha\omega_\gamma)N_0(N_0 + 1) \quad (21)$$

is the quasiequilibrium displacement of the distribution function maintained by loading. The form of the nonlinear system of equations (18)–(20) is similar to that of the system of equations describing the radiation generation in a laser [15]. It can be solved only numerically at the appropriate values of the microparameters. In the processes of self-organization, the relaxation time for normal modes is usually much less than the relaxation time $\tau_C$ for the order parameter and the relaxation time $\tau_r$, which signifies that the adiabatic approximation is applicable, and one can use the method of multiscale expansions [15, 16] by introducing fast variables for $\tilde{a}_\alpha$. It is also possible to obtain the equation for the critical mode (the order parameter) in the form

$$\dot{\tilde{b}}_n = -\alpha_0\tilde{b}_n - \beta_0\tilde{b}_n^+\tilde{b}_n\tilde{b}_n, \quad (22)$$

where

$$-\alpha_0 = -1/\tau_r + \tau_F\sum_{\alpha\gamma,\,m}\beta_\alpha(m, n)\zeta_{\alpha\gamma}(m, n)\Delta N_*,$$

$$\beta_0 = \tau_C\tau_F\sum_{\alpha\gamma,\,m}\frac{\pi}{h^2}\left|V_{\alpha\gamma}^k\right|^2\beta_\alpha(m, n)\zeta_{\alpha\gamma}^2(m, n). \quad (23)$$

Equation (22) is, in fact, the equation of an anharmonic oscillator in a two-well potential. If $\alpha_0 < 0$, the mode is a conventional relaxation mode. The temperature and stress fluctuations are almost Gaussian, therefore the amplitude $\tilde{b}_n$ corresponds to conventional thermally-activated fluctuations in the displacements of atoms from their equilibrium positions. If $\alpha_0 = 0$, a befurcation arises and $\tilde{b}_n$ acquires two new equilibrium positions. At $\alpha_0 > 0$, we have

$$\Delta N > \Delta N_C = 1/\tau_C\tau_F\sum_{\alpha\gamma,\,m}\beta_\alpha(m, n)\zeta_{\alpha\gamma}(m, n), \quad (24)$$

and the mode can be interpreted as an amplitude of an acoustic wave generated by a dislocation (soliton) in the process of its nucleation. Thus, for homogeneous nucleation of dislocations, it is necessary to increase the critical degree of nonequilibrium of the phonon sys-

tem (24). Equation (22) can be obtained from the synergetic potential of the Ginzburg–Landau type [15, 16].

To determine the correlation radius $l_C$ of the order parameter, which corresponds to the size of a newly formed dislocation loop, one has to solve the inhomogeneous problem with an inhomogeneous potential involving a term $C|\nabla b_n|^2$. For such synergetic potential [15], equation of the order parameter (22) acquires an additional term and takes the form

$$\dot{\tilde{b}}_n = -\alpha_0\tilde{b}_n - \beta_0\tilde{b}_n^+\tilde{b}_n\tilde{b}_n + C\nabla^2 b_n, \qquad (25)$$

where $C$ is the dimensional constant. Using the spatial correlation function $\langle b_n(x, t)b_n(x', t')\rangle$ [15], we can obtain the expression for the correlation length (the dimension of the critical fluctuation) in the form

$$l_C \cong \left(aC/\left(-1/\tau_r + \tau_F\sum_{\alpha\gamma,\,m}\beta_\alpha(m, n)\zeta_{\alpha\gamma}(m, n)\Delta N\right)\right)^{1/2}. \qquad (26)$$

In this model, the time of homogeneous dislocation nucleation is determined by the time of formation of the critical phonon packet. The exact value of time $t_C$ is determined by the dynamics of the dislocation (soliton) formation and by the requirement that the time-dependent energy of the critical phonon packet, $E_C(t)$, should attain the intrinsic mechanical energy of the nucleated dislocation, $E_0$. The energy of the phonon packet is determined from the kinetic equation for the order parameter. To determine the nucleation time, we use the following equation [1, 2, 15]:

$$E_0 = 8\pi K_1\int_0^{t_C} dt\int_{-\infty}^{\infty}\left|\tilde{A}(k)\right|^2 d\mathbf{k}, \qquad (27)$$

where $K_1$ is the dimensional constant, $\tilde{A}(k)$ is the amplitude of the wave packet in the $k$ representation. Using the relaxation time approximation (the Debye model) and the Grüneisen coefficient $\gamma$ [10], we can solve equation (27) and obtain an expression for the nucleation time in the form

$$t_C = t_0\exp(-(U_0 - \gamma_0\sigma)/k_0T), \qquad (28)$$

where

$$t_0 = \tau_r,\ \gamma_0 = \gamma c_V l_C^3/16\pi K_1,$$

$$U_0 = 16\pi^3 E_0\gamma\tau_C\tau_F\sum_{\alpha\gamma,\,m}\beta_\alpha(m, n)\zeta_{\alpha\gamma}(m, n),$$

$$c_V = (k_0T)^{-2}\times\sum_\alpha\omega_\alpha^2 N_\alpha(N_\alpha + 1).$$

Expression (28) corresponds to the formula of thermal activation [3, 7], where macroscopic parameters $U_0$ and $\gamma_0$ are expressed in terms of the microscopic characteristics of the nonequilibrium phonon system.

The soliton solutions are obtained at the appropriate initial conditions. It should be remembered that the energy of the critical phonon packet would necessarily exceed the intrinsic energy of the soliton (dislocation). In the general case, it can be necessary to impose a more rigorous condition on the packet profile. The force conditions for defect nucleation can be found with due regard of the phonon contribution to the elastic stress tensor [10]

$$\sigma_{ij}^F = \sum_j\int\frac{d^3k}{(2\pi)^3}h\Omega M_{ij}\Delta N_C, \qquad (29)$$

where $M_{ij}$ is the strain potential tensor. Substituting $\Delta N_C$ from (24) into (29), we can see that the force condition of nucleation has the classical form [3, 7, 8] $\sigma \geq \sigma_C$, where $\sigma_C$ is the theoretically predicted strength of the ideal crystal.

The force condition for homogeneous nucleation of a dislocation in the critical phonon packet can be written as

$$E_0 = \frac{\beta}{2}\sum_j\int\frac{d^3k}{(2\pi)^3}\frac{(\Delta N)^2}{N_0(N_0 + 1)}, \qquad (30)$$

where $E_0$ is the intrinsic elastic energy of an already nucleated soliton (dislocation), $\beta = 1/k_0T$, and $k_0$ is the Boltzmann constant. Using the Heisenberg model, we can write $\Delta N_C \cong N_0^2\exp(h\omega_\alpha\beta)(h\omega_\alpha\beta)\gamma\varepsilon_{ii}$. Then, condition (30) takes the form

$$\frac{3Nk_0T}{16\pi^3}\left(\frac{T}{\theta}\right)\int_0^{l_C} d^3r\gamma\varepsilon_{ii}\int_0^{\theta/T}\frac{e^z z^4}{(e^z - 1)^2}dz = E_0, \qquad (31)$$

where $\varepsilon_{ii}$ is the relative change in the packet volume and $\theta$ is the Debye temperature.

Now, compare the estimates made by our formula with the known experimental data. Using the typical parameters for Al and Cu at the Debye temperatures, we obtain from (26) the correlation radius $l_C$ of the critical phonon packet, which is of the order of $10^{-5}$ cm. This value agrees with the theoretical predictions made within the kinetic theory of nucleation [7, 8]. Using the typical values of the quantities in (28), we obtain that the nucleation time of the critical packet is $t_C \leq 10^{-3}$ s, which is consistent with the data reported in [7].

## ACKNOWLEDGMENTS

I should like to thank V. L. Indenbom for helpful discussions and critical comments.

## RFERENCES

1. R. K. Dodd, G. Eilenberger, G. Gibbon, and H. Morris, *Solitons and Nonlinear Wave Equations* (Academic, New York, 1982; Mir, Moscow, 1988).

2. A. C. Newel, *Solitons in Mathematics and Physics* (Society for Industrial and Applied Mathematics, Philadelphia, Pa., 1985; Mir, Moscow, 1989), p. 386.
3. *Modern Crystallography. Structure of Crystals*, Ed. by B. K. Vaĭnshtein, V. M. Fridkin, and V. L. Indenbom (Nauka, Moscow, 1979), Vol. 4, p. 360.
4. V. L. Indenbom, Kristallografiya **3**, 197 (1958).
5. G. N. Dubnova and V. L. Indenbom, Kristallografiya **11**, 642 (1996) [Crystallogr. Rep. **11**, 554 (1996)].
6. J. Kratovil and V. L. Indenbom, Chechosl. J. Phys. B: At. Mol. Opt. Phys. **13**, 814 (1963).
7. J. P. Hirth and J. Lothe, *Theory of Dislocations* (Wiley, New York, 1982; Moscow, Atomizdat, 1972).
8. A. M. Kosevich, *Dislocations in Elastic Theory* (Naukova Dumka, Kiev, 1978).
9. U. E. Zasimchuk and S. I. Selitser, Fiz. Tverd. Tela (Leningrad) **26**, 1148 (1984) [Sov. Phys.–Solid State **26**, 695 (1984)].
10. H. Böttger, *Principles of the Theory of Lattice Dynamics* (Physik, Weinheim, 1983; Mir, Moscow, 1986).
11. I. D. Morokhov, V. I. Petinov, L. I. Trusov, and V. F. Petrunin, Usp. Fiz. Nauk **132**, 653 (1981) [Sov. Phys.–Usp. **24**, 295 (1981)].
12. H. Gleiter, Nanostructured Mater. **6**, 3 (1995).
13. R. Z. Valiev, Ann. Chim. (Paris) **21**, 369 (1996).
14. A. Kadic and D. G. B. Edelen, *A Gauge Theory of Dislocations and Disclinations* (Springer, Berlin, 1983; Mir, Moscow, 1987).
15. H. Haken, *Synergetics: An Introduction: Nonequilibrium Phase Transitions and Self-Organization in Physics, Chemistry, and Biology* (Springer, Berlin, 1977; Mir, Moscow, 1980).
16. G. Nicolis and I. Prigogine, *Self-Organization in Nonequilibrium Systems: From Dissipative Structures to Order through Fluctuations* (Wiley, New York, 1977; Mir, Moscow, 1979) [Sov. Phys.–Solid State **11**, 2871 (1969)].
17. A.V. Subaishev, Fiz. Tverd. Tela (Leningrad) **11**, 3417 (1969) [Sov. Phys.–Solid State **11**, 2871 (1969)].
18. V. I. Alshits and V. L. Indenbom, Usp. Fiz. Nauk **115**, 3 (1975) [Sov. Phys.–Usp. **18**, 1 (1975)].

*Translated by K. I. Kugel*

*Crystallography Reports, Vol. 45, No. 2, 2000, pp. 270–276. Translated from Kristallografiya, Vol. 45, No. 2, 2000, pp. 301–307.*


**LATTICE DYNAMICS**

# Dynamic and Static Orientational Disorder in Mixed $K_{1-x}(NH_4)_xI$ Crystals

**L. A. Shuvalov*, U. Natkaniec**, and L. S. Smirnov*****

** Shubnikov Institute of Crystallography, Russian Academy of Sciences, Leninskiĭ pr. 59, Moscow, 117333 Russia*

*** Frank Laboratory of Neutron Physics, Joint Institute for Nuclear Research, Dubna, 141980 Russia*

*Niewodniczanski Institute of Nuclear Physics, Krakow, 31-342 Poland*

**** Research Center of the Russian Federation Institute of Theoretical and Experimental Physics, Moscow, 117259 Russia*

Received January 26, 1999; in final form, November 3, 1999

**Abstract**—Earlier, we have shown that, at low temperatures, the mixed $K_{1-x}(NH_4)_xI$ crystals show two low-energy resonance modes in the dynamically orientationally disordered region of the α-phase and statically orientationally disordered phase of the orientational glass, absent in the orientationally ordered γ-phase. Below, we report the results of the experimental study of the low-energy resonance and local modes in $K_{1-x}(NH_4)_xI$ crystals obtained by the method of inelastic incoherent neutron scattering (IINS) over the wide temperature range. © *2000 MAIK "Nauka/Interperiodica".*

## INTRODUCTION

The α-phase of mixed ammonium–alkali halide crystals has attracted the attention of numerous researchers already for several decades. The *x*–*T* phase diagram of mixed $K_{1-x}(NH_4)_xI$ crystals has been continuously refined for the last decade [1–4]. It was shown [5] that with an increase of the temperature, the high-temperature α-phase (sp. gr. $Fm\bar{3}m$, the dynamically orientationally disordered NaCl-type structure) undergoes the following phase transitions: α ⟶ β ⟶ γ in the concentration range $x_{\beta\gamma} < x < 1.0$, α ⟶ β in the range $x_{\varepsilon\beta} < x < x_{\beta\gamma}$, α ⟶ ε in the range $x_{s_\varepsilon} < x < x_{\varepsilon\beta}$, α ⟶ *SRO* in the range $x_{gs} < x < x_{s_\varepsilon}$, and α ⟶ *OG* in the range $x_{\alpha g} < x < x_{gs}$. The crystal structures of the γ-, β-, and ε-phases are known: the space group of the γ-phase is $P\bar{4}3m$, the space group of the disordered β-phase is $Pm\bar{3}m$, and the space group of the ε-phase is $R3m$ [6]. The abbreviations *SRO* and *OG* denote the regions of the short-range order and the static orientational disorder of the orientational glass formed with lowering of the temperature because of freezing of the dynamically disordered orientational degrees of freedom of $NH_4^+$ ions. The concentration values $x_{\beta\gamma}$, $x_{\varepsilon\beta}$, $x_{s_\varepsilon}$, $x_{gs}$, and $x_{\alpha g}$ correspond to the boundaries between the adjacent phases on the *x*–*T* phase diagram. It should be emphasized that the boundary concentrations obtained in various studies are inconsistent, which can be explained by different quality of the samples studied. Thus, the boundary of the transition from the α- to the *OG*-phase at the temperature 1 K corresponds to the concentration $x_{\alpha g} = 0.16$ [4].

The early studies of ammonium dynamics in $K_{1-x}(NH_4)_xI$ crystals in the concentration range $0 < x \leq 0.60$ performed by the method of inelastic incoherent neutron scattering (IINS) showed the existence of the resonance modes $E_r^1$ (1.8–2.9 meV) at 10 K [7, 8] and $E_r^2$ (7–10 meV) at 10 [7, 8] and 20 K [9].

To identify the nature of the resonance modes observed in $K_{1-x}(NH_4)_xI$ crystals in [10], we studied a deuterated sample with $x = 0.45$ by the IINS method at 20 K. This experiment provided the answer to the question about the nature (translational or librational) of the resonance modes. It was shown that the modes $E_r^1$ and $E_r^2$ are of the translational nature, whereas Tomkinson *et al.* [9], who first observed the resonance mode $E_r^2$, considered it to be librational. It was also confirmed that among the local modes observed earlier [11] in protonated crystals, the mode with the energy of about 20 meV is the translational one, $\nu_5$, whereas the mode with the energy of about 30 meV is librational, $\nu_6$.

Below, we report our study of the effect of $NH_4^+$ concentration and temperature on the evolution of the IINS intensities from protonated $K_{1-x}(NH_4)_xI$ crystals. It was important to establish how one can study the transition from the "frozen" static orientational disorder of the *OG*-phase to the dynamic orientational disorder of the α-phase by the IINS method, what changes

1063-7745/00/4502-0270$20.00 © 2000 MAIK "Nauka/Interperiodica"

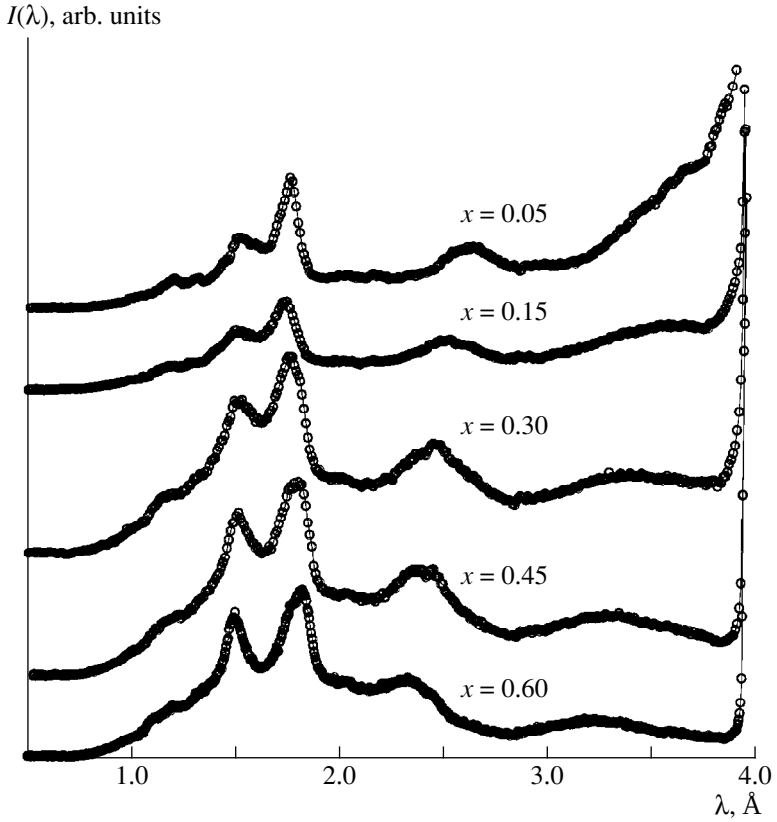


**Fig. 1.** Intensities of inelastic incoherent neutron scattering $I(\lambda)$ of mixed $K_{1-x}(NH_4)_xI$ crystals at various ammonium concentrations obtained at 10 K.

in the concentration and temperature dependences of the IINS intensities can occur during this transition, and what effect it can produce onto the resonance and local modes.

## EXPERIMENT AND RESULTS

Polycrystal $K_{1-x}(NH_4)_xI$ samples in the concentration range $0 < x < 0.60$ were prepared by evaporating the corresponding stoichiometric aqueous solutions under a pressure of 6.5 Pa at room temperature. The IINS spectra of the thus prepared crystals were measured at a 2% resolution on a neutron NERA-PR spectrometer of the back-scattering geometry with a pulsed neutron source IBR-2 (Laboratory of Neutron Physics, Joint Institute for Nuclear Research, Dubna) in the temperature range from 10 to 290 K. The NERA-PR spectrometer allows the simultaneous study of the crystal structure of the samples by the method of the neutron powder diffraction. The energies of inelastically scattered neutrons were determined by pyrolytic-graphite crystals-analyzers adjusted to the wavelength $\lambda_0$ = 4.15 Å [12]. The measured IINS intensities, $I(\lambda)$, were recalculated into the spectra of the generalized densities of phonon states $G(E)$ in the one-phonon incoherent approximation using the programs described elsewhere [13, 14].

We studied the dependence of the IINS spectra, $I(\lambda)$, of $K_{1-x}(NH_4)_xI$ crystals along the concentration section of the $x$–$T$ phase diagram in the concentration range $0 < x \le 0.6$ at 10 K and along the temperature sections of the $x$–$T$ diagram from 10 to 290 K for the crystals with the concentrations $x$ = 0.15 and 0.45. As showed diffraction measurements, both these crystals possess the NaCl-type long-range order in the temperature range 10–290 K. The temperature section of the phase diagram for a crystal with the concentration $x$ = 0.15 is located in the region of the α-phase, whereas the temperature section for the sample with $x$ = 0.45 enters, at $T$ = 10 K, the region of the *OG* phase, passes through it, and intersects the "defreezing" boundary in the transition to the α-phase.

The IINS intensities, $I(\lambda)$, along the concentration section of the $x$–$T$ phase diagram of the $K_{1-x}(NH_4)_xI$ crystals at 10 K are shown in Fig. 1. As shown in [7, 8], four maxima of the $I(\lambda)$ dependence corresponds to the resonance modes $E_r^1$ and $E_r^2$ and the local translational, $\nu_5$, and librational, $\nu_6$, modes. The contribution of the quasielastic incoherent neutron scattering (QEINS) to the $I(\lambda)$ dependence in the wavelength

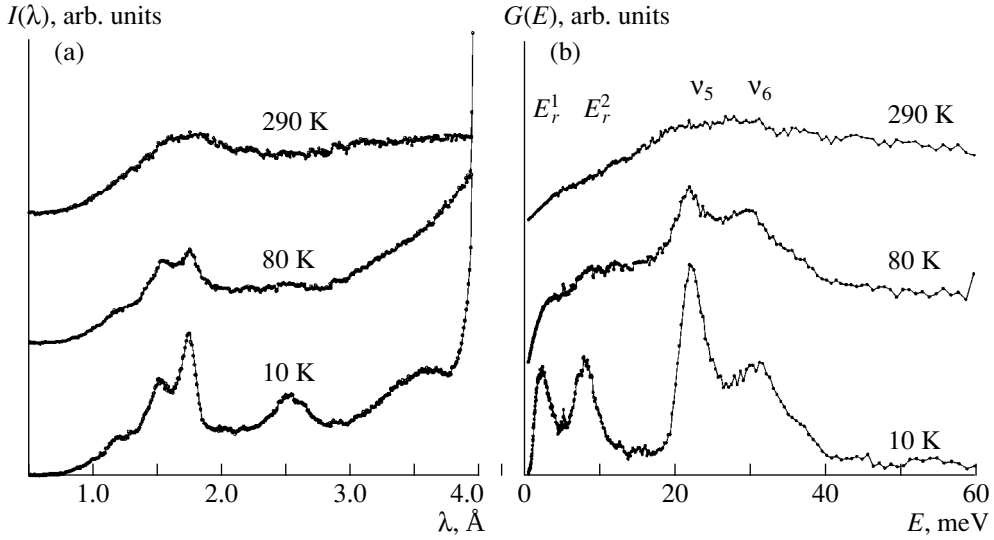


**Fig. 2.** (a) $I(\lambda)$ curves and (b) the generalized phonon-state densities $G(E)$ for a $K_{0.85}(NH_4)_{0.15}I$ crystal at different temperatures.

range 4.15–3.0 Å manifests itself with a decrease of the ammonium concentration $x$ from 0.60 to 0.30. With a further decrease of the ammonium concentration, one observes a considerable increase in the intensity of the quasielastic incoherent neutron scattering, which, in turn, can give rise to fluctuations in the reorientation of ammonium ions. An increase of the intensities of quasielastic incoherent neutron scattering can be explained by the fact that, moving along the concentration section of the *x*–*T* diagram, we go outside the region of the *OG* phase in the vicinity of $x = 0.30$ at 10 K and enter the region of the α-phase.

Studying the changes in the IINS spectra on the temperature sections, we can determine the position of the above the boundary of defreezing on the *x*–*T* diagram and also establish the effect of the dynamic and static orientational disorder in the arrangement of ammonium ions on the resonance and local modes, i.e., on the dynamics of the crystal lattice of $K_{1-x}(NH_4)_xI$ crystals.

The IINS spectra from a crystal with $x = 0.15$ at various temperatures are shown in Fig. 2a. The generalized densities of the phonon states $G(E)$ calculated from these spectra are shown in Fig. 2b.

The detailed study of the IINS spectra $I(\lambda)$ and $G(E)$ for $K_{0.55}(NH_4)_{0.45}I$ crystals at various temperatures is illustrated by Figs. 3a and 3b. One can follow the changes in the behavior of the resonance and local modes with an increase of the temperature from 10 to 290 K. The modification of the $I(\lambda)$ and $G(E)$ spectra starts with broadening of the resonance-mode maximum $E_r^1$ and a considerable increase of the QEINS intensities. At temperatures as low as 30 K, the contribution of this mode to the IINS intensities can hardly be seen against the background of the QEINS intensities. The effect of the temperature on the resonance mode $E_r^2$ is similar, broadening of the maximum of this mode is accompanied by a considerable reduction of its intensity against the continuing increase of the QEINS intensity at 80 K. There are almost no contributions of the resonance modes $E_r^1$ and $E_r^2$ to the $I(\lambda)$ and $G(E)$ spectra at 80 K, but the translational, $\nu_5$, and librational, $\nu_6$, modes still contribute to the intensity, although the intensities of their maxima decrease with the temperature rise. The intensities of the maxima of the local $\nu_5$ and $\nu_6$ modes on the $I(\lambda)$ and $G(E)$ dependences at 160 K overlap due to the broadening of their maxima caused by an increased anharmonicity of these modes.

Comparing the IINS spectra, $I(\lambda)$, and $G(E)$ of the crystals with $x = 0.15$ and 0.45 at 80 and 290 K, we see their almost complete identity. At 80 K, one observes only a pronounced QEINS contribution to the intensity in the wavelength range, where, at 10 K, the scattering from the resonance modes $E_r^1$ and $E_r^2$ takes place, and which then is transformed into the scattering from the local modes, $\nu_5$ and $\nu_6$. At 290 K, the spectra of both crystals have broad maxima in the range of the local modes.

## RESULTS AND DISCUSSION

We analyzed the effect of the temperature on the characteristics of the resonance and the local modes determined for the samples of $K_{1-x}(NH_4)_xI$ crystals with $x = 0.15$ and $x = 0.45$.

For a crystal with $x = 0.15$, the $I(\lambda)$ dependence at 10 K shows the presence of the QEINS contribution (Fig. 2a) [contrary to the case of $I(\lambda)$ for a crystal with $x = 0.45$ in Fig. 3a]. This indicates the dynamic disorder in the orientational degrees of freedom of an $NH_4^+$ ion. It should be emphasized that the IINS spectra, $I(\lambda)$, and $G(E)$ for crystals with $x = 0.15$ and 0.45 at 80 K show

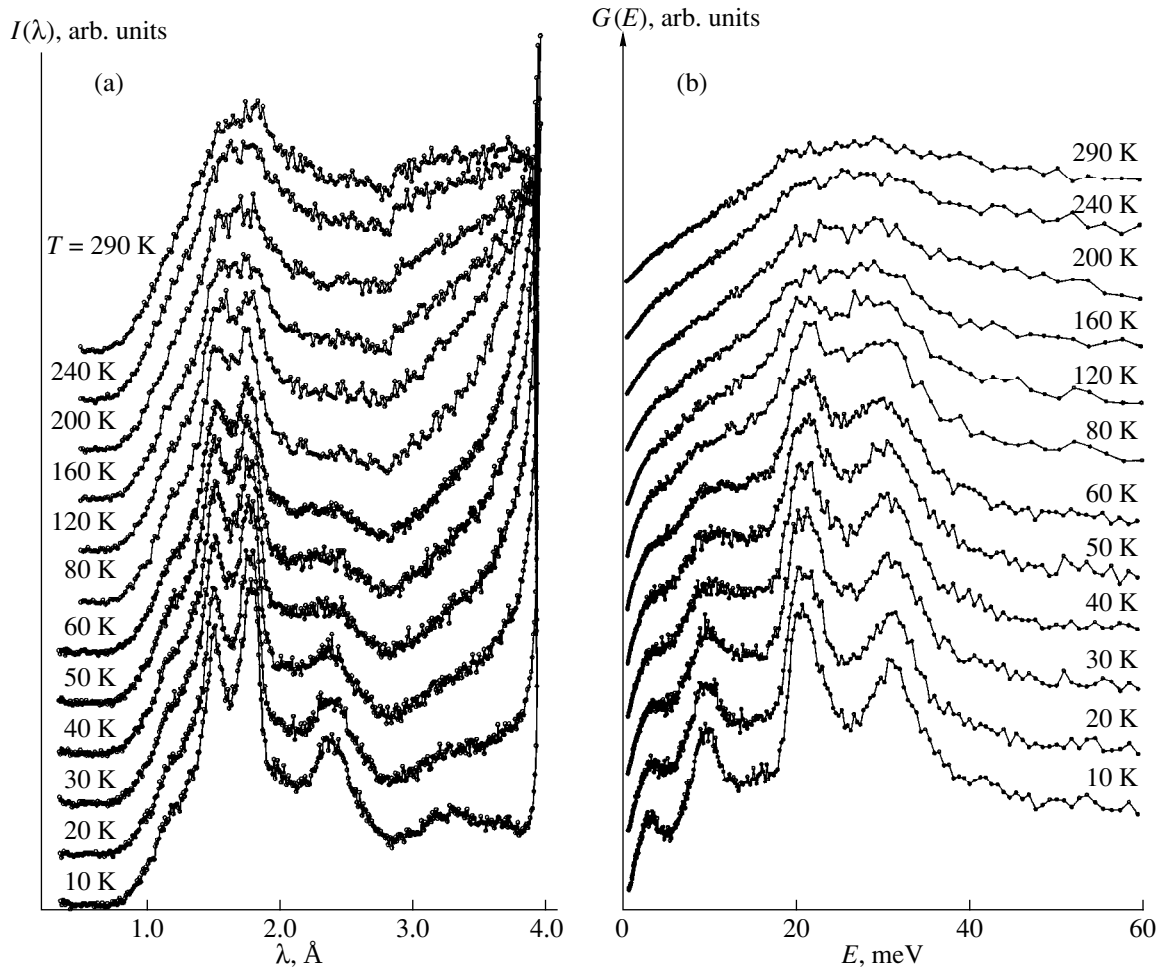


**Fig. 3.** (a) $I(\lambda)$ curves and (b) generalized densities of phonon states $G(E)$ for a $K_{0.55}(NH_4)_{0.45}I$ crystal at various temperatures.

almost no contributions due to the resonance modes $E_r^1$ and $E_r^2$; they consist mainly of the contributions of the local modes $\nu_5$ and $\nu_6$, whereas the corresponding spectra obtained at 290 K are absolutely identical (Figs. 2 and 3). However, the change in the QEINS contribution to the IINS intensities $I(\lambda)$ for the crystal with $x = 0.15$ at various temperatures reflects the influence of the temperature on the behavior of the orientational degrees of freedom of ammonium ions in the $\alpha$-phase—in that part of the concentrational range of the $\alpha$-phase, where weak (but still pairwise) $NH_4^+$–$NH_4^+$ interactions give no rise to the collective $NH_4^+$ interactions resulting in the formation of the *OG* phase.

Analyzing the characteristics of the resonance, $E_r^1$ and $E_r^2$, and the local, $\nu_5$ and $\nu_6$, modes for a crystal with $x = 0.45$, it is possible to study the effect of the transition from the state of the orientational glass to the state of the dynamic orientational order. With this aim, each $G(E)$ curve in Fig. 3b is considered as consisting of the background of the multiphonon scattering and the maxima of the resonance modes, $E_r^1$ and $E_r^2$, and the local translational, $\nu_5$, and librational, $\nu_6$, modes, whose shapes are approximated by Gaussians. In this approximation, one can determine the area $S$ of each maximum, its position $E$, and its width at the half-height (FWHM). These characteristics are determined for each mode with an increase of the temperature from 10 up to 290 K until the moment that the mode can still be distinguished against the background. The thus determined temperature dependences are shown in Fig. 4a for the resonance modes $E_r^1$ and $E_r^2$ and in Fig. 4b for the local modes $\nu_5$ and $\nu_6$. The analysis shows that the run of these curves shows considerably changes at two temperatures—40 and 80 K.

The areas of the maxima corresponding to the resonance modes monotonically decrease almost to their complete disappearance with the temperature rise from 10 to 80 K. The temperature dependence of the energy of the resonance mode $E_r^1$ has an anomaly at 40 K,

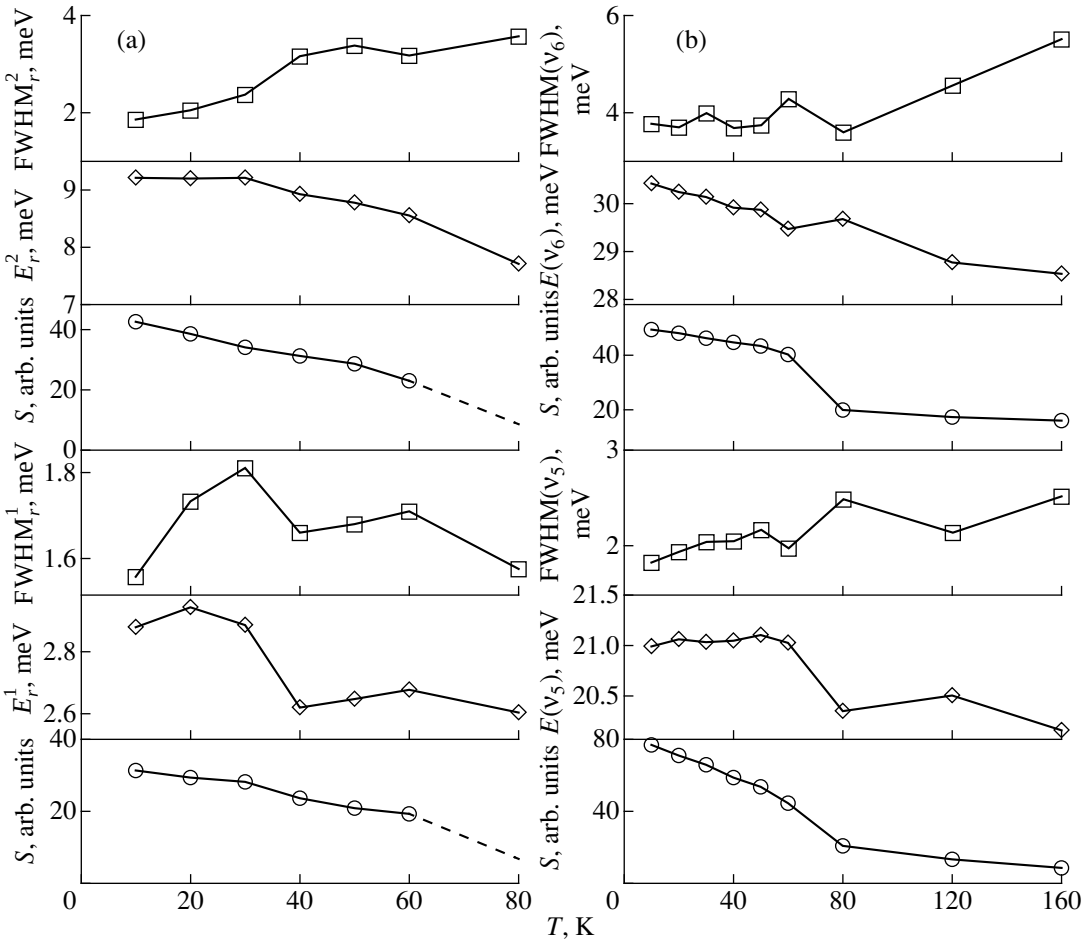


**Fig. 4.** (a) Temperature curves of the areas $S$, energy values $E$, and the width at a half-heights, FWHM, of the resonance modes $E_r^1$ and $E_r^2$ and (b) the local modes $\nu_5$ and $\nu_6$ of a $K_{0.55}(NH_4)_{0.45}I$ crystal.

because, in the vicinity of this temperature, its value changes in a jumpwise manner and then, with the further increase of the temperature, becomes constant. The energy of the resonance mode $E_r^2$ monotonically decreases with the change of the temperature from 10 to 80 K. The FWHM value of the resonance mode $E_r^1$ increases with the temperature rise from 10 K, decreases in the vicinity of 40 K, and somewhat increases with an approach to the temperature of the intensity disappearance in the vicinity of 80 K. The FWHM value for the resonance mode $E_r^2$ increases in the temperature range from 10 to 40 K and also, but at a lower rate, with an increase of the temperature from 40 to 80 K.

The variation in the decreasing rate of the areas for the local mode, $\nu_5$ and $\nu_6$, with an increase of the temperature from 10 to 160 K (the temperature of their overlap) is observed at 80 K. The temperature dependences of the energies of the local modes $\nu_5$ and $\nu_6$ at 80 K also indicate the change in the rate of the energy decrease, although, for the local modes, the corresponding temperature dependences noticeably differ. The temperature dependence of the FWHM values for the local modes shows their monotonic increase with the temperature change from 10 to 160 K.

For a more convenient comparison of the temperature dependences of the areas of the maxima and the energies of the resonance and the local modes, we constructed special plots of the reduced $Z(T)$ values in the temperature range from 10 to 80 K:

$$Z(T) = [Y(T) - Y(80\ \text{K})]/[Y(10\ \text{K}) - Y(80\ \text{K})] = \Delta Y/Y_{\max},$$

where $Y$ are the experimental values for the resonance and local modes. The thus determined reduced temperature dependences of the area of the maxima of the resonance and local modes are shown in Fig. 5a; the reduced temperature dependences of the energies of the resonance and local modes are shown in Fig. 6.

The reduced temperature dependences of the areas, $\Delta S/S_{\max}$, of the resonance and the local ($\nu_5$) modes are

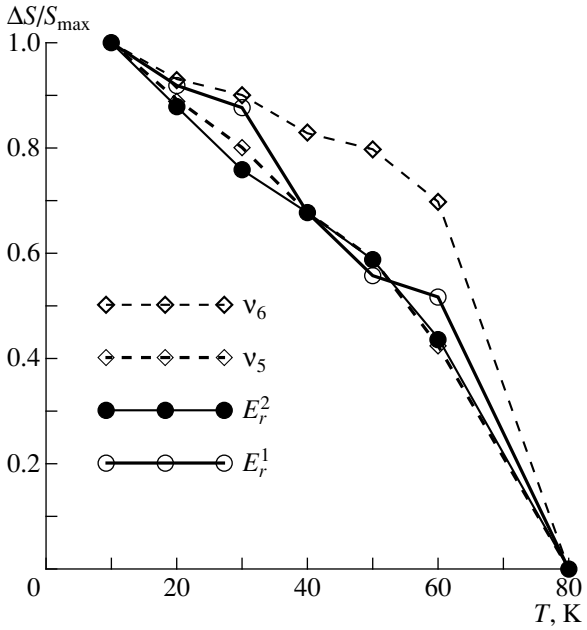


**Fig. 5.** Reduced temperature dependences for the area of the maxima, $\Delta S/S_{max}$, of the resonance modes $E_r^1$ and $E_r^2$ and the local modes $\nu_5$ and $\nu_6$ of a $K_{0.55}(NH_4)_{0.45}I$ crystal.

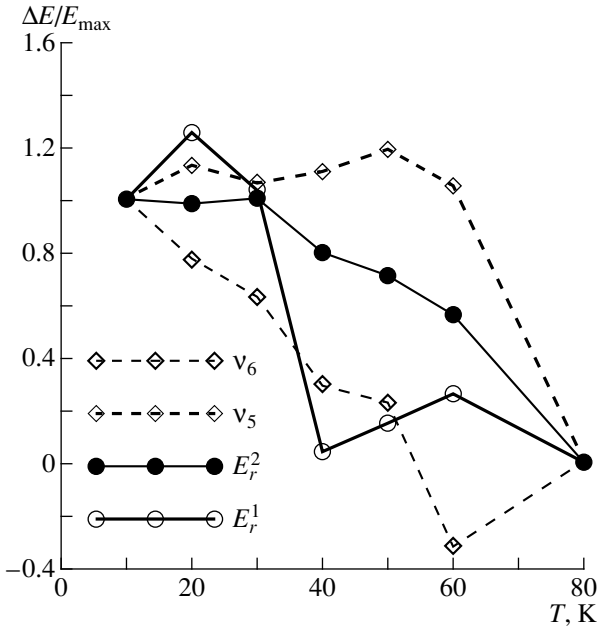


**Fig. 6.** Reduced temperature dependences for the energies $\Delta E/E_{max}$ of the resonance $E_r^1$ and $E_r^2$ modes and the local modes $\nu_5$ and $\nu_6$ of a mixed $K_{0.55}(NH_4)_{0.45}I$ crystal.

similar, but the temperature dependence of the maximum area of the local mode $\nu_6$ noticeably differs from them (Fig. 5). Similar behavior of the temperature dependences of the areas of the maxima for the resonance and the local modes $\nu_5$ seems to be associated with their similarity to phonons. The reduced temperature dependences of the energies $\Delta E/E_{max}$ for the resonance and the local modes are considerably different. As has already been indicated, the resonance mode $E_r^1$ shows an anomaly at 40 K, whereas the energy of the resonance mode $E_r^2$ monotonically decreases from 10 to 80 K. With an increase of the temperature from 10 K, the energy of the local mode $\nu_6$ decreases faster than that of the local mode $\nu_5$. This difference in the temperature dependences of the energies of the local modes ($\nu_5$ and $\nu_6$) can be caused by the fact that the librational mode $\nu_6$ is determined mainly by the distance between the ammonium ions and the nearest neighboring iodine ions [15]. The temperature dependence of the lattice parameter $a$ of the cubic lattice of the mixed crystal with $x = 0.45$ is shown in Fig. 7. With an increase of the temperature, the noticeable change in the lattice parameter of the cubic lattice is already seen at temperatures above 50 K, which correlates with the temperature variation in the energies of the local modes $\nu_5$ and $\nu_6$.

Thus, the above qualitative analysis based on the consideration of the temperature dependences of the resonance and local modes shows that each mode has its own individual characteristics. The local modes $\nu_5$ and $\nu_6$ in the temperature evolution of the $G(E)$ spectra show no noticeable dependence on concentration in the range $0 < x \le 0.60$, which distinguish them from the temperature evolution of the $G(E)$ spectra of the resonance modes $E_r^1$ and $E_r^2$.

The resonance modes $E_r^1$ and $E_r^2$ disappear against the background of an increasing intensity of the QEINS

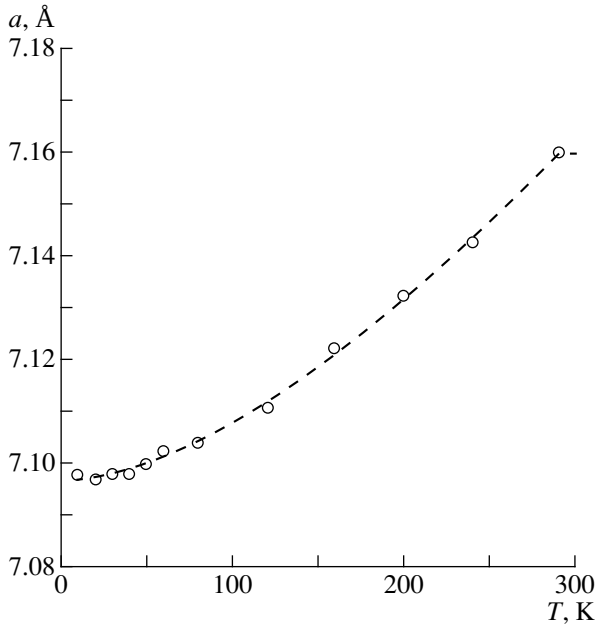


**Fig. 7.** Temperature dependence of the cubic-lattice parameter $a$ of a $K_{0.55}(NH_4)_{0.45}I$ crystal.

at 80 K. However, their disappearance does not uniquely determine the defreezing temperature of the orientational degrees of freedom of ammonium ions, because the disappearance of the orientational degrees of freedom can be indicative to the fact that ammonium ions participate in the diffusion reorientational motion in the α-phase. It seems that the anomaly of the temperature dependence of the position of the resonance-mode energy $E_r^1$ in the $G(E)$ spectrum of a $K_{0.55}(NH_4)_{0.45}I$ crystals in the vicinity of the temperature of 40 K reported above can be considered as the defreezing temperature.

## CONCLUSION

The study of the IINS intensities for the $K_{1-x}(NH_4)_xI$ crystals at various concentrations and temperatures with the aim to determine the influence of the dynamic and static orientational disorder on the phonon spectrum yielded the following results.

It is shown that the presence of the dynamic orientational disorder in a crystal indicates that the quasielastic incoherent neutron scattering makes a certain contribution to the lattice dynamics. The intersection of the boundary between the *OG*- and the α-phases shows that the individual characteristics of the resonance and the local modes along the temperature section show both similar and dissimilar features. It is established that at the temperature 80 K [at which the width of the maxima of the resonance modes in the $G(E)$ spectra become zeroes], the rate of the area decrease under the maxima of the local modes also starts changing and continues doing so until their final merge at 160 K. The temperature dependences of the area of the maxima of the resonance and local translation mode $\nu_5$ on the $G(E)$ spectrum are similar up to 80 K, which reflects the translational nature of the resonance modes. At the intersection of the boundary between the *OG* and the α-phases, the resonance mode energy $E_r^1$ decreases in a jumpwise manner at 40 K, which can be associated with defreezing of the orientational degrees of freedom.

## ACKNOWLEDGMENTS

The study was supported by the Grant for Leading Schools, project no. 96-15-96504 and the Russian Foundation for Basic Research, project no. 98-02-16944.

## REFERENCES

1. I. Fehst, R. Böhmer, W. Ott, *et al.*, Phys. Rev. Lett. **64**, 3139 (1990).
2. J. F. Berret, C. Bostoen, and B. Hennion, Phys. Rev. B: Condens. Matter **46**, 13747 (1992).
3. M. Winterlich, R. Böhmer, and A. Loidl, Phys. Rev. Lett. **75**, 1783 (1995).
4. M. Paasch, M. Winterlich, R. Böhmer, *et al.*, Z. Phys. B: Condens. Matter **99**, 333 (1996).
5. F. Güthoff, M. Ohl, M. Reehuis, and A. Loidl, Physica B (Amsterdam) **266**, 310 (1999).
6. M. Paasch, G. L. McIntyre, M. Reehuis, *et al.*, Z. Phys. B: Condens. Matter **99**, 339 (1996).
7. I. Natkaniec and L. S. Smirnov, Physica. B **234–236**, 409 (1997).
8. I. Natkaniec, L. S. Smirnov, S. I. Bragin, *et al.*, Kristallografiya **43**, 246 (1998) [Crystallogr. Rep. **43**, 211 (1998)].
9. J. Tomkinson, B. A. Dasannacharya, A. S. Goal, *et al.*, J. Chem. Soc., Faraday Trans. **87**, 3431 (1991).
10. I. Natkaniec, L. S. Smirnov, and L. A. Shuvalov, Ferroelectrics (in press).
11. A. B. Gardner, T. C. Waddington, and J. Tomkinson, J. Chem. Soc. Faraday Trans. **73**, 1191 (1977).
12. I. Natkaniec, S. I. Bragin, J. Brankowski, *et al.*, ICANS-XII, Abingdon, RAL Report 94-025, **1**, 89 (1993).
13. E. L. Bokhenkov, I. Natkaniec, and E. F. Sheka, Zh. Éksp. Teor. Fiz. **70**, 1027 (1976) [Sov. Phys.–JETP **43**, 536 (1976)].
14. E. F. Sheka, I. V. Markichev, I. Natkaniec, *et al.*, Part. and Nuclei **27**, 493 (1996).
15. I. Natkaniec, L. S. Smirnov, and A. I. Solov'ev, in *Proceedings of National Conference on Application of X-ray and Synchrotron Radiation, Neutrons and Electrons in Materials Science, Dubna, Russia*, 1997 (Nauka, Dubna, 1997), Vol. 3, p. 25.

*Translated by L. Man*

*Crystallography Reports, Vol. 45, No. 2, 2000, pp. 277–281. Translated from Kristallografiya, Vol. 45, No. 2, 2000, pp. 308–312.*


**PHASE TRANSITIONS**

# Entropy Theory of Metamorphic Transitions in Coals

**M. I. Novgorodova*, Yu. M. Gufan**, N. F. Losev**†, and I. N. Moshchenko****

** Fersman Mineralogy Museum, Russian Academy of Sciences, Leninskiĭ pr. 18/2, Moscow, 117071 Russia*
*e-mail min@minmuz. msk. su*

*** North Caucasian Scientific Center of Higher School,*
*Rostov-on-Don, ul. Pushkinskaya 140, 344006 Russia*
*e-mail: gufan@gufan. rnd. runnet. ru*

Received February 4, 1998

**Abstract**—A model of a metamorphic phase transition in coals has been suggested, which explains the change of the superionic conduction of coals at early stages of metamorphism by the electronic conductivity of anthracites. The model is based on a concept of quasiplane fragments of aromatic rings, the main component of microstructure of coals, the percolation approximation for determining the carbon concentration responsible for the formation of infinite clusters of aromatic rings, and the Lichtenecker approximation for determining the conductivity of the object "coal substance + rock". *© 2000 MAIK "Nauka/Interperiodica".*

## INTRODUCTION

Enrichment of the coal mass with carbon on the geological time scale (the metamorphism) gives rise to changes in the physical characteristics of coals. The time characteristics of coal metamorphism are studied insufficiently and thus cannot be used to construct physical models. However, it is well-known that the carbon content in highly metamorphized coals is also rather high. An increase of carbon concentration up to 92% (the boundary between lean coals and anthracite) drastically changes the physical properties of coals. The anthracites are known to have the electronic (metallic) conductivity five orders of magnitude higher than the ionic conductivity of lean coals [1]. In what follows, the transition superionic conductor–metal occurring on the geological time scale will be referred to as the metamorphic transition. Depending on the carbon content, this phase transition manifests itself as a sharp (morphotropic) transition in the physical properties.

The change of the physical properties of coals showing metamorphism is determined by their molecular structure. We had the aim to develop a model to describe the changes in the coal microstructure showing metamorphism in the vicinity of the above metamorphic phase transition.

## MODELS OF COAL MICROSTRUCTURE

The first models of coal microstructure were suggested by Fuchs and further developed by Storch, van Krevelen, and Hirsch [2–6]. In these models, C, H, O, and other atoms have covalent bonds and form various aromatic structures, short aliphatic chains, and hydroxyl, ether, and other functional groups, randomly bonded, but located in a layer that can be continuously deformed into a planar one. The molecular structure in these models is transformed in the process of coalification from the cellulose and lignin structures (which are fibrous polymers formed mainly by aliphatic chains) to a glassy graphite—a three-dimensional layer polymer whose main functional element is an aromatic ring.

When modeling the coal structure, we focused our attention on the formation and the changes occurring during metamorphism of quasiplanar fragments. Let us assume that there is a planar hexagonal network whose points are randomly occupied by carbon atoms in accordance with carbon concentration in the coal at the given stage of metamorphism (Fig. 1). The remaining points are occupied by H, O, and S impurity atoms or by vacancies. It is possible to use the carbon concentration as a qualitative parameter of the coalification degree directly dependent on the metamorphism stage. The hexagonal network in Fig. 1 can be regarded as a specific topological coordinate system. In the chosen model, this network can be continuously deformed and bent, its bond angles can be varied, etc. However, at all distortions of the network, the system of bonds between its points shoud remain unchanged. Filling the points of this hypothetical hexagonal network, one can model the whole ensemble of quasiplanar fragments existing in coals.

The resulting structure is determined proceeding from the principle of the minimum free energy ($F = E - TS$, where $E$ is the internal energy, $S$ is the entropy, and $T$ is the temperature) as a function of the external parameters (temperature, pressure, and composition) [7]. The problem of free-energy ($F$) minimization is solved with the aid of models that differ by the methods of approximation and calculation of $E$ and $S$. One of the methods of the approximate calculation of the mini-

† Deceased.

1063-7745/00/4502-0277$20.00 © 2000 MAIK "Nauka/Interperiodica"

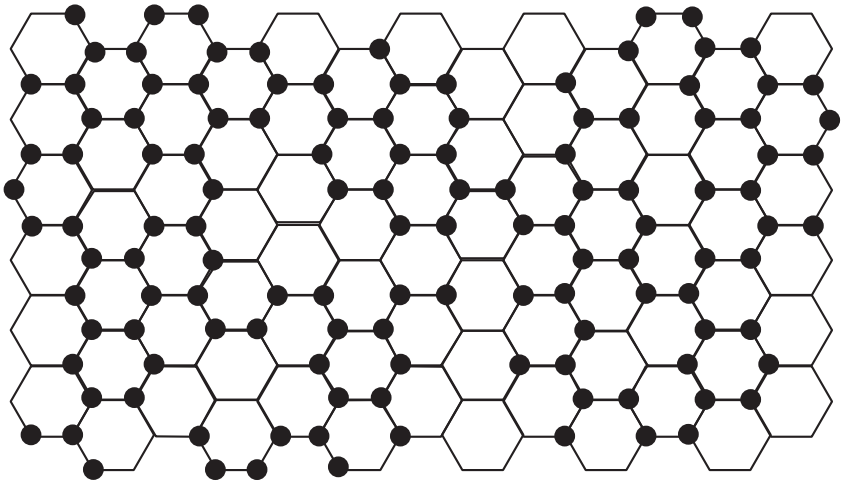

**Fig. 1.** Model of the coal structure: a hexagonal network with the points statistically occupied by carbon atoms.

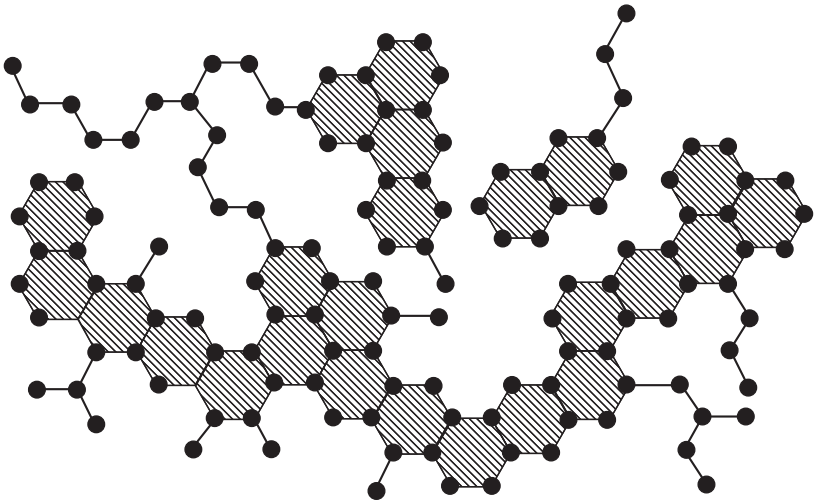

**Fig. 2.** Model of the coal structure. An isolated fragment of an infinite graphite-like cluster.

mum $F$ is based on the percolation theory [8, 9] corresponding to the limiting case, where the internal energy and its variations are ignored and the main contribution to the free energy comes from entropy, or, more precisely, from the configurational part of entropy. This approach is applicable only at high temperatures sufficient for the description of the properties in "frozen" or "solidified" nonequillibrium states and thus provides the adequate description of polymer properties. One can expect that this approach would also be successful in the description of the properties of metamorphic coals subjected to high-temperature annealing under high pressures and then "frozen" in a stressed state.

It is well known that the electronic structure of a benzene ring of carbon atoms drastically differs from all the other molecular formations of carbon atoms by the presence of shared electron states [10]. In fact, this molecular structure can be used as the basis for the transition of the coal substance in anthracite into the metal state. The formation of infinite clusters of aromatic rings at a certain carbon concentration in a coal substance "shunts" the weak ionic conductivity and changes it into the electronic one. The formation of infinite clusters of aromatic rings (determined from the maximum of the configuration entropy) is essentially dependent on the carbon concentration and the structure of the network.

A carbon atom is considered to belong to a cluster if it enters at least one completely formed aromatic ring, otherwise its electronic states do not form a conduction band. In other words, a graphite-like cluster is understood as a system consisting of one or several condensed aromatic rings (cores) (Fig. 2).

The growth of graphite-like clusters in the process of coalification can be most conveniently analyzed not in the hexagonal coordinate system, but in a triangular

one, which is dual to hexagonal but is more natural for the model considered upon the definition of a carbon atom belonging to the cluster. The points of a dual lattice are located at the centers of the hexagonal rings of the initial lattice. A point of a triangle network is considered to be occupied, if it is surrounded by the completely formed aromatic ring of carbon atoms from the initial network, otherwise the point is considered to be vacant. Thus, the problem of growth of graphite-like clusters on the hexagonal network is equivalent to the problem of growth of arbitrary clusters on the triangle network. The concentration of occupied points on the triangle network is equal to the concentration of the aromatic rings in the initial hexagonal network.

The analysis of cluster growth at stochastic filling of points in various networks is one of the problems soluble within the framework of the percolation theory. Consider some results directly related to our problem. For lattices of any geometries, there exists a critical concentration $Z_{cr}$ such that if the concentration of occupied points is lower that the critical one, the probability of formation of an infinite cluster equals zero. The system contains only finite, most probably, one-point clusters. For a triangle lattice, $Z_{cr} = 0.5$. The "condensation" of single points into clusters begins at the concentration $Z \approx Z_{cr}$; the dimensions of the maximum cluster $I_{max}$ increase as

$$I_{max} \sim (Z_{cr} - Z)^{-1.3}, \quad (Z < Z_{cr}).$$

At $Z = Z_{cr}$, the first infinite cluster is formed. The fraction of the occupied points, $V_\infty$, in an infinite cluster depends on the concentration $Z$ as

$$V_\infty \sim (Z - Z_{cr})^{0.14} \quad (Z > Z_{cr}).$$

The above results can be applied to the structure of quasiplanar fragments of the coal substance upon the establishment of the dependence concentration $Z$ of aromatic clusters on the carbon concentration $c$ in the hexagonal network.

Let us consider the hexagonal network completely filled with carbon atoms. Taking away one atom from the network point, we break three aromatic rings. Stochastically introducing a vacancy, we make the ratio 1 : 3 to be valid in a certain vicinity of $Z = 1$. Taking into account that the total number of points in hexagonal network is two times higher than in the triangular one, we have that $(1 - Z) \approx 6(1 - c)$ in the vicinity of $Z = 1$. This relation correctly determines the lower boundary, $Z \geq 6c - 5$. If the average distance $r$ between vacancies is greater than or equals to $3a$ ($a$ is a lattice constant of the hexagonal lattice), the probability of breaking three rings by one vacancy is higher than of two or one ring. Thus, the condition of validity of the relation $Z \sim 6c - 5$ is $r \gg 3a$. Taking into account that $[2(1 - c)]^{-\frac{1}{2}} \times 3^{\frac{3}{4}} a = r \geq 3a$, we obtain that the above estimate of the dependence of the concentration aromatic cores on the carbon concentration is valid at $c \geq 0.86$ or $Z \geq 0.16$.

It is necessary to take into account that with an increase of the number of vacancies in the hexagonal network at $3a \geq r \geq 2a$, the addition of one vacancy will break three or two aromatic rings, which leads to $(4c - 3) \geq Z \geq (6c - 5)$ at $c > 0.833$.

However, the above results are still insufficient for establishing the relationship between $Z$ and the measured carbon concentration in coals. In a real structure of a coal substance, the network points can be occupied by nitrogen and oxygen atoms not considerably changing the electronic bands of its quasiplanar fragments. Thus, the carbon concentration $c$ in our model exceeds the measured atomic concentration of carbon and is, in fact, only a phenomenological parameter of the theory. Proceeding from a good agreement of the results discussed below within the framework of percolation theory which neglects the interactions between the neighboring carbon atoms, we may assume that $c$ equals the mass concentration of carbon in coals. This hypothesis of "accidental coincidence" is justified by the numerical ratio of the bending energies of the "defect" fragments of the network, $(C_3O + 4C_3N)/5$, in comparison with $C_3C$, and, as a consequence, by the probability of oxygen and nitrogen substitution. However, this result requires a special consideration and is taken here as a mere postulate.

## METAMORPHISM PROCESS IN TERMS OF THE PERCOLATION THEORY

Thus, in accordance with the model of planar hexagonal fragments, an increase in the number of aromatic rings $Z$ determined by the relationship $Z \geq 6c - 5$ begins with the gas coals (G) at $c \approx 83\%$.

The poor (P) and long-flame (LF) coals have almost no aromatic rings. The coals characterized by the moderate metamorphism [gas (G), fat (F), coking (C), and the coals of trademarks (G–LS)] show no formation of aromatic rings into multiparticle clusters. The coal substance at this stage of metamorphism has only individual aromatic rings. The coals with the trademarks from LS to the L (lean) show the condensation of aromatic rings into graphite-like clusters. The dimension of the maximum cluster depends on the coalification in the following way [8, 9]: $I_{max} = 2a(Z - 0.5)^{1.3} = 2a(6c - 5.5)^{1.3}$. At the boundary between the charcoal and anthracite ($c_c \approx 92\%$), the first infinite graphite-like clusters are formed. This signifies that in the process of metamorphism, the attainment of the critical carbon concentration in the coal substance should initiate a metamorphic (percolating, in our model) phase transition. The relative volume ($V$) of infinite clusters in the vicinity of the critical concentration drastically increases [8, 9]: $V = V_0[2(6c - 5.5)]^{0.14}$.

It should be emphasized that the results of the percolation theory are not much sensitive to the network

geometry used in the study of cluster formation. They are much more sensitive to the system dimension. This leads to a conclusion that the essential aspect of the model is the assumption about the formation quasiplanar fragments in the system. Topologically, a hexagonal lattice is the most appropriate for description of actual carbon bonds in coal at the microlevel. However, for a complicated polymer, such as coal, a more suitable network seems to be a stochastic network modeling a random packing. The percolation threshold for both models is the same, and therefore, in this case, the numerical coincidence of the critical concentrations corresponding to the metamorphic transition and appearance of electronic conductivity in coals cannot be used as a criterion.

Thus, the main advantage of the model consists in that it provides the establishment of a metamorphic phase transition (structural rearrangement) upon the attainment of the carbon concentration $c = 92\%$ in the carbon substance. This phase transition is associated with the formation of infinite graphite-like clusters. The terminology used in this paper is borrowed from the theory of phases in solid solutions and alloys based on the concept of "phase transitions occurring with the change of composition." The analogy with the real phase transitions, which allowed us to use this terminology, consists in the fact that the changes of the substance composition in the vicinity of the critical concentrations should drastically change the dependences of the physical characteristics of the system (in particular, of conductivity) on the composition.

## APPLICATION OF THE RESULTS TO THE DESCRIPTION OF PROPERTIES OF REAL COALS

The data on electrical conductivity of coals having different degrees of metamorphism show that the carbon concentration corresponding to the metamorphic phase transition determined for the model coincides with the onset of a steep rise in conductivity.

Figure 3 shows a typical dependence of resistivity ρ on the degree of coalification (solid line) obtained by averaging of the experimental data [1]. At the boundary of bituminous coals and anthracites (corresponding to the carbon concentration of 92%), the resistivity drops beginning with the value of $10^4$ Ω m and attains the value of $10^{-5}$ Ω m for highly metamorphized anthracites. The change in the carbon content by only 3% gives rise to an increase in conductivity by a factor exceeding $10^5$. Such a dependence of resistivity on carbon concentration and the change of the conductivity type correspond to a metal–dielectric phase transition well-known in solid state physics.

The point of the metamorphic metal–dielectric-type phase transition in coals is compared with the point of the percolation phase transition in a planar network randomly filled with carbon atoms. If the concentration of

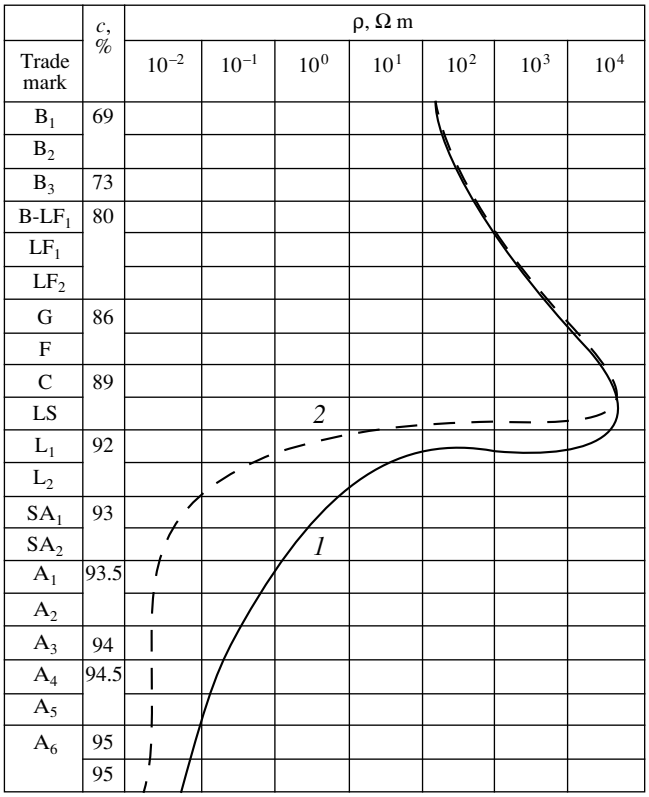


Notation: (B) brown coal; (LF) long-flame coal; (G) gas coal; (F) fat coal; (C) coking coal; (LS) lean sintering coal; (L) lean coal; (SA) semianthracite; (A) anthracite.

**Fig. 3.** Electrical resistivity of coals at different metamorphism stages: (*1*) experiment; (*2*) theory.

aromatic rings exceeds the threshold value ($Z_{cr} = 0.5$), the conductivity attains the value $\sigma = \sigma_0(Z - Z_{cr})^{1.3}$, where $\sigma_0$ is the phenomenological parameter. The total conductivity of coals equals $\sigma = \sigma_i + \sigma_0\ (5.5–6c)^{1,3}$, where $\sigma_i$ corresponds to the conductivity of poor coals. This dependence, shown in by the dashed line Fig. 3 describes qualitatively the characteristic features of the experimental dependence $\sigma(c)$. In the regions far from the concentration $c_{cr} \approx 92\%$, the dependence of conductivity on carbon concentration should be linear.

We should like to emphasize that the results of modeling are in a fairly good agreement with the data of the chemical analysis, which yielded the same numbers of aromatic rings and the degrees of aromatization in coals at various degrees of metamorphism [2]. This also confirms the adequacy of the model that describes the molecular structure of coals with various degree of metamorphism developed in this study.

## REFERENCES

1. V. V. Grechukhin, *The Study of Coal-Bearing Formations by Geophysical Methods* (Nedra, Moscow, 1980).

2. Ya. Yurkevich and S. Rosin'skiĭ, *Chemistry of Coals* (Nedra, Moscow, 1973).
3. S. G. Gigirin and G. B. Skripchenko, Khim. Tverd. Topl. (Moscow), No. 3, 3 (1986).
4. P. W. Atkins, *Molecules* (HPHLP Division, New York, 1987; Nauka, Moscow, 1991).
5. V. N. Saranchuk, A. T. Airuni, and K. E. Kovalev, *Supramolecular Organization, Structure, and Properties of Coal* (Naukova Dumka, Kiev, 1988).
6. *Proceedings of the 24th International Conference of Research Institutes Working for Safety of Mining Industry, Donetsk, 1991* (Donetsk, 1991).
7. L. D. Landau and E. M. Lifshitz, *Theoretical Physics, vol. 5: Statistical Physics* (Nauka, Moscow, 1964; Pergamon Press, Oxford, 1960).
8. A. P. Éfros, *Physics and Geometry of Disorder* (Kvant, Moscow, 1982).
9. J. M. Ziman, *Models of Disorder* (Cambridge University Press, Cambridge, 1979; Mir, Moscow, 1982).
10. P. R. Wallace, Phys. Rev. B: Condens. Matter **71**, 623 (1947).

*Translated by A. V. Zalesskiĭ*

*Crystallography Reports, Vol. 45, No. 2, 2000, pp. 282–287. Translated from Kristallografiya, Vol. 45, No. 2, 2000, pp. 313–318.*


**PHASE TRANSITIONS**

# New Type of a Shear Surface Acoustic Wave in Piezoelectric Crystals

**S. V. Tarasenko**

*Donetsk Physicotechnical Institute, National Academy of Sciences of Ukraine, Donetsk, 340114 Ukraine*

Received March 18, 1998; in final form, July 20, 1998

**Abstract**—The study of a phase transition from para- to ferroelectric state has shown that the three-dimensional dispersion in the nonpolar phase of the piezoelectric medium results in the formation of a new type of a shear surface acoustic wave whose dispersion characteristics drastically change in the vicinity of the phase transition.


Of special importance in the studies of the critical dynamics of phase transitions in optically nontransparent polarized crystals by the methods of surface optical spectroscopy is the determination of those types of surface excitations whose characteristics undergo considerable changes in the vicinity of a phase transition [1]. It is shown [2] that in the phase transitions from the para- to the ferroelectric state, the consistent description of the transition dynamics in the vicinity of the Curie point $T_C$ requires the allowance for interactions between the soft optical mode and the acoustic phonons. In this case, with the approach to $T_C$ ($T \longrightarrow T_C + 0$), the spectrum of the soft optical mode for the model of an infinite crystal acquires an "elastic gap" [2]. The conditions of a drastic decrease of the velocity (down to zero on the line of a second-order phase transition) and an increase in the attenuation of the Rayleigh-type surface acoustic wave (SAW) at the mechanically free boundary of the piezoelectric in the vicinity of the proper phase transition were indicated in [3]. For a one-component ferroelelastic phase transition, this phenomenon is observed if the directions, which are mutually perpendicular in the **k**-space (in an infinite crystal, to these directions there correspond anomalously divergent critical fluctuations), would coincide with the surface normal $n$ of the piezoelectric and the direction of the propagation of elastic vibrations in the boundary plane $\mathbf{k}_\perp$. A similar situation is also observed for the dispersion characteristics of the Bleustein–Gulyaev-type shear surface acoustic waves in the structural phase transitions associated with softening of acoustic phonons [4]. Such a SAW can exist at a mechanically free boundary of a dielectric crystal only if (i) the crystal symmetry is described by one of the 6*mm*, 4*mm*, 43*m*, 23, *mm*2, and ∞*m* classes [5], (ii) the direction of the propagation of the shear SAW coincides with the direction along which an anomalous increase of critical fluctuations in the model of an infinite crystal occurs at $T \longrightarrow T_C$.

If none of the above conditions is met, no Rayleigh or Bleustein–Gulyaev-type SAWs with the dispersion characteristics substantially varying in the vicinity of the bulk structural phase transition can be generated at all. A similar situation also takes place for SAWs in the case of dipole-active structural transitions in polarized media (i.e., the media possessing magnetic or electric dipole moments).

Up to now, one usually neglected the effect of the three-dimensional dispersion on the conditions of SAW generation in polar crystals undergoing bulk ferroelastic structural phase transitions. At the same time, it is well known that, with due regard for the finite dimensions of a real specimen, the analysis of the dynamic phenomena related to the soft mode should be performed with due regard for both three-dimensional medium dispersion and lattice effect in the vicinity of the proper ferroelastic phase transition [6, 7].

Below, it is shown that the three-dimensional dispersion of the soft mode may result in the formation of a new type of a shear surface acoustic wave in the vicinity of a mechanically free surface of a piezoelectric crystal in the paraelectric phase. The dispersion characteristics of this type of surface acoustic waves experience considerable changes in the vicinity of the proper ferroelastic phase transition.

The first section of the article is devoted to the basic relationships and formulation of the boundary-value problem of determining a spectrum of normal acoustic vibrations in the model of a semi-infinite piezolectric crystal with due regard for the three-dimensional dispersion. The second section is devoted to the classification of possible types of propagating ferroacoustic excitations for a one-component ferroelectric phase transitions depending on the degree of their proximity to the surface of a piezoelectric crystal. In this case, we assumed that the displacement vector of the lattice, **u**, is normal to the directions of both wave propagation and surface normal **n**. In the next section, the conditions of the generation of a surface acoustic SH-wave

1063-7745/00/4502-0282$20.00 © 2000 MAIK "Nauka/Interperiodica"

induced by the three-dimensional dispersion are analyzed together with its dispersion properties. The calculation is performed for two types of elastic boundary conditions important for practice—for a mechanically free surface of a piezoelectric crystal and a rigidly glued piezoelectric–dielectric interface. We formulate a criterion which provides the determination of the conditions for generation of a new type of a shear SAW from the analysis of the spectrum of a soft optical mode of an infinite piezoelectric crystal. Finally, we present the conclusions drawn from the analysis of the results obtained.

## BASIC RELATIONSHIPS

As an example, consider a piezoelectric crystal described by the sp. gr. $D_{2d}$ with the known dispersion characteristics of a Rayleigh-type SAW in the vicinity of the Curie point of the bulk proper ferroelastic phase transition [3]. The corresponding density of the thermodynamic potential can be represented in the form [3]

$$\begin{aligned} W &= \frac{1}{2}\kappa^2(\nabla P_z)^2 + \frac{a}{2}P_z^2 + \frac{a_\perp}{2}P_1^2 + \gamma_{36}P_z u_{xy} \\ &+ \gamma_{14}(P_x u_{yz} + P_y u_{xz}) + \frac{c_{11}}{2}(u_{xx}^2 + u_{yy}^2) + \frac{c_{33}}{2}u_{zz}^2 \\ &+ c_{12}u_{xx}u_{yy} + c_{13}(u_{xx} + u_{yy})u_{zz} + 2c_{66}u_{xy}^2 \\ &+ 2c_{44}(u_{xz}^2 + u_{yz}^2), \end{aligned} \tag{1}$$

where $\nabla \equiv (\partial/\partial x, \partial/\partial y, \partial/\partial z)$, $\mathbf{P}$ is the polarization vector, $\kappa$ is the parameter of the gradient energy, $a_\perp^{-1}$ is the polarizability in the $XY$ plane, $a^{-1}$ is the polarizability along the $0Z$-axis, $a = a_1(T - T_C)$ [3], $\gamma_{ik}$ are the coefficients of the piezoelectric interaction, $\hat{c}$ is the tensor of elastic constants, and $u_{ik}$ is the tensor of elastic strains.

Similar to the case considered in [6–8], in order to simplify the necessary calculations, we limit ourselves to the approximation $|P_z| \gg |P_\perp|$ corresponding to the condition that the longitudinal susceptibility considerably exceeds the transverse susceptibility (a one-component ferroelectric phase transition). Then the dynamics of the model of the piezoelectric crystal under consideration is described by a closed system of equations including the equation of motion for the $z$ component of the polarization vector $\mathbf{P}$ and the equations of the elasticity theory

$$f\frac{\partial^2 P_z}{\partial t^2} = \frac{\partial W}{\partial P_z}, \quad \rho\frac{\partial^2 u_i}{\partial t^2} = \frac{\partial^2 W}{\partial u_{ik}\partial x_k}, \tag{2}$$

where $f$ is the coefficient corresponding to the effective mass [9] and $\rho$ is the crystal density.

We also assume that the surface ($\eta = 0$) of a semiinfinite piezoelectric crystal ($\eta < 0$, where $\eta$ is the current coordinate along the surface normal $\mathbf{n}$) forms a rigid glued interface between the substrate and a nonpolarized dielectric coating of thickness $d$. If the external surface of this coating ($\eta = d$) is mechanically free, the corresponding system of boundary conditions for $P_z$, the tensor of elastic stresses $\sigma_{ik}$, and the displacement vector of the lattice, $\mathbf{u}$, can be represented in the form

$$\begin{aligned} \kappa\frac{\partial P_z}{\partial \eta} - \delta P_z = 0, \ \sigma_{ik}n_k = \tilde{\sigma}_{ik}n_k, \ \eta = 0, \\ \mathbf{u}(0) = \tilde{\mathbf{u}}(0), \ \tilde{\sigma}_{ik}n_k(\eta = d) = 0, \end{aligned} \tag{3}$$

where $\delta$ is the constant of the uniaxial surface anisotropy [9], and a tilde indicates a nonpolar dielectric medium.

To simplify the calculations and to make the representation clearer, we assume that a nonpolar dielectric at $0 < \eta < d$ is an elastically isotropic medium with the Lamé coefficients $\lambda$ and $\mu$. Since our aim is to analyze the surface dynamics of the medium under study, then, in addition to conditions (3), the following conditions should also be fulfilled

$$\rho_z(-\infty) \longrightarrow 0; \ |\mathbf{u}(-\infty)| \longrightarrow 0, \tag{4}$$

where $\rho_z$ is a small deviation of $P_z$ from its equilibrium value.

At $T > T_C$, $\mathbf{k} \in XZ$, and $\mathbf{u} \parallel 0Y$, the dispersion equation determining the spectrum of normal piezoacoustic vibrations with the participation of the soft optical mode in the model of an infinite crystal (1) is represented in the form

$$\begin{aligned} (\omega_0^2 + \kappa_*^2\mathbf{k}^2 + \omega_{me}^2 - \omega^2)(c_{66}^*(k_x^2 + \alpha k_z^2) - \omega^2) \\ - \omega_{me}^2 c_{66}^* k_x^2 = 0, \end{aligned} \tag{5}$$

where $\mathbf{k}^2 \equiv k_x^2 + k_z^2$, $\omega_0^2 \equiv a/f$; $\omega_{me}^2 \equiv \gamma_{36}^2(c_{66}f)$; $\alpha \equiv c_{44}/c_{66}$, $c_{44}^* \equiv c_{44}/\rho$, $c_{66}^* \equiv c_{66}/\rho$, and $\kappa_*^2 \equiv \kappa^2/f$, whence it follows, in particular, that a three-dimensional structure $u_y$ satisfying (3) and (4) is a two-partial-type wave

$$\begin{aligned} u_y &= \sum_{j=1}^{2} A_j \exp(q_j\eta)\exp(i\omega t - ik_\perp r_\perp), \\ q_{1,2}^2 &= \frac{P_1}{2} \pm \left(\left(\frac{P_1}{2}\right)^2 - P_2\right)^{1/2}, \end{aligned} \tag{6}$$

where $\eta < 0$; $k_\perp = k_z$, and $r_\perp = z$ at $\mathbf{n} \parallel 0X$ and $k_\perp = k_x$, $r_\perp = x$ at $\mathbf{n} \parallel 0Z$, and $A_1$ and $A_2$ are arbitrary constants.

In the case $\mathbf{n} \parallel 0X$ ($\mathbf{k} \in XZ$), the $P_{1,2}$ values are deter-

mined by the following relationships

$$P_1 = \frac{\omega_0^2 + \kappa_*^2(1+\alpha)k_\perp^2 - \omega^2\left(1 + \kappa_*^2/c_{66}^*\right)}{\kappa_*^2},$$
$$P_2 = \frac{\omega_0^2 + \kappa_*^2 k_\perp^2 + \omega_{me}^2 - \omega^2}{\kappa_*^2}\left(\alpha k_\perp^2 - \frac{\omega^2}{c_{66}^*}\right) \quad (7)$$

and, in the case $\mathbf{n} \parallel 0Z$ ($\mathbf{k} \in XZ$), by the relationships

$$P_1 = \frac{\kappa_*^2(1+\alpha)k_\perp^2 + (\omega_{me}^2 + \omega_0^2)\alpha - \omega^2(\alpha + \kappa^2/c_{66}^*)}{\kappa_*^2\alpha},$$
$$P_2 = \frac{(\omega_0^2 + \kappa_*^2 k_\perp^2 + \omega_{me}^2 - \omega^2)(k_\perp^2 - \omega^2/c_{66}^*) - \omega_{me}^2 k_\perp^2}{\kappa_*^2\alpha}.$$

Assuming that the vibration frequencies ω and the wave-vector $\mathbf{k}_\perp$ component tangential to the surface are set by the external parameters and invoking (6) and (7), one can classify possible types of propagating ferroacoustic vibrations depending on the type of their three-dimensional localization in the vicinity of the specimen surface.

## CLASSIFICATION OF POSSIBLE TYPES OF PROPAGATING FERROELASTIC EXCITATIONS

The analysis of equations (6) and (7) in the case, where $\mathbf{k} \in XZ$ ($u_y \neq 0$), shows that two-partial surface ferroelastic excitations ($q_{1,2}^2 > 0$) can be generated in a piezoelectric crystal only if the frequency ω and the wave number $k_\perp$ at $\mathbf{n} \parallel 0X$ satisfy one of the following systems of equations

$$\omega^2 < \omega_-^2(k_\perp),\ k_c^2 \le k_\perp^2 \le k_0^2,$$
$$\omega^2 \le c_{44}^* k_\perp^2,\ 0 \le k_\perp^2 \le k_c^2,\ k_c^2 \equiv \frac{\omega_0^2}{\alpha c_{66}^* - \kappa_*^2},$$

$$\omega_+^2(k_\perp) \le \omega^2 \le \omega_0^2 + \omega_{me}^2 + \kappa_*^2 k_\perp^2,\ k_\perp > k_*,$$
$$k_*^2 \equiv \left(\omega_0^2 + \omega_{me}^2\frac{c_{66}^* + \kappa_*^2}{\kappa_*^2}\right)\left(\alpha c_{66}^* - \kappa_*^2\right)^{-1},$$

$$\omega_\pm^2(k_\perp) = \frac{B}{2A} \pm \left(\left(\frac{B}{2A}\right)^2 - C\right)^{1/2},\ A \equiv \left(1 - \frac{\kappa_*^2}{c_{66}^*}\right)^2, \quad (8)$$

$$B \equiv 2\left(1 + \frac{\kappa_*^2}{c_{66}^*}\right)[\omega_0^2 + \kappa_*^2(1+\alpha)k_\perp^2]$$
$$- 4\kappa_*^2\left[\frac{\omega_0^2 + \omega_{me}^2 + \kappa_*^2 k_\perp^2}{c_{66}^*} + \frac{\alpha k_\perp^2}{\kappa_*^2}\right],$$
$$C \equiv (\omega_0^2 + \kappa_*^2(1+\alpha)k_\perp^2)^2$$
$$- 4\kappa_*^2\alpha k_\perp^2(\omega_0^2 + \kappa_*^2 k_\perp^2 + \omega_{me}^2),$$

where $k_0$ is given by the condition $\omega_-^2(k_0) = 0$.

The condition for a generalized two-partial traveling ferroacoustic surface wave ($\mathrm{Re}\, q_{1,2}^2 \neq 0$; $\mathrm{Im}\, q_{1,2}^2 \neq 0$) at $\mathbf{k} \in XZ$ and $\mathbf{n} \parallel 0X$ for model (1) has the form

$$\omega_-^2(k_\perp) \le \omega^2 \le \omega_+^2(k_\perp),\ k_\perp \ge k_c. \quad (9)$$

Two-partial pseudosurface ($q_1^2 > 0$, $q_2^2 < 0$) excitations in this piezoelectric crystal can be generated only if

$$c_{44}^* k_\perp^2 \ge \omega^2 \ge \omega_0^2 + \omega_{me}^2 + \kappa_*^2 k_\perp^2,$$
$$k_\perp^2 \ge k_{00}^2 \equiv \frac{\omega_0^2 + \omega_{me}^2}{\alpha c_{66}^* - \kappa_*^2}, \quad (10)$$

$$c_{44}^* k_\perp^2 \le \omega^2 \le \omega_0^2 + \omega_{me}^2 + \kappa_*^2 k_\perp^2,\ k_\perp^2 < k_{00}^2.$$

Two-partial bulk ferroacoustic vibrations ($q_{1,2}^2 < 0$) at $\mathbf{k} \in XZ$ and $\mathbf{n} \parallel 0X$ are generated at ω and $k_\perp$ satisfying the following relationships

$$\omega^2 \ge \omega_0^2 + \omega_{me}^2 + \kappa_*^2 k_\perp^2,\ k_\perp^2 < k_{00}^2,$$
$$\omega^2 > c_{44}^* k_\perp^2,\ k_\perp^2 \ge k_{00}^2,$$
$$\omega_0^2 + \omega_{me}^2 + \kappa_*^2 k_\perp^2 > \omega^2 > \omega_+^2(k_\perp),\ k_{00}^2 < k_\perp^2 < k_*^2, \quad (11)$$
$$c_{44}^* k_\perp^2 > \omega^2 > \omega_+^2(k_\perp),\ k_c^2 < k_\perp^2 < k_{00}^2.$$

The analysis of equations (6) and (7) shows that if $\mathbf{k} \in XZ$ and $\mathbf{n} \parallel 0Z$, then only bulk ($q_{1,2}^2 < 0$) excitations are possible at $\omega^2 \ge \omega_A^2$ and only surface ($q_{1,2}^2 > 0$) two-partial ferroelastic excitations with $\mathbf{u} \perp \mathbf{k}$ are possible at $\omega^2 \le \omega_B^2$. If $\omega_B^2 \le \omega^2 \le \omega_A^2$, then the elastic wave propagating along the crystal surface is a two-partial pseudosurface piezoacoustic wave ($q_1^2 > 0$, $q_2^2 < 0$).

The characteristic frequencies $\omega_{A,B}$ are the positive roots of the following equation ($\mathbf{k}_\perp \parallel 0X$):

$$(\omega_0^2 + \kappa_*^2 k_\perp^2 + \omega_{me}^2 - \omega^2)\left(k_\perp^2 - \frac{\omega^2}{c_{66}^*}\right) - \omega_{me}^2 k_\perp^2 = 0. \quad (12)$$

However, the domains of existence of a ferroacoustic wave with $\mathbf{k} \in XZ$ and $\mathbf{u} \parallel 0Y$ localized in the vicinity of the piezoelectric surface for $\mathbf{n} \parallel 0X$ and $\mathbf{n} \parallel 0Z$ should be considered as the necessary but not sufficient condition of their generation. The dispersion relationship for a surface acoustic wave propagating along the piezoelectric boundary is a condition for the existence of a nontrivial solution of the boundary-value problem (3) and (4) with respect to the unknown amplitudes $A_{1,2}$ for the three-dimensional structure $u_y$ of the form (6), (7).

## GENERALIZED SHEAR SURFACE ACOUSTIC WAVE

Since none of the types of shear SAWs considered earlier for a model of a piezolectric (1) in the geometry where $\mathbf{k} \in XZ$, $\mathbf{n} \parallel 0X$, and $\mathbf{u} \parallel 0Y$ in the vicinity of the proper ferroelastic phase transition, the further analysis of the boundary-value problem (3), (4) is performed here just for this geometry. The calculation shows that for any $d \neq 0$ ($\delta = 0$), the corresponding dispersion equation, with due regard for (6) and (7), can be represented in the form

$$\left(k_\perp^2 - \frac{\omega^2}{c_{44}^*}\right)\left(q_1^2 + q_2^2 + q_1 q_2 - \alpha k_\perp^2 + \frac{\omega^2}{c_{66}^*}\right) + \tilde{k}_\perp \tanh(\tilde{k}_\perp d)\frac{\mu}{c_{44}} q_1 q_2 (q_1 + q_2) = 0, \quad (13)$$

where $s$ is the minimum phase velocity of shear elastic wave propagation in an elastically isotropic medium at $d > \eta > 0$ and $\tilde{k}_\perp^2 \equiv k_\perp^2 - \omega^2 \tilde{\rho}/s^2$.

One can readily show that the spectrum of the given surface acoustic wave terminates at the point lying in the range of small wave numbers

$$k_\perp^2 = k_c^2, \quad \omega^2 = \omega_0^2 \frac{\alpha c_{66}^*}{\alpha c_{66}^* - \kappa_*^2}. \quad (14)$$

In the general form, the solution of (13) for arbitrary values of $\omega$, $k_\perp$, and $d$ can be obtained only by numerical methods; therefore, in what follows, we limit ourselves to solving (13) only in practically important particular cases. As shows the analysis, at $d = 0$ and $\delta = 0$ (mechanically free isotropic surface of a piezoelectric having no surface anisotropy[1]), the exact solution of (13) in the explicit form can be determined at an arbitrary value of the wave number $|\mathbf{k}_\perp|$:

$$\omega_s^2(k_\perp) = \frac{N_1}{2} + \left(\left(\frac{N_1}{2}\right)^2 - N_2\right)^{1/2},$$

$$N_1 = \frac{2\tilde{\omega}_0^2 - \alpha\kappa_*^2 k_\perp^2 - \kappa_*^2(\tilde{\omega}_0^2 + \omega_{me}^2)/c_{66}^*}{1 - \kappa_*^2/c_{66}^*}, \quad (15)$$

$$\tilde{\omega}_0^2 \equiv \omega_0^2 + \kappa_*^2 k_\perp^2,$$

$$N_2 = \frac{\tilde{\omega}_0^4 - \alpha\kappa_*^2 k_\perp^2(\omega_{me}^2 + \tilde{\omega}_0^2)}{1 - \kappa_*^2/c_{66}^*}.$$

To be sure that this solution really describes a shear SAW, compare the dispersion relationship (15) with the classification of possible types of ferroacoustic waves (6)–(10) propagating along the surface of a piezoelectric crystal. The analysis shows that dispersion relationship (15) obtained at $k_\perp < k_{**}$ [$\omega_s(k_{**}) = \omega_+(k_{**})$] is a generalized two-partial surface elastic SH-wave with $\mathrm{Re}\, q_{1,2}^2 \neq 0$ and $\mathrm{Im}\, q_{1,2}^2 \neq 0$. At $k_\perp = k_{**}$, the corresponding dispersion curve is smoothly transformed into the dispersion curve for a two-partial surface acoustic wave with $q_{1,2}^2 > 0$ generated at $k_\perp > k_{**}$. Thus, the character of the three-dimensional localization of the determined shear elastic surface wave (15) in the vicinity of the piezoelectric boundary depends on its wave number $|\mathbf{k}_\perp|$. Introducing the notation $q_{1,2} = q_r \pm iq_i$ ($q_i \neq 0$ at $\mathrm{Re}\, q_{1,2}^2 \neq 0$ and $\mathrm{Im}\, q_{1,2}^2 \neq 0$), we see that (6) and (7) yield for the SAW under study, which is described by (15) at $\omega = \omega_s$

$$q_r^2 = \frac{1}{2}\left(P_2^{1/2} + \frac{P_1}{2}\right), \quad q_i^2 = \frac{1}{2}\left(P_2^{1/2} - \frac{P_1}{2}\right). \quad (16)$$

A generation of such type of SAWs on a mechanically free surface of the crystal without the three-dimensional medium dispersion ($\kappa = 0$) is impossible.

From (13), it also follows that the type of the surface SH-phonon established for the polarized medium can also exist in the another limiting case, namely, at $d \longrightarrow \infty$, corresponding to the piezoelectric–nonpolarized dielectric interface, where, at $x = 0$, the conditions of acoustic continuity are fulfilled, and the surface anisotropy is absent ($\delta = 0$). Now, the dispersion law for the surface acoustic SH-wave cannot be determined in the explicit form from (13) at an arbitrary value of the wave number $k$. However, in the short-wavelength approximation ($k_\perp \gg k_*$), the corresponding expressions for the spectrum of a SAW propagating along the piezoelectric–nonpolarized dielectric interface can be repre-

[1] In this paper, we neglect the surface effects [10] and consider only the classical boundary conditions.

sented in the form

$$\omega^2 = \tilde{\omega}_0^2 + \omega_{me}^2 - \Delta^2, \quad (17)$$

$$\Delta(k_\perp) = \omega_{me}^2\left[\kappa_* k_\perp \alpha^{1/2}\left(1 + \frac{\mu}{c_{44}}\alpha^{1/2}\tanh(k_\perp d)\right)\right]^{-1}.$$

In both cases, with an approach to the phase-transition point ($T \longrightarrow T_C + 0$), $\omega_0^2 \longrightarrow 0$, and the dynamic characteristics of this type of SAWs show considerable changes in the vicinity of the bulk ferroelastic phase transition. Therefore, in the paraelectric phase of an optically nontransparent piezoelectric crystal this type of surface acoustic excitations can readily be studied by the methods of optical spectroscopy used in the studies of the bulk proper ferroelastic phase transition.

The calculations show that the localization of the surface acoustic wave of this type in the vicinity of the crystal surface also strongly depends on the presence and the nature of the surface anisotropy. In the particular case of strongly pronounced surface anisotropy ($1/\delta = 0$), the type of the shear SAW considered above cannot be generated at all. The dispersion properties of the SAW under study are substantially modified also with the change of the elastic boundary conditions. This is illustrated by the case, where, as earlier, the conditions of acoustic continuity for a dielectric elastically isotropic condition for a coating of thickness $d$ are fulfilled at the surface of a semiinfinite crystal (1) at $\eta = 0$, but, contrary to (3), the external surface ($\eta = d$) is not mechanically free but is rigidly fixed, i.e., $\mathbf{u}(\eta = d) = 0$. Then, if all the other relationships of the boundary-value problem (3), (4) are the same, the corresponding dispersion equation for a SAW of the type under study with due regard for (6) and (7) at $\mathbf{n} \parallel 0X$, $\mathbf{k} \in XZ$, and $\mathbf{u} \parallel 0Y$ can be represented in the form

$$\left(k_\perp^2 - \frac{\omega^2}{c_{44}^*}\right)\left(q_1^2 + q_2^2 + q_1 q_2 - \alpha k_\perp^2 + \frac{\omega^2}{c_{66}^*}\right) + \tilde{k}_\perp \coth(\tilde{k}_\perp d)\frac{\mu}{c_{44}} q_1 q_2 (q_1 + q_2) = 0. \quad (18)$$

Limiting ourselves, as earlier, to the short-wavelength limit, we can represent the solution of (18) in form (17) within the accuracy of the substitution $\tanh(k_\perp d) \longrightarrow \coth(k_\perp d)$. Relationships (17) and (18) also determine the spectrum of a new type of an acoustic wave with a gap. Phonons of this type are localized in a nonpolar dielectric layer of thickness $2d$ whose both surfaces have a continuous acoustic contact with the semiinfinite piezoelectric medium (1).

In the case of acoustic continuity of the piezoelectric–nonpolar dielectric interface, one can establish a direct analogy between the conditions for the generation of a SAW and the surface magnetic TE polaritons [11]. The surface acoustic wave of the type under study is generated due to coupling of the soft optical mode and a shear elastic wave polarized normally to the sagittal plane in the presence of a quasi-two-dimensional defect (crystal surface).

As is shown in [12], the surface of the wave vectors of normal vibrations of an infinite crystal is an important characteristic of its interaction with the crystal surface. In connection with this, of practical interest is the establishment of the criterion for a spectrum of the soft optical mode of the piezoelectric under study, which would provide the generation of the type of a SAW considered above (15), (17) along the selected direction of the elastic-wave propagation [$\omega/ck_\perp \longrightarrow 0$; $c \equiv \max(c_{66}, c_{44})$] on its surface. Using (5), consider the structure of isofrequency surface of the soft optical mode in the model of an infinite piezoelectric (1) in the elastostatic approximation:

$$k^2 = \frac{\omega^2 - \omega_0^2 - \omega_{me}^2\cos^2\vartheta}{\kappa_*^2},\ \cos^2\vartheta \equiv \frac{c_{44}k_z^2}{c_{66}k_x^2 + c_{44}k_z^2}. \quad (19)$$

The analysis shows that at

$$\omega^2 \le \omega_0^2 + 2\omega_{me}^2, \quad (20)$$

the sign of the surface curvature changes without breaking the continuity. The maximum curvature is attained for the directions in the **k**-space, that correspond to the condition

$$\vartheta = 0, \pi. \quad (21)$$

As follows from (6)–(10), the condition $k_\perp = k_* \cong \omega_{me}/\kappa_*$ and $\omega^2 \cong \omega_0^2 + 2\omega_{me}^2$ in the elastostatic approximation corresponds to the point where the boundaries of the domains of existence of two-partial surface ($q_{1,2}^2 > 0$), bulk ($q_{1,2}^2 < 0$), and pseudosurface ($q_1^2 > 0$; $q_2^2 < 0$) elastic SH waves merge together in the plane of the parameters $\omega$ and $k_\perp$ at $\mathbf{n} \parallel 0X$ ($\mathbf{k} \in XZ$).

Comparing (20) and (21) with (6)–(10) and (15) and (16), we see that the existence of a region with the maximum negative curvature on the isofrequency surface of the optical mode in an infinite crystal for the given propagation direction of an acoustic SH wave can be considered as the sufficient condition for generation of the traveling surface acoustic wave of the SH-type in the specimen satisfying the boundary conditions (3) and (4).

## CONCLUSION

Thus, the results obtained allow us to draw the following conclusions:

(i) The successive allowance for the three-dimensional dispersion still in the paraelectric phase of a piezoelectric crystal is consistent with the generation of a new type of shear surface acoustic wave in the vicinity of the bulk ferroelastic phase transition.

(ii) For a mechanically free surface in the absence of surface anisotropy, the spectrum of this new SAW can be determined in the explicit form for any arbitrary value of the wave number $k_\perp$.

(iii) There exists a one-to-one correspondence between the shape of the corresponding section of the isofrequency surface of the soft optical mode for an infinite piezoelectric crystal and the generation of a new type of shear surface acoustic wave whose frequency is softened in the vicinity of the bulk proper ferroelastic phase transition.

(iv) If a crystal possesses no piezoelectric properties, the bilinear relation between the order parameter and the deformation tensor, which provides the generation of such a surface acoustic wave can be induced by electrostriction caused by an external field applied to the crystal.

A similar mechanism of generation of surface acoustic waves in the vicinity of the Curie point takes place for the paramagnetic phase of a piezomagnetic crystal undergoing a bulk proper ferroelastic phase transition.

## ACKNOWLEDGMENTS

The author is grateful to A.N. Bogdanov and T.N. Tarasenko for their interest in this study and fruitful discussions.

## REFERENCES

1. *Surface Polaritons* [in Russian], Ed. by V. M. Agranovich and D. L. Mills (Nauka, Moscow, 1985).
2. R. Blinc and B. Zeks, *Soft Modes in Ferroelectrics and Antiferroelectrics* (North Holland, Amsterdam, 1974; Mir, Moscow, 1975).
3. S. V. Gerus, I. E. Dikshteĭn, V. V. Tarasenko, *et al.*, Fiz. Tverd. Tela (Leningrad) **19**, 218 (1977).
4. Yu. A. Kosevich and E. S. Syrkin, Fiz. Tverd. Tela (Leningrad) **28**, 248 (1986).
5. I. B. Yakovkin and D. V. Petrov, *Diffraction of Light by Surface Acoustic Waves* [in Russian] (Nauka, Novosibirsk, 1979).
6. A. F. Andreev, Pis'ma Zh. Éksp. Teor. Fiz. **32**, 654 (1980).
7. I. E. Dikshteĭn, Fiz. Tverd. Tela (Leningrad) **28**, 1748 (1986).
8. E. V. Chenskiĭ and V. V. Tarasenko, Zh. Éksp. Teor. Fiz. **83**, 1089 (1982).
9. M. G. Cottam, D. R. Tilley, and B. Zeks, J. Phys. C: Solid State Phys. **17**, 1793 (1984).
10. S. V. Biryukov, Yu. V. Gulyaev, V. V. Krylov, *et al.*, *Surface Acoustic Waves in Inhomogeneous Media* [in Russian] (Nauka, Moscow, 1991).
11. R. E. De Wames and T. J. Wolfram, *J. Appl. Phys.* **41**, 987 (1970).
12. V. M. Balakirev and I. A. Gilinskiĭ, *Waves in Piezocrystals* [in Russian] (Nauka, Novosibirsk, 1982).

*Translated by L. Man*

*Crystallography Reports, Vol. 45, No. 2, 2000, pp. 288–293. Translated from Kristallografiya, Vol. 45, No. 2, 2000, pp. 319–325.*


**PHASE TRANSITIONS**

# Phase Transition and Domain Structure in Iodoform Crystals

**N. V. Sidorov*, Yu. N. Krasyukov**, É. I. Mukhtarova**, and D. M. Shkrabo*****

** Institute of Chemistry and Technology of Rare Elements and Mineral Raw Materials, Kola Research Center, Russian Academy of Sciences, Apatity, Murmansk oblast, 184200 Russia*

*** Research Industrial Association "Kompleks," Rzavki, Moscow oblast, 141552 Russia*

**** Institute of Spectroscopy, Russian Academy of Sciences, Troitsk, Moscow oblast, 142092 Russia*

Received March 18, 1998; in final form, November 11, 1998

**Abstract**—Phase transition in an iodoform crystal has been established from the temperature dependence of the Raman spectra of "external" crystal vibrations at 260 K. The transformation mechanism is interpreted under the assumption on the existence in the crystal of domains where dipole moments of the molecules have parallel or antiparallel orientations. Below the phase-transition temperature, the structure is more ordered, and the crystal consists mainly of domains with the parallel orientation of dipole moments of the molecules, whereas above this point, the domains with the antiparallel orientation of dipole moments prevail. The crystal as a whole is not a pyroelectric. © *2000 MAIK "Nauka/Interperiodica".*

According to the X-ray and neutron diffraction analyses [1–3], the crystal structure of iodoform ($CHI_3$) is characterized by a hexagonal unit cell, sp. gr. $P6_{3/m}$, $Z = 2(C_{3/m})$ and the static (rigid) orientational disorder in the arrangement of dipole molecules—the positions of iodine atoms are fixed, whereas carbon and hydrogen atoms are statistically (with equal probabilities) distributed below and above the planes of iodine atoms (Fig. 1). The molecular dipoles can be either parallel or antiparallel to the crystallographic *c*-axis (with the equal probabilities).

It is well known that the diffraction experiment yields the data averaged over the whole crystal consisting of an infinite number of unit cells. In the actual fact, the structural arrangement of dipole molecules in a iodoform crystal can be much more complicated. In particular, according to dielectric measurements, the α-phase of bromoform, which is isomorphous to iodoform, shows the considerable orientational mobility of the dipole moments [4].

The disorder of the crystal structure is reflected in the range of crystal lattice vibrations in the Raman spectra: one observes line broadening and the change in the parameter characterizing the line shape [5, 6]. The contribution to the line width caused by the static orientational disorder in the molecular arrangement is almost temperature independent. At the same time, the contribution caused by the anharmonic dynamic disorder (molecule reorientations) exponentially increases with the temperature [6]. The simultaneous presence in the Raman spectrum of both contributions can be established from the temperature dependence of these spectra.

Raman spectra were recorded on a modified DSF-24 spectrometer by counting photons at the excitation of the 514.5 nm line with the aid of a 0.02 Wt argon ILA-120 laser. Crystalline iodoform was purified by slow evaporation in vacuum at 300 K. Low-temperature measurements were performed using a cryostat with a special system for precise specimen thermostating [7]. The line parameters were determined using the programs described elsewhere [8]. The spectra were processed in such a way that the area under the total theoretical contour differed from the area under the experimental contour by not more than 5%. The frequencies were determined within an accuracy of ±1 $cm^{-1}$, the line widths, within the accuracy of ±0.3 $cm^{-1}$, and the shape parameters and the line intensities, within ±5 %.

Figure 2 shows the Raman spectra of external vibrations of polycrystalline iodoform at various temperatures. At 77 K, the iodoform spectrum has four lines at the frequencies of 15, 32, 38, and 65 $cm^{-1}$. The line at the frequency 32 $cm^{-1}$ is very narrow ($s < 2$ $cm^{-1}$). Narrow line widths are typical of the spectra of external vibrations of highly ordered molecular crystals. This fact contradicts the assumed static orientational disorder in the arrangement of dipole molecules in the iodoform structure (Fig. 1). All the other lines of the Raman spectrum of these crystals are rather broad, with the line widths being slightly temperature-dependent, which is characteristic of crystals with a rigid static orientational disorder. The temperature dependence of the spectra shows that with an increase of the temperature, the width of the narrow line at 32 $cm^{-1}$ considerably increases and, at 300 K, becomes almost equal to the widths of all the other lines on the Raman spectra of the lattice vibrations.

1063-7745/00/4502-0288$20.00 © 2000 MAIK "Nauka/Interperiodica"

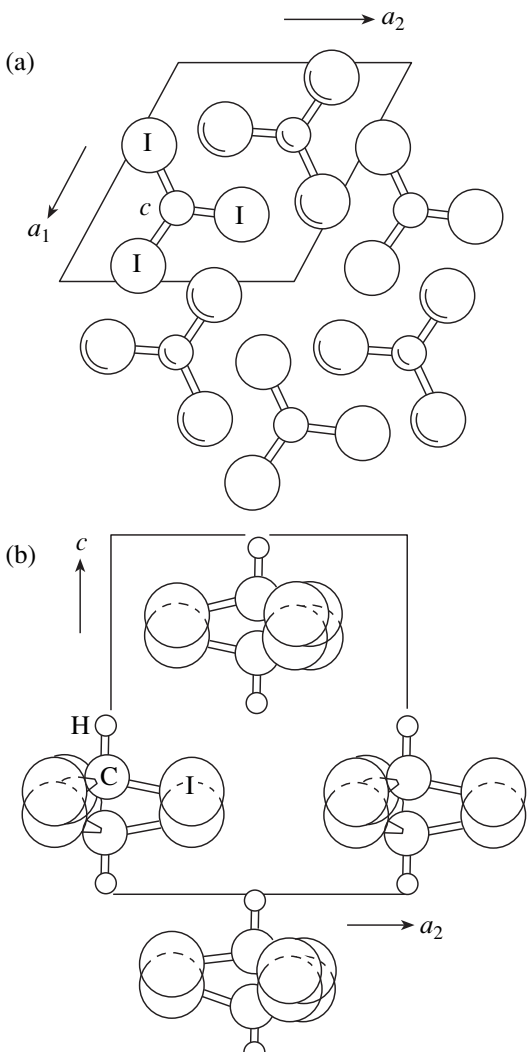


**Fig. 1.** Crystals structures of (a) iodoform and (b) α-bromoform [3, 15].

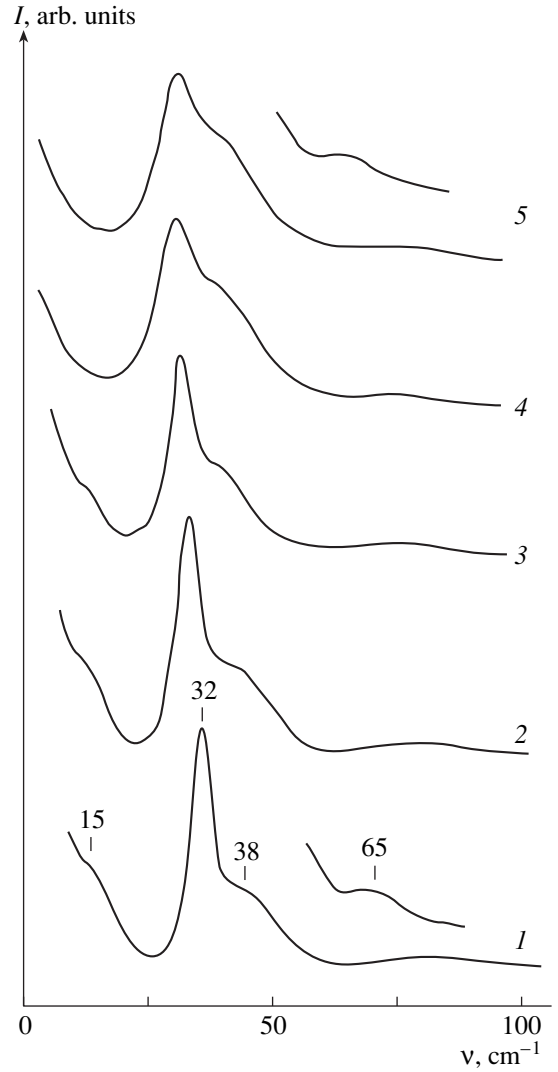


**Fig. 2.** Raman spectra of external vibrations of an iodoform polycrystal at various temperatures: (*1*) 77, (*2*) 160, (*3*) 240, (*4*) 293, and (*5*) 320 K. Frequencies for four spectrum lines are indicated at curve *1*.

The observed changes in the Raman spectra are inconsistent with the assumption about the statistical distribution of the dipole moments of molecules parallel and antiparallel to the crystallographic *c*-axis (Fig. 1).

Such a behavior of the line widths in the Raman spectrum of external vibrations of a iodoform crystal allows us to assume that the structure consists of two types of domains—the orientationally ordered domains with the parallel orientation of the dipole moments of all the molecules and the statically orientationally disordered domains, where the dipole moments of the neighboring molecules are antiparallel to one another. The domains of the first type are polar and possess the dipole moments that can be either parallel or antiparallel to the crystallographic *c*-axis. The domains of the second type have no dipole moments at all. Thus, the Raman spectrum of the external vibrations of a real iodoform crystal is the superposition of the spectra of three different orientationally ordered structures.

The changes in the Raman spectra (Fig. 2) indicate that with an increase of the temperature, the fraction of domains in which the structure is statically orientationally disordered increases, whereas the fraction of the domains with the parallel orientation of dipole moments decreases. There are grounds to believe that the crystal structure inside the domains with the parallel orientation of dipole moments is ordered and characterized by the polar space group $P6_3$, $Z = 2(C_3)$. According to the X-ray diffraction data, the unit cell of an iodoform crystal with completely ordered structure should be described by this space group as well and the dipole moments of all the molecules should be parallel to the crystallographic *c*-axis [1, 2]. The crystal struc-

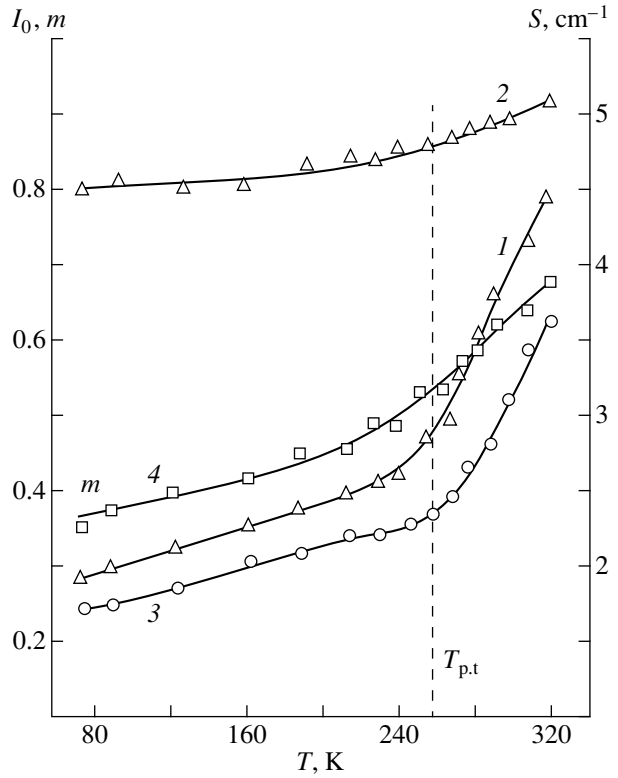


**Fig. 3.** Temperature dependences of the main parameters of the lines at the frequencies 32 and 28 cm$^{-1}$ in the Raman spectrum of external vibrations of an iodoform crystal; (*1*, *2*) the width $s$ of the lines at (*1*) 32 and (*2*) 38 cm$^{-1}$; (*3*) the relative intensity $I_0 = I_1/I_2$, where $I_1$ and $I_2$ are the integrated intensities of the lines at 32 and 38 cm$^{-1}$, respectively, and (*4*) the parameter $m$ characterizing the line shape [8]. For the Gaussian contour $m = 1$; for the Lorentzian contour $m = 0$; for intermediate contours, $0 < m < 1$.

ture inside a domain characterized by the antiparallel orientation of dipole moments is statically orientationally disordered and, thus, can be described by the sp. gr. $P\bar{3}$, $Z = 2(C_3)$ [9]. At a certain ratio of the domains with the parallel and the antiparallel orientations of dipole moments, averaging over the crystal would result in the space group $P6_{3/m}$, $Z = 2(C_{3/m})$. In all the remaining cases, the real iodoform structure corresponds to one of the above structures, depending on the temperature. The ratio of the domains of different types should vary in such a way that the crystal as a whole would remain nonpolar.

Thus, with an increase of the temperature of the iodoform crystal, one can observe the orientational phase transition from the structure with mainly ordered orientations of dipole moments within domains to the structure with mainly antiparallel orientations of dipole moments of the molecules within domains with the accompanying breaking of the pseudosymmetry of the crystal unit-cell. Since the orientations of the dipole moments of molecules are necessarily changed (the activation-type transition), the phase transition should be determined from the temperature dependence of the line width in the Raman spectrum and from the calorimetry and the dielectric spectroscopy data.

The studies of the temperature dependence of the main parameters of the lines in the Raman spectrum of external vibrations of iodoform crystal by the method described in [8] showed that the temperature dependences of line width, relative intensity, and the parameter of the line shape have a pronounced kink at the frequency 32 cm$^{-1}$ in the temperature range 240–280 K (Fig. 3). This may indicate the occurrence of a diffuse phase transition in the crystal accompanied by a considerable increase of the dipole mobility of molecules along the normal to the molecular $C_3$-axis. The temperature dependences of the parameters of a broad line at the frequency 38 cm$^{-1}$ show no pronounced anomalies. The occurrence of the phase transition in crystalline iodoform at 260 K is confirmed by the calorimetry data [10].

The classification of the frequencies of the Raman spectra from ordered organic crystals depending on the type of vibrations is usually performed by calculating the shape and the frequencies of vibrations by the method of atom–atom potentials (AAP) [6]. We calculated the spectrum of external vibrations of a iodoform crystal under the assumption on the existence of hypothetical ordered structures described by space groups $P6_3$ ($Z = 2$) and $P\bar{3}$ ($Z = 2$). In the former space group, an iodoform molecule has the positional symmetry $C_3$. The group-theoretical analysis yields the following representations for the external vibrations:

$$\Gamma_{tr} = B + E_1(\mathrm{R}),$$

$$\Gamma_{libr} = A(\mathrm{R, IR}) + B + E_1(\mathrm{R, IR}) + E_2(\mathrm{R}).$$

The $B$-type vibrations of the vibrational spectrum are inactive. In the second structure, a molecule is also characterized by the positional symmetry $C_3$ and the representations

$$\Gamma_{tr} = A_g(\mathrm{R}) + E_g(\mathrm{R}),$$

$$\Gamma_{libr} = A_g(\mathrm{R}) + E_g(\mathrm{R}) + A_u(\mathrm{IR}) + E_u(\mathrm{IR}).$$

The lattice dynamics for an iodoform crystal were calculated with the use of the atom–atom potential of the (6-exp)-type with the set of parameters suggested for crystalline 1,2-diiodobenzene [11]. Similar calculations were also performed for the crystal of the α-modification of bromoform (isomorphous to iodoform) with the set of parameters suggested in [12] for bromosubstituted methanes. The maximum distance at which the molecular interactions still were taken into account was 9 Å. The lattice energy was minimized over the Eulerian angles of the molecule orientation with the use of the lattice parameters at room temperature [3]. The calculated molecule orientation differed by about three degrees from the experimental by observed orientation [3]. The calculated lattice energies for these two struc-

**Table 1.** Interpretation of the Raman spectrum of external vibrations of iodoform and α-bromoform crystals based on the hypothetical ordered structures described by the space groups $P6_3$ and $P\bar{3}$

| Sp. gr. | Symmetry | Polarization | Experiment, ν, $cm^{-1}$ | | | | Calculation, ν, $cm^{-1}$ | |
|---|---|---|---|---|---|---|---|---|
| | | | $CHBr_3$ | $CHI_3$ | | | $CHBr_3$ | $CHI_3$ |
| $P6_3$ | $A$ | ($YY$) | 60 | 65 | 65* | 36**(IR) | 51 | 57 |
| | $E_1$ | ($YZ$) | 43 | 38 | 38* | 24**(IR) | 29 | 31 |
| | $E_2$ | ($YY$) | 36 | 32 | 32* | | 49 | 35 |
| | $E_2$ | ($YY$) | 22 | 15 | 25* | | 11 | 17 |
| $P\bar{3}$ | $A_g$ | ($YY$) | 60 | 65 | 65* | | 61 | 66 |
| | $A_g$ | ($YY$) | 43 | 38 | 38* | | 54 | 52 |
| | $E_g$ | ($YY$) ($YZ$) | 36 | 32 | 32* | | 36 | 41 |
| | $E_g$ | ($YY$) ($YZ$) | 22 | 15 | 25* | | 25 | 24 |
| | $A_u$ | | | | | | 55 | 56 |
| | $E_u$ | | | | | | 35 | 38 |

* According to [17].
** According to [18].

tures differ only insignificantly and are equal to 14.5 kcal/mol for the structure described by the sp. gr. $P6_3$ and 13.5 kcal/mol for the structure described by $P\bar{3}$. Indirectly, this fact confirms the existence in the iodoform structure with domains characterized by parallel and antiparallel orientations of dipole moments of the molecules. The experimental and the calculated frequencies of external vibrations of iodoform and α-bromoform crystals are listed in Table 1. The calculated iodoform frequencies equal to 66 and 24 $cm^{-1}$ (for the structure described by the sp. gr. $P\bar{3}$) and the 17 $cm^{-1}$ (for the structure described by the sp. gr. $P6_3$) correspond to the translational vibrations, whereas all the remaining frequencies correspond to the libration modes.

It is seen from Table 1 that, proceeding from an assumption that iodoform crystals can have at least one of the hypothetical ordered structures (described by $P6_3$ or $P\bar{3}$), it is impossible to fit the experimentally observed and the calculated frequencies of the spectrum of external vibrations and the states of their polarizations.

At present, such complicated calculations for statically and orientationally disordered iodoform crystals [$P6_{3/m}$, $Z = 2$ ($C_{3/m}$)] with considerably disturbed and temperature-dependent short-range order cannot be performed. However, it is possible to preliminarily identify the lines by comparing the Raman spectra of iodoform with the Raman spectra of a much better studied bromoform.

As is well known, iodoform crystals are isomorphous to the orientationally disordered α-modification of bromoform crystals existing in a narrow (about 10 K) temperature range in the vicinity of the melting point [9, 13–16]. The Raman spectra of external vibrations of poly- and single crystals of these compounds in the polarized light with due regard for a slight frequency shift agree quite well (Table 1) [16]. The detailed interpretation of the spectra of external vibrations of the α-, β-, and γ-modifications of bromoform based on the calculation of the frequencies, type of vibrations, and the barriers for molecule reorientation in the ordered β- and γ-phases by the AAP method is given elsewhere [9]. According to [9], the lines at the frequencies of 43 and 38 $cm^{-1}$ in the spectrum of the α-bromoform, which are preserved during the β–α and γ–α phase transitions, correspond to librations with respect to the axis coinciding with the $C_3$-axis of the molecule and the axis normal to it. Thus, taking into account isomorphism between the α-bromoform and iodoform and the calculated spectra of external vibrations (Table 1), the lines at 38 and 32 $cm^{-1}$ on the iodoform spectrum can be reliably interpreted as those due to librations with respect to the $C_3$-axis of the molecule and the axis normal to it, respectively. According to the calculations performed for a bromoform crystal, the diffuse line at a frequency of 65 $cm^{-1}$ corresponds to the translational vibrations of the molecules along the crystallographic $c$-axis [9]. A considerable width of the line at 65 $cm^{-1}$ (Figs. 2 and 4) additionally confirms the static orientational disorder of dipole moments of the molecules along the $c$-axis in iodoform and α-bromoform crystals.

The data obtained in this study allowed us to refine the isomorphism of the iodoform and α-bromoform crystals. Both low-temperature β- and high-temperature α-modifications of iodoform crystals have the structures similar to that of α-bromoform. However,

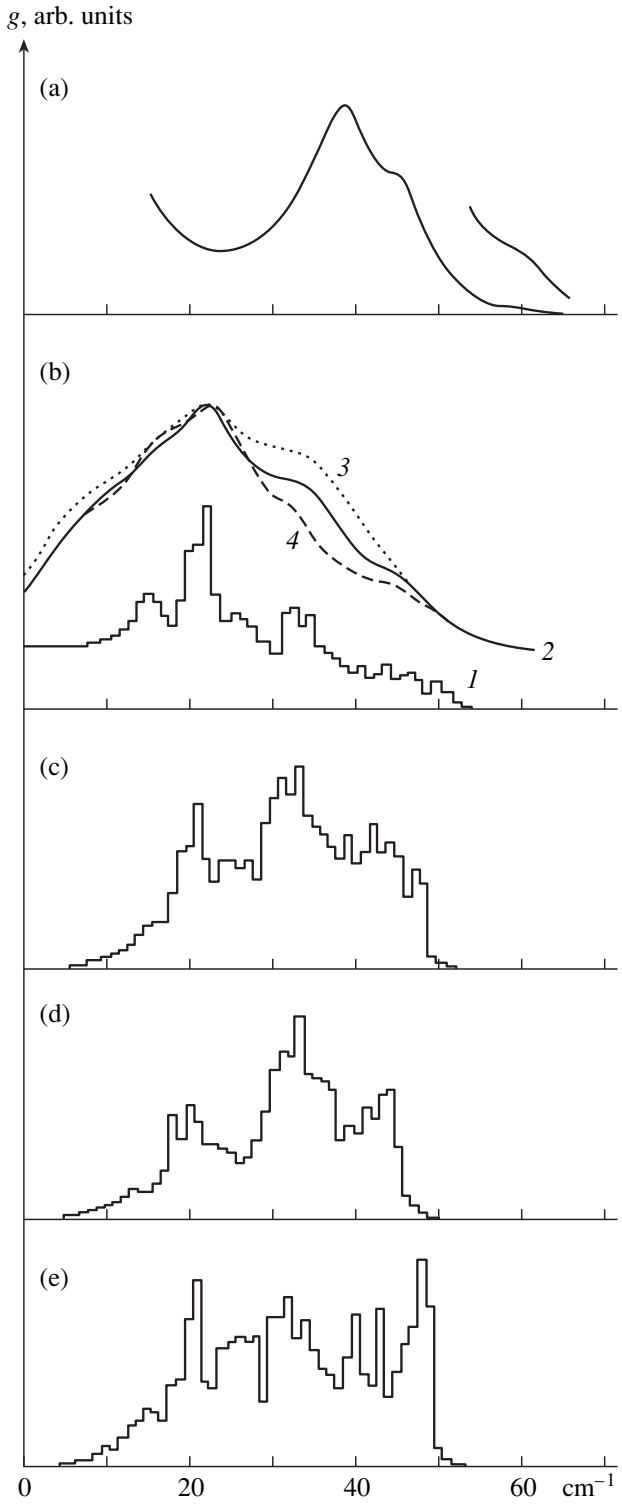


**Fig. 4.** Densities $g$ of the phonon states of differently ordered crystal structures of α-bromoform calculated with the use of the atom–atom potential: (a) the Raman spectrum of the external vibrations of a polycrystals and (b) (*1*) the total and (*2*, *3*, *4*) broadened reduced densities of states corresponding to the hypothetical structures $P6_3 + P\bar{3}$, $P\bar{3}$, and $P6_3$, respectively; (c) $g(\omega) = g_1(\omega) + g_2(\omega)$; (d) $g_2(\omega)$, and (e) $g_1(\omega)$; $T = 275$ K.

the high-temperature iodoform is closest to the α-bromoform, because it is also characterized by an elevated dipole mobility of the molecules. In dipole-ordered low-temperature β-bromoform, the reorientations of the molecules with respect to the axis normal to the $c_3$-axis of the molecule are frozen [16]. In low-temperature β-iodoform, such reorientations are noticeably activated.

The iodoform spectrum (Fig. 2) has a rather broad line at a frequency of 38 cm$^{-1}$ corresponding to molecule vibrations about the molecular axis $c_3$. In the spectrum of α-bromoform, this type of librations is reflected by the line at a frequency 43 cm$^{-1}$ [9], which indicates that, although the reorinetations of the molecules about the $c_3$-axes are rather intense, but they are still not completely activated. One can see from Fig. 3 that the width of this line only slightly depends on the temperature within a rather wide temperature range. This fact indicates that with the change of the temperature, the reorientation barrier with respect to the $c_3$-axis of the molecule (and therefore also the frequency of these reorientations) are almost constant. This can be caused by possible hydrogen bonding in the iodoform structure [17, 18] hindering the molecule reorientation around the $c_3$-axis.

Interpreting the α–β phase transitions in iodoform and bromoform crystals as the transitions between the structures with different kind of the orientational order of dipole moments of the molecules in domains, one can describe the dynamics of such transitions in terms of the calculated densities of phonon states in the crystals. As is well known, the Raman spectrum of a disordered crystal should reflect the main characteristics of the phonon-state densities. We calculated the densities of phonon states $g(\omega)$ for the orientationally disordered α-modification of bromoform using the AAP and the hypothetical ordered structures with the short-range order described by the space groups $P6_3$ and $P\bar{3}$ reflecting the structure within the domains with the parallel and antiparallel orientation of dipole moments of the molecules, respectively. The $g(\omega)$ values were calculated by the method described in detail elsewhere [9, 19]. We scanned the wave vector over the symmetrically independent part of the Brillouin zone at a step of $0.1\pi/a$, where $a$ is the unit-cell parameter. The parameters of the potential used are indicated in Table 2.

The calculated densities of states $g_1(\omega)$ and $g_2(\omega)$ corresponding to the bromoform structures described by $P\bar{3}$ and $P6_3$ are shown in Fig. 4 together with the total density of states $[g_1(\omega) + g_2(\omega)]$, which approximately reflects the spectrum of external vibrations of α-bromoform with the same numbers of domains having the structures described by the space groups $P6_3$ and $P\bar{3}$. Despite the noticeable shift (by about 15 cm$^{-1}$) of the calculated spectrum toward low frequencies in

**Table 2.** Parameters of the atom–atom potential $\varphi_{12} = -A_{12}/r^6 + B_{12}/\exp(-\alpha_{12}/r) + 332.07 q_1 q_2/r$ used in the calculation of the phonon-state densities in α-bromoform crystals [6, 9]

| Type of interactions | $A_{12}$, Å$^6$ kcal/mol | $B_{12}$, kcal/mol | $\alpha_{12}$, Å$^{-1}$ | $q$ |
|---|---|---|---|---|
| H···Br | 555 | 18050 | 3.44 | – |
| C···Br | 730 | 78500 | 3.37 | – |
| Br···Br | 4580 | 14900 | 3.14 | – |

comparison with the experimental one, both spectra agree rather well. The calculated spectrum consists of broad lines with the maxima at 14, 21, 31, and 46 cm$^{-1}$.

The calculations show that the relative intensities of the maxima at a frequency of 31 cm$^{-1}$ considerably differ for two differently oriented ordered structures described by $P6_3$ and $P\bar{3}$ (Fig. 4). These differences can be used for the qualitative estimation of the short-range order and its temperature variations. In particular, these calculations allow one to follow the changes in the ratio of the numbers of domains with the equally and oppositely oriented dipole moments. It is seen from Fig. 4 that the relative intensity of the maximum at 31 cm$^{-1}$ in the transitions from the orientationally disordered structure (described by $P\bar{3}$) to the ordered structure with oriented dipoles (described by $P6_3$) considerably increases, whereas the width of this maximum decreases, which is in good qualitative agreement with the changes observed in the Raman spectrum of iodoform (Fig. 2). Similar temperature variations should also be observed for the the α-bromoform. However, it is impossible to follow the changes in α-bromoform spectrum because of a narrow (~10 K) temperature range of its existence.

Thus, our calculations qualitatively confirmed the gradual increase of the degree of order in iodoform crystals with a decrease of the temperature because of an increased fraction of domains with the equivalently oriented dipole moments of the molecules. The change in the number of domains with ordered dipoles gives rise to the α–β phase transitions in iodoform and bromoform crystals. However, the natures of the transformations in these crystals are different. The α–β phase transition in bromoform proceeds abruptly with the change of the space group at 270 K and is an order–disorder phase transition [13–16], whereas the analogous transition in iodoform is not accompanied by considerable changes in the structure or the pseudosymmetric sp. gr. $P6_{3/m}$, which describes the unit cell of the crystal.

## REFERENCES


1. A. I. Kitaigorodsky, T. L. Khotsyanova, and Yu. T. Struchkov, Dokl. Akad. Nauk SSSR **78**, 1161 (1951).
2. T. L. Khotsyanova, A.I. Kitaigorodsky, and Yu.T. Struchkov, Zh. Fiz. Khim. **27**, 647 (1956).
3. Y. Iwata and T. Watanabe, Ann. Rep. Res. Reactor Inst. Kyoto Univ. **7**, 87 (1979).
4. A. K. Sharma and V. K. Agarwal, Chem. Phys. Lett. **68**, 151 (1979).
5. V. M. Burlakov, Doctoral Dissertation in Physics and Mathematics (Troitsk, 1993).
6. G. N. Zhizhin and E. I. Mukhtarov, *Optical Spectra and Lattice Dynamics of Molecular Crystals. Vibrational Spectra and Structure. A Series of Advances*, Ed. by J.R. Durin (Elsevier, Amsterdam, 1995), Vol. 21.
7. N. V. Sidorov and É. I. Mukhtarov, *Fourier-Spectroscopy and Current Problems of Surface Physics and Chemistry* [in Russian] (Nauka, Moscow, 1989), p. 186.
8. Yu. V. Rakitin, V. M. Mitrofanov, and N. V. Sidorov, Zh. Prikl. Spektrosk. **55**, 693 (1991).
9. É. I. Mukhtarov and Yu. N. Krasyukov, Preprint No. 4, Institute of Spectroscopy, Russian Academy of Sciences (1992).
10. J. Boerio-Goates and B. F. Woodfield, Can. J. Chem. **66**, 645 (1988).
11. C. Faerman and H. Bonadeo, Chem. Phys. Lett. **69**, 91 (1980).
12. A. Gavezzotti and M. Simonetta, Acta Crystallogr., Sect. A: Cryst. Phys., Diffr., Theor. Gen. Crystallogr. **31**, 645 (1975).
13. T. Kawaguchi, K. Takashina, T. Tanaka, *et al.*, Acta Crystallogr., Sect. B: Struct. Crystallogr. Cryst. Chem. **28**, 967 (1972).
14. C. A. Coulson and D. Emerson, Proc. Roy. Soc. A (London) **37**, 151 (1974).
15. R. Myers and B. H. Torrie, J. Chem. Phys. **79**, 1495 (1983).
16. N. V. Sidorov, Yu. N. Krasyukov, É. I. Mukhtarov, *et al.*, Khim. Fiz. **10**, 1320 (1982).
17. P. Dawson and B. I. Berenblat, Spectrochim. Acta A **31**, 1049 (1975).
18. N. Neto, O. Oehler, and R. M. Nexter, J. Chem. Phys. **58**, 5661 (1973).
19. G. Fillippini, C.M. Gramaccioli, M. Simonetta, *et al.*, J. Chem. Phys. **59**, 5088 (1973).


*Translated by L. Man*

*Crystallography Reports, Vol. 45, No. 2, 2000, pp. 294–299. Translated from Kristallografiya, Vol. 45, No. 2, 2000, pp. 326–331.*


**REAL STRUCTURE**

# X-ray Diffraction Study and Quantitative Measurements of High Dislocation Densities in Superlattices and Single Crystal Layers of Heteroepitaxial Systems with Pronounced Lattice Mismatch

**G. F. Kuznetsov**

*Institute of Radio Engineering and Electronics, Russian Academy of Sciences, Fryazino, Moscow oblast, Russia*
*e-mail: gfk217@ire216.msk.su*

Received July 13, 1995; in revised form, June 6, 1995 and March 25, 1998; in final form, April 15, 1999

**Abstract**—Plastic deformation in a single-crystal layer of the $In_{0.12}Ga_{0.88}As/(111)InP$ solid solution is identified by the methods of X-ray diffractometry (XRD) and the double-crystal pseudorocking curves (DCPRC). X-ray topographs showed the generation of three intersecting systems of straight dislocations in the layer. In a one-layer ZnSe/GaAs structure and multilayer $ZnSe/ZnSe_{1-x}S_x/ZnSe/GaAs$ structures, the elastic and plastic strains were detected by the combined XRD–DCPRC method. The major components of the thermoelastic and plastic-deformation tensors were determined as $\varepsilon_{xx} = \varepsilon_{yy} = 3.5 \times 10^{-3}$ and $\varepsilon_{zz} = 2.35 \times 10^{-3}$. Using these data, the dislocation densities were determined as $N_d \sim 2.5 \times 10^8$ cm$^{-2}$ and $N_d \sim 3 \times 10^{10}$ cm$^{-2}$ for the 7 μm-thick ZnSe and 1 μm-thick InAs layers, respectively. In a superlattice of the $Al_xGa_{1-x}As/GaAs/\cdots/$GaAs-type with a large lattice parameter, the plastic deformation was detected. X-ray topography confirmed that the dislocation density in this superlattice equals ~$10^5$ cm$^{-2}$. © *2000 MAIK "Nauka/Interperiodica".*

The main prerequisites for identifying, measuring, and separating the components of elastic and plastic deformation in single-crystal layers of one- and multilayer aperiodic and periodic (superlattice) epitaxial systems were laid in [1, 2] and the following publications [3–9].

It was suggested to identify the elastic and plastic strains in the single-crystal layers of heteroepitaxial systems by the combined method X-ray diffractometry (XRD) and the double-crystal pseudorocking curves (DCPRC) [4, 7–9]. Such curves are obtained on a double-crystal diffractometer with the zero dispersion in the *n*, *–n* geometry using the and θ–2θ scan and any monochromatic (in particular, $CuK_{\alpha_1}$) radiation. In the X-ray diffractometry, scanning is performed with the use of a narrow (50 μm) slit placed in front of the counter window with the flare angle ~3° [4, 7–9]. The standard method of double-crystal rocking curves consists in scanning the specimen by a counter fixed at an angle of 2θ [4].

Identification of plastic deformation in single-crystal layers of heteroepitaxial systems is based on the well-known phenomenon of broadening of X-ray diffraction maxima. In practice, the numerical value of the maximum widths at its halfheight (halfwidth) is often used as an integral characteristic indicating the lattice perfection, especially in epitaxially grown materials [10–12].

As was shown in [4, 7–9], the diffraction maxima on the conventional XRD curves and double-crystal pseudorocking curves from the elastically deformed single-crystal layers almost coincide [8], whereas the maxima widths on double-crystal rocking curves of single-crystal layers with pronounced dislocation density can be several times broader than the analogous maxima on conventional X-ray diffractometry curves [9].

Below, we report the results of our study of single- and multilayer heteroepitaxial $In_{1-x}Ga_xAs/(001)InP$, ZnSe/(001)GaAs, and $ZnSe/ZnSe_{1-x}S_x/ZnSe/(001)GaAs$ systems obtained by deposition of organometallic compounds and also of the $Al_xGa_{1-x}As/GaAs/\ldots/(001)GaAs$-type superlattices grown by the molecular-beam epitaxy (MBE).

Figure 1 shows the X-ray diffraction spectra obtained by the method of double-crystal X-ray diffractometry from the epitaxial $In_{0.88}Ga_{0.12}As/(111)GaAs$ system. It is seen that the width of diffraction maximum *2* for the solid-solution layer obtained by the XRD–DCPRC method (dashed line) exceeds by four times the width of the analogous maximum on the curve obtained by the conventional XRD method (solid line), whereas the widths of maxima *1* from the GaAs substrate on these curves differ much less.

For a more reliable interpretation of this result, we also obtained an X-ray topograph from this heterostructure (Fig. 2) by the method of anomalous transmission

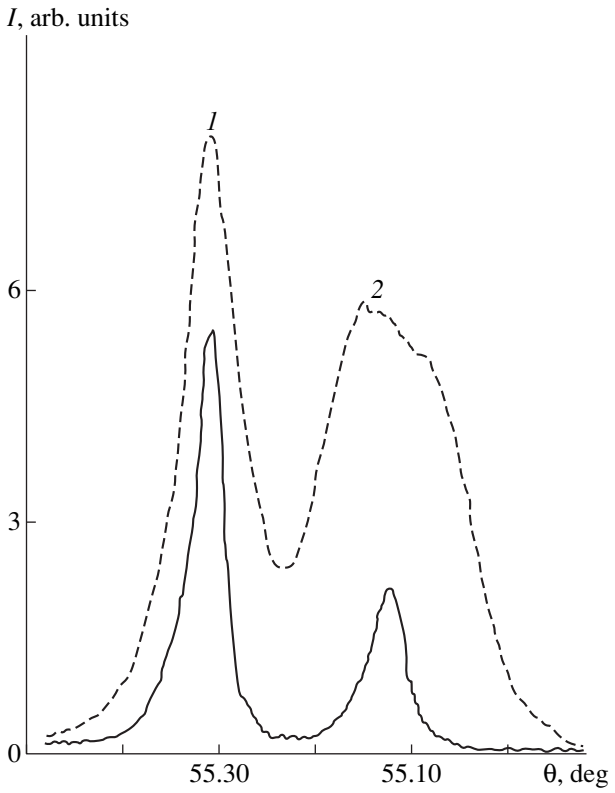


**Fig. 1.** X-ray diffraction spectra obtained in the (333) reflection (Cu$K_{\alpha_1}$ radiation) from the epitaxial $In_{0.88}Ga_{0.12}As$/(111)GaAs system obtained by the DCPRC (dashed lines) and the XRD (solid line) methods. (*1*) The maximum due to the GaAs substrate, (*2*) the maximum due to the heteroepitaxial layer of the $In_{0.88}Ga_{0.12}As$ solid solution.

[4]. This topograph clearly demonstrates that the $In_{0.88}Ga_{0.12}As$ layer is really characterized by strong plastic deformation due to generation of three groups of gliding systems of straight dislocations intersecting at angles of 120° (region *2* in Fig. 2). The linear density of dislocation groups along each of the three directions roughly estimated from the topograph is 300 $cm^{-1}$. The single-crystal layer is divided into numerous fragments misoriented within angles of up to 0.2° (estimated from the difference between the maximum halfwidths on the curves obtained by the XRD–DCPRC method).

The X-ray topograph of the part of the InP substrate not coated with an epitaxial layer (region *1* in Fig. 2) shows several short dislocation segments inclined to the substrate surface. Thus, the substrate is almost free of dislocations. A small number of inclined dislocations cannot "suppress" the generation of lines of straight dislocations in the heteroepitaxial solid-solution layer caused, first and foremost, by the lattice mismatch between the layer and the InP substrate. The lattice mismatch calculated from the XRD spectrum at room temperature is $\varepsilon = 3.5 \times 10^{-3}$; at the epitaxial temperature, the mismatch value is even higher.

The widths of the maxima on the curves obtained from single-crystal ZnSe/(001)GaAs layers with thicknesses $h$ ranging from 5 to 15 μm by the DCPRC method were almost three times larger than the halfwidths of the maxima on conventional XRD curves. This indicates that the single crystal ZnSe layers with such thicknesses also experience considerable plastic deformation during growth. The maximum misorientation angle for individual fragments in plastically deformed ZnSe layers attains ~0.1°.

The model suggested for single-crystal layers of heteroepitaxial systems in [2] is based on the assumption that the lines of generated dislocations are parallel to the heteroboundary and emerge at the end surfaces of the heterostructure. The use of the model suggested in [2] allows one to measure by the XRD method rather high dislocation densities ($N_d > 10^5$ $cm^{-2}$) in single-crystal layers of heteroepitaxial systems with pronounced lattice mismatch ($0.02 \le \varepsilon \le 0.20$) [4]. Here, it is most convenient to measure the lattice mismatch by the transmission Laue method in the (220) reflection as the components of the tensor of thermoelastic and thermoplastic deformation under the assumption that $\varepsilon_{xx}$ and $\varepsilon_{yy}$ coincide with the [110]- and $[1\bar{1}0]$-directions and $\varepsilon_{zz}$, with the [001]- or the [111]-direction, depending on the substrate orientation in the heterostructure. Then, using the thus obtained experimental data

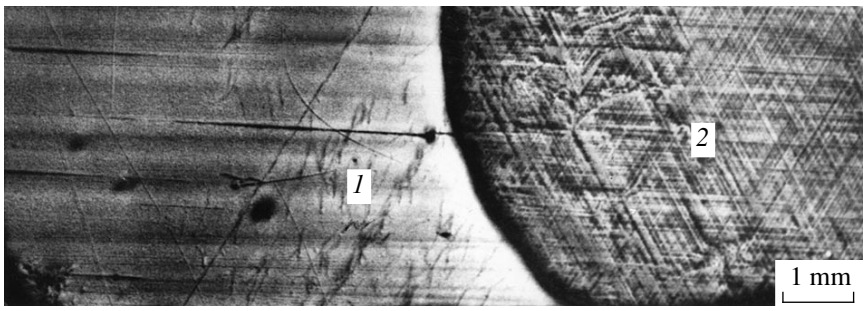


**Fig. 2.** X-ray topograph of the same specimen as in Fig. 1 obtained by the method of anomalous transmission of the Cu$K_{\alpha_1}$ radiation in the (220) reflections: (*1*) the part of the (111)GaAs substrate not covered with an epitaxial layer, (*2*) heterostructure.

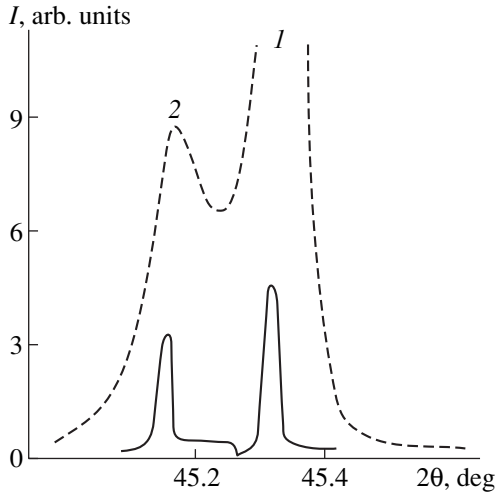


**Fig. 3.** X-ray diffraction spectra obtained by the DCPRC method (dashed line) and the transmission Laue diffraction method in the (220) reflection (solid line) from the heteroepitaxial ZnSe/(001)GaAs system (Cu$K_{\alpha_1}$ radiation): (*1*) the maximum due to the GaAs substrate, (*2*) the maximum due to the ZnSe layer.

(Fig. 3), one can roughly estimate the dislocation density $N_d$ in plastically deformed single-crystal heterolayers from the following formula [4]:

$$N_d = m\varepsilon_{xx}/hb, \quad (1)$$

where $m = 2$ and $m = 3$ for the (001)- and (111)-orientations of hcp substrates, $h$ is the thickness of the single-crystal layer, and $b$ is the Burgers vector of dislocations.

The thus measured values, $\varepsilon_{xx} \approx \varepsilon_{yy} = 3.50 \times 10^{-3}$ (Fig. 3) for the plastically deformed single crystal ZnSe layer only slightly differ (by $\Delta\varepsilon \approx 2 \times 10^{-4}$) from the mismatch calculated from the tabulated values of the lattice periods of unstrained crystals at room temperature reduced to the epitaxy temperature by the method suggested elsewhere [4, 7, 8]. Substituting $\varepsilon_{xx}$ and $\varepsilon_{yy}$ into (1), we determine the dislocation density in the transverse section of a 7 μm-thick layer of the crystal as $N_d \approx 2.5 \times 10^8$ cm$^{-2}$.

The deformation component $\varepsilon_{zz} = 2.35 \times 10^{-3}$ normal to the heteroboundary measured by the XRD method is lower than the values of the deformation components measured in the direction parallel to the heteroboundary, $\varepsilon_{xx} \approx \varepsilon_{yy} = 3.50 \times 10^{-3}$. This signifies that the single-crystal ZnSe layer on the (001)GaAs substrate at room temperature is elastically deformed by tensile stresses. Reducing the $\varepsilon_{zz}$, $\varepsilon_{xx}$, and $\varepsilon_{yy}$ values to the mismatch for the unstrained or free ZnSe/(001)GaAs lattices by formula (2) taking into account the anisotropy and the contribution of the components of the elastic and plastic strains [4, 7],

$$\varepsilon_f = C_{11}\varepsilon_{zz} + C_{12}(\varepsilon_{xx} + \varepsilon_{yy})/(C_{11} + 2C_{12}), \quad (2)$$

we obtain the value $\varepsilon_f = 3.73 \times 10^{-3}$ coinciding (within an accuracy of $\pm 4 \times 10^{-5}$) with the value calculated by (1) in [8] at $T_{ex}$ from the tabulated lattice parameters with due regard for the thermal-expansion coefficients of the heterolayer and the substrate at room and growth temperatures.

Thus, one can see that in the heterostructures of the ZnSe/(001)GaAs type, the almost complete (~100%) relaxation of elastic stresses occurs still at the growth temperature via the plastic deformation of a single-crystal heterolayer. In other words, relaxation of elastic stresses proceeds via generation and accumulation of dislocations up to the attainment of high densities ($N_d \sim 2 \times 10^8$ cm$^{-2}$) in the grown single-crystal ZnSe layer. During the subsequent cooling of the epitaxial system from the growth temperature down to room temperature, the elastic strains increase without transformation into plastic deformation, whence it follows that the plastic deformation of the epitaxial layer of thickness $h$ exceeding its critical thickness ($h \geq h_{cr}$) occurs only within a narrow temperature range in the vicinity of the epitaxy temperature $T_{ex}$.

This XRD method and the calculation of high dislocation densities ($N_d > 1 \times 10^5$ cm$^{-2}$) was also used for studying other heterostructures with considerably higher mismatch in free or elastically unstrained states. Thus, for the InAs/(001)GaAs heterostructure with a 1.1 μm-thick InAs/(001)GaAs heterolayer with $\varepsilon_f = 6.9 \times 10^{-2}$, the dislocation density is $N_d \approx 3 \times 10^{10}$ cm$^{-2}$, for the 1.8 μm-thick layer of GaAs/(001)Si heterostructure with $\varepsilon_f = 4.2 \times 10^{-2}$, it is $N_d \approx 5 \times 10^9$ cm$^{-2}$.

It should be indicated that the dislocation density obtained for the heteroepitaxial InAs/(001)GaAs layer by the XRD method coincided with the dislocation density determined for such type of heterostructures measured by the method of transmission electron microscopy (TEM) in [13].

The accuracy of the above calculations depends on the degree of applicability of the model used. However, at $N_d \geq 1 \times 10^6$ cm$^{-2}$, there are no more reliable methods for control and measurement of dislocation density. When analyzing the quantitative characteristics of mosaicity of single-crystal layers [4, 12] grown by the method of nonisostructural epitaxy, one has also invoke the method of divergent-beam from a quasipoint source [4, 12] or the destructive method of transmission electron microscopy [13].

A generation of dislocations as a mechanism of plastic deformation in growing single-crystal heterolayers is "switched on" at $h \approx h_{cr}$ [4–10] and "works" mainly at the epitaxy temperature $T_{ex}$ [4, 7]. The critical thicknesses $h_{cr}$ and the lattice mismatch for any heteropair are in advance calculated theoretically [4–8, 10] from the tabulated data for the lattice parameters $a_j$. One has also to take into account the variation in the lat-

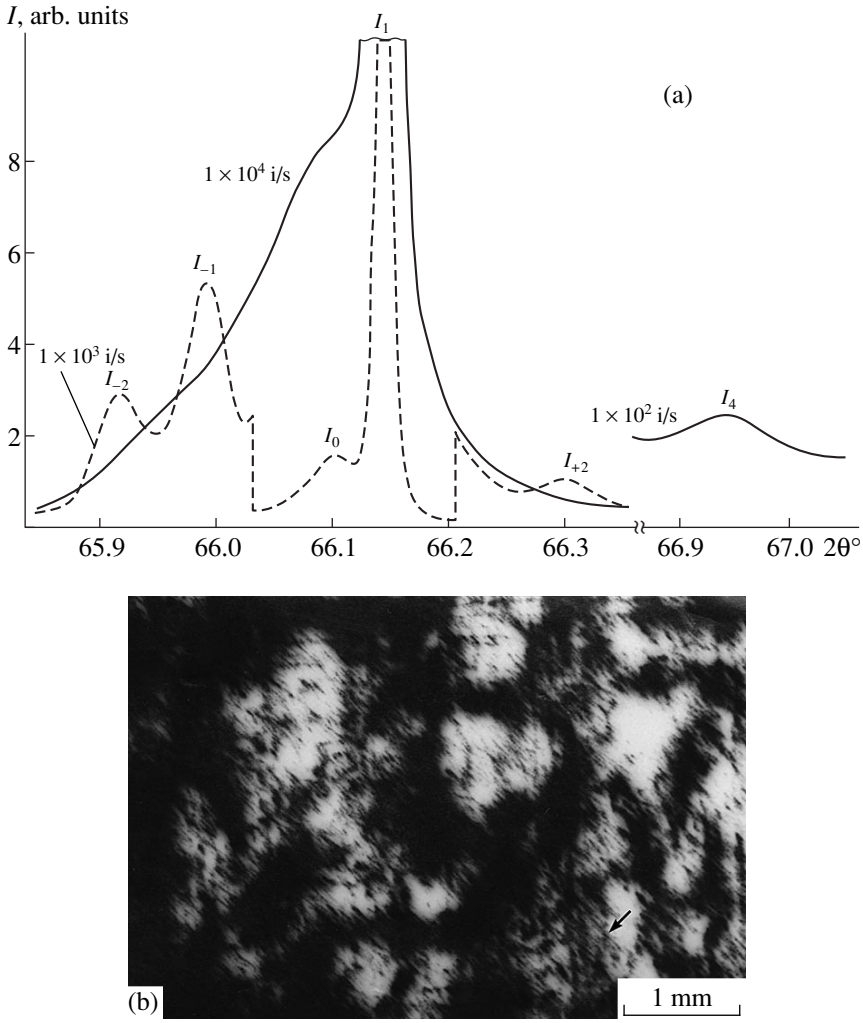


**Fig. 4.** (a) X-ray diffraction spectra from complex system of the $Al_xGa_{1-x}As/GaAs/\ldots/(001)GaAs$ type obtained by the DCPRC method (solid line) and conventional XRD method (dashed line) in the (004) Bragg reflection ($CuK_{\alpha_1}$-radiation): (a) $J_1$ is the maximum due to the substrate, $J_0$ is the main maximum due to the large-period superlattice and its satellites $J_{+2}$, $J_{-1}$ and $J_{-2}$ ($J_4$ is the maximum due to the satellite from the active small-period superlattice) and (b) X-ray topograph from the same specimen as in (a) obtained by the method of anomalous transmission of the $CuK_{\alpha_{1.2}}$ radiation in the (220) reflection.

tice parameters during material heating up to the epitaxial temperature $T_{ex}$ [4, 7, 8].

On the basis of the data obtained, the physics of the process of plastic deformation and its mechanism during growth of epitaxial multilayer systems can be described as follows.

The coherent single-crystal ZnSe and the solid-solution $ZnSe_{1-x}S_x$ layers cease to grow when $h \approx h_{cr}$ [4, 9, 11]. The larger the grown layer thickness in comparison with the critical thickness, $h_{cr} \leq h \geq h_{cr}$, the greater the number of the generated dislocations. The dislocation density drastically increases from the zeroth value to a certain limiting value $0 < N_d \geq 10^6$ cm$^{-2}$ dependent on the thickness of the single-crystal heterolayer and determined by its conjugacy with the substrate (mismatch) at the epitaxy temperature. In other words, at all $h > h_{cr}$, the growth process is accompanied by simultaneous plastic deformation and "pumping" of dislocations into the growing single-crystal layer. At the moment of the film growth cessation, the plastically relaxed single-crystal layer has almost no elastic stresses any more. The energy of "mismatch elastic stresses" is completely transformed into the energy of newly generated dislocations in the heterolayer. At the epitaxy temperature, the system is in equilibrium. The fragments of the thus formed crystal lattice undergo no elastic deformations.

However, during cooling of the epitaxial system, which underwent plastic deformation and lattice fragmentation, one observes the reappearance of elastic stresses. However, these are thermoelastic stresses due

to lattice mismatch of the opposite sign. Thus, prior to the cessation of coherent growth, the single-crystal ZnSe layer is under the action of misfit compressive stresses caused by lattice mismatch. Upon completion of the plastic relaxation at the epitaxy temperature, the fragmented single-crystal layer is almost unstressed. When the growth temperature is lowered to room temperature, the thermoelastic tensile stresses appear. This explains the sign reversal of elastic stresses in some heteroepitaxial systems revealed in [2].

It is very important to identify by a nondestructive X-ray method the type of deformation (elastic or plastic) of each of the superlattices in complex MBE-grown superlattice structures obtained in the same process and on the same substrate [8, 14]. In some cases, the use of the combined XRD-DCPRC method can solve this problem as well. We studied about 30 specimens of complicated MBE-grown superlattice structures of the type $Al_xGa_{1-x}As/GaAs/\ldots/(001)GaAs$ [7, 10, 14–16] consisting of one large-period ($T \geq 100$ nm) superlattice–mirror and a small-period ($T_3 \leq 15$ nm) active superlattice–optical modulator. On both sides of the latter lattice, there are also two small-period ($T_2 \approx T_4 <$ 10 nm) superlattices. For most of such specimens, both XRD and DCPRC methods and conventional classical rocking curves (obtained at a fixed fully open counter window) from the superlattice–mirror were almost the same. Along with the substrate maximum, they showed the main maximum from the superlattice–mirror and two-three orders of the satellites of the opposite sign. However, the low-intensity satellite lines from the fourth up to the sixth orders were recorded only by the DCPRC method. It was established that the DCPRC method is more sensitive, because it provides the intensity accumulation in he process of slow scanning of comparatively narrow weak satellite lines by a counter with a completely open entrance window (the flare angle of the counter is ~3°).

However, several specimens of the superstructures of such type studied by the DCPRC method had only clearly pronounced (004) diffraction line from the (001)GaAs substrate against the background of a broad curve of a considerably less intensity (solid line in Fig. 4a) instead of the spectrum with the satellite structure. However, as soon as we returned back to the conventional method [i.e., the use of a narrow (50 μm) slit in front of the counter], the θ–2θ scanning of the same specimen allowed us to record the diffraction spectrum with a well-pronounced main maximum and two orders of different satellites from its superlattice–mirror (dashed line in Fig. 4a). The period of this superlattice–mirror equals $T = 105.5 \pm 5.5$ nm.

Such a considerable difference between the XRD and DCPRC spectra from complicated superlattice structures can be explained only under the assumption of considerable plastic deformation in alternating layers, resulting in a drastic increase in the diffuse-scattering intensity of the X-ray radiation from the superlattice–mirror "absorbing" the maxima of the main diffraction line and its satellites.

Thus, the drastic differences in the XRD and DCPRC spectra (the XRD spectrum shows the well pronounced satellite structure, whereas the DCPRC spectrum, only the substrate maximum against the background of a broad diffuse-scattering curve) can serve as a reliable criterion for the existence of the plastic deformation in single-crystal layers of the large-period superlattices.

The additional confirmation of this conclusion is given by a topograph obtained by the method of anomalous transmission from one of the structures with the plastic deformation of the layers of the superlattice–mirror (the data obtained by the XRD–DCPRC method). This topograph is characterized by the cellular dislocation structure typical of Cr-doped GaAs substrates [17] and by considerable striation, which seems to be a topographic image of short dislocation lines or, more precisely, segments of dislocation loops generated in the process of epitaxial growth of the layers of the large-period superlattice. The rough estimate of the dislocation density in the layers of the superlattice–mirror made from the topograph in Fig. 4b yields the value $N_d \sim 1 \times 10^5$ cm$^{-2}$.

We believe that the plastic deformation of the layers of the large-period superlattices revealed in some specimens is caused by the deviation of the set growth parameters from their optimum values often observed for the MBE method.

Concluding the article, we should like to indicate that we observed one more maximum, $J_4$, of the positive satellite of the active superlattice (Fig. 4a). This low-intensity satellite is revealed by the DCPRC method due to integrating properties of the completely open moving counter. The lattice period of the active superlattice determined from this satellite is $T_a$ = 13.0 nm. The use of the XRD method with the system of computer intensity accumulation provided the observation of two orders of satellites of opposite signs from the active superlattice of the specimen. The same width of the XRD–DCPRC lines of this satellite (with the period of the active superlattice being $T_a$ = 13 nm) indicates that the layers of the active small-period superlattice in this specimen experience mainly elastic deformation.

## REFERENCES

1. J. Hornstra and W. J. Bartels, J. Cryst. Growth **5**, 513 (1978).
2. S. N. G. Chu, A. T. Macrender, K. E. Strage, *et al.*, J. Appl. Phys. **126**, 249 (1985).
3. G. F. Kuznetsov and A. A. Khazanov, Kristallografiya **35**, 1267 (1990).
4. G. F. Kuznetsov, Doctoral Dissertation in Physics and Mathematics (Moscow, 1989).

5. G. F. Kuznetsov, in *Proceedings of 4th All-Union Conference on Structural Defects in Semiconductors* (Novosibirsk, 1984), part 2, p. 58.
6. G. B. Bokiĭ and G. F. Kuznetsov, Dokl. Akad. Nauk SSSR **279**, 876 (1984).
7. G. F. Kuznetsov, in *Proceedings of Conference on Electronic Materials* (Novosibirsk, 1992), p. 32.
8. G. F. Kuznetsov, Kristallografiya **40**, 936 (1995) [Crystallogr. Rep. **40**, 869 (1995)].
9. G. F. Kuznetsov, Zh. Tekh. Fiz. **1**, 181 (1996).
10. Krishan Lal, Nirajana N. Goswami, and G.F. Kuznetsov, in *Semiconductor Devices* (Narosa, New Dehli, 1996), p. 113.
11. M. G. Milvidskiĭ and V. B. Osvenskiĭ, Kristallografiya **22**, 431 (1977).
12. G. F. Kuznetsov and S. A. Semiletov, Diffraction Methods of Nondestructive Control of the Real Structure of Epitaxial and Polycrystalline Films in Microelectronics in *Review on Electronics. Ser. Microelectronics* (TsNII Electronics, Moscow, 1975), No. 1 (280).
13. A. K. Gurakovskiĭ, Yu. K. Kanter, M. A. Revenko *et al.*, Kristallografiya **34**, 706 (1989).
14. G. F. Kuznetsov, A. S. Ignat'ev, V. G. Mokerov, *et al.*, Available from VINITI, no. 200-B93 (1993).
15. G. F. Kuznetsov, A. S. Ignat'ev, V. G. Mokerov, *et al.*, in *Proceedings of Conference on Electronic Materials* (Novosibirsk, 1992), p. 248.
16. A. S. Ignat'ev, G. F. Kuznetsov, V. G. Mokerov, *et al.*, in *Proceedings of Conference on Physics of Semiconductors* (Nizhniĭ Novgorod–Moscow, 1993), p. 331.

*Translated by L. Man*

*Crystallography Reports, Vol. 45, No. 2, 2000, pp. 300–303. Translated from Kristallografiya, Vol. 45, No. 2, 2000, pp. 332–336.*


**PHYSICAL PROPERTIES OF CRYSTALS**

# Thermal Expansion of Sm–Tb Orthoferrites in the Region of the Spin Reorientation Transition

**I. D. Lomako* and V. P. Popov****

** Institute of Solid State and Semiconductor Physics, Belarussian Academy of Sciences, ul. Brovki 17, Minsk, 220072 Belarus*

*** Kharkov State University, pl. Svobody 4, Kharkov, 310077 Ukraine*

Received June 27, 1998; in final form, April 23, 1999

**Abstract**—A new model of spin reorientation is discussed on the basis of the analysis of experimental data on thermal expansion of samarium–terbium orthoferrite and the earlier studies of its magnetic and crystallooptical properties. During the orientational phase transitions, the zero values of the thermal and optical parameters of rare earth orthoferrites correspond to the alignment of the magnetization vector along the [110] crystallographic directions. For orthorhombic Sm–Tb orthoferrite crystals, these directions coincide with the twofold axes in the (001) plane. © *2000 MAIK "Nauka/Interperiodica".*

## INTRODUCTION

Samarium–terbium orthoferrites (STO) have the distorted perovskite-type structure and belong to the crystals of the orthorhombic system. In terms of optics, they are biaxial, birefringent, and absorbing in the visible and the near infrared ranges. STO are weak ferromagnets, and they can exhibit an orientational phase transition in magnetic fields and at high temperatures [1, 2].

In spite of a large number of papers concerning the crystal chemistry physics, magnetism, and optics of the rare earth orthoferrites, there are still a lot of unsolved problems. For example, it is still unclear what crystallographic directions (except the well-known [100]- and [001]-directions) are involved in the orientational phase transitions in STO. These papers are reviewed in detail elsewhere [3, 4]. In orthoferrites, the dominant contribution to the magnetic anisotropy of iron ions comes from the antisymmetric exchange [3] stabilizing the $G_xF_z(\Gamma_4)$ spin configuration corresponding to the orientation of the magnetic moments along the [001]-direction.

For the detailed analysis of the orientational phase transition, it is of particular interest to study the characteristics of the model compound $Sm_{0.55}Tb_{0.45}FeO_3$ using different techniques. Such a study would allows us to reveal the correlation between the structural, thermal, optical, and magnetic properties of the compound. In STO of this composition, the easy magnetization axis at $T < T_1$ coincides with the [100] crystallographic axis, whereas at $T > T_2$, it is directed along the [001]-direction, where $T_1$ and $T_2$ are the onset and offset temperatures of the orientational phase transition. These transitions in the rare earth orthoferrites can be classified as the transitions related to the changes in the type of magnetic ordering [5]. As a result of the orientational phase transition, the crystal state at $T > T_2$ is characterized by a higher symmetry than at $T_1$. In addition, in most orthoferrites, especially in substituted binary ones, the orientational phase transitions proceed gradually within the wide temperature range ($\Delta \geq 70$ K).

In the present paper, we describe our study of thermal expansion of STO crystals along three directions and perform a more detailed analysis of the mechanisms underlying the orientational phase transition in the intermediate state.

## EXPERIMENTAL

We studied single crystals of Sm–Tb orthoferrites grown by from flux in the static mode. As a solvent, we used the $PbO–PbF_2–B_2O_3$ system. In this growth technique, lead is an inevitable technology-related (noncontrollable) impurity. Its concentration can vary depending on the content of rare earth elements and can be as high as 0.4 wt %. According to the data of neutron activation analysis, in the course of terbium substitution by samarium, the samarium content gradually decreases in comparison with the calculated values. This occurs, because it is more favorable for lead to substitute samarium (having a larger ionic radius) than terbium. The terbium content in the solid solutions of rare earth orthoferrites is slightly lower than it could be expected from the nominal composition [7]. The crystal structure of $Sm_{0.55}Tb_{0.45}FeO_3$ is characterized by the sp. gr. $D_{2h}^{16}$–*Pbnm* and the lattice parameters $a = 5.372$, $b = 5.597$, and $c = 7.696$ Å. The sample in the shape of a rectangular bar ($4.584 \times 4.699 \times 6.236$ mm in size) was placed into the measurement unit to determine its relative elongation $\Delta l(T)$ caused by the temperature variation under the quasi-steady-state conditions ($l_i$ are the sample dimensions along each of its three sides measured at room temperature). In our experiments, the

1063-7745/00/4502-0300$20.00 © 2000 MAIK "Nauka/Interperiodica"

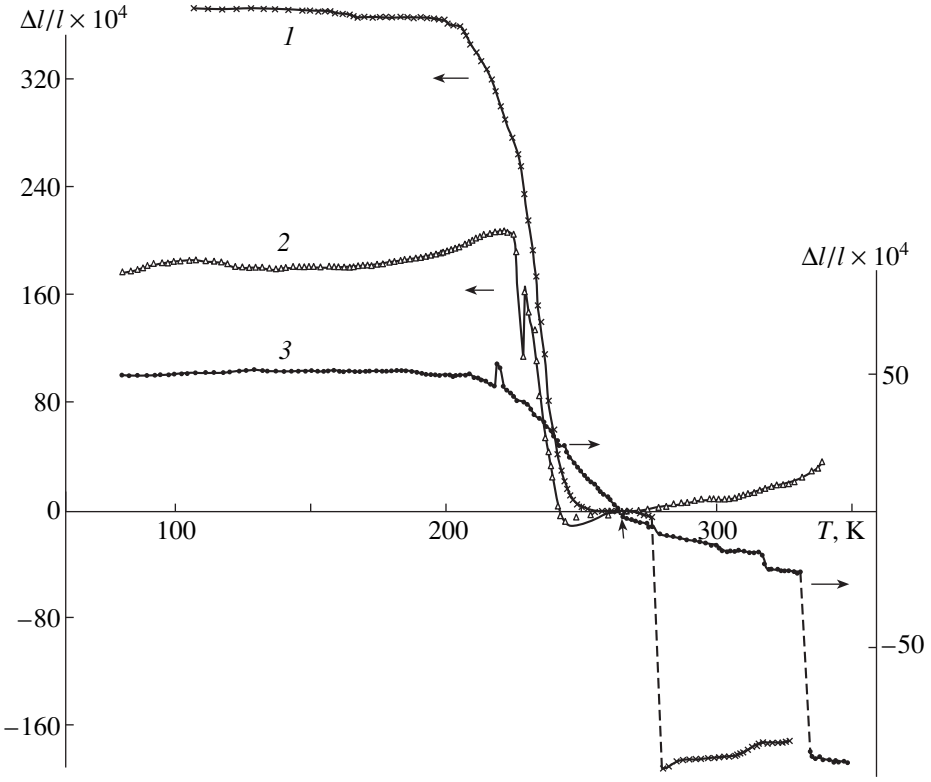


Temperature dependence of the relative elongation of $Sm_{0.55}Tb_{0.45}FeO_3$ single crystal measured along three sides of the sample: $l_a$ = 4.584, $l_b$ = 4.699, and $l_c$ = 6.236 mm (the [001] axis); curves *1–3*, respectively.

step of the temperature variation was equal to 2–2.8 K in the 80–200 K range and 1–1.5 K in the 200–340 K range. The starting $\Delta l/l$ values correspond to 80 K for each orientation (with $l_a$ = 4.584 Å, $l_b$ = 4.699 Å, and $l_c$ = 6.236 Å). The end face of the Sm–Tb orthoferrite bar coincides with the (001) plane; its larger diagonal coincides with the [010]-crystallographic direction, as was demonstrated in [8]. The direction normal to [010] corresponds to [100], and it is almost coincident with the smaller diagonal of the end face of the crystal. Therefore, the magnetization in the $\Gamma_2$ phase ($G_zF_x$) at $T < T_1$ is characterized by a rather large projection on the smaller edge of the crystal. The [010]-axis has a non-zero projection on the larger side of the STO crystal, and the longest side of the crystal is parallel to the [001]-direction.

Thermal expansion of the Sm–Tb orthoferrite single crystal was measured within the 80–350 temperature range. For the sample under study, the yield strength under compression was equal to 0.5 MPa. The maximum sensitivity of the optomechanical dilatometer used was about $10^{-9}$ m.

In the vicinity of the orientational phase transition, the easy magnetization axis is reorientated from [100] to a certain intermediate direction. This causes the decrease in the magnetization $M_a$ along the *a*-axis and gives rise to a non-zero magnetization $M_c$ along the *c*-axis. For the material under study, we determined temperatures $T_1$ = 220 and $T_2$ = 290 K. These values were found from the measured temperature dependence of spontaneous magnetization $\sigma$ at a low magnetic field (about 100 Oe). The intersection of $\sigma_a$ and $\sigma_c$ plots was observed at $T \simeq 265$ K. In the vicinity of orientational phase transition, one has to take into account the existence of the domain structure because this structure undergoes significant changes (the domains become smaller). In the temperature dependence of coercive force $H_c$ in the middle of the range corresponding to the orientational phase transition, the magnetization processes for the (100) and the (001) planes exhibit a pronounced anisotropy. For the material of the composition $Sm_{0.65}Tb_{0.2}Eu_{0.15}FeO_3$, it was shown that $H_c$ has the minimum value (about 2 Oe) at the point of intersection of these curves in the temperature range 260–265 K [10].

## RESULTS AND DISCUSSION

The obtained experimental data on the relative elongation of a STO crystal for three different orientations in the temperature range 80–350 K are presented in the figure. One can see that the observed $\Delta l/l$ values are almost constant for all the three directions over the wide temperature range (80–200 K). This clearly indicates that such characteristics as the effective crystal

field, domain structure, interaction between $Fe^{3+}$ and rare earth ions remain unchanged at $T < T_1$. Similar features were also observed for the temperature dependence of magnetization along the *c*-axis for $Sm_{0.2}Tb_{0.8}FeO_3$, where $\sigma$ = const at $T$ = 25–100 K [2].

In the temperature range 80–200 K, the minimum $\Delta l/l$ values were observed along the [001]-axis (curve *3* in the figure). This can be interpreted as a consequence of the anisotropy in interactions: the interactions between atoms located in the layer or the chain are stronger than the interlayer or interchain interactions [11]. Therefore, at $T < T_1$, $\Delta l/l$ along the chain in the perovskite structure has a much lower value (almost by a factor of seven) than in the [100]-direction (curve 1).

At $T < T_1$, the $\Delta l/l$ value along the *a*-axis (curve *1*) is twice as large as its value along the *b*-axis (curve *2*). In the latter case, there is no magnetic contribution under the same conditions. Figure demonstrates that the additional contribution at $T < T_1$, constitutes one half of the total value, and is comparable with the sum of the lattice and the electron contributions [12].

The "detachment" of magnetization vector from [100]-axis occurs in several steps. At $T > 210$ K, the relative elongation along the *a*-axis decreases by a factor of 1.5 in the temperature range $\Delta \simeq 15$ K, whereas along the *b*-axis, first, an increase in $\Delta l/l$ is observed and then, its steep drop down to zero. Beginning from 235 K, the temperature dependences of $\Delta l/l$ along the *a*- and the *b*-axes are similar until their intersection with the horizontal axis. Curve *2* is of interest, because a pronounced $\Delta l/l$ peak is observed in the narrow temperature range ($\Delta \simeq 4$ K), and then $\Delta l/l$ returns to the region of its positive values. It is possible that these peaks of $\Delta l/l$ of different intensities in curves *2* and *3* can be related to the so-called critical fluctuations, usually observed in the "detachment" of the magnetization vector from its equilibrium orientations, as was predicted in [13]. It was also assumed that both uniform and strongly nonuniform fluctuations of magnetization should be observed in the vicinity of $T_1$ and $T_2$ in rare earth orthoferrites.

Note that large crystals of rare earth orthoferrites have numerous structural defects (dislocations, vacancies, nostoichiometric regions) giving rise to the fluctuations in the energy of the magnetic anisotropy and, as a result, also to the magnetization fluctuations. We performed the X-ray fluorescent analysis of the material under study using the $Cd^{109}$ isotope to determine the content of the main components (Sm, Tb, Fe) at different faces of the crystal. The ratio $\Sigma$(Sm + Tb)/Fe had the following values on different faces of the crystal: 0.92, 0.95, 1.0005, and 0.963. The presence of different kinds of defects, including the nonstoichiometric regions and the regions with composition fluctuations, can cause a significant broadening of the range of spin reorientation for samarium–terbium orthoferrite in comparison with the data obtained in the magnetization measurements on a high-quality $0.8 \times 1 \times 1$ mm-large sample by the vibrating-sample magnetometer sample.

Analyzing the experimental dilatometric data along the three principal axes of the STO crystal, we established three stages in recording of the temperature dependence of $\Delta l/l$. At the first stage (220–240 K), we observed a steep drop of $\Delta l/l$ down to zero. At the second stage (240–270 K), $\Delta l/l$ had almost zero values for all the three orientations. Such a temperature dependence of relative elongation for three crystal orientations indicates the pronounced nonuniformity in the rotation of the magnetization vector in the (101) plane. This nonuniformity manifests itself at the intermediate stage ($\Delta$ = 240–270 K), when the angle between the magnetization vector and the *c*-axis is close to $\pi/4$. Note that this last stage has a characteristic feature: all the three curves intersect the horizontal axis at 265 K (the vertical arrow in the figure).

The third stage is somewhat similar to the first one for the *a*- and *c*-orientations: the stepwise decrease in $\Delta l/l$ occurs at 276 K (curve *1*) and at 333 K (curve *3*); these temperatures correspond to the offset of the phase transition. For the last orientation (the magnetization is parallel to [001]), the behavior of $\Delta l/l$ is more complicated. For this orientation, we observe a stepwise decrease in $\Delta l/l$ and the segments with the constant $\Delta l/l$ value ($\Delta$ = 10–15 K). In our opinion, the extended range of the orientational phase transition is explained by an unsatisfactory quality of large STO crystals. In this connection, we should like to cite B.M. Mogilevskiĭ, a well-known expert in thermal properties, who wrote: "The transport phenomena allow us to determine the mechanisms of various physical processes. The transport in crystals occurs mainly over the defect centers, so that the study of the transport is equivalent to the study distributions of defect states in crystal lattices". For the [100]-direction, the orientational phase transition proceeded within the 220–280 K range. The orientational phase transition is accompanied by the rearrangement of domain structure, which proceeds either in the stepwise manner (within one or more stages) or gradually within a wide temperature range. For two directions (curves *1* and *3*), the negative $\Delta l/l$ values are observed in the vicinity of $T_2$, which is characteristic for metals with so called open (porous) structure [14].

Different values were reported for the range of the orientational phase transition in the Sm–Tb orthoferrite. As an example, indicate here the results obtained from the temperature dependence of the specific Faraday rotation [15]. It was found that the orientational phase transition occurs within the temperature range from $T_1$ = 273 K to $T_2$ = 170 K." In another paper, the following conclusion was made: "In $Sm_{0.55}Tb_{0.45}FeO_3$ crystals, the reorientation of spontaneous magnetization from the *a*- to the *c*-axis occurs within the temperature range 300–210 K. The "domain-memory effect" observed in the reorientation range is an indication to the delay in the reorientation of the easy magnetization

axis in the surface layer within the temperature range 120–180 K [16]. The published data show that STO crystals studied were of different quality and sometimes had nonstoichiometric compositions, various inclusions and defects. In other words, the crystals were inhomogeneous over the volume and along different crystallographic directions. Such an inhomogeneity leads to the scatter in the temperature ranges of orientational phase transition, which, in the latter case, amounts to 300–120 K.

Note that [100]-type directions are characterized by the lowest energies, and, therefore, they provide the largest contributions to the domain rearrangement. Under the applied magnetic and temperature fields, new domains arising in STO start aligning in the [100]-type directions.

Earlier [17], we established the correlation between the anisotropy of optical and magnetic properties of STO crystals. We also paid attention to the existence of the relation between the measured polar diagrams describing the rotation angles of the longest axis in the polarization ellipse $\gamma(\varphi)$ in STO and the polar diagrams for magnetic torque (for the same orientations) constructed using the data reported in [3]. It was shown in [1] that the zero values of $\gamma(\varphi)$ in (001)-oriented $Sm_{0.55}Tb_{0.45}FeO_3$ plates are observed along the crystallographic [110]-type directions. They correspond to the quasi-linear polarization of light. The similar character of the optical anisotropy and the crystallographic magnetic anisotropy was established with due regard for the orientation of Sm–Tb orthoferrites under study.

Thus, we demonstrated that dilatometry provides the useful information on the thermal properties of samarium–terbium orthoferrites in the vicinity of the orientational phase transition. Taking into account the analogous behavior of the structural, optical, and thermal characteristics of these crystals, we put forward a hypothesis that the zero values of the relative linear elongation in the existence range of the intermediate state can be observed if the magnetization vector coincides with the crystallographic [110]-type directions, whence it follows that the magnetization vector rotates during the orientational phase transition not only within the (101) plane—in fact, if proceeds in a more complicated way. The [110]-directions in the orthorhombic samarium–terbium orthoferrite crystals are the twofold symmetry axes located in the (001) plane.

## CONCLUSIONS

At the initial stage of the "detachment" of the magnetization vector from the equilibrium [100]-direction, we observed the pronounced peaks in $\Delta l/l$ in the vicinity of the spin-reorientation transition for two orientations of the STO crystal. These peaks seem to be associated with the so-called critical fluctuations predicted in [13].

We revealed the nonmonotonic temperature dependence of the magnetization rotation within the whole range of the orientational phase transition, and especially in the intermediate region ($\Delta$ = 240–270 K), where $\Delta l/l$ has almost zero values for all three orientations.

The comparison of the temperature dependence of the relative elongation with the earlier published optical data for Sm–Tb orthoferrite allowed us to put forward a hypothesis that the zero values of the linear elongation can be observed in STO crystals only if the magnetization vector coincides with the crystallographic directions of the [110]-type, whence it follows that the magnetization vector rotates during the orientational phase transition not only in the (101) plane but also in a more complicated way in the three-dimensional space.

## ACKNOWLEDGMENTS

We are grateful to A.N. Igumetsev for X-ray fluorescent analysis of the samples.

## REFERENCES

1. N. N. Sirota and I. D. Lomako, Krist. Tech. **13**, 873 (1978).
2. N. N. Sirota and I. D. Lomako, Fiz. Nizk. Temp. (Kharkov) **5**, 664 (1979).
3. K. P. Belov, A. K. Zvezdin, A. M. Kadomtseva, and R. Z. Levitin, *Orientational Transitions in the Rare Earth Magnetic Materials* [in Russian] (Nauka, Moscow, 1979).
4. A. K. Zvezdin, V. M. Matveev, A. A. Mukhin, and A. I. Popov, *Rare Earth Ions in the Crystals with Magnetic Order* [in Russian] (Nauka, Moscow, 1985).
5. E. A. Turov and V. G. Shavrov, Usp. Fiz. Nauk **140**, 429 (1983).
6. V. G. Bar'yakhtar, A. N. Bogdanov, and D. A. Yablonskiĭ, Fiz. Tverd. Tela (Leningrad) **29**, 116 (1987).
7. I. D. Lomako and G. V. Leushkina, Dokl. Akad. Nauk BSSR **21**, 592 (1977).
8. J. R. Patel, L. G. van Uitert, and A. Mathiot, J. Appl. Phys. **44**, 3763 (1973).
9. V. P. Popov, V. M. Valiev, and I. N. Rybalko, USSR Inventor's Certificate, no. 11164854 (1985).
10. A. P. Ges', I. N. Kondrat'ev, and V. V. Fedotova, Vesti Akad. Nauk BSSR **5**, 67 (1983).
11. I. M. Lifshits, Zh. Éksp. Teor. Fiz. **22**, 475 (1952).
12. S. I. Novikova, *Thermal Expansion of Solids* [in Russian] (Nauka, Moscow, 1974).
13. Yu. M. Kolesnikov, A. A. Nersesyan, and A. A. Kharadze, Fiz. Tverd. Tela (Leningrad) **17**, 715 (1975).
14. G. Dolling and R. A. Cowley, Proc. Phys. Soc. (London) **88**, 463 (1966).
15. G.S. Kandaurova, V. O. Vas'kovskiĭ, *et al.*, Fiz. Tverd. Tela (Leningrad) **30**, 838 (1988).
16. V. O. Vas'kovskiĭ, G. S. Kandaurova, and E. V. Sinitsyn, Fiz. Tverd. Tela (Leningrad) **19**, 1245 (1977).
17. N. N. Sirota and I. D. Lomako, Cryst. Res. Technol. **22**, 1085 (1987).

*Translated by K. I. Kugel*

*Crystallography Reports, Vol. 45, No. 2, 2000, pp. 304–306. Translated from Kristallografiya, Vol. 45, No. 2, 2000, pp. 337–339.*


**PHYSICAL PROPERTIES OF CRYSTALS**

# Spectroscopy Studies of Pure and Chromium-Doped Calcium Gallogermanate Crystals, $Ca_3Ga_2Ge_4O_{14}$

**Z. B. Perekalina[1], T. F. Veremeĭchik[1], K. A. Kaldybaev[2], and A. D. Tynaev[2]**

[1] *Shubnikov Institute of Crystallography, Russian Academy of Sciences, Leninskiĭ pr., Moscow, 117333 Russia*

[2] *Issyk-Kul' State University, Karakol, Kyrgizstan*

Received July 12, 1999

**Abstract**—Absorption spectra, the spectra of circular dichroism and magnetic circular dichroism of pure and Cr-doped $Ca_3Ga_2Ge_4O_{14}$ crystals have been studied. The crystal-field parameters and the transition frequencies of $Cr^{3+}$ ions are calculated. The location of $Cr^{3+}$ and $Cr^{4+}$ ions in oxygen octahedra and tetrahedra is confirmed. The spectra of circular dichroism show the maxima due to $Cr^{3+}$ ions and growth-induced defects. © *2000 MAIK "Nauka/Interperiodica".*

Activated calcium gallogermanite (CGGO) crystals of the composition $Ca_3Ga_2Ge_4O_{14}$ are promising materials for quantum electronics and acoustics [1].

CGGO crystals belong to the trigonal-trapezohedral 32 class of the trigonal system, sp. gr. *D*23-*P*321, and have one molecule per unite cell. The structure of this crystal is described in detail elsewhere [2].

We studied the optical properties of pure and Cr-doped CGGO crystals. The specific feature of our approach consists in the simultaneous use of the method of circular dichroism, including the magnetic-field-induced dichroism, and the absorption spectroscopy. These methods allow to make measurements of the difference between the intensities of right- and left-circularly polarized waves with a high precision and at high resolution.

The absorption spectra of Cr-doped CGGO crystals and oriented normally to the optical axis were studied in the range of 250–900 nm on a Specord-40 spectrophotometer at 300 K (Figs. 1a–1c). The absorption spectra showed the same peaks (285, 440, 635 nm) as were observed in [3]. We recorded the bending point at 695–700 nm and weak absorption bands at 830, 570, and 475 nm. In addition to the data obtained in [3], a purely electronic transition was revealed at a wavelength of 11374 $cm^{-1}$ (879 nm), which was attributed to the band at 12000 $cm^{-1}$ (830 nm) and started the electron-vibration series of peaks with a period of 130 $cm^{-1}$ within the wavelength range of 11500–12500 $cm^{-1}$ (870–800 nm) (Fig. 1c).

We calculated the following parameters of the crystal field: $Dq$ = 1575 $cm^{-1}$, $B$ = 761 $cm^{-1}$, $C$ = 2811 $cm^{-1}$, $\alpha$ = 70 $cm^{-1}$. Then, these values were used to calculate the frequencies of transitions in $Cr^{3+}$ ion. The data obtain are consistent with the experimental values (see table). However, the weak absorption bands at 830 and 570 nm and a purely electronic transition do not fit this scheme. The estimation showed that these peaks correspond to a tetrahedrally coordinated $Cr^{4+}$ ion, which confirms the results obtained in [3].

The circular dichroism spectra of CGGO crystals were measured aid of a dichrograph at the wavelengths of 250–800 nm on the samples oriented normally to the optical axis. In Cr-doped CGGO crystals the circular dichroism peaks were recorded at all the peak frequencies of the absorption spectra of $Cr^{3+}$ ion (Fig. 2, curve *1* and table). In addition, a peak at 335 nm and a shoulder

(1) Calculated and (2) observed wavelengths (nm) corresponding to the absorption spectrum peaks; (3) peaks of circular dichroism of $Cr^{3+}$-doped and (4) of pure CGGO crystals

| Transition | 1 | 2 | 3 | Transition | 1 | 2 | 3 | 4 |
|---|---|---|---|---|---|---|---|---|
| $^4A_2 \longrightarrow {}^2E$ | 694 | 700 | 700 | $a\ ^4T_1 \longrightarrow {}^4A_2$ | 441 | 440 | 453 | |
| $^4A_2 \longrightarrow {}^2T_1$ | 660 | | | | | | | 440 |
| $^4A_2 \longrightarrow {}^4T_2$ | 635 | 635 | 635 | | | | 390* | 390 |
| $^4A_2 \longrightarrow {}^2T_2$ | 474 | | 470* | | | | 330 | 330 |
| | | | | $b\ ^4T_1 \longrightarrow {}^4A_2$ | 283 | 285 | 275 | 275 |

* Measured at 77 K.

1063-7745/00/4502-0304$20.00 © 2000 MAIK "Nauka/Interperiodica"

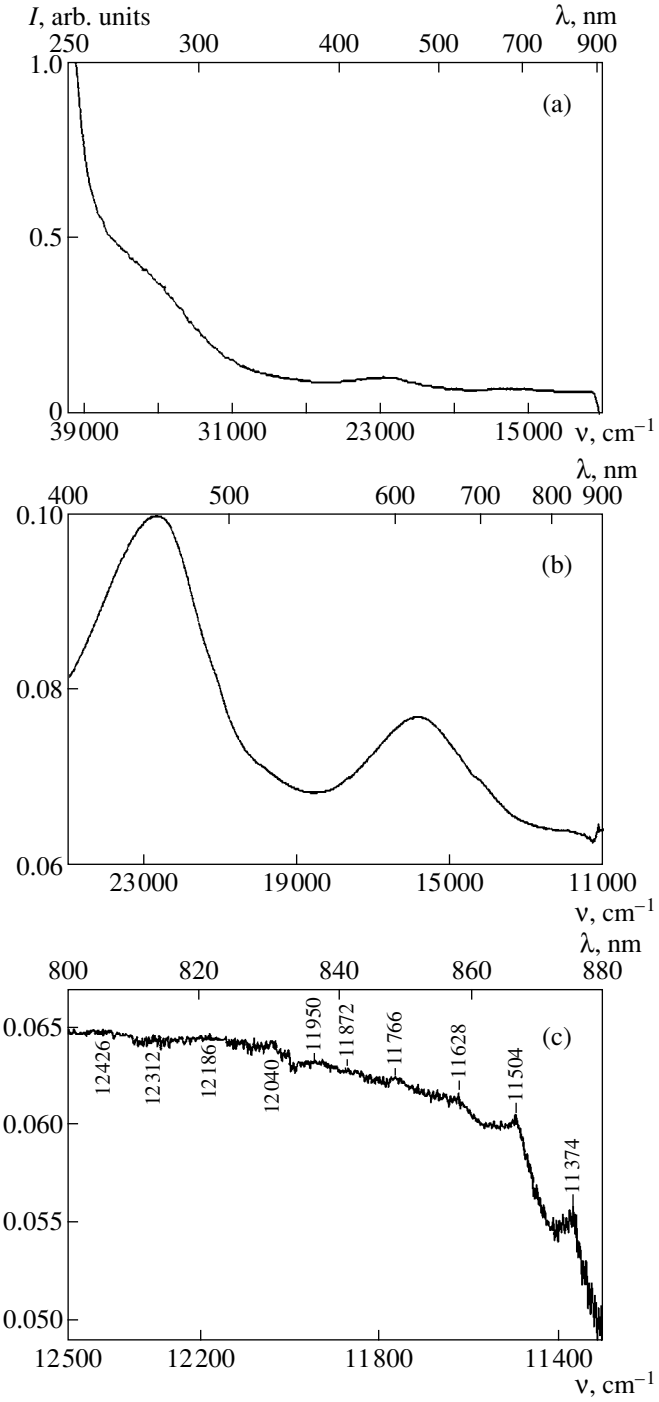


**Fig. 1.** Absorption spectra of chromium-doped CGGO crystal in various spectral ranges: (a) 250–900; (b) 400–900; (c) 800–880 nm.

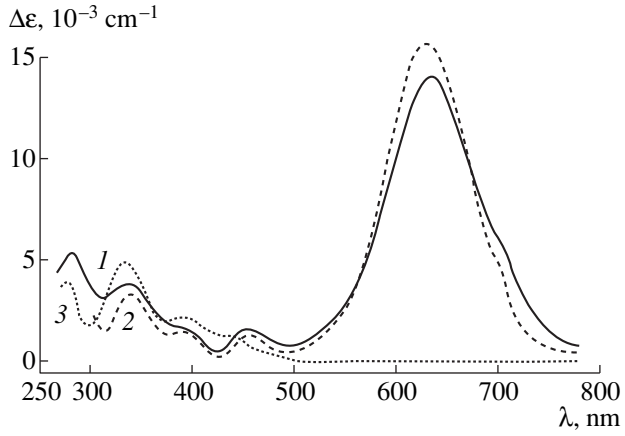


**Fig. 2.** Spectra of circular dichroism of CGGO crystals for (*1*) $Cr^{3+}$ in the spectral range 250–800 nm at $T$ = 300 K and (*2*) at $T$ = 77 K and (*3*) for a pure crystal.

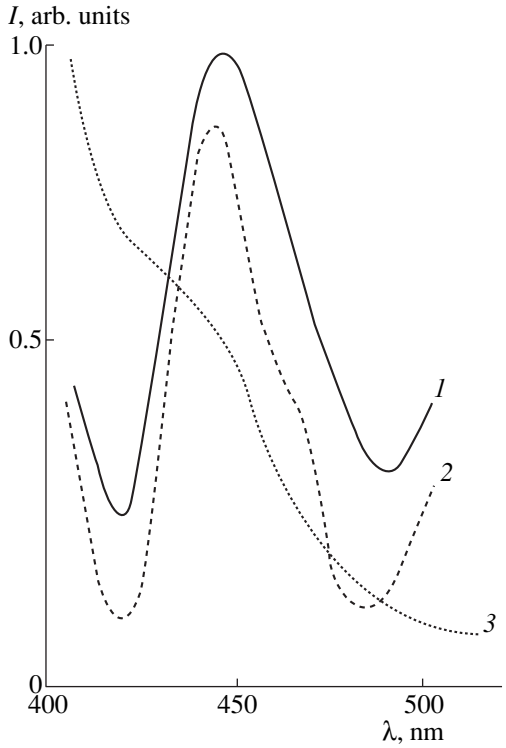


**Fig. 3.** Spectra of circular dichroism of CGGO crystals: (*1*) for $Cr^{3+}$ in the spectral range 400–500 nm at $T$ = 300 K and (*2*) at $T$ = 77 K and (*3*) for a pure crystal.

in the range 380–400 nm were observed on the circular dichroism spectra. The calculations showed that these peaks cannot be attributed to $Cr^{3+}$ ions.

At a temperature of 77 K, two more peaks were observed: one in the ultraviolet spectrum range at 390 nm (Fig. 2, curve *3*) and the other at a long-wave wing of the 450 nm band at about 470 nm (Fig. 3, curve *2*). The calculations show that the latter wavelength corresponds to the transition $^4A_2 \longrightarrow {}^2T_2$ (see table).

The spectra of magnetically-induced circular dichroism were obtained with the aid of a dichrograph combined with a permanent magnet inducing a field of about 14 kOe. In the visible range, we observed the same bands as in circular dichroism. In addition, at

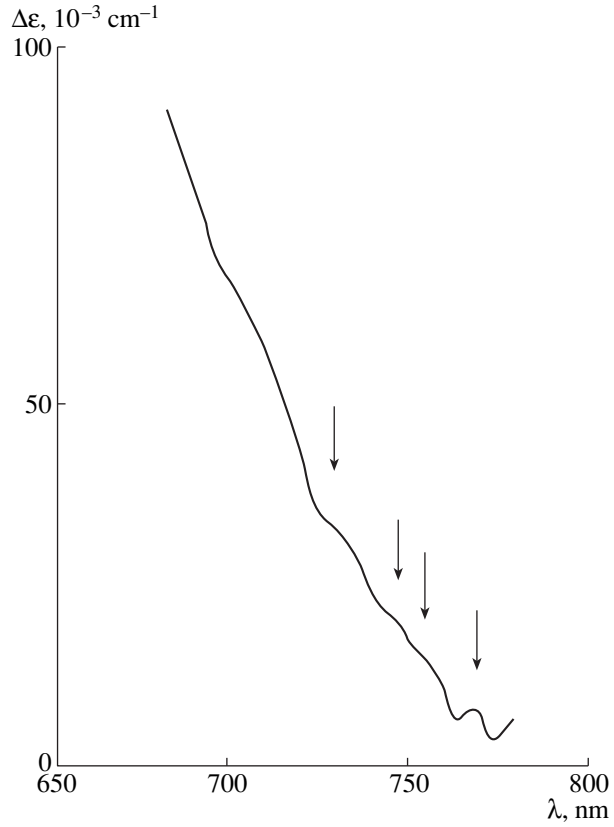


**Fig. 4.** Spectrum of magnetic circular dichroism of CGGO: $Cr^{3+}$ crystal.

300 K, we recorded the maximum 765 nm (13072 $cm^{-1}$) at the long-wavelength wing of $Cr^{3+}$ at 635 nm and its vibration recurrences at 190 $cm^{-1}$ (Fig. 4).

The circular dichroism spectra of pure crystals had well-resolved absorption bands with the maxima at 275, 330, 390 nm and a shoulder at 440 nm (Fig. 2, curve *2*, Fig. 3, curve *3*). The peaks at 275 and 440 nm and the bands at 276 and 453 nm observed on the circular dichroism spectrum of $Cr^{3+}$ ions overlap. Thus, these spectra show that the band at 453 nm consists of three components located at 440, 453, and 470 nm.

The bands observed in circular dichroism spectra of a pure crystal seem to be caused by absorption at the centers associated with growth defects. They seem to be caused by the prevalent evaporation of $GeO_2$ in the process of crystal growth [2]. However, these defects were observed in absorption spectra only upon X-ray irradiation of a crystal. We believe that we managed to observe them for non-irradiated crystals only because of the high sensitivity of the dichrograph ($10^{-5}$ opt. dens./mm). According to [4], these defects are most probably holes localized at oxygen in the vicinity of the $Ge^{4+}$ vacancy in the tetrahedral *d*-positions.

Since the CGGO crystal belongs to the symmetry class 32, sp. gr. *P*321, and contains one molecule per unit cell, it cannot have a "helical structure". The optical activity of such crystals is not associated with the symmetry of the crystal, but is caused by the asymmetry of individual centers. The structure only provides the conditions for formation of these centers. The role of such centers in the CGGO crystals is played by octahedra *a* and tetrahedra *d* with the symmetries 32 and 3, respectively. It is because of the symmetries of these polyhedra, that the absorption bands due to impurity centers and defects localized in these polyhedra can possess circular dichroism.

Thus, our work confirms that the dopant in Cr-doped CGGO crystals is incorporated into the structure and the $Cr^{3+}$ and $Cr^{4+}$ ions occupy the octahedral and tetrahedral positions, respectively.

Using the spectra of magnetically-induced dichroism for octahedrally-coordinated $Cr^{3+}$ ion and the absorption spectra for tetrahedrally-coordinated $Cr^{4+}$ ion, we determined the characteristics of oscillations caused by excitation of electron transitions in these chromium ions.

The dichroism spectra obtained at 300 and 77 K provided the information additional to the data obtained from the absorption spectra about a purely electronic transition $^4A_2$–$^2T_2$. The dichroism spectra of pure and doped crystals showed the absorption bands due to $Cr^{3+}$ and growth defects.

## REFERENCES

1. *Physics and Spectroscopy of Laser Crystals*, Ed. by A. A. Kaminskiĭ (Nauka, Moscow, 1986).
2. *Crystallochemical Systematics of Minerals*, Ed. by V. S. Urusova (Mosk. Gos. Univ., Moscow, 1985).
3. P. I. Macfarlane, T. P. J. Han, B. Henderson, and A. A. Kaminskiĭ, Opt. Mater., No. 3, 15 (1994).
4. A. E. Nosenko, R. E. Leshchuk, B. V. Podlyak, and A. A. Sel'skiĭ, Fiz. Tverd. Tela (St. Petersburg) **39**, 1044 (1997) [Phys. Solid State **39**, 938 (1997)].

*Translated by A. V. Zalesskiĭ*

*Crystallography Reports, Vol. 45, No. 2, 2000, pp. 307–309. Translated from Kristallografiya, Vol. 45, No. 2, 2000, pp. 340–342.*


**LIQUID CRYSTALS**

# Helical Disclinations in a Cylindrical Capillary with Nematic Liquid Crystal

**V. K. Pershin* and I. I. Klebanov****

** Ural State University of Railway Transport, Yekaterinburg, Russia*

*** Chelyabinsk State Pedagogical University, pr. Lenina 69, Chelyabinsk, 454080 Russia*

Received February 24, 1998; in final form, July 20, 1998

**Abstract**—A new type of linear disclinations in a cylindrical capillary with a nematic liquid crystal (NLC) has been studied. It can be considered as a generalized linear disclination of the unit strength. The exact analytical expressions for the elastic field components, lines of force, and the free energy of deformation have been derived. © *2000 MAIK "Nauka/Interperiodica".*

The director field $\mathbf{n}(\mathbf{r})$ of a nematic liquid crystal (NLC) in a cylindrical capillary of a radius smaller than a certain critical value $\rho_c$ under the normal boundary conditions, possesses a singularity along capillary axis [1]. Under the boundary conditions other than normal, the elastic field has a more complicated structure. We had the aim to study the structures of this field in the one-constant approximation of the continuum NLC theory under the boundary conditions such that the director lying in the plane normal to the capillary axis does not coincide with the surface normal.

Consider a nematic in a cylindrical capillary of radius $\rho_0 < \rho_c$. In the cylindrical system of coordinates, the dimensionless quantity $\mathbf{n}$ may depend on polar angle $\varphi$ and the dimensionless combinations of $z/\rho$ and $\rho/\rho_0$. We restrict ourselves to the case, where the director depends only on the ratio $\rho/\rho_0$.

In the one-constant approximation, the equation of equilibrium has the form [1]:

$$\Delta\mathbf{n} - \mathbf{n}\cdot(\mathbf{n}\cdot\Delta\mathbf{n}) = 0. \quad (1)$$

The director components in the cylindrical coordinates are represented as

$$n_\rho = \cos\alpha(\rho/\rho_0); \quad n_\varphi = \sin\alpha(\rho/\rho_0); \quad n_z = 0, \quad (2)$$

where $\alpha$ is the angle between the director and radius-vector $\boldsymbol{\rho}$ in the plane $z$ = const (a flat structure).

Substituting (2) into (1), we find

$$\alpha''_{\xi\xi} = 0, \quad (3)$$

where $\xi \equiv \ln(\rho/\rho_0)$, whence

$$\alpha = a\xi + \alpha_0, \quad (4)$$

with the constants $a$ and $\alpha_0$ being defined by the boundary conditions. Integrating the equation along the lines of force,

$$\rho d\varphi/n_\varphi = d\rho/n_\rho \quad (5)$$

with due regard for (2) and (4), we obtain

$$\varphi - \varphi_0 = -\frac{1}{a}\ln\left|\frac{\cos(a\ln(\rho/\rho_0) + \alpha_0)}{\cos\alpha_0}\right|, \quad (6)$$

where $\varphi_0$ is integration constant. If $a = 0$, expression (6) is transformed to the equation of a logarithmic helix

$$\varphi - \varphi_0 = \tan\alpha_0\ln(\rho/\rho_0). \quad (6a)$$

The families of lines of force at $a = 0$ and $a \neq 0$ are shown in Figs.1 and 2. In the former case, we have a conventional linear disclination of the unit strength [2]. In the latter case, $a \neq 0$, the elastic field has an infinite number of cylindrical surfaces, passing which the director changes its orientation to the opposite one. With an approach to the capillary axis, the radii of these surfaces decrease in the geometrical progression as

$$\rho_n = \rho_0\exp(-\pi n/|a|), \quad n = 0, 1, 2\ldots. \quad (7)$$

It should be emphasized that the above surfaces cannot be considered as defects, since, in nematics, the directions $\mathbf{n}$ and $-\mathbf{n}$ are equivalent and, in the case under consideration, there is no preferred director orientation (that can be set, e.g., by an external field). The elastic field has only one singularity along the capillary axis which will be referred to a helical disclination.

Now, let us calculate the free energy $F$ of a helical disclination. In the one-constant approximation [1], we have

$$F = \frac{K}{2}\int_{(V)}((\mathrm{div}\mathbf{n})^2 + (\mathrm{curl}\mathbf{n})^2)dV, \quad (8)$$

where $K$ is the Frank elastic constant and $V$ is the volume of the nematic. Substitution of (2) and (4) into (8)

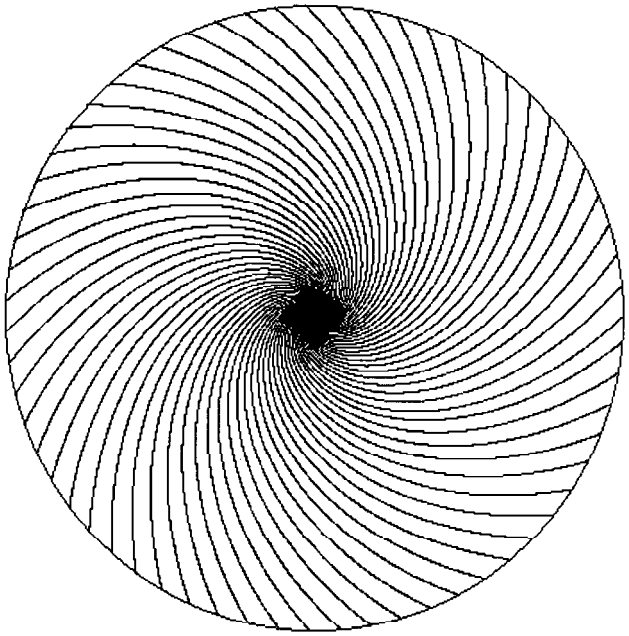

**Fig. 1.** Linear disclination of strength $m = 1$ in a cylindrical capillary: $\alpha(\rho = \rho_0) = \pi/4$.

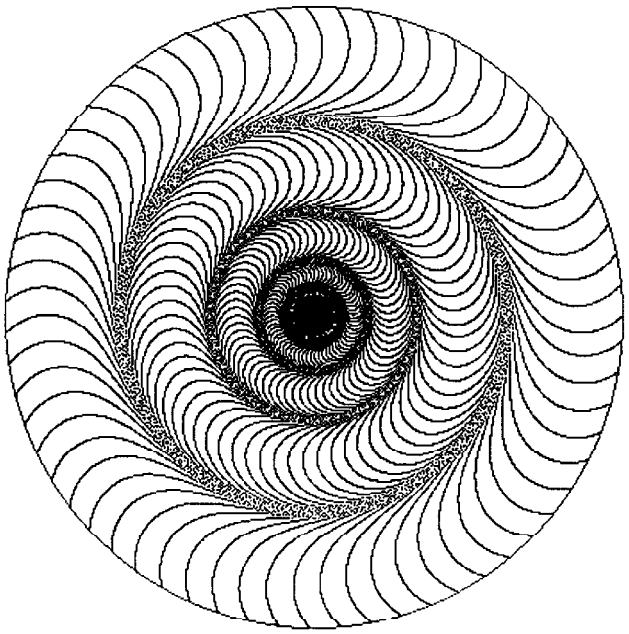

**Fig. 2.** Helical disclination in cylindrical capillary: $\alpha(\rho = \rho_0) = \pi/4$; $a = 10$.

yields:

$$F = \pi KL(a^2 + 1)\ln(\rho_0/b) + F_0, \tag{9}$$

where $L$ is the capillary length; $b$ is the order parameter on a molecular scale, having the sense of the radius of a disclination core radius; and $F_0$ is the disclination core energy, which cannot be estimated within the framework of the continuum theory [1]. Expression (9) shows that the energy of helical disclination is of the same order of magnitude as the energy of a conventional linear disclination of integral strength.

It is well known, that at the capillary radii $\rho_0 > \rho_c$, the structure with the above a singularity becomes unstable and "flows out" or "escapes" into the third dimension [3]. The preliminary calculations show that this property is also inherent in helical disclinations. This is obvious if $a = 0$. This case allows the complete analytical examination, will be considered in detail. (The singularity escape under the normal boundary conditions was considered elsewhere.)

Using the analogy with the Cladis–Kleman problem, we represent the director components in the form:

$$\begin{aligned} n_\rho &= \sin\beta(\rho/\rho_0)\cos\alpha(\rho/\rho_0), \\ n_\varphi &= \sin\beta(\rho/\rho_0)\sin\alpha(\rho/\rho_0), \\ n_z &= \cos\beta(\rho/\rho_0), \end{aligned} \tag{10}$$

where $\beta$ is the angle formed by a line of force and the capillary axis. Substituting (10) into (1), we arrive at the system of differential equations

$$\begin{aligned} &\sin(2\beta)(1 + (\alpha'_\xi)^2) = 2\beta''_{\xi\xi}, \\ &\sin\beta\alpha''_{\xi\xi} + 2\cos\beta\alpha'_\xi\beta'_\xi = 0, \\ &\xi \equiv \ln(\rho/\rho_0), \end{aligned} \tag{11}$$

whose simplest solution is

$$\begin{aligned} &\alpha = \text{const} \equiv \alpha_0, \\ &\beta_1 = 2\arctan(\rho/\rho_0) \quad \text{or} \quad \beta_2 = \pi - \beta_1. \end{aligned} \tag{12}$$

Integrating the system of equations for lines of force

$$\rho d\varphi/n_\varphi = d\rho/n_\rho = dz/nz, \tag{13}$$

with allowance for (10) and (12), we obtain

$$\begin{aligned} &\varphi - \varphi_0 = \tan\alpha_0 \ln(\rho/\rho_0), \\ &z - z_0 = \frac{\rho_0}{2\cos\alpha_0}\left(\ln(\rho/\rho_0) + \frac{1 - (\rho/\rho_0)^2}{2}\right), \end{aligned} \tag{14}$$

which is the equation of a helix (logarithmic helix "flowing out" into the third dimension), where $\varphi_0$ and $Z_0$ are integration constants. Now, substituting (10) and (11) into (8), we find the energy of helical structure

$$F = 3\pi KL. \tag{15}$$

Thus, one-sided escape of a linear disclination of the unit strength under the boundary conditions other than normal occurs at the same critical value of the capillary radius $\rho_c$, as in the Cladis–Kleman problem, and results in the formation of nonsingular helical structure. One can readily show, that in the case of two-sided escape (more natural for a nematic), the helical structure can has a radial or a hyperbolic point defect [4]. The study of structures formed upon the escape of helical disclination is more complicated and requires a special analysis.

Concluding the article, we should like to emphasize that the experimental observation of the structures with helical disclinations requires the knowledge of the director orientation on the capillary walls in the plane normal to the capillary axis. Otherwise, one has to introduce an additional boundary condition providing free director rotation about the normal to capillary walls, with the tilt angle being constant [5]. However, if such conditions are imposed, the above structures are not formed. If the director orientation is rigidly fixed in the plane normal to capillary axis, the equal probabilities of the director deviation in any direction from the normal is described by the trivial replacement of $\alpha_0$ by $2\pi - \alpha_0$ in (4) not changing the final result.

## REFERENCES

1. P. G. de Gennes, *The Physics of Liquid Crystals* (Clarendon Press, Oxford, 1974; Mir, Moscow, 1977).
2. S. Chandrasekhar and G. S. Ranganath, Adv. Phys. **35**, 507 (1986).
3. P. E. Cladis and M. Kleman, J. Phys. (Paris) **33**, 591 (1972).
4. V. K. Pershin and T. V. Kushnareva, Mol. Cryst. Liq. Cryst. **302**, 415 (1997).
5. L. D. Landau and E. M. Lifshitz, *The Theory of Elasticity* (Nauka, Moscow, 1987; Pergamon, Oxford, 1981).

*Translated by A.S. Zolot'ko*

*Crystallography Reports, Vol. 45, No. 2, 2000, pp. 310–311. Translated from Kristallografiya, Vol. 45, No. 2, 2000, pp. 343–344.*


**LIQUID CRYSTALS**

# The Energy of Radial and Hyperbolic Defects in a Long Cylindrical Capillary[1]

**V. K. Pershin* and T. V. Kouchnareva****

** Ural State University of Railway Transport, Yekaterinburg, Russia*
*e-mail: pershin@vitaly.csu.ac.ru*

*** University of British Columbia, Vancouver, Canada*
*e-mail: tania@physics.ubc.ca*

Received April 22, 1998

It is well known [1] that the planar linear disclination of the integral force $k = 1$ ($L_{+1}^{(p)}$) in a cylindrical capillary under the normal boundary conditions on its surface becomes unstable if the capillary radius $\rho_0$ exceeds a certain critical value $\rho_0^*$. In this case, an "escape" results in the disappearance of the singular core of the linear defect and the formation of a nonsingular disclination ($L^{(ns)}$).

The present paper studies the formation of unit point defects (*R*) and (*H*) formed due to two-sided escape of the disclination $L_{+1}^{(p)}$ in circular cylindrical capillary under the normal boundary conditions. The calculations and the analysis of the results are performed for a thin long cylindrical capillary.

To solve the above problem, calculate the energy of point defects formed as a consequence of the two-sided escape of the disclination $L_{+1}^{(p)}$. With this aim, use the expression for the free energy of a deformed nematic liquid crystal (NLC) in the one-constant approximation of the theory of elasticity [2]:

$$\hat{F} = \frac{1}{4\pi}\int\limits_{(V)} \{(\nabla\alpha)^2 + \sin^2\alpha(\nabla\beta)^2 + 2\sin\alpha(\mathbf{n}[\nabla\alpha, \nabla\beta])\}dV. \quad (1)$$

The symbol "^" is used to denote the energy normalized to $2\pi K$ (where *K* is the Frank elastic constant), and the symbol "(^)" marks the quantities related to the defects bound by the cylindrical surface. The angular functions $\alpha$ and $\beta$ define the position of the director $\mathbf{n}(\mathbf{r})$ in the local system of the coordinates [2] and satisfy the normal boundary conditions and the equilibrium condition, which in the cylindrical coordinate system $(\rho, \varphi, z)$ have the form:

$$\frac{\partial^2\beta}{\partial\varphi^2} = 0, \quad \frac{\partial^2\alpha}{\partial z^2} + \frac{\partial^2\alpha}{\partial\rho^2} + \frac{1}{\rho}\frac{\partial\alpha}{\partial\rho} - \frac{\sin\alpha\cos\alpha}{\rho^2} = 0. \quad (2)$$

Proceeding from symmetry of the problem, we assume that $\beta = \varphi$ and make use of the following approximate solution of (2) for *R*- and *H*-defects [3]:

$$\alpha^{(R)}(\rho, z) = 2\arctan\left\{\frac{\sqrt{\rho^2 + z^2q_+^2} - zq_-}{\sqrt{\rho^2 + z^2q_+^2} + zq_-}\right\}^{\frac{1}{2}},$$

$$\alpha^{(H)} = \pi - \alpha^{(R)}, \quad q_\pm(\rho) = 1 \pm \frac{\rho^2}{\rho_0^2}.$$

Now, single out a coaxial cylinder of the radius $\rho_1 \le \rho_0$ and the halfhight $z_1 \gg \rho_0$ in the capillary under consideration in such a way that the center of gravity coincides with the origin of the coordinate system and the core of the point defect. Then, it is possible to pass to the limit $\rho_0 \longrightarrow \infty$ in the formulas given below and to compare the results obtained with the data known for the corresponding defects in a free space.

Substituting $\alpha^{(i)}$ and $\beta = \varphi$ into (1), expanding it into power series in small parameter $\frac{\rho_1}{z_1} \ll 1$, retaining only the first nonvanishing term, and integrating over the variable *z*, we can represent the energy of the system as the following sum:

$$\hat{F}^{(i)} = \frac{\pi}{2}\chi_{i0}\rho_0 - \frac{3}{4}\frac{\rho_0^2}{z_1} + 3z_1 + \Delta F(\rho_0), \quad (3)$$

where

$$\chi_{i0} = \begin{cases} \frac{1}{6} + \frac{7}{8}\pi \approx 2.916, & i = R \\ \frac{13}{6} - \frac{1}{8}\pi \approx 1.774, & i = H. \end{cases}$$

[1] The full text of the paper is deposited at VINITI, June 9, 1999, no. 1858 B99.

1063-7745/00/4502-0310$20.00 © 2000 MAIK "Nauka/Interperiodica"

The term $\Delta\hat{F}(\rho_0)$ (weakly dependent on $z$ and vanishing at $\rho_0 \longrightarrow \infty$) can formally be regarded as the energy of interaction between a free point defect and a nonsingular disclination. Their superposition results in the formation of a structure which can be formed due to escape of $L_{+1}^{(p)}$.

Comparing (3) with the energy $\hat{F}^{(L)}$ of the linear disclination $L_{+1}^{(p)}$ [4]

$$\hat{F}^{(L)} = z_1 f_c + z_1 \ln\frac{\rho_0}{\rho_c}, \quad (4)$$

we arrive at the critical value of the capillary radius $\rho_0^*$. In the expression (4), $f_c$ and $\rho_c$ are the normalized energy of the disclination core per unit length and its radius, respectively. Indeed, from the equality of the energies $\hat{F}^{(L)} = \hat{F}^{(i)}$ we obtain

$$\rho_0^* = \rho_c e^g\left(1 + \frac{\pi}{2}\tilde{\chi}_{i0} e^g \frac{\rho_c}{z_1}\right), \quad (5)$$

where

$$g = 3 - f_c \text{ and } \tilde{\chi}_{i0} = \begin{cases} -\frac{7}{3} + \frac{41}{24}\pi \approx 3.0336, & i = H \\ -\frac{13}{3} + \frac{65}{24}\pi \approx 4.1752, & i = R. \end{cases}$$

The correcting term in (5) slightly increases the critical radius. However, the most important fact is not the value of the correcting term but rather its dependence on the cylinder length $z_1$, which, in principle, takes no place for a one-sided escape $L_{+1}^{(p)} \longrightarrow L^{(ns)}$ [1]. The dependence of the correcting term on $z_1$ implies, in fact, another size effect, which influences the stability of the disclination $L_{+1}^{(p)}$ within the cylindrical capillary but related not to the cylinder radius but to its length.

Thus, at the capillary radius exceeding the critical value $\rho_0^*$, the disclination $L_{+1}^{(p)}$ loses stability and escapes into the third dimension and forms the defects of the *R*- or *H*-type. Energetically, the formation of *H*-defects is more advantageous. However, almost twice decrease of the energy gap between the *R*- and *H*-defects in the bound state in comparison with the gap value for the free ones provides the real possibility for formation of *R*-defects as well.

## REFERENCES

1. P. E. Cladis and M. Kleman, J. Phys. **33**, 591 (1972).
2. S. Chandrasekhar and G. S. Ranganath, Adv. Phys. **35**, 507 (1986).
3. V. K. Pershin and T. V. Kushnareva, Mol. Cryst. Liq. Cryst. Sci. Technol., Sect. A **302**, 414 (1997).
4. P. G. de Gennes and J. Prost, *The Physics of Liquid Crystals.* 2nd ed. (Clarendon, Oxford, 1993).

*Crystallography Reports, Vol. 45, No. 2, 2000, pp. 312–317. Translated from Kristallografiya, Vol. 45, No. 2, 2000, pp. 345–351.*


**THIN FILMS**

# On an Unusual Azimuthal Orientational Relationship in the System Gallium Nitride Layer on Spinel Substrate

**A. N. Efimov, A. O. Lebedev, V. V. Lundin, and A. S. Usikov**

*Ioffe Physicotechnical Institute, Russian Academy of Sciences, Politekhnicheskaya 26, St.-Petersburg, 194021 Russia*

Received March 18, 1998; in final form, November 11, 1998

**Abstract**—Possible types of orientational relationships for hexagonal and cubic gallium nitride layers on aluminum–magnesium spinel substrates with various crystallographic orientations have been determined as a result of the theoretical and the experimental studies of this system. Most of the experimental data and the data obtained in the present study are consistent with the theoretical considerations. The causes of some apparent inconsistencies are discussed. *© 2000 MAIK "Nauka/Interperiodica".*

## 1. INTRODUCTION

Epitaxial gallium nitride layers are of great interest for optoeletronics. Usually, gallium nitride GaN is crystallized in the hexagonal wurtzite-type structure and sometimes also in the cubic sphalerite-type structure. Since it is impossible to grow large gallium nitride crystals, in optoelectronics, one uses epitaxial GaN layers grown on foreign substrates.

Earlier, we studied in detail, both experimentally and theoretically, the factors that can influence the orientational relationships in the III–V-type nitrides on sapphire [1–3]. The invocation of a large number of the experimental data on epitaxial growth of AlN, GaN, InN, and $Al_xGa_{1-x}N$ layers grown on various cuts (all the close-packed and nonsingular faces, i.e., the "faces of the general positions") and the use of the symmetry analysis and Monte-Carlo modeling of growth lead to the following conclusions:

(a) Metric matching of the layer and the substrate lattices does not essentially affect orientational relationships and degree of the structural perfection of the grown layers.

(b) The whole set of the orientational relationships formed in the system can be reliably predicted and classified on the basis of the analysis of the point symmetries of the layer and the substrate.

(c) The symmetry analysis admits two azimuthal orientations of the epitaxial layer, whereas the contacting plane of the layer for each chosen substrate cut is rigidly determined. All the attempts of *a priori* determination of one of these two orientations on the basis of the principle of the minimum lattice mismatch in the interface plane have been failed.

At the same time, an important information on the azimuthal misorientation can be obtained by computer simulation of the initial stages of nucleation. Thus, the dependence of the orientational relationships on the composition of the {0001}- and $\{11\bar{2}0\}$-oriented sapphire faces was successfully described without using any fitting parameters by the computer Monte–Carlo simulation of the initial stage of epitaxy [2].

The widespread use of sapphire substrates for epitaxial growth of nitrides with the wurtzite structure is explained by its stability to the aggressive high-temperature growth medium, availability of large sapphire substrates, and a high degree of their structural perfection rather than by their favorable crystallogeometrical parameters. Of great scientific and practical interest is also the study of the basic crystallographic characteristics of epitaxial growth of nitrides on some other chemically inert crystals. Such studies can lead to better characteristics of the structures used in various devices.

The use of the $MgAl_2O_4$ spinel (sp. gr. $Fd\bar{3}m$, $a \approx 8$ Å) as a substrate material is usually explained by two main factors. First, spinel substrates provide growth of high-quality epitaxial layers, whose structural characteristics are comparable with those of GaN layers grown on sapphire, the design of light-diode and laser structures [4–7]. Second, according to modern concepts, cubic spinel can be a favorable substrate for growing epitaxial cubic gallium nitride layers, which may be more attractive for optoelectronics.

## 2. METHODS OF EPITAXIAL GROWTH AND STUDY OF ORIENTATIONAL RELATIONSHIPS

### *2.1. Growth Methods*

Gallium nitride (GaN) layers were grown by the method of organometallic synthesis (OMS) in a horizontal flowing reactor with inductive heating under a low pressure (0.2 atm). The initial components were ammonia ($NH_3$) and trimethylgallium (TMG). The gas-carrier was hydrogen purified via diffusion through

1063-7745/00/4502-0312$20.00 

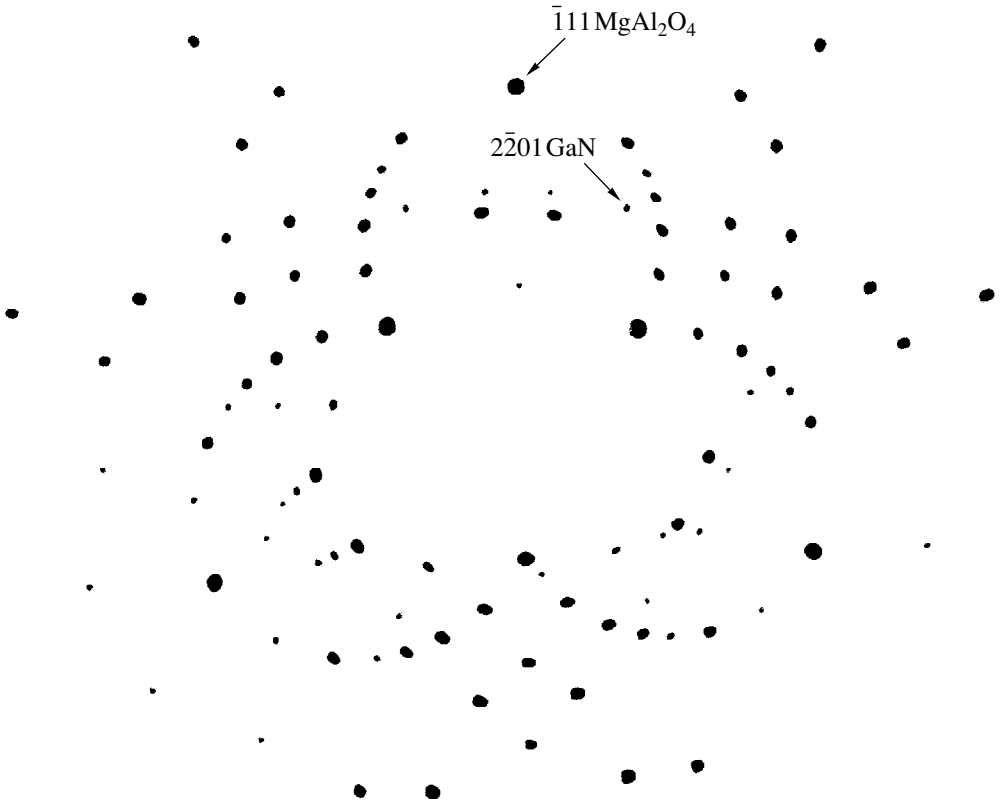


**Fig. 1.** Transmission Laue diffraction pattern from the GaN layer on the {111} $MgAl_2O_4$ substrate.

a palladium filter. The substrates were the {111}-oriented $MgAl_2O_4$ plates. At the first stage of growth, the buffer Al-doped GaN or GaN layers were grown on the substrate surfaces at temperatures 500°C. Epitaxial gallium nitride layers were grown in the reactor at 800–1000°C. The buffer gallium nitride layer was deposited at the following consumption of the reagents: TMG 24–96 μmol/min, $NH_3$ 1.5 l/min, and $H_2$ 45 l/min. The epitaxial GaN layer was grown at the TMG, $NH_3$, and $H_2$ flow rates equal to 36 μmol/min, 2.5 l/min, and 4.5 l/min, respectively. The typical thickness of the thus grown epitaxial layers ranged within 1.5–3.0 μm.

### *2.2. Results*

The orientational relationships in the heterostructures were studied by the traditional Laue method. The Laue patterns were indexed using the computer simulation by the method suggested elsewhere [8]. A typical transmission Laue diffraction pattern is shown in Fig. 1, the arrows indicate the $\bar{1}11$ $MgAl_2O_4$ and $2\bar{2}01$ GaN reflections. The corresponding orientational relationships can be formulated as follows: the {0001} plane of the layer is parallel to the {111} plane of the substrate, whereas the $\langle 01\bar{1}0\rangle$ direction of the layer is parallel to the $\langle 011\rangle$ direction of the substrate.

It should be emphasized that the above orientational relationship has not been observed for the method of organometallic synthesis (OMS) as yet. The conventional relationships observed for the heterostructures obtained by the method of organometallic synthesis are

$$\{111\}MgAl_2O_4//\{0001\}GaN,$$

$$\langle 110\rangle MgAl_2O_4//\langle 11\bar{2}0\rangle GaN.$$

They differ from the orientational relationship determined in our study by the layer rotation by 30°. Thus, we have to interpret the orientational relationships in the system gallium nitride on spinel.

## 3. SYMMETRY CONSTRAINTS IMPOSED ON THE ORIENTATIONAL RELATIONSHIPS IN THE SYSTEM (III–V)-TYPE NITRIDES ON SPINEL

Since gallium nitride and spinel have different symmetries and lattice parameters, one cannot predict *a priori* which crystallographic orientation will be implemented on the spinel substrate.

Earlier [1], we described the method providing the *a priori* prediction of the constraints imposed on single crystal growth in the system and the orientational relationships formed by analyzing two-dimensional point

**Table 1.** Orientational relationships allowed by the point symmetry in the system gallium nitride on spinel

| Type of relationship | Substrate orientation and its symmetry group | Layer orientation and its symmetry group | Direction in the substrate | Parallel direction in the layer |
|---|---|---|---|---|
| | | Hexagonal gallium nitride | | |
| *h*1 | {111}, 3*m* | {0001}, 6*mm* | $\langle \bar{1}\bar{1}2 \rangle$ | $\langle 10\bar{1}0 \rangle$ |
| *h*2 | {111}, 3*m* | {0001}, 6*mm* | $\langle \bar{1}\bar{1}2 \rangle$ | $\langle 11\bar{2}0 \rangle$ |
| *h*3 | {110}, 2*mm* | {0001}, 6*mm* | ⟨001⟩ | $\langle 11\bar{2}0 \rangle$ |
| *h*4 | {110}, 2*mm* | {0001}, 6*mm* | ⟨001⟩ | $\langle 10\bar{1}0 \rangle$ |
| *h*5 | {*hk*0}, *m* | {*HH*2*HL*}, *m* | $\langle \bar{k}h0 \rangle$ | $\langle \bar{L}\bar{L}2L6H \rangle$ |
| *h*6 | {*hk*0}, *m* | {0*KKL*}, *m* | $\langle \bar{k}h0 \rangle$ | $\langle 0\bar{L}L2K \rangle$ |
| *h*7 | {*hh*1}, *m* | {*HH*2*HL*}, *m* | $\langle \bar{1}\bar{1}2h \rangle$ | $\langle \bar{L}\bar{L}2L6H \rangle$ |
| *h*8 | {*hh*1}, *m* | {0*KKL*}, *m* | $\langle \bar{1}\bar{1}2h \rangle$ | $\langle 0\bar{L}L2K \rangle$ |
| | {001},4*mm* | No epitaxial growth is possible | | |
| | | Cubic gallium nitride | | |
| *c*1 | {111}, 3*m* | {111}, 3*m* | $\langle \bar{1}\bar{1}2 \rangle$ | $\langle \bar{1}\bar{1}2 \rangle$ |
| *c*2 | {111}, 3*m* | {111}, 3*m* | $\langle \bar{1}\bar{1}2 \rangle$ | $\langle 11\bar{2} \rangle$ |
| *c*3 | {110}, 2*mm* | {100}, 2*mm* | ⟨001⟩ | ⟨011⟩ |
| *c*4 | {110}, 2*mm* | {100}, 2*mm* | ⟨001⟩ | $\langle 01\bar{1} \rangle$ |
| *c*5 | {*hk*0}, *m* | {*HHL*}, *m* | $\langle \bar{k}h0 \rangle$ | $\langle \bar{L}\bar{L}2H \rangle$ |
| *c*6 | {*kk*1}, *m* | {*HHL*}, *m* | $\langle \bar{1}\bar{1}2h \rangle$ | $\langle \bar{L}\bar{L}2H \rangle$ |
| | {100}, 4*mm* | No epitaxial growth is possible | | |

symmetry of a bicrystal. The symmetry analysis for the heteroepitaxial system considered in the present article leads to several types of the orientational relationships for the layers of hexagonal and cubic gallium nitride allowed by the point symmetry (Table 1).

It is seen from Table 1 that single crystal hexagonal gallium nitride with the {0001} planes parallel to the substrate surface (the orientational relationships of the *h*1- and *h*2-types in Table 1) and cubic gallium nitride with the {111} planes parallel to the substrate surface (the orientational relationships of the *c*1- and *c*2-types) can grow on the {111} face of spinel. Most probably, the implementation of these orientational relationships in the experiment is dependent on the physical and chemical conditions existing during the growth process. The relationships of the *h*1- and *h*2-types differ by the 30°-rotation of the epitaxial layer with respect to the substrate around the ⟨0001⟩ axis. In these cases, the lattices match in different ways (Fig. 2).

The orientational relationships of the *c*1- and *c*2-type differ by the 180°-rotation of the layer about the {111}-axis of GaN whereas their lattices match the substrate lattice in the same way.

Thus, we can make an important practical conclusion: no epitaxial growth of cubic or hexagonal gallium nitride on the {001} face of spinel is possible.

It should also be emphasized that the above classification of the allowed orientational relationships for epitaxial growth on spinel substrates is valid not only for gallium nitride but also for any other material having the wurtzite- and sphalerite-type structures.

## 4. PUBLISHED DATA

The published experimental data on the epitaxial growth of gallium nitride on various spinel cuts are listed in Table 2. It is seen from Table 2 that the substrates used for growth of gallium nitride layers were the {111} and {001} spinel cuts, despite the possibilities provided by the cuts of other orientations (Table 1). However, with due regard for the above stated, the choice of the {001} orientation cannot be recognized as quite successful, despite the fact that it is the plane of natural cleavage that can readily be obtained.

On the {111}-oriented substrate, both orientational relationships predicted from the symmetry considerations of relationships *h*1 and *h*2 for the hydrochloride

(HC) method (Table 1) are possible (orientations 1 and 2 in Table 2). It should also be indicated that the competing formation of these orientations on the same substrate was observed [9]. No {111}-oriented cubic gallium nitride (relationships *c*1 and *c*2 in Table 1) grew on this spinel face, which can be explained by the fact that single crystal growth of more stable thermodynamically hexagonal gallium nitride is also allowed on such substrate.

On the {001}-orientated substrates, we also obtained mainly hexagonal gallium nitride, the cubic phase was detected only in some microregions [10]. Three orientational relationships were determined which, formally, do not satisfy the symmetry relationships obtained in the present study. At the same time, it was indicated [9, 10] that these orientational relationships can be attributed to microregions twinned at the macrolevel. In [10], it was stated that the films formed on the {001}-oriented spinel substrates had five different phases (instead of only one sphalerite phase, as was to be expected from the symmetry constraints), namely, four variants of the wurtzite-type phases (orientation) and one sphalerite-type phase (orientation). Using the symmetry consideration, we obtained that the $\{10\bar{1}1\}$ GaN face having the symmetry *m* is formed on the substrate having the symmetry 4*mm* (four variants). The appearance of the orientational relationships forbidden by the point symmetry can be explained by the fact that the {001} plane of the spinel cut was somewhat inaccurate and that the real symmetry of this cut was somewhat lower than 4*mm*. Thus, it was indicated [10] that the characteristics of the layer formed on the {001}, spinel face were essentially dependent on the errors in the substrate orientation. The exact orientation of such a substrate was not {001}, but rather {*hhl*} (depending on the deviation azimuth) with $h \ll l$ or {*hk*0}, where $h \ll k$. For such substrate cuts, the orientational relationships allowed by the point symmetry are those of the types *h*5–*h*8 in Table 1. Therefore, forbidden relationships 3–5 from Table 2 can be interpreted as the allowed ones from Table 1 for the substrate orientation very close but not equal to {001}. Table 3 represents the symmetry-forbidden orientational relationships as the limiting cases of the corresponding allowed relationships and indicates the corresponding limiting conditions imposed onto the crystallographic indices.

## 5. DISCUSSION

The critical analysis of the orientational relationships for the epitaxial systems formed by the components with considerably different structures and types of chemical bonding (i.e., not forming isomorphous series of solid solutions) such as silicon on sapphire, (III–V)-type nitrides with the sphalerite structure on spinel [1], (III–V)-type nitrides with the wurtzite structure on sapphire [2], and gallium nitride on spinel (the present study) allows us to formulate the following statements of the general character.

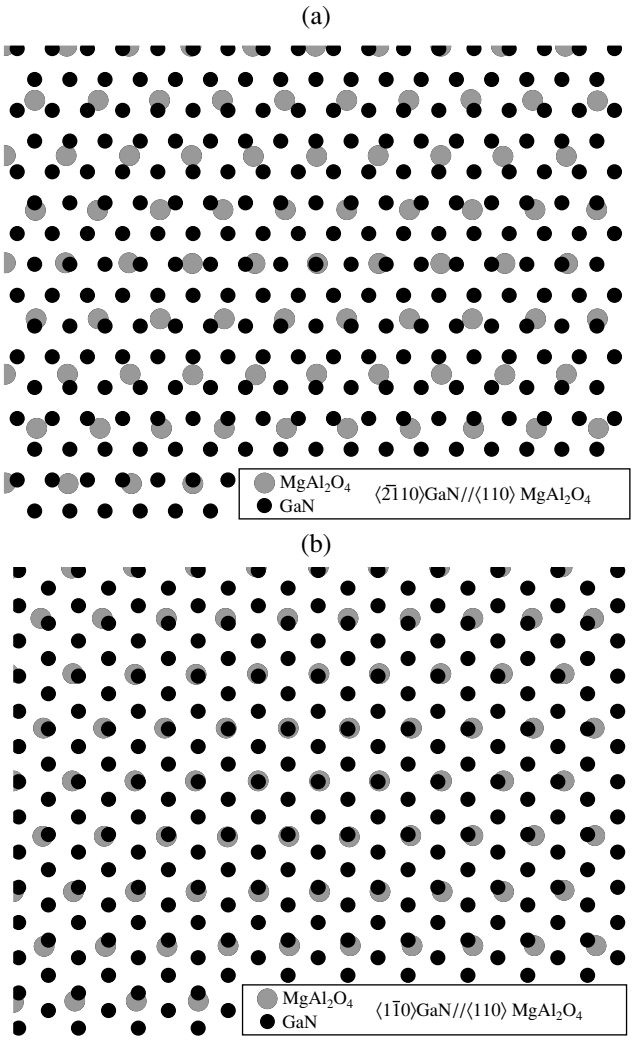


**Fig. 2.** Illustrating matching of the atomic nets at the gallium nitride–spinel interface: (a) the orientational relationship of the *h*1-type (observed experimentally in [4, 5]), (b) orientational relationship of *h*2-type (observed experimentally in the present study and in [9]).

One standpoint has it that the formation of an orientational relationship in an epitaxial system can be considered in terms of the minimum dimensional mismatch, namely, the layer orientation should be such that the difference in the lattice parameters in the interface plane would be minimal. This inevitably leads to a conclusion that the best substrate is the substrate providing the minimum mismatch. However, the comparative analysis of the 30°-rotation of the indium nitride layer and gallium and aluminum nitrides epitaxially grown on the basal plane of sapphire and a similar situation in the present study (the existence of two orientational relationships with different mismatch on the {111} plane of spinel) do not support this standpoint. Thus, for the {111} spinel substrate, the most often orientational relationship corresponds to the maximum mismatch of the layer and substrate lattice parameters

**Table 2.** Experimental data on epitaxial growth of gallium nitride on various spinel cuts

| Type of relationship | Plane and direction in the substrate | Plane and direction in the layer | Growth method, deposition temperature $T$, °C | Reference |
|---|---|---|---|---|
| 1 | (111), $(\bar{2}11)$ | (0001), $(1\bar{1}00)$ | OMS | [5] |
| | (111), $[1\bar{1}0]$ | (0001), $[11\bar{2}0]$ | OMS | [4] |
| | $\{111\}, \langle 1\bar{1}0\rangle$ | $\{0001\}, \langle 1\bar{2}10\rangle$ | HC | [9] |
| 2 | $\{111\}, \langle 1\bar{1}0\rangle$ | $\{0001\}, \langle 10\bar{1}0\rangle$ | HC | [9] |
| | $\{111\}, \langle 1\bar{1}0\rangle$ | $\{0001\}, \langle 10\bar{1}0\rangle$ | OMS | this work |
| 3 | $\{100\}, \langle 110\rangle$ | $\{0001\}, \langle 1\bar{2}10\rangle$ | HC, $850 < T < 950$ | [9] |
| 4 | $\{100\}, \langle 110\rangle$ | $\{10\bar{1}1\}, \langle 1\bar{2}10\rangle$ | HC, $T > 950$ | [9] |
| | $\{100\}, \langle 011\rangle$ | $\{10\bar{1}1\}, \langle 1\bar{2}10\rangle$ | OMS | [9] |
| 5 | $\{100\}, \langle 100\rangle$ | $\{10\bar{1}1\}, \langle 1\bar{2}10\rangle$ | HC, $500 < T < 600$ | [9] |

**Table 3.** Symmetry-forbidden experimentally observed orientational relationships represented as the limiting cases of the allowed relationships

| Experimental orientational relationship (Table 2) | Allowed orientational relationship (Table 1) | Experimental orientational relationship represented as the limiting case of the allowed relationship | | | | |
|---|---|---|---|---|---|---|
| | | substrate orientation | layer orientation | direction in the substrate | direction in the layer | limiting conditions |
| 3 | $h7$ | $\{1hh\}$ | $\{HH\overline{2H}L\}$ | $\langle\overline{2h}\,ll\rangle$ | $\langle\bar{L}\bar{L}\,2L6H\rangle$ | $l \longrightarrow 1, h \longrightarrow 0$<br>$H \longrightarrow 0, L \longrightarrow 1$ |
| 3 | $h8$ | $\{1hh\}$ | $\{0K\bar{K}L\}$ | $\langle\overline{2h}\,ll\rangle$ | $\langle 0\bar{L}\,L2K\rangle$ | $l \longrightarrow 1, h \longrightarrow 0$<br>$K \longrightarrow 0, L \longrightarrow 1$ |
| 4 | $h8$ | $\{1hh\}$ | $\{K0\bar{K}L\}$ | $\langle\overline{2h}\,ll\rangle$ | $\langle\bar{L}\,0L2K\rangle$ | $l \longrightarrow 1, h \longrightarrow 0$<br>$K \longrightarrow 1, L \longrightarrow 1$ |
| 5 | $h6$ | $\{hk0\}$ | $\{K0\bar{K}L\}$ | $\langle kh0\rangle$ | $\langle\bar{L}\,0L2K\rangle$ | $h \longrightarrow 1, k \longrightarrow 0$<br>$K \longrightarrow 1, L \longrightarrow 0$ |

(Fig. 2). Moreover, the numerous published experimental data show that the widespread opinion on the direct relation between the crystal perfection and the lattice mismatch in nonisomorphous epitaxy is not always correct. Thus, Kung *et al.* [11] reported growth of gallium nitride layers on {001} $LiGaO_2$ substrates. In terms of the dimensional lattice mismatch, this substrate can hardly be recognized as the optimum one (the mismatch value ~1–2%). However, the diffraction data show that the crystal perfection of these layers (the minimum halfwidth of the X-ray rocking curve 300″) is much worse than the degree of perfection of the layers grown on the basal plane of sapphire (the best data show less than 60″ with the mismatch of 14%). Moreover, in many other studies, gallium nitride layers were grown on silicon carbide substrates. Proceeding from small mismatch and closeness of the crystal structures and types of chemical bonding in the layer and the substrate, one could expect rather high degree of perfection for such layers, but, in fact, the crystal perfection of gallium nitride layers was not higher than for layers grown on the basal plane of sapphire.

Another interpretation of the orientational relationships obtained during nonisomorphous epitaxy is based on the structural and chemical aspects of bicrystal formation, i.e., on the consideration of the structural and chemical models of a real surface of the substrate and the attempts to describe the possible formation of the directional bonding between the concrete types of atoms in the layer and the substrate [12]. Despite the

fact that this approach seems to be promising, the above examples make it rather dubious. Thus, the application of this approach to AlN, GaN, and InN grown on the {0001} plane of sapphire should yield the same orientational relationships because of the similar structures and bonding in these isomorphous nitrides. However, this contradicts the known experimental data. Moreover, this approach does not allow one to interpret the reliably established existence of two different orientational relationships on the {111} plane of spinel.

At the same time, a simple but effective method of symmetry analysis developed in the present study can provide an important *a priori* information on possible types of orientational relationships. The already accumulated experimental data on new nontraditional substrates, growth media, and temperature–time modes show that most of the orientational relationships predicted earlier within the framework of the symmetric approach [13] are also confirmed experimentally.

## ACKNOWLEDGMENTS

The study was supported by the Russian Foundation for Basic Research, project no. 97-02-18017. One of the authors (A.O.L) was supported by the State Committee for Higher Education of the Russian Federation, project no. 96-26-3.5-28.

## REFERENCES

1. A. N. Efimov and A. O. Lebedev, Thin Solid Films **260**, 111 (1995).
2. A. N. Efimov, A. O. Lebedev, and A. M. Tsaregorodtsev, J. Appl. Crystallogr. **31**, 461 (1998).
3. A. N. Efimov and A. O. Lebedev, Surf. Sci. **344**, 276 (1995).
4. C. J. Sun, J. W. Yang, Q. Chen, *et al.*, Appl. Phys. Lett. **68**, 1129 (1996).
5. A. Kuramata, K. Horino, K. Domen, *et al.*, Appl. Phys. Lett. **67**, 2521 (1995).
6. J. W. Yang, Q. Chen, C. J. Sun, *et al.*, Appl. Phys. Lett. **69**, 369 (1996).
7. Sh. Nakamura, M. Senoh, S. Nagahama, *et al.*, Appl. Phys. Lett. **68**, 2105 (1996).
8. A. O. Lebedev, Zavod. Lab.: Diagnostika Mater. **64**, 16 (1998).
9. A. Tempel, W. Seifert, J. Hammer, *et al.*, Krist. Tech. **10**, 747 (1975).
10. T. George, E. Jacobsohn, W. T. Pike, *et al.*, Appl. Phys. Lett. **68**, 337 (1996).
11. P. Kung, A. Saxler, X. Zhang, *et al.*, Appl. Phys. Lett. **69**, 2116 (1996).
12. M. J. Davies, S. C. Parker, and G. W. Watson, J. Mater. Chem. **4**, 813 (1994).
13. A. N. Efimov, A. O. Lebedev, and A. M. Tsaregorodtsev, Izv. Leningrad Élektrotekh. Inst., No. 365, 24 (1986).

*Translated by L. Man*

*Crystallography Reports, Vol. 45, No. 2, 2000, pp. 318–322. Translated from Kristallografiya, Vol. 45, No. 2, 2000, pp. 352–356.*


**THIN FILMS**

# Model of Packing of Cellulose Acetomyristinate in Langmuir–Blodgett Films

**A. K. Khripunov*, Yu. G. Baklagina*, N. D. Stepina**, L. G. Yanusova**, L. A. Feigin**, V. M. Denisov*, A. Ya. Volkov*, and V. K. Lavrent'ev***

** Institute of Macromolecular Compounds, Russian Academy of Sciences, St.-Petersburg, Bol'shoĭ pr. 31, St.-Petersburg, 199004 Russia*

*** Shubnikov Institute of Crystallography, Russian Academy of Sciences, Leninskiĭ pr. 59, Moscow, 117333 Russia*

Received April 28, 1998

**Abstract**—The variation of the structural characteristics in the transition from a block polymer to a Langmuir–Blodgett film has been investigated for cellulose acetomyristinate by the methods of X-ray diffraction analysis. The effect of length and number of acid residues on the diffraction pattern of block cellulose acetomyristinate is studied. The role of acyl substituent in the formation of an ordered structure of multilayer Langmuir–Blodgett films is established. A model of packing of cellulose acetomyristinate molecules in the *Y*-type films is suggested. The model is based on a two-domain structure in which close-packed myristic-acid residues are located either normally or at a certain angle to the plane of glucoside rings on one side of the polymer chain. © *2000 MAIK "Nauka/Interperiodica"*.

To synthesize new materials based on natural macromolecular compounds, which meet the requirements of supramolecular chemistry, one has to know their detailed molecular characteristics and the structures of the starting polymers. It it well known [1, 2] that the experimental data on the properties of monolayers of the same polysaccharide derivatives are inconsistent. Therefore, it is clear that only the systematic study of chemical structures and molecular characteristics of homologous series of polysaccharide derivatives can provide more reliable interpretation of the results.

We had the aim to study the possibilities of synthesizing ordered Langmuir–Blodgett (LB) films from mixed cellulose esters of the myristic and acetic acids with regularly varying chemical structures and to establish the relation between the block polymer and the structure formed as a result of the forced organization of macromolecules in an LB film.

## EXPERIMENTAL

Cellulose acetomyristinate (CAM) was synthesized by acylation of linter cellulose with the mixture of the acetic and myristic acids with the use of trifluoroacetic acid anhydride in the atmosphere of the trifluoroacetic acid by the method described elsewhere [3]. The substitution degree $\gamma$ of the mixed cellulose ester with respect to the myristic and acetic acids was established by analyzing the corresponding proton magnetic-resonance spectra of the CAM solutions in the trifluoroacetic acid and deuterated chloroform. The spectra were recorded on a JEOL-C-60HL (Japan) and a Bruker AC-200 (Germany) spectrometers. We synthesized a number of cellulose acetomyristinates denoted as 290/10, 275/25, 250/50, 200/100, 150/150, 100/200, 50/250, 10/290 (the numerator indicates the $\gamma$ value with respect to the myristic acid and the denominator, the $\gamma$ value with respect to the acetic acid).

Langmuir–Blodgett films were obtained on a Joyce–Loebl Langmuir Trough-4 (United Kingdom). Cellulose esters were applied onto a subphase (water tridistillate) from a 1 mg/ml benzene solution. A CAM-1 solution was applied onto the subphase upon the preliminary dissolution of a dry substance in benzene without no subsequent treatment. Prior to the application of a CAM-2 solution onto the subphase, it was subjected to centrifuging. The rate of monolayer compression on the subphase was 0.01 $m^2$/min. Then the layers were transferred onto silicon or glass substrates by the Langmuir–Schaefer method of horizontal lift under various surface pressures and times of layer keeping on the subphase prior to its compression.

The small-angle X-ray study of LB films consisting of 40 monolayers on a silicon substrate was performed on an AMUR-K diffractometer with the two-dimensional position-sensitive detector with a copper anode and a nickel filter at the 30 kV voltage. The X-ray study of block samples was performed on a DRON-II diffrac-

1063-7745/00/4502-0318$20.00 © 2000 MAIK "Nauka/Interperiodica"

tometer and in a Kratky camera with the use of the Ni-filtered Cu$K_\alpha$-radiation.

## RESULTS AND DISCUSSION

The X-ray diffraction study of the compressed CAM samples showed that with an increase of the myristic acid content the degree of the mutual order of polymer molecules also increases. Indeed, both position and half-width of the small-angle reflection ($2\theta$ = 2°–3°) characterizing the lateral periodicity on the diffraction patterns from mesomorphic cellulose esters depend on the $\gamma$ value. The interplanar spacing for CAM samples with $\gamma$ = 290/10, 275/25, 250/50, and 200/100 ranges from 42.2 to 35.5 Å (Fig. 1, curves *1* and *2*). A further reduction of the number of myristic residues ($\gamma$ = 150/150, 100/200) results in a decrease of the intensity of the small-angle reflection and its shift to the range of large angles (Fig. 1, curves *3* and *4*). The interplanar spacing in CAM 150/150 is 29 Å, and in CAM 100/200, 26 Å. The intensities of reflections in the angular range $2\theta$ = 20° (Fig. 1) is stable for CAM samples with the $\gamma$ ranging from 290/10 to 100/200. With a decrease of the substitution degree with respect to the myristic acid (50/250 and 10/290), the samples undergo amorphization (Fig. 1, curve *5*).

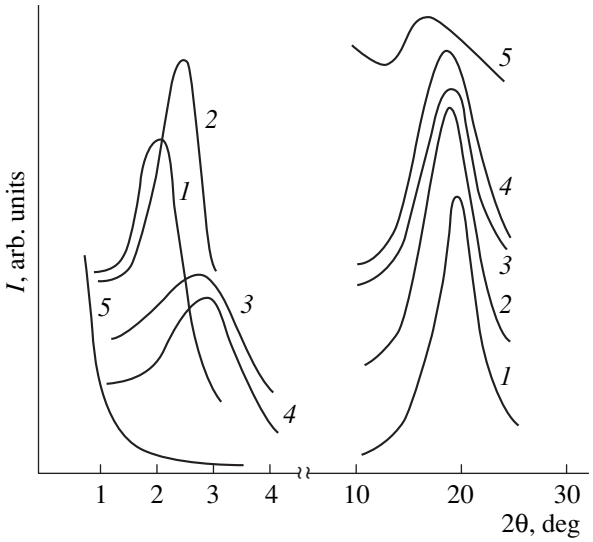


**Fig. 1.** Diffraction patterns from compressed CAM samples with various substitution degrees: (*1*) 290/10, (*2*) 200/100, (*3*) 150/150, (*4*) 100/200, and (*5*) 10/290.

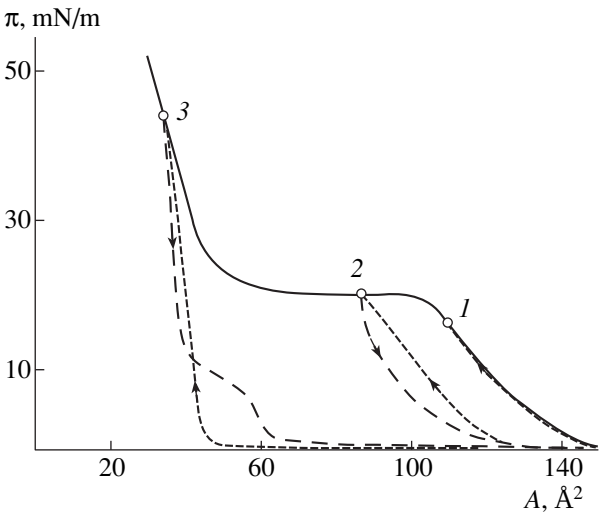


**Fig. 2.** The $\pi$–*A* isotherm for CAM (290/10).

Figure 2 shows the $\pi$–*A* isotherms (the dependence of the surface pressure $\pi$ on the area *A* per glucoside unit) in a CAM layer ($\gamma$ = 290/10) on the subphase. Under a surface pressure of about 18 mN/m, we observed the formation of a characteristic plateau accompanied by the change of a glucoside ring area from 106 to 55 Å$^2$. The isotherm has three characteristic regions. Under a surface pressure less than 18 mN/m, the isotherm in region *1* is reversible. At a pressure exceeding 18 mN/m, the isotherm in region *2* stops being reversible. Upon extension of a monolayer preliminarily compressed under a surface pressure of 18.5 mN/m and then compressed again, the plateau on the isotherm became shorter, and the curve started rising at a smaller monolayer area. In region *3* (under a pressure exceeding 20 mN/m), upon the second secondary compression of a monolayer preliminarily compressed under a surface pressure of 35 mN/m, the plateau disappears at all, and the curve showed only a feebly marked bending. The character of the $\pi$–*A* isotherm depends on the rate of monolayer compression, the initial density of a monolayer, and the time of its keeping on the subphase prior to its compression. The reversibility of the isotherm depends on the pressure applied for the initial monolayer compression. This effect is essential in the range of the condensed monolayer and indicates the formation of different structures in the layer.

Analyzing the $\pi$–*A* isotherms, we estimated the area per glucoside ring under a certain value of surface pressures. Using the CAM-2 solution, we determined the area at the initial stage of the isotherm rise as 144 Å$^2$; at the beginning of the plateau, it was equal to 106 Å$^2$; and under the surface pressure of 34 mN/m, it was 37 Å$^2$, whereas the area estimated along the tangent to the $\pi$–*A* isotherm in the range of a condensed layer was equal to 56 Å$^2$. The theoretically calculated area of the repeating unit is about 60 Å$^2$. Using the CAM-1 solution, we observed somewhat smaller areas. At the beginning of the isotherm rise, the area was equal to 131 Å$^2$, at the beginning of the plateau (the phase transition), 88 Å$^2$, and under the surface pressure of 34 mN/m, it was equal to 31 Å. The larger area per glucoside ring obtained with the use of the preliminarily treated CAM-2 solution seems to be associated with the formation of a more homogeneous film on the subphase

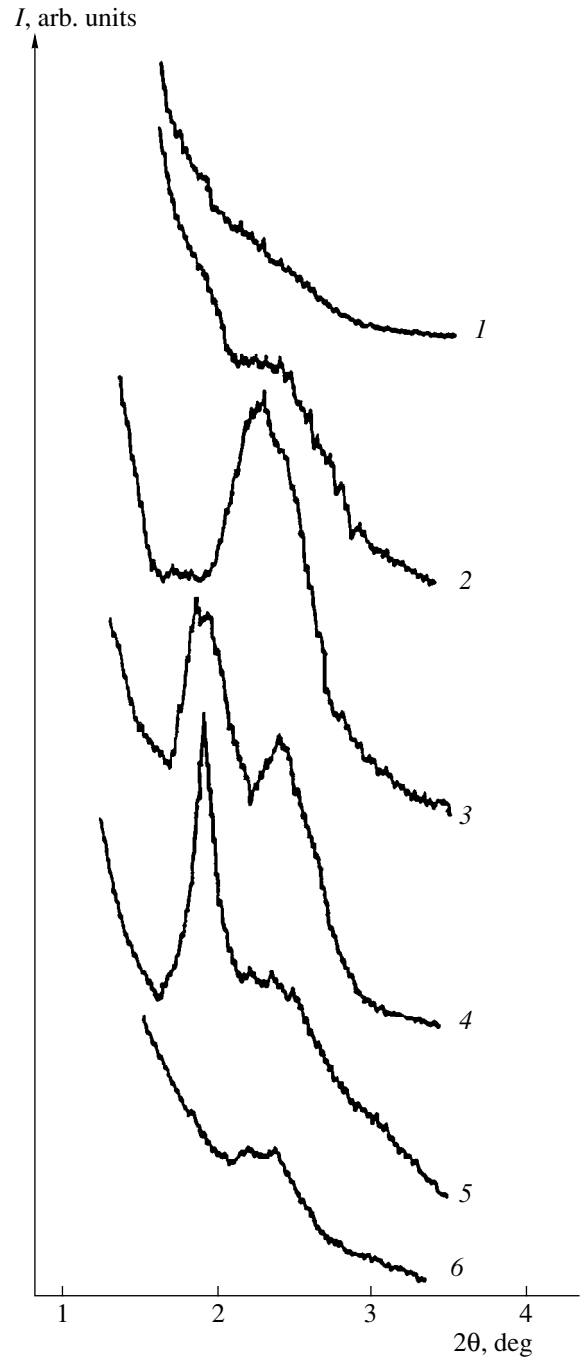


**Fig. 3.** Small-angle diffraction patterns from LB films consisting of 40 layers obtained upon 4 h-keeping of a monolayer on the subphase prior to its compression at various surface pressures: (*1*–*4*) CAM-2 and (*5*, *6*) CAM-1, (*1*) 5, (*2*) 12, (*3*) 17, (*4*, *5*) 35, and (*6*) 35 mN/m.

surface. The CAM-1 solution can contain aggregates of the molecules preserved on the subphase. These aggregates would decrease the area calculated per glucoside ring [4]. The *A*-values at various characteristic points of the $\pi$–*A* isotherms for CAM are well consistent with the known data [5].

X-ray studies of CAM-1 multilayers ($\gamma$ = 290/10) were performed on samples obtained under various surface pressures (5, 12, 17, 28, and 35 mN/m) and times of keeping monolayers on the subphase prior to their compression. The corresponding diffraction patterns from a multilayer film formed under a surface pressure of 5 mN/m showed no Bragg maxima (Fig. 3, curve *1*). The films obtained under surface pressures of 12 mN/m showed a diffuse arm corresponding to the periodicity of 39–49 Å (Fig. 3, curve *2*). A close packed layer structure with a period of 37 Å was obtained under surface pressures of 17 mN/m and higher (Fig. 3, curve *3*). Under a surface pressure of 35 mN/m, the films obtained provided the formation of two systems of Bragg reflections corresponding to the periods of 40 and 50 Å (Fig. 3, curve 4). At the same time, the diffraction curve from the LB-film of CAM-2 formed upon 4-h keeping monolayers on the subphase prior to their compression showed only a broad diffuse reflection (Fig. 3, curve *6*).

The construction of a model for a dimer fragment using the Alchemy program [6] allowed us to estimate the thickness of a monolayer proceeding from the steric model of the repeating unit of the cellulose ester macromolecule. The values obtained, 20.7 and 24.1 Å, agree quite well with the known X-ray data under the assumption that the formation of an LB film is accompanied by the formation of the structure of the *Y*-type (Fig. 4a). This conclusion contradicts the results obtained in [5], where the formation of the *X*-type structure was assumed. In our case, the formation of the *Y*-type structure is also confirmed by the fact that the substrate remained dry upon the layer removal.

It is well known that an elevated stiffness of the chains of cellulose derivatives and the tendency to the formation of helical structures lead to the formation of self-ordered mesomorphic regions [2]. The X-ray studies and the conformation analysis of a number of cellulose esters showed that, depending on the relationship between the length, the orientation, the number of side substituents, and the methods of sample "planting," one can obtain different types of diffraction patterns similar to those from amorphous, mesomorphous, or crystalline samples [7, 8]. Since the glucopyranose rings of cellulose esters have mainly the chair conformation, whereas the polymer chains have the helical structure, these chains are usually considered as pseudocylindrical helical molecules with the statistically averaged arrangement of the side substituents. The molecule section can be depicted as a circle with the average diameter dependent on the dimensions of the side substituents. Usually, aggregation of such molecules is described in terms of the hexagonal packing of the chains [9] and therefore the small-angle reflection of the block CAM ($\gamma$ = 290/10) with $d = 41 \pm 2$ Å (Fig. 1,

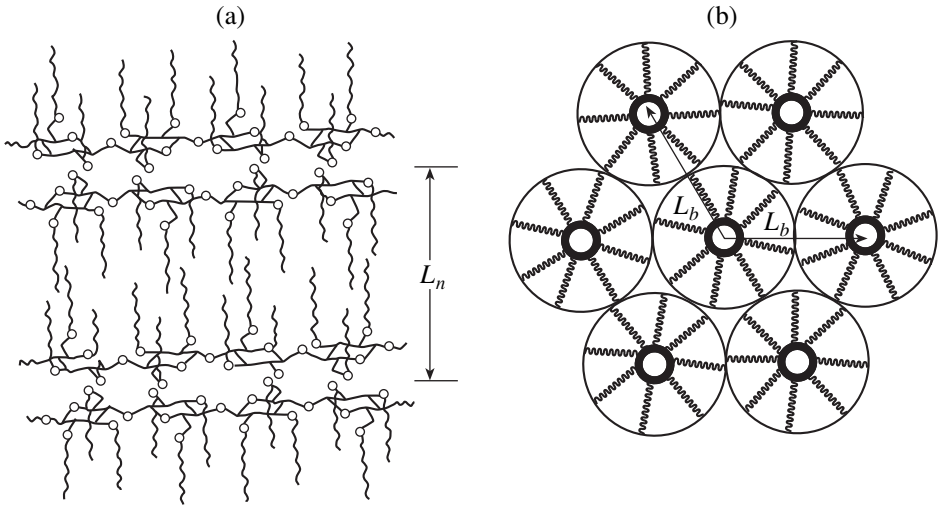


**Fig. 4.** Schematic of (a) *Y*-type packing of CAM molecules (290/10) in an LB film, where $L_n$ is the period along the surface normal and (b) the hexagonal packing of molecules in block CAM samples, where $L_b$ is the average interchain distance.

curve *1*) corresponds to the distance between the axes of such polymer chains, $L_b = 47.6$ Å (Fig. 4b).

The model of mutual CAM packing ($\gamma$ = 290/10) suggested for the block sample correlates with the results obtained for multilayer LB film of the same sample. The multilayer structure built by CAM bilayers can be considered as a single-domain crystal with the period $L_n$ along the substrate normal (Fig. 4a). Depending on the conditions of LB preparation, the position and the halfwidth of reflections characterizing the period $L_n$ vary and give the values 40 or 50 Å, whereas in the case of the film obtained under the surface pressure $\pi$ = 35 mN/m, both these periods are formed simultaneously. We believe that the existence of domains with two values of the one-dimensional periodicity along the substrate normal can be explained in terms of the conformational polymorphism in CAM chains.

It is shown [7] that, depending on the angles of internal rotation about the glucoside bonds on the conformation maps of dimer fragments of the cellulose ester, there are two conformational regions with the minimum energies. It is shown that, for many esters, the energies necessary for the conformational transitions from one minimum to another are very close. The absence of any experimental proof of the existence of crystal structures corresponding to these two regions, even in highly oriented fibers of the cellulose ester, is explained by the conformational polymorphism of the macrochain, which hinders the formation of stereoregular polymers. A great variety of structural models of cellulose esters is also associated with the rotational properties of the side groups, although, according to the calculations, the conformations with the perpendicular arrangement of the substituents with respect to the chain backbone dominate in the structure [7, 8].

It is well known that the organization of a Langmuir layer on the subphase is essentially dependent on the conformational mobility of the polymer chain and the number and the length of the side hydrophobic groups. In our case, the interactions between the myristic hydrocarbon radicals increase the cohesion between the main CAM chains. As has already been indicated, a CAM layer can have at least two stable conformations. The constructions of models for a fragment consisting of two rings of the CAM chain (Fig. 4) indicates the possible formation of two types of structural groupings depending on the mutual rotation of the glucoside rings. In the first case, the normal orientation of hydrophobic substituents with respect to the cellulose-chain backbone yields the bilayer period equal to 48.1 Å, whereas its experimental value is $L_n = 50$ Å. In the second case, the bilayer period equals 41.4 Å, whereas its experimental value, 40 Å, can be determined even at a slight deviation of the myristic residues from the normal to the polymer-chain backbone.

Thus, two regions of stable conformation states, which were predicted theoretically for a number of cellulose esters but were not observed experimentally even for highly-oriented fibers, were revealed in the process of forced organization of a two-dimensional structure of CAM molecules ($\gamma$ = 290/10) on the water surface. We believe that the model of two-domain packing in the *Y*-type LB films suggested on the basis of the above analysis can be of the theoretical and practical interest for obtaining multilayer structures of cellulose derivatives.

## REFERENCES

1. V. V. Arslanov, Usp. Khim. **63**, 3 (1994).
2. N. V. Tsvetkov, A. K. Khripunov, E. P. Astapenko, and S. D. Didenko, Vysokomol. Soedin., Ser. A **37**, 1306 (1995).
3. A. K. Khripunov, O. P. Koz'mina, I. N. Shteinikova, *et al.*, Zh. Prikl. Khim. (Leningrad) **43**, 2581 (1970).
4. L. Zatz Joel, J. Colloid Interface Sci. **33**, 465 (1970); K. Borgin and P. Johuson, J. Chem. Soc., Faraday Trans. **49**, 956 (1953).
5. T. Kawaguchi, H. Nakahara, and K. Fukuda, Thin Solid Films **133**, 29 (1985).
6. W. H. Press, B.P. Flannery, S. A. Tenkolsky, and W. T. Vetterling, *Numerical Recipes. The Art of Scientific Computing* (Cambridge Univ. Press, Cambridge, 1986), p. 160.
7. V. P. Panov and R. G. Zhbanov, *Molecular Interactions in Carbons* (*Nonvalent Interactions and Conformation*) (Nauka i Tekhnika, Minsk, 1988).
8. P. Zugenmaier and U. Vogt, Makromol. Chem. **184**, 1749 (1983).
9. B. K. Vainshtein, *Diffraction of X-rays by Chain Molecules* (Isd. AN SSSR, Moscow, 1963; Elsevier, Amsterdam, 1996).

*Translated by L. Man*

*Crystallography Reports, Vol. 45, No. 2, 2000, pp. 323–328. Translated from Kristallografiya, Vol. 45, No. 2, 2000, pp. 357–363.*


**CRYSTAL GROWTH**

# Migration of Liquid Inclusions in a Solid under Asymmetric Temperature Oscillations

**V. Yu. Gershanov*, S. I. Garmashov, and I. Yu. Nosuleva**

*Rostov State University, Rostov-on-Don, Russia*

** e-mail: vgersh@jeo.ru*

Received February 10, 1997; in final form, July 27, 1999

**Abstract**—The existence of a new type of thermal migration has been found—the migration of the layer of a liquid phase between two substrates possessing different properties (e.g., two different cuts of a crystal) occurring under the action of asymmetric temperature oscillations. The effect can arise if three following conditions are simultaneously fulfilled: (1) the kinetic properties of the solid–liquid interfaces should be different, (2) the dependence of the growth (dissolution) kinetics on supersaturation should be nonlinear at least at one of the interfaces, and (3) the temperature oscillations should be asymmetric. It is shown that both sign and absolute value of the migration velocity depend on the shape of temperature oscillations. The velocities of migration for liquid layers of various thicknesses as functions of the amplitude of thermal oscillations, their shape, and frequency are calculated for the model Si–Al system. *© 2000 MAIK "Nauka/Interperiodica".*

## INTRODUCTION

The effect of liquid-inclusion migration under the effect of a chemical-potential gradient caused by various external factors in a solid has long been known [1, 2]. The theory of flat liquid-layer motion through an anisotropic crystal with due regard of three possible mechanisms of interphase processes for the stationary case under the effect of the temperature gradient was considered in [2]. Three growth (dissolution) mechanisms were considered, i.e., the normal, dislocation- and the nucleation-controlled mechanisms. The possible differences in the growth and the dissolution kinetics were taken into account. It should be emphasized that the limitations imposed on mass transport by the interphase kinetics result in the characteristic decrease in the migration velocity in the range of small layer thicknesses. At large thicknesses, the rate of thermal migration (hereafter called the diffusion rate) is limited mainly by the mass transport in the volume of the liquid phase. Earlier [3, 4], the theory of thermal migration was extended to the nonstationary process temperature. Two types of temperature oscillations are considered—those with the rectangular and sinusoidal profiles, with all the remaining assumptions being the same as in the model described in [2]. It is shown that if the growth and dissolution processes are nucleation-controlled, temperature oscillations with the amplitudes of the order of several hundredths (tenths) of a degree increase the thermal-migration rate for thin (<100 μm) planar inclusions up to the diffusion rate. This effect is caused by the nonlinearity of the dependence of interfacial kinetics on the real supersaturation, resulting in the fact that the instantaneous magnitude of the effective concentration gradient in the liquid phase under nonstationary temperature conditions deviates from the concentration gradient under the stationary conditions.

It should be indicated that in [2, 3], the properties of both interfaces were assumed to be the same. Moreover, taking into account the nonstationary temperature conditions, it was assumed [3] that the growth and the dissolution kinetics was the same and the profile of temperature oscillations was symmetric. Under these assumptions, an increase in the effective temperature gradient in the liquid led to an increase of the migration velocity of the liquid layer. We shall show that the asymmetry of temperature oscillations, the difference in the interface kinetics, and the nonlinearity of the dependence of the growth (dissolution) kinetics on supersaturation (at least for one of the interfaces) should give rise to an additional force, which, in the absence of any temperature gradient, sets the liquid layer in motion.

We believe that migration of a liquid layer under the action of only asymmetric temperature oscillations is a qualitatively new effect. We had the aim to reveal the factors responsible for this effect and to analyze the influence of their variation on the migration velocity of the liquid layer. For simplicity, we assume the external temperature gradient to be zero. Obviously, in the general case, the effect under consideration and thermal migration, can take place simultaneously, then the total velocity of migration is determined by their superposition.

## THE MODEL

Prior to the qualitative analysis of the effect under study, calculate the velocity of migration of a plane-parallel layer of the solution of the substance A in the

1063-7745/00/4502-0323$20.00 © 2000 MAIK "Nauka/Interperiodica"

melt of the substance B sandwiched between two differently oriented single-crystal plates of the substance A caused by the temperature variation occurring at a constant rate $a_{c(h)} = dT/dt$, where the subscripts c and h correspond to cooling and heating, respectively. The interface located at $x = 0$ (Fig. 1) is taken to be nonsingular and therefore can be considered as absorbing, in other words, supersaturation at this interface is always zero, irrespectively of the influx of the substance A. The other interface located at $x = l$ is singular. At this interface, the growth and the dissolution processes proceed by the two-dimensional nucleation. The thickness of the liquid phase layer is assumed to be so small that no convective stirring can occur. The segregation coefficient of the solvent is taken to be zero to avoid the variation in the volume of the liquid layer during its motion. As is shown in [2], the effect of the interface motion on the concentration field in the liquid and the heat effects of phase transitions can also be neglected.

The mass transport in the liquid is described by the nonstationary diffusion equation:

$$\frac{\partial C}{\partial t} = D\frac{\partial^2 C}{\partial x^2}, \quad (1)$$

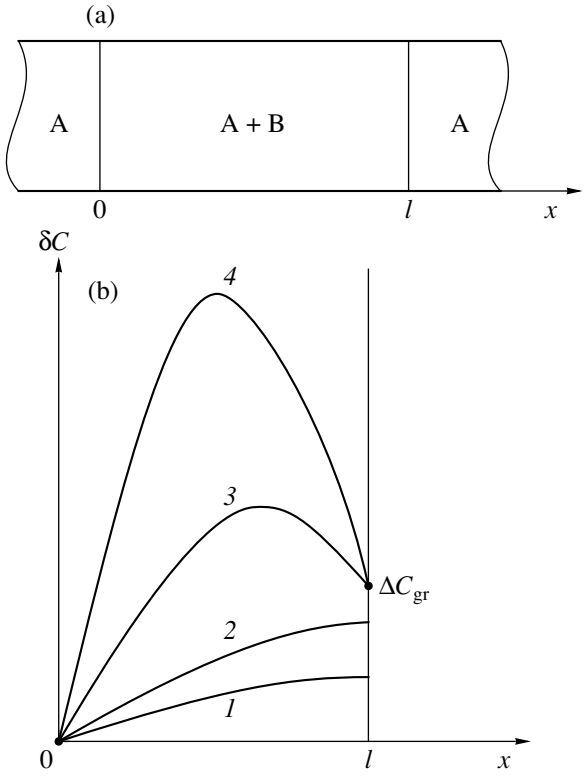


**Fig. 1.** (a) Geometry of the problem and (b) supersaturation profiles in the liquid obtained during system cooling at the rates (*1*, *2*) violating and (*3*, *4*) satisfying criterion (11). The absolute value of the cooling rate increases with the serial number of the curve.

where $D$ is the coefficient of mutual diffusion of the components in the A–B system and $C$ is the concentration of the substance A in the melt of the substance B.

The equilibrium concentrations at the solid–liquid interfaces are time-dependent and can be written as

$$C_e(0, t) = C_e(l, t) = C_e(t) = C_e(0) + a_{c(h)}t/m, \quad (2)$$

where the subscript $e$ indicates the equilibrium concentrations, determined from the liquidus line on the phase diagram of the A–B system and $m$ is the slope of this liquidus line.

## ANALYTICAL APPROXIMATION

Beginning at a certain moment, the temperature starts to increase at a constant rate, the supersaturation in the liquid phase attains its stationary value for a certain time interval $t$ exceeding the relaxation time $\tau_r$

$$t \gg \tau_r = l^2/(\pi^2 D). \quad (3)$$

Then, the problem can be simplified by passing in equation (1) from distribution of concentrations to that of supersaturations measured from the equilibrium concentrations,

$$\delta C(x) = C(x, t) - C_e(0, t). \quad (4)$$

In this case,

$$\frac{\partial C}{\partial t} = \frac{a_{c(h)}}{m}, \quad \frac{\partial^2 C}{\partial x^2} = \frac{d^2\delta C(x)}{dx^2}. \quad (5)$$

If inequality (3) holds, equation (1) is reduced to the following ordinary differential equation:

$$\frac{d^2\delta C}{dx^2} = \frac{a_{c(h)}}{mD}. \quad (6)$$

In accordance with the above assumptions, the true concentration at the interface located at $x = 0$ is equal to the equilibrium concentration at any moment. In other words, the supersaturation at this interface should be zero at any moment

$$\delta C(0) = 0. \quad (7)$$

The other interface (located at $x = l$) is considered to be a reflecting one until the absolute value of the supersaturation dependent on the rate of the temperature variation would exceed the absolute value the critical supersaturation necessary for the formation of two-dimensional growth (dissolution) nuclei, $\Delta C_{gr(ds)}$ ($\Delta C_{gr} > 0$, $\Delta C_{ds} < 0$):

$$\left.\frac{d\delta C(x)}{dx}\right|_{x = l} = 0. \quad (8)$$

If, on the contrary, the supersaturation exceeds the critical one, the growth (dissolution) rate is controlled only by the diffusion of the substance A into the volume of the liquid. Thus, at relatively high rates of the tem-

perature variation (the corresponding criterion will be introduced later), the second solid–liquid interface can also be considered absorbing if the supersaturation at this interface is

$$\delta C(l) = \Delta C_{\mathrm{gr(ds)}}. \quad (9)$$

Integrating of equation (6) at the boundary conditions (7) and (9), we obtain the stationary concentration profile in the liquid layer in the form:

$$\delta C(x) = \frac{a_{\mathrm{c(h)}} x(x-l)}{2mD} + \frac{\Delta C_{\mathrm{gr(ds)}} x}{l}. \quad (10)$$

This solution is valid for the rates of temperature variation obeying the equation

$$|a_{\mathrm{c(h)}}| > 2mD|\Delta C_{\mathrm{gr(ds)}}|/l^2 \quad (11)$$

[for the sake of brevity, the rates of temperature variation obeying criterion (11) will be referred to as high ones and the rates not obeying it, as low].

If criterion (11) is invalid, equation (6) should be integrated at the boundary conditions (7) and (8). Then, the supersaturation profile is written as

$$\delta C(x) = \frac{a_{\mathrm{c(h)}} x(x-2l)}{2mD}. \quad (12)$$

The velocity of the motion of the liquid layer as a rule, $\langle V \rangle$, can be calculated as the average velocity of the motion of an arbitrary point of the layer for a period of the temperature oscillations. Let us follow the velocity $V^{\mathrm{ms}}$ of the layer section lying between the two interfaces which can be represented as the half-sum of the velocities of the interfaces motion determined by the fluxes of the growth substance moving toward the interfaces or from them

$$V_{0,l} = \frac{D}{C_{\mathrm{S}} - C_{\mathrm{L}}} \left.\frac{d\delta C(x)}{dx}\right|_{x=0,l}, \quad (13)$$

where $C_{\mathrm{S}}$ and $C_{\mathrm{L}}$ are the concentrations of the substance A in the solid and the liquid, respectively. With due regard for (7) and (10), the motion velocity of the mean section of the layer at high rates of the temperature variation is

$$V^{\mathrm{ms}}_{\mathrm{c(h)}} = \frac{D}{C_{\mathrm{S}} - C_{\mathrm{L}}} \frac{\Delta C_{\mathrm{gr(ds)}}}{l}, \quad (14)$$

and at low rates of the temperature variation it is

$$V^{\mathrm{ms}}_{\mathrm{c(h)}} = -\frac{1}{C_{\mathrm{S}} - C_{\mathrm{L}}} \frac{a_{\mathrm{c(h)}} l}{2m}. \quad (15)$$

The average velocity of the layer motion for the period of the temperature variation is

$$\langle V^{\mathrm{ms}} \rangle = \frac{V^{\mathrm{ms}}_{\mathrm{c}} \tau_{\mathrm{c}} + V^{\mathrm{ms}}_{\mathrm{h}} \tau_{\mathrm{h}}}{\tau_{\mathrm{c}} + \tau_{\mathrm{h}}}, \quad (16)$$

where $\tau_{\mathrm{c(h)}}$ is the duration of the cooling and heating stages.

If both cooling and heating rates are low, the velocity of layer motion averaged over the period of the temperature oscillation equals zero. At high rates of the temperature oscillation, the average velocity of the layer migration can be written as

$$\langle V^{\mathrm{ms}} \rangle = \frac{D}{C_{\mathrm{S}} - C_{\mathrm{L}}} \frac{(\Delta C_{\mathrm{gr}} \tau_{\mathrm{c}} + \Delta C_{\mathrm{ds}} \tau_{\mathrm{h}})}{l(\tau_{\mathrm{c}} + \tau_{\mathrm{h}})}. \quad (17)$$

At low cooling rates and high heating rates, the average velocity of the layer migration is

$$\langle V^{\mathrm{ms}} \rangle = \frac{D}{(C_{\mathrm{S}} - C_{\mathrm{L}}) l(\tau_{\mathrm{c}} + \tau_{\mathrm{h}})} \left( \Delta C_{\mathrm{ds}} \tau_{\mathrm{h}} - \frac{a_{\mathrm{c}} l^2}{2mD} \tau_{\mathrm{c}} \right). \quad (18)$$

At high cooling rates and low heating rates we have

$$\langle V^{\mathrm{ms}} \rangle = \frac{D}{(C_{\mathrm{S}} - C_{\mathrm{L}}) l(\tau_{\mathrm{c}} + \tau_{\mathrm{h}})} \left( \Delta C_{\mathrm{gr}} \tau_{\mathrm{c}} - \frac{a_{\mathrm{h}} l^2}{2mD} \tau_{\mathrm{h}} \right). \quad (19)$$

## SOLUTION TO THE PROBLEM AT GENERAL BOUNDARY CONDITIONS

The above expressions show that flat liquid layers can migrate at asymmetric temperature oscillations. This effect is explained by the formation of a nonzero concentration gradient (and, which is equivalent, the gradient of the chemical potential) averaged over the period of temperature oscillation. Indeed, the layer migration is associated with the flux of the substance A through the volume of the liquid. Provided that the kinetic properties of the interfaces are different, the temperature variation results in an asymmetric distribution of the substance A in the liquid, which give rise to the displacement of the mean section of the layer. The velocity of the mean section motion for a steady-state process (that is, at $t \gg \tau_{\mathrm{r}}$) can be determined as the half-sum of the velocities of the two interfaces. The solution to equation (6) with due regard for (13) under the condition that the supersaturations at the interfaces during the steady-state process are constant and equal to $\delta C_0$ and $\delta C_l$, respectively, yields

$$V^{\mathrm{ms}} = \frac{D}{C_{\mathrm{S}} - C_{\mathrm{L}}} \frac{\delta C_l - \delta C_0}{l}. \quad (20)$$

Thus, under stationary conditions, it follows from (20) that the velocity of the motion of the mean section of the liquid layer is proportional to a certain effective concentration gradient $(\delta C_l - \delta C_0)/l$.

Let us derive the mean-section velocity averaged over the period of temperature oscillation under the assumption that one of the interfaces (the left one) is absorbing, whereas at the other interface, one of the well-known mechanisms acts—normal dislocation- or nucleation-controlled. Then, at the left interface, the condition $\delta C_0 = 0$ is met, whereas at the right interface, the dependence of the growth (dissolution) on supersaturation is described by one of the following equations:

$$V_{\mathrm{gr(ds)}} = \mu_1^{\mathrm{gr(ds)}}\delta C_l, \quad (21)$$

$$V_{\mathrm{gr(ds)}} = \mu_2^{\mathrm{gr(ds)}}(\delta C_l)^2, \quad (22)$$

$$V_{\mathrm{gr(ds)}} = \mu_3^{\mathrm{gr(ds)}}\exp\left(-\frac{\mu_4^{\mathrm{gr(ds)}}}{|\delta C_l|}\right). \quad (23)$$

Under the above assumptions, the equation for the average motion velocity of the mean layer section can be written in the form

$$\langle V^{\mathrm{ms}}\rangle = \frac{D}{l(C_\mathrm{S}-C_\mathrm{L})}\frac{\delta C_{l,\mathrm{gr}}\tau_\mathrm{c} + \delta C_{l,\mathrm{ds}}\tau_\mathrm{h}}{\tau_\mathrm{c}+\tau_\mathrm{h}}. \quad (24)$$

Now, consider the case when the kinetic properties of both interfaces are identical and are described by any of equations (21)–(23) with the equal coefficients $\mu_i$, i.e.,

$$\mu_i^{\mathrm{ds}} = \mu_i^{\mathrm{gr}}, \quad (25)$$

where $i$ = 1–4. The fluxes of the substance A to the interfaces, which are induced by a steady-state temperature variation, are proportional to the rate of the temperature variation. If the velocity of an interface motion depends on the supersaturation as indicated by (21), the supersaturation will be proportional to the rate of the temperature variation. If the temperature oscillations occur with a constant amplitude, the numerator in equation (24) equals zero for any profile of temperature oscillations, because $a_\mathrm{c}\tau_\mathrm{c} = -a_\mathrm{h}\tau_\mathrm{h}$.

If the function $V = V(\delta C_l)$ is nonlinear [even if (25) is valid], the velocity of layer migration differs from zero only at the symmetric profile of temperature oscillation ($|a_\mathrm{c}| = a_\mathrm{h}$). If profile of the temperature oscillations is asymmetric, the migration velocity depends not only on the oscillation amplitude, but also on oscillation sign. If the heating rate is higher than the cooling rate, the layer moves from $x = 0$ to $x = l$. At the inverse heating-to-cooling rate ratio, the migration velocity changes the sign to the opposite one.

If the growth and dissolution kinetics are described by equations (21)–(23) with different coefficients $\mu_i$ (that is, $\mu_i^{\mathrm{gr}} \neq \mu_i^{\mathrm{ds}}$), the migration velocity differs from zero even at the symmetric profile of temperature oscillations.

In any particular case, the appropriate ratio of heating-to-cooling rates $(a_h/a_c)_0$ can be found such that the average migration velocity can be zero. If $a_\mathrm{h}/a_\mathrm{c} > (a_\mathrm{h}/a_\mathrm{c})_0$, the migration velocity is directed from the absorbing interface to the singular one; for the reverse ratio, the migration occurs in the opposite direction. The only exception is the case of the linear interfacial kinetics where the migration velocity is independent of the profile of temperature oscillations and is determined only by the values of the coefficients $\mu_1^{\mathrm{gr}}$ and $\mu_1^{\mathrm{ds}}$.

The requirement of the zero supersaturation at one of the interfaces was imposed only for more clear analysis of the results obtained. Obviously, in the general case, the migration velocity will differ from zero if the following conditions are met:

(1) The kinetic properties of the interfaces are different;

(2) The dependence of growth (dissolution) on supersaturation is nonlinear at least at one of the interfaces;

(3) The $a_\mathrm{h}/a_\mathrm{c}$ ratio differs from unity if kinetics properties of the interfaces are the same or, in a more general case, differs from $(a_\mathrm{c}/a_\mathrm{h})_0$.

Now, estimate the order of magnitude of the migration velocity and determine the temperature conditions providing the motion of liquid layers of various thicknesses. With this aim, consider Si–Al liquid layers sandwiched between two silicon plates of different crystallographic orientations—that parallel to the (111) plane and that limited by the planes of arbitrary orientations characterized by high Miller indices. The interface with low indices is assumed to be singular. The diffusion coefficient in the liquid is of the order of $10^{-4}$ cm$^2$ s$^{-1}$ [5]. To estimate the growth kinetics of Si(111) from the Al-based flux we used the data on velocities of thermal migration measured at 1000 K [6]. The shape of the dependence of the migration velocity on the layer thickness measured under the stationary temperature conditions indicates the nucleation mechanism of the mass transfer through the layer by operating at the interfaces. It is possible to separate the influence of various factors at the dissolution and growth fronts of planar solution layers. Assuming that all the factors have the same influence, we obtain $\mu_3^{\mathrm{gr(ds)}} = 10^5$ cm s$^{-1}$ and $\mu_4^{\mathrm{gr(ds)}} = 3.4 \times 10^{-2}$ at. %, which, in turn, yields $\Delta C_{\mathrm{gr(ds)}} = 1.35 \times 10^{-3}$ at. %. The slope of the liquidus line for the Si–Al system is $m$ = 10 K/at. %.

Under the above assumptions, the migration velocity was calculated functions of layer thickness (Fig. 2) amplitude of temperature oscillations (Fig. 3). The calculation was performed by (17)–(19) and the numerical calculations by equation (1) at boundary conditions (7) and (23) on a computer. The results obtained correspond to the profile of temperature oscillations with $|a_\mathrm{h}/a_\mathrm{c}| = 2.5$. At the inverse ratio of heating-to-cooling rates, only the sign of the migration velocity changes.

At large $l$ values, the function $V = V(l)$ is hyperbolic. At low $l$ values, the velocity drastically decreases. The existence of the maximum is explained by the condition (11): at $l \ll l_{\max}$, the rate of temperature variations is insufficient to initiate the growth or the dissolution process at the singular interface. With an increase of the amplitude of temperature oscillations, ever thinner liquid layers are involved into the migration process, and the maximum migration velocity also increases. The migration velocity of thick liquid layers only slightly

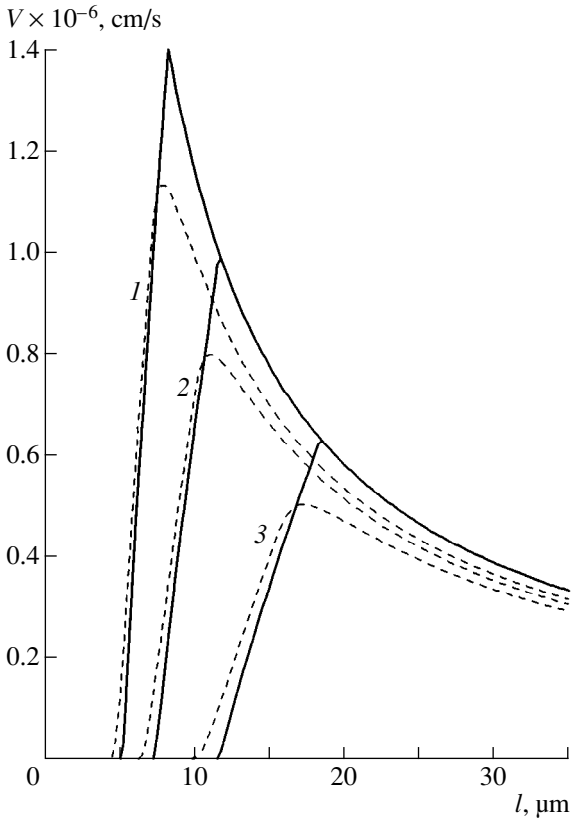


**Fig. 2.** Migration velocity as a function of the layer thickness calculated by solving equations (17)–(19) analytically (solid lines) and by solving equation (1) numerically under the boundary conditions (7) and (23) (dashed lines). $a_h/a_c$ = 5 : 2; $a_h$ = (*1*) 10, (*2*) 5, and (*3*) 2 K/s.

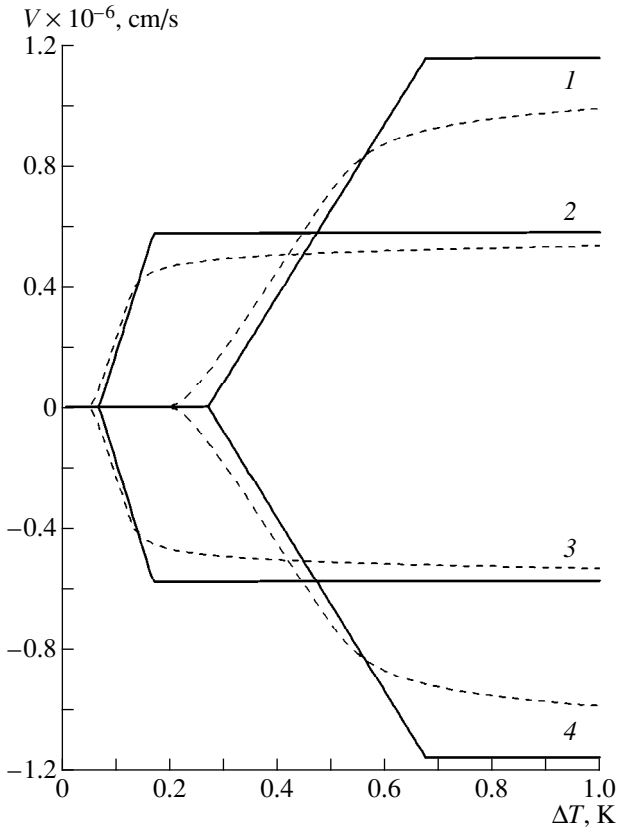


**Fig. 3.** Migration velocity as a function of the amplitude of temperature oscillations calculated by solving equations (17)–(19) analytically (solid lines) and by solving equation (1) numerically under the boundary conditions (7) and (23) (dashed lines). $a_h/a_c$ = (*1*, *2*) 5 : 2 and (*3*, *4*) 2 : 5; $l$ = (*1*, *4*) 10 and (*2*, *3*) 20 μm.

depends on the amplitude of temperature oscillations for numerical calculations and is independent of it for the analytical ones. This is explained by a weak dependence of supersaturation on the velocity of interfacial process for nucleation-controlled growth (dissolution) kinetics.

The dependence of the migration velocity on the period of temperature oscillations (Fig. 4) was calculated numerically. The rates of temperature variations were assumed to be constant, i.e., the amplitude of temperature oscillations was proportional to the oscillation period. The results shown in Fig. 4 are normalized to the velocities corresponding to large periods of temperature oscillations.

A dramatic fall in the migration rate in the range of short oscillation periods is explained by two factors. If the duration of the cooling or the heating stage (strictly speaking, the duration of the process occurring with the maximum rate) is too small for the attainment of the stationary solute distribution in the liquid phase, the velocity of the motion of the mean layer section decreases. The characteristic duration of this process is of the order of $4l^2/(\pi^2 D)$ at low rates of temperature variations and of the order of $l^2/(\pi^2 D)$ at high rates. Moreover, the asymmetric concentration distribution in the liquid arises only once during the time interval $\Delta t$,

$$\Delta t = \frac{(\Delta C_{gr} - \Delta C_{ds})m}{|a_{c(h)}|}$$

at the moment when cooling is changed to heating or vice versa.

Of course, the fall in the migration velocity takes place when the duration of the fastest stage of temperature variations becomes less than (or equal to) the sum of both above time intervals.

The attainable migration velocities are usually of the order comparable with the velocity of conventional thermal migration; for thin liquid layers, they are even higher. However, it should be emphasized that, unlike conventional thermal migration, the velocity of migration in our case has the maximum in the range of small layer thicknesses. The position and the height of its maximum depend on the shape of the profile of temperature oscillations and on the heights of the barriers hindering the kinetic processes at the interfaces. It can

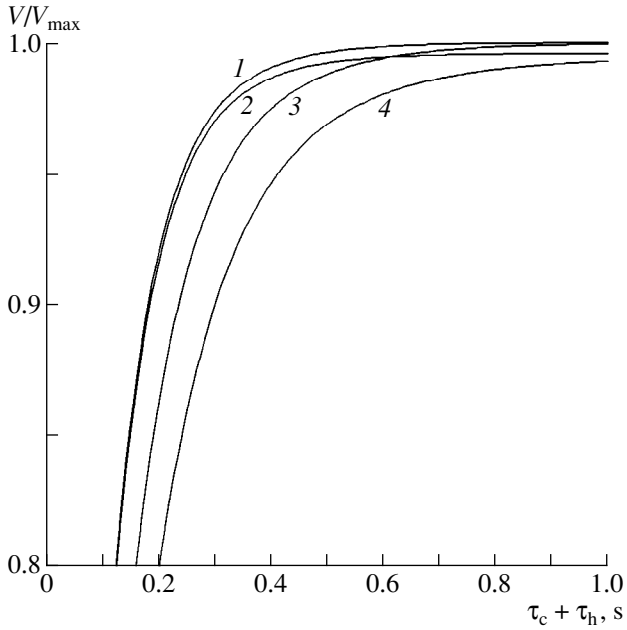


**Fig. 4.** Normalized migration velocity as a function of the period of temperature oscillations at $|\Delta C_{gr(ds)}| = 1.35 \times 10^{-3}$ at. % and $l$ = (*1*) 5, (*2*) 10, and (*3*) 20 μm; and at (*4*) $|\Delta C_{gr(ds)}| = 2.7 \times 10^{-3}$ at. % and $l$ = 10 μm.

therefore be expected that change in the profile of temperature oscillations can be used for controlling not only the magnitude of the migration velocity but also the direction of this migration.

The direct dependence of the migration velocity on the kinetic properties of the interfaces can make this effect very useful for studying the mechanisms and kinetics of the growth and the dissolution processes. It should be remembered that uncontrolled temperature fluctuations can contribute to the velocity of thermal migration of thin liquid layers and thus affect the results of the experimental studies of the kinetics of thermal migration. This can be caused either because the temperature fluctuations can become nonsymmetric because of the power fluctuations of the heater or because the differences in the kinetics of the growth and the dissolution processes make these oscillations symmetric.

## CONCLUSIONS

Analyzing the mass transport in the liquid layer sandwiched between differently oriented single-crystal plates, we discovered a new effect—migration of a planar liquid layer in a crystal in the absence of a temperature gradient. The migration is driven by asymmetric temperature oscillations. The effect arises if the following three conditions are simultaneously fulfilled: (1) the nonlinear interfacial kinetices is observed on at least at one of the interfaces; (2) the properties of the interfaces are different; and (3) the profile of temperature oscillations is asymmetric. The sign and the value of the migration velocity are determined by the shape and the height of the profile of temperature oscillations and by the degree of nonlinearity of the dependence of growth (dissolution) rate on supersaturation.

The velocity of migration induced by the temperature oscillations is comparable with the velocity of conventional thermal migration, and, at small layer thicknesses (~10 μm) can be considerably higher than the velocity of thermal migration.

The fact that the attainable migration velocities increase with the height of the barriers hindering interfacial processes and lesser layer thickness allows one to expect that the migration of liquid layers can also be implemented at low temperatures and extremely small layer thicknesses. The direct dependence of the migration velocity on the kinetic properties of the interfaces will allow to use it in the studies of the mechanisms and kinetics of the growth and dissolution processes.

## REFERENCES

1. W. G. Pfann, J. Metals **7**, 961 (1955).
2. W. A. Tiller, J. Appl. Phys. **34**, 2757 (1963).
3. V. Yu. Gershanov and S. I. Garmashov, Kristallografiya **37**, 34 (1992) [Sov. Phys. Crystallogr. **37**, 14 (1992)].
4. V. Yu. Gershanov and S. I. Garmashov, in *Proceedings of the 1994 Spring Meeting MRS* (San Francisco, 1994), p. 473.
5. D. A. Frank-Kamenetskiĭ, *Diffusion and Heat Transfer in Chemical Kinetics* (Nauka, Moscow, 1987).
6. V. Yu. Gershanov, L. Z. Golovanova, and N. I. Nikitin, in *Proceedings of VI International Conference on Crystal Growth* (Moscow, 1980), vol. 2, p. 10.

*Translated by V. Tokarev*

*Crystallography Reports, Vol. 45, No. 2, 2000, pp. 329–335. Translated from Kristallografiya, Vol. 45, No. 2, 2000, pp. 364–370.*




# Fluctuations in Growth Rate of Gypsum Crystals

**V. F. Komarov, A. V. Severin, and I. V. Melikhov**

*Moscow State University, Vorob'evy gory, Moscow, 119899 Russia*

Received November 25, 1997; in final form, April 23, 1998

**Abstract**—Growth of needlelike gypsum crystals from highly supersaturated aqueous solutions has been studied by the methods of the optical and electron microscopies. The average growth rates of the end faces and their fluctuations are determined. It is shown that the fluctuations in the growth rates of end faces are described by the Fokker–Planck equation and that the end faces of gypsum crystals grow by the layer mechanism with the layer nucleation in the vicinity of one of the crystal vertices. *© 2000 MAIK "Nauka/Interperiodica".*

## PROBLEM FORMULATION

As is well known, crystal growth is often accompanied by macroscopic fluctuations in growth rates [1, 2]. Growth of many crystals is characterized by long periods of growth cessation and acceleration [3]. It seems that equivalent crystals can grow in the same homogeneous supersaturated medium with rates that can differ by several times [4]. Usually, fluctuations in the growth rate are described in the continuum approximation by introducing random curvature and time functions into the equation of the motion of the growth front and making some arbitrary assumptions about their character [5, 6]. It is most often assumed that random functions are centered and delta-correlated. As a result, the equation of the front motion is reduced to the Fokker–Planck equation for the probability of the front displacement [7–9]. The Fokker–Plank equation is most often used to describe growth fluctuations [10–12]. However, this procedure has never been reliably justified. Therefore, this article is devoted to the study of growth of gypsum crystals with the aim to establish the most adequate method for describing growth fluctuations. Growth of gypsum crystals has been studied repeatedly, but in all these studies only the average values and dispersions of the growth rate were determined [13–15].

The model used for establishing the role of growth fluctuations can be described as follows.

Let several crystals be in homogeneous isothermal supersaturated medium. We consider growth of $N$ faces of these crystals assuming that each of them is characterized by the same molecular relief and grows independently from the other. Each face can be characterized by the distance $L$ of its location from the crystal center. The whole set of the faces at any moment $t$ is characterized by the average distance

$$\bar{L}(t) = \int_0^\infty L\beta(L, t)dL,$$
$$\beta(L, t) = \frac{1}{N}\frac{\partial N_L}{\partial L}, \quad (1)$$

where $N_L$ is the number of faces lying at a distance less than $L$ from the crystal center. The distribution function $\beta(L, t)$ of the faces over distances $L$ is determined by the integral Smoluchowski equation

$$\beta(L, t) = \int_0^\infty \beta(L_0, t_0)\omega(L_0, L, t_0, t)dL_0, \quad (2)$$

where $\omega(L_0, t_0, L, t)$ is the probability density of the face displacement from the position $L_0$ to the position $L$ for the time period from $t_0$ to $t$, which satisfies the condition

$$\int_0^\infty \omega(L_0, t_0, L, t)dL = 1. \quad (3)$$

Equation (2) implies that any crystal in a supersaturated medium does not necessarily grow at each moment; on the contrary, at some moments, it can be dissolved due to thermal fluctuations. This equation does not contradict the fact that crystals cannot be considerably dissolved in the supersaturated media, because it implies that with a decrease of $L$ the dissolution probability can become infinitely low although finite. Equations (1) and (2) allow one to compare the functions $L_0(t_0)$ and $L(t)$ for the given time interval $\tau = t - t_0$. Introducing the function $L(t) = Z(L_0, \tau)$, one can

1063-7745/00/4502-0329$20.00 © 2000 MAIK "Nauka/Interperiodica"

represent $L(t)$ as a series

$$L(t) = L_0(t_0) + \sum_{n=1}^{\infty} \frac{1}{n!}\frac{\partial^n Z}{\partial L_0^n}(L - L_0)^n. \quad (4)$$

For a face growing without any fluctuations, we have $Z(L_0, \tau) = L_0(t_0) + G_M\tau$, where $G_M$ is the normal growth rate constant at low $\tau$ values. For a face undergoing some fluctuations, $Z(L_0, \tau)$ can be an arbitrary complicate function. Substituting relationships (2) and (4) into (1), integrating the thus obtained equations by parts, and passing to the limit of small $\tau$ (as was made in [16]) under the conditions

$$\beta(\infty, t) = 0, \quad \lim_{L_0 \to 0}\left(\frac{\partial^n Z}{\partial L_0^n}\right)_{n \geq 2} = 0, \quad (5)$$

we obtain

$$\frac{d\bar{L}}{dt} = \int_0^{\infty}\frac{\partial\beta}{\partial t}L dL = \sum_{n=1}^{\infty}(-1)^n\int_0^{\infty}\left[\frac{\partial^n}{\partial L^n}(G_n\beta)\right]L dL, \quad (6)$$

where

$$G_0 = \frac{1}{n!}\lim_{\tau \to 0}\int_0^{\infty}\frac{(L - L_0)^n}{\tau}\omega(L, L_0, t_0, t)dL_0.$$

It follows from (6) that

$$\frac{\partial\beta}{\partial t} = \sum_{n=1}^{\infty}(-1)^n\frac{\partial^n(G_n\beta)}{\partial L^n}. \quad (7)$$

At small $\tau\omega(L_0, t_0, L, t) = \Omega(L_0, t_0, t)\tau$, where $\Omega(L_0, t_0, t)$ is the frequency of molecules transition into the solution within the interval $\tau$. Therefore

$$G_n = \frac{1}{n!}\langle b^n\rangle\omega, \quad (8)$$

where

$$b = L - L_0, \quad \omega = \int_0^{\infty}\Omega(L_0, t_0, L)dL_0.$$

Equation (7) differs from the Fokker–Plank equation by the terms containing $G_n$ at $n \geq 3$. Using the Fokker–Plank equation, one implicitly assumes that these terms are negligible. However, their smallness is not always obvious [10].

As is shown in [7], at $G_{n \geq 3} = 0$, $G_1 = \text{const}$, $G_2 = \text{const}$, and under the conditions

$$\beta(L, t) = \delta(t), \quad \beta(\infty, t) = 0, \quad \int_0^{\infty}\beta dL = 1, \quad (9)$$

the solution of equation (7) has the form

$$\beta(L, t) = \frac{1}{(\pi p G_1 t)^{1/2}}\exp(-x_-^2) - \frac{1}{p\sqrt{\pi}}e^{L/p}\int_{x_+}^{\infty}e^{-x^2}dx, \quad (10)$$

where $\delta(t)$ is the Dirac function, $p = G_2/G_1$, and $x_{\pm} = \dfrac{L \pm G_1 t}{\sqrt{4pG_1 t}}$.

Conditions (9) signify that the face positions at the beginning of the observation are taken to be the zero positions ($L_0 = 0$). Crystals in the solution cannot grow indefinitely because of the limited time of observation, whereas, the only cause of the change in $L$ can be face overgrowth.

If during the growth process neither the molecular relief of the faces, nor the medium supersaturation are changed, equations (7)–(9) characterize the behavior not only of the set of crystals, but also the behavior of each individual crystal. In accordance with the ergodic hypothesis (the values of various physical quantities averaged over time and characterizing the system are equal to their statistically averaged values), upon time $t$ after the beginning of growth, the state of each face of an individual crystal can be taken to be equivalent to its initial state. Therefore, the growth of an individual crystal continuing for a rather long time can be considered as a number of successive independent events of face growth (each taking the time $t$), resulting in the face displacement by a distance $L$. Repeating the derivation of equation (7) to the set under consideration, one arrives at the formula (10) for the $\beta(L, t)$ distribution of successive increments in $L$ at the given $t$.

Using equation (10), one can pass from the $\beta(L, t)$ distribution to the distribution over the instantaneous growth rates for an individual crystal. Thus, under the assumption that the growth rate of the face $G = dL/dt$ within a short time interval from $t$ to $t + \tau_0$ undergoes no fluctuations and is equal to the instantaneous growth rate $G_M$, one can introduce the function

$$\varphi(G_M) = \tau_0\beta(L, \tau_0) \text{ at } L = G_M\tau_0.$$

From equation (10), it follows that

$$\varphi(G_M) = G_1^{-1}\left[\sqrt{\frac{A}{\pi}}\exp(-x_-^2) - \frac{A}{2}\exp\left(\frac{AG_M}{G_1}\right)\text{erfc}(x_+)\right], \quad (11)$$

where

$$x_{\pm} = (G_M \pm G_1)/(4G_2/\tau_0)^{1/2}, \quad A = \frac{G_1^2\tau_0}{G_2}.$$

Relationship (11) is valid only at $\tau_0 > \omega^{-1}$. However, using this relationship at $\tau_0 = \omega^{-1}$ together with (8), we arrive at

$$\varphi(G_M) = \frac{1}{\omega b}\left[\sqrt{\frac{2}{\pi}}\exp(-x_-^2) - \exp\left(\frac{2G}{\omega b}\right)\mathrm{erfc}(x_+)\right], \quad (12)$$

where

$$x_\pm = \left(\frac{G}{\omega b} \pm 1\right)/\sqrt{2}.$$

Relationships (10) and (12) are also used in our study. We had the aim to determine the function $\beta(L, t)$ by measuring the increments in the dimensions of the crystals growing in a steady-state mode within equal time intervals, to determine the parameters $G_n$, in order to answer the question whether the transition from (7) to the Fokker–Plank equation is sufficiently justified. Moreover, we planned to study the face relief of gypsum crystals and to see whether it is expedient to application (8) to describe the fluctuations and justify the use of the ergodic hypothesis to crystal growth.

## EXPERIMENTAL

We studied growth of gypsum crystals in an optical flat continuous-flow cell with the thermostated walls. The necessary temperature was maintained within an accuracy of ±0.1°C with the aid of a MLW-UH thermostat. During growth, crystals were observed and photographed with the aid of an MBI-1594.2 microscope. A flow of supersaturated solution through the cell was provided by the peristaltic pump providing the dosage or the flow of a liquid or a gas with the given velocity and operating on the principle of pushing out the liquid because of a gradual flattening of the elastic-hose (tube) walls. The average solution consumption was 22 ml/h at the Reynolds number for the cell Re = 15.

Each experiment was performed as follows. About thirty gypsum crystals were placed into a thermostated cell filled with the saturated gypsum solution. The crystals were located at the cell bottom in a way to provide their independent growth so that the distance between the crystals was not less than 10 μm. Then, a supersaturated solution was prepared and supplied to the cell, thus forcing out the saturated solution. All the crystals introduced into solution had the dimensions such that the solution flow could not take them off or change their orientation on the cell bottom.

The seeding $CaSO_4$ crystals were obtained by mass crystallization during mixing and stirring (Re = 300) of the chemically pure 0.5 M $CaCl_2$ and $Na_2SO_4$ solutions. The crystals thus obtained were kept in the saturated solution for two weeks, then the solution was poured into the optical cell directly before the experiment.

The supersaturated solution was prepared by mixing the equal volumes (9 ml) of equimolar $CaCl_2$ and $Na_2SO_4$ solutions in a special two-chamber ampule—a vessel consisting of two connected Λ-like test tubes (chambers) with the volumes relating as 2 : 1. Each ampule was filled with the solution of initial reagents mixed directly before the experiment by a careful transfusion of the solutions from one test tube to another performed three times under the minimum hydrodynamic effect. The supersaturated solution thus prepared was supplied to the system. The solutions of the reagents were preliminarily purified from the impurities by their centrifuging and filtration via the nuclear filter with a pore diameter of 0.05 μm. Prior to mixing, the solutions were degassed and thermostated at the experimental temperature. The concentrations of the reagent solutions were such that upon mixing, they would provide the supersaturation with respect to gypsum within the range $S = (a/a_\infty) - 1 = 3$–11, where $a$ and $a_\infty$ are the products of the $Ca^{2+}$- and $SO_4^{2-}$-ion activities in the solution used and in the saturated solution, respectively. The ion activities in the solution were calculated by the equation of the second Debye–Hückel approximation as is described in [17].

The time necessary for the appearance of the first newly formed gypsum microcrystal was determined in a visual field of the microscope at each supersaturation value. The time of the experiment $t_c$ (i.e., the total time of all the observations made on one crystal) was deliberately chosen to be less than the time necessary for the appearance of new crystals.

The exposure times in photographing ranged within 5–7 s; the time intervals between the frames was $t$ = 60–180 s.

The photographs obtained were used to measure the edge length along the [001] direction of each crystal and the crystal width in the direction normal to [001]. Then, we calculated the change in the length $L$ and the width $H$ of each crystal for time $t$. The measurements were made with the aid of the optical ruler on eight-times magnified photographic image in a microscope. The accuracy of the $L$ and $H$ measurements was ±0.07 μm.

Knowing the dimension $L$, we can determine the function

$$\theta(L) = \frac{N_L}{N} = \int_0^L \beta(L, t)dL,$$

where $N_L$ is the number of all the measurements in which an increase of the crystal dimension per one growth event does not exceed $L$ and $N$ is the total number of measurements. The function $\theta(L)$ was determined for the whole set of crystals and then was estimated for each crystal separately. The thus determined functions $\theta(L)$ were compared with the integral in (10) calculated at different $G_1$ and $p$. Then those values of these parameters were selected at which the calculated data best fitted the experimental ones. The consistency of the calculated and the experimental data was

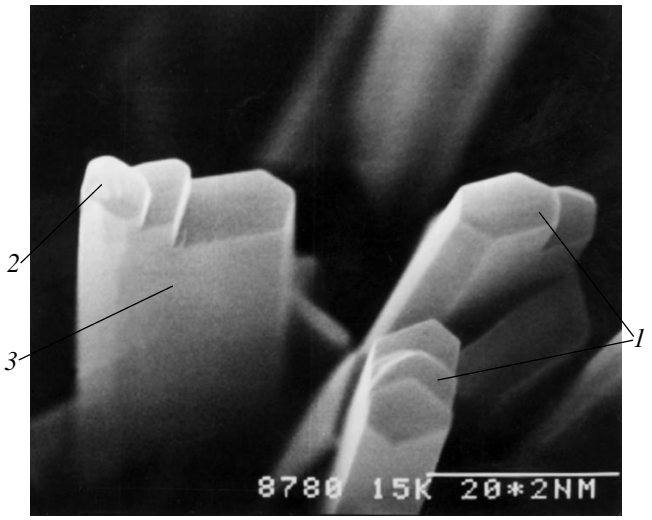


**Fig. 1.** Initial gypsum crystals: (*1*) crystal ends, (*2*) (001) face, (*3*) side faces

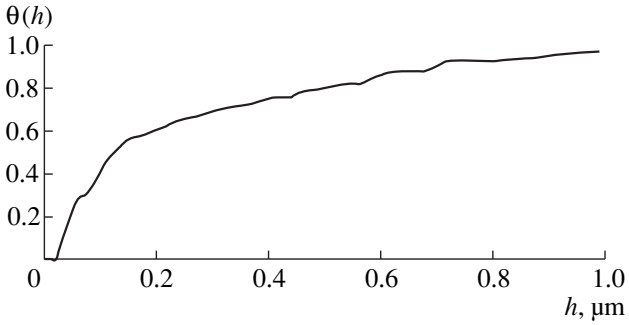


**Fig. 2.** Integral distribution function of the steps over the height $h$ of the end faces ($S$ = 6.6, $T$ = 18°C).

checked against the Kolmogorov criterion whose value should not exceed 0.21 (a value conventional for the apparatus scatter in the experimental data).

The X-ray phase analysis of the initial and final crystals was performed on a DRON-2a diffractometer (Cu$K_\alpha$ radiation).

Some crystals were separated from the mother solution by filtering it via a microfilter, then they were dried in air and were studied it in a Hitachi-S-405 scanning electron microscope at a resolution of 50 Å or in a JEM-100V transmission electron microscope at a resolution of 3 Å.

## EXPERIMENTAL RESULTS

The initial crystals had a needlelike (filament) prismatic habit and gave the diffraction patterns consistent with the typical gypsum pattern. The crystal length ranged within $L_0$ = 3–15 μm and their width ranged within $H_0$ = 0.2–1.5 μm. The preferable crystal faces were (001) and (110), with the latter being elongated in the [001] direction. The (001) planes faceted the needle ends and had a stepwise relief (Fig. 1) with the step height distribution shown in Fig. 2, where θ($h$) is the fraction of steps with the height less than $h$. In a transmission electron microscope providing the observation of steps with heights as small as 1 nm, we observed only the steps with the heights exceeded 10 nm, which indicated that the minimum step height was $h_{min}$ = 10 nm. The steps on some crystals formed regular echelons, whereas the steps on some other crystals located irregularly. The distribution of crystal ends over the angle α is shown in Fig. 3, where θ(α) is the fraction of crystals with the end face forming an angle less than α.

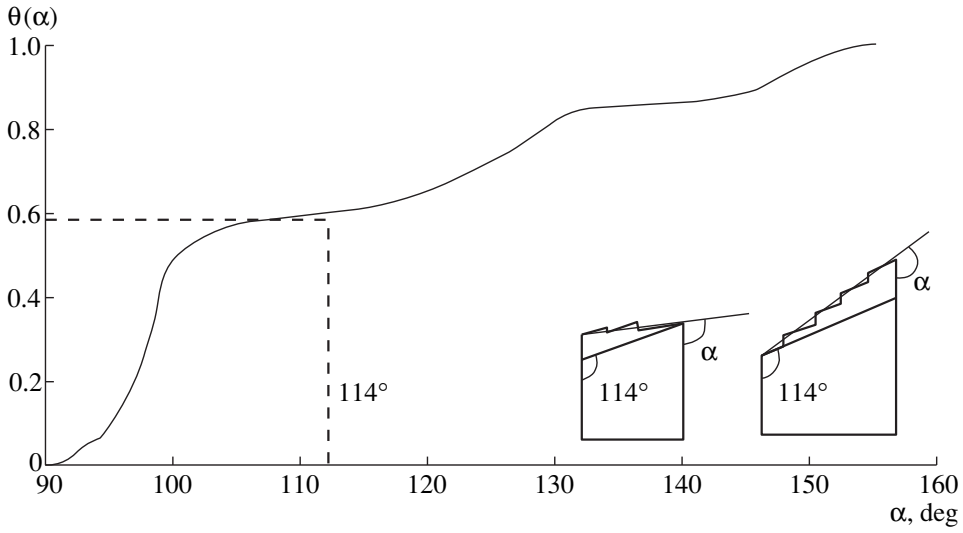


**Fig. 3.** Distribution of the end faces over the angle α of their inclination toward the (100) face ($S$ = 6.6, $T$ = 18°C). The right-hand part of the figure illustrates layer nucleation at various face vertices.

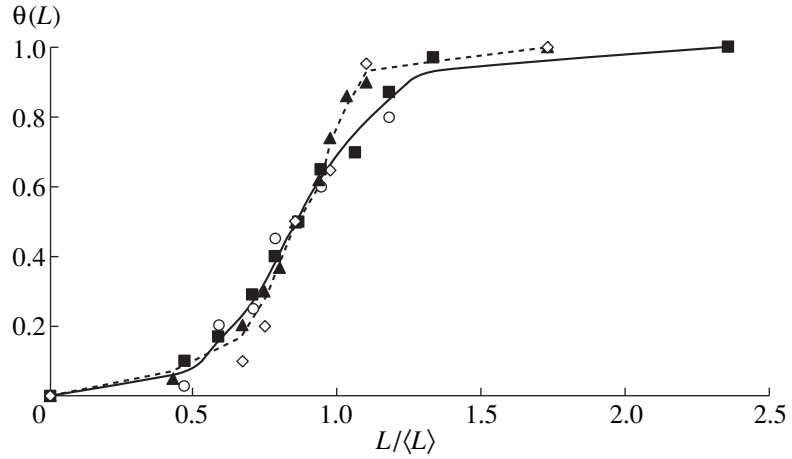


**Fig. 4.** Distribution of the increments in edge lengths $L/\langle L\rangle$ along the [001]-direction for time $t$ under the conditions (1) $t$ = 3 min, $S$ = 6.6, $T$ = 18°C. ■ experimental data observed for a set of crystals, —— calculation by formula (10), ○ experimental data obtained from observation of an individual crystal; (2) $t$ = 2 min, $S$ = 6.6, $T$ = 30°C. ▲ experimental data obtained from observation of a set of crystals, - - - - - calculation by formula (10), ◇ experimental data obtained from observation of an individual crystal.

During crystal growth, the face relief remained unchanged. For the time $t$, only the end faces of the crystals had enough time to noticeably grow, with the $L$ values being considerably different in each of the successive observations. Figure 4 shows the fractions $\theta(L)$ of the number of observations in which the increments in the crystal length were less than $L$. Each of the functions $\theta(L)$ was determined from the data for all the crystals grown under the same supersaturation and the same temperature. Figure 4 also shows the estimates of the function $\theta(L)$ made over the data for only one crystal. Table 1 shows the growth rates for the end faces averaged over time and the set of crystals

$$\langle G\rangle = \frac{1}{t}\int_0^\infty L\beta(L, t)dL,$$

where

$$\beta(L, t) = d\theta(L)/dL.$$

Table 1 also lists the average growth rates $\langle G_s\rangle = (1/2t_c)(H_c - H_0)$ for the side faces of the crystals, whose average width for the observation time $t_c$ (at the beginning and at the end of the growth process) was equal to $H_0$ and $H_c$, respectively. The $\langle G_s\rangle$ values were determined with a lower accuracy than $\langle G\rangle$ because of a low growth rate of the side faces.

The $\langle G\rangle$ values were independent of the crystal dimensions (Table 2).

## RESULTS AND DISCUSSION

The experimental values of the functions $\theta(L)$ correspond, with a high accuracy, to equation (10). Figure 4 shows the results obtained by integration of this equa-

**Table 1.** Data on crystal growth

| $T$, °C | Supersaturation $S$ | Average growth rate $\langle G\rangle \times 10^9$, m/s | Growth rate of a side face $\langle G_s\rangle \times 10^9$, m/s | Parameter in the Fokker–Planck equation $G_1 \times 10^9$, m/s | Fluctuation parameter $p$, nm | Kolmogorov criterion, λ |
|---|---|---|---|---|---|---|
| 18 | 6.6 | 7.6 ± 0.3 | 0.5 ± 0.1 | 5.2 ± 0.3 | 6.2 ± 0.7 | 0.16 |
| | 8.4 | 16.1 ± 0.7 | 1.2 ± 0.3 | 14.2 ± 0.6 | 6.8 ± 0.9 | 0.21 |
| | 9.3 | 25.0 ± 0.7 | 1.7 ± 0.4 | 22.8 ± 0.7 | 9.5 ± 1.0 | 0.09 |
| | 10.3 | 32.1 ± 1.0 | 2.2 ± 0.4 | 28.6 ± 0.9 | 11.8 ± 1.0 | 0.12 |
| | 11.3 | 39.2 ± 3.0 | 2.6 ± 0.5 | 31.4 ± 2.5 | 19.0 ± 1.1 | 0.19 |
| 30 | 6.6 | 21.2 ± 1.7 | 1.6 ± 0.3 | 17.8 ± 2.5 | 6.6 ± 0.8 | 0.07 |
| | 8.4 | 49.1 ± 3.0 | 3.3 ± 0.4 | 42.7 ± 3.5 | 19.0 ± 1.0 | 0.14 |
| | 9.3 | 66.0 ± 4.5 | 4.4 ± 0.4 | 60.1 ± 3.0 | 20.0 ± 1.2 | 0.09 |
| | 10.3 | 72.6 ± 4.5 | 4.8 ± 0.7 | 56.6 ± 6.0 | 47.2 ± 2.3 | 0.14 |
| | 11.3 | 83.3 ± 6.0 | 5.5 ± 0.8 | 61.6 ± 7.0 | 58.3 ± 3.0 | 0.09 |

**Table 2.** Growth rates $\langle G \rangle \times 10^{-9}$ m/s for crystals of various dimensions

| $T$, °C | Supersaturation $S$ | Growth rate (m/s) at the initial crystal dimensions, $L_0$, μm | |
|---|---|---|---|
| | | 3 ± 2 | 10 ± 4 |
| 18 | 8.4 | $(16.4 \pm 1.8) \times 10^{-9}$ | $(17.0 \pm 0.6) \times 10^{-9}$ |
| 30 | 8.4 | $(48.9 \pm 3.6) \times 10^{-9}$ | $(50.1 \pm 3.6) \times 10^{-9}$ |

tion over $L$ at the values of the parameters $G_1$ and $p$ indicated in Table 1. As is seen, the calculated and the experimental data agree at any $T$ and $S$ values. This is also confirmed by the fact that in all the experiments, the Kolmogorov criterion yielded the values not exceeding $\lambda = 0.21$ characteristic of the apparatus scatter in the experimental data (Table 1).

The data in Fig. 4 indicate that growth of gypsum crystals is described by the Fokker–Planck equation. All the terms in equation (7) (except of the two first terms) turned out to be unessential for gypsum. The ergodic hypothesis proved to be justified, which is indicated by the independence of the function $\theta(L)$ of the fact whether it is determined for the simultaneous growth of several crystals or "multiple overgrowth" of the same crystal

Crystals grew in the kinetic mode, which is proved by the independence of $\langle G \rangle$ of the crystal dimensions (Table 2). Therefore, one can state that the growth fluctuations were not associated with the solution state; they reflected the processes occurring on the crystal surfaces. The $\langle G \rangle$ values (Tables 1 and 2) thus determined are close to the growth rates of gypsum crystals

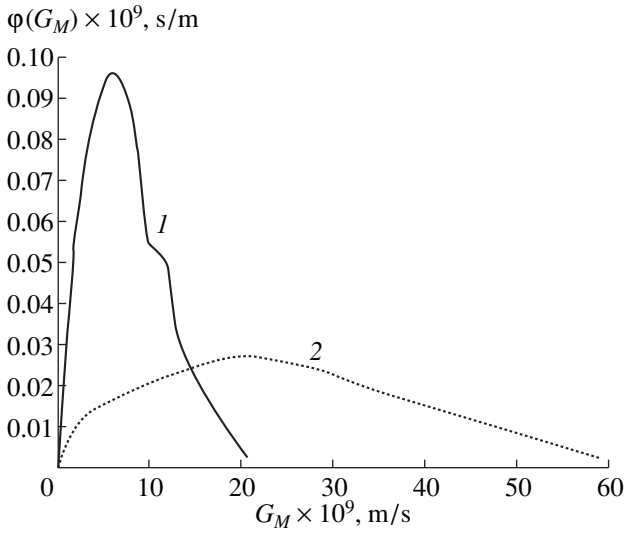


**Fig. 5.** The distribution function $\varphi(G_M)$ of the instantaneous growth rates of the end faces for the steady-state growth of a gypsum crystal. (*1*) $T$ = 18°C, $S$ = 6.6; (*2*) $T$ = 30°C, $S$ = 6.6.

indicated in [13–15], but do not coincide with them because they were obtained at higher $S$ values.

The end faces of crystals grew according the layer growth mechanism with the layer nucleation in the vicinity of the crystal vertices, which is illustrated by Fig. 1. Layer nucleation and propagation over the (001) faces proceeded with some macrofluctuations and resulted in broadening of the functions $\theta(h)$ and $\theta(\alpha)$. At $S$ = 6.6 and $T$ = 18°C, the minimum step height, $h_{min} = 10 \pm 2$ nm, was close to $2p$ (Table 1), thus indicating the validity of formula (10) in this case. Indeed, the parameter $p$ was determined from the experimental $\theta(L)$ distribution and, thus, is a measured value. The comparison of $\theta(L)$ with formula (10) makes the physical sense of the parameter $p$ quite clear: according to the model described by (7)–(9), it was equal to $b/2$ and led to the conclusion that, e.g., at $S$ = 6.6 and $T$ = 18°C, $b = 12.4 \pm 1.4$ nm (Table 1). At the same time, the thickness of the layers grown under these conditions was determined by the electron microscopy method. It was established that the layers had the thicknesses ranging within $h$ = 10–100 nm (Fig. 2), with the lowest limit, $h_{min} = 10 \pm 2$ nm, being coincident with the calculated $b$ value. If this coincidence is not accidental, then, one can take that $h_{min} = b$. Against the background of the layer thickening (because of their merging together), the electron microscopy data confirm the validity of formula (8).

With due regard for the above stated, growth of the end faces of the crystals can be described as follows. The elementary growth layers are nucleated in the vicinity of the vertices of the (001) faces and, having not enough time to propagate for long distances from the nucleation site, they merge and form macrosteps of height $b = h_M = 2p$. The frequency of formation of such steps is $\omega = G_1/2p$ = 0.4–1.5 $s^{-1}$. According to the data listed in Table 1, the frequency $\omega$ of step formation only weakly depends on $S$ and $T$, but in all the cases it is so low that the nonuniformity of nucleation becomes the major factor promoting growth fluctuations. The layers can be nucleated at different face vertices with comparable probabilities. This is seen from the bending of the function $\theta(\alpha)$ in Fig. 3, which begins at $\alpha = 114°$. In order to interpret this bending, one has to take into account that at $\alpha < 114°$, the layers are nucleated at the "obtuse vertex" (57% of the total number of the layers), whereas at $\alpha > 114°$, at the "acute vertex" (43% of the total number of the layers). In both cases, the step height was exponentially dependent on $S$:

$$b = B\exp(kS), \tag{13}$$

where $B$ = 0.25 nm at 18 and 30°C, $k$ = 0.46 at 18°C, and $k$ = 0.58 at 30°C. One can see it by comparing the data from Table 1 with formula (13), from which it follows that the formation of macrosteps is decelerated with a decrease in $S$, so that in a slightly supersaturated solution, the $b$ value approaches the monolayer thickness. Deceleration would have been more pronounced

if nucleation had occurred at an obtuse vertex, which would be seen from the behavior of the function $\theta(h)$ (Fig. 2). The initial branch of this function ($h < 0.2$ μm) characterizes the layers nucleated at the obtuse vertices, whereas the final branch characterizes all the other layers. This is confirmed by the fact that 57% of all the layers, i.e., exactly the percentage of the layers nucleated at obtuse vertices, are described by the initial branch. However, layer thickening does not influence the parameters $G_n$ determined, in accordance with condition (8), only by the frequency ω and the initial thickness of the layers immediately upon their nucleation. Therefore, the problem of layer thickening and motion is beyond the scope of our study.

The correspondence between the experimental data and relationships (8) and (10) allowed us to calculate the function $\varphi(G_M)$ by formula (11) (Fig. 5). One can see that the distribution over the instantaneous growth rates of the end faces of gypsum crystals considerably differs from the normal distribution.

## REFERENCES


1. E. T. White and P. G. Whright, Chem. Eng. Prog., Sympos. Series **67** (110), 81 (1971).
2. I. V. Melikhov, M. Ya. Belousova, N. A. Rudnev, and N. T. Bludov, Kristallografiya **19**, 1263 (1974) [Sov. Phys. Crystallogr. **19**, 784 (1974)].
3. I. V. Melikhov and B. D. Nebylitsyn, in *Crystal Growth* (Izd. Yerevan Gos. Univ., Yerevan, 1977), Vol. 12, p. 108.
4. N. S. Tavare and J. Garside, Chem. Eng. J. (Lausanne) **25**, 229 (1982).
5. S. T. Chui and J. D. Weeks, Phys. Rev. Lett. **40**, 733 (1978).
6. H. Muller-Krumbhaar, T. W. Burkhordt, and D. M. Kroll, J. Cryst. Growth **38**, 13 (1977).
7. I. V. Melikhov and L. B. Berliner, Teor. Osn. Khim. Tekhnol. **19**, 158 (1985).
8. P. Noizieres and F. Galeet, J. Phys. (Paris) **48**, 353 (1987).
9. T. Hwa, M. Kardar, and M. Paczuski, Phys. Rev. Lett. **66**, 441 (1991).
10. L. V. Mikheev, Phys. Rev. Lett. **71**, 2347 (1993).
11. S. Balibar and Bouchaud, Phys. Rev. Lett. **69**, 862 (1992).
12. M. Kotrla and A. C. Levi, Surf. Sci. **317**, 183 (1994).
13. G. H. Nancollas, M. M. Reddy, and F. Tsai, J. Cryst. Growth **20**, 125 (1973).
14. S.-T. Liu and G. H. Nancollas, J. Cryst. Growth **6**, 281 (1970).
15. B. Mile, A. T. Vincent, and C. R. Wilding, J. Chem. Technol. Biotechnol. **32**, 975 (1982).
16. N. N. Tunitskiĭ, V. A. Kaminskiĭ, and S. F. Timashev, *Methods of Physicochemical Kinetics* (Khimiya, Moscow, 1972).
17. L. Amathieu and R. Boistelle, J. Cryst. Growth **88**, 183 (1988).


*Translated by L. Man*

*Crystallography Reports, Vol. 45, No. 2, 2000, pp. 336–339. Translated from Kristallografiya, Vol. 45, No. 2, 2000, pp. 371–374.*




# Polarization Characteristics of Polydimethylsiloxane-Based Composites during First-Order Phase Transitions

**N. N. Matveev and A. S. Sidorkin**

*Voronezh State University, Voronezh, 394893 Russia*

Received March 25, 1999

**Abstract**—Crystallization of polydimethylsiloxane (PDMS) filled with insulating carbon has been studied in an inhomogeneous temperature field. It is shown that the material polarization during the melt–crystal transitions depends on the concentration of the filler.This results in a decrease of the temperature coefficient of polarization with the concentration of dielectric carbon. The temperature dependences of thermodynamic functions are calculated for the crystallization range of the crystals under study. © *2000 MAIK "Nauka/Interperiodica".*

Polydimethylsiloxane (PDMS) is a polymer material widely used in electronics and radio engineering as a sealer and insulator. It has the low vitrification temperature (150 K) and high thermal stability (up to 573 K). PDMS crystals can be used over a wide temperature range (their dielectric characteristics remain almost constant) [1]. At the same time, high flexibility of a PDMS macromolecular chain provides the tendency to crystallization during cooling still in the vicinity of 213 K [2]. Such a tendency results in significant changes in its rheological and dielectric parameters and leads to the drastic deterioration in the performance of PDMS-based devices.

The parameters characterizing thermal polarization and pyroelectricity of PDMS crystals during first-order phase transitions were analyzed in [2, 3]. It was shown that the conformation-induced polarization depends on the crystallization rate and the filler concentration in the objects under study. Both these characteristics depend on the presence of defects or impurities in the material. Bearing this in mind, we describe below our study of the process of PMDS crystallization in inhomogeneous temperature fields using the method of polarization currents [4]. An inhomogeneous temperature field modifies the crystallization mechanism and provides the formation of the crystallization front normal to the direction of the temperature gradient. The difference in the trapping coefficients for the impurities of opposite signs and some other phenomena promote the generation of an electric field normal to the crystallization front. This field can orient dipoles, which are "frozen" in the course of crystallization. The orientation of these dipoles can also be caused by purely mechanical factors; the role of these factors was analyzed in [4].

In this paper, we report the results concerning PDMS with different content of the insulating carbon filler (from zero to 50 wt %). As an example, Figure 1 shows thermograms of polarization current densities in PDMS with 5 wt % of insulating carbon. The experiment was performed at the rate of temperature variation $\beta$ equal to 3 K/min under the constant temperature gradient $\Delta T = 10^4$ K/m. Two peaks in the $j = j(T)$ curves indicate the two-stage character of the crystallization

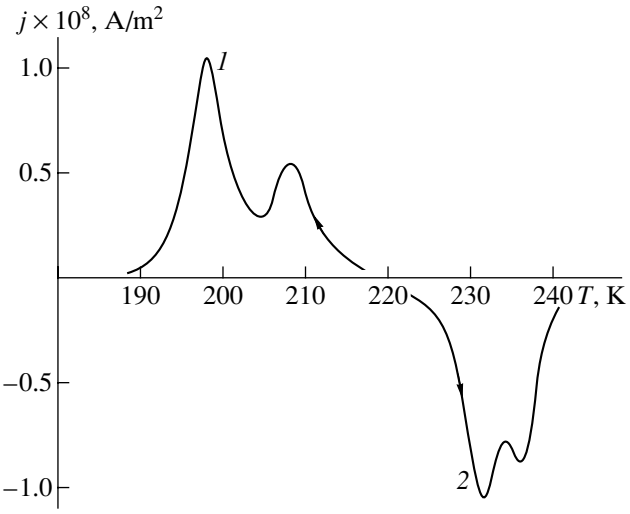


**Fig. 1.** Thermograms of polarization current densities during (*1*) crystallization and (*2*) melting of PDMS + 5 wt % of insulating carbon.

1063-7745/00/4502-0336$20.00 © 2000 MAIK "Nauka/Interperiodica"

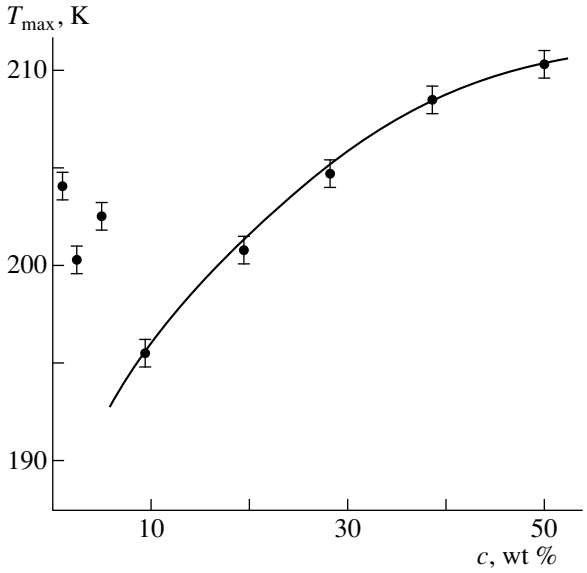


**Fig. 2.** Position of the peak in $j(T)$ thermograms corresponding to PDMA crystallization versus concentration of insulating carbon.

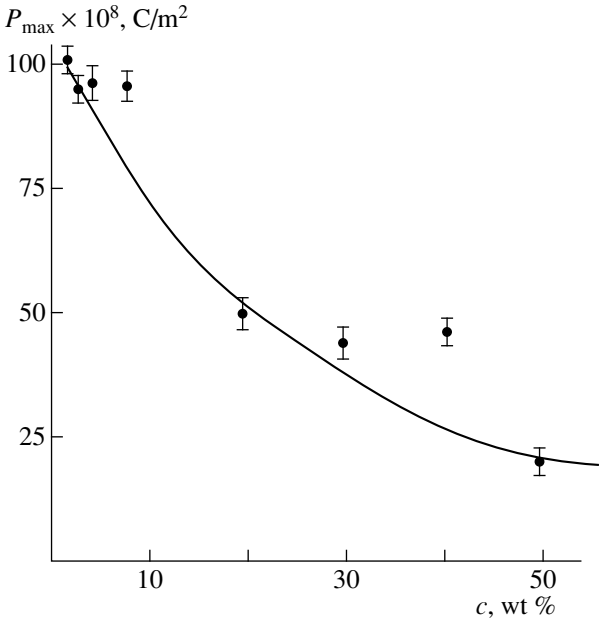


**Fig. 3.** Maximum value of polarization during PDMS crystallization versus concentration of insulating carbon.

and the melting processes. With the variation of filler content, the temperature value corresponding to the main crystallization peak (Fig. 1, curve *1*) changes, and at concentrations exceeding 10 wt %, the position of this peak steadily shifts toward higher temperatures with the growth of the filler content (Fig. 2).

The experiment was performed at the constant rate temperature variation, $\beta$ = const; thus, polarization $P$ can be defined as

$$P(T) = \frac{1}{\beta}\int_{T_0}^{T} j(T')dT'. \quad (1)$$

Using the numerical integration of the $j = j(T)$ functions, we determined the values of the maximum polarization $P_{max}$ corresponding to the crystallization of the composite materials under study (Fig. 3). It was observed that $P_{max}$ steadily decreased with an increase of the filler content.

With due account taken for the linear temperature variation $T = T_0 + \beta t$, the temperature coefficient of polarization,

$$\gamma = \frac{\partial P}{\partial T}, \quad (2)$$

can be determined using the relationship

$$\gamma = \frac{\partial P}{\beta \partial t}. \quad (3)$$

Relationship (3) implies that the maximum current density at $\beta$ = const corresponds to the maximum value $\gamma_{max}$ of the temperature coefficient of polarization. The experimental data demonstrate that the temperature coefficient of polarization slightly decreases with the growth of the filler content (Fig. 4, curve *1*). A decrease in $\gamma_{max}$ is an indication of the deterioration of the polarization characteristics of PDMS filled with insulating carbon. Such deterioration occurs despite the fact that the growth of the filler content causes the decrease in the half-period of crystallization $\tau_{0.5}$, i.e., despite the enhancement of the crystallization rate (Fig. 4, curve *2*) [5]. This can also be true for the formation of spatial

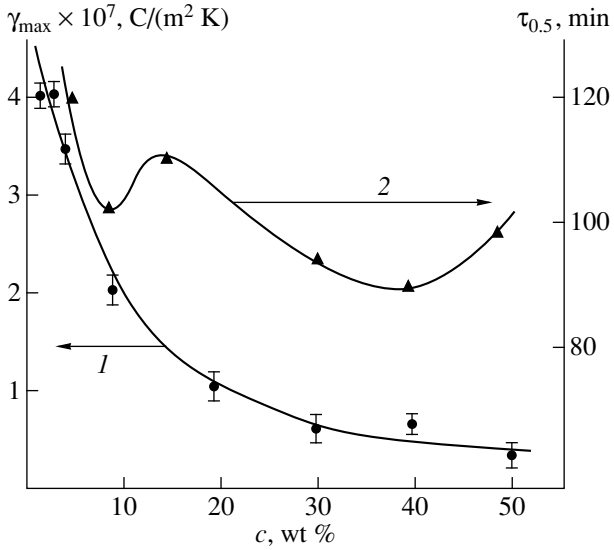


**Fig. 4.** (*1*) $\gamma_{max}$ and (*2*) $\tau_{0.5}$ during PDMS crystallization versus concentration of insulating carbon.

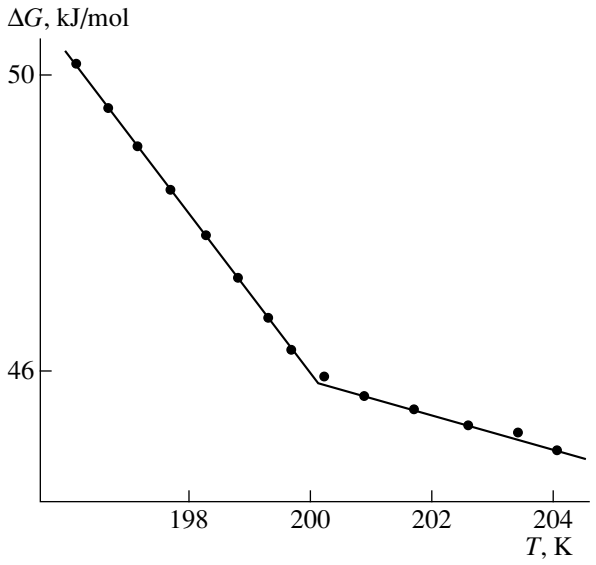


**Fig. 5.** Temperature dependence of $\Delta G$ during crystallization of PDMS with 5 wt % of insulating carbon filler.

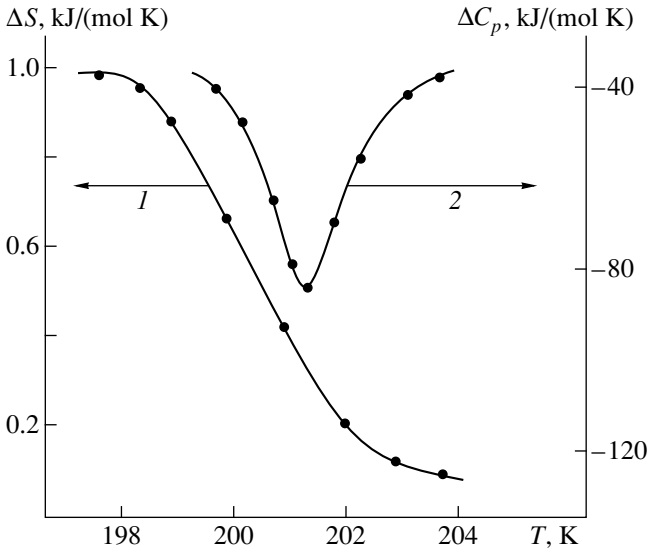


**Fig. 6.** Temperature dependence of (*1*) $\Delta S$ and (*2*) $\Delta C_p$ during crystallization of PDMS with 5 wt % of insulating carbon filler.

network accompanying the filling of PDMS with insulating carbon. The density of this network increases with the filler concentration [6]. This increase of density inhibits the process of conformation-induced polarization in the direction specified by the temperature gradient.

In our opinion, the observed behavior of the polarization current is determined mainly by the phase transformations taking place in the polymer during the melt-crystal transition [7]. Let us prove this statement by calculating the thermodynamic functions in the crystallization range of the material under study.

If the polarization current are measured under the isobaric conditions, one can use the Eyring equation

$$\tau = h/kT\exp(\Delta G/RT), \quad (4)$$

where $\Delta G$ is the variation in the Gibbs free energy in the process under study, $h$, $k$, and $R$ are the Planck, Boltzmann, and universal gas constants, respectively. Using this equation, we can determine the temperature dependence of the following thermodynamic functions:

$$\Delta G(T) = RT(\ln(k/h) + \ln(\tau T)), \quad (5)$$

$$\Delta H(T) = -RT(1 + T\partial\ln\tau/\partial T) - T\Delta S, \quad (6)$$

$$\Delta S(T) = (\Delta H - \Delta G)/T, \quad (7)$$

$$\Delta C_p(T) = T\partial\Delta S/\partial T. \quad (8)$$

Thus, the equations determining the temperature dependence of enthalpy $\Delta H(T)$, entropy $\Delta S(T)$, and specific heat $\Delta C_p(T)$ provide the necessary information on the thermal processes. Note that $\tau$ in (4) is the characteristic time of the polarization changes related to the polarization currents at a given temperature. The plots of thermodynamic functions versus temperature for PDMS filled with insulating carbon in the crystallization range of PDMS are presented in Figs. 5 and 6.

The analysis of the thermodynamic functions of the activation-type demonstrates that the melt-crystal transformations discussed here should be related to the first-order phase transitions [8].

## CONCLUSIONS

The results presented in this paper lead to the following conclusions:

An increase in the concentration of insulating carbon within the PDMS bulk from zero to 50 wt % increases the crystallization temperature from 190 to 210 K.

An increase in the concentration of insulating carbon is accompanied by the deterioration of the polarization characteristics: the temperature coefficient of polarization decreases from $4 \times 10^{-7}$ (0 wt %) to $0.7 \times 10^{-7}$ C/(m$^2$ K) (50 wt %), the polarization (accompanying crystallization) decreases from $12 \times 10^{-7}$ (0 wt %) to $2 \times 10^{-7}$ C/m$^2$ (50 wt %).

The temperature behavior of the activation-type thermodynamic functions demonstrates that the observed polarization currents are related to the first order phase transitions (of the melt-crystal type) occurring within the specified temperature range.

## REFERENCES


1. M. V. Sobolevskiĭ, O. A. Muzovskaya, and G. S. Popeleva, *Properties and Applications of Organosilicon Materials* [in Russian] (Moscow, Khimiya, 1975).
2. N. N. Matveev, Candidate's Dissertation in Mathematical Physics (Voronezh, 1987).
3. A. F. Klinskikh and N. N. Matveev, Polym. Sci. B **37**, 56 (1995).
4. N. N. Matveev and A. S. Sidorkin, Fiz. Tverd. Tela (St. Petersburg) **36**, 2440 (1994).
5. *Physical Properties of Elastomers* [in Russian], Ed. by A. I. Mareĭ (Moscow, Khimiya, 1975).
6. L. Sperling, *Interpenetrating Polymer Networks and Related Materials* (New York, Plenum, 1981; Moscow, Mir, 1984).
7. N. N. Matveev and A. S. Sidorkin, Fiz. Tverd. Tela (St. Petersburg) **36**, 2791 (1994).
8. G. M. Bartenev and A. A. Remizova, Zh. Fiz. Khim. **31**, 2534 (1957).


*Translated by K. I. Kugel*

*Crystallography Reports, Vol. 45, No. 2, 2000, pp. 340–342. Translated from Kristallografiya, Vol. 45, No. 2, 2000, pp. 375–377.*


**CRYSTALLOGRAPHIC SOFTWARE**

# A Windows Application: Program for Qualitative Phase Analysis of Polycrystalline Mixtures

**E. M. Burova and B. M. Shchedrin**

*Moscow State University, Vorob'evy gory, Moscow, 119899 Russia*

Received November 10, 1997

**Abstract**—The use of modern methods of programming (the Delphi system) for the further development or adaptation of the programs designed earlier and providing their functioning as 32-bit applications controlled by the operation system Windows-95 has been considered. New possibilities of the user dialog with a computer are described on an example of the developed FAZAN–Windows program for the phase analysis of polycrystalline mixtures. *© 2000 MAIK "Nauka/Interperiodica".*

At present, one of the main methods for designing modern programs for processing the data of the qualitative phase analysis is the visual programming [1]. The previous DOS-version of our program was written in Pascal [2]. The program described below is written in Pascal-based 32-bit Delphi-2 [3]. The program is designed as a Windows application, with a mouse being used in a conventional way. The numerical values of the rejection parameters are changed by two spin buttons increasing or decreasing the standard rejection value. A click with the simultaneous change of the color is used for marking individual elements of the data lists (such as the list of chemical elements and radicals forbidden to be used in the mixture; the list of sample lines to be interpreted by the user; or the list of the phases known to be present in the mixture). The elements of these lists can be treated by the group operations. Thus, if one singles out low-probable phases in the Table of results obtained, these phases can be excluded from the further analysis with the aid of the "Reject" button. Using a mouse, one can change the order of the rows in the Table of results. Thus, a more attractive phase can be transferred to the first position in the list, the low-probable phase can be transferred to the end of the list; it is also possible to place a series of standards (reference spectra) into the same row for their more convenient comparison. For better visual comparison, the Table of results indicates not only the numerical characteristics, but also yields the graphical information in the form of X-ray line diagrams or spectra. When developing the program for the qualitative phase analysis as a Windows application, we envisaged the performance of a number of special operations such as: (1) the input of the spectra and their preliminary processing; (2) selection of the most probable phases in the mixture using a flexible system of spectrum characteristics (including the chemical information); (3) selection of the most probable phases from the complete data set (spectra) computation of the criteria of the corresponding phase spectrum to the standard spectrum; (4) the arrangement of the list of selected phases against any of the computed criterion selected by the user; (5) the possible manual arrangement of selected phases by placing the selected phases to the beginning of the list; (6) indication of the standards which *a priori* are absent in the specimen and their subsequent rejection; (7) modeling of the spectrum of a multiphase sample using the standard spectra indicated by the user; (8) the analysis of the modeling results by statistical methods, including the estimation of individual components of the polycrystalline mixture and its checking against the Fisher criterion; (9) output of the information on the phases with similar line positions in the spectra; (10) output of the information on the phases with large correlation coefficients; (11) output of the information about the reference data base; (12) output of the lists of chemically similar standards; (13) correction, introduction, and storage of new initial data and the phase composition determined; and, finally, (14) elements of self-education. The main window of the program is shown in Fig. 1. The "Spectrum processing" button opens the window of the experimental datafile. The preliminary dialogue processing generates the diffraction line diagram (a set of diffraction maxima with their intensities). Traditionally [4], the line positions are input in terms of the reciprocal spacings (in the values of $H = 1000/d$)), the intensities are input in relative units within a scale of 100 values. The diffraction line diagram can be stored for its further processing. If the spectral data on a magnetic carrier are absent (i.e., if there is only a list of the line positions and intensities), the button "New line diffraction pattern" is used. The dialogue window "Rejection parameters and line information" is shown in Fig. 2. This window includes of three main elements: rejection parameters, forbidden chemical elements, and table of intensities and line positions. When the user fills this table, the program checks whether the data introduced are reasonable enough and arrange them in the table. Upon setting the rejection parameters and establishing the list of forbid-

1063-7745/00/4502-0340$20.00 © 2000 MAIK "Nauka/Interperiodica"

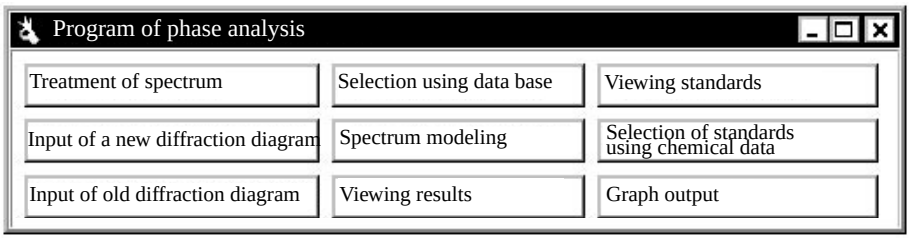


**Fig. 1.** Main window of the FAZAN–Windows system for the phase analysis.

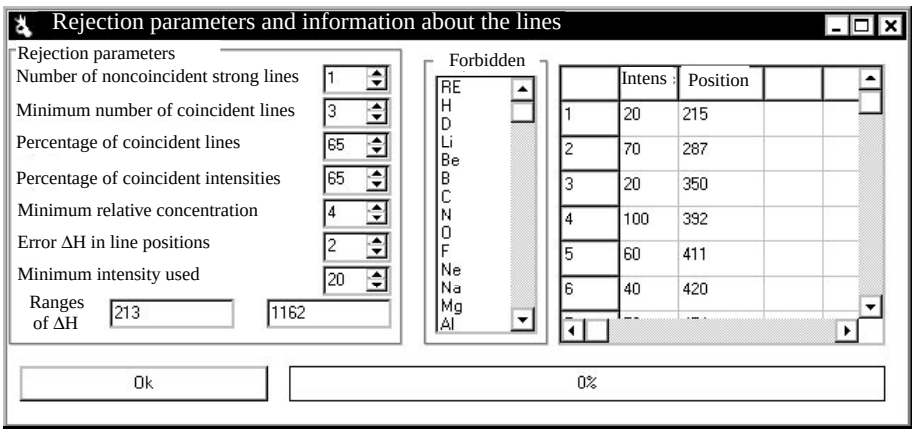


**Fig. 2.** One of the dialogue windows of the FAZAN–Windows system providing setting of the rejection parameters and information about the lines on diffraction diagram including the list of forbidden chemical elements and radicals and introduction of the spectral data.

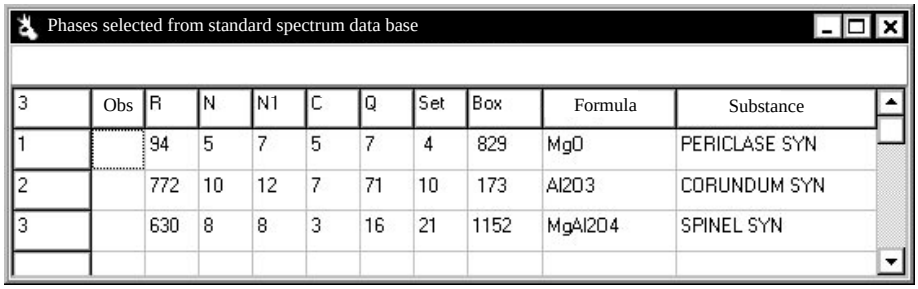


| 3 | Obs | R | N | N1 | C | Q | Set | Box | Formula | Substance |
|---|---|---|---|---|---|---|---|---|---|---|
| 1 | | 94 | 5 | 7 | 5 | 7 | 4 | 829 | MgO | PERICLASE SYN |
| 2 | | 772 | 10 | 12 | 7 | 71 | 10 | 173 | Al2O3 | CORUNDUM SYN |
| 3 | | 630 | 8 | 8 | 3 | 16 | 21 | 1152 | MgAl2O4 | SPINEL SYN |

**Fig. 3.** Window “Phases selected from standard spectrum data base” providing viewing of the list of selected phases and criteria of their correspondence to the total spectrum. The user can introduce the determined values into the column of the expert estimates.

den elements, the user closes the window of the set parameters pushing the “OK” button. Now, pushing the button “Selection from reference data base” one can display in the main window the list of the phases determined by the computer in the window “Results of phase selection from standard base” (Fig. 3). The user can rearrange the list automatically (by checking it against any of the computed criteria [5]) or manually (by placing the most favorable phases at the beginning of the list).

The composition refinement [6] is started by pushing the button “Spectrum modeling”. This stage also includes the refinement of the model by analyzing the validity of each individual phase for the interpretation of the spectrum as a whole against the Fisher criterion [7].

The composition determined is also shown in the graphical form for the sample and its model constructed on the basis of the selected phases and can be displayed on the screen by pushing the button “Graphic output”. Upon the selection of the phases, the results can be revised, edited, and output using the button “Viewing of results”.

The computer system for phase analysis is designed not only for the direct solution of the main problem of the phase analysis—the selection of a group of phases

whose superimposed spectrum fits best the experimental data—but also for providing the reference information (i.e., the known standard phases) from the data base. The button "Viewing of standards" provides the output of the spectral data for one-phase substances. The button "Selection using chemical data" provides the display of the lists of phases either including or not including certain chemical elements or their combinations.

## REFERENCES

1. N. J. Rubeking, *Delphi Programming for Dummies* (IDG Books Worldwide, Foster City, Ca.; Dialektika, Kiev, 1996).
2. E. M. Burova and B. M. Shchedrin, Kristallografiya **22**, 1182 (1977) [Sov. Phys.–Crystallogr. **22**, 672 (1977)].
3. Ch. Kalvert, *Delphi 2 Unleashed* (SAMS, Indiannopolis, In., 1996; Dia Soft, Kiev, 1996).
4. G. G. Johnson and V. Vand, Ind. Eng. Chem. **59**, 18 (1967).
5. E. M. Burova and B. M. Shchedrin, Zavod. Lab., No. 6, 38 (1993).
6. E. M. Burova and B. M. Shchedrin, *Library of Programs for Studying Structure and Composition of Compounds* (Izd. MGU, Moscow, 1989), p. 35.
7. J. B. Peacock and N. A. Hastings, *Statistical Distributions: A Handbook for Students and Practicioners* (Butterworth, London, 1975; Statistika, Moscow, 1980).

*Translated by L.Man*

*Crystallography Reports, Vol. 45, No. 2, 2000, pp. 343–344. Translated from Kristallografiya, Vol. 45, No. 2, 2000, pp. 379–380.*


**JUBILEES**

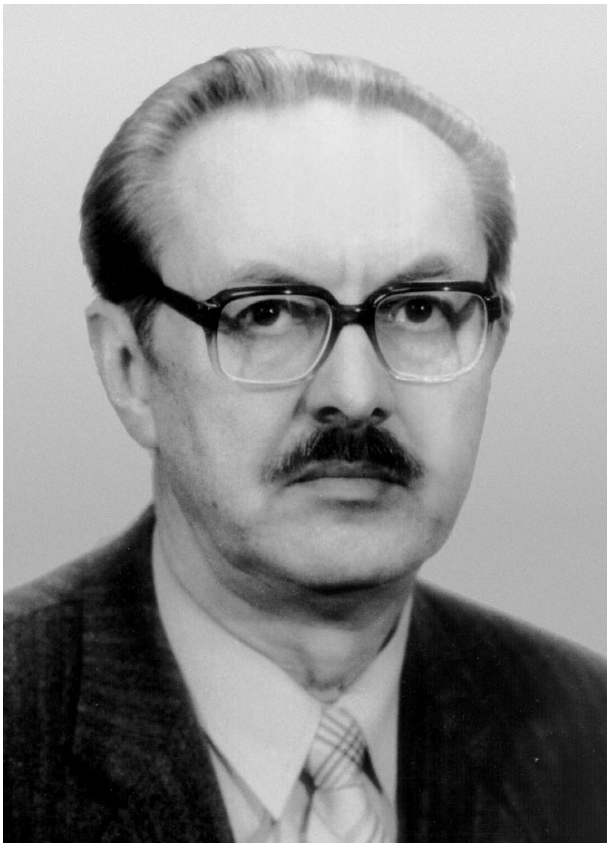

# Valentin Ivanovich Simonov (On the Occasion of His Seventieth Birthday)

Valentin Ivanovich Simonov was born on March 8, 1930 in the city of Nizhne-Chirskaya of Volgograd oblast. In 1955, he graduated from the Faculty of Physics and Mathematics of Gor'kiĭ (nowadays Niznii Novgorod) State University, where he studied at the Chair headed by the late Academician N. V. Belov. From 1955 to 1958 he was Belov's post-graduate student at the Institute of Crystallography of the USSR Academy of Sciences, Moscow, and then started to work at Belov's laboratory. In 1958, he defended his Candidate Dissertation, and in 1971, his Doctoral Dissertation in Physics and Mathematics. In 1981, he became a professor.

In 1968, the scientific group headed by Simonov was reorganized into an independent scientific unit—the Sector of Automation of Structural Studies. In 1981, the Sector had completed its program and was transformed into the Laboratory of Precision Structural Studies. After Belov's death, Simonov's laboratory and the oldest Russian laboratory of X-ray Structure Analysis organized by Belov were merged into one laboratory headed by Professor Simonov.

Simonov is a well-known expert in structural crystallography. The main direction of Simonov and his students' research is the establishment of the regular relationship between the structure and the physical properties of crystalline materials on the basis of the precision structural data. Simonov put forward and implemented the idea of the direct interpretation of the function of interatomic vectors (Patterson function) with the simultaneous analysis of the Fourier coefficients of the electron-density expansion for solving the central problem of the structure analysis—determination and refinement of structure-factor phases. The methods developed by Simonov in this field were implemented in the corresponding computer programs and are widely used in the practice of structure investigations. Simonov also suggested, developed, and formalized the methods for

1063-7745/00/4502-0343$20.00 © 2000 MAIK "Nauka/Interperiodica"

determining various deviations from the symmetry of the atomic structures of crystals from the diffraction data. Thus, the precision studies provided the establishment of the mechanism of ionic transport at the atomic level and the character of atomic rearrangements during phase transitions in superionics. These data allowed one to synthesize a new type of crystal with high conductivity with respect to lithium, the most important element for autonomic power sources.

The neutron-diffraction studies of nonstoichiometric fluorides performed by Simonov and his coworkers provided important modifications of the classical structural models of fluorites. A new approach to the atomic structure of these materials resulted in the development of new methods for controling cluster structures of fluorites and modification, on this base, of such physical factors and properties as the melting point, hardness, refractive indices, ionic conductivity, etc. In the row of $BaF_2$–$Ba_{0.69}La_{0.31}F_{2.31}$ solid solutions, the conductivity with respect to fluoride ions can purposefully be varied within six orders of magnitude.

Simonov and his group actively and successfully studied atomic structures of single crystals of high-temperature superconductors. They established that the temperature of transition into the superconducting state in lanthanum-containing phases depends not only on the amount of strontium, but also on the character of its distribution over the lanthanum positions. It was shown that the crystals of yttrium-containing phases with different oxygen concentrations have three characteristic local regions with different ordered arrangement of oxygen atoms. It has also been established that the so-called superconducting tetragonal Y-123-type phases are, in fact, microtwins with a deficit of copper or with a partial substitution of copper by other chemical elements. Usually, twin components are orthorhombic. It was also established that some structural parameters in the vicinity of the transition to the superconducting state in single crystals of the T1-2212 and Y-124 phases behave anomalously. It was shown that atomic thermal vibrations in the vicinity of the second-order phase transition can provide valuable information on the rearrangement in the electronic structure of the crystal during such transition.

The experimental determination of the absolute configurations (chirality) of the atomic structures of crystalline materials and the deviations of the atomic thermal vibrations from the harmonic law are of great importance for understanding the fact that the physical properties of optically active crystals and crystals with nonlinear characteristics are conditioned by their structural characteristics. The determination of the anharmonic components of the atomic thermal motion in crystals provided qualitatively new information on the mechanisms of second-order phase transitions. The knowledge of the parameters of anharmonic atomic thermal vibrations allows one to predict the character of possible phase transitions in crystals at temperatures tens of degrees above the temperatures of these transitions. Such structural studies proved to be very effective for ferroelectric materials.

Another important aspect of Simonov's scientific biography is his interest in the structural studies of biologically active compounds such as cyclic peptides (enniatin B, sporidesmolide, valinomycin, etc.) and steroid hormones and their synthetic analogs. Simonov and his group established molecular structures and conformational parameters determining the activity of a modified progesterone-type steroid hormone with the gestagenic and contraceptive functions.

Simonov's students work not only in Moscow and Moscow oblast, but also in Vladivostok, Ulan-Ude, Krasnoyarsk, Nizhniĭ Novgorod, Saransk, and also in Poland, China and South Korea. They actively use crystallographic methods in solving various problems of solid-state physics, chemistry, mineralogy, and materials science. Simonov supervised twenty-one Candidate and two Doctoral dissertations.

Simonov is a member of the Scientific Council on Condensed Matter of the Russian Academy of Sciences, and is also the Vice-Chairman of the National Committee of Russian Crystallographers. Simonov was a member of the Executive Committee of the International Union of Crystallography (1978–1984) and a Vice-President of this organization (1984–1987).

Simonov is a member of the Editorial Boards of two scientific journals *Kristallografiya* (Crystallography Reports) and *Zeitschrift für Kristallographie*. For twelve years he was a co-editor of *Acta Crystallographica*.

Simonov's successful activity in science has been highly valued. He was awarded the title of an Honored Scientist of the Russian Federation and decorated with *Badge of Honor* and the medal *For Services to Country.* In 1992, Simonov was awarded the prestigious Fedorov prize of the Russian Academy of Sciences.

Simonov greets his 70th birthday, being full of new scientific plans and projects. His colleagues from *Kristallografiya* and the Shubnikov Institute of Crystallography of the Russian Academy of Sciences and his numerous Russian and foreign students and admirers of this scientific talent wish Valentin Ivanovich Simonov good health, prosperity, and success in his scientific work.

*Translated by L. Man*

*Crystallography Reports, Vol. 45, No. 2, 2000, pp. 345–346. Translated from Kristallografiya, Vol. 45, No. 2, 2000, pp. 381–382.*


**JUBILEES**

# Daniel Moiseevich Kheiker (On the Occasion of His Seventieth Birthday)

Daniel Moiseevich Kheiker, a leading figure in the fields of the X-ray diffraction analysis and design and construction of scientific instruments, was born on April 4, 1930 in the city of Zhitomir, Ukraine. He graduated with a silver medal from middle school in the city of Orekhovo-Zuevo, Russia and entered the Moscow Physical Engineering Institute, where he studied physics and, in parallel, performed research under the guidance of Professor G.S. Zhdanov at the Department of Solid State Physics. In those years, he published his first articles entitled *Structure of Superconductors. X-ray Diffraction Study of BiPd* and *A Simple Method for Calculating Absorption Coefficient for Strongly Absorbing Samples in X-ray Diffraction Analysis* in the *Journal of Experimental and Theoretical Physics*.

In 1953, Kheiker graduated with distinction from the Moscow Physical Engineering Institute and started working as an engineer at the All-Union Research Institute for Asbestos and Cement. There, Kheiker organized the Laboratory of Physical Methods and became its first head. The laboratory used the most advanced methods for studying various materials such as electron microscopy and infrared spectroscopy, differential thermal analysis (DTA), X-ray diffractometry, etc. Under Kheiker's guidance, a scintillation and high-resolution proportional counters and various goniometric attachments to an industrially manufactured X-ray diffractometer used in the laboratory were designed and constructed in cooperation with other institutes and organizations. These devices were then used as the basis for designing a universal X-ray diffractometer DRON produced by the Research and Production Association "Burevestnik." In 1958, Kheiker defended his Candidate dissertation entitled "Diffractometric Methods for Solving Some Basic Problems of X-ray Diffraction Analysis."

The development of X-ray diffractometric methods for precision measurements of the unit-cell parameters, determination of crystallite dimensions, phase analysis, and small-angle scattering provided the solution of numerous scientific problems from the study of various cements and products of their hydration to the kinetics of copper and lead ferrite formation and the determination of fiber diameters and wall thicknesses in chrysotile asbestos.

Since 1964, Kheiker's scientific life has been closely related to the Shubnikov Institute of Crystallography of the Russian Academy of Sciences. At this Institute, Kheiker elaborated highly sensitive precision diffractometric methods for studying single crystals of various substances, including proteins and viruses, polycrystalline materials, polymers, and liquid crystals. He has also developed original methods that could be used at both the preliminary stage of the structural

1063-7745/00/4502-0345$20.00 © 2000 MAIK "Nauka/Interperiodica"

study and at the stage of precision measurements of the integrated intensities from single crystals on four-circle and inclined diffractometers. Another interesting direction of Kheiker's studies is modeling of the shape and dimensions of the reciprocal-lattice points in the diffractometric study of single crystals. In 1972, Kheiker defended his Doctoral dissertation in physics and mathematics entitled "X-ray Diffractometry."

Kheiker made a unique contribution to designing Russian X-ray diffractometers. In cooperation with the Special Design Bureau of the Institute of Crystallography and the Research and Production Association "Burevestnik," Kheiker designed and constructed DAR-type and a RED-type automated inclined four-circle single-crystal diffractometers. The DAR- and RED-type diffractometers were manufactured in small series and installed at numerous laboratories of the former Soviet Union. From the mid-seventies, Kheiker was engaged in the design of automated X-ray diffractometers with two-dimensional position-sensitive detectors. In coordination with the Special Design Bureau of the Institute of Crystallography and the Research and Production Association "Burevestnik," Kheiker designed and scaled-up a multichannel DARK-2.0 diffractometer for protein studies. In 1980, Kheiker, together with the Special Design Bureau of the Institute of Crystallography and the colleagues from the Joint Institute of Nuclear Research in Dubna, designed a KARD diffractometer with a two-dimensional position-sensitive detector based on the proportional chamber with $256 \times 256$ pixels. For many years, this unique device has been used for studying hundreds of protein single crystals and their derivatives and viruses.

Despite the crisis in Russian science, Kheiker, in cooperation with the Laboratory of High Energies of the Joint Institute for Nuclear Research in Dubna, designed a diffractometer with a Franks focusing collimator and a two-dimensional detector with the spherical entrance window with $500 \times 500$ channels. At present, Kheiker participates in the design of two stations for a SIBIR-2 storage ring.

Professor Kheiker is the head of the Russian school of X-ray diffractometry. Many of his students successfully work in the best laboratories in Russia and abroad. Three monographs written by Kheiker have remained an indispensable tool for all the experimenters working in the X-ray diffraction analysis. He is the author of more than 200 publications. Professor Kheiker is highly respected both at home and abroad. For many years, he was a member of the Commission on Crystallographic Apparatus and Commission on Synchrotron Radiation of the International Union of Crystallography. At present, Professor Kheiker is a member of the National Committee of Russian Crystallographers and of the Council of Technical Equipment of the Presidium of the Russian Academy of Sciences. Professor Kheiker is decorated with the medals *For Valiant Labor* and *Veteran of Labor* and also with six Medals of the All-Union Exhibition of Advances in the National Economy. He was also awarded a title of Honorary Scientist of the Russian Federation.

The Editorial Board of *Kristallografiya* (Crystallography Reports), all Kheiker's colleagues and students congratulate Daniel Moiseevich Kheiker on his seventieth birthday and wish him good health and new achievements in the development of fundamental and applied crystallography.

*Translated by L. Man*

*Crystallography Reports, Vol. 45, No. 2, 2000, pp. 347–348. Translated from Kristallografiya, Vol. 45, No. 2, 2000, pp. 383–384.*


**OBITUARY**

# Galina Nikolaevna Tishchenko (1926–1999)

When a brilliant and eminent person and a prominent scientist who is a kind, well-liked, and beautiful woman, passes away, one can feel nothing but a sense of loss and injustice.

Galina Nikolaevna Tishchenko, a leading researcher of the Institute of Crystallography of the Russian Academy of Sciences, died suddenly on October 12, 1999. She was one of the first students of Academician Boris Konstantinovich Vaĭnshteĭn, who made a considerable contribution to the organization of the Laboratory of Biocrystal Structures of the Institute of Crystallography. At this laboratory, she herself worked fruitfully for many years. Tishchenko was engaged in the X-ray structure analysis of biologically active compounds.

Her scientific career was successful right from the start. In 1950, Tishchenko graduated with distinction from the Department of Chemistry of Moscow State University and began working as a post-graduate student at the same department. In 1954, she brilliantly defended her candidate dissertation in chemistry. In those years, her research was predominantly focused on the structures of coordination compounds by the methods of X-ray and electron diffraction analyses. She approached scientific problems creatively and was the first to apply the rotation method to collect three-dimensional data sets by the electron diffraction method.

In December 1959, Tishchenko entered the Institute of Crystallography of the USSR Academy of Sciences. With her characteristic energy, Tishchenko devoted herself to the study of biologically active compounds and proteins by the methods of X-ray structure analysis. The Institute of Crystallography had become her second home, where she lived for the rest of her life. Tishchenko started to work as a young researcher and had become a leading. In 1985, she defended her doctorate dissertation in chemistry. In February 1993, Tishchenko became a full Professor.

Tishchenko made a valuable contribution to the X-ray structure studies of physiologically active compounds, such as psychotropic and anticancer drugs and drugs used in the treatment of alcoholism, the antibiotics of the enniatin, valinomycin, and gramicidin series, prostaglandins, and gossypol. The characteristic established during the studies of the structure and the activity of the various objects can be used for developing recommendations for the design of new drugs. Tishchenko and her co-workers studied the structures of the

1063-7745/00/4502-0347$20.00 © 2000 MAIK “Nauka/Interperiodica”

enzyme ribonuclease C2 and its complexes and also that of histidine decarboxylase from *Micrococcus sp. n.*

All who worked with Tishchenko were infected with her energy and enthusiasm. She was highly respected because of her great knowledge and erudition. The scope of her scientific interests went beyond particular objects and was constantly broadened. In every field of research, Tishchenko always managed to achieve impressive progress. Apparently, the chief trait of her character was to find the essence of the phenomenon and the energy to complete the study. Her native talents and great erudition always brought a successful results. Thus, Tishchenko managed to obtain new important results in studies of the deformation electron density distributions in perfect crystals of amino acids and enzyme inhibitors and substrates. In 1989–1990, Tishchenko together with V.I. Andrianov studied a complicated crystal structure of the complex of a membrane-active antibiotic—the cyclodecapeptide gramicidin S with urea and discovered the gramicidin channels. Tishchenko and her coworkers were awarded a medal of the Exhibition of the Achievements in the People's Economy of the USSR and a prize of the Mendeleev All-Union Chemical Society for their studies of the structures of ionophoric antibiotics and their analogs and the mechanisms of their biological action. She was also a winner of several scientific competitions at the Institute of Crystallography of the Russian Academy of Sciences. Tishchenko published more than 190 scientific articles in Russian and foreign journals.

Tishchenko never limited herself to scientific research alone and always took an active part in the public activities at the Institute of Crystallography. She was a member of the Comission on Small Molecules of the International Union of Crystallography and a member of the Special Academic Council on Defence of Dissertations at the Institute of Crystallography. Tishchenko devoted much energy to preparing scientific staff for X-ray diffraction analysis in Uzbekistan. She was a good teacher and encouraged many students and young scientists, who now continue and develop further the investigations started by her. Six young scientists defended their candidate dissertations under her supervision and one of them defended his doctoral dissertation.

Tishchenko took an active part in the establishment of scientific relations and consolidation of the international crystallographic community. She succeeded in coordinating the efforts of scientists from various research institutions in Russia and abroad. She knew many outstanding scientists in person, among them Dorothy Hodgkin, with whom she extensively and fruitfully discussed the structure of gramicidin; Dr. E. Dodson and Professors M.M. Woolfson and G. Dodson from the University of York; Professor D. Phillips from Oxford University; and many other prominent scientists. Tishchenko participated in numerous international crystallographic meetings. Her studies received due recognition of the international scientific community.

All those who knew Galina Nikolaevna Tishchenko and were fortunate to communicate and to work with her remember her generosity, benevolence, professional knowledge, and devotion to science. She was an incredibly charming, responsive, and amicable person always cheerful and enthusiastic. Tishchenko was a very beautiful, delicate, and compassionate woman and a good mother who brought up two sons. One should always remember her bright scientific presentations, participation in scientific discussions, the oratorical gift, and the ability to penetrate the crux of the matter. Tishchenko was always ready to give a helping hand in one's hour of need. That is how we shall always remember her.

*Translated by T. Safonova*